

STUDIES ON THE HOT CORROSION BEHAVIOUR OF HVOF COATINGS ON SOME Ni-AND Fe-BASED SUPERALLOYS

A THESIS

*Submitted in partial fulfilment of the
requirements for the award of the degree
of*

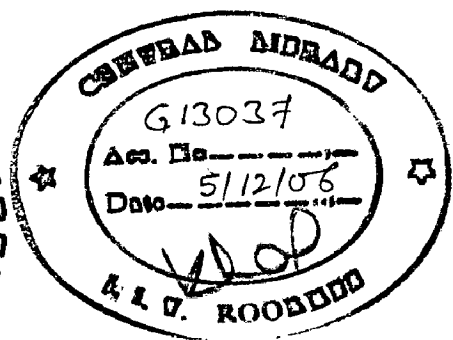
DOCTOR OF PHILOSOPHY

in

METALLURGICAL AND MATERIALS ENGINEERING

By

TEJINDER SINGH



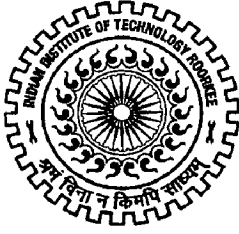
**DEPARTMENT OF METALLURGICAL AND MATERIALS ENGINEERING
INDIAN INSTITUTE OF TECHNOLOGY ROORKEE
ROORKEE-247 667 (INDIA)**

MAY, 2006

© INDIAN INSTITUTE OF TECHNOLOGY, ROORKEE, 2006
ALL RIGHTS RESERVED

6th Annual Convocation- 2006
Degree conferred on 11.11.2006


Supdt. (PGS&R)



CANDIDATE'S DECLARATION


I hereby certify that the work which is being presented in the thesis entitled "STUDIES ON THE HOT CORROSION BEHAVIOUR OF HVOF COATINGS ON SOME Ni- AND Fe-BASED SUPERALLOYS" in partial fulfilment of the requirements for the award of the Degree of Doctor of Philosophy and submitted in the Department of Metallurgical and Materials Engineering of the Institute is an authentic record of my own work carried out during a period from January, 2004 to May, 2006 under the supervision of **Dr. Satya Prakash** and **Dr. R.D. Agrawal**.

The matter presented in this thesis has not been submitted by me for the award of any other degree of this or any other University/Institute.


(TEJINDER SINGH) 08.05.06

Signature of the Candidate

This is to certify that the above statement made by the candidate is correct to the best of our knowledge.



Date: 03.05.06 (Dr. R.D. AGRAWAL)
Professor

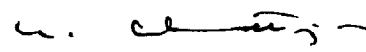

(Dr. SATYA PRAKASH)
Professor

Department of Metallurgical and Materials Engineering
Indian Institute of Technology Roorkee
Roorkee – 247 667, India

The Ph.D. Viva-Voice examination of Tejinder Singh,
been held on 08.09.2006.

Research Scholar, has


Signature of Supervisor(s)


Signature of External Examiner

ABSTRACT

Hot corrosion degradation of metals and alloys has been identified as a serious problem for many high temperature aggressive environment applications such as boilers, internal combustion engines, gas turbines, fluidized bed combustion and industrial waste incinerators. Hot corrosion has become a topic of continuous investigations and great concern as it consumes the material at an unpredictably rapid rate. Consequently, the load-carrying ability of the components reduces quickly, leading eventually to their catastrophic failure. The inability to either totally prevent the hot corrosion or at least detect it at an early stage has resulted in several accidents, leading to loss of life and/or destruction of engines/infrastructures.

Super-heater and re-heater components of boilers used in steam-generating systems are subjected to fireside corrosion due to condensation/accumulation of low melting-point salts on tube surface such as alkali-iron trisulphates compounds in the coal fired boilers or compounds of vanadium, sodium and sulphur, mainly as $\text{Na}_2\text{SO}_4\text{-V}_2\text{O}_5$ complex and sodium-vanadates mixtures in the case of oil fired boilers. Some combinations of these compounds have low melting points 550°C . These compounds easily liquefy at the operating temperatures of boilers and cause accelerated corrosion (hot corrosion). The hot corrosion problem of the boilers has become more alarming as the increasing demand for electricity is forcing the power plants to increase steam temperature and pressure of the boilers. Increased steam parameters in turn lead to accelerated corrosion of boiler components.

Currently, the superalloys are used to increase the service life of the boilers especially in the super-heater zones of the new generation ultra-supercritical boilers. However, the presence of combustion gases constitutes an extreme environment and the hot corrosion is inevitable when the superalloys are used at high-temperatures for longer periods of time. A number of countermeasures are presently in use or under investigation to combat the hot corrosion such as, the use of inhibitors, control of the process parameters, development of suitable industrial alloys, and deposition of protective coatings. However, the use of protective coatings is most practical, reliable, and economically viable method to control or prevent the hot corrosion problems of the super-heater and re-heater tubes of the boilers.

Among the various techniques used for deposition of coatings, the high velocity oxy-fuel (HVOF) process has been widely adopted by many industries due to its flexibility, cost effectiveness and the superior quality of the coatings produced. The HVOF has the advantage of being a continuous and most convenient process for applying the coating to industrial installations at site. Hitherto the hot corrosion behaviour of the HVOF coatings is not much reported.

The present research programme aims to comparatively evaluate the hot corrosion behaviour of four HVOF sprayed coatings on five types of Ni- and Fe based superalloys, with the objectives to protect the boiler super-heaters and re-heaters for use at temperatures significantly above that used in the existing steam-generating systems. Five superalloys were selected for the present investigation, as at higher temperatures coatings on various superalloys behave differently. Differences in chemical compositions between a coating and a substrate alloy can lead to inter-diffusion between these materials which can modify the oxidation and hot corrosion resistance of the coating and also the mechanical properties of the coating-substrate system.

Four types of commercially available feedstock materials: $\text{Cr}_3\text{C}_2\text{-NiCr}$, NiCrBSi and Stellite-6 in the powder form and Ni-20Cr in the wire form were used for spraying coatings on five superalloys using HVOF process. These superalloys, namely Superni 75, Superni 600, Superni 601 and Superni 718 as Ni-based, and Fe-based Superfer 800H, were provided by Mishra Dhatu Nigam Limited, Hyderabad (India), for devising some means to protect them against high temperature corrosive environment applications. As-sprayed coatings were characterized by using the combined techniques of optical microscopy, microhardness testing, X-ray diffractometry (XRD), scanning electron microscopy/energy-dispersive analysis (SEM/EDAX) and electron probe micro analyzer (EPMA).

The coatings have dense and nearly uniform lamellar structure consisting of flat splats with average porosity less than 2% and surface roughness in the range of 4-6 μm . The XRD analysis of the as-sprayed $\text{Cr}_3\text{C}_2\text{-NiCr}$, NiCrBSi, and Ni-20Cr coatings revealed the formation of Ni-based fcc structure as the principal phase, whereas Stellite-6 coating revealed Co-based fcc structure as the principal phase. The EDAX analysis has confirmed that HVOF coatings obtained in the present investigation meet the required compositions.

The coatings have higher hardness values than the substrates. The $\text{Cr}_3\text{C}_2\text{-NiCr}$ coating showed maximum values of hardness 950 Hv in the range of 870-950 Hv, followed by Stellite-6 and NiCrBSi coatings, whereas the Ni-20Cr wire coating exhibited the least hardness 600 Hv in the range of 600-630 Hv. The hardness of the substrates has

increased near the coating-substrate interface for all the coating-substrate combinations partly due to high impact of the sprayed droplets and partly due to sand blasting of the specimens prior to HVOF coatings. The inter-diffusion of various elements occurred to some extent across the interface between the substrates and the HVOF coatings.

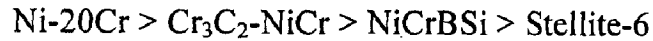
The hot corrosion behaviour of the bare and HVOF coated superalloys was studied in the laboratory tube furnace in molten salt ($\text{Na}_2\text{SO}_4\text{-60\%V}_2\text{O}_5$) environment at 900 °C for 50 cycles. Each cycle consisted of 1 hour heating at 900 °C followed by 20 minutes cooling in open air. A uniform layer ($3\text{-}5\text{ mg/cm}^2$) of $\text{Na}_2\text{SO}_4\text{-60\%V}_2\text{O}_5$ salt mixture was coated on the touch to warm surface of the specimens with the help of a camel hair brush. In order to establish an understanding of the behaviour of these coatings and bare superalloys in the actual working conditions, where these coatings are intended to be used, the specimens were exposed for 1000 hours to platen super-heater zone of the coal fired boiler at Guru Nanak Dev Thermal Power Plant, Bathinda, Punjab. This zone was selected for the present study as many breakdowns occurred in this power plant due to the hot corrosion degradation of the platen superheater tubes of the coal fired boilers. The samples were hanged in this zone, having temperature 900 ± 10 °C, with the help of stainless steel wires for 10 cycles, each cycle consisting of 100 hours of heating followed by 1 hour of cooling in open air. At the end of each cycle, the specimens were visually examined with respect to colour, luster, spallation tendency and adherence of the scale. Thereafter, the specimens were subjected to weight measurements. XRD and SEM/EDAX techniques were used for detecting the phases present and for elemental analysis of the surface scale after exposure to both the environments. The EPMA analysis was used for elemental mappings along cross-section of the scale.

The hot corrosion resistance of the bare superalloys, based on the overall weight gains after 50 cycles in the molten salt environment, has been found to be in the following order:

Superni 75 > Superni 600 > Superni 601 > Superfer 800H

The nickel-based superalloys have shown better hot corrosion resistance than the iron-based superalloy, except Superni 718. Superni 718 suffered accelerated hot corrosion in the given molten salt environment and its weight gain could not be measured after 16th cycle due to severe spalling and sputtering of the scale. Molybdenum present in Superni 718 forms MoO_3 which reacts with molten salt to form low melting-point Na_2MoO_4 that causes severe hot corrosion of Superni 718 by acidic fluxing.

All the coatings have imparted resistance to hot corrosion in the molten salt environment for all the substrate superalloys. The Ni-20Cr coating has shown highest hot corrosion resistance, whereas Stellite-6 coating indicated least resistance at 900 °C under cyclic conditions. The overall protective behaviour of the coatings in this environment on different superalloys used in the present study, except on Superni 718, has been found in the following sequence:



All the coated superalloys follow nearly parabolic behaviour for all 50 cycles of the study and their parabolic rate constants are found to be significantly less than that for the bare alloys. The coatings show good adherence to their respective substrates during exposure to the molten salt environment. In some cases the coated superalloys show slight deviations from the parabolic rate law due to minor spallation of the scale, or superficial spallation from outer layer of the coatings or from edges of the specimens.

All the coated alloys have shown higher rate of oxidation during earlier cycles of exposure and thereafter oxidation rate decreases and finally stabilises. Initially the oxygen permeates inward along the splat boundaries and pores and causes rapid oxidation. Subsequently, these oxides plug/seal all possible diffusion paths of the coatings and, therefore, block or slow down the penetration of oxygen. The oxidation is then confined mainly to the surface of the coatings, thereby making the oxidation rate to reach a steady state.

In the molten salt environment, the substrate superalloys have affected to some extent the performance of different coatings due to outward diffusion of the substrate elements at higher temperature. The performance of the coatings on different substrates follows the following sequences:

Cr₃C₂-NiCr coating : Superni 75>Superni 718>Superni 601>Superni 600>Superfer 800H

NiCrBSi coating : Superni 75>Superni 600>Superfer 800H>Superni 601>Superni 718

Stellite-6 coating : Superni 75>Superni 601>Superni 718>Superni 600>Superfer 800H

Ni-20Cr coating : Superfer 800H>Superni 718>Superni 601>Superni 600>Superni 75

Similar to the molten salt environment, the bare nickel-based superalloys have performed better than the bare iron-based superalloy in the actual working conditions of the coal fired boiler. However, in contrast to the molten salt environment, Superni 718 performed well in the coal fired boiler environment. This may be attributed to the presence of a protective scale consisting of chromia, alumina and silica, in the boiler environment which has restricted the diffusion of molybdenum to reach the surface. The

hot corrosion resistance of the superalloys based on the material depth affected by corrosion after 1000 hours of cyclic exposure has been found in the following order:

Superni 75 > Superni 600 > Superni 718 > Superni 601 > Superfer 800H

The coated superalloys performed better than the uncoated one. The degradation of bare superalloys in the boiler environment has been attributed to the dissolution of the protective oxides due to fluxing actions of the low melting-point alkali-iron trisulphates compounds.

The coatings have successfully imparted the hot corrosion resistance to the superalloys in the boiler environment and have shown no thickness loss due to spallation during experimentations. Minor internal corrosion attack on the substrate, in some cases of coated alloys, is due to the penetration of corrosive species through pores or splat boundaries during the initial hours of exposure before the paths get sealed. The coatings have shown the following trend of hot corrosion resistance on different superalloys, except on Superni 718:

Ni-20Cr > Stellite-6 > NiCrBSi > Cr₃C₂-NiCr

In case of Superni 718 superalloy, the Cr₃C₂-NiCr coating performed better in the boiler environment than the Stellite-6 and NiCrBSi coatings. In the molten salt environment, mainly the upper part of the NiCrBSi coating gets oxidized and the rest portion of the coating remains similar to what has been noted in the as-sprayed coatings. However, the NiCrBSi coating partially oxidised up to the coating-substrate interface in the boiler environment.

The hot corrosion resistance of all the coatings under study, in both the environments, has been attributed mainly to the formation of oxides at the surface of the coatings, and at the splat boundaries. The XRD and EDAX analyses show that the scale formed on the surface of all the coated superalloys after exposure to both the environments consists of oxides of mainly chromium, silicon, and nickel; and their spinels containing nickel-chromium/cobalt-chromium type mixed oxides. EPMA analysis has confirmed these results. These oxides are reported to be protective in nature against hot corrosion due to their low growth rate, strongly bounded compositions and ability to act as effective barriers against ionic migration. Due to much lower diffusion coefficients of the cations and anions in the spinal phases than that in the parent oxide phases, the spinal phases further increase the oxidation resistance.

In addition to surface oxides, it has been established that the splat boundaries of the coatings are more active in imparting the hot corrosion resistance as compared to the rest

of the coating regions. In both the environments, the oxide scale has preferentially formed at the splat boundaries due to oxidation of active elements of the coatings. The $\text{Cr}_3\text{C}_2\text{-NiCr}$, NiCrBSi and Ni-20Cr coatings form oxides mainly of chromium and spinel of nickel and chromium at the boundaries of nickel-rich splats, whereas Stellite-6 coating forms the oxides of silicon and chromium, and spinels of cobalt-chromium and nickel-chromium at the boundaries of Co-rich splats. Both the Ni-rich and Co-rich splats remained mostly in an un-oxidised state.

Additionally, the very low porosity and the flat splat structure of the HVOF sprayed coatings have also contributed to hot corrosion resistance as this is the desired structure, when the coatings have to perform in corrosive environment at higher temperature. In the flat splat structure the distance from the coating surface to coating/substrate interface along splat boundaries, through which the corrosive species mostly permeate, is very long.

The base superalloys affect the hot corrosion behaviour of the coatings in both the environments. However, in some coating-substrate combinations, their effect is noted to be relatively more in the boiler environment as compared to that in the molten salt environment. The performance of the coatings on different substrates, in the boiler environments, follows the following sequence:

$\text{Cr}_3\text{C}_2\text{-NiCr}$ coating : Superni 718 > Superni 600 \approx Superni 75 > Superni 601

NiCrBSi coating : Superni 75 \approx Superni 600 > Superfer 800H > Superni 601 > Superni 718

Stellite-6 coating : Superni 600 > Superni 75 > Superfer 800H > Superni 601 > Superni 718

Ni-20Cr coating : Superni 75 > Superni 718 > Superni 600 > Superni 601 > Superfer 800H

The Ni-20Cr coating has given the best performance on all the substrates under study in both the environments and is, therefore, recommended as the best coating under the given conditions. The $(\text{Ni-20Cr})\text{-Superfer 800H}$ and $(\text{Ni-20Cr})\text{-Superni 75}$ combinations have the highest hot corrosion resistance in the molten salt and in the coal fired boiler environments, respectively.

Based on the findings of the present study, all the coatings under investigations are recommended for applications to super-heater and re-heater tubes of the boilers for protecting them against high temperature corrosive environment applications.

ACKNOWLEDGEMENTS

Perhaps there is not enough space or time to thank the many individuals who at some point or another helped me to complete this thesis.

I would first like to acknowledge my thesis supervisor, **Dr. Satya Prakash**, Professor and Ex-Head, Department of Metallurgical and Materials Engineering (MMED), Indian Institute of Technology (IIT), Roorkee, for his patient guidance, encouragement and untiring efforts throughout the tenure of this work. Many sincere thanks go to my co-supervisor **Dr. R.D. Agrawal**, Professor, MMED, IIT, Roorkee, for his constructive guidance and support. They have been an inspiring and driving force during the course of this work. Without their timely help, intellectual input, constructive criticism and painstaking efforts, it would not have been possible for me to complete this thesis in the present form.

I express sincere thanks to my research committee members: Professor P.S. Misra, Professor A.K. Jain, and Professor D. Puri for their time and energy in reviewing this thesis.

Deep sense of gratitude is acknowledged to Mr. C.S. Nagpal, Additional Director, Department of Technical Education, Punjab, who was kind enough to sponsor me to pursue Ph.D under MHRD Scheme of Govt. of India. The financial support rendered by MHRD, Govt. of India, is highly acknowledged.

I wish to record deep my gratitude to Dr. P.S. Misra, Professor and Head, and Dr. V.K. Tiwari, Ex-Head, MMED, IIT, Roorkee, for their co-operation and support in carrying out the experimental and analysis work in the department.

Several individuals of the technical and administrative staff of MMED, IIT, Roorkee, deserve my sincere thanks and gratitude, in particular Mr. S.K. Seth, Mr. Shamsher Singh, Mr. Rajinder Sharma, Mr. Shakti Gupta, Mr. Vidya Prakash, Mr. T.K. Sharma, Mr. V.P. Verma, Mr. M. Aslam, Mr Pritam Singh, and Mr. Sahdev.

Many thanks go to Mr. S.K. Saini, Mrs. Rekha Sharma, and Mr. T.K. Ghosh of Institute Instrumentation Centre, IIT, Roorkee for carrying out XRD, SEM and EPMA work respectively. Thanks are also due to Mr. Narendra Kumar for typesetting of thesis manuscript.

I am highly obliged to Dr. Ajay Gupta, Director IUC DAE, Indore, Dr. M. Srinivas, Scientist 'F', Defense Metallurgical Research Laboratory (DMRL), Hyderabad, and Dr. V.P. Dimri, Director, National Geophysical Research Institute (NGRI), Hyderabad, for

extending their support and facilities to perform the analysis work. Special thanks are due to Mr. S.C. Modi, Managing Director, Metallizing Equipment Company Pvt. Ltd, Jodhpur, for providing facilities to deposit the coatings with HVOF process.

I convey my sincere thanks to Dr. D.M Phase and Mr. Vinay Ahire of IUC DAE, Indore and Mr. Dr. Rabindranath Maiti of CRF IIT Khargpur for performing the EDAX analysis. Thanks are due to Mr. V.V. Rama Rao of DMRL, Hyderabad and Dr. EVSSK. Babu of NGRI, Hyderabad, for doing EPMA analysis.

I would like to express my sincere gratitude for the library staff of IIT Roorkee, IIT Mumbai, IIT Kharagpur, IIT Madras, and DMRL Hyderabad for their kind co-operation to carry out the literature survey.

Many thanks are due to my colleagues from Mechanical and Production Engineering Department of Shaheed Bhagat Singh College of Engineering and Technology, Ferozepur, Punjab, who have to put extra efforts during the period of my sponsorship.

I wish to thank my friends and colleagues for their moral support and camaraderie help to keep things in perspective, in particular Mr. Balwinder Singh, Dr. Harpreet Singh, Dr. Buta Singh, Mr. A.K. Kohli, Mr. R.S. Walia, Mr. S.B. Misra, Mr. Pawan Kumar Sapra, Mr. Vikas Chawla, Mr. M.R. Ramesh, and Mr. Arivazaghan. Special thanks go to Mr. Sukhwant Singh, Mr. Vinod Verma, Mr. Gurpreet Singh Lakhoke, Mr. Raminderpal Singh, and Mr. Jatinder Agarwal, for their everlasting support.

I would like to humbly dedicate this thesis to my parents who are the spirit and source of inspiration behind this research work. I would like to express my reverence and great admiration for parents-in-law, sisters-in-law, and brothers-in law, who have always been the inspiring and encouraging force for me. I am highly grateful to my brothers, sisters, sisters-in-law, nephews and nieces for their continual co-operation during the course of this work. I am especially grateful to my brother, M.S.Sidhu, who motivates me to try to be as creative and to work hard as he is.

A sense of apology is due from my sweet and loving sons Arbaaz Sidhu and Arsh Pratap Singh Sidhu, who missed many precious moments of their childhood from fatherly love and care. A sense of forgiveness is recorded for them as they missed the help and enthusiasm expected from me during their birthday celebrations. The wife, Ravinder Kaur, deserves special thanks and grand appreciation who gave her best in looking after the growing kids during the tenure of this work by sacrificing her comforts. I am falling short of words to express gratitude to her for the determination she has shown to bear extra household responsibilities during the tenure of this work.

Above all, I am highly indebted to almighty God who blessed me with spiritual support and fortitude at each and every stage of this work.

The entire work carried out for this investigation has been presented into nine chapters.

Chapter-1 contains introductory remarks on the hot corrosion, its disastrous consequences and prevention methods, and the method used in present research.

Chapter-2 presents critical review of the published literature relevant to the present study. First part of the chapter contains a comprehensive review of the existing literature on the hot corrosion, its characteristics and mechanism, and the hot corrosion of nickel- and iron-based superalloys in the molten salt and boiler environments. In the second part, literature review concerning the protective coatings and the HVOF process has been discussed. The studies related to the behaviour of the coatings at high temperatures have been reviewed in the third part of the chapter.

Chapter-3 highlights the scope and objectives of the present study.

Chapter-4 gives details of the experimental equipments used and the procedures adopted for deposition and characterization of the coatings, the hot corrosion studies and analyses of the corrosion products.

Chapter-5 presents the results and discussion on the characterisation of the as-sprayed coatings.

Chapter-6 describes the results for the hot corrosion behaviour of the HVOF coated as well as uncoated superalloys subjected to an aggressive environment of molten salt ($\text{Na}_2\text{SO}_4\text{-60\%V}_2\text{O}_5$) at $900\text{ }^\circ\text{C}$ under cyclic conditions. Results are discussed critically in view of the existing literature to suggest the plausible hot corrosion mechanisms.

Chapter-7 contains the results and discussions for the experiments performed in the platen super-heater zone of the coal fired boiler of a thermal power plant at $900\pm 10\text{ }^\circ\text{C}$ for 1000 hours under cyclic conditions.

In Chapter-8 the important results of the study obtained from both the molten salt and boiler environments have been discussed. Further, a comparison of the hot resistance of different coatings, in the similar environments, has also been made.

Finally, **Chapter-9** summarises the salient conclusions resulting from the present investigation, and also presents recommendations for future work.

	Page No.
<i>Candidate's Declaration</i>	i
<i>Abstract</i>	ii
<i>Acknowledgements</i>	viii
<i>Preface</i>	x
<i>List of Figures</i>	xx
<i>List of Tables</i>	xxxviii
<i>Research Papers Presented/Published</i>	xl
<i>Abbreviations</i>	xlii
CHAPTER 1 INTRODUCTION	1
1.1 HOT CORROSION	1
1.2 PREVENTIVE MEASURES	3
1.3 HIGH VELOCITY OXY-FUEL (HVOF) PROCESS	5
CHAPTER 2 LITERATURE REVIEW	6
PART-I	6
2.1 HIGH-TEMPERATURE MATERIALS	6
2.1.1 Nickel-Based Superalloys	7
2.1.2 Iron- and Cobalt-Based Superalloys	7
2.2 EFFECT OF DEPOSITS ON SUPERALLOYS	7
2.3 HOT CORROSION	8
2.3.1 Hot corrosion Characteristics	8
2.3.1.1 Type-I Hot Corrosion (HTHC)	9
2.3.1.2 Type II Hot Corrosion (LTHC)	9
2.3.2 Hot Corrosion Degradation of the Superalloys	12
2.3.3 Mechanisms of Hot Corrosion Degradation of the Superalloys	13
2.3.3.1 Failure of Oxide Scale	13

2.3.3.2	<i>Sulfidation-Oxidation and Salt-Fluxing</i>	
	<i>Mechanisms</i>	15
2.3.3.3	<i>Oxide Solubility</i>	15
2.3.3.4	<i>Effect of Vanadium</i>	14
2.3.3.5	<i>LTHC Mechanism</i>	16
2.3.4	Salt Chemistry	16
2.3.4.1	<i>Chemistry of Sulphate Solution</i>	16
2.3.4.2	<i>Chemistry of Vanadate Solution</i>	17
2.3.4.3	<i>Chemistry of Salts Present in the Combustion</i>	
	<i>Products of Coal/Fuel Oils</i>	17
2.4	HOT CORROSION IN THE MOLTEN SALT	
	(Na₂SO₄-V₂O₅) ENVIRONMENT	18
2.4.1	Hot Corrosion of the Iron and Iron-Based Alloys	22
2.4.2	Hot Corrosion of the Nickel and Nickel-Based Alloys	24
2.5	SOME STUDIES ON ENERGY GENERATION	
	SYSTEMS	30
2.6	PREVENTIVE AND CONTROL AGAINST HOT	
	CORROSION	36
	PART-II	37
2.7	PROTECTIVE COATINGS	37
2.7.1	Use of Coatings at High Temperature	38
2.7.2	Coating Techniques	40
	<i>2.7.2.1 Thermal Spray Techniques</i>	40
2.8	HIGH VELOCITY OXY-FUEL (HVOF)	
	THERMAL SPRAYING	41
2.8.1	HVOF Spraying-The Process	44
2.8.2	Splat Formation and Building up a Coating	46
	<i>2.8.2.1 Splat Formation</i>	46
	<i>2.8.2.2 Building up a Coating</i>	47
2.8.3	Selected Properties of HVOF Coatings	
	for High Temperature Applications	47

2.8.3.1	<i>Physical and Mechanical Properties of the Coatings</i>	47
2.8.3.2	<i>Microstructural Properties</i>	49
2.8.3.3	<i>Corrosion Behaviour of the Coatings</i>	49
2.8.3.4	<i>Adhesion of the Coatings</i>	49
2.8.4	Advantages of the HVOF System	50
PART-III		53
2.9	ROLE OF THE COATINGS	53
2.9.1	Behaviour of Cr₃C₂-NiCr Coating	54
2.9.2	Behaviour of NiCrBSi Coating	56
2.9.3	Behaviour of Cobalt-Based Coating	57
2.9.4	Behaviour of nickel-chromium Coating	60
CHAPTER 3 PROBLEM FORMULATION		65
3.1	SCOPE	65
3.2	OBJECTIVES	68
CHAPTER 4 EXPERIMENTAL EQUIPMENTS AND PROCEDURES		72
4.1	SUBSTRATE MATERIALS	72
4.2	FEEDSTOCK MATERIALS FOR COATINGS	72
4.3	DEPOSITION OF THE COATINGS	72
4.3.1	Preparation of the Substrate Materials	72
4.3.2	Deposition of the Coatings	74
4.4	CHARACTERISATION OF THE FEEDSTOCK MATERIALS AND COATINGS	75
4.4.1	Preparation of Specimens	75
4.4.2	Measurement of Coating Thickness	75
4.4.3	Porosity Measurement	75
4.4.4	Metallographic Studies	75
4.4.5	Measurement of Microhardness	77

4.4.6	X-Ray Diffraction (XRD) Analysis	77
4.4.7	Scanning Electron Microscopy (SEM) and Energy Dispersive X-Ray (EDAX) Analysis	77
	4.4.7.1 <i>Surface Morphology/EDAX Analysis</i>	77
	4.4.7.2 <i>Cross Section Analysis</i>	78
4.4.8	Electron Probe Micro Analyser (EPMA)	78
4.5	HOT CORROSION STUDIES	78
4.5.1	Studies in Molten Salt (Na_2SO_4-60%V_2O_5) Environment	78
	4.5.1.1 <i>Experimental Setup</i>	78
	4.5.1.2 <i>Na_2SO_4-60%V_2O_5 Salt Coating</i>	79
	4.5.1.3 <i>Hot Corrosion Runs</i>	79
4.5.2	Studies in Industrial Environment	80
4.6	ANALYSIS OF CORROSION PRODUCTS	80
4.6.1	Visual Observation	80
4.6.2	Thermogravimetric Studies	81
4.6.3	Evaluation of Corrosion Rate	82
4.6.4	Measurement of Scale Thickness and Depth of Internal Attack	82
4.6.5	Measurement of Scale Thickness Lost	82
4.6.6	X-Ray Diffraction (XRD) Analysis	83
4.6.7	SEM/EDAX Analysis	83
	4.6.7.1 <i>Surface Morphology</i>	83
	4.6.7.2 <i>Cross-Section Analysis</i>	83
4.6.8	Electron Probe Micro Analyser (EPMA)	83
 CHAPTER 5 SUBSTRATE SUPERALLOYS AND CHARACTERISATION OF THE COATINGS		 84
5.1	FEED STOCK MATERIALS	84
	5.1.1 SEM Analysis	84
	5.1.2 XRD Analysis	84
5.2	SUBSTRATE SUPERALLOYS	85

5.3	COATED SUPERALLOYS	85
5.3.1	Visual Examinations	85
5.3.2	Measurements of Coating Thicknesses	85
5.3.3	Porosity Analysis	91
5.3.4	Microhardness Measurements	91
5.3.5	Metallographic Studies of the Coatings	92
	5.3.5.1 <i>Surface Microstructures</i>	92
	5.3.5.1(a) <i>Cr₃C₂-NiCr Coating</i>	92
	5.3.5.1(b) <i>NiCrBSi Coating</i>	92
	5.3.5.1(c) <i>Stellite-6 Coating</i>	92
	5.3.5.1(d) <i>Ni-20Cr Wire Coating</i>	98
	5.3.5.2 <i>Cross-Section Microstructures</i>	98
5.3.6	XRD Analysis	98
5.3.7	SEM Analysis	99
5.3.8	EDAX Analysis	99
	5.3.8.1 <i>Surface Analysis</i>	99
	5.3.8.2 <i>Cross-section Analysis</i>	112
5.3.9	EPMA Analysis	112
5.4	DISCUSSION	113

CHAPTER 6	HOT CORROSION STUDIES IN MOLTEN SALT ENVIRONMENT	124
6.1	RESULTS AND DISCUSSION	124
6.1.1	Visual Examination	124
	6.1.1.1 <i>Bare Superalloys</i>	124
	6.1.1.2 <i>HVOF Coated Superalloys</i>	125
6.1.2	Hot Corrosion of Bare and Coated Superni 75	130
	6.1.2.1 <i>Corrosion Kinetics</i>	130
	6.1.2.2 <i>Scale Thickness Measurement</i>	131
	6.1.2.3 <i>X-ray Diffraction Analysis</i>	131
	6.1.2.4 <i>SEM/EDAX Analysis</i>	137

6.1.2.4(a) <i>Surface Analysis</i>	137
6.1.2.4(b) <i>Cross-Section Analysis</i>	137
6.1.2.5 <i>EPMA Analysis</i>	138
6.1.3 Hot Corrosion of Bare and Coated Superni 600	143
6.1.3.1 <i>Corrosion Kinetics</i>	143
6.1.3.2 <i>Scale Thickness Measurement</i>	143
6.1.3.3 <i>X-ray Diffraction Analysis</i>	151
6.1.3.4 <i>SEM/EDAX Analysis</i>	151
6.1.3.4(a) <i>Surface Analysis</i>	151
6.1.3.4(b) <i>Cross-Section Analysis</i>	152
6.1.3.5 <i>EPMA Analysis</i>	153
6.1.4 Hot Corrosion of Bare and Coated Superni 601	163
6.1.4.1 <i>Corrosion Kinetics</i>	163
6.1.4.2 <i>Scale Thickness Measurement</i>	163
6.1.4.3 <i>X-ray Diffraction Analysis</i>	163
6.1.4.4 <i>SEM/EDAX Analysis</i>	164
6.1.4.4(a) <i>Surface Analysis</i>	164
6.1.4.4(b) <i>Cross-Section Analysis</i>	169
6.1.4.5 <i>EPMA Analysis</i>	169
6.1.5 Hot Corrosion of Bare and Coated Superni 718	175
6.1.5.1 <i>Corrosion Kinetics</i>	175
6.1.5.2 <i>Scale Thickness Measurement</i>	176
6.1.5.3 <i>X-ray Diffraction Analysis</i>	176
6.1.5.4 <i>SEM/EDAX Analysis</i>	176
6.1.5.4(a) <i>Surface Analysis</i>	176
6.1.5.4(b) <i>Cross-Section Analysis</i>	177
6.1.5.5 <i>EPMA Analysis</i>	178
6.1.6 Hot Corrosion of Bare and Coated Superfer 800H	189
6.1.6.1 <i>Corrosion Kinetics</i>	189
6.1.6.2 <i>Scale Thickness Measurement</i>	190
6.1.6.3 <i>X-ray Diffraction Analysis</i>	190
6.1.6.4 <i>SEM/EDAX Analysis</i>	197
6.1.6.4(a) <i>Surface Analysis</i>	197
6.1.6.4(b) <i>Cross-Section Analysis</i>	197
6.1.6.5 <i>EPMA Analysis</i>	198

6.2	SUMMARY OF RESULTS	203
6.3	COMPREHENSIVE DISCUSSION	212
6.3.1	Uncoated Superalloys	212
6.3.2	HVOF Coated Superalloys	215
6.3.2.1	<i>Cr₃C₂-NiCr Coating</i>	216
6.3.2.2	<i>NiCrBSi Coating</i>	222
6.3.2.3	<i>Stellite-6 Coating</i>	225
6.3.2.4	<i>Ni-20Cr Coating</i>	226

CHAPTER 7 HOT CORROSION STUDIES IN INDUSTRIAL ENVIRONMENT

7.1	RESULTS AND DISCUSSION	233
7.1.1	Visual Examination	233
7.1.1.1	<i>Bare Superalloys</i>	233
7.1.1.2	<i>HVOF Coated Superalloys</i>	233
7.1.2	Hot Corrosion of Superalloys	234
7.1.3	Hot Corrosion of Bare and Coated Superni 75	240
7.1.3.1	<i>Corrosion Kinetics</i>	240
7.1.3.2	<i>Average Scale Thickness and Depth of Internal Attack</i>	240
7.1.3.3	<i>X-ray Diffraction Analysis</i>	240
7.1.3.4	<i>SEM/EDAX Analysis</i>	241
7.1.3.4(a)	<i>Surface Analysis</i>	241
7.1.3.4(b)	<i>Cross-Section Analysis</i>	246
7.1.3.5	<i>EPMA Analysis</i>	246
7.1.4	Hot Corrosion of Bare and Coated Superni 600	253
7.1.4.1	<i>Corrosion Kinetics</i>	253
7.1.4.2	<i>Average Scale Thickness and Depth of Internal Attack</i>	253
7.1.4.3	<i>X-ray Diffraction Analysis</i>	254
7.1.4.4	<i>SEM/EDAX Analysis</i>	254
7.1.4.4(a)	<i>Surface Analysis</i>	254
7.1.4.4(b)	<i>Cross-Section Analysis</i>	255
7.1.4.5	<i>EPMA Analysis</i>	256

7.1.5	Hot Corrosion of Bare and Coated Superni 601	267
	7.1.5.1 <i>Corrosion Kinetics</i>	267
	7.1.5.2 <i>Average Scale Thickness and Depth of Internal Attack</i>	267
	7.1.5.3 <i>X-ray Diffraction Analysis</i>	268
	7.1.5.4 <i>SEM/EDAX Analysis</i>	268
	7.1.5.4(a) <i>Surface Analysis</i>	268
	7.1.5.4(b) <i>Cross-Section Analysis</i>	269
	7.1.5.5 <i>EPMA Analysis</i>	269
7.1.6	Hot Corrosion of Bare and Coated Superni 718	282
	7.1.6.1 <i>Corrosion Kinetics</i>	282
	7.1.6.2 <i>Average Scale Thickness and Depth of Internal Attack</i>	282
	7.1.6.3 <i>X-ray Diffraction Analysis</i>	282
	7.1.6.4 <i>SEM/EDAX Analysis</i>	282
	7.1.6.4(a) <i>Surface Analysis</i>	282
	7.1.6.4(b) <i>Cross-Section Analysis</i>	288
	7.1.6.5 <i>EPMA Analysis</i>	288
7.1.7	Hot Corrosion of Bare and Coated Superfer 800H	289
	7.1.7.1 <i>Corrosion Kinetics</i>	289
	7.1.7.2 <i>Average Scale Thickness and Depth of Internal Attack</i>	290
	7.1.7.3 <i>X-ray Diffraction Analysis</i>	290
	7.1.7.4 <i>SEM/EDAX Analysis</i>	291
	7.1.7.4(a) <i>Surface Analysis</i>	291
	7.1.7.4(b) <i>Cross-Section Analysis</i>	301
	7.1.7.5 <i>EPMA Analysis</i>	301
7.2	SUMMARY OF RESULTS	308
7.3	COMPREHENSIVE DISCUSSION	312
	7.3.1 Uncoated Superalloys	312
	7.3.2 HVOF Coated Superalloys	314
	7.3.2.1 <i>Cr₃C₂-NiCr Coating</i>	314
	7.3.2.2 <i>NiCrBSi Coating</i>	316

	<i>7.3.2.3 Stellite-6 Coating</i>	324
	<i>7.3.2.4 Ni-20Cr Coating</i>	325
CHAPTER 8	COMPARATIVE DISCUSSION	330
8.1	MOLTEN SALT ENVIRONMENT	330
8.2	INDUSTRIAL ENVIRONMENT	333
CHAPTER 9	CONCLUSIONS & RECOMMENDATIONS FOR FUTURE WORK	338
9.1	AS-SPRAYED HVOF COATING	338
9.2	HOT CORROSION IN MOLTEN SALT ENVIRONMENT	339
9.3	HOT CORROSION IN THE INDUSTRIAL ENVIRONMENT OF COAL FIRED BOILER	340
9.4	RECOMMENDATION FOR FUTURE WORK	344
	APPENDIX	346
	REFERENCES	355

LIST OF FIGURES

Figure No.	Particulars	Page No.
Fig. 2.1	Schematic diagram showing a Na_2SO_4 deposit upon an alloy separating the alloy from the gas phase (Pettit and Meier, 1985).	10
Fig. 2.2	Thermodynamic stability diagram for the Na-O-S system showing how composition of Na_2SO_4 may change due to alloy reacting with the deposit.	10
Fig. 2.3	Schematic of hot corrosion mechanisms (Natesan, 1976).	11
Fig. 2.4	Schematic diagram illustrating the conditions that develop during the initiation and the propagation of hot corrosion attack and to identify the factors that determine the time at which the transition from the initiation to the propagation stage occurs (Pettit and Meier, 1985).	14
Fig. 2.5	Schematic representation of the reaction sequence during LTHC of a Co-30%Cr alloy exposed to O_2 - SO_2 - SO_3 environment where Na_2SO_4 - CoSO_4 liquid and Co_3O_4 are stable. At higher concentration of SO_3 where Co_3O_4 is unstable at the gas-salt interface, the outward migrating cobalt will form CoSO_4 (s) or Co_3O_4 and CoSO_4 (s) (Luthra, 1983).	19
Fig. 2.6	Na-Cr-S-O phase stability diagram for 1200 K (Rapp, 1986).	19
Fig. 2.7	Phase stability diagram for Na-V-S-O system at 900 °C (Hwang and Rapp, 1989).	20
Fig. 2.8	Phase Diagram for Na_2SO_4 - V_2O_5 System (Otero et al, 1987).	27
Fig. 2.9	Schematic diagram showing probable hot corrosion mechanism in Na_2SO_4 -60% V_2O_5 after exposure for 50 cycles at 900 °C for alloys (Gitanjaly, 2003) (a) Superni 75 (b) Superni 601.	32
Fig. 2.10	Sequential steps in the vanadic corrosion of metals (Pantony & Vasu, 1968A).	32
Fig. 2.11	Schematic illustration of the growth of chromia scales in (i) the absence of oxygen active elements and with predominant outward transport of chromia through the scale, and (ii) the presence of oxygen active elements and with predominant inward transport of oxygen (Kofstad, 1990).	33
Fig. 2.12	Coating deposition technologies (Bhushan and Gupta, 1991).	42
Fig. 2.13	Schematic of a Thermal Spray Process (Stokes, 2003).	45

Fig. 2.14	Schematic cross-section of diamond-jet spray gun (Stokes & Looney, 2001).	45
Fig. 2.15	Schematic diagram of spherical particle impinged onto a flat surface (Stokes, 2005).	48
Fig. 2.16	Two morphological forms of lamellae splashed on the substrate (a) Pancake, (b) Flower; I: Top View, II: X-Section View.	48
Fig. 2.17	(a) A cross-section of lamella splat in diagram (1) is shown in diagram (2), which represents the possible microstructure of lamellae resulting from solidification (columnar). (b) Another cross-section through a lamella, showing a 'Brick-wall' type microstructure resulting from solidification. (c) Schematic of adhesion of a particle to a substrate asperity (Stokes, 2005).	51
Fig. 2.18	Characteristics of HVOF and standard plasma process coatings (Helali and Hashmi, 1992).	52
Fig. 3.1	Types of high-temperature attack for metallic coatings (aluminide, chromide, MCrAlY, etc.) on nickel-base superalloys with approximate temperature regimes and severity of attack (National Materials Advisory Board, 1996).	69
Fig. 4.1	High velocity oxy-fuel systems used in the current research.	76
Fig. 5.1	SEM of different coating powder (a) $\text{Cr}_3\text{C}_2\text{-NiCr}$ powder, (b) NiCrBSi Powder, (c) stellite-6 powder.	86
Fig. 5.2	X-ray diffraction patterns for the HVOF feedstock materials.	87
Fig. 5.3	Optical micrographs of the substrate superalloys (a) Superni 75 (b) Superni 600 (c)Superni 601 (d) Superni 718 (e)Superfer 800H.	88
Fig. 5.4	Optical macrographs of as-sprayed specimens with (a) $\text{Cr}_3\text{C}_2\text{-NiCr}$ coating (b) NiCrBSi coating (c) Stellite-6 coating (e) Ni-20Cr coating.	89
Fig. 5.5	BSEI micrographs showing cross-section morphologies of different HVOF coatings on Superni 75 superalloy, (a) $\text{Cr}_3\text{C}_2\text{-NiCr}$ coating (b) NiCrBSi coating (c) Stellite-6 coating (d) Ni-20Cr coating.	90
Fig. 5.6	Microhardness profiles of HVOF sprayed coatings for different superalloys along the cross section (a) $\text{Cr}_3\text{C}_2\text{-NiCr}$ coating, (b) NiCrBSi coating.	93
Fig. 5.7	Microhardness profiles of HVOF sprayed coatings for different superalloys along the cross section (a) Stellite-6 coating, (b) Ni-20Cr coating.	94

Fig. 5.8	Optical micrographs showing surface morphology of HVOF sprayed $\text{Cr}_3\text{C}_2\text{-NiCr}$ coating on substrate superalloys: (a) Superni 75 (b) Superni 600 (c) Superni 601 (d) Superni 718 (e) Superfer 800H.	95
Fig. 5.9	Optical micrographs showing surface morphology of HVOF sprayed NiCrBSi coating on substrate superalloys: (a) Superni 75 (b) Superni 600 (c) Superni 601 (d) Superni 718 (e) Superfer 800H.	96
Fig. 5.10	Optical micrographs showing surface morphology of HVOF sprayed Stellite-6 coating on substrate superalloys: (a) Superni 75 (b) Superni 600 (c) Superni 601 (d) Superni 718 (e) Superfer 800H.	97
Fig. 5.11	Optical micrographs showing surface morphology of HVOF sprayed Ni-20Cr coating on substrate superalloys: (a) Superni 75 (b) Superni 600 (c) Superni 601 (d) Superni 718 (e) Superfer 800H.	100
Fig. 5.12	Optical micrographs showing cross-section microstructures of different coatings on Superfer 800H superalloy: (a) $\text{Cr}_3\text{C}_2\text{-NiCr}$ coating (b) NiCrBSi coating (c) Stellite-6 coating (d) Ni-20Cr coating.	101
Fig. 5.13	X-ray diffractions for the $\text{Cr}_3\text{C}_2\text{-NiCr}$ coatings on different superalloy: (a) Superni 75 (b) Superni 600 (c) Superni 601 (d) Superni 718 (e) Superfer 800H.	102
Fig. 5.14	X-ray diffractions for the NiCrBSi coatings on different superalloy: (a) Superni 75 (b) Superni 600 (c) Superni 601 (d) Superni 718 (e) Superfer 800H.	103
Fig. 5.15	X-ray diffractions for the Stellite-6 coatings on different superalloy: (a) Superni 75 (b) Superni 600 (c) Superni 601 (d) Superni 718 (e) Superfer 800H.	104
Fig. 5.16	X-ray diffractions for the Ni-20Cr wire coatings on different superalloy: (a) Superni 75 (b) Superni 600 (c) Superni 601 (d) Superni 718 (e) Superfer 800H.	105
Fig. 5.17	SEM micrographs showing surface morphology of HVOF sprayed $\text{Cr}_3\text{C}_2\text{-NiCr}$ coating on substrate superalloys: (a) Superni 75 (b) Superni 600 (c) Superni 601 (d) Superni 718 (e) Superfer 800H.	106
Fig. 5.18	SEM micrographs showing surface morphology of HVOF sprayed NiCrBSi coating on substrate superalloys (a) Superni 75 (b) Superni 600 (c) Superni 601 (d) Superni 718 (e) Superfer 800H.	107

Fig. 5.19	SEM micrographs showing surface morphology of HVOF sprayed Stellite-6 coating on substrate superalloys: (a) Superni 75 (b) Superni 600 (c) Superni 601 (d) Superni 718 (e) Superfer 800H.	108
Fig. 5.20	SEM micrographs showing surface morphology of HVOF sprayed Ni-20Cr wire coating on substrate superalloys: (a) Superni 75 (b) Superni 600 (c) Superni 601 (d) Superni 718 (e) Superfer 800H.	109
Fig. 5.21	SEM/EDAX analysis of the HVOF sprayed coatings showing elemental composition (wt%) at selected points: (a) Cr ₃ C ₂ -NiCr Coating (b) NiCrBSi Coating.	110
Fig. 5.22	SEM/EDAX analysis of the HVOF sprayed coatings showing elemental composition (wt%) at selected points: (a) Stellite-6 coating (b) Ni-20Cr coating.	111
Fig. 5.23	EDAX analysis (wt%) across the cross-section of the HVOF coatings on Superfer 800H: (a) Cr ₃ C ₂ -NiCr coating (b) NiCrBSi coating (c) Stellite-6 coating (d) Ni-20Cr coating.	114
Fig. 5.24	Composition image (BSEI) and X-ray mappings at the cross-section of the as-sprayed Cr ₃ C ₂ -NiCr coating on Superni 75 superalloy.	115
Fig. 5.25	Composition image (BSEI) and X-ray mappings at the cross-section of as-sprayed NiCrBSi coating on Superni 601 superalloys.	116
Fig. 5.26	Composition image (BSEI) and X-ray mappings at the cross-section of the as-sprayed Stellite-6 coating on Superni 75 superalloys.	117
Fig. 5.27	Composition image (BSEI) and X-ray mappings at the cross-section of the as-sprayed Ni-20Cr coating on Superfer 800H superalloy.	118
Fig. 5.28	SEM micrograph of HVOF sprayed coating reported by Ak et al. (2003), using Ni-20Cr powder as feedstock alloy.	123
Fig. 5.29	SEM micrograph of HVOF sprayed coating using Ni-20Cr wire as feedstock alloy.	123
Fig. 6.1	Macrographs of the bare superalloys subjected to hot corrosion in Na ₂ SO ₄ -60%V ₂ O ₅ environment at 900 °C for 50 cycles: (a) Superni 75 (b) Superni 600 (c) Superni 601 (d) Superni 718 (e) Superfer 800H.	126
Fig. 6.2	Cracks developed in the scale of uncoated superalloy Superni 601 subjected to hot corrosion in Na ₂ SO ₄ -60%V ₂ O ₅ environment at 900 °C after 10 th cycles.	127

Fig. 6.3	Macrographs of the Cr ₃ C ₂ -NiCr coated superalloys subjected to hot corrosion in Na ₂ SO ₄ -60%V ₂ O ₅ environment at 900 °C for 50 cycles: (a) Superni 75 (b) Superni 600 (c) Superni 601 (d) Superni 718 (e) Superfer 800H.	128
Fig. 6.4	Macrographs of the NiCrBSi coated superalloys subjected to hot corrosion in Na ₂ SO ₄ -60%V ₂ O ₅ environment at 900 °C for 50 cycles: (a) Superni 75 (b) Superni 600 (c) Superni 601 (d) Superni 718 (e) Superfer 800H.	129
Fig. 6.5	Macrographs of the Stellite-6 coated superalloys subjected to hot corrosion in Na ₂ SO ₄ -60%V ₂ O ₅ environment at 900 °C for 50 cycles: (a) Superni 75 (b) Superni 600 (c) Superni 601 (d) Superni 718 (e) Superfer 800H.	132
Fig. 6.6	Macrographs of the Ni-20Cr wire coated superalloys subjected to hot corrosion in Na ₂ SO ₄ -60%V ₂ O ₅ environment at 900 °C for 50 cycles: (a) Superni 75 (b) Superni 600 (c) Superni 601 (d) Superni 718 (e) Superfer 800H.	133
Fig. 6.7	Weight gain vs. number of cycles plot for coated and uncoated Superni 75 subjected to hot corrosion for 50 cycles in Na ₂ SO ₄ -60%V ₂ O ₅ environment at 900 °C.	134
Fig. 6.8	Bar charts showing cumulative weight gain per unit area for coated and uncoated Superni 75 subjected to hot corrosion for 50 cycles in Na ₂ SO ₄ -60%V ₂ O ₅ environment at 900 °C	134
Fig. 6.9	(Weight gain/area) ² vs. number of cycle plots for coated and uncoated superalloy Superni 75 subjected to hot corrosion for 50 cycles in Na ₂ SO ₄ -60%V ₂ O ₅ environment at 900 °C.	134
Fig. 6.10	SEM back scattered images for the bare and HVOF coated Superni 75 superalloy subjected to hot corrosion in Na ₂ SO ₄ -60%V ₂ O ₅ environment at 900 °C for 50 cycles: (a) Bare superalloy (b) Cr ₃ C ₂ -NiCr coated (c) NiCrBSi coated (d) Stellite-6 coated (e) Ni-20Cr coated.	135
Fig. 6.11	X-ray diffraction patterns for the bare and coated superalloy Superni 75 subjected to hot corrosion in Na ₂ SO ₄ -60%V ₂ O ₅ environment at 900 °C for 50 cycles.	136
Fig. 6.12	SEM/EDAX analysis showing elemental composition (wt.%) for the bare and coated Superni 75 subjected to hot corrosion in Na ₂ SO ₄ -60%V ₂ O ₅ environment at 900 °C for 50 cycles: (a) Bare Superni 75 (b) Cr ₃ C ₂ -NiCr coated (c) NiCrBSi coated (d) Stellite-6 coated (e) Ni-20Cr coated.	139

Fig. 6.13	Oxide scale morphologies and variations of elemental composition across the cross section of HVOF coated Superni 75 superalloy hot corroded in Na ₂ SO ₄ -60%V ₂ O ₅ environment at 900 °C for 50 cycles (a) Bare Superni 75 (b) NiCrBSi coated (c) Stellite-6 coated.	140
Fig. 6.14	Composition image (BSEI) and X-ray mappings of the cross-section of the bare Superni 75 subjected to hot corrosion at 900 °C in Na ₂ SO ₄ -60%V ₂ O ₅ environment for 50 cycles.	141
Fig. 6.15a	Composition image (BSEI) and X-ray mappings of the cross-section of the Cr ₃ C ₂ -NiCr coated Superni 75 superalloy subjected to hot corrosion at 900 °C in Na ₂ SO ₄ -60%V ₂ O ₅ environment for 50 cycles.	144
Fig. 6.15b	Composition image (BSEI) and X-ray mappings, using oxygen detection crystal, of the cross-section of the Cr ₃ C ₂ -NiCr coated Superni 75 superalloy subjected to hot corrosion at 900 °C in Na ₂ SO ₄ -60%V ₂ O ₅ environment for 50 cycles.	145
Fig. 6.16	Composition image (BSEI) and X-ray mappings of the cross-section of the NiCrBSi coated Superni 75 superalloy subjected to hot corrosion at 900 °C in Na ₂ SO ₄ -60%V ₂ O ₅ environment for 50 cycles.	146
Fig. 6.17	Composition image (BSEI) and X-ray mappings of the cross-section of the Stellite-6 coated Superni 75 superalloy subjected to hot corrosion at 900 °C in Na ₂ SO ₄ -60%V ₂ O ₅ environment for 50 cycles.	147
Fig. 6.18	Composition image (BSEI) and X-ray mappings of the cross-section of the Ni-20Cr coated Superni 75 superalloy subjected to hot corrosion at 900 °C in Na ₂ SO ₄ -60%V ₂ O ₅ environment for 50 cycles.	148
Fig. 6.19	Weight gain vs. number of cycles plot for coated and uncoated Superni 600 subjected to hot corrosion for 50 cycles in Na ₂ SO ₄ -60%V ₂ O ₅ environment at 900 °C.	149
Fig. 6.20	Bar charts showing cumulative weight gain per unit area for coated and uncoated Superni 600 subjected to hot corrosion for 50 cycles in Na ₂ SO ₄ -60%V ₂ O ₅ environment at 900 °C.	149
Fig. 6.21	(Weight gain/area) ² vs. number of cycles plot for coated and uncoated superalloy Superni 600 subjected to hot corrosion for 50 cycles in Na ₂ SO ₄ -60%V ₂ O ₅ environment at 900 °C.	149
Fig. 6.22	SEM back scattered images for the bare and HVOF coated Superni 600 superalloy subjected to hot corrosion in Na ₂ SO ₄ -60%V ₂ O ₅ environment at 900 °C for 50 cycles: (a) Bare superalloy (b) Cr ₃ C ₂ -NiCr coated (c) NiCrBSi coated (d) Stellite-6 coated (e) Ni-20Cr coated	150

Fig. 6.23	X-ray diffraction patterns for the bare and coated superalloy Superni 600 subjected to hot corrosion in Na_2SO_4 -60% V_2O_5 environment at 900 °C for 50 cycles.	155
Fig. 6.24	SEM/EDAX analysis showing elemental composition (wt.%) for the bare and coated Superni 600 subjected to hot corrosion in Na_2SO_4 -60% V_2O_5 environment at 900 °C for 50 cycles: (a) Bare Superni 600 (b) Cr_3C_2 -NiCr coated (c) NiCrBSi coated (d) Stellite-6 coated (e) Ni-20Cr coated.	156
Fig. 6.25	Oxide scale morphologies and variations of elemental composition across the cross section of uncoated and coated Superni 600 hot corroded in Na_2SO_4 -60% V_2O_5 environment at 900 °C for 50 cycles: (a) Bare Superni 600 (b) NiCrBSi coated (c) Ni-20Cr coated.	157
Fig. 6.26	Composition image (BSEI) and X-ray mappings of the cross-section of the bare Superni 600 subjected to hot corrosion at 900 °C in Na_2SO_4 -60% V_2O_5 environment for 50 cycles.	158
Fig. 6.27	Composition image (BSEI) and X-ray mappings of the cross-section of the Cr_3C_2 -NiCr coated Superni 600 superalloy subjected to hot corrosion at 900 °C in Na_2SO_4 -60% V_2O_5 environment for 50 cycles.	159
Fig. 6.28	Composition image (BSEI) and X-ray mappings of the cross-section of the NiCrBSi coated Superni 600 superalloy subjected to hot corrosion at 900 °C in Na_2SO_4 -60% V_2O_5 environment for 50 cycles.	160
Fig. 6.29	Composition image (BSEI) and X-ray mappings of the cross-section of the Stellite-6 coated Superni 600 superalloy subjected to hot corrosion at 900 °C in Na_2SO_4 -60% V_2O_5 environment for 50 cycles.	161
Fig. 6.30	Composition image (BSEI) and X-ray mappings of the cross-section of the Ni-20Cr coated Superni 600 superalloy subjected to hot corrosion at 900 °C in Na_2SO_4 -60% V_2O_5 environment for 50 cycles.	162
Fig. 6.31	Weight gain vs. number of cycles plot for coated and uncoated Superni 601 hot corroded for 50 cycles in Na_2SO_4 -60% V_2O_5 environment at 900 °C.	165
Fig. 6.32	Bar charts showing cumulative weight gain per unit area for coated and uncoated Superani 601 subjected to hot corrosion for 50 cycles in Na_2SO_4 -60% V_2O_5 environment at 900 °C.	165
Fig. 6.33	(Weight gain/area) ² vs. number of cycles plot for coated and uncoated Superni 601 hot corroded for 50 cycles in Na_2SO_4 -60% V_2O_5 environment at 900 °C.	165

Fig. 6.34	SEM back scattered images for the bare and HVOF coated Superni 601 subjected to hot corrosion in Na_2SO_4 -60% V_2O_5 environment at 900 °C for 50 cycles: (a) Bare superalloy (b) Cr_3C_2 -NiCr coated (c) NiCrBSi coated (d) Stellite-6 coated (e) Ni-20Cr coated.	166
Fig. 6.35	X-ray diffraction patterns for the bare and coated Superni 601 subjected to hot corrosion in Na_2SO_4 -60% V_2O_5 environment at 900 °C for 50 cycles.	167
Fig. 6.36	SEM/EDAX analysis showing elemental composition (wt.%) for the bare and coated Superni 601 subjected to hot corrosion in Na_2SO_4 -60% V_2O_5 environment at 900 °C for 50 cycles: (a) Bare Superfer 800H (b) Cr_3C_2 -NiCr coated (c) NiCrBSi coated (d) Stellite-6 coated (e) Ni-20Cr coated.	168
Fig. 6.37	Oxide scale morphologies and variations of elemental composition across the cross section of HVOF coated Superni 601 hot corroded in Na_2SO_4 -60% V_2O_5 environment at 900 °C for 50 cycles: (a) Cr_3C_2 -NiCr coated (b) Stellite-6 coated (c) Ni-20Cr coated.	171
Fig. 6.38	Composition image (BSEI) and X-ray mappings of the cross-section of the bare Superni 601 subjected to hot corrosion at 900 °C in Na_2SO_4 -60% V_2O_5 environment for 50 cycles.	172
Fig. 6.39	Composition image (BSEI) and X-ray mappings of the cross-section of the Cr_3C_2 -NiCr-coated Superni 601 subjected to hot corrosion at 900 °C in Na_2SO_4 -60% V_2O_5 environment for 50 cycles.	173
Fig. 6.40	Composition image (BSEI) and X-ray mappings of the cross-section of the NiCrBSi coated Superni 601 subjected to hot corrosion at 900 °C in Na_2SO_4 -60% V_2O_5 environment for 50 cycles.	174
Fig. 6.41	Composition image (BSEI) and X-ray mappings of the cross-section of the Stellite-6 coated Superni 601 subjected to hot corrosion at 900 °C in Na_2SO_4 -60% V_2O_5 environment for 50 cycles.	179
Fig. 6.42	Composition image (BSEI) and X-ray mappings of the cross-section of the Ni-20Cr coated Superni 601 subjected to hot corrosion at 900 °C in Na_2SO_4 -60% V_2O_5 environment for 50 cycles.	180
Fig. 6.43	Weight gain vs. number of cycles plot for coated and uncoated Superni 718 subjected to hot corrosion for 50 cycles in Na_2SO_4 -60% V_2O_5 environment at 900 °C.	181
Fig. 6.44	Bar charts showing cumulative weight gain per unit area for coated and uncoated Superni 718 subjected to hot corrosion for 50 cycles in Na_2SO_4 -60% V_2O_5 environment at 900 °C.	181

Fig. 6.45	(Weight gain/area) ² vs. number of cycles plot for coated and uncoated Superni 718 subjected to hot corrosion for 50 cycles in Na ₂ SO ₄ -60%V ₂ O ₅ environment at 900 °C.	182
Fig. 6.46	SEM back scattered images for the bare and HVOF coated Superni 718 subjected to hot corrosion in Na ₂ SO ₄ -60%V ₂ O ₅ environment at 900 °C for 50 cycles: (a) Bare superalloy (b) Cr ₃ C ₂ -NiCr coated (c) NiCrBSi coated (d) Stellite-6 coated (e) Ni-20Cr coated.	183
Fig. 6.47	X-ray diffraction patterns for the bare and coated Superni 718 subjected to hot corrosion in Na ₂ SO ₄ -60%V ₂ O ₅ environment at 900 °C for 50 cycles.	184
Fig. 6.48	SEM/EDAX analysis showing elemental composition (wt.%) for the bare and coated Superni 718 subjected to hot corrosion in Na ₂ SO ₄ -60%V ₂ O ₅ environment at 900 °C for 50 cycles: (a) Bare Superni 718 (b) Cr ₃ C ₂ -NiCr coated (c) NiCrBSi coated (d) Stellite-6 coated (e) Ni-20Cr coated.	185
Fig. 6.49	Oxide scale morphologies and variations of elemental composition across the cross section of HVOF coated Superni 718 hot corroded in Na ₂ SO ₄ -60%V ₂ O ₅ environment at 900 °C for 50 cycles: (a) Cr ₃ C ₂ -NiCr coated (b) NiCrBSi coated.	186
Fig. 6.50	Composition image (BSEI) and X-ray mappings of the cross-section of the bare Superni 718 subjected to hot corrosion at 900 °C in Na ₂ SO ₄ -60%V ₂ O ₅ environment for 50 cycles.	187
Fig. 6.51	Composition image (BSEI) and X-ray mappings of the cross-section of the Cr ₃ C ₂ -NiCr coated Superni 718 subjected to hot corrosion at 900 °C in Na ₂ SO ₄ -60%V ₂ O ₅ environment for 50 cycles.	188
Fig. 6.52	Composition image (BSEI) and X-ray mappings of the cross-section of the NiCrBSi coated Superni 718 subjected to hot corrosion at 900 °C in Na ₂ SO ₄ -60%V ₂ O ₅ environment for 50 cycles.	191
Fig. 6.53	Composition image (BSEI) and X-ray mappings of the cross-section of the Stellite-6 coated Superni 718 subjected to hot corrosion at 900 °C in Na ₂ SO ₄ -60%V ₂ O ₅ environment for 50 cycles.	192
Fig. 6.54	Composition image (BSEI) and X-ray mappings of the cross-section of the Ni-20Cr coated Superni 718 subjected to hot corrosion at 900 °C in Na ₂ SO ₄ -60%V ₂ O ₅ environment for 50 cycles.	193
Fig. 6.55	Weight gain vs. number of cycles plot for coated and uncoated Supfer 800H hot corroded for 50 cycles in Na ₂ SO ₄ -60%V ₂ O ₅ environment at 900 °C.	194

Fig. 6.56	Bar charts showing cumulative weight gain per unit area for coated and uncoated Superfer 800H hot corroded for 50 cycles in Na ₂ SO ₄ -60%V ₂ O ₅ environment at 900 °C.	194
Fig. 6.57	(Weight gain/area) ² vs. number of cycles plot for coated and uncoated Superfer 800H hot corroded for 50 cycles in Na ₂ SO ₄ -60%V ₂ O ₅ environment at 900 °C.	194
Fig. 6.58	SEM back scattered images for the bare and HVOF coated Superfer 800H subjected to hot corrosion in Na ₂ SO ₄ -60%V ₂ O ₅ environment at 900 °C for 50 cycles:(a) Bare superalloy (b) Cr ₃ C ₂ -NiCr coated (c) NiCrBSi coated (d) Stellite-6 coated (e) Ni-20Cr coated.	195
Fig. 6.59	X-ray diffraction patterns for the bare and coated Superfer 800H subjected to cyclic oxidation in Na ₂ SO ₄ -60%V ₂ O ₅ environment at 900 °C after 50 cycles.	196
Fig. 6.60	SEM/EDAX analysis showing elemental composition (wt.%) for the bare and coated Superfer 800H subjected to hot corrosion in Na ₂ SO ₄ -60%V ₂ O ₅ environment at 900 °C for 50 cycles: (a) Bare Superfer 800H (b) Cr ₃ C ₂ -NiCr coated (c) NiCrBSi coated (d) Stellite-6 coated (e) Ni-20Cr coated.	199
Fig. 6.61	Oxide scale morphology and variations of elemental composition across the cross section of HVOF coated Superfer 800H hot corroded in Na ₂ SO ₄ -60%V ₂ O ₅ environment at 900 °C for 50 cycles: (a) Cr ₃ C ₂ -NiCr coated (b) Stellite-6 coated (c) Ni-20Cr coated.	200
Fig. 6.62	Composition image (BSEI) and X-ray mappings of the cross-section of the bare Superfer 800H subjected to hot corrosion at 900 °C in Na ₂ SO ₄ -60%V ₂ O ₅ environment for 50 cycles.	201
Fig. 6.63	Composition image (BSEI) and X-ray mapping of the cross-section of the Cr ₃ C ₂ -NiCr coated Superfer 800H subjected to hot corrosion at 900 °C in Na ₂ SO ₄ -60%V ₂ O ₅ after 50 cycles.	208
Fig. 6.64	Composition image (BSEI) and X-ray mapping of the cross-section of the NiCrBSi coated Superfer 800H subjected to hot corrosion at 900 °C in Na ₂ SO ₄ -60%V ₂ O ₅ after 50 cycles.	209
Fig. 6.65	Composition image (BSEI) and X-ray mapping of the cross-section of the Stellite-6 coated Superfer 800H subjected to hot corrosion at 900 °C in Na ₂ SO ₄ -60%V ₂ O ₅ after 50 cycles.	210
Fig. 6.66	Composition image (BSEI) and X-ray mapping of the cross-section of the Ni-20Cr coated Superfer 800H subjected to hot corrosion at 900 °C in Na ₂ SO ₄ -60%V ₂ O ₅ after 50 cycles.	211

Fig. 6.67	Bar charts showing cumulative weight gain per unit area for uncoated superalloys hot corroded for 50 cycles in Na ₂ SO ₄ -60%V ₂ O ₅ environment at 900 °C.	214
Fig. 6.68	Weight gain vs. number of cycles plot for uncoated superalloys subjected to hot corrosion for 50 cycles in Na ₂ SO ₄ -60%V ₂ O ₅ environment at 900 °C.	214
Fig. 6.69	Schematic diagram showing probable hot corrosion mechanism for the uncoated Superni 600 exposed to Na ₂ SO ₄ -60%V ₂ O ₅ environment at 900 °C for 50 cycles.	219
Fig. 6.70	Weight gain vs. number of cycle plots for uncoated and Cr ₃ C ₂ -NiCr coated superalloys subjected to hot corrosion for 50 cycles in Na ₂ SO ₄ -60%V ₂ O ₅ environment at 900 °C.	220
Fig. 6.71	Schematic diagram showing possible hot corrosion mode for the Cr ₃ C ₂ -NiCr coated Superni 75 exposed to Na ₂ SO ₄ -60%V ₂ O ₅ environment at 900 °C for 50 cycles.	221
Fig. 6.72	Schematic diagram showing possible hot corrosion mode for the NiCrBSi coated Superni 601 exposed to Na ₂ SO ₄ -60%V ₂ O ₅ environment at 900 °C for 50 cycles.	224
Fig. 6.73	Weight gain vs. number of cycles plot for uncoated and Stellite-6 coated superalloys subjected to hot corrosion for 50 cycles in Na ₂ SO ₄ -60%V ₂ O ₅ environment at 900 °C.	229
Fig. 6.74	Schematic diagram showing possible hot corrosion mode for the Stellite-6 coated Superni 600 exposed to Na ₂ SO ₄ -60%V ₂ O ₅ at 900 °C for 50 cycles.	230
Fig. 6.75	Weight gain vs. number of cycles plot for uncoated and Ni-20Cr coated superalloys subjected to hot corrosion for 50 cycles in Na ₂ SO ₄ -60%V ₂ O ₅ environment at 900 °C.	231
Fig. 6.76	Schematic diagram showing possible hot corrosion mode for the Ni-20Cr coated Superni 600 exposed to Na ₂ SO ₄ -60%V ₂ O ₅ at 900 °C for 50 cycles.	232
Fig. 7.1	Macrographs of the bare superalloys after 1000 hrs exposure to platen superheater zone of the coal fired boiler at 900 °C: (a) Superni 75 (b) Superni 600 (c) Superni 601 (d) Superni 718 (e) Superfer 800H.	235
Fig. 7.2	Macrographs of the Cr ₃ C ₂ -NiCr coated superalloys after 1000 hrs exposure to platen superheater zone of the boiler at 900 °C : (a) Superni 75 (b) Superni 600 (c) Superni 601 (d) Superni 718 (e) Superfer 800H.	236

Fig. 7.3	Macrographs of the NiCrBSi coated superalloys after 1000 hrs exposure to platen superheater zone of the boiler at 900 °C : (a) Superni 75 (b) Superni 600 (c) Superni 601 (d) Superni 718 (e) Superfer 800H.	237
Fig. 7.4	Macrographs of the Stellite-6 coated superalloys after 1000 hrs exposure to platen superheater zone of the boiler at 900 °C: (a) Superni 75 (b) Superni 600 (c) Superni 601 (d) Superni 718 (e) Superfer 800H.	238
Fig. 7.5	Macrographs of the Ni-20Cr coated superalloys after 1000 hrs exposure to platen superheater zone of the boiler at 900 °C: (a) Superni 75 (b) Superni 600 (c) Superni 601 (d) Superni 718 (e) Superfer 800H.	239
Fig. 7.6	Weight change vs. time plots for coated and uncoated Superni 75 subjected to 1000 hrs cyclic exposure to platen superheater zone of the coal fired boiler at 900 °C.	242
Fig. 7.7	(Weight change/area) ² vs. time plots for coated and uncoated superalloy Superni 75 subjected to 1000 hrs cyclic exposure to platen superheater zone of the coal fired boiler at 900 °C.	242
Fig. 7.8	BSE images for the bare and HVOF coated Superni 75 after 1000 hrs exposure to platen superheater zone of the coal fired boiler at 900 °C: (a) Bare superalloy (b) Cr ₃ C ₂ -NiCr coated (c) NiCrBSi coated (d) Stellite-6 coated (e) Ni-20Cr coated.	243
Fig. 7.9	Bar charts indicating the extent of corrosion for the bare and HVOF coated Superni 75 after 1000 hrs exposure to the coal fired boiler at 900 °C.	243
Fig. 7.10	X-ray diffraction patterns for the bare and coated superalloy Superni 75 after 1000 hrs exposure to platen superheater zone of the coal fired boiler at 900 °C.	244
Fig. 7.11	SEM/EDAX analysis showing elemental composition (Wt.%) for the bare and coated Superni 75 after 1000 hrs exposure to platen superheater zone of the coal fired boiler at 900 °C: (a) Bare Superni 75 (b) Cr ₃ C ₂ -NiCr coated (c) NiCrBSi coated (d) Stellite-6 coated (e) Ni-20Cr coated.	245
Fig. 7.12	Oxide scale morphologies and variations of elemental composition (wt%) across the cross section of bare and HVOF coated Superni 75 after 1000 hrs exposure to platen superheater zone of the coal fired boiler at 900 °C : (a) Bare Superni 75 (b) NiCrBSi coated.	248

Fig. 7.13	Composition image (BSEI) and X-ray mappings across the cross-section of bare Superni 75 after 1000 hrs exposure to platen superheater zone of the coal fired boiler at 900 °C.	249
Fig. 7.14	Composition image (BSEI) and X-ray mappings across the cross-section of Cr ₃ C ₂ -NiCr coated Superni 75 after 1000 hrs exposure to platen superheater zone of the coal fired boiler at 900 °C.	250
Fig. 7.15	Composition image (BSEI) and X-ray mappings across the cross-section of NiCrBSi coated Superni 75 after 1000 hrs exposure to platen superheater zone of the coal fired boiler at 900 °C.	251
Fig. 7.16	Composition image (BSEI) and X-ray mappings across the cross-section of Stellite-6 coated Superni 75 after 1000 hrs exposure to platen superheater zone of the coal fired boiler at 900 °C.	252
Fig. 7.17	Composition image (BSEI) and X-ray mappings across the cross-section of Ni-20Cr coated Superni 75 after 1000 hrs exposure to platen superheater zone of the coal fired boiler at 900 °C.	257
Fig. 7.18	Weight change vs. time plots for coated and uncoated Superni 600 subjected to 1000 hrs cyclic exposure to platen superheater zone of the coal fired boiler at 900°C.	258
Fig. 7.19	(Weight change/area) ² vs. time plots for coated and uncoated superalloy Superni 600 subjected to 1000 hrs cyclic exposure to platen superheater zone of the coal fired boiler at 900 °C.	258
Fig. 7.20	BSEIs for the bare and HVOF coated Superni 600 after 1000 hrs exposure to platen superheater zone of the coal fired boiler at 900°C: (a) Bare superalloy (b) Cr ₃ C ₂ -NiCr coated (c) NiCrBSi coated (d) Stellite-6 coated (e) Ni-20Cr coated.	259
Fig. 7.21	Bar charts indicating the extent of corrosion for the bare and HVOF coated Superni 600 after 1000 hrs exposure to the coal fired boiler at 900 °C.	259
Fig. 7.22	X-ray diffraction patterns for the bare and coated superalloy Superni 600 after 1000 hrs exposure to platen superheater zone of the coal fired boiler at 900 °C.	260
Fig. 7.23	SEM/EDAX analysis showing elemental composition (wt.%) for the bare and coated Superni 600 after 1000 hrs exposure to platen superheater zone of the coal fired boiler at 900 °C: (a) Bare Superni 75 (b) Cr ₃ C ₂ -NiCr coated (c) NiCrBSi coated (d) Stellite-6 coated (e) Ni-20Cr coated.	261

Fig. 7.24	Oxide scale morphologies and variations of elemental composition (wt%) across the cross section of HVOF coated Superni 600 after 1000 hrs exposure to platen superheater zone of the coal fired boiler at 900 °C : (a) Stellite-6 coated (b) Ni-20Cr coated.	262
Fig. 7.25	Composition image (BSEI) and X-ray mappings across the cross-section of bare Superni 600 after 1000 hrs exposure to platen superheater zone of the coal fired boiler at 900 °C.	263
Fig. 7.26	Composition image (BSEI) and X-ray mappings across the cross-section of Cr ₃ C ₂ -NiCr coated Superni 600 after 1000 hrs exposure to platen superheater zone of the coal fired boiler at 900 °C.	264
Fig. 7.27	Composition image (BSEI) and X-ray mappings across the cross-section of NiCrBSi coated Superni 600 after 1000 hrs exposure to platen superheater zone of the coal fired boiler at 900 °C.	265
Fig. 7.28	Composition image (BSEI) and X-ray mappings across the cross-section of a Stellite-6 coated Superni 600 after 1000 hrs exposure to platen superheater zone of the coal fired boiler at 900 °C.	266
Fig. 7.29	Composition image (BSEI) and X-ray mappings across the cross-section of Ni-20Cr coated Superni 600 after 1000 hrs exposure to platen superheater zone of the coal fired boiler at 900 °C.	271
Fig. 7.30	Weight change vs. time plots for coated and uncoated Superni 601 subjected to 1000 hrs cyclic exposure to platen superheater zone of the coal fired boiler at 900 °C.	272
Fig. 7.31	(Weight change/area) ² vs. time plots for coated and uncoated superalloy Superni 601 subjected to 1000 hrs cyclic exposure to platen superheater zone of the coal fired boiler at 900 °C.	272
Fig. 7.32	BSEIs for the bare and HVOF coated Superni 601 after 1000 hrs exposure to platen superheater zone of the coal fired boiler at 900 °C: (a) Bare superalloy (b) Cr ₃ C ₂ -NiCr coated (c) NiCrBSi coated (d) Stellite-6 coated (e) Ni-20Cr coated.	273
Fig. 7.33	Bar charts indicating the extent of corrosion for the bare and HVOF coated Superni 601 after 1000 hrs exposure to the coal fired boiler at 900 °C.	273
Fig. 7.34	X-ray diffraction patterns for the bare and coated superalloy Superni 601 after 1000 hrs exposure to platen superheater zone of the coal fired boiler at 900 °C.	274

Fig. 7.35	SEM/EDAX analysis showing elemental composition (wt.%) for the bare and coated Superni 601 after 1000 hrs exposure to platen superheater zone of the coal fired boiler at 900 °C: (a) Bare Superni 75 (b) Cr ₃ C ₂ -NiCr coated (c) NiCrBSi coated (d) Stellite-6 coated (e) Ni-20Cr coated.	275
Fig. 7.36	Oxide scale morphologies and variations of elemental composition (wt%) across the cross section of HVOF coated Superni 601 after 1000 hrs exposure to platen superheater zone of the coal fired boiler at 900 °C :(a) Cr ₃ C ₂ -NiCr coated (b) NiCrBSi coated.	276
Fig. 7.37	Composition image (BSEI) and X-ray mappings across the cross-section of a bare Superni 601 after 1000 hrs exposure to platen superheater zone of the coal fired boiler at 900 °C.	277
Fig. 7.38	Composition image (BSEI) and X-ray mappings across the cross-section of a Cr ₃ C ₂ -NiCr coated Superni 601 after 1000 hrs exposure to platen superheater zone of the coal fired boiler at 900 °C.	278
Fig. 7.39	Composition image (BSEI) and X-ray mappings across the cross-section of a NiCrBSi coated Superni 601 after 1000 hrs exposure to platen superheater zone of the coal fired boiler at 900 °C.	279
Fig. 7.40	Composition image (BSEI) and X-ray mappings across the cross-section of a Stellite-6 coated Superni 601 after 1000 hrs exposure to platen superheater zone of the coal fired boiler at 900 °C.	280
Fig. 7.41	Composition image (BSEI) and X-ray mappings across the cross-section of a Ni-20Cr coated Superni 601 after 1000 hrs exposure to platen superheater zone of the coal fired boiler at 900°C.	281
Fig. 7.42	Weight change vs. time plots for coated and uncoated Superni 718 subjected to 1000 hrs cyclic exposure to platen superheater zone of the coal fired boiler at 900 °C.	284
Fig. 7.43	(Weight change/area) ² vs. time plots for coated and uncoated Superni 718 subjected to 1000 hrs cyclic exposure to platen superheater zone of the coal fired boiler at 900 °C.	284
Fig. 7.44	BSEIs for the bare and HVOF coated Superni 718 after 1000 hrs exposure to platen superheater zone of the coal fired boiler at 900°C: (a) Bare superalloy (b) Cr ₃ C ₂ -NiCr coated (c) NiCrBSi coated (d) Stellite-6 coated (e) Ni-20Cr coated.	285
Fig. 7.45	Bar charts indicating the extent of corrosion for the bare and HVOF coated Superni 718 after 1000 hrs exposure to the coal fired boiler at 900 °C.	285

Fig. 7.46	X-ray diffraction patterns for the bare and coated Superalloy Superni 718 after 1000 hrs exposure to platen superheater zone of the coal fired boiler at 900 °C.	286
Fig. 7.47	SEM/EDAX analysis showing elemental composition (wt.%) for the bare and coated Superni 718 after 1000 hrs exposure to platen superheater zone of the coal fired boiler at 900 °C: (a) Bare Superni 75 (b) Cr ₃ C ₂ -NiCr coated (c) NiCrBSi coated (d) Stellite-6 coated (e) Ni-20Cr coated.	287
Fig. 7.48	Oxide scale morphologies and variations of elemental composition (wt%) across the cross section of Ni-20Cr coated Superni 718 after 1000 hrs exposure to platen superheater zone of the coal fired boiler at 900 °C.	292
Fig. 7.49	Composition image (BSEI) and X-ray mappings across the cross-section of a bare Superni 718 after 1000 hrs exposure to platen superheater zone of the coal fired boiler at 900 °C.	293
Fig. 7.50	Composition image (BSEI) and X-ray mappings across the cross-section of Cr ₃ C ₂ -NiCr coated Superni 718 after 1000 hrs exposure to platen superheater zone of the coal fired boiler at 900 °C.	294
Fig. 7.51	Composition image (BSEI) and X-ray mappings across the cross-section of a NiCrBSi coated Superni 718 after 1000 hrs exposure to platen superheater zone of the coal fired boiler at 900 °C.	295
Fig. 7.52	Composition image (BSEI) and X-ray mappings across the cross-section of a Ni-20Cr coated Superni 718 after 1000 hrs exposure to platen superheater zone of the coal fired boiler at 900 °C.	296
Fig. 7.53	Weight change vs. time plots for coated and uncoated Superfer 800H subjected to 1000 hrs cyclic exposure to platen superheater zone of the coal fired boiler at 900 °C.	297
Fig. 7.54	(Weight change/area) ² vs. time plots for coated and uncoated Superfer 800H subjected to 1000 hrs cyclic exposure to platen superheater zone of the coal fired boiler at 900 °C.	297
Fig. 7.55	BSEIs for the bare and HVOF coated Superfer 800H after 1000 hrs exposure to platen superheater zone of the coal fired boiler at 900°C: (a) Bare superalloy (b) Cr ₃ C ₂ -NiCr coated (c) NiCrBSi coated (d) Stellite-6 coated (e) Ni-20Cr coated.	298
Fig. 7.56	Bar charts indicating the extent of corrosion for the bare and HVOF coated Superfer 800H after 1000 hrs exposure to the coal fired boiler at 900 °C.	298

Fig. 7.57	X-ray diffraction patterns for the bare and coated Superfer 800H after 1000 hrs exposure to platen superheater zone of the coal fired boiler at 900 °C.	299
Fig. 7.58	SEM/EDAX analysis showing elemental composition (wt.%) for the bare and coated Superfer 800H after 1000 hrs exposure to platen superheater zone of the coal fired boiler at 900 °C: (a) Bare Superfer 800H (b) Cr ₃ C ₂ -NiCr coated (c) NiCrBSi coated (d) Stellite-6 coated (e) Ni-20Cr coated .	300
Fig. 7.59	Oxide scale morphologies and variations of elemental composition (wt%) across the cross section of bare and HVOF coated Superfer 800H after 1000 hrs exposure to platen superheater zone of the coal fired boiler at 900 °C :(a) Bare Superfer 800H (b) Stellite-6 coated.	303
Fig. 7.60	Composition image (BSEI) and X-ray mappings across the cross-section of a bare Superfer 800H after 1000 hrs exposure to platen superheater zone of the coal fired boiler at 900 °C.	304
Fig. 7.61	Composition image (BSEI) and X-ray mappings across the cross-section of a Cr ₃ C ₂ -NiCr coated Superfer 800H after 1000 hrs exposure to platen superheater zone of the coal fired boiler at 900 °C.	305
Fig. 7.62	Composition image (BSEI) and X-ray mappings across the cross-section of a Stellite-6 coated Superfer 800H after 1000 hrs exposure to platen superheater zone of the coal fired boiler at 900 °C.	306
Fig. 7.63	Composition image (BSEI) and X-ray mappings across the cross-section of a Ni-20Cr coated Superfer 800H after 1000 hrs exposure to platen superheater zone of the coal fired boiler at 900 °C.	307
Fig. 7.64	(a) (Weight change/area) ² vs. time plots, and (b) Weight change vs. time plots for uncoated superalloys subjected to 1000 hrs cyclic exposure to platen superheater zone of the coal fired boiler at 900 °C.	318
Fig. 7.65	Bar charts indicating the extent of corrosion for the bare superalloys after 1000 hrs exposure to the coal fired boiler at 900 °C.	318
Fig. 7.66	Schematic diagram showing probable hot corrosion mechanism for the uncoated superalloy exposed to 1000 hours in the actual environment of the coal fired boiler at 900 °C.	319
Fig. 7.67	Weight change vs. time plots for Cr ₃ C ₂ -NiCr coated superalloys subjected to 1000 hrs cyclic exposure to platen superheater zone of the coal fired boiler at 900 °C.	320

Fig. 7.68	Bar charts indicating the extent of corrosion for the Cr ₃ C ₂ -NiCr coated superalloys after 1000 hrs exposure to the coal fired boiler at 900 °C.	320
Fig. 7.69	Schematic diagram showing probable hot corrosion mode for the Cr ₃ C ₂ -NiCr coated superalloy exposed to 1000 hours in the actual environment of the coal fired boiler at 900 °C.	321
Fig. 7.70	Bar charts indicating the extent of corrosion for the NiCrBSi coated superalloys after 1000 hrs exposure to the coal fired boiler at 900 °C.	322
Fig. 7.71	Weight change vs. time plots for NiCrBSi coated superalloys subjected to 1000 hrs cyclic exposure to platen superheater zone of the coal fired boiler at 900 °C.	322
Fig. 7.72	Schematic diagram showing probable hot corrosion mode for the NiCrBSi coated superalloy exposed to 1000 hours in the actual environment of the coal fired boiler at 900 °C.	323
Fig. 7.73	Bar charts indicating the extent of corrosion for the Stellite-6 coated superalloys after 1000 hrs exposure to the coal fired boiler at 900°C.	328
Fig. 7.74	Schematic diagram showing probable hot corrosion mode for the Stellite-6 coated superalloy exposed to 1000 hours in the actual environment of the coal fired boiler at 900 °C.	328
Fig. 7.75	Bar charts indicating the extent of corrosion for the Ni-20Cr coated superalloys after 1000 hrs exposure to the coal fired boiler at 900 °C.	329
Fig. 7.76	Schematic diagram showing probable hot corrosion mode for the Ni-20Cr coated superalloy exposed to 1000 hours in the actual environment of the coal fired boiler at 900 °C.	329
Fig. 8.1	Bar charts showing cumulative weight gain (mg/cm ²) for the coated and uncoated superalloys subjected to cyclic oxidation in Na ₂ SO ₄ -60%V ₂ O ₅ environment at 900 ⁰ C for 50 cycles.	332
Fig. 8.2	Bar charts showing the extent of corrosion for the coated and uncoated superalloys after exposure to platen super-heater zone of the coal fired boiler at 900 °C for 1000 hours.	337
Fig. 8.3	Bar charts showing net weight change (mg/cm ²) for the coated and uncoated superalloys after exposure to platen super-heater zone of the coal fired boiler at 900 °C for 1000 hours.	337

LIST OF TABLES

Table No.	Particulars	Page No.
Table 2.1	General property criteria for coating systems for elevated temperature services (Sidky and Hocking, 1999).	39
Table 2.2	Comparison of characteristics for various thermal spray processes (Bhushan and Gupta, 1991; Stokes, 2003; Sobolev et al., 2004; Sidhu et al., 2005).	43
Table 2.3	Benefits of using HVOF coatings.	53
Table 4.1	Nominal composition and industrial applications of the superalloys used.	73
Table 4.2	Composition of the feedstock alloys, and shape and size of the particles.	74
Table 4.3	Spray parameters employed for HVOF coating.	74
Table 4.4	Chemical analysis of ash and flue gases inside the boiler.	81
Table 5.1	Major and minor phases identified by XRD analysis of the feedstock alloys.	84
Table 5.2	Average coating thickness and porosity of the HVOF coatings.	91
Table 5.3	Major and minor phases identified by XRD analysis of the as-sprayed coatings.	99
Table 6.1	Major and minor phases identified by XRD analysis of the hot corroded bare and coated Superni 75.	131
Table 6.2	Major and minor phases identified by XRD analysis of the hot corroded bare and coated Superni 600.	151
Table 6.3	Major and minor phases identified by XRD analysis of the hot corroded bare and coated Superni 601.	164
Table 6.4	Major and minor phases identified by XRD analysis of the hot corroded bare and coated Superni 718.	176

Table 6.5	Major and minor phases identified by XRD analysis of the hot corroded bare and coated Superfer 800H after 50 cycles.	190
Table 6.6	Summary of the results for uncoated and coated superalloys exposed to molten salt (Na_2SO_4 -60% V_2O_5) at 900 °C for 50 cycles.	203
Table 7.1	Major and minor phases identified by XRD analysis for the bare and coated Superni 75 hot corroded in actual boiler environment.	241
Table 7.2	Major and minor phases identified by XRD analysis for the bare and coated Superni 600 after 1000 hrs exposure to actual environment of the coal fired boiler.	254
Table 7.3	Major and minor phases identified by XRD analysis for the bare and coated Superni 601 after 1000 hrs exposure to actual environment of the coal fired boiler.	268
Table 7.4	Major and minor phases identified by XRD analysis for the bare and coated Superni 718 after 1000 hrs exposure to actual environment of the coal fired boiler.	283
Table 7.5	Major and minor phases identified by XRD analysis for the bare and coated Superfer 800H after 1000 hrs exposure to actual environment of the coal fired boiler.	291
Table 7.6	Summary of the results for the uncoated and coated superalloys exposed to platen superheater zone of the coal fired boiler at around 900 °C for 1000 hours.	308
Table A.1	Summary of oxidation of Fe-, Ni- & Co- base alloys in Na_2SO_4 and V_2O_5 environments.	346
Table A.2	Thermal expansion coefficients of substrate steels, coatings and oxides.	354

RESEARCH PUBLICATIONS

Research papers published out of the present investigation, in the peer-reviewed journals as well as presented/published in the conferences, are as follows:

(A) REFERRED JOURNALS

1. T.S. Sidhu, S. Prakash, and R.D. Agrawal, (2005) "State of the Art of HVOF Coating Investigation-A Review," *Marine Technology Society Journal*, Vol. 39, No. 2, pp. 55-66.
2. T.S. Sidhu, R.D. Agrawal, and S. Prakash, (2005), "Hot Corrosion of Some Superalloys and Role of High-Velocity Oxy-Fuel Spray Coatings—A Review," *Surf. Coat. Technol.* (Elsevier), Vol. 198, pp. 441-446.
3. T.S. Sidhu, S. Prakash, and R.D. Agrawal, (2005) "Studies on the Properties of High Velocity Oxy-Fuel Thermal Spray Coatings for Higher Temperature Applications", "*Physicochemical Mechanics of Materials*," Vol. 41, No. 6, pp. 80-95.
4. T.S. Sidhu, S. Prakash, and R.D. Agrawal, (2006), "Hot Corrosion Behaviour of HVOF Sprayed NiCrBSi Coatings on Ni- and Fe- Base Superalloys in Na₂SO₄-60%V₂O₅ Environment at 900 °C," *Acta Materialia* (Elsevier), Vol. 54, No. 3, pp. 773-784
5. T.S. Sidhu, S. Prakash, and R.D. Agrawal, (2006), "Characterisation of NiCr Wire Coatings on Ni- and Fe- Based Superalloys by HVOF Techniques," *Surf. Coat. Technol.* (Elsevier), Vol. 200, No. 18-19, pp. 5542-5549.
6. T.S. Sidhu, S. Prakash, and R.D. Agrawal, (2006), "Performance of High Velocity Oxy-Fuel Sprayed Coatings on a Fe-Based Superalloy in Na₂SO₄-60%V₂O₅ Environment at 900 °C. Part I: Characterisation of the Coatings, *J. Mater. Engg. Perform.* (ASM International), Vol. 15 No. 1, pp. 122-129.
7. T.S. Sidhu, S. Prakash, and R.D. Agrawal, S., (2006), "Performance of High Velocity Oxy-Fuel Sprayed Coatings on a Fe-Based Superalloy in Na₂SO₄-60%V₂O₅ Environment at 900 °C. Part II: Hot Corrosion Behaviour of the Coatings, *J. Mater. Engg. Perform.* (ASM International), Vol. 15, No.1, pp. 130-138.
8. T.S. Sidhu, S. Prakash, and R.D. Agrawal, (2006), "Hot Corrosion and Performance of Nickel Based Coatings," *Current Science*, Vol.90, No.1, pp. 41-47.
9. T.S. Sidhu, S. Prakash, and R. D. Agrawal, " Studies of the Metallurgical and Mechanical Properties of High Velocity Oxy-Fuel Sprayed Stellite-6 Coatings on Ni and Fe- Based Superalloys," *Surf. Coat. Technol.* (Elsevier), In Press, Available on-line.
10. T.S. Sidhu, S. Prakash, and R.D. Agrawal, (2006) "Characterisations of HVOF Sprayed NiCrBSi Coatings on Ni- and Fe- Based Superalloys and Evaluation of Cyclic Oxidation Behaviour of Some Ni-Based Superalloys in Molten Salt Environment" *Thin Solid Films* (Elsevier), In Press, Available on-line.

11. **T.S. Sidhu, S. Prakash, and R. D. Agrawal, (2006),** “Hot Corrosion studies of HVOF sprayed Cr_3C_2 -NiCr and Ni-20Cr Coatings on Nickel Based Superalloy at 900 °C,” *Surf. Coat. Technol.* (Elsevier), In Press, Available on-line.
12. **T.S. Sidhu, S. Prakash, and R. D. Agrawal, (2006)** “Hot Corrosion Resistance of HVOF Sprayed Coatings on a Ni-Based Superalloy in Molten Salt Environment,” *J. Therm. Spray Technol.* (ASM International), In Press.
13. **T.S. Sidhu, S. Prakash, and R. D. Agrawal, (2006),** “Hot Corrosion Studies of HVOF NiCrBSi and Stellite-6 Coatings on a Ni-Based Superalloy in an Actual Industrial Environment of a Coal Fired Boiler,” *Surf. Coat. Technol.* (Elsevier), In Press, Available on-line.
14. **T.S. Sidhu, S. Prakash, and R. D. Agrawal, (2006),** “Hot Corrosion Performance of a NiCr Coated Ni-based Alloy,” *Scripta Materialia* (Elsevier), Accepted for publication, Corrected Proofs submitted.
15. **T.S. Sidhu, S. Prakash, and R.D. Agrawal,(2006),** “Evaluation of Hot Corrosion Resistance of HVOF Coatings on a Ni-Based Superalloy in Molten Salt Environment,” *Mater. Sci. Engg. A* (Elsevier), Under review, Minor revisions submitted.
16. **T.S. Sidhu, S. Prakash, and R. D. Agrawal, (2006),** “Performance of HVOF sprayed Cr_3C_2 -NiCr Coating in Actual Boiler Environment of a Thermal Power Plant,” *Mater Letters* (Elsevier), Under Review.
17. **T.S Sidhu, S. Prakash and R.D. Agrawal, (2006)** “Characterisations and Hot Corrosion Resistance of Cr_3C_2 -NiCr Coating on Ni-base Superalloys in an aggressive Environment,” *J. Therm. Spray Technol.* (ASM International), Under Review.

(B) CONFERENCES

18. **T.S Sidhu, R.D. Agrawal and S. Prakash, (2004),** “Hot Corrosion of Some Superalloys and Role of High-Velocity Oxy-Fuel Spray Coatings—A Review,” 2nd International Conference on Technological Advances of Thin Films & Surface Coatings, THIN FILMS 2004, 13-17 July, 2004, Singapore, Paper ID: 34-TCR-A801.
19. **T.S, Sidhu, S. Prakash and R.D.Agarwal, (2004),** “Hot Corrosion Behaviour of Nickel Based Coatings”, Indo-Japan Conference on “Damage Tolerant Design and Materials”, December 16-18, 2004, IITM, Chennai, India.
20. **T.S Sidhu, S. Prakash and R.D. Agrawal, (2005),** “Characterisation of NiCrBSi Coatings on Ni- and Fe- Base Superalloys by HVOF Techniques”, International Conference on Surfaces, Coatings and Nanostructured Materials” 6-9 September 2005, University of Aveiro, Portugal. Paper No. FO-17.
21. **T.S Sidhu, S. Prakash and R.D. Agrawal, (2006)** “Characterisations and Corrosion Resistance of HVOF Sprayed Cr_3C_2 -NiCr Coating on Ni-base Superalloys at 900 °C in Molten Salt Environment, International Thermal Spray Conference & Exposition May 15-18, 2006 , Seattle, Washington, USA, Accepted for presentation

ABBREVIATIONS

APS	Air Plasma Spray
CVD	Chemical Vapour Deposition
PVD	Physical Vapour Deposition
HVOF	High Velocity Oxy-Fuel
LPSS	Low Pressure Plasma Spray
VPS	Vacuum Plasma Spray
LTHC	Low Temperature Hot Corrosion
HTHC	High Temperature Hot Corrosion
Bal	Balance
BSEI	Back Scattered Electron Image
XRD	X-ray Diffraction
SEM	Scanning Electron Microscopy
EDAX	Energy Dispersive X-ray Analysis
EPMA	Electron Probe Micro Analyser
hr	Hour
Kcps	Kilocycles per Second
k_p	Parabolic Rate Constant
M.P.	Melting Point
min	Minute
Wt. Gain	Weight Gain
Wt%	Weight Percentage
h.c.p.	Hexagonal Close-Packed
fcc	Face-Centered Cubic
FBC	Fluidized Bed Combustor
LPG	Liquefied Petroleum Gas
Hv	Vickers Hardness
mpy	Miles Per Year

Chapter 1

INTRODUCTION

Corrosion is the destruction or deterioration of a material over time due to its reaction with environment to form oxides or sulphides, or other metallic compounds, generally considered to be ores, as material's compositional elements have a natural tendency to return to their most thermodynamically stable state. Corrosion is both costly and dangerous. In addition to indirect costs due to shutdown and loss of efficiency, billions of dollars are spent annually for the replacement of corroded structures, machineries and equipments. Koch et al. (2002) reported that metallic corrosion costs in the United States are about \$300 billion per year, which is approximately 3.1% of the nation's Gross Domestic Product (GDP). This report on corrosion costs in the United States has drawn worldwide attention in every industry. In India, corrosion costs may exceed Rs. 240000 million per annum (Gupta, 2003). Apart from monetary costs it diminishes our natural resources. From human safety point of view, corrosion is considered more disastrous, as premature failure of bridges, structures or operating equipments can result in human injury or even loss of life.

1.1 HOT CORROSION

At higher temperatures degradation due to corrosion is known as oxidation or dry corrosion. Sometimes metals and alloys experience accelerated oxidation when their surfaces are covered with a thin film of fused salt in an oxidizing atmosphere at elevated temperatures. This mode of attack is called hot corrosion, where a porous non-protective oxide scale is formed at the surface and sulphides in the substrate. This form of corrosion, unlike oxidation, can consume the material at an unpredictably rapid rate. Consequently, the load-carrying^{*} ability of the components reduces quickly, leading eventually to catastrophic failure.

Hot corrosion can be defined as deposit modified gas-induced degradation of materials at higher temperatures. Eliaz et al. (2002) have defined the hot corrosion as an accelerated corrosion, resulting from the presence of salt contaminants such as Na_2SO_4 , NaCl , and V_2O_5 that combine to form molten deposits, which damage the protective surface oxides. The inability to either totally prevent hot corrosion or at least detect it at

an early stage has resulted in several accidents, leading to loss of life and/or destruction of engines/infrastructures.

Hot corrosion has been observed in boilers, internal combustion engines, gas turbines, fluidized bed combustion and industrial waste incinerators since 1940's. However, it became a topic of importance and popular interest in the late 1960's when gas turbine engines of military aircrafts suffered severe corrosion attacks while operating over and near sea water during the Vietnam conflict (Rapp, 1986 and 2002).

Due to depletion of high-grade fuels and for economic reasons, use of residual fuel oil in energy generation systems is well known. Residual fuel oil contains sodium, vanadium and sulphur as impurities. Sodium and sulphur react to form Na_2SO_4 (melting point $884\text{ }^\circ\text{C}$) in the combustion system, whereas during combustion of the fuel, vanadium reacts with oxygen to form an oxide V_2O_5 (melting point $670\text{ }^\circ\text{C}$). These compounds, known as ash, deposit on the surface of materials and induce accelerated oxidation (hot corrosion). Corrosion occurs when these molten compounds dissolve the protective oxide layers, which naturally form on materials during boiler/gas turbine operation. Moreover, the vanadium compounds are also good oxidation catalysts and allow oxygen and other gases in the combustion atmosphere to diffuse rapidly to the metal surface and cause further oxidation. As soon as the metal is oxidized, the cycle starts over again resulting into high corrosion rates. Similarly, in coal-gasification processes, hot corrosion is expected to be a serious problem because the gas environment generally has large sulphur and low oxygen activities and also contains substantial amount of salts (Natesan, 1976; Sharma, 1996).

Corrosion problems caused by low-quality fuels can be avoided by decreasing the steam temperature in superheaters. The boilers combusting low-chlorine coals operate with steam temperatures up to $570\text{ }^\circ\text{C}$ (Natesan, 1993), whereas boilers burning high-chlorine fuels, like waste (Kawahara, 1997) or black liquor (Tran et al., 1988) operate with steam temperatures below $500\text{ }^\circ\text{C}$. Unacceptable corrosion rates have occurred when biofuel fired boiler has been operated with steam temperature of 530°C (Salmenoja et al., 1996). However, these lower steam temperatures drastically decrease the efficiency of electricity production. On the other hand, in order to meet the demand for more electricity, the operating temperature and pressure of pulverized coal-fired boilers have to be increased (Blum, 1997). The combination of such high-temperatures with contaminants of environment and low grade fuels require special attentions to the phenomenon of hot corrosion.

The first technical publication on hot corrosion was contributed by Simons et al. (1955). They called it sulphidation and outlined a reaction mechanism involving metal sulphidation by Na_2SO_4 with emphasis on the accelerated oxidation of a sulphide–base eutectic. Seybolt (1968) modified the sulphidation mechanism and attributed Na_2SO_4 –induced hot corrosion of the Ni-Cr alloys to accelerated oxidation of the Cr-depleted alloy following the preferential internal sulphidation of chromium. By this mechanism, sulphide formation was considered as a prerequisite for the occurrence of accelerated oxidation, and this phenomenon was even called sulphidation. However, it has been found that sulphidation is not necessarily the critical mechanistic step in the hot corrosion. Bornstein and DeCrescente (1969 and 1971) did not observe the accelerated kinetics during the oxidation of three different presulphidised superalloys. However, a Na_2CO_3 or NaNO_3 coating gave rise to accelerated kinetics similar to Na_2SO_4 in spite of the absence of sulphur in the salt. They proposed a hot corrosion mechanism based on the (basic) dissolution of the protective oxide scale by a reaction involving Na_2O , the basic minority component of the fused salt. Goebel et al. (1970B and 1973) extended this mechanism to include acidic fluxing and oxide reprecipitation to account for the catastrophic oxidation caused by Na_2SO_4 for the alloys containing strong acidic components, such as V or Mo. These fluxing mechanisms are still accepted, and some quantitative aspects of oxide solubility (Otsuka et al., 1990; Rapp, 2002) and electrochemical reaction steps have been added in the literature (Kapoor, 1991).

1.2 PREVENTIVE MEASURES

Although corrosion is inevitable, its cost can be reduced considerably. It is reported that about 25% to 30% of annual corrosion costs can be saved if optimum corrosion control measures are employed (Koch et al., 2002). A number of countermeasures are currently in use or under investigation to combat hot corrosion such as using inhibitors, controlling the process parameters, designing a suitable industrial alloy and depositing protective coatings. However, the protection system to be selected for a particular application must be practical, reliable and economically viable.

Commercially available inhibitors can be used to reduce the severity of oil ash corrosion, particularly Mg and Mn-based inhibitors (Paul and Seeley, 1991). Use of inhibitors like MgO , CeO_2 , CaO , MnO_2 , etc. have already been investigated (Tiwari and Prakash, 1998; Gitanjaly et al., 2002) and the decrease in the extent of hot corrosion in the most aggressive environment of Na_2SO_4 -60% V_2O_5 at 900 °C has been achieved. However, their use in actual industrial environment is limited due to the practical

problems of injecting these inhibitors along with the fuel in the combustion chamber. Controlling the various process parameters of the boiler and gas turbine such as air/fuel ratio, temperature, pressure etc., are also useful to some extent to combat the corrosion, but these parameters can be controlled only within certain limits.

The iron- and nickel- base superalloys are commonly used for high-temperature applications and in aggressive environments of steam boilers, gas turbines etc. However, the presence of combustion gases constitutes an extreme environment and hot corrosion is inevitable when these alloys are used at high-temperatures for longer periods of time (Goebel et al., 1973). The corrosion resistance of the superalloys can be improved by adding fair amounts of Al and Cr, and small amounts of Y, Zr and Hf (Wang et al., 1989). However, these elements (such as Al, Cr) can be added only up to a limited extent as their higher concentrations adversely affects the mechanical properties of the alloys (Eliaz et al., 2002; Pomeroy, 2005). Another method to resist corrosion is coating the alloy with a protective layer using various surface treatment techniques. These composite materials perform better under extreme conditions, the base material provides the required mechanical strength and the coatings protect them against wear, erosion or corrosion (Li et al., 2003; Sidky and Hocking, 1999; Liu et al., 2001).

Due to continuously rising cost of the materials as well as increased material requirements, the coating techniques have been given much more importance in recent times. Coatings can add value to products up to 10 times the cost of the coating (Matthews et al., 1998). Diffusion coating and overlay coating are two basic coating systems that are often used to provide improved corrosion and oxidation resistance at higher temperatures, and, thereby extend the component life (Nicholls and Stephenson, 1991). Mevrel (1989) reported that as the operating temperatures of gas turbines have increased, it has become more difficult to achieve the required service lives using diffusion coatings, whereas overlay coatings have greater potential in aggressive environments at elevated temperatures.

Bai et al. (2004) have proposed many coating techniques for higher temperature applications such as pack cementation, plasma spraying and chemical vapour deposition. Among these coating techniques, the thermal spraying has grown into a well-accepted industrial technology for applying overlay coatings onto the surfaces of engineering components to allow them to function under the extreme conditions of wear, erosion-corrosion, high-temperature oxidation and hot corrosion (Yamada et al., 2002). Amongst the various thermal spray techniques, the High Velocity Oxy-Fuel (HVOF) process has been chosen for the current research.

1.3 HIGH VELOCITY OXY-FUEL (HVOF) PROCESS

The HVOF process is one of the most popular thermal spraying technologies and has been widely adopted by many industries due to its flexibility, cost effectiveness and the superior quality of the coatings produced. The HVOF process is a relatively recent thermal spray process (the Sulzer METCO Diamond Jet HVOF was developed in 1988), offering coatings with higher bond strengths and hardness, together with lower porosity, as compared with other thermal spray counterparts such as flame spraying, arc spraying, and plasma spraying (Parker and Kutner, 1991). The HVOF thermally sprayed coatings are used in a wide range of applications such as gas turbines, petroleum (Moskowitz, 1992), chemical, paper and pulp (Matsubara and Tomiguchi, 1992), energy conversion, automotive industries (Byrnes and Kramer, 1994; Fukutome et al., 1995), manufacturing industries (Perkin Elmer, 1989B), boiler super-heaters and pre-heaters, valve bodies and trim, and pipe systems (Tan et al., 2005).

As compared to vacuum plasma spraying (VPS), which is frequently used for deposition of corrosion and oxidation resistant materials, the HVOF systems operate in the open atmosphere, their investment costs are roughly one tenth of the cost of VPS, and process monitoring is easier (Irons and Zanchuk, 1993; Meyer, 1995). Moreover, the HVOF has the advantage of being a continuous and most convenient process for applying coatings to industrial installations on site.

The composition and structure of the coatings are determined by the role that they have to play in the various material systems and performance environments (Hocking, 1993). During service, the coatings are expected to form slowly growing protective oxides which should not allow the corrosive species to diffuse into the coating. These protective oxides should have a resistance to cracking or spallation under mechanical and thermal stresses induced during operation of the components. Further the coatings should also serve as a reservoir for the elements forming protective surface oxides (Gurrappa, 2001 and 2003; Hocking, 1993). Therefore, identification/development of suitable coatings is of great interest for higher temperature applications in boilers and gas turbines. In the present investigation, $\text{Cr}_3\text{C}_2\text{-NiCr}$, NiCrBSi , Ni-20Cr and Stellite-6 feedstock alloys have been selected to evaluate their hot corrosion behaviour in the laboratory as well as in the actual industrial environments, for applications of these coatings on the hot section components of boilers.

Chapter 2

LITERATURE REVIEW

Literature review relevant to the present study has been divided into three parts. First part contains a comprehensive review of the existing literature on hot corrosion, its characteristics and mechanisms, and the hot corrosion of nickel- and iron-based superalloys in the molten salt and boiler environments. In the second part, literature review concerning the protective coatings and High velocity oxy-fuel (HVOF) process has been described. The studies related to the behaviour of the coatings at higher temperatures have been reviewed in the third part of this chapter.

PART-I

2.1 HIGH-TEMPERATURE MATERIALS

Alloys that are used for structural components at higher temperatures in corrosive environments are generally austenitic and ferritic stainless steels and superalloys based on nickel, iron, and cobalt. They serve in a wide variety of environments where oxygen, sulphur, sodium, vanadium, halogens, and nitrogen are the aggressive reactive species most frequently encountered (Stroosnijder et al., 1994).

An increasing demand for more electricity, reduced plant emissions and greater efficiency is forcing power plants to increase the steam temperature and pressure of the boilers. Ultra-supercritical steam conditions greater than 31 MPa and 600 °C have been adopted and the thermal efficiency up to 45% have been obtained for the pulverized coal-fired boilers. Efforts are being made to further improve the efficiency of the boilers. Therefore, superheater and re-heater materials which have high creep rupture strength and high corrosion resistance at temperatures of about 750 °C and above are required (Blum, 1997; Evans et al., 2004). To meet this new strength and temperature requirement of boiler tube alloy, the usual ferritic and solid solution austenitic alloys must be excluded. Superalloy can be used to meet these stringent material targets in corrosive environments up to 1200 °C (Smith et al., 1999; Pettit and Meier, 1985).

The superalloys exhibit outstanding strength and surface stability at temperature up to 85% of their melting points. Usually the superalloys are used at temperatures above 540 °C (Metal Handbook, 1990). However, compared with steels, corrosion resistance of the superalloys is relatively less known (Smith et al., 1999; Castello et al. 2000). The superalloys are broadly classified as nickel-, cobalt- and iron-based alloys.

2.1.1 Nickel-Based Superalloys

The nickel-based superalloy may contain both chromium and aluminium at concentration levels sufficient to permit the selective oxidation of either aluminium or chromium. Hence, nickel base superalloys may be either alumina or chromia formers. Pettit and Meier (1985) reported that chromia scales can be stable up to temperature about 1000 °C and after this the formations of gaseous oxides of chromium becomes significant.

2.1.2 Iron-and Cobalt-Based Superalloys

The iron- and cobalt-based superalloys usually cannot be made to contain enough aluminium to permit them to be alumina formers while maintaining the necessary mechanical properties. Such alloys utilize a Cr₂O₃ scale to develop resistance against the oxidation/hot corrosion. Hence, their oxidation/hot corrosion resistance is less than that of the nickel-based superalloys which are alumina formers. Furthermore, even when considering the nickel-based superalloys that are chromia formers, as degradation begins the chromia scales are damaged, and a less protective oxide of nickel in significant quantities is formed on the nickel-based alloys as compared to iron and cobalt oxides on iron- and cobalt-based alloys, respectively. Since nickel oxides are more protective than iron and cobalt oxides, the drop-off in oxidation resistance is more abrupt in the case of iron- and cobalt-based alloys as compared to the nickel-based alloys (Pettit and Meier, 1985).

Pettit and Meier (1985) further reported that when sulphur is present in the environment, the nickel-based superalloys too have poor corrosion resistance as nickel sulphide phases result in the formation of non-protective scales. Chromium can be used to inhibit the onset of the effects produced by the reactants such as sulphur and carbon. Furthermore, carbides present in all the superalloys are preferentially attacked. Chromia is the only protective scale that can be formed over the carbides.

2.2 EFFECTS OF DEPOSITS ON THE SUPERALLOYS

Several very important engineering systems operating at high-temperatures (650-1100 °C) involve contact of metallic or ceramic materials with the gaseous combustion products or other oxidizing gases containing inorganic impurities, e.g. steam generators, incinerators, gas turbines, and numerous petrochemical process vessels. As the gases are cooled, fused salt deposits are formed on the hardware (Rapp, 1990).

Deposit of Na₂SO₄ upon the surface of superalloy is depicted schematically in Fig. 2.1. As evident from this figure, an important effect of the deposit is that it separates the superalloy from the gas environment. Since superalloys always contain elements that have high affinities for oxygen, an oxygen gradient is established across the deposit. This situation usually results in a lower oxygen activity over the surface of the alloy than what

would have been established in the absence of a deposit. Moreover, the activities of other reactants in the gas are increased. Such conditions make formation of selective oxide difficult. Further, as the exposure time increases and the scale is damaged by thermally induced stresses, eventually less protective oxides will be formed in the case of superalloys with foreign deposits on its surface (Pettit and Meier, 1985).

These condensed phases (deposits) can have undesirable effects on the protective oxide scales formed on the surface of the superalloys to develop resistance against attack. This type of deposit-modified corrosion (hot corrosion) is very severe when the condensed phase is liquid (Petit and Meter, 1985). Deposition of the condensed liquid film on the system hardware can result generally from one of the two processes (Rapp, 2002):

- Chemical deposition: when the vapour pressure of Na_2SO_4 in the vapour phase exceeds its equilibrium partial pressure for the substrate temperature, or
- Physical deposition: when some solid or liquid salt is attached to a hot substrate upon impact.

The effects of deposits on the superalloys have further been described by Pettit and Meier (1985) more effectively by using thermodynamic stability diagram shown in Fig. 2.2. This figure depicts the conditions that could develop when a deposit is formed on an alloy such as shown in Fig. 2.1. As a result of oxygen depletion, the sulphur pressure over the alloy increases, and the deposit also may become either basic or acidic in regards to its initial composition. Figure 2.3 shows the various examples of ash-deposition induced hot corrosion.

2.3 HOT CORROSION

Degradation of the metal and alloys induced by the condensed phases of the fused salts (deposits) in an oxidizing atmosphere at elevated temperatures is called hot corrosion. This type of deposit modified corrosion (hot corrosion) is more severe than the oxidation.

2.3.1 Hot Corrosion Characteristics

Hot Corrosion can crop up at high-temperatures, where the deposit is in the liquid state right from the beginning, or the solid deposit turns into liquid during the exposure as a result of reaction with the environment. These two types of hot corrosion processes are termed as Type I and Type II hot corrosions, and also called High Temperature Hot Corrosion (HTHC) and Low Temperature Hot Corrosion (LTHC), respectively (Eliaz et al., 2002; Khanna and Jha, 1998)

2.3.1.1 Type I Hot Corrosion (HTHC)

High temperature hot corrosion (HTHC), also called Type I hot corrosion, is observed mainly within the temperature range of 850–950°C (Hancock, 1987; Wright, 1987). This type of corrosion commences with the condensation of fused alkali metal salts on the surface of the components. Subsequently, a cycle of chemical reactions takes place, initially attacking the protective oxide film and progressing to deplete the chromium element from the substrate materials. With chromium depletion, oxidation of the base material accelerates and porous scale begins to form (Eliaz et al., 2002). Type I hot corrosion involves the transport of sulphur from a sulphatic deposit (generally Na_2SO_4) across a preformed oxide into the metallic material with the formation of the most stable sulphides. Once stable sulphide formers (e.g. Cr) have fully reacted with the sulphur moving across the scale, then base metal sulphides can form with catastrophic consequences as they are molten at the temperatures at which Type I hot corrosion is observed (Pomeroy, 2005). The dominant salt in HTHC is Na_2SO_4 due to its high thermodynamic stability. Other impurities present either in the fuel or in the air, such as vanadium, phosphorous, lead, and chlorides, can combine with Na_2SO_4 to form compounds with lower melting points, thus broadening the range of attack. For example, Na_2SO_4 (M.P. 884 °C) when combined with V_2O_5 (M.P. 670 °C), a eutectic is formed with a melting point of 550 °C, thus providing a very aggressing environment (Tiwari, 1997).

The macroscopic appearance of HTHC is characterized in many cases by severe peeling of the metal and by significant colour changes. For instance, greenish tone appears on the surface of metals and alloys due to the formation of NiO in the area of accelerated attack. Microscopically, the morphology of Type I is characterized by a sulphidised and depleted region beneath the porous, non-productive, scale. The reaction products frequently exhibit oxide precipitates dispersed in the salt film (Rapp, 1986).

2.3.1.2 Type II Hot Corrosion (LTHC)

Low temperature hot corrosion (LTHC), also called Type II hot corrosion, is observed mainly within the temperature range of 650–800°C (Jaffee and Stringer, 1979; Driver et al., 1981; Wright, 1987). It involves the formation of base metal sulphates which require a certain partial pressure of SO_3 for their stabilisation. These sulphates react with alkali metal sulphates to form low melting point eutectics (the melting temperature of the Na_2SO_4 – CoSO_4 eutectic is 540 °C) which prevent the formation of protective oxides (Pomeroy, 2005). In this type of corrosion, typical pitting occurs in the localized areas. A high partial pressure of SO_3 in the gaseous phase is required for the LTHC reactions to occur, in contrary to HTHC (Wright, 1987). The localized nature of

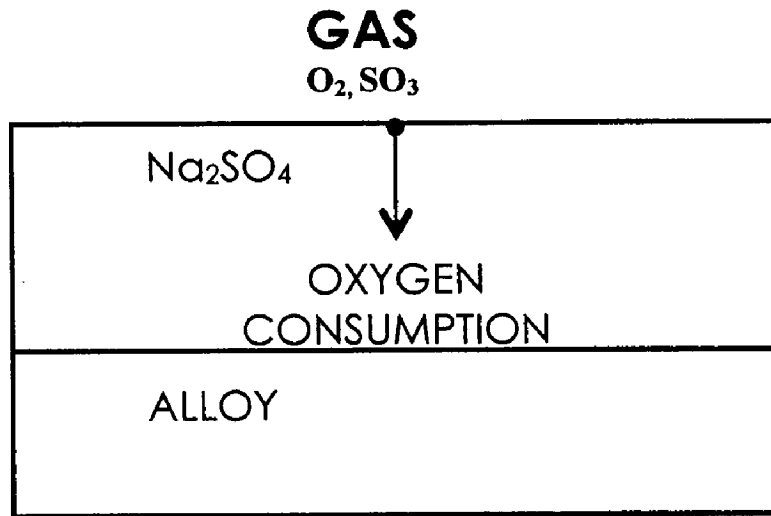


Fig. 2.1 Schematic diagram showing a Na₂SO₄ deposit upon an alloy separating the alloy from the gas phase (Pettit and Meier, 1985).

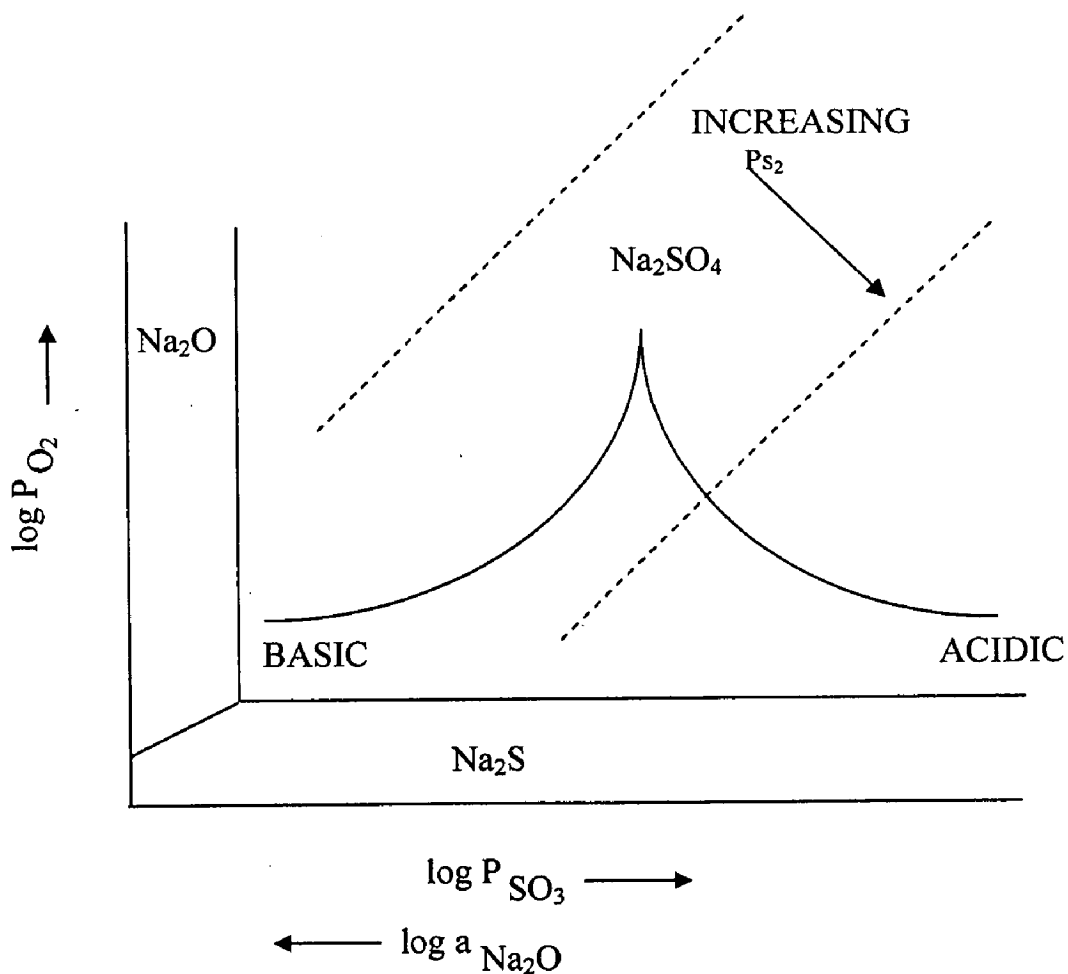


Fig. 2.2 Thermodynamic stability diagram for the Na-O-S system showing how composition of Na₂SO₄ may change due to alloy reacting with the deposit.

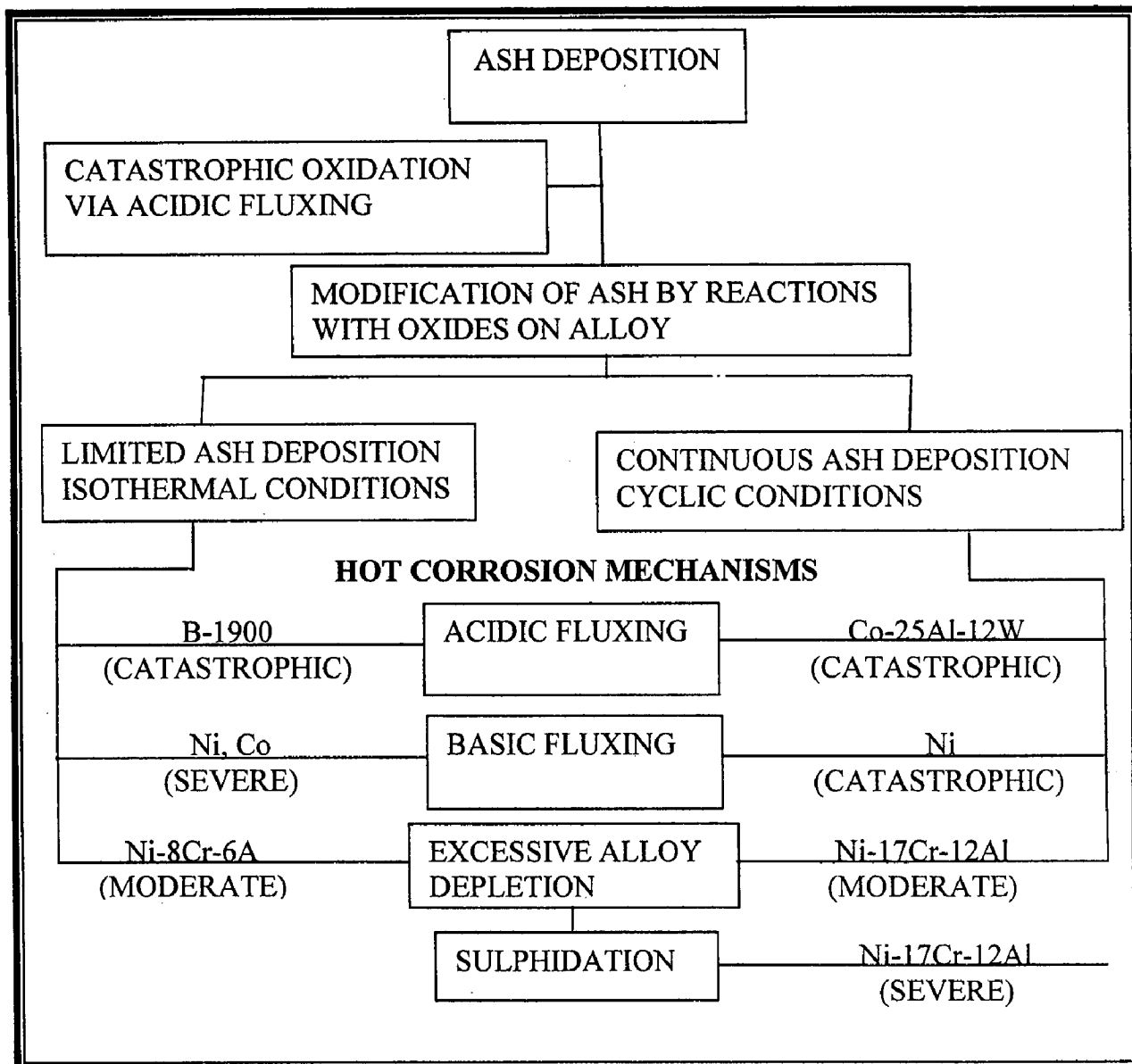


Fig. 2.3 Schematic of hot corrosion mechanisms (Natesan, 1976).

attack is related to localized failure of the scale as a result of thermal cycling, erosion, or chemical reactions. As opposed to Type I hot corrosion, in Type II neither microscopic sulphidation nor chromium depletion are generally observed (Driver et al., 1981; Santorelli et al., 1989).

2.3.2 Hot Corrosion Degradation of the Superalloys

The hot corrosion degradation of superalloys usually consists involves two stages (Pettit and Meier, 1985; Pettit and Giggins, 1987).

- An initiation stage during which the alloys behave much the same way as they would have behaved in the absence of the deposit, and
- A propagation stage when the deposit causes the protective properties of the oxide scales to become significantly different than the properties they would have in the absence of deposit. Such conditions are depicted schematically in Fig. 2.4.

Pettit and Meier (1985) reported that all corrosion resistant alloys degrade via these two stages, and it is the result of using selective oxidation to develop oxidation or corrosion resistance. The conditions causing hot corrosion, therefore, do nothing more than shortening the time for which the superalloys can form protective alumina or chromia scales via selective oxidation. During the initiation stage, the superalloys are preconditioned by the deposits in a way that determines the time after which selective oxidation is no longer possible and also determines the type of corrosion product scale that will be formed as the alloy enters the propagation stage.

The propagation stage of the hot corrosion sequence is the stage for which the superalloy must be removed from service since this stage always has much higher corrosion rates than that in the initiation stage (Pettit and Meier, 1985; Pettit and Giggins, 1987). Pettit and Giggins (1987) further opined that the hot corrosion degradation sequence is not always clearly evident. Sometimes, the initiation stage does not exist at all and the degradation process directly enters into the propagation stage. In some cases of hot corrosion, an increasing amount of sulphide particles are evident in the alloy beneath the protective reaction product barrier. In others, small holes are evident in the protective reaction product barrier where the molten deposit begins to penetrate. Eventually the protective barrier formed via selective oxidation is rendered ineffective, and the hot corrosion process enters into the propagation stage. Obviously in attempting to develop resistance to hot corrosion one should strive to see that the superalloys remain in the initiation stage as long as possible (Pettit and Meier, 1985).

Numerous factors, as shown in Fig. 2.4, affect the time at which the hot corrosion process moves from the initiation stage into the propagation stage. These factors also play the dominant role in determining the type of reaction product that is formed in the propagation stage (Pettit and Meier, 1985).

2.3.3 Mechanisms of Hot Corrosion Degradation of the Superalloys

From the literature review, it has been observed that there are varieties of conditions which can be considered for hot corrosion degradation of the superalloys. Research workers have proposed number of mechanisms for this type of degradation such as failure of oxide scale, sulphidation-oxidation and salt fluxing, oxide solubility, and effect of vanadium (Goebel and Pettit, 1970A; Goebel and Pettit, 1970B; Beltran and Shores, 1972; Rapp and Goto, 1981B; Pettit and Meier, 1985; Rapp, 1986; Stringer, 1987; Baxter and Natesan, 1989; Otsuka and Rapp, 1990; Zhang et al., 1993; Eliaz et al., 2002). These mechanisms can be considered in relation to each other rather than as completely different and unrelated corrosion process.

2.3.3.1 Failure of Oxide Scale

The initiation of high-temperature hot corrosion (HTHC) is often attributed to failure of the protective oxide layer, which allows the molten salt to access directly the substrate metal. Mechanical failure and sulphur penetration (or sulphide formation) are the two primary modes of breakdown of protective oxide scales (Baxter and Natesan, 1989). The mechanical failure is mainly due to stress build-up in the oxide and at the scale-metal interface that causes cracking and delamination of oxide scales or the failure may result from erosion or erosion-corrosion, etc.

Nucleation and growth of base-metal sulphides at the scale-gas interface are initiated by the penetration of sulphur into the oxide scale. The penetration of sulphur into the oxide can be either through solute diffusion along oxide grain boundaries (short-circuit diffusion) (Atkinson, 1988) or gas molecular transport via physical defects (pores or cracks) (Singh and Birks, 1979). The presence of sulphur in the oxide and at the scale-metal interface increases the outward flux of cations which form sulphides on the oxide surface (Singh and Birks, 1979).

Stott et al. (1984) proposed that sulphur-containing species, penetrating through localized short-circuit paths in the oxide, develop sulphide ducts from the scale-metal interface to the scale-gas interface. The sulphide ducts provide easier diffusion paths for the base-metal ions through the oxide to the surface, and eventually allow more rapid growth of sulphide nodules above the oxide. However, Natesan (1985) reported that no transport of sulphur into the oxide, or sulphide duct formation was necessary to form massive mixed iron and chromium sulphides at the oxide-gas interface. Based on the experimental results of sulphidation-oxidation of Incoloy 800, he reported that adsorption of sulphur by the oxide scale accelerates the transport of cations such as Fe and Ni from the substrate to the gas/scale interface and if the sulphur partial pressure in the gas is above that needed for base-metal sulphidation, the transported cations react with sulphur to form sulphides as an outer scale, external to the preformed chromium oxide layer.

HOT CORROSION CHRONOLOGY

Initiation Stage

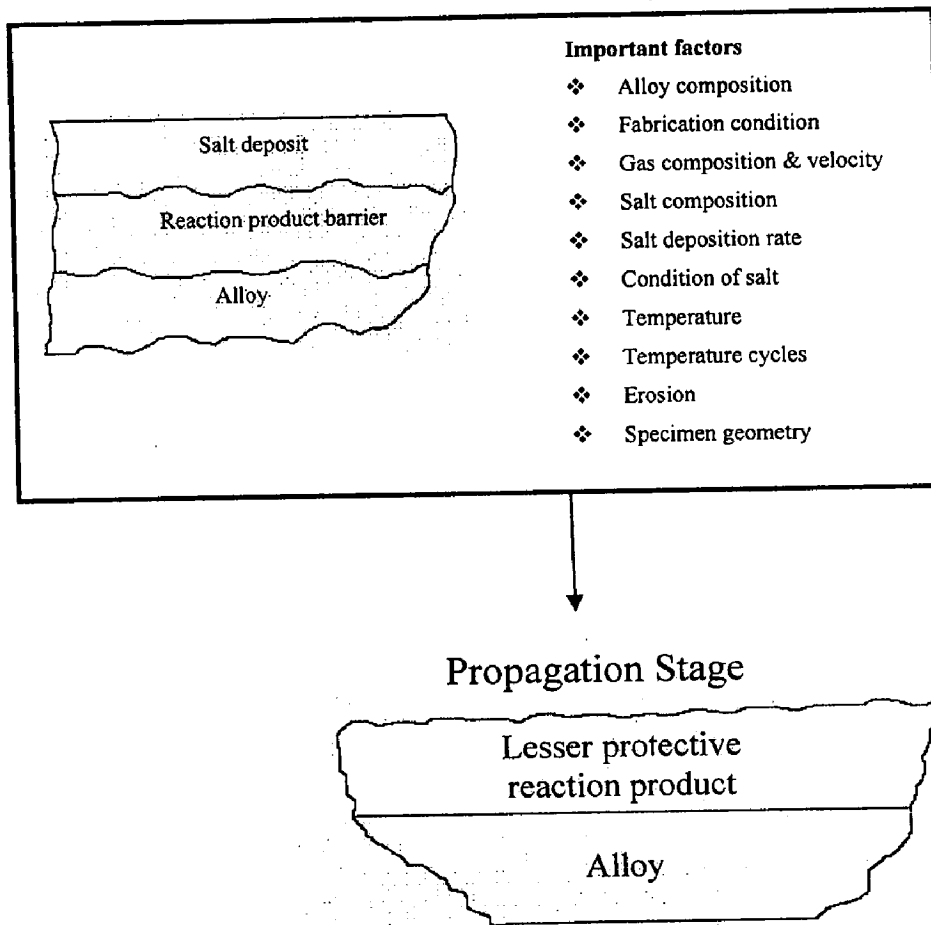


Fig. 2.4 Schematic diagram to illustrate the conditions that develop during the initiation and the propagation of hot corrosion attack, and to identify the factors that determine the time at which the transition from the initiation to the propagation stage occurs (Pettit and Meier, 1985).

2.3.3.2 Sulphidation-Oxidation and Salt-Fluxing Mechanisms

The mechanisms proposed for the HTHC propagation stage are the sulphidation-oxidation mechanism and the salt-fluxing mechanisms (Pettit and Meier, 1985; Stringer, 1987). Earlier works were focused on the effects of sulphur, as sulphides were often found in the microstructures of failure components. But it proved difficult to develop a coherent description of the process on this basis alone. It was not until about 1969 that the logical mechanisms which recognize the acid-base properties of molten Na_2SO_4 began to emerge (Bornstein and DeCrescente, 1969; Cutler, 1971; Goebel et al., 1973). Molten Na_2SO_4 containing dissolved sulphur trioxide (SO_3), from sulphur in fuels, is acidic, whereas the salt deficient in SO_3 or high in oxide ion concentration is basic. Dissolution of protective oxides on the acidic side is termed as 'acidic fluxing' and on the basic side as 'basic fluxing'.

According to the salt fluxing mechanism proposed by Goebel and Pettit (1970A and 1970B), the protection efficiency of the surface oxide layer might be lost as a result of fluxing of this layer in the molten salt. The fluxing can be caused either by combination of oxides with O^{2-} to form anions (i.e. 'basic fluxing'), or by decomposition of oxides into the corresponding cations and O^{2-} (i.e. 'acidic fluxing').

It is important to notice that the concentration of oxygen ions available for basic fluxing is limited by the amount of deposit present upon the surface of the superalloy. Hence basic fluxing reactions are not self-sustaining but require a continuous source of Na_2SO_4 in order to precede this type of degradation indefinitely. As opposed to the basic fluxing, the acidic fluxing can be self-sustaining, since the displacement of the salt from stoichiometry does not become progressively more difficult as the reaction proceeds (Stringer, 1987; Pettit and Meier, 1985). Therefore, acidic fluxing is more severe as compared to basic fluxing.

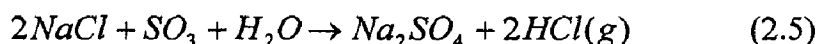
In general, the hot corrosion of the superalloys with high contents of aluminium and chromium is often reported to occur according to the basic fluxing mechanism. On the other hand, the hot corrosion of alloys with high contents of tungsten, molybdenum and vanadium is often reported to follow the acidic fluxing mechanism (Eliaz et al., 2002) and these elements, when oxidised in the presence of Na_2SO_4 , deposit on superalloys causing catastrophic self-sustaining hot corrosion (Pettit and Meier, 1985).

2.3.3.3 Oxide Solubility

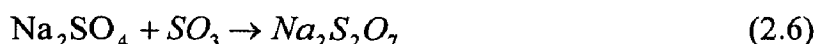
Rapp and Goto (1981B) proposed that protective scales on alloy become non-protective when the solubility gradients of the protective oxides in the molten deposit are negative, since continuous dissolution and re-precipitation of oxide is then possible. On the basis of oxide solubilities measurement in molten Na_2SO_4 as a function of the

together with fly ash on the pendant superheater and re-heater tubes in the boiler. Corrosion has been attributed to the fluxing action of the molten salt deposits on the oxide scales formed on the tubes, leading to rapid localised corrosion, accompanied by Sulphidation (Beltran and Shores, 1972; Rapp et al., 1981A).

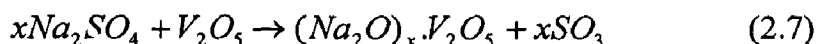
Khanna and Jha (1998) reported that the sulphur present in fuel oils yields SO₂ on combustion which is partially oxidised to SO₃. The NaCl (either as impurities in the fuel or in the air) reacts with SO₃ and water vapours at combustion temperatures to yield Na₂SO₄ as below:



At lower temperatures, Na₂SO₄ can further react with SO₃ to form sodium pyrosulphate, Na₂S₂O₇ with melting point (m. p.) of 401 °C:



Small amounts of vanadium may be present in fuel oils, which on combustion forms V₂O₅. This may further react with Na₂SO₄ to form low melting sodium vanadates, which are highly corrosive.



Thus metals and alloys in combustion gases are exposed to various corrosives such as O₂, SO₂/SO₃, molten salts, e.g. Na₂SO₄ or sulphate mixtures, sodium vanadates, NaCl etc. (Khanna and Jha, 1998).

2.4 HOT CORROSION IN THE MOLTEN SALT (NA₂SO₄-V₂O₅) ENVIRONMENT

Molten sulphate-vanadate deposits, resulting from the condensation of combustion products of residual fuels, are extremely corrosive to high-temperature materials in the combustion systems (Natesan, 1976). Luthra and Spacil (1982) carried out a thermochemical analysis of deposits in gas turbines for liquid fuels containing Na, S and V. They observed that the predominant species in the salt deposits formed on the gas turbine surfaces were Na₂SO₄, V₂O₅ and Na₂V₂O₆. This environment is also pertinent to the boilers. Barbooti et al. (1988) revealed that sodium vanadyl vanadate (Na₂O.V₂O₄.5V₂O₅), which melts at a relatively low temperature 550 °C, is found to be the most common salt deposit on boiler superheaters. Tiwari (1997) reported that the mixture of Na₂SO₄ and V₂O₅ in the ratio of 40:60 constitutes a eutectic with a low melting point of 550 °C and provides a very aggressive environment for hot corrosion to occur.

Kofstad (1988) has proposed that during combustion, the vanadium contaminants are oxidized to the higher valence vanadium oxides (V₂O₄ and V₂O₅) which react with sodium salts to form low melting point sodium vanadates (lowest M.P. 535 °C) such as (Na₂O)_xV₂O₄(V₂O₅)_{12-x}, (Na₂O)₅(V₂O₄)_x(V₂O₅)_{12-x}, NaVO₃, Na₄V₂O₇ and Na₃VO₄.

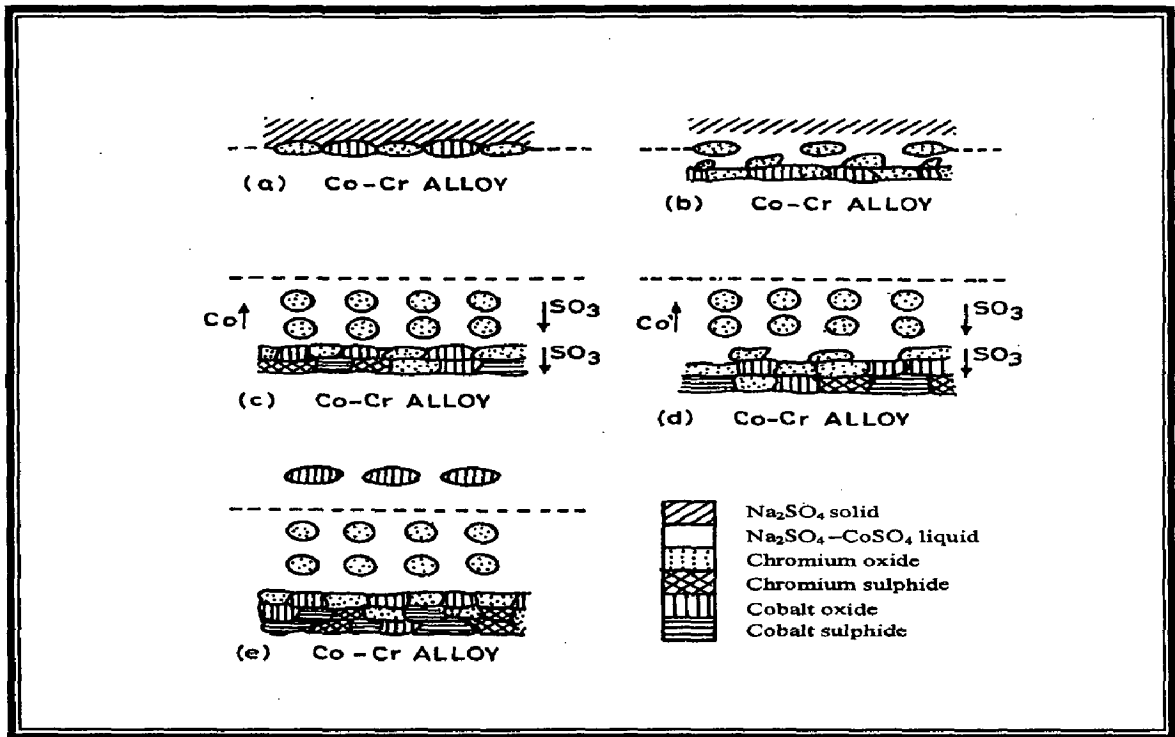


Fig. 2.5 Schematic representation of the reaction sequence during LTHC of a Co-30%Cr alloy exposed to O_2 - SO_2 - SO_3 environment where Na_2SO_4 - CoSO_4 liquid and Co_3O_4 are stable. At higher concentration of SO_3 where Co_3O_4 is unstable at the gas-salt interface, the outward migrating cobalt will form CoSO_4 (s) or Co_3O_4 and CoSO_4 (s) (Luthra, 1983).

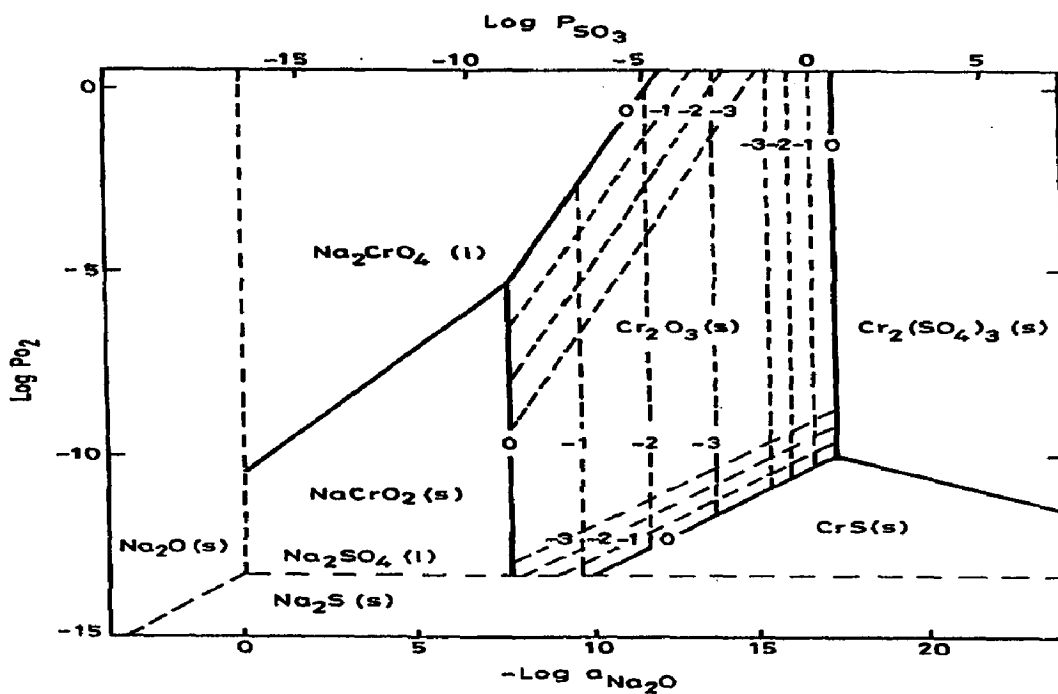


Fig. 2.6 Na-Cr-S-O phase stability diagram for 1200 K (Rapp, 1986).

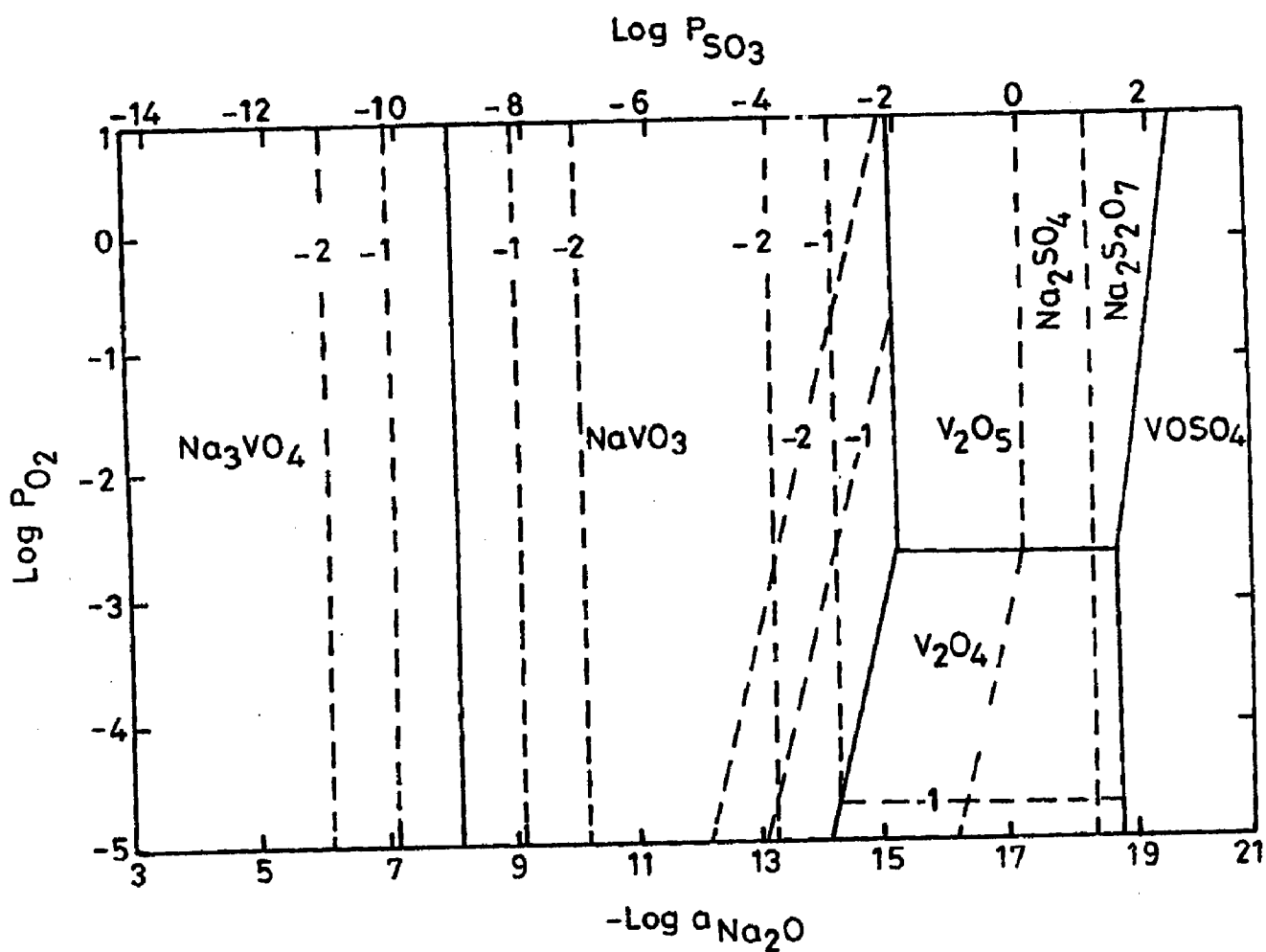


Fig. 2.7 Phase stability diagram for Na-V-S-O system at 900 °C (Hwang and Rapp, 1989).

Metal oxides dissolved in the vanadates may suppress the melting points and eutectic temperatures even further. He further reported that the slags developed on valves in diesel engines consist predominantly of sodium sulphate and sodium vanadates and have melting points as low as 400 °C. Singh (2003B) reported that a strong ability of vanadium to reduce in its lower oxidation state by consuming electrons released by sulphate ion oxidation is mainly responsible for the enhancement of the corrosion of the metals and alloys in the sulphates melts. Presence of V_2O_5 seems to act as an electron sink in the sulphate melts that consume electrons released by oxidizing components of the system. Electrons released during oxidation of sulphate ion, are consumed by vanadium which get reduced to its lower oxidation states. This process appears to enhance the hot corrosion of metals in sulphate melts.

Kolta et al. (1972) studied the kinetics of reactions between Na_2SO_4 and V_2O_5 . They concluded that the rate of reaction depends both on the temperature (600-1300 °C) and the molar ratios of Na_2SO_4 and V_2O_5 . They further revealed that with increase in the reaction period (>30 min.), the reaction rate decreased and finally reached to zero order. They attributed this decrease in the reaction rate to the formation of vanadosulphate complexes such as $(NaV_3O_8)_2 \cdot Na_2SO_4$ and $(NaVO_3)_2 \cdot Na_2SO_4$ which are decomposed at higher temperatures giving the meta- and pyro-vanadates respectively.

Hwang and Rapp (1989) studied the solubilities of oxides in the mixed sodium sulphate-vanadate solution containing 30 mole% vanadates. They reported that the basicity of the melt, oxygen partial pressure and proportion of V^{5+} and V^{4+} states of vanadate in the sulphate-vanadate solution decide the solubilities of oxides. Kofstad (1988) revealed that the solubilities of metal oxides may be high and are dependent on the Na:V ratio. The solubilities of Cr_2O_3 and Fe_2O_3 are highest (≈ 50 mol. %) at Na : V ratios close to 5 : 12. For NiO, the solubility is about 60 mol. % at Na : V = 3 : 2 which decreases to about 55 mol.% at Na : V = 5 : 12. As V_2O_5 is acidic, it will react with more basic oxides to form the corresponding vanadates.

Zhang and Rapp (1994) measured the solubility of CeO_2 as a function of melt basicity in a Na_2SO_4 -10mol.% $NaVO_3$ solution at 900 °C and 1 atm. oxygen. A comparison of the solubility in Na_2SO_4 -10mol.% $NaVO_3$ with the solubilities in both pure Na_2SO_4 and in Na_2SO_4 -30mol.% $NaVO_3$ was made. Their results indicated that CeO_2 dissolves in the salt solution either as a basic or as an acidic solute.

Sidhu et al. (2003) studied the hot corrosion behaviour of boiler tube steels namely ASTM-SA210 grade A1, ASTM-SA213-T-11 and ASTM-SA213-T-22 in air and molten salt environments of Na_2SO_4 -60% V_2O_5 at 900 °C. They found that all the steels show less resistance in the molten salt environment than in air. They reported that the presence

of vanadium, sodium and sulphur accelerates the rate of corrosion of boiler steels in the molten salt environment.

2.4.1 Hot Corrosion of the Iron and Iron-Based Alloys

Fairman (1962) reported severe corrosion of some metal specimens in an ash mixture ($V_2O_5 + 10\% Na_2SO_4$) environment in air. The corrosion attack was found to be greatest where the concentration of O_2 and V_2O_5 was higher, suggesting the transfer of oxygen atoms or ions by the pentoxide to the metal surface: $2V_2O_5 \rightarrow 2V_2O_4 + 2O \downarrow$. He opined that the accelerated oxidation is a diffusion controlled process of the incorporation of defects into the oxide scale. He further suggested that the mechanism of accelerated attack could be most satisfactorily explained by the catalytic action of V_2O_5 operating with an increase in the defect concentration of the scale.

Thilkan et al. (1967) studied the hot corrosion of nickel free austenitic stainless steel, Cr-Ni stainless steel and Inconel in an oxygen atmosphere at different temperatures and in an aggressive environment of vanadium-sodium salt of varying composition. They justified the use of saturated solution of Na_2SO_4 as the liquid medium because of its low gas solubility, vapour pressure and viscosity. They reported that threshold temperature lie between 700 and 800 °C. Above the threshold temperature the extent of attack initially increased but with increasing temperature either it became constant (as observed for Inconel) or decreased (for other alloys). Oxidation first increased and then decreased with increase in the amounts of Na_2SO_4 in the mixtures of sodium sulphate-vanadium pentoxide in temperature range 820-870 °C. However, at 950 °C all Na_2SO_4 additions decreased the corrosive effect of V_2O_5 . They revealed that fluidity of slag was important in allowing diffusion of oxygen. At lower temperatures, the fluidity might have a marked effect in increasing the attack. At higher temperatures, however, this may not have any effect on the corrosion rate as there may be negligible difference in the fluidity of fused V_2O_5 and $V_2O_5-Na_2SO_4$ mixture. They found an interesting observation that nickel free stainless steel has a high resistance to attack against $V_2O_5-Na_2SO_4$ mixture and under the experimental conditions shows a resistance superior to that of even Inconel at temperatures 850 °C specially in 70% V_2O_5 -30% Na_2SO_4 .

Kerby and Wilson (1972) revealed that the liquid vanadates increase the corrosion rate of metals by fluxing of the normally protective oxide layers present on the surface of the alloys and by providing a source of oxide ion for the corrosion reaction. The electrical conductivity increased with increase in temperature and with decreasing oxygen pressure. Incorporation of sodium into the V_2O_5 lattice structure caused a reduction in the valency of the vanadium atoms from V^{5+} to V^{4+} due to donation of the alkali metal valence electron to a vanadium atom.

Valdes et al. (1973) studied AISI 446 stainless steel under V_2O_5 and $Na_2O.6V_2O_5$ environment in the temperature range 700-900 °C in air and found that the oxide scale was mainly Cr_2O_3 with some vanadium oxide which acted as a moderate barrier to

corrosion. Above 850 °C in V₂O₅, a breakaway corrosion reaction occurred. No Cr₂O₃ oxide barrier was present but there was a continuous oxide scale that comprised of Cr₂O₃, Fe₂O₃ and V₂O₅ at the metal/oxide interface from which a region of crystals grew. They suggested that the addition of Na₂O to V₂O₅ increased the oxide ion (O²⁻) content of the melt and made it more aggressive to acidic oxides such as Cr₂O₃.

Kerby and Wilson (1973) examined the rates of liquid vanadate corrosion of iron, nickel and several other Ni, Cr containing alloys and the rates of corrosion were found to depend on temperature, oxygen partial pressure, the composition, amount and turbulence of the liquid vanadates, composition of the metal or alloys in contact with the liquid vanadates and duration of the corrosion tests. They observed that the corrosion scales present on Armco iron specimens after cooling consisted of a thick, porous, outer oxide scale and a compact, slightly porous, inner oxide scale.

Tiwari and Prakash (1996 and 1997) and Tiwari (1997) have reported hot corrosion studies on some industrial superalloys in temperature range 700-900 °C in the environments comprising of pure Na₂SO₄, Na₂SO₄-15%V₂O₅ and Na₂SO₄-60%V₂O₅. The corrosion rates were observed to be very high in the environment having Na₂SO₄-60%V₂O₅ composition. The extremely corrosive nature of this composition was attributed to its low melting point i.e. 550 °C. Tiwari and Prakash (1997) further revealed that in Na₂SO₄-60%V₂O₅ melt, the degradation was due to the cracking of the protective scale under the influence of the fluxing action of the melt for both Fe-base alloy Superfer 800H and Co- base alloy Superco 605. The enhanced degradation was reported to be due to the presence of tungsten in form of Na₂WO₄-WO₃ compound. No oxidation and sulphidation into the substrate was observed by them in Co-based alloy. Tewari (1997) concluded that the Co-based alloy has inferior corrosion resistance than the Ni-base alloy in Na₂SO₄-60%V₂O₅ environment at 900 °C.

Almeraya et al. (1998A) conducted electrochemical studies on AISI-SA-213-TP-347H steel in 80 wt% V₂O₅ + 20 wt% Na₂SO₄ at temperature 540 °C–680 °C and reported the corrosion rate values of around 0.58-7.14 mm/year. They found an increase in the corrosion rate with time. However, the corrosion potential was observed to be decreasing with increase in temperature from 540 °C to 680 °C. Almeraya et al. (1998B) further conducted electrochemical studies of hot corrosion of type 347H stainless steel under same environment and temperature range, and revealed that with change in temperature from 540 °C to 680 °C the corrosion potential decreased.

Cuevas-Arteaga et al. (2001) used LPR (Linear Polarisation Resistance) and weight loss techniques, in their hot corrosion study on alloy 800 in Na₂SO₄-20%V₂O₅, and reported a slightly higher corrosion rate at 900 °C than at 700 °C. They further reported

that in both the techniques, the corrosion rate increased in the beginning of the experiment but decreased later on until steady values reached.

Singh (2003A) studied the hot corrosion of GrA1, T11 and T22 boiler steels in an environment of Na_2SO_4 -60% V_2O_5 at 900 °C and observed that the Mo containing T22 steel showed least resistance to the hot corrosion attack. This was attributed to the formation of a low melting point MoO_3 phase, which reacted with molten salt resulting in formation of Na_2MoO_4 . This low melting point oxide was suggested to cause the acidic fluxing of the protective scale.

Singh et al. (2005C) investigated the hot corrosion behaviour of an iron-base superalloy in molten salt (Na_2SO_4 -60% V_2O_5) environment at 900 °C under cyclic conditions for 50 hours and found that the superalloy underwent severe spalling and sputtering and the weight gain was enormous during the course of study.

Sidhu et al., 2006C reported that iron-base superalloy Superfer 800H underwent intense spalling, sputtering (disintegration of the scale accompanied by cracking sound during cooling) and peeling of the scale in an aggressive environment of Na_2SO_4 -60% V_2O_5 at 900 °C. During the cyclic study for 50 hours, the mass gained by the superalloy was enormous. It was found that the mass increased continuously, although the rate of increase was high during the initial period of exposure. This rapid increase in mass gain was attributed to the formation of NaVO_3 compound. This NaVO_3 acts as a catalyst and also serves as an oxygen carrier to the base alloy that leads to the rapid oxidation of the basic elements of the superalloy to form the protective oxide scale. Slower increase in mass gain after initial mass gain was due to the simultaneous growth and dissolution of oxide scale in the molten salt due to the reaction $\text{Cr}_2\text{O}_3 + 4\text{NaVO}_3 + 3/2\text{O}_2 \rightarrow 2\text{Na}_2\text{CrO}_4 + 2\text{V}_2\text{O}_5$. This Na_2CrO_4 gets evaporated as a gas.

2.4.2 Hot Corrosion of the Nickel and Nickel-Based Alloys

Several studies have been reported on the hot corrosion of Ni-based high-temperature alloys in a vanadate-sulphates melt. Bornstein et al. (1973) studied the vanadium oxide and Na_2SO_4 induced accelerated oxidation for nickel-based superalloy B-1900 and seven binary nickel-based alloys. They reported that the protective oxide scale formed on the superalloy was dissolved into the fused salt. The dissolution occurred by a reaction between oxide ions present in melt and the oxide scale. They opined that the sulphidation attack can be inhibited by decreasing the oxide ion content of the fused salt.

Bornstein et al. (1975) again studied the effect of vanadium and sodium on the accelerated oxidation of the nickel based alloys. Liquid V_2O_5 has been proposed to be an excellent flux and easy path for oxygen diffusion. They attributed the initial rapid rate of oxidation between V_2O_5 and metal substrate to the reduction of V_2O_5 by the substrate. They concluded that the sulphidation attack can be attenuated if the initial oxide ion

content of the melt is prevented from increasing. Oxides such as Cr_2O_3 have been reported to react preferentially with oxide ions.

Dooley and Wilson (1975) hot corroded a 50Cr-50Ni commercial alloy in a pure V_2O_5 and in a vanadate melt containing sodium sulphate and chloride in the temperature range 750 to 950 °C in a rotating disc apparatus. The authors reported the formation of chromium rich oxide scale in pure V_2O_5 melt, which dissolved slowly into the liquid melt and thus acts as a barrier layer. However in $\text{Na}_2\text{O} \cdot 0.6\text{V}_2\text{O}_5$, this barrier layer was not observed. A marked internal oxidation of the Cr-rich α -phase was noticed in the chloride containing melts throughout the temperature range 750-950 °C.

Rapp and Goto (1981B) have hypothesized that presence of multivalent metal ions in vanadate-sulphates melt could greatly accelerate the hot corrosion rate either by counter diffusion of multivalent cations or else by electron hopping which provides the fast transport of charge through the deposited layer.

Iyer et al. (1987A) studied the hot corrosion cracking behaviour of Nimonic 80A in a flue gas atmosphere containing Na, S, V at 600-700 °C under tensile stress. They explained hot corrosion degradation of the alloy on the basis that sulphur reacts with chromium to form CrS at 600 °C which decomposes into Cr_2O_3 and SO_2 and then SO_2 escapes into atmosphere. In case of vanadium, large quantities of oxides such as NiO, Cr_2O_3 , $\text{Ni}(\text{VO}_3)_2$, $\text{NiO} \cdot \text{Cr}_2\text{O}_3$ were formed. Cr_2O_3 formed a non-protective sodium chromate (yellow stains) and hence further oxidation of nickel took place and the scale spalled off. They suggested that the mechanism was not self sustaining at 600 °C and attack of S was not very severe. They further reported that a eutectic of Ni-Ni₃S₂ formed at 650 °C penetrated along the grain boundaries at 700 °C and caused severe self sustaining attack.

The mechanisms of the hot corrosion by the molten sulphate-vanadate deposits were investigated by Sidky and Hocking (1987). They studied the hot corrosion of Ni-10Cr, Ni-30Cr, Ni-20Cr-3Al, Ni-21Cr-0.3Si, Ni-20Cr-5V and IN738 superalloys. The effect of addition of Cr to Ni was found to be beneficial in the Na_2SO_4 melt. However, on increasing the VO_3^- concentration in the melt, this effect diminished, and became harmful in pure NaVO_3 due to the formation of the non protective CrVO_4 . According to them, alloying element Al was found to be harmful in Na_2SO_4 - NaVO_3 melts. Cr depletion was observed in rich VO_3^- melts but internal corrosion was more obvious in the SO_4^{2-} rich melts. Corrosion in rich VO_3^- melts was aggressive due to the fluxing action of the salt, which takes place along internally sulphidised areas. According to their study, IN738 suffered tremendous internal attack due to its γ precipitates which became sulphidation prone areas, and were fluxed by the VO_3^- melt.

Seiersten and Kofstad (1987) studied the sulphate and vanadate induced corrosion at 650 to 800 °C. They reported that the corrosion caused by the sodium sulphate/sodium vanadate mixtures have a complex mechanism. Samples coated with sodium vanadate were exposed to O₂ + 4% SO₂ and the initial reaction was observed to be same as that observed in pure oxygen. After an incubation period, the duration was found to decrease with increasing temperature and sufficient SO₃ got dissolved in the molten vanadate that formed a mixture of NiSO₄ and Na₂SO₄ near the metal. When a molten NiSO₄-Na₂SO₄ solution containing small amounts of vanadate, was formed as an intermediate layer, the reaction reportedly proceeded as sulphate-induced hot corrosion. They concluded that the corrosion mechanism changed from initial vanadate-induced to essentially sulphate induced hot corrosion when the sulphur trioxide pressure was high enough to form sodium sulphate.

Otero et al. (1987) investigated the hot corrosion behaviour of IN657 (46.5 Cr, 1.32 Nb, bal-Ni) at 635 °C in a molten salt environment of 60:40 V₂O₅:Na₂SO₄ (Mol%). They characterised the morphology and chemical compositions of the corrosion products and found that the presence of sulphur and its oxidised compounds favour the formation of isolated lobes with radial morphology. These lobes had great permeability which facilitated the access of oxygen; therefore the protection character of the scale was reduced. They reported that the presence of vanadium and its oxidised products generate compounds with aciculate morphology, which is not very much covering and reduces the protective character of the scale. The equilibrium diagram for varying composition of Na₂SO₄ is shown in Fig. 2.8 and the mixture of Na₂SO₄-60%V₂O₅ is seen to have the lowest eutectic temperature.

Otero et al. (1990) again studied the hot corrosion behaviour of the same alloy IN657 in same molten salt environment 60%V₂O₅-40%Na₂SO₄. They observed that for duration less than 100 hours, the corrosion kinetics increased with temperature when the temperature was less than 727 °C. For temperatures greater than 727 °C, corrosion rate decreased. An increase in corrosion rate with temperature observed during the initial stages of exposure was related to the higher fluidity of the molten salt mixture. At temperatures greater than 727 °C, once the appropriate fluidity was achieved, the corrosion rate decreased due to the decrease in the oxygen solubility in the molten salt.

Otsuka and Rapp (1990) examined the effects of chromate and vanadate anions on the hot corrosion of Ni by a thin fused Na₂SO₄ film in an SO₂-O₂ gas atmosphere at 900°C. The results indicate that the inhibition of sulphidation may be due to the precipitation of solid Cr₂O₃ from the melt which partially seals/plugs the crack defects and grain boundaries of the original protective oxide layer. Further, they found that

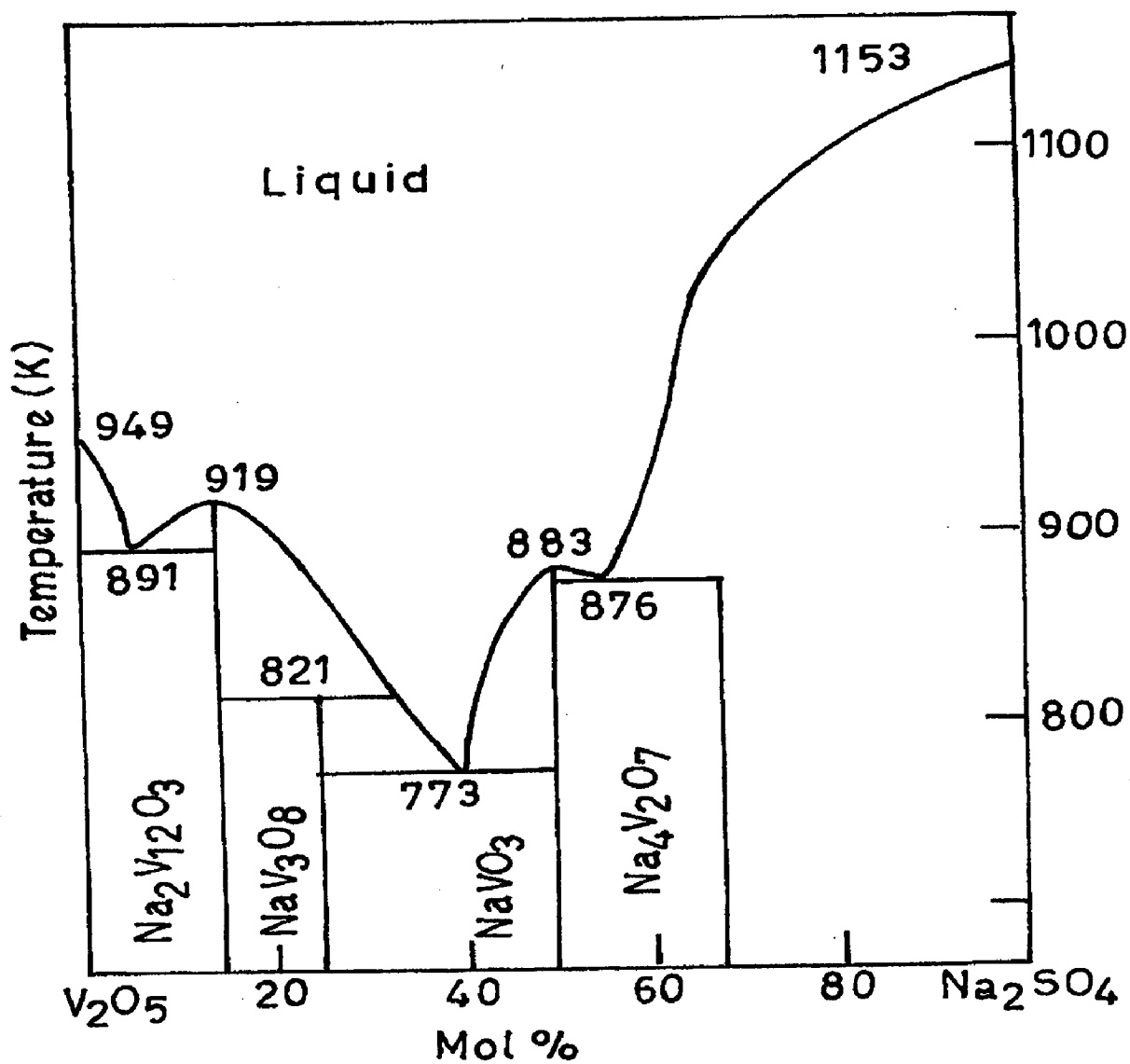


Fig. 2.8 Phase Diagram for Na_2SO_4 - V_2O_5 System (Otero et al, 1987).

vanadate anions enhanced the onset of the hot corrosion and sulphidation probably via rapid dissolution of the protective oxide scale at cracks/defects or grain boundaries.

The oxidation and hot corrosion studies of nickel based alloys in Na_2SO_4 -60% V_2O_5 environment at 700 °C were carried out by Lambert et al. (1991) to investigate the effects of Si addition. The chemical compositions (wt.%) of these alloys were Ni-17Cr-6Al-0.5Y and Ni-16Cr-5.7Al-0.47Y-5Si. They found that an outer layer of NiO developed on the surface of the standard alloy whereas a thin Al_2O_3 scale formed on the Si enriched alloy. They opined that the condensed vanadates of sodium are highly corrosive and can markedly increase the rate of oxidation of nickel-based superalloys. According to them, the development of protective oxide barrier was considerably affected by the corrosive coating, particularly in the Si-enriched alloy. They detected Ni, Cr, Al and Si complex oxides in the inner oxide layer.

Swaminathan and Raghvan (1992) reported that the cracking and fluxing of the protective scales together with easier crack nucleation and growth at grain boundaries in the presence of liquid deposits of sodium metavanadate and sodium metavanadate plus 15wt% sodium sulphate at 650-750 °C account for the enhanced creep rates and reduced rupture life for Superni-600.

Swaminathan and Raghvan (1994) further studied Superni-C276 in the presence of NaVO_3 and NaVO_3 -15% Na_2SO_4 at 650, 700 and 750 °C. They reported similar findings of an enhanced creep damage at all test temperatures. They opined that the degradation of the alloy in case of NaVO_3 melt was due to the cracking of the protective scales under the influence of the applied stress and the fluxing action of the melt. They further reported that eutectic $\text{NaVO}_3 + 15\text{wt}\% \text{Na}_2\text{SO}_4$ mixture was more severe in degrading the creep properties. They found that addition of sodium sulphate to sodium metavanadate increased the corrosivity of the deposit by lowering the melting point and by the formation of molten Ni-NiS₂ eutectic which initiates a self sustaining hot corrosion. Further, they revealed that the additional presence of molybdenum compounds Na_2MoO_4 - MoO_3 enhanced the degradation.

Swaminathan et al. (1993) studied the hot corrosion behaviour of Ni-base superalloy Nimonic 80A, Hastelloy C-276 and Superni 600 coated with different amounts of V_2O_5 for a period of 100 hrs at 650, 700 and 800 °C in air by the weight change measurement. They revealed that the hot corrosion kinetics obeyed a parabolic rate law. The rapid increase in weight of alloys at the initial hours was due to the ease of diffusion of nickel and oxygen ions in the molten V_2O_5 . Once the compact solid vanadate $\text{Ni}_3\text{V}_2\text{O}_8$ layer was formed, the short circuit diffusion paths were blocked and diffusion became difficult for the oxygen ions to move towards the metal surface.

Deb et al. (1996) in their study on the hot corrosion behaviour of a cast nickel-based superalloy coated with 60% Na₂SO₄-30% NaVO₃-10% NaCl observed a thin layer of NiO, followed by a thick layer of Ni₃(VO₄)₂ and a inner porous duplex layer of oxides of Ni and Cr and CrS. They observed that the corrosion rate decreased with time, which they attributed to the formation of refractory nickel vanadate layer over the surface. The authors also conducted studies in 100% Na₂SO₄ and 75% Na₂SO₄ + 25% NaCl molten salt environment. They revealed that the presence of sulphur in the form of sulphates caused internal sulphidation of the alloy beneath the external oxide layer. Further, volatile species of chlorides led to formation of voids and pits at grain boundaries, which provide easy path for the corrodents to penetrate into the alloys. They observed that the presence of vanadate in conjunction with sulphate and chloride provided additional fluxing action, which destroyed the integrity of the alloy and weakened its mechanical properties.

Gurrappa (1999) studied the hot corrosion behaviour of Ni-base superalloy CM 247 LC in Na₂SO₄ and Na₂SO₄+NaCl mixtures at 900 °C. The author observed that the superalloy CM 247 LC got severely corroded in just 4 hr, while it was completely consumed in 70 hr when tested in 90%Na₂SO₄+10%NaCl at 900 °C. The life of the superalloy, however, further decreased to just 2 hours when studied in 90%Na₂SO₄+5%NaCl+5%V₂O₅ environment at 900 °C.

Gitanjaly (2003) studied the hot corrosion performance of some Ni-, Fe- and Co-based superalloys in an environment of Na₂SO₄+60%V₂O₅ at 900 °C. In general, the author observed significant corrosion rates in all the superalloys. However, the Ni-based superalloy Superni 75 showed lowest rate of corrosion compared to Co-base superalloy Superco-605. The better corrosion resistance of Ni-base superalloys was attributed to the presence of refractory nickel vanadate Ni(VO₃)₂ which acted as a diffusion barrier for the oxidising species. The proposed hot corrosion mechanisms of this study for the superalloys Superni 75 and Superni 601 have been schematically shown in Fig. 2.9.

Tzvetkoff and Gencheva (2003) reviewed the mechanism of formation of corrosion layers on nickel and nickel-based alloys in melts containing oxyanions. They reported that acidic oxides such as those of V and Mo induce rapid fluxing of the oxide scale and therefore catastrophic hot corrosion. The chromates were stated to be beneficial for the repassivation of the surfaces following fluxing of the oxide scale by the molten salt. Further, they reported that the molten sulphate mixtures are aggressive towards Ni superalloys. In such environments, the formation of Cr-rich passive films such as spinel-type oxides could be protective to some extent. They further detected the presence of sulphides at metal/oxide interface which do not offer plausible protection except for a possible positive role of MoS₂ formed on Ni alloys containing significant amounts of Mo.

Singh (2003B) studied the effect of V_2O_5 on the sulphate ion reduction and its influence on the hot corrosion of metal in the sulphates melt. The author reported that addition of V_2O_5 in the melt increases the hot corrosion of nickel extensively. According to Tafel plots measurement, corrosion or oxidation rate of nickel increases more than two orders of magnitude higher in the presence of 3% V_2O_5 in $(Li,Na,K)_2SO_4$ melt at 550 °C.

Singh et al. (2005D) investigated the corrosion behaviour of a nickel-base superalloy in Na_2SO_4 -60% V_2O_5 environment at 900 °C under cyclic conditions for 50 cycles of one hour each. They used thermogravimetric technique to establish the kinetics of corrosion. They revealed that superalloy Superni 601 showed intense spalling of the scale and the weight gain, including the spalled scale, was enormous during hot corrosion studies in the given aggressive environment. They reported continuous increase in the weight of the superalloys, but the rate of increase was high during the initial period of exposure. They revealed that $NaVO_3$ formed due to the reaction of Na_2SO_4 -60% V_2O_5 acts as a catalyst and also serves as a oxygen carrier to the metal. The chromium has high affinity for oxygen to form Cr_2O_3 and so in the earlier stages of hot corrosion, there was rapid increase in weight.

Prakash et al. (2005) studied the hot corrosion behaviour of another Ni-based superalloy under the same conditions and at same temperature. They reported that the superalloy suffered a catastrophic corrosion in the form of intense spalling and sputtering of the scale. They attributed this behaviour to the presence of Mo in the alloy, as oxides of Mo cause an alloy-induced acidic fluxing.

2.5 SOME STUDIES ON ENERGY GENERATION SYSTEMS

The phenomenon of accelerated corrosion at high-temperatures occurs on the heating surfaces of furnaces super-heaters or re-heaters of power station boilers, due to the deposition of ashes during combustion processes. Ashes usually have high concentrations of compounds of vanadium, sodium and sulphur, mainly as Na_2SO_4 - V_2O_5 complex and sodium-vanadates mixtures. Vanadium, sodium and sulphur are often present as impurities in residual oils used as fuel (Harada and Kawamura, 1980; Harada et al., 1981; Wong-Moreno and Salgado, 1995). Some mixtures of these compounds have low melting points (480 to 510 °C) which are lower than the metallic surface temperatures. Therefore, these compounds turn into liquid state and increase the corrosion rates (Cuevas-Arteaga et al., 2004).

Pantony and Vasu (1968A) explained the process of the fire side corrosion of boilers and gas turbines in the presence of vanadium pentoxide with the help of a schematic diagram Fig. 2.10. They divided the process into six stages, any of which can be a rate-controlling. In the system, stages 1, 2 and 6 would be governed by the physical properties of the melt while stage 4 would be controlled by the physical nature and

impurities of metal surface, together with the chemical properties of the metal and the melt. Stages 3 and 5 would be influenced by the physical and chemical properties of both the melt and products of corrosion to such an extent that the associated barrier may not exist at all. They mentioned that if any of the stages 1, 2, 3, 5 or 6 were rate controlling, the process was likely to be diffusion controlled with relatively low activation energy while if stage 4 was rate-controlling, then the whole process would be activation-controlled with relatively high activation energy. Pantony and Vasu (1968B) further mentioned that the vanadic corrosion could be viewed as a two-stage diffusion process, viz. an inward diffusion of oxygen and an outward diffusion of the corrosion products away from the surface. Kofstad (1990) explained these diffusion processes with the help of neat sketches shown in Fig. 2.11, which illustrate the growth of chromia scale in the presence or absence of oxygen active elements.

Boilers and other steam power plant equipments are subjected to a wide variety of failures involving one or more of several mechanisms. Overheating is reported to be the main cause of failure in steam generators. A survey compiled by one laboratory over a period of 12 years, encompassing 413 investigations, listed overheating as the cause in 201 failures or 48.7% of those investigated. Fatigue and corrosion fatigue were listed as the next most common causes of failure accounting for 89 failures or 21.5%. Corrosion, stress corrosion and hydrogen embrittlement caused a total of 68 failures or 16.5%. Defective or improper material has been cited as the cause of most of the remaining failures (13.3%). Although "defective material" is often blamed for a failure but this survey indicates that statistically it is one of the least likely cause of failure in power plant equipments (Metals Handbook, 1975).

Iyer et al. (1987B) studied the hot corrosion behaviour of Nimonic 80A under tension using combustion gases environment at 600-700 °C and reported the presence of NiO, Cr₂O₃, Ni(VO₃)₂ and NiO.Cr₂O₃ on the surface of the corroded alloy. Accelerated oxidation was observed and the scale was reported to be spongy. They observed that the lowest melting liquid was formed even at 550 °C. They suggested that the presence of stresses enhanced the damage due to spalling, allowing fresh surface to be exposed to hot corrosion. They proposed that as vanadium content increases some of the vanadium participates as vanadates and, therefore, increase in vanadium beyond a certain level is not monotonically aggressive. This critical level was found to be around 20 ppm vanadium. Also at high-temperature, the stability of V₂O₅ would decrease resulting in critical level of V for the worst corrosion attack.

Moujahid (1987) observed severe ash corrosion, mechanical deformation and cracks on the cast iron chains of moving grate used to air burning of coal. Liquid coal ash at 1300 °C, strongly acidic, dissolves the basic wustite/spinel layers which formed on the chains at elevated temperature. The fused ash embeds coal particles and also reduces the

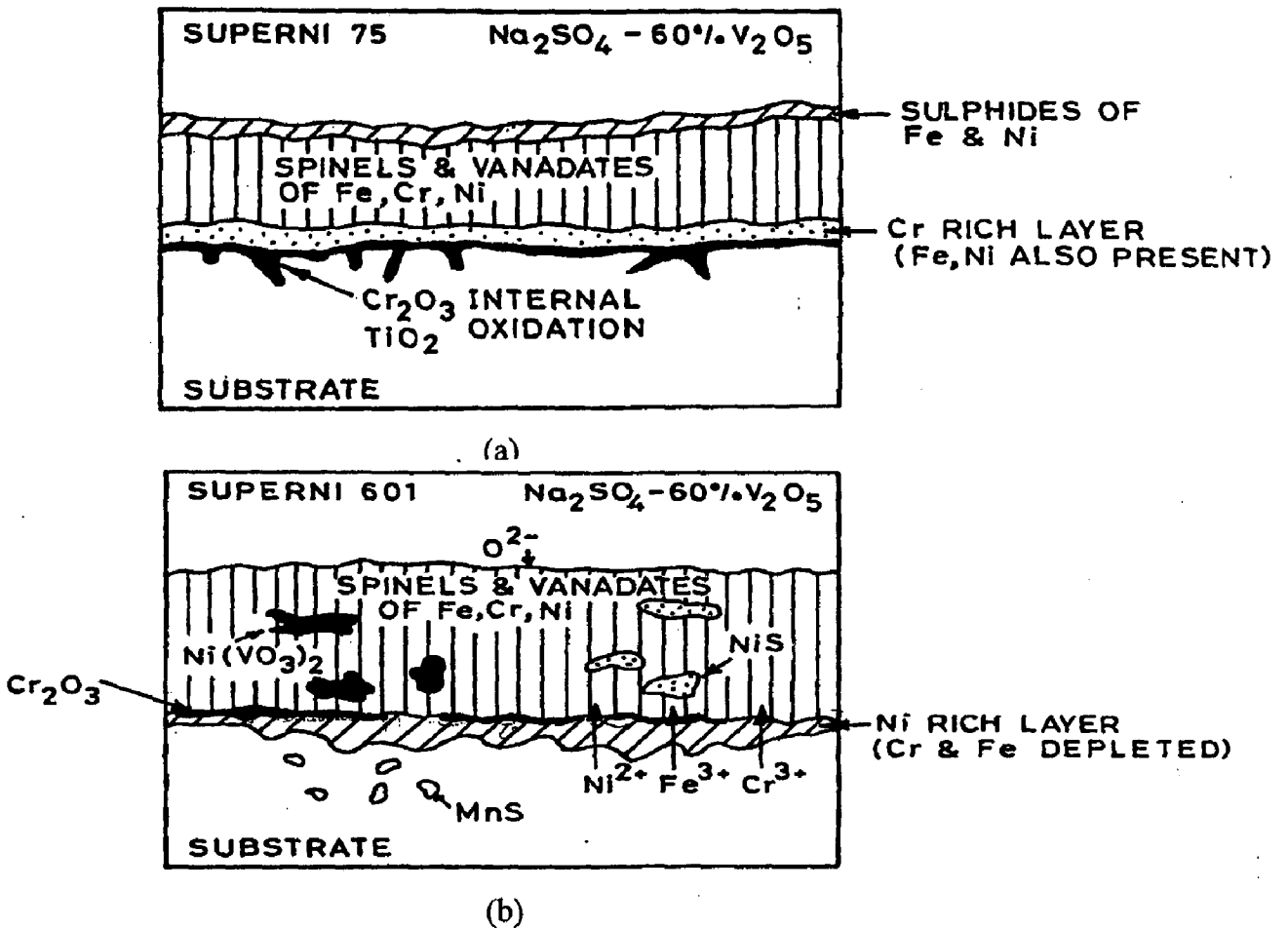


Fig. 2.9 Schematic diagram showing probable hot corrosion mechanism in Na_2SO_4 - $60\%\text{V}_2\text{O}_5$ after exposure for 50 cycles at 900°C for alloys (Gitanjaly, 2003)
 (a) Superni 75 (b) Superni 601.

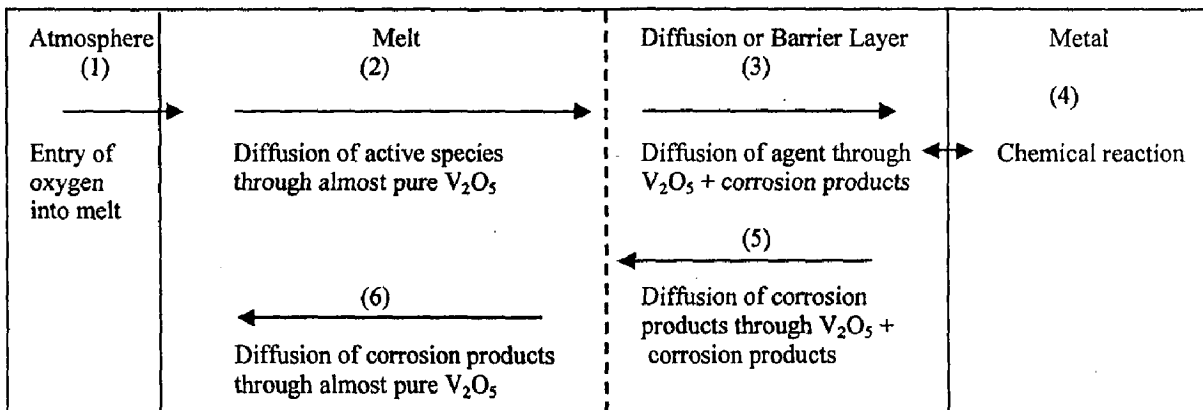


Fig. 2.10 Sequential steps in the vanadic corrosion of metals (Pantony & Vasu, 1968A)

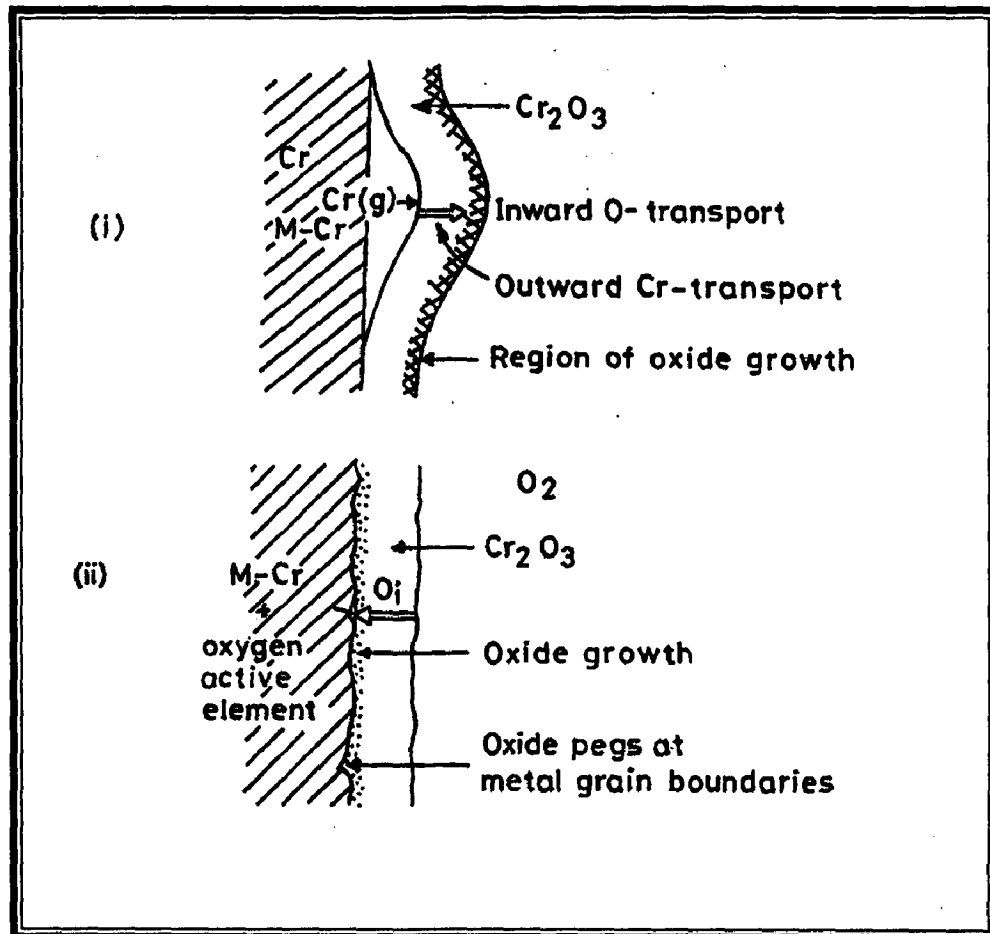


Fig. 2.11 Schematic illustration of the growth of chromia scales in (i) the absence of oxygen active elements and with predominant outward transport of chromia through the scale, and (ii) the presence of oxygen active elements and with predominant inward transport of oxygen (Kofstad, 1990).

thermal efficiency of the equipment. Drastic enhancement in ash corrosion rate has been attributed to the mechanical damages.

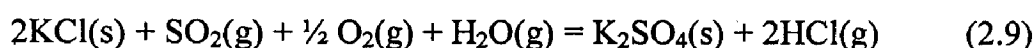
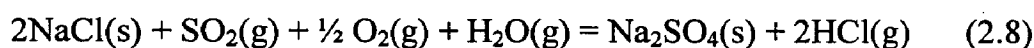
Levy (1993) observed unacceptable levels of degradation of heat exchanger tubes in some boilers, particularly fluidized bed combustors, by a combined mechanism of erosion-corrosion. The author noticed that the extent of such degradation varied considerably, both between different boilers and within the same boiler operating on different feedstocks. However, primarily same erosion-corrosion mechanism occurred in all cases that has integrated both chemical and mechanical behaviour of the base metal and the boiler particles. They revealed the formation of a continuous and dynamic surface layer that consists of a mechanical mixture of particles from the boiler gases and oxide scale growing from the base metal. It was constantly refurbished and removed at a rate that resulted in an essentially constant thickness of the deposit/scale layer during steady state operation of the boiler. So the loss of sound metal is related to the rate of oxidation of metal.

Colot et al. (1997) investigated the corrosion of 9 Cr-Mo (T91 and EM12) steels in synthetic environments similar to those experienced by tubes in the coal-fired boilers. They compared the effects of water vapour, SO₂ and ash deposits with and without alkali salts on the corrosion of steels in ambient air in the temperature range 460 -800 °C. In the synthetic atmospheres, maximum corrosion rate was observed approximately at 600 °C which they attributed to the effect of water vapour and/or SO₂. They reported that the alkali silicates are responsible for high rates of corrosion as temperature reaches 800 °C.

Saunders et al. (1997) studied high-temperature corrosion behaviour of FeCr alloy and three iron aluminides alloys containing 16 and 28 at% Al with up to 5 at% Cr in simulated coal gasification conditions containing 1000 ppm HCl at 450 and 550 °C and 3283 ppm HCl at 550 °C for 1000 hrs. They used higher HCl level at 1 bar in the laboratory experiments to simulate a gasifier operating at 10 bar with a coal containing 0.3% Cl. According to them, intermetallic alloys containing 28 at% Al and 2-5 at% Cr showed exceptional resistance to attack even in the most aggressive conditions with mass gains of generally less than 1 g m⁻². The corrosion resistance was somewhat reduced for the lower Cr alloy. For the most aggressive test conditions, the intermetallic alloys were found to exhibit superior resistance to attack as compared with FeCr alloy, but a 16 at% Al intermetallic with 5 at% Cr showed the lowest corrosion resistance among the materials investigated.

Prakash et al. (2001) reported a case study on boiler tube failure in the coal fired power plants in north-western region of India, covering a period of one year. . They described that total 89 failures occurred in the study period, out of which 50 failures were attributed to the hot corrosion and erosion by ash. They further investigated five samples of failed boiler tubes selected randomly from the same installation. They found overheating as another main cause of tube failures.

Otsuka (2002) studied the effects of fuel impurities on the fireside corrosion of boiler tubes in advanced power generating systems. He reported that high-temperature corrosion of boiler tubes in the coal-fired boiler results from formation of liquid phase, complex sulphates such as $(\text{Na,K})_3\text{Fe}(\text{SO}_4)_3$ in the deposits. He observed that Na_2SO_4 and K_2SO_4 compounds were vapour condensed from flue-gas on tube surfaces, while Fe_2O_3 is considered to accumulate by impingement/adhesion of fly-ash particles, containing solid Fe_2O_3 , onto superheater tube surfaces. For boilers firing high-chlorine high-sulphur coal, he concluded that sodium and potassium sulphates vapours condensed from flue-gases to form deposits on the metal surface, whereas chloride condensation was not evident. This was attributed to the high-sulphur content of coal, which changed chloride salts to sulphate salts in tube deposits, according to the following reactions:



Krishna and Sidhu (2002) observed severe pitting corrosion of carbon steel tube in the air preheater of a power plant. They reported that corrosive species settled at the tube surface due to the extended non operation of the plant. The complete failure of the tubes occurred due to diffusion of these elements into the base metal and precipitation of potassium and chlorine compounds along the grain boundaries with subsequent dislodging of grains. Further they reported that the nonmetallic inclusions acted as nucleating sites for local pitting bursting. Nonuniform heat transfer during operation accelerated the selective corrosion of front-end tubes and relatively high heat transfer resulted in condensation of some corrosive gases and consequent corrosion. Continuous operation of the plant with some precautions during assembly of the tubes reduced the corrosion problem.

Wang and Pan (2003) studied the high-temperature corrosion of a boiler material (SB450) using simulated combustion environment of an actual boiler's service conditions, at 750 and 850 °C using carbon steel with 2 mg cm^{-2} NaCl coating. The combustion environment was produced by burning ASTM 2D diesel oil or an emulsion thereof with 10% water. The experimental results indicate that both the higher temperature and the water vapours in the atmosphere promoted metal loss. The metal loss of SB450 in the atmosphere that contained water vapours, resulting from the burning of emulsified oil, was more than that obtained by burning just the diesel oil. They reported that water vapour contributed to higher SO_2 concentrations in the gas produced, thus, SB450 suffers sulphidation more seriously in an atmosphere that contains water vapours than in one obtained by burning diesel oil and, therefore, it deteriorates more rapidly.

Uusitalo et al. (2003) performed high-temperature corrosion tests on ferritic and austenitic boiler steels, using simulated biofuel combustion conditions at 550 °C for 1000 h. The tests were performed in oxidizing atmosphere containing 500 vppm HCl, 20% H₂O, 3% O₂, and Ar the balance. The author reported that the chromium oxide layer formed on the austenitic steel was more protective than the iron oxide layer on the ferritic steel. He further reported that oxides formed in presence of chlorine reduced the corrosion rate but they were not protective. The oxides on the ferritic steel spalled off. The chromium oxide layer on the austenitic steel was observed to be discontinuous and cracks in the oxide layer were also detected. Some chlorine-containing corrosion products of iron, chromium and nickel are reported to be volatile at test temperature.

Zhao et al. (2005A) studied the corrosion of a new nickel-based superalloy, INCONEL alloy 740, at 550 and 700 °C using a simulated pulverized coal-fired environment as coal ash plus flue gas. The synthetic coal ashes were composed of (wt.%): 5 Na₂SO₄, 5 K₂SO₄, 30 Al₂O₃, 30 SiO₂, 30 Fe₂O₃ and the synthetic flue gas were composed of (vol.%): 15 CO₂, 3.5 O₂, 0.25 SO₂, 81.25 N₂. They reported the formation of thin oxide scale on the samples corroded at 550 °C. The hot corrosion, which was characterized by a pitting attack with no internal sulphidation and alloy depletion, resulted from sulphidation mechanism. The corrosion products consisted of Cr₂O₃, CrS, NiO, and Ni₃S₂. They further reported that the hot corrosion of the alloy at 700 °C consisted of two stages. The oxidation and sulphidation of alloy took place in the initial stage, during which the fluxing of oxide scale did not occur. The compact and protective Cr₂O₃ scale was formed and Al₂O₃, TiO₂, CrS, and Ti-Nb-sulphide precipitated at the interface of scale/alloy and in Cr-depletion zone. Due to the oxidation of cobalt on the surface of oxide scale, the hot corrosion proceeded to the propagation stage during which stable CoSO₄ melt formed by inward migration of SO₃ and the outward migration of cobalt, and the internal sulphidation reaction proceeded as well. The porous outer layer of oxide scale consisted of CoCr₂O₄, Fe(Cr,Al)₂O₄, and NiCr₂O₄ spinels. The inner layer of scale consisted of Cr₂O₃, Al₂O₃, TiO₂, and internal sulphides formed, in the initial stage, at the interface and in Cr-depletion zone.

Some of hot corrosion studies conducted by various investigators in Na₂SO₄ or V₂O₅ environments are summarised in Appendix A.1.

2.6 PREVENTIVE AND CONTROL AGAINST HOT CORROSION

Material losses due to erosion and corrosion are the major problems in many industries (Das et al., 2005). Corrosion and its associated losses can not be eliminated completely. However, 25 to 30% of annual corrosion related costs could be saved with the use of optimum corrosion preventive and control strategies (Koch et al., 2002;

Priyantha et al., 2003). Preventive measures against metal losses and failures due to corrosion should be economically devised to ensure safety and reliability in the use of metallic components (Chatterjee et al., 2001).

Heath et al. (1997) proposed a number of countermeasures corresponding to the variety of corrosive environments including proper selection of alloy, optimum design of components, use of chemical additives to neutralise the corrosive components in the flue gases, shielding the substrate, and/or use of protective coatings. Eliaz et al. (2002) also, in their review of hot corrosion in gas turbine components, suggested several approaches to control the hot corrosion of gas turbine components. These approaches are proper selection of structural alloys, application of coatings, washing of hot parts, air filtering, and control of both fuel cleanliness and composition.

Hot corrosion preventive and control methods used in the aggressive environment can be classified as corrosion inhibitors, selection of proper alloy, cathodic protection and coatings (Priyantha et al., 2003; Bai et al., 2004).

For adequate corrosion protection of a metal in an aggressive environment, it is important to select materials and techniques that are compatible. For example, addition of an organic inhibitor (e.g. pyridines, pyrimidines, quinolines) is sufficient to mitigate corrosion of metals in many corrosive media. However, these inhibitors have shown only limited success due to solubility and/or thermal stability problems in high –temperature, concentrated salt solutions (Priyantha et al., 2003). The corrosion control in highly aggressive applications requires careful selection of materials. Nickel-based superalloys have good mechanical properties and superior corrosion resistance at higher temperatures and are used as base materials for many hot components. However, the hot corrosion is inevitable when these alloys are used at higher temperatures for longer periods of time in an extreme environment (Goebel et al., 1973; Sims, 1987).

Another method of hot corrosion prevention is to coat the alloy with a protective layer, which has been used in the current investigation. This is the preferred approach, even when relatively hot corrosion-resistant alloys are used (Eliaz et al., 2002).

PART-II

2.7 PROTECTIVE COATINGS

In a wide variety of applications, materials have to operate under severe conditions such as erosion, corrosion and oxidation at higher temperature in hostile chemical environments. Therefore, surface modification of these components is necessary to protect them against various types of degradation (Pawłowski, 1995).

Only composite materials are able to meet such a demanding spectrum of requirements, the base material provides the necessary mechanical strength and coatings provide a way of extending the limits of use of materials at the higher temperatures

(Sidky and Hocking, 1999; Li et al., 2003). Even if the material withstands high-temperature without a coating, the coating enhances the lifetime of the material.

A coating is a layer of material, formed naturally or synthetically or deposited artificially on the surface of an object made of another material, with the aim of obtaining required technical or decorative properties. Heath et al. (1997) have summarised the main advantages of coatings as follows:

- Very high flexibility concerning alloy selection and optimization for specific resistance to corrosion environments and particle abrasion/erosion. Surface properties can be separated from required mechanical properties of the structural component.
- Coating systems (multi-layered or functionally graded) can be used, combining, for example, good adhesion with optimised corrosion and erosion behaviour.
- Unique alloys and microstructures can be obtained with thermal spraying which are not possible with a wrought material. These include continuously graded composites and corrosion resistant amorphous phases.
- Costs of a coating solution are normally significantly lower than those of a highly alloyed bulk material; thermal spray coatings are especially interesting for their cost/performance ratio.
- Thermal spray coatings additionally offer the possibility of on-site application and repair of components, given a sufficient accessibility for the sprayer and his equipment. However, thermal spraying in the workshop is preferred, whenever possible, to achieve optimum results.

2.7.1 Use of Coatings at High Temperature

Protective surface treatments are widely used at low temperature, but the use of these at elevated temperature is more recent. High-temperature applications are limited largely to the aerospace industry. An enormous challenge exists to develop and apply these techniques to other high-temperature applications (Stroosnijder et al., 1994). Porcayo-Calderon et al. (1998) have reported the use of protective coatings for the superheater/re-heater components of boiler where the material severely suffers high-temperature corrosion. Sidky and Hocking (1999) have summarised the coating properties required for application at elevated temperature as is given in Table 2.1.

Table 2.1: General property criteria for coating systems for elevated temperature services (Sidky and Hocking, 1999).

Component system criteria/property	Coating criteria/property
Aerodynamic property	Smooth surface finish for coating; must conform to appearance of precision cast component
Mechanical strength and microstructural stability	Coating must be resistant to all types of stress (impact, fatigue, creep, and thermal) to which system will be exposed
System adhesion, bonding and interface stability	Coating/substrate must be compatible without gross thermal or structural mismatch; diffusion rates at interface must be at minimum at operating temperatures, as must compositional changes; development of embrittling phases must be avoided
Surface resistance to erosion and oxidation/hot corrosion	Coating composition must have sufficient reserve of all reactant constituents to meet scale reformation needs without marked deterioration in protection ability; coating must be ductile, and must develop uniform, adherent, and ductile scale at low rates

The demand for protective coatings has increased recently even for almost all types of superalloys, since high-temperature corrosion problem become much more significant for these alloys with increasing operating temperatures of boilers, turbines and heat engines. The necessities for higher performance and increased efficiency have resulted in the progressive increase in their operation temperatures (Yoshida, 1993; Stott et al., 1994; Conner and Connor, 1994). As a result, components operating at high-temperature within such plants are coated or surface treated (Nicholls, 2000).

Though superalloys have been designed for high temperature applications, however, protective coatings are applied to enhance their life for use in corrosive environments as they are not able to meet the requirement of high-temperature strength and high-temperature corrosion resistance simultaneously (Liu et al., 2001).

According to Taylor and Evans (2001), a few earlier attempts have been made for applying the thermal sprayed protective coatings for fossil power plants though the thermal spray process is extensively used for gas turbine applications. Sundararajan et

al. (2003A and 2003B) advocated the need for applying thermal spray coatings on the boiler components.

2.7.2 Coating Techniques

There are many coating deposition techniques available, and choosing the best process depends on the functional requirements, adaptability of the coating material to the technique intended, level of adhesion required, (size, shape, and metallurgy of the substrate), and availability and cost of the equipment. The commonly employed coating deposition techniques have been enlisted in Fig. 2.12 (Bhushan and Gupta, 1991). These techniques are divided into metallic and non-metallic categories. Metallic coating deposition can be considered under three categories, hard facing being the technique most important to this research.

Nicoll (1984) reported that from production point of view, chemical vapour deposition (CVD) from a pack, physical vapour deposition (PVD) and thermal spraying (metal spraying), are in current use. Since CVD process is a non-line-of-site technique, proper masking and tooling are the major design considerations and it is expensive. Another shortcoming of the CVD process is the inclusion of pack particles in the coating which can lead to coating failure (DeMasi-Marcin and Gupta, 1994)

Ilavsky et al. (2000) reported that the thermally sprayed coatings have often superior properties, lower application cost and less environmental issues as and when compared to other industrially used coatings such as CVD, PVD, hard chromium plating. Moreover, Nicholls and Stephenson (1995) revealed that overlay coatings performed better than diffusion coatings at higher temperatures. For depositing overlay coatings, thermal spray technologies are often considered (Singh, 2005E).

2.7.2.1 Thermal Spray Techniques

In the early nineteen hundreds, a young Swiss inventor named Dr. Max Schoop invented thermal spraying, after watching his son playing with his toy cannon. Dr. Schoop observed that the hot lead shots that were projected out of the cannon, stuck to almost any surface, the result of which gave him the idea that if metal could be melted and projected in a spray like manner, then a surface could be built up with that material.

The technology continued, but expanded in the 70s due to development of the thermal plasmas and the increasing demand of high-temperature and wear resistant materials and coating systems (Knotek, 2001). Thermal spraying is one of the most versatile hard facing techniques available for the application of coating materials used to protect components from abrasive wear, adhesive wear, erosive wear or surface fatigue and corrosion (such as that caused by oxidation or seawater) (Marceau and Adjorlolo, 1995; Groshart, 1995; Ishikawa et al., 1993). Generally, any material which does not decompose, vaporize, sublime, or dissociate on heating, can be thermally

sprayed. Consequently a large class of metallic and nonmetallic materials (metals, alloys, ceramics, cermets, and polymers) can be deposited by thermal spraying. In thermal spraying the initial coating material (materials in the form of rod, wire, or powder) is heated, generally to a molten state and projected onto a receiving surface, known as a substrate, as shown in Fig. 2.13 (Stokes, 2005). A variety of engineering problems have been solved using thermal spraying applications. The use of thermal spraying ranges across many manufacturing processes, from the automotive (Nakagawa et al., 1994; Nicoll, 1994), through to the space exploration industry (Nguyentat et al., 1992). Metals, carbides and cermets are the most widely used coating materials, however the spraying of polymers has also been researched (Varacalle et al., 1996; Kawase and Nakano, 1996). The HVOF coatings are widely used in various engineering components for combating wear and corrosion including propellers, pump impellers and casings, superheaters and pre-heaters of boilers, valve bodies/trim and pipe systems (Tan et al., 2005)

The Thermal spray processes that have been used to deposit the coatings for the protection against the high-temperature corrosion are enlisted below, summarised by Heath et al. (1997):

- Flame spraying with a powder or wire
- Electric arc wire spraying
- Plasma spraying
- Spray and fuse
- High Velocity Oxy-fuel (HVOF) spraying
- Detonation Gun

Table 2.2 shows some of the important characteristics associated with these thermal spray techniques (Bhushan and Gupta, 1991; Stokes, 2005; Sobolev et al., 2004; Sidhu et al., 2005B). Particle speed, flame temperature and spray atmosphere are the main parameters which differentiate the various spraying techniques. Coating porosity, bond strength and oxide content are typical properties influenced by the coating procedure. In 1988, METCO introduced the Diamond Jet HVOF (High Velocity Oxy-Fuel) system, the process used in the current investigation.

2.8 HIGH VELOCITY OXY-FUEL (HVOF) THERMAL SPRAYING

High velocity oxy-fuel (HVOF) processes belong to the family of thermal spraying technologies and are capable of producing coatings with lower porosity, higher hardness, superior bond strength and less decarburization than many of the other thermal spraying methods (Pawlowski, 1995; Smith and Knight, 1995; Herman et al., 2000; Modi and Calla, 2001; Wang and Shui, 2002; Sidhu et al., 2005B). In recent years, there has been considerable growth in the use of this spraying process to deposit cermets, metallic and

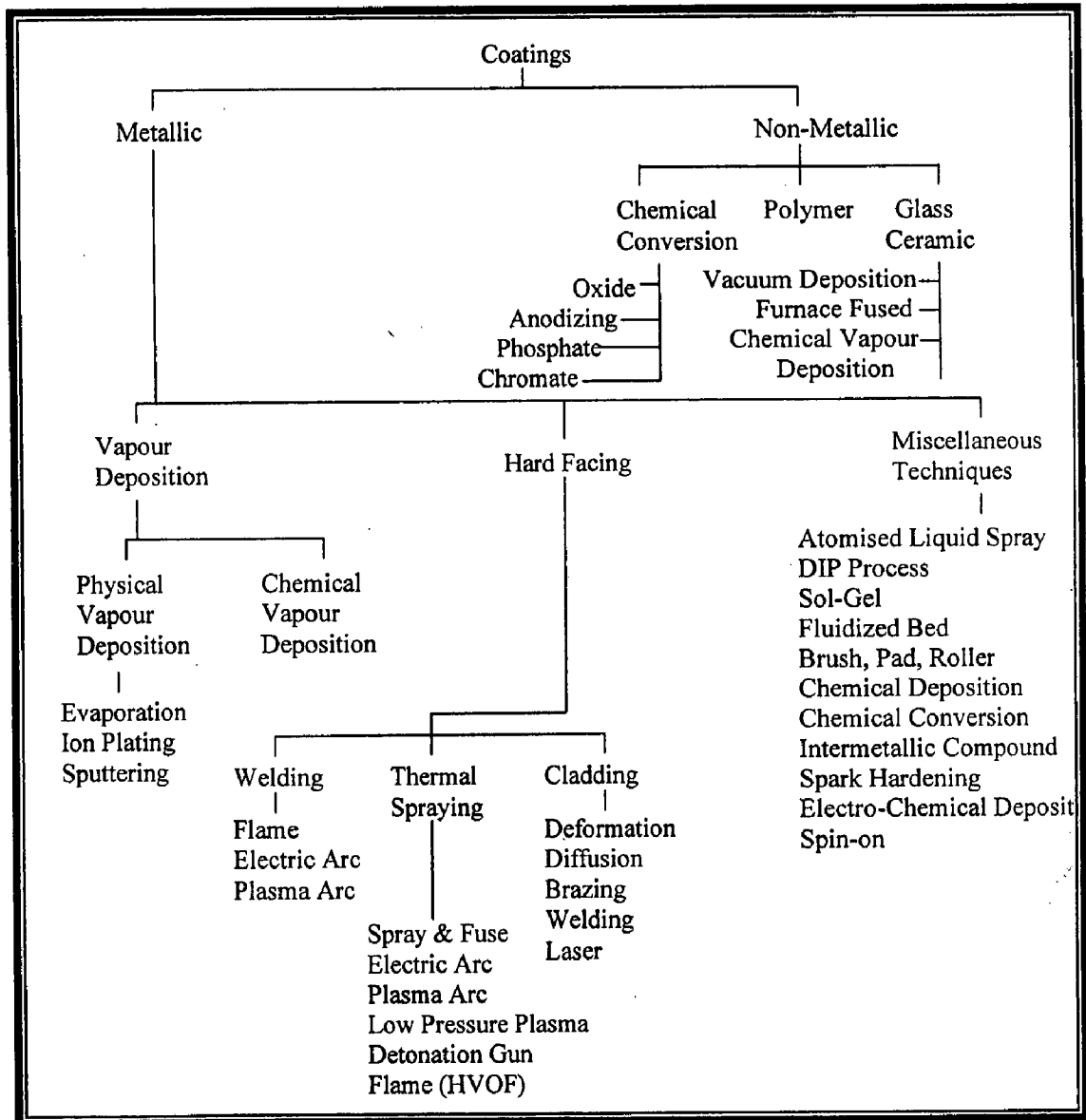


Fig. 2.12 Coating deposition technologies (Bhushan and Gupta, 1991).

Table 2.2: Comparison of characteristics for various thermal spray processes (Bhushan and Gupta, 1991; Stokes, 2003; Sobolev et al., 2004; Sidhu et al, 2005).

Deposition Technique	Heat source	Propellant	Material feed type	Spray Gun temp. (°C)	Particle velocity m/s	Coating materials	Relative bond strength	Porosity level %volume
Electric Arc	Arc between electrodes	Air	Wire	6000	240	Ductile materials	Good	8-15
Plasma Arc Spraying	Plasma Arc	Inert Gas	Powder	16000	120-600	Metallic, ceramic, plastic and compounds	Very Good to Excellent	2-5
Low Pressure Plasma Spraying	Plasma Arc	Inert Gas	Powder	16000	900	Metallic, ceramic, plastic and compounds	Excellent	<5
Spray & Fuse	-	-	Powder	-	-	Fusible metals	Excellent	<0.5
Flame Spraying	Oxyacetylene/ Oxyhydrogen	Air	Powder	3000	30-120	Metallic and ceramics	Fair	10-20
Detonation Gun Spraying	Oxygen/ Acetylene/ Nitrogen Gas Detonation	Detonation Shock Waves	Powder	4500	800	Metallic, ceramic, plastic and compounds	Excellent	0.1 to 1
High Velocity Oxy-fuel (HVOF)	Oxy-propylene/ hydrogen/ propane/ LPG	Combustion Jet	Powder/wire	3000	800	Metallic and ceramic	Excellent	0.1-2

ceramic protective overlay coatings, which are typically 100-300 μm thick, onto the surfaces of engineering components to allow them to function under extreme conditions (Parker and Kutner, 1991; Smith and Knight, 1995). Vacuum plasma-based coatings have considerable potential for reducing wear and corrosion. However, due to high investment costs they have not been widely applied to engineering components other than tools such as those used in metal cutting (Matthews et al., 1995). Due to low investment costs, the HVOF coatings have now gained popularity and are being studied extensively for their corrosion resistant properties (Perkin, 1989A). Several HVOF sprayed coatings have been subjected to corrosion testing in seawater, including cermets (Guilemany et al., 1998; Collazo et al., 1999; Tani et al., 2000) and corrosion resistant

alloys (Gu et al., 1998; Sturgeon and Buxton, 2000; Harvey et al., 2000). These studies concluded that the HVOF method produce coatings with higher corrosion resistance when compared with other spraying technologies.

The HVOF sprayed coatings have found wide application in marine, aircraft, automotive and other industries. For reclaiming a wide range of petrochemical-process components such as storage vessels, heat exchangers, pipe end fittings and valves, which are subjected to severe erosive, wear and corrosive conditions, Amoco Oil Company routinely employs the HVOF process by applying AISI 316 L and Hastalloy C-276 coatings (Moskowitz, 1992).

The HVOF spraying techniques are predominantly being used as wear, corrosion and oxidation resistant barriers, resulting in increased lifetimes as compared with the uncoated substrate components. However, as the technology has advanced, through new deposition techniques and improved tool design, the range of materials that can be effectively deposited by this process has increased to include low melting point ceramics such as alumina and materials for biomedical applications such as bio-ceramic coatings for dental implants (Haman et al., 1995; Sampath and McCune, 2000). Recently, the HVOF coatings are increasingly used in many areas such as petrochemical and offshore industries, automotive components and general engineering applications including printing, textiles and mining (Sturgeon et al., 1994; Sidhu et al., 2005C).

2.8.1 HVOF Spraying-The Process

The basic scheme of the HVOF spray system is shown in Fig. 2.14 using the Diamond Jet gun as an example (Stokes and Looney, 2001). In the HVOF process, powder/wire material is melted and propelled at high velocity, with the use of oxygen and fuel gas mixtures, towards a surface. Propylene, propane, hydrogen, acetylene, methane, ethylene, crylene, SPRAL 29 kerosene, MAPP (methyleacetylene-propadiene-stabilised gas), LPG etc. are used as combustion fuels. The HVOF system consists of a spray gun, powder feed unit, flow meter unit, and an air and gas supply unit. The powder feed unit comprises a hopper assembly, air vibrator, feed rate meter and control cabinet. The desired powder is fed from the powder feed unit by means of a carrier gas to the gun, where combustion occurs. The amount of powder required for deposition may be regulated using the powder feed-rate meter. In the combustion zone, the powder material enters the flame, where it becomes molten or semi-molten, depending on the melting temperature and the feed rate of the material. The flame temperature for the HVOF process is around 3000 °C (Sobolev et al., 2004). The molten or semi-molten particles are then propelled out of the gun nozzle at very high velocities towards the target/substrate, where the material is deposited. Powder particles, typically in the range 10-63 μm , attain velocities of 300-800 ms^{-1} at the

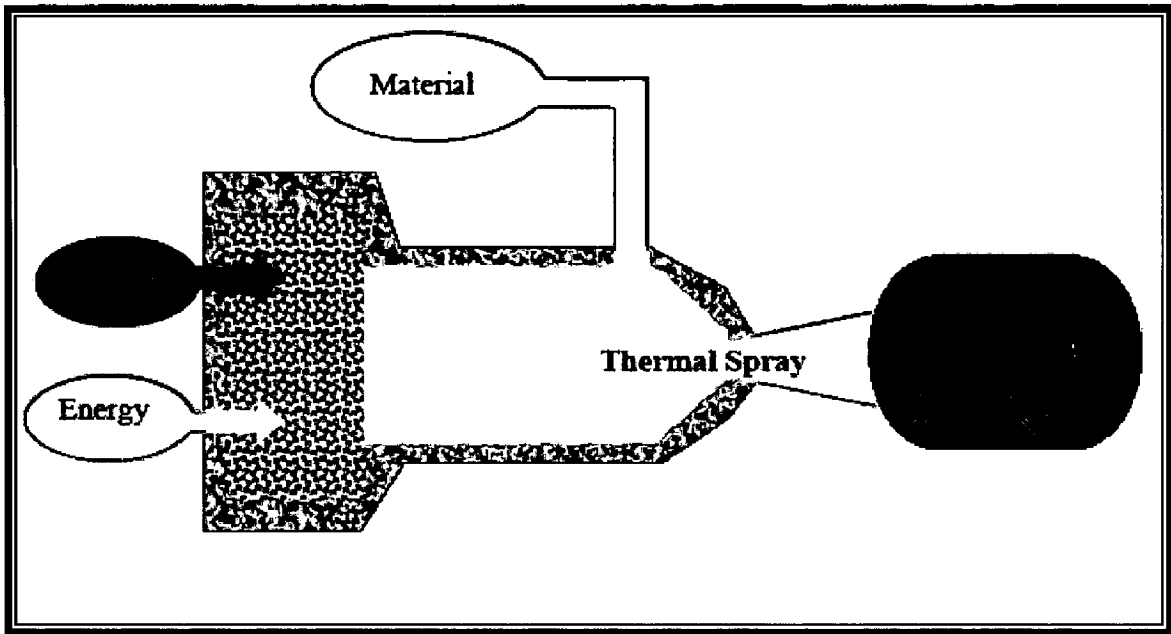


Fig. 2.13 Schematic of a Thermal Spray Process (Stokes, 2003).

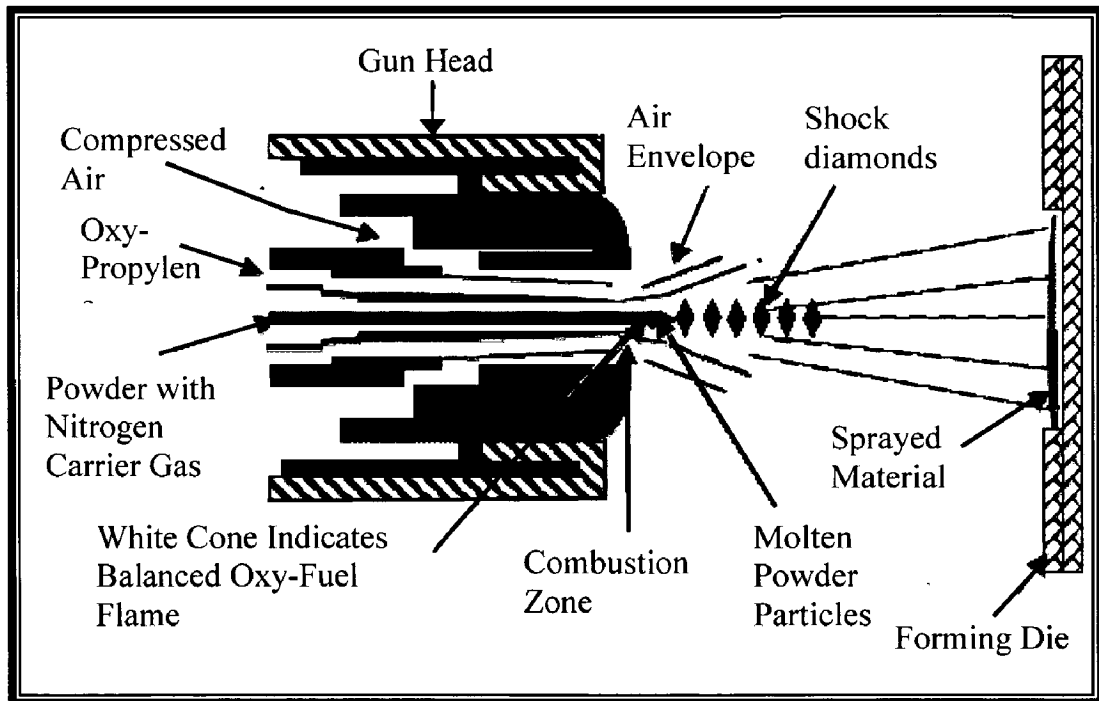


Fig. 2.14 Schematic cross-section of diamond-jet spray gun (Stokes & Looney, 2001).

substrate to be coated (Kowalsky et al., 1991; Irving et al., 1993; Knight et al., 1994; Smith and Knight, 1995; Herman et al., 2000).

Quality of the coatings depends significantly on the velocity and temperature of the powder particles impinging onto the substrate surface, which in turn is associated with the gas pressure developed in the combustion chamber. In the HVOF spray systems of the first and second generations (Continuous Detonation Spraying, Top Gun, Jet-Kote and Diamond Jet) combustion occurs at pressures in the range of 3-5 bar and the flame attains a supersonic velocity in the process of expansion at the nozzle exit. These systems produce comparable particle velocities with the standard spray parameters and the same fuel gases and powders (Sidhu, 2005B). For instance, during spraying of the WC-17%Co powder with these systems using particle size distribution of $-45+10\ \mu\text{m}$ and propane as fuel, the particle velocities obtained were about 450 m/s (Kreye, 1997).

The HVOF systems of the third generation (Diamond Jet Hybrid 2600 and 2700, JP-5000, OSU Carbide jet, and TOP Gun K) operate at higher combustion pressures in the range of 6-10 bar. These systems permit higher particle velocities and higher spray rates. For examples, in the case of the WC-Co powder the velocities are about 600-650 m/s and the spray rates increase up to 10 kg/h and in JP-5000 system even up to 18 kg/h without any deterioration of the coating quality (Kreye, 1997).

2.8.2 Splat Formation and Building up a Coating

2.8.2.1 Splat Formation

Depending on the melting temperatures of the particle relative to the flame temperature, the particle may be molten, semi-molten or solid when it impacts a substrate or pre-coated surface. The state of the particle as it exits the combustion zone has an effect on the final microstructure of the coating (Pawłowski, 1995).

The spray deposition process consists of three steps, which occur in succession, viz. atomization, droplet flight and deposition (Dube, 2000). The HVOF coatings have lenticular or lamellar grain structure, resulting from rapid solidification of small globules, which flattened upon striking a colder surface at high velocities. Figure 2.15 shows a schematic of the formation of a splat from its globular form (Stokes, 2005). Initially, the particle is melted and propelled out from the gun in the form of a sphere then, at its first contact with the substrate, the impact creates a shock wave inside the lamella and in the substrate. Post-impact forms the particle into a 'pancake' shape lamella or splat (associated with moderate particle velocities and moderate heat contents), shown in Fig 2.16(a), or a flower type lamella (connected with an elevated velocity of the particle and an elevated heat content), as shown in Fig. 2.16 (b), when the solidification process takes place (Fantassi et al., 1992; Moreau et al., 1992). When a

molten droplet arrives at a surface at high velocity, spreading of the splat is restrained by surface tension. Otherwise the extremities of the splat will either become weak, and break off or form small spherical drops (Stokes, 2005).

The substrate surface roughness also influences the splat formation, and adherence loss occurs if an inadequate amount of surface roughness is present whilst spraying (Gawne et al., 1995; Kanouff et al., 1998).

2.8.2.2 Building up a Coating

A coating is the build up of individual particles which strike a substrate. In one pass of the spray gun, a layer of 5-15 lamellae thickness is formed depending on the processing parameters such as powder feed rate, spray distance, particle size and the torch's linear speed. So, several passes of spray gun are required to build-up a coating across the work-piece. Meanwhile, the layer deposited by the first pass may be submitted to oxidation (for highly oxidizable materials) and cooling. On the second pass, the temperature of the first layer (which may be partially solidified) cools the second layer due to the difference in temperatures between the first and second layer. The final coating may comprise of 5-200 passes of deposited material. Afterwards, the coating is allowed to cool down to room temperature. During this period thermal stresses generate, often leading to crack formation in the coating or separation from the substrate (Stokes, 2005).

Once a molten or semi-molten particle strikes the substrate or previously deposited material, solidification starts and a columnar deposit structure is formed as shown in Fig. 2.17a (Stokes, 2005). The deposit structure may change to a 'brick wall' type structure shown in Fig. 2.17b (Pawlowski, 1995), where a low rate of heat removal is experienced between the particle and the adjoining material interface, due to substrate oxidation and/or surface roughness. In either case the solidification within each lamella will repeat itself as the coating builds up to the required thickness

2.8.3 Selected Properties of HVOF Coatings for High Temperature Applications

The HVOF coatings in comparison with other thermal spraying processes have low roughness, high bond strength, higher hardness, lower porosity, low oxide content and higher thickness (Halling, 1985; Perkin, 1989B). The overall result is a coating with reproducible coating characteristics and high erosion, corrosion and wear resistance.

2.8.3.1 Physical and Mechanical Properties of the Coatings

Due to high velocity and high impact of the sprayed powder particles, the coatings produced by HVOF spraying process are less porous and have higher bond strength than that produced by other methods such as plasma spraying, flame spraying, and electric arc spraying

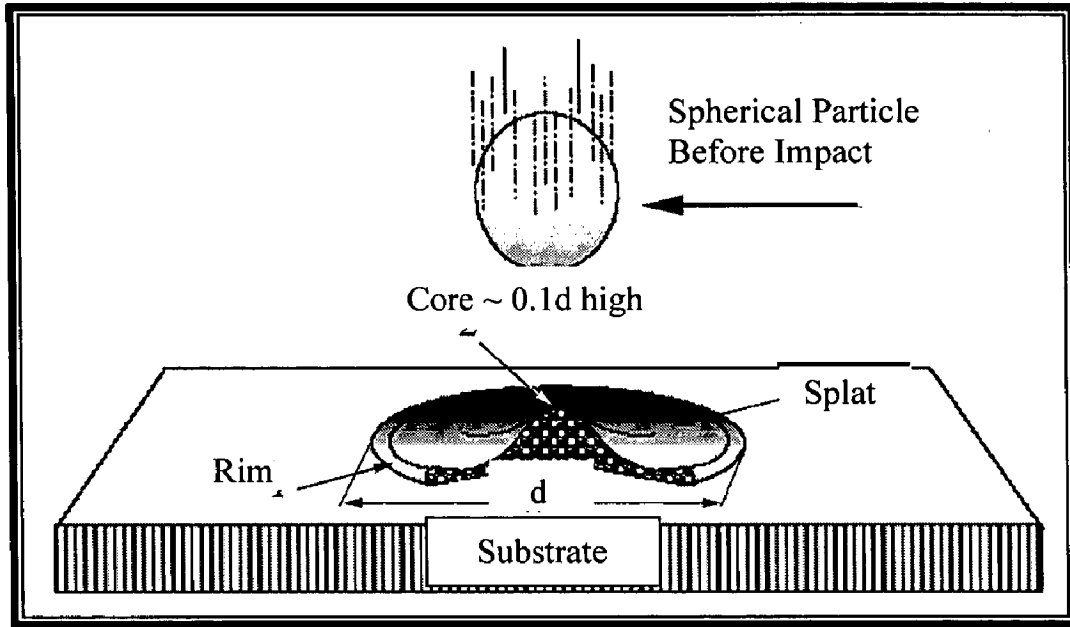


Fig. 2.15 Schematic diagram of spherical particle impinged onto a flat surface (Stokes, 2005).

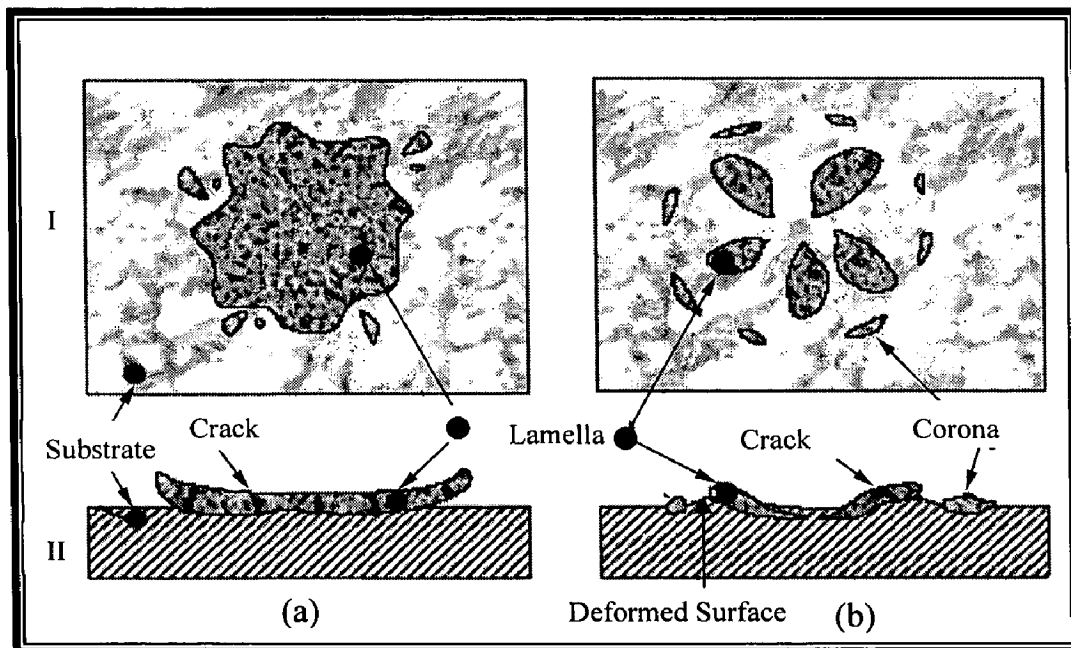


Fig. 2.16 Two morphological forms of lamellae splashed on the substrate (a) Pancake, (b) Flower; I: Top View, II: X-Section View.

(Crawmer et al., 1992; Jarosinski et al., 1993; Provot et al., 1993). The physical properties of the materials depend upon their developed structure (Buchanan and Park, 1998).

The high kinetic energy of the particles in the HVOF process deformed the particles in a plastic state rather than a molten state. As a result, oxidation of spray metal during flight and flattening is relatively less, since oxidation can occur only by a relatively slow diffusion mechanism. In spite of the plastic state, the high kinetic energy of the particles still allows flattening by deformation and leads to dense and pore-free coating with low oxygen content. This characteristic of the HVOF process is of high importance for spraying mechanically alloyed material (Provot et al., 1993; Lugscheider et al., 1998; Zhao et al., 2001; Zhao and Lugscheider, 2002).

2.8.3.2 Microstructural Properties

Detailed microstructural examination of the HVOF sprayed surfaces shows that coatings exhibit characteristic splatlike, layered morphologies due to the deposition and re-solidification of molten or semi-molten powder particles. During the HVOF spraying, powder particles are generally comprised of three separate zones; fully melted regions, partially melted zones, and an unmelted core. However, the relative proportions of the zones formed in an individual powder depends on its particle size, trajectory through the gun, the gas dynamics (velocity/temperature) of the thermal spray gun and the type of gun employed (Dent et al., 2001; Kong et al., 2003; Zhang et al., 2003; Sidhu et al., 2005C).

2.8.3.3 Corrosion Behaviour of the Coatings

Dense coatings provide better corrosion resistance than the porous coatings as porosities can do harm to the persistent corrosion resistance of the coating (Guilemany et al., 1997A and 1998; Zhao, 2004A; Zhao 2005 B). In the HVOF process, the powder particles are propelled out of the gun nozzle at high velocities towards the substrate. Due to high velocity and high impact of the sprayed powder particles, the coatings produced by HVOF spraying process are very dense. A number of research workers has reported that the HVOF coatings have higher corrosion resistance as compared with other thermal sprayed coatings (Barbezat et al., 1993; Russo and Dorfmann, 1995; Zimmermann and Kreye, 1996; Gu et al., 1998; Collazo et al., 1999; Stein et al., 1999; Anfenz et al., 2003, Kawakita et al., 2003; Zhao et al., 2004A; Zhao et al., 2005B). Uusitalo et al. (2003) attributed better corrosion resistance property of the HVOF coatings to their flat splat structures.

2.8.3.4 Adhesion of the Coatings

The HVOF coatings have higher bond strengths as compared to most of other thermal spraying processes, due to the high kinetic energy experienced by the impinging particles (Sidhu et al. 2005B). The bond strength achieved by the HVOF system is 25% greater than that found using a plasma thermal spraying process (Stokes, 2005).

The adhesion strength of the impinging particle to the substrate is dependent on mechanical and metallurgical-chemical mechanisms. An impinging particle will flatten and conform to a suitably prepared surface, then mechanically lock itself to the receptive asperities as shown in Fig. 2.17c. Subsequently, diffusion or alloying may occur, forming intermetallic compounds. This is known as the metallurgical-chemical adhesion mechanism (Batchelor et al., 2003; Stokes, 2005).

Increased bond strength depends not only on the deposition process utilized, but also on cleanliness (with respect to oxides and other foreign elements), adequate roughness and adhesion to a substrate surface, along with plastic deformation exhibited by the particle on the substrate surface. Cohesive strength depends on the roughness, temperature difference and bond/cohesive strength of the previously coated surface. Coating properties are also governed by the splat layering which further depends on the particle parameters at impact, the shape and topology of already deposited layers, the ability of the flattening particle to accommodate their pores, asperities etc, and finally, on their temperature at the moment of impact (Fauchais, 2004).

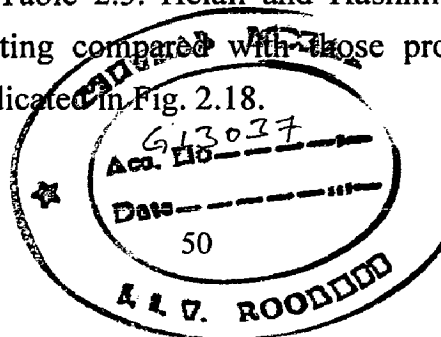
The full melting of spray particles does not contribute to the increase in the adhesion of HVOF metallic coating. On the other hand, the deposition of partially melted large particle contributes to the substantial improvement of adhesion strength to over 76 MPa, which is double compared to the strength of the coating deposited with completely molten particles (Li et al., 2000).

2.8.4 Advantages of the HVOF System

The HVOF process is designed to produce high velocities in spray particles, and this contributes to the advantages that HVOF has over other thermal spray processes in terms of particle condition (De Villiers Lovelock et al., 1998; Jacobs et al., 1998) including:

- More uniform and efficient particle heating, due to the high turbulence experienced by the particles within the combustion chamber
- Much shorter exposure time of flight due to the high particle velocities
- Lower surface oxidation due to short particle exposure time compared to other thermal spraying techniques
- Reduced mixing with ambient air once jet and particles leave the gun
- Lower ultimate particle temperatures compared to other processes such as plasma or arc guns which operate at temperatures of 16000 and 6000°C as opposed to 3000 °C in the HVOF (oxygen/propylene mixture) process

Stokes (2005) summarised the reasons for such high quality coatings produced by the HVOF process as shown in Table 2.3. Helali and Hashmi (1992) reported the main characteristics of HVOF coating compared with those produced using the standard plasma spraying process as indicated in Fig. 2.18.



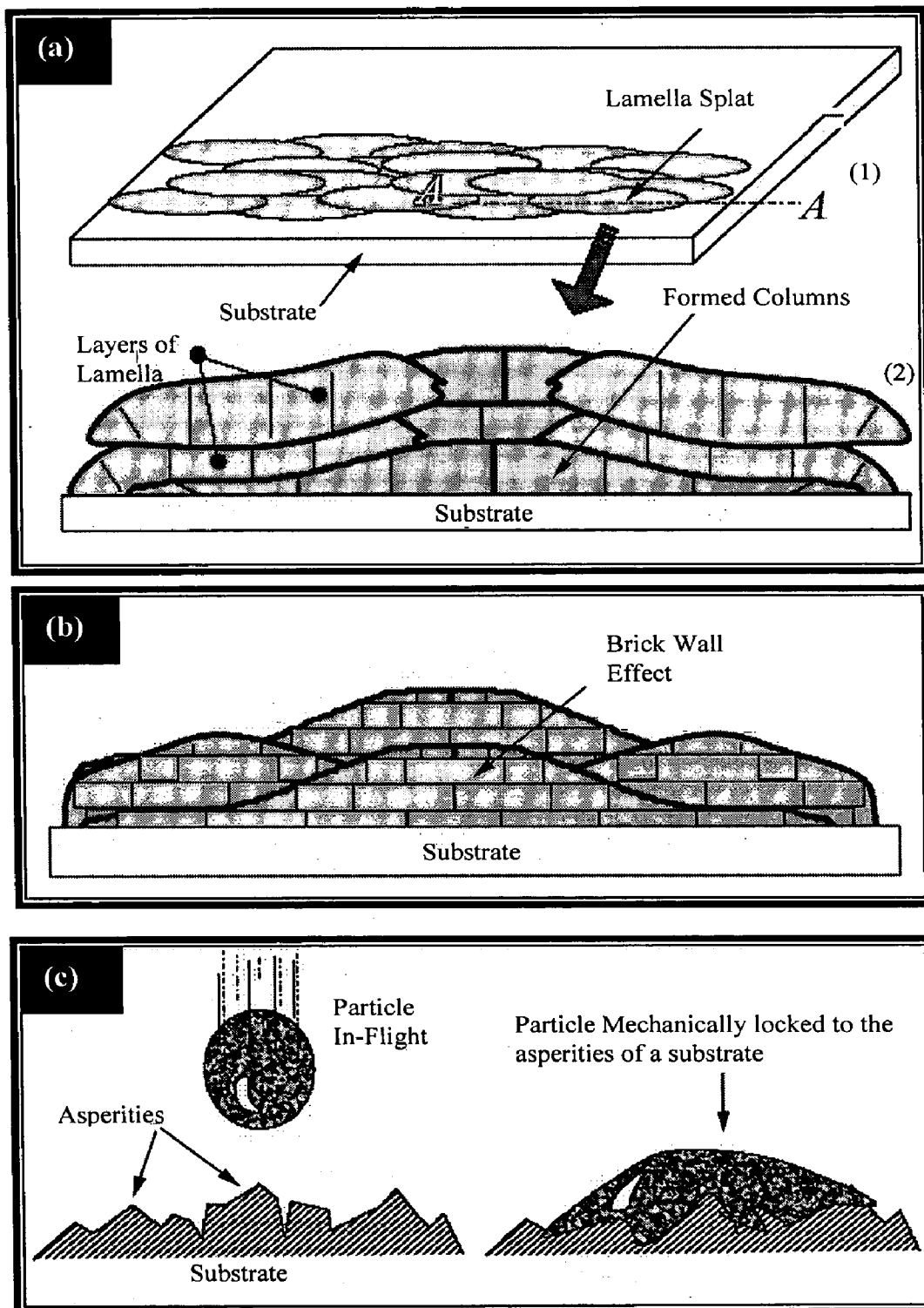


Fig. 2.17 (a) A cross-section of lamella splat in diagram (1) is shown in diagram (2), which represents the possible microstructure of lamellae resulting from solidification (columnar).
 (b) Another cross-section through a lamella, showing a 'Brick-wall' type microstructure resulting from solidification.
 (c) Schematic of adhesion of a particle to a substrate asperity (Stokes, 2005).

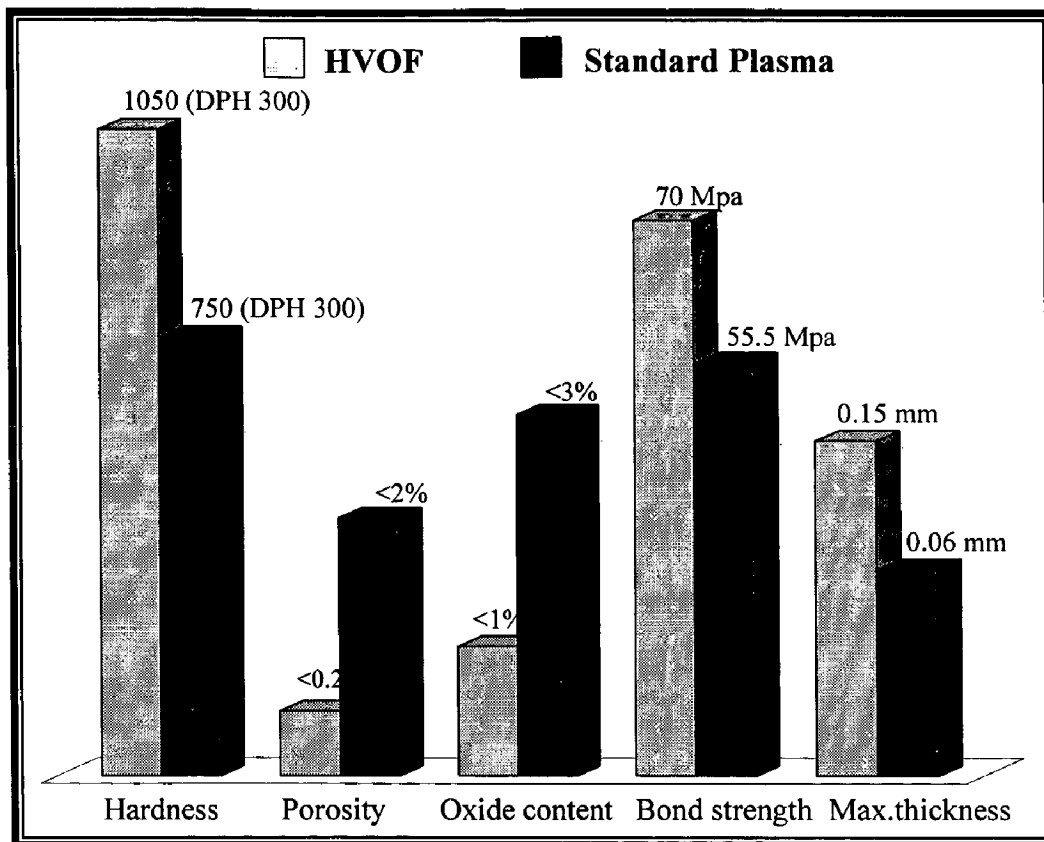


Fig.2.18 Characteristics of HVOF and standard plasma process coatings (Helali and Hashmi, 1992).

PART III

2.9 ROLE OF THE COATINGS

The thermal spray coatings used at high temperatures must be dense enough so that the protective oxides can form within and fill voids, and thick enough to postpone the diffusion of corrosive species to the substrate material before the protective oxide can form within the coating (Bluni and Marder, 1996). Guilemany et al. (2002) have also reported that a thicker coating provides better resistance against corrosion.

Gurrappa (2003) suggested that the coating used at high-temperature should have a composition that will react with the environment to produce the most protective scale possible, provide corrosion resistance with long term stability and have resistance to cracking or spallation under mechanical and thermal stresses induced during operation of

Table 2.3: Benefits of using HVOF coatings.

Coating Benefit	Main reasons for this benefit
Higher Density (lower porosity)	Higher Impact Energy
Improved Corrosion Barrier	Less porosity
Higher Hardness Ratings	Better Bonding, Less Degradation
Improved Wear Resistance	Harder, Tougher Coating
Higher Bond and Cohesive Strengths	Improved Particle Bonding
Lower Oxide Content	Less In-flight Exposure Time to Air
Fewer Un-melted Particle Content	Better Particle Heating
Greater Chemistry and Phase Retention	Reduced Time at Higher Temperatures
Thicker Coatings (per pass & total)	Less Residual Stress
Smoother As-sprayed Surfaces	Higher Impact Energies

the components. Further, the protective oxide scale should not react with the corrosive environment and at the same time, it should not allow the corrosive species to diffuse through the coating.

Alloys and coatings designed to resist oxidizing environments at high-temperatures should be able to develop a surface oxide layer, which is thermodynamically stable, slowly growing and adherent (Brand et al., 2004).

2.9.1 Behaviour of Cr₃C₂-NiCr Coatings

The Cr₃C₂-NiCr coatings can be used at temperatures between 600 and 900 °C, in steam turbine blades or in boiler tubes for power generation (Calero, 1997; Guilemany et al., 1997A), due to their behaviour against aggressive corrosion and erosive-abrasive atmospheres, and their thermal stability at high-temperatures (Dwyer et al., 1995). Because of their good resistance to high-temperature corrosion and erosion, these coatings are considered as protective coatings for heat exchanger pipes and fluidized bed combustors (Fukuda and Kumon, 1995). HVOF sprayed Cr₃C₂-NiCr coatings have high erosion-corrosion, and wear resistance properties (Vuoristo et al., 1994; Zimmermann and Kreye, 1996; Guilemany et al., 1997B; Suegama et al., 2002; Fedrizzi et al., 2004; Murthy and Venkataraman, 2004). Guilemany et al. (2005) reported that HVOF sprayed Cr₃C₂-NiCr coating has best wear and corrosion resistance and are replacing hard chromium coatings.

Vuoristo et al. (1994) reported that plasma spraying, detonation gun spraying and high velocity oxy-fuel spraying method are mostly used to apply chromium carbide coatings to work as wear resistant coatings against abrasion and erosion in corrosive environments at high-temperatures up to 900 °C. The room temperature abrasion and erosion wear resistance of Cr₃C₂-25%NiCr coatings, applied by these methods has been compared and high velocity combustion process is reported to have the highest wear resistance.

Seong et al. (2000) evaluated the corrosion resistance of the HVOF sprayed Cr₃C₂-NiCr coatings to protect the heat exchanger pipes of recuperators used in steel mills. They detected that these pipes corroded via oxidation, sulphidation, and molten salt corrosion. They carried out three kinds of corrosion tests under cyclic conditions: high-temperature oxidation tests in air; cyclic oxidation tests in SO₂-containing environment; and a molten salt corrosion test. High-temperature oxidation tests were carried out in a box furnace for 50 h at 1000°C. Another high-temperature corrosion test was conducted in a N₂-4.8%O₂-0.2%SO₂ atmosphere at 1000°C for 100 h. Molten salt corrosion test of the coating was carried out at 700°C for 20 h in a sodium sulphate (Na₂SO₄) and iron sulphate Fe₂(SO₄)₃ salt environment carrying a gas mixture of O₂-0.5%SO₂. In this experiment, a platinum catalyst was used for the fast transformation of SO₂ to SO₃. They observed that Cr₃C₂-NiCr coatings have shown excellent corrosion resistance in the molten salt as well as in the oxidation environment. Further they recommended Cr₃C₂-

NiCr coatings as the promising coatings for the heat exchanger pipes where they encounter molten salt corrosion attack.

Wang and Luer (1994) reported that HVOF sprayed Cr_3C_2 -NiCr coatings are used in elevated temperature service environments including fluidized bed boilers, coal-fired boilers and municipal waste incinerators, in light of the excellent corrosion and oxidation resistance of the nickel chromium alloy and reasonable wear resistance of chromium carbides at temperatures up to 900 °C. They investigated the erosion-corrosion (oxidation) behaviour of the HVOF Cr_3C_2 -NiCr coating at elevated temperature and found that the erosion-oxidation resistance of the HVOF Cr_3C_2 -NiCr coating was higher than the substrate 1018 steel and other thermal-spray coatings including FeCrSiB (Amarcor M), Ni-base, Cr_2O_3 -6SiO₂-4Al₂O₃ (Rokide C), Cr_2O_3 -12SiO₂-2Al₂O₃-4MgO (Rokide MBC) and WC-NiCrCo (SMI 712). They attributed the high erosion-oxidation resistance of the HVOF Cr_3C_2 -NiCr coating to its low porosity, fine grain structure and homogeneous distribution of hard carbides/oxides which form a skeletal network within a ductile and corrosion-resistant metal binder.

Hidalgo et al. (1999) studied the corrosion behaviour of plasma sprayed Cr_3C_2 -25%NiCr coatings onto an austenitic stainless steel (AISI 304) for high temperature applications. Corrosion tests were carried out at 800 °C for 24 hours under cyclic conditions in a 210 kW laboratory combustion unit using propane as a fuel. They reported that weight gain versus time graph for the coating showed typical parabolic law behaviour. They also noticed some micro-spallation of the coatings after 15 hours of the study.

Isothermal oxidation behaviour of detonation sprayed Cr_3C_2 -NiCr coating onto conticaster rolls made of high-temperature structural steel DIN 12CrMo44, has been studied by Wang et al. (2000). Tests were carried out in an electric muffle furnace at 750 and 850 °C in air. They revealed that the coated specimens exhibited a much better improvement in high-temperature corrosion resistance than the uncoated specimens. The total weight gain of the coated specimens was approximately 10 times and 100 times less than that of the uncoated specimens after 70 h oxidation at 750 and 850 °C, respectively. They concluded that the high chromium content and the dense coating protected the substrate from the inward permeation of oxygen and promoted the selective oxidation of chromium which improves the high-temperature corrosion resistance of the steel.

Wang et al. (2000) further carried out in service testing of detonation sprayed Cr_3C_2 -NiCr coating on the same conticaster rolls at steelmaking plant of Bao Shan Steel Company since 1998. They reported that after 3740 heats, there were many alligator cracks formed on the surfaces of the uncoated rolls, some of which had to be repaired. However, compared with the original feature, no changes were detected on the surfaces

of coated ones. Their first report from the in-service test shows that the use of the coating is an efficient means of prolonging the life of the contecaster rolls.

Sidhu et al. (2006K) studied the role of HVOF coatings in improving hot corrosion resistance of ASTM-SA210 GrA1 steel in the presence of $\text{Na}_2\text{SO}_4\text{-V}_2\text{O}_5$ salt deposits at 900 °C under cyclic conditions. They reported that $\text{Cr}_3\text{C}_2\text{-NiCr}$ coating showed better hot corrosion resistance as compared to the uncoated boiler steel. They attributed better performance of the $\text{Cr}_3\text{C}_2\text{-NiCr}$ coating to the formation of protective oxides like Cr_2O_3 , NiO and NiCr_2O_4 in the scale. They also observed that $\text{Cr}_2\text{C}_3\text{-NiCr}$ coating showed some spalling during the cyclic exposure of the specimens.

Sidhu et al., 2006C, 2006E and 2006F reported the performance of HVOF sprayed $\text{Cr}_3\text{C}_2\text{-NiCr}$ coatings on a Fe-based superalloy in $\text{Na}_2\text{SO}_4\text{-60}\%\text{V}_2\text{O}_5$ environment at 900 °C under cyclic conditions. The thermogravimetric technique was used to study the kinetics of corrosion. The coating has successfully imparted the hot corrosion resistance to the molten salt environment. The corrosion resistance of the $\text{Cr}_3\text{C}_2\text{-NiCr}$ coated alloys has been ascribed to the formation of phases like Cr_2O_3 , NiO , and NiCr_2O_4 in the oxide scales.

2.9.2 Behaviour of NiCrBSi Coatings

The Ni based powder Ni-B-Si, with the addition of other alloying elements can be used for higher temperature applications. The addition of chromium promotes the oxidation and corrosion resistance at elevated temperatures and increases the hardness of the coating by the formation of hard phases. Boron depresses the melting temperature and also contributes to the formation of hard phases. Silicon is added to increase the self-fluxing properties. Carbon produces hard carbides with elevated hardness that promotes the wear resistance of the coatings (Otsubo, 2000; Lebaili and Hamar, 1987).

Ni-Cr-B-Si alloy powders were used for corrosion and wear resistant coatings by Knotek et al. (1975). Different methods such as dipping into molten alloys and fusing of metal powders have been developed but powder spraying has been reported to be the main method for applying these coatings. Microstructural characterization of HVOF sprayed NiCrBC coating applied on low carbon mild steel has been carried out by Dent et al. (2001). The results show that the coatings have layered morphologies due to the deposition and solidification of successive molten or semi-molten splats. Coating microhardness value is found to be ~ 6.0 GPa.

Cha et al. (2002) studied the high-temperature corrosion behaviour of HVOF sprayed Ni-20Cr, NiCrBSi and $\text{Cr}_3\text{C}_2\text{-NiCr}$ coatings applied on high-temperature steel 15 Mo 3 in HCL- $\text{H}_2\text{O-O}_2\text{-N}_2$ corrosive atmosphere at 500 °C. They revealed that Ni-20Cr coating is more corrosion resistant than NiCrBSi and $\text{Cr}_3\text{C}_2\text{-NiCr}$ coatings. Further they found that $\text{Cr}_3\text{C}_2\text{-NiCr}$ coating has shown slightly better corrosion resistant behaviour than NiCrBSi coating under the similar conditions.

Cha and Wolpert (2003) also studied high-temperature erosion and corrosion behaviour of HVOF sprayed coatings on 15Mo3 base materials in the environment containing HCl, H₂O, O₂ and N₂ at a temperature of 500 °C for 168 hours. The coatings used were Ni-based Colmonoy 62 (NiCrFeBSi) and Co-based material T800. They reported that Co-based T800 coatings show poor corrosion resistance as compared to Ni-based Colmonoy 62 coatings. They further indicated that Colmonoy 62 applied by HVOF or the APS process show almost the same corrosion rate. However, HVOF produces less oxide, particularly along the fusion line and the coalescence of the oxides is stronger with the AP process.

Miguel et al. (2003) studied the wear resistance and wear mechanisms of NiCrBSi coatings obtained by spray and fuse and as-sprayed coatings obtained by Atmospheric Plasma Spraying (APS) and High Velocity Oxy Fuel (HVOF). They found that HVOF sprayed as well as spray and fused coatings perform well, whereas Plasma sprayed coating show the worst sliding wear resistance.

Wang et al. (2004) tested the hot corrosion behaviour of arc ion plating NiCoCrAlY (SiB) coatings deposited on nickel base superalloys DZ 125 and DSM 11, in molten 75 Na₂SO₄ + 25K₂SO₄ (wt%) at 900 °C in air for 90 h. The coating improved the hot corrosion resistance of DZ125 and DSM11 superalloys. The authors concluded that the additions of Si and B can promote the selective oxidation of the protective scale-forming elements resulting in the formation of a continuous scale in the initial corrosion stage and improve the adherence of the outer scale to the coating in the subsequent hot corrosion process.

Zhao et al. (2004A) used electrochemical tests to evaluate the corrosion resistance of HVOF sprayed NiCrBSi coatings onto a steel substrate. They reported that NiCrBSi coating has excellent corrosion resistance in alkali solution, because the surface can keep in a self-passivation condition. He reported that the effects of porosities on the early corrosion of coating are not serious unless there are penetrating porosities. However, presence of porosities can do harm to the persistent corrosion resistance of coatings.

2.9.3 Behaviour of Cobalt-Based Coating

Cobalt-based alloys containing chromium, tungsten and carbon, are known as 'Stellite' alloys. One of the common Co-based alloys in use is Stellite-6 (Kong et al., 2003). In Stellite-6 alloys, Cr provides oxidation and corrosion resistance, as well as strength by the formation of M₇C₃ and M₂₃C₆ carbides. Refractory metals such as Mo and W, which are known to be solid-solution hardening elements also contribute to the strength via precipitation hardening by forming MC and M₆C carbides and intermetallic phases such as Co₃(Mo,W). Further, alloying addition of Ni, C and Fe promotes the stability of an f.c.c. structure of Co-rich matrix, which is stable at high-temperatures up to the melting point (1495°C), whilst Cr, Mo, and W tend to stabilize at low-temperature,

hexagonal close-packed (h.c.p.) crystal structure, which is stable at temperatures below 417 °C. Stellite-6 has high hardness at high-temperature, high corrosion resistance and wear resistance (Antony, 1983; Crook, 1993).

Schmidt and Ferriss (1975) studied wear and corrosion resistance of cobalt-based Tribaloy (registered trade name) in corrosion environments and found that alloy has outstanding wear resistance. There were no signs of corrosion on the test surfaces and weight loss was low or moderate. Cermet (WC/Co) thermal spray coatings are widely used in wear situations because they combine several advantages such as resistance to abrasion, erosion, high-temperature and corrosive atmospheres (Chuanxian et al., 1984; Liao et al., 2000).

Co-25 wt% Cr, Co-25 wt% Cr-1 wt% Y and yttrium-implanted Co-25 wt% Cr alloy specimens were oxidised at 1000 °C by Hou and Stringer (1988). The unimplanted binary alloy was reported to be oxidised to duplex Co-rich scale, but the Y-containing ternary alloy formed a continuous Cr₂O₃ layer. They revealed that a temporarily stable Cr₂O₃ scale is formed on the most heavily implanted specimens (1×10^{18} Y⁺/cm²). This Cr₂O₃ scale consists of very fine grained oxide, which is permeable to the outward transport of Cr and Co. Internal oxidation during pre-treatment of the ion-implanted specimens has been reported to convert the Y metal to its oxide prior to the oxidation experiment, which enhances the development of an external Cr₂O₃ scale that has also been reported to be unstable. Selective oxidation of chromium in an ordinarily non-Cr₂O₃-forming alloy has been reported to be due to the reactive element oxides acting as preferential nucleation sites on the alloy surfaces.

Loss of WC was observed by Lovelock et al. (1998) during thermal spraying primarily by a combination of decarburisation and dissolution in the binder metal during spraying, whereas WC-Co transformed to phases such as W₂C, Co₃W₃C (η phases), Co₆W₆C (ϵ phase), WC_{1-x}, WO₃ and W. According to them, the original cobalt binder phase of the powder is replaced in the coating by an amorphous or nanocrystalline binder phase.

The high-temperature wear characteristics of Stellite-6 alloy containing Cr₃C₂ after thermal fatigue and oxidation treatment at 700 °C, has been investigated by Aoh and Chen (2001). Plasma transferred arc (PTA) process was used to form hard facing layers of alloy powders Stellite-6 and Stellite-6 with Cr₃C₂ on medium carbon steel. They found that thermal fatigue cracks initiated from the surface of Stellite-6 with Cr₃C₂ and propagated into the clad layer along the carbide boundaries, whereas no thermal fatigue crack was observed on the Stellite-6 clad layer. They further noticed that the formation of the oxide layer was enhanced by Cr₃C₂ content in the alloy and the surface oxidation was beneficial to the improvement of wear resistance.

Kong et al. (2003) studied microstructural characterisation of HVOF sprayed Stellite-6 coatings deposited on low carbon mild steel. They revealed that the microstructure of

the as-sprayed coatings comprised, principally, of a microcrystalline, fcc Co-based metallic matrix, with some regions accounting for ~20% partially melted dendritic structure. A small proportion of unmelted feedstock powder particles were also present in the coating. They further reported that M_7C_3 carbide phase was not present in the coatings, although it was present in the original feedstock powder. They suggested that its formation in the coatings might have been suppressed by the high cooling rates occurring during splat solidification.

Cha and Wolpert (2003) studied the high-temperature erosion and corrosion of thermally sprayed coatings on 15Mo3 and 13CrMo44 base materials. The coatings were Ni-based materials like Colmonoy 62 (NiCrFeBSi) and NiCrBSi/WC and Co-based material T800 fabricated by thermal spray processes like HVOF, Flame sprayed and sintered (FS/sinter) and air plasma spray (APS). The corrosion studies in the environment containing HCl, H_2O , O_2 and N_2 at a temperature of 500 °C indicated that the Colmonoy 62 applied by HVOF or by APS show the same corrosion rates. HVOF sprayed T800 coating experienced the highest corrosion rate. NiCrBSi/WC coating formed by FS/sinter proved to be a fair combination of erosion and corrosion resistance.

Singh et al. (2005C) evaluated the hot corrosion performance of plasma sprayed coatings on a Fe-based superalloy in Na_2SO_4 -60% V_2O_5 environment at 900°C for 50 hrs under cyclic conditions. They used thermogravimetric technique to establish kinetics of corrosion. They reported that Stellite-6 coating has decreased the weight gain to around 60% of that of the bare superalloy. They suggested that the protection provided by the Stellite-6 coatings may be due to the formation of phases CoO, $CoCr_2O_4$, and Cr_2O_3 . Spalling of the coating as well as of the oxide scale was also observed by them during the investigation.

Singh et al. (2005D) further studied the corrosion behavior of plasma-sprayed Stellite-6 coatings on a Ni-Base Superalloy in the same environment at same temperature under cyclic conditions. They reported that the Stellite-6 coating was successful in developing resistance against hot corrosion. They attributed hot corrosion resistance of Stellite-6 coatings to the formation of oxides of cobalt and chromium, and spinel containing chromium and cobalt. Luthra (1985) proposed that the formation of spinels might stop the diffusion activities through the cobalt oxide (CoO), which in turn suppresses the further formation of this oxide. He further opined that increases in the growth of $CoCr_2O_4$ and Cr_2O_3 in competition with CoO and Co_3O_4 formation increases the corrosion resistance of alloys.

Sidhu et al., 2006C and 2006 E reported the hot corrosion performance of HVOF sprayed Stellite-6 coatings on a Fe-based superalloy in Na_2SO_4 -60% V_2O_5 environment at 900 °C under cyclic conditions. Study showed that the Stellite-6 coating was successful

in decreasing the mass gain to about one-fourth as compared to the uncoated superalloy. The protection shown by this coating has been attributed to the formation of the oxides of chromium and spinels of chromium and cobalt.

Sidhu and Prakash (2006I and 2006J) investigated the performance of plasma sprayed Stellite-6 coatings on boiler steels in the simulated molten salt environment as well as in the actual boiler conditions. The author reported that Stellite-6 coatings are effective in both the environments. They revealed that the formation of CoCr_2O_4 spinel in both the environments contributes to requisite resistance, which blocks the diffusion activities through the CoO by suppressing the further formation of CoO , as has also been suggested by Luthra (1985).

Sidhu et al. (2006K) studied the HVOF sprayed Stellite-6 coating deposited on ASTM-SA210 GrA1 steel in the molten salt environment of Na_2SO_4 –60% V_2O_5 salt mixture at 900 °C under cyclic conditions. They reported that Stellite-6 coating is successful in providing the necessary hot corrosion resistance to the bare steel substrate. They concluded that the protection shown by stellite-6 coating is due to the formation of cobalt oxide and spinels of chromium and cobalt.

2.9.4 Behaviour of Nickel-Chromium Coatings

Nickel–chromium alloys are well known as coatings to resist oxidation and corrosive environments at high-temperature. When nickel is alloyed with chromium, the chromium may oxidize to produce a surface oxide of Cr_2O_3 at rates slow enough to make it suitable for use up to about 1000 °C (Goward, 1986). Higher temperatures present the problem of evaporation of Cr_2O_3 vapour. The more rapidly this surface oxide layer is formed, the better is the protection offered (Link et al., 1998). There is an increasing interest in the deposition of Ni-based metallic alloys for protection against corrosion. Ni-based coatings are used in applications where wear resistance combined with oxidation or hot corrosion resistance is required (Edris et al., 1997).

The high resistance of high-chromium, nickel-chromium alloys to high-temperature oxidation and corrosion makes them widely used as welded and thermally sprayed coatings in fossil fuel-fired boilers, waste incineration boilers, and electric furnaces (Kawahara, 1997). Modern thermal spray processes such as HVOF and plasma spraying are often applied to deposit high-chromium, nickel coatings onto the outer surface of various parts of the boilers, e.g. tubes, to prevent the penetration of hot gases, molten ashes, and liquids to the less noble carbon steel boiler tubes (Tuominen et al., 2002)

Longa and Takemoto (1992) investigated high-temperature oxidation of as-sprayed as well as gas flame-sprayed NiCr coatings in a mixed salt of 15% Na_2SO_4 – V_2O_5 at 900 °C. They revealed that the NiCr coatings offers better corrosion resistance in as-sprayed condition than that in laser glazed condition. Laser glazed NiCr coating showed

exfoliation from its substrate after high-temperature testing, which is ascribed to poor adhesion of the coating to the substrate.

High-temperature oxidation and corrosion resistance of plasma transferred arc welded Ni-Cr alloy coatings have been studied by Yamamoto and Hashimoto (1995). They observed that the Ni-20Cr coatings show a good oxidation resistance, while the Ni-50Cr coating collapse because of a large amount of oxide scales. In the case of the vanadium induced corrosion, they noticed that the resistance of the coatings improves with an increase in Cr content.

Longa-Nava et al. (1996) investigated the hot corrosion behaviour of as sprayed LPPS Ni-20Cr coating on type 304 stainless steel, induced by thin fused films of Na₂SO₄ and 0.7 mole fraction Na₂SO₄-0.3 mole fraction of NaVO₃ at 900 °C in a 1% SO₂-O₂ gas atmosphere. They found that the coating is successful in resisting the hot corrosion. They observed that the formation of Cr-rich oxide layer of approximately 30µm after 16 hours exposure prevents sulphidation of the alloy.

The oxidation behaviour of Ni-20Cr foils of 100- and 200-µm thickness has been investigated by Calvarin et al. (2000) in air between 500 and 900 °C. The scale formed at all the temperatures was complex with an outer NiO layer having columnar grains and an inner layer of equiaxed NiCr₂O₄+NiO+Cr₂O₃ grains. They found that at low temperatures (500-600 °C), the chromium content was insufficient to form a continuous Cr₂O₃ layer, whereas such a continuous layer formed at the inner interface at oxidation temperatures of 700 to 900 °C. The formation of all these oxides layers was found to be in agreement with the Wagner Theory and was justified on the basis of effective diffusion coefficients.

Hidalgo et al. (2001) studied the behaviour of plasma sprayed NiCr coatings under simulated coal-fired boiler atmosphere at 500 and 800 °C. They reported that high-temperature oxidation rates of the coatings in post-combustion gases from coal-fired boilers are low and the oxidation kinetics laws are parabolic, revealing the protective behaviour of the oxide scales.

High-temperature corrosion resistance of Ni-20Cr, Ni-50Cr and Cr coated boiler tubes in an actual refuse incineration plant as well as in laboratory tests have been evaluated by Yamada et al. (2002). It was observed that detonation sprayed Ni-50Cr coating exhibit a highest corrosion resistance in the laboratory test at 600 °C, followed by the HVOF coatings among the detonation gun sprayed, plasma sprayed and HVOF sprayed coatings. The detonation sprayed Ni-50Cr coated tubes performed very well for seven years of testing in the actual plant without any problems and were expected to have a longer life. They further concluded that the Incolloy 825 and Inconel 625, having high nickel content possessed higher corrosion resistance than the stainless steels.

Gudenau et al. (2002) compared the corrosion behavior of thermal sprayed and diffusion-coated materials. The results of the high-temperature corrosion test showed that the layers with NiCr applied by atmospheric plasma spraying (APS) and high velocity oxy fuel flame spraying (HVOF) are more resistant than the layers with NiCrBSi and Cr₃C₂/NiCr.

Uusitalo et al. (2003) studied the high-temperature corrosion behaviour of HVOF sprayed Ni/Cr coatings on ferritic and austenitic boiler steels in an oxidising atmosphere of 500 vppm HCl, 3%O₂, 14%CO₂, 20% H₂O and argon as balance for 1000 h. The Ni-49Cr-2 Si coating performed well as no corrosion products were detected at the coating surface. No internal attack or attack on the substrate through this coating was observed. Whereas Ni-57CrMoSiB and Ni-21Cr-9MoFe coatings were proved to be poor in resisting the high-temperature oxidation as the substrates were attacked by corrosive species through the voids and oxides.

Uusitalo et al. (2004) also investigated the high-temperature behaviour of the same coatings in the presence of a salt environment of 40% Na₂SO₄-40% K₂SO₄-10NaCl-10KCl in two environments viz. oxidising environment of N₂-20H₂O-14CO₂-3O₂-500 vppm HCl, reducing environment of N₂-20H₂O-5CO-0.06H₂S-500 vppm HCl. They found that the corrosion was more severe in oxidising environments as compared to the corrosion in reducing environment. An active oxidation was responsible for the accelerated corrosion in oxidising environments. The coatings were prone to the chlorine attack in both the atmospheres through the interconnected oxide network at the splat boundaries. The Ni-57CrMoSiB coating was the only material forming a protective oxide layer. Whereas in reducing conditions the materials with high chromium content were found to be able to form a protective layer containing chromium, sulphur, and sodium. The corrosion resistance of this layer increased with increasing chromium content. Further, it was concluded that the corrosion resistance of the nickel-based, high chromium coating materials was satisfactory in the test conditions.

Ul-Hamid (2003) investigated the isothermal oxidation behaviour of the Ni-20Cr binary alloy at 750 and 1000 °C in air for 50 h. They reported the formation of the oxide phases as α-Cr₂O₃, NiCr₂O₄ and NiO. The outer oxide constituted mainly of NiO and the inner oxide consisted of a mixture of NiCr₂O₄, α-Cr₂O₃, and NiO.

Singh (2003A) evaluated the oxidation and hot corrosion performance of plasma sprayed Ni-20Cr coatings on some boiler steels at 900 °C in the molten salt environment (Na₂SO₄-60%V₂O₅) in laboratory tests. The coatings were tested in the actual boiler environment also. He observed that the coated boiler steels show very high oxidation as well as hot corrosion resistance as compared to uncoated steels. The formation of phases

like Cr_2O_3 and NiCr_2O_4 in the scale of the coatings was suggested to induce the requisite resistance in the boiler steels.

Sundararanjan et al. (2003A) evaluated the steam oxidation resistance of HVOF as well as air plasma sprayed Ni-20Cr metallic coatings on 9Cr-1Mo type steel at four steam temperatures in the range of 600-750 °C. The results showed that thick and dense HVOF coating yield a better steam oxidation resistance than the thin and porous APS coating. The formation of a continuous protective oxide scale of Cr_2O_3 has been reported on the HVOF coating surfaces, despite their low concentration in the coating material. The diffusion of nickel from the coatings to the substrate and iron from the substrate to the coatings for longer exposures to steam oxidation has also been noticed. The rate of diffusion of Ni and Fe has been found to be almost similar. The diffusion of iron caused formation of Fe_2O_3 scale, which is suggested to be reason for non-protectiveness of coatings for longer exposure times. In the case of the Ni-50Cr coatings, the HVOF coating forms a complete Cr_2O_3 healing layer, which prevents the scale growth. Additionally, in the case of APS coating, the scale initiation has also been reported at the interface between the coating and the substrate, where as it is absent in HVOF coating (Sundararanjan et al., 2003B).

In view of the severe sulphidation of boiler tubes used in coal-burning power plants, Xuefeng (2004) studied the corrosion behaviour of two arc sprayed coatings (70Ni-30Cr and 56Ni-43Cr) on a mild steel substrate in a mixed gas environments containing 10% H_2S at 400, 500 and 600 °C. They found a duplex scale consisting of an outer Ni-rich layer and an inner Cr-rich layer, on both the coatings. An excellent sulphidation resistance has been shown by the high-chromium coating.

Lianyong et al. (2005) reported that oxidation, sulphidation and molten salt corrosion are the main high-temperature corrosion problems for the water-wall tubes of boilers used in thermal power plants where the most severe corrosion occurs in the molten salt corrosion environment. They studied the corrosion resistance of the high velocity electric arc sprayed (HVAS) coatings. By comparison, they recommended NiCr (Ni-45Cr-4Ti) as a promising alloy coating for the water-wall tubes, which can resist molten salt corrosion attack. They found that (i) the corrosion resistances of NiCr and FeCrAl coatings are much better than that of 20 g steel, (ii) NiCr coatings showed the best anti-corrosion properties, and that (iii) the NiCr coatings have slightly lower porosity than FeCrAl coatings. They concluded that the corrosion resistance of the coatings is mainly determined by the chromium content, whereas the microstructure of a coating is also as important as the chemical composition of the material.

Sidhu et al., 2006G reported that HVOF sprayed Ni-20Cr wire coatings have a dense and nearly uniform lamellar microstructure with porosity less than 1% and hardness values in the range of 600-630 Hv. The author (Sidhu et al., 2006C, 2006E, 2006F, and 2006H) further examined the performance of this coating on a Fe-based superalloy in a Na_2SO_4 -60% V_2O_5 environment at 900 °C as well as in the actual working condition of the coal fired boiler of a thermal power plant under cyclic conditions. It has been found that the Ni-20Cr wire coating show excellent hot corrosion resistance in both the environments. The corrosion resistance of this coating have been attributed to the presence of the oxides of nickel and chromium and their spinels.

Sidhu et al. (2006K) studied the hot corrosion resistance of HVOF sprayed Ni-20Cr coating in the molten salt environment (Na_2SO_4 -60% V_2O_5) at 900 °C for 50 cycles. They reported that Ni-20Cr coating show best hot corrosion resistance as compared to Cr_3C_2 -NiCr, Stellite-6 and WC-Co coatings. They attributed better performance of the Ni-20Cr coating to the formation of protective oxides like Cr_2O_3 , NiO and NiCr_2O_4 in the scale. They further reported that the hot corrosion resistance of Cr_2C_3 -NiCr coating is better than Stellite-6 coating.

PROBLEM FORMULATION

After reviewing the literature critically, the scope of the problem and the objectives of the present study have been formulated. The present investigation is mainly focused on the hot corrosion problems of boilers.

3.1 SCOPE

Hot corrosion of boiler tubes used for super-heaters and re-heaters in the steam-generating systems has been recognized as a severe problem. These tubes are subjected to fireside corrosion, resulting in tube wall thinning and premature failure. Attempts to decrease maintenance costs of these components have increased interest in shielding them with protective coatings. Hot corrosion degradation of materials has also been identified as a serious problem in other high-temperature applications such as in waste incinerations, diesel engines, gas turbines, coal gasification plants, and chemical plants.

Combustion of coal generates very corrosive media particularly near the superheater tubes of the boilers (Weulersse-Mouturat et al., 2004). In the boiler tubes suffering severe fireside corrosion, sulphate salts concentrate at the deposit/scale interface and become partially fused since these salts contain alkali metals of sodium and potassium (Otsuka, 2002). In the combustion systems, much of the sodium and potassium is volatilized from the mineral matters in the flame to form Na_2O and K_2O vapours. The sulphur released from the coal, forms SO_2 with a minor amount of SO_3 and reacts with the volatilized alkalis to form Na_2SO_4 vapours, which then condense together with fly ash on the pendant superheater and reheater tubes in the boiler. These are the major areas where critical high-temperature fireside corrosion problems are encountered, particularly on the leading tubes in a bank. The corrosion has been attributed to the fluxing action of the molten salt on the oxide scales formed over the tubes, leading to a rapid localized corrosion, accompanied by the sulphidation (Beltran and Shores, 1972).

In the boilers burning residual oil, the compounds formed by vanadium, sodium and sulphur, mainly as $\text{Na}_2\text{SO}_4\text{-V}_2\text{O}_5$ complex and sodium–vanadates mixtures condense on the heating surfaces of furnace super-heaters or re-heaters (Harada et al., 1981; Wong-Moreno and Salgado, 1995). The condensation /accumulation of these low melting-point salts from flue-gas on the tube surface is considered to be a root cause for the severe wastage of the tube materials, since these compounds easily liquefy at the operating metal temperatures and induce accelerated oxidation (hot corrosion) (Otsuka, 2002).

High-temperature erosion-corrosion and oxidation of the heat transfer pipes and other structural materials in the coal fired boilers are recognized as being the main cause of downtime at power generating plants, accounting for 50% to 75% of the total arrest time (Cutler, 1978). Maintenance costs for replacing the broken pipes in such installations are also very high and are estimated to be up to 54% of the total production costs (Chandler and Quigley, 1986). Lee and Lin (2003) reported that the primary corrosion problem in fluidized bed combustor (FBC) systems has been identified as the internal sulfidation–oxidation of alloys beneath the oxide scale at metal temperatures above 600°C, which reduce the stability of the protective oxides and destroy the continuous adherent oxide scales by forming fast-growing sulphides, and degrade the mechanical properties of the alloy.

Although natural gas has been considered as an alternative to the traditional fuels for generation of electricity in the combined cycle power plants, there is a strong interest in the development of clean, high efficiency coal-base systems for the power generation (Saunders et al., 1997). This might be due to anticipated saving of the high grade energy such as natural gas. Similarly, in coal conversion processes, which are known to produce clean environmentally acceptable fuels, technical problem arises from the interaction of sulphur and ash in the coal with plant construction materials at high-temperatures and pressures (Natesan, 1985). Although superalloys have been developed for high-temperature applications, the presence of combustion gases constitutes an extreme environment and the hot corrosion is inevitable when these alloys are used at high-temperatures for longer periods of time (Goebel et al., 1973).

These facts emphasize that the hot corrosion problems of the superheaters and reheaters of the boilers require some preventive measures. It is learnt from the published literature that one possible, practical, reliable and economically viable way to control or prevent the hot corrosion problems of the superheaters and reheaters of the boilers is an application of a thin layer of corrosion resistant coatings having good thermal conductivity such as nickel based or cermet (carbide-metal) alloys. Due to the continuously rising cost of the bulk materials as well as increased material requirements, the coating techniques have been given more importance in the recent times. Therefore, the use of protective overlay coatings has been identified as a potential area for the present research.

Porosity, stress generation and interlayer separation between the different deposited layers are the prominent parameters to be considered for selecting a particular process for deposition of the corrosion resistant coating as they are the preferential corrosion paths where the corrosion species can penetrate through the coating to reach the substrate and

may cause rapid corrosion attack. The easiness, economy and convenience of operations are the other major factors that must be considered for applying the coatings to industrial installations at site. The HVOF and plasma thermal spray techniques are commonly considered to deposit the overlay coatings for industrial applications.

The HVOF is a relatively recent and promising process which can yield high density coatings with porosity less than 1%, having high hardness values and a good adhesive strength (Sidhu et al., 2005B). This process is used extensively due to its properties being superior to even vacuum plasma spraying (VPS) process. In contrast to the VPS, the HVOF spray systems are operated at atmospheric pressure, the process monitoring is easier and the investment costs are roughly $1/10^{\text{th}}$ compared to the VPS (Irons and Zanchuk, 1993). Further, in comparison with the plasma spraying, the HVOF has the advantage of being a continuous process and has been widely adopted in many industries due to its flexibility and cost effectiveness for on-site coating applications to industrial installations. Therefore, in the present investigation, the HVOF process has been selected to deposit the coatings for evaluating their hot corrosion behaviour.

Chatterjee et al. (2001) have reported that, in general, the behaviour of the protective coatings in environments of their use and their interactions with the substrate during high-temperature performance is not well understood. Uusitalo et al. (2003) have also suggested that there is a need to investigate the high-temperature corrosion behaviour of the thermal spray coated materials in different aggressive environments.

Some research workers have reported against post laser melting of the thermal spray coatings. Streiff (1987) revealed that the trapped oxygen in the coatings causes unfavourable oxide inclusions during the laser remelting process. These inclusions may develop into sites of oxidation attack. Longa and Takemoto (1992) observed that the laser glazed Ni-Cr coating showed exfoliation from the substrate after high-temperature testing, due to a poor adhesion to the substrate, and indicated less corrosion resistance to a mixed salt (15% $\text{Na}_2\text{SO}_4\text{-V}_2\text{O}_5$) corrosion at 900 °C in comparison to the coating in the as-sprayed condition. Kinoshita et al. (1994) reported that the corrosion resistance of the HVOF sprayed coating cannot be improved by the post treatment. Singh (2003A) attempted laser remelting of the plasma sprayed coatings to decrease/eliminate the porosity. However, he observed that these laser remelted coatings showed slightly inferior hot corrosion resistance in molten salt environment as compared to the as coated samples. This behaviour was attributed to the presence of vertical cracks in the laser remelted samples after exposure to the hot corrosion, through which the oxidising environment could reach the substrate steels.

3.2 OBJECTIVES

The present research programme aims to comparatively evaluate the hot corrosion behaviour of four commercial feedstock alloys deposited on five types of Ni- and Fe-based superalloys using an HVOF process, with an objective to protect the boiler superheaters and re-heaters for use at temperatures significantly above that used in the existing steam-generating systems. It is aimed to study the hot corrosion behaviour of HVOF sprayed $\text{Cr}_3\text{C}_2\text{-NiCr}$, NiCrBSi , Stellite-6 and Ni-20Cr coatings by the accelerated corrosion testing in the molten salt environment using a laboratory tube furnace as well as in the actual industrial environment of a power plant where these coatings are intended to be used.

The research programme was designed to compare the hot corrosion performance of the HVOF coated superalloys with uncoated ones, to compare and rank the hot corrosion performance of these coatings and coating-substrate systems, and to select the best performing coating and coating-substrate combination for implementation in the boiler superheaters and re-heaters, and for other future hot section components for use in similar corrosive environments. An attempt would be made to understand and propose mechanisms for the high-temperature corrosion of the substrate superalloy and coated alloys, wherever possible.

In the laboratory tube furnace, the tests have been planned to be carried out in a molten salt environment comprising of $\text{Na}_2\text{SO}_4\text{-60}\%\text{V}_2\text{O}_5$ at an elevated temperature of 900 °C under cyclic conditions. The behaviour of bare superalloys has also been investigated under similar conditions to assess the effectiveness of the HVOF coatings. The exposure time for the laboratory test has been selected as 50 cycles; each cycle consisting of 1 hour heating followed by 20 minutes cooling in air. The oxidising time of 50 hours is considered adequate for the study of the steady-state oxidation of materials (Wood and Hodgkiess, 1966; Ul-Hamid, 2003). The temperature of study has been purposely kept high (900 °C) as this will take into consideration the overheating effects in case of boilers, which has been identified as the major cause of failure (Metals Handbook, 1975). Moreover, near 900 °C, the rate of high-temperature hot corrosion (HTHC) has been reported to be the severest, Fig. 3.1 (National Materials Advisory Board, 1996). Experiments have been proposed to be conducted in a silicon tube furnace because both the furnaces as well as the burner rig tests are capable of reproducing the corrosion observed in service (Saunders and Nicholls, 1984). Further, the testing in the tube furnace provides a means to control conditions, such as temperature and environment, more precisely.

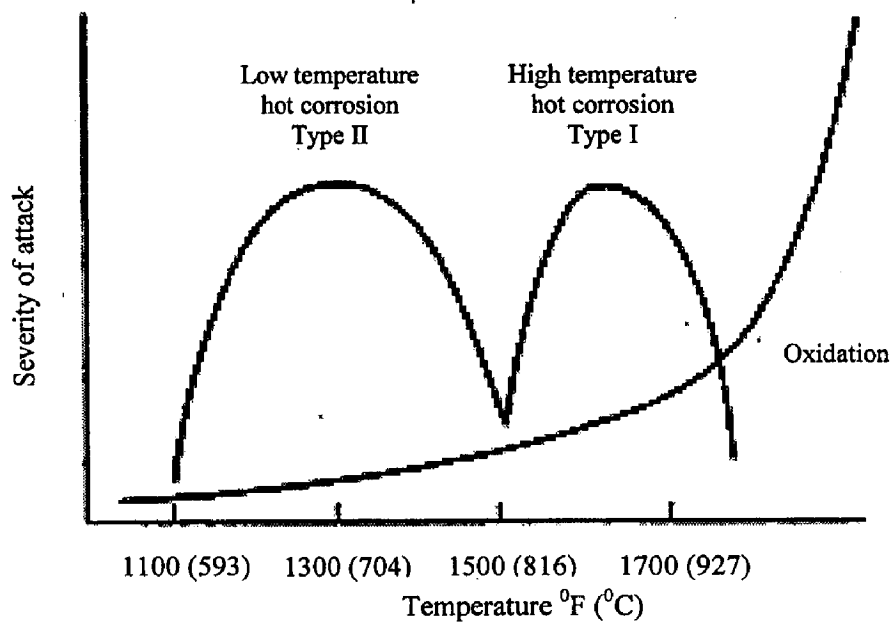


Fig. 3.1 Types of high-temperature attack for metallic coatings (aluminide, chromide, MCrAlY, etc.) on nickel-base superalloys with approximate temperature regimes and severity of attack (National Materials Advisory Board, 1996).

The hot corrosion environment Na_2SO_4 -60% V_2O_5 has been selected for the laboratory tests as the molten sulphate-vanadate deposits resulting from the condensation of combustion products of low grade fuels are extremely corrosive to the high-temperature materials (Rapp, 1986). Furthermore, sodium vanadyl vanadate ($\text{Na}_2\text{O} \cdot \text{V}_2\text{O}_4 \cdot 5\text{V}_2\text{O}_5$), which melts at a relatively low temperature 550 °C is found to be the most common salt deposit on the boiler superheaters (Barbooti et al., 1988). This environment will also be pertinent to the gas turbines as the predominant species in the salt deposits forming on gas turbine surfaces are expected to be Na_2SO_4 , V_2O_5 and $\text{Na}_2\text{V}_2\text{O}_6$. According to Goward (1986) the corrosions in the boilers and turbines have much in common.

In order to establish the behaviour of these coatings and bare superalloys in the actual working conditions in which they may be used, it has been planned to study the coatings in the operational environment of the coal fired boiler at Guru Nanak Dev Thermal Plant, Bathinda, Punjab, India. The tests have been designed to expose the coated as well as the uncoated samples for 1000 hours to the combustion environment of the coal fired boiler in the regions of the platen superheater, where temperature is around 900 °C with variation of ± 10 °C. It has been aimed to conduct the study under cyclic conditions for 10 cycles, each cycle consisting of 100 hour duration heating followed by 1 hour cooling at the ambient conditions.

In both the laboratory as well in industrial environments, it has been planned to conduct the experiments under cyclic conditions as the cyclic study provides the severest conditions for testing and represents the actual industrial environment where breakdown and shutdown occur frequently. Metal corrosion problems in actual applications are more or less cyclic rather than isothermal (Sadique et al., 2000). Cyclic modes of testing introduce strain between the coating and the substrate, and between the coating and the scale. Further, the oxide scale formation and spalling can be followed from the weight changes that occur per cycle (Nicoll, 1984). Moreover, all potential commercial alloys should be subjected to thermal cyclic mode of testing to consider the effect of surface stresses developed due to disparity in the coefficients of expansion of the base alloy, coating and oxide (Hancock and Hurst, 1974). It is seen from the literature survey that relatively very few studies are reported on hot corrosion behaviour of the HVOF coatings under the cyclic conditions.

Numerous research workers have reported the inter-diffusion of the elements between the coating and the substrate during the high temperature exposures (Smeggil and Bornstein, 1983; Singh, 2003A; Sundararajan et al., 2004A; Prakash et al., 2005; Singh et al., 2005C and 2005D; Xiao et al., 2006). Shifler (2004) discovered that the

high-temperature coatings on various superalloy substrates behaved differently during 1000 hours of exposure in a Type I hot corrosion environment at 899°C. He reported that differences in chemical compositions between a coating and a substrate alloy can lead to inter-diffusion between these materials that can modify the oxidation and corrosion resistance of the coating and the mechanical properties of the coating-substrate system. He further suggested that the stress state may also significantly influence and increase the magnitude of the inter-diffusion that may lead to deleterious precipitation reactions. Sundararajan et al. (2005) reported that diffusion of elements adjacent to the coating-substrate interface induces microstructural changes. Therefore, several superalloys have been chosen for the study to understand the effect of the composition of the substrate alloy on the hot corrosion behaviour of a particular coating. Besides, the study would be useful to rank the alloys under investigation with respect to their hot corrosion performance in the given environments of the study.

Ni- and Co-based metallic coatings are frequently considered for the protection against oxidation, corrosion, wear and erosion at high temperatures. Many researchers have reported high erosion, corrosion, and wear resistance of HVOF sprayed Cr₃C₂-NiCr and Ni-20Cr coatings, whereas HVOF sprayed NiCrBSi and Stellite-6 Coatings are less reported. However, it is found from the open literature that very little attempt is made to evaluate the hot corrosion behaviour of these coatings in the simulated as well as in actual working environment of the boilers. The HVOF systems are the most convenient processes for applying coatings to in-service boilers at site. Therefore, it has been planned to deposit the feedstock materials namely Cr₃C₂-NiCr, NiCrBSi and Stellite-6 in the powder form and Ni-20%Cr in the wire form on all the chosen superalloys by using the HVOF process to evaluate their hot corrosion behaviour in the molten salt environment as well as in the actual environment of the boiler, with an aim to protect the boiler tubes used for the super-heaters and re-heaters in the steam-generating systems.

Thermogravimetric studies have been proposed to be conducted under the cyclic conditions in Na₂SO₄-60%V₂O₅ environment as well as in actual industrial environment of the boiler to establish the kinetics of corrosion. Standard techniques such as X-ray Diffractometer (XRD), Scanning Electron Microscope (SEM), Energy Dispersive X-ray Analysis (EDAX) and Electron Probe Micro Analyser (EPMA) are proposed to be used to characterise the as sprayed coatings and the corrosion products.

EXPERIMENTAL EQUIPMENTS AND PROCEDURES

This chapter contains description of the experimental equipments used and the procedures adopted for deposition and characterizations of the coatings, the hot corrosion studies and analyses of the corrosion products.

4.1 SUBSTRATE MATERIALS

The Ni-based superalloys namely Midhani Grades Superni 75, Superni 600, Superni 601, and Superni 718, and Fe-based superalloy namely Superfer 800H have been selected for the present study as the substrate materials. These alloys were provided by Mishra Dhatu Nigam Limited, Hyderabad (India) in the rolled sheet form, for protecting them against high temperature corrosive environment applications. The nominal chemical compositions of these alloys are given in Table 4.1. These superalloys have applications in steam boilers, heat exchangers and piping in the chemical industry, gas turbines, jet engines, furnace equipment, reformers and baffle plates/tubes in fertilizer plants.

4.2 FEEDSTOCK MATERIALS FOR THE COATINGS

Four types of commercially available feedstock materials: Cr_3C_2 -NiCr, NiCrBSi and Stellite-6 in the powder form and Ni-20Cr in the wire form have been used for depositing the coatings on the five types of substrate superalloys. The chemical composition and particle size of all the feedstock materials have been reported in Table 4.2. It is pertinent to mention here that the commercially available feedstock materials have been selected in the present study for depositing the coatings to evaluate their hot corrosion behaviour as many researchers have reported that these coatings have high wear and erosion-corrosion resistance for high temperature applications.

4.3 DEPOSITION OF THE COATINGS

4.3.1 Preparation of the Substrate Materials

The specimens with dimensions of approximately 20mmX15mmX5mm were cut from the alloy sheets. The specimens were ground with SiC papers down to 180 grit and subsequently grit blasted by alumina (Grit 45) before deposition of the coatings by the HVOF Processes, for developing better adhesion between the substrates and the coatings. The specimens were prepared manually and all care was taken to avoid any structural changes in the specimens.

Table 4.1: Nominal composition and industrial applications of the superalloys used.

S. No.	Alloy Midhani Grade (Similar grade)	Chemical Composition (wt.%)										Recommended Application (Manufacturer's Catalogue)		
		Fe	Ni	Cr	Ti	Al	Mo	Mn	Si	Cu	Ta		C	
1.	Superni 75 (Nimonic 75)	3.0	Bal	19.5	0.3	-	-	-	-	-	-	-	0.100	Boiler, Gas Turbine
2.	Superni 600 (Inconel 600)	10.0 max	Bal	15.5	-	-	-	0.30	-	-	-	-	0.200	Furnace parts, heat treatment jigs
3.	Superni 601 (Inconel 601)	Bal	62	23.0	-	1.48	-	0.80	0.37	0.10	-	-	0.025	High temperature heat resistant alloy
4.	Superni 718 (Inconel 718)	18.5	Bal	19.0	0.9	0.50	3.05	0.18	0.18	0.15	5.13	-	0.040	Jet engines, pump bodies and parts
5.	Superfer 800H (Incoloy 800H)	Bal	32	21.0	0.3	0.30	-	1.50 max	1.00 max	-	-	-	0.100 max	Steam boilers, heat exchangers and piping in chemical industry, furnace equipment, reformer, baffle plates/tubes in fertilizer plants

Table 4.2: Composition of the feedstock alloys, and shape and size of the particles.

Feedstock Alloys	Chemical Composition (Wt. %)	Shape	Particle Size	Weight %age
Cr ₃ C ₂ -NiCr Powder (LA-6875, Blend of 75%LA-6304 and 25% LA-7319)	75 Cr ₃ C ₂ -25 (Ni-20Cr)	Irregular	+45μ	1.05
			-45μ	98.95
NiCrBSi Powder (PA 101HV)	Ni-15.3Cr-3.1B-4.8Si- 4.2Fe-0.6C	Spherical	+45μ	1.02
			-45 μ	98.98
Stellite-6 Powder (Jet-Kote 7206)	Co-28Cr-4.9W-2.7Fe-2.3Ni-1.1Si -1.2C	Spherical	-53μ	0.22
			+45μ	2.23
			-45μ	97.55
Ni-20Cr wire	Ni-20Cr	----	Wire diameter 3.17 mm	

4.3.2 Deposition of the Coatings

The coatings were sprayed at M/S Metallizing Equipment Co. Pvt. Ltd., Jodhpur (India) by using two types of commercial high velocity oxy-fuel (HVOF) thermal spray systems. A Hipojet-2100 HVOF system was used for the powder spraying and a Hijet-9600 HVOF system for the wire spraying, as shown in Fig. 4.1. Standard spray parameters, as mentioned in the manual of the Hipojet-2100 and Hijet-9600 HVOF systems, were used for depositing the coatings. In both the HVOF systems, the prominent spray parameters such as spray distance, air flow rate, air pressure, and type of fuel were the same. Liquefied petroleum gas (LPG) was used as a fuel. The process parameters were kept constant throughout the coating process. The specimens were cooled with the compressed air jets during and after spraying. The employed spraying parameters are presented in Table 4.3.

Table 4.3: Spray parameters employed for HVOF coating.

Parameters	Hipojet-2100	Hijet-9600
Oxygen flow rate (SLPM*)	250	200
Fuel (LPG) flow rate (SLPM)	60	50
Air flow rate (SLPM)	900	900
Spray distance (cm)	20	20
Feed rat (gm/min)		
• Cr ₃ C ₂ -NiCr powder	38	-
• NiCrBSi	21	-
• Stellite-6	26.5	-
• Ni-20%Cr wir	-	80
Ni-20%Cr wire dia (cm)	-	0.317
Fuel pressure (kg/cm ²)	6	4
Oxygen Pressure (kg/cm ²)	8	6
Air Pressure (kg/cm ²)	6	6
* SLPM =Standard Litres Per Minute		

4.4 CHARACTERISATION OF THE FEEDSTOCK MATERIALS AND COATINGS

4.4.1 Preparation of Specimens

For cross-section analysis, the as-sprayed specimens were cross-sectioned with a diamond cutter (Buehler's Precision Diamond Saw, Model ISOMET 1000, USA make). Thereafter, they were hot mounted in Buehler's transoptic powder (20-3400-080) and polished manually down to 1000 grit using SiC emery papers. Final polishing was carried out on a cloth polishing wheel machine with 1 μm lavigated alumina powder suspension. Subsequently the specimens were washed properly with flowing water, and dried in hot air to remove any moisture. For taking the surface microstructures, the as-sprayed specimens were polished similarly down to 1 μm alumina on a cloth polishing wheel.

4.4.2 Measurement of Coating Thickness

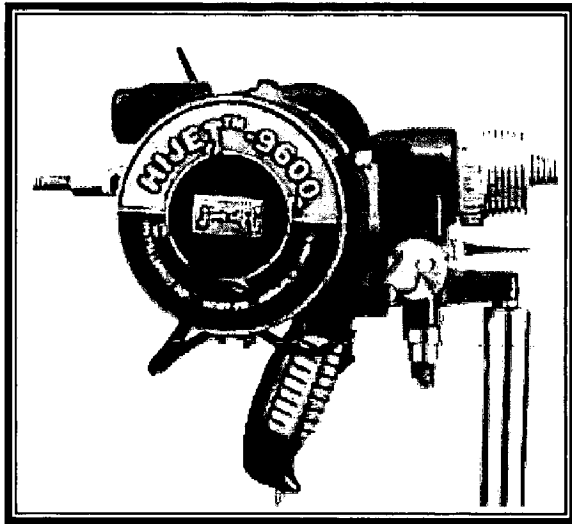
The thickness was monitored during the process of depositing the coatings with a Minitest-2000 thin film thickness gauge (Elektro-Physik Koln company, Germany, precision $\pm 1 \mu\text{m}$), to obtain the coatings with uniform thickness. Further to verify the thickness of the deposited coatings, the as-sprayed specimens were cut along the cross-section and mounted, as explained in Section 4.4.1. A Scanning Electron Microscope (LEO 435VP, Leo Electron Microscopy Ltd., Cambridge, UK, Resolution of 4.0 nm) with an attached Robinson Back Scattered Detector (RBSD) was used to obtain the back scattered electron (BSE) images. The average thicknesses of the coatings, as measured from the BSE images, have been reported in Chapter 5 of the present study.

4.4.3 Porosity Measurement

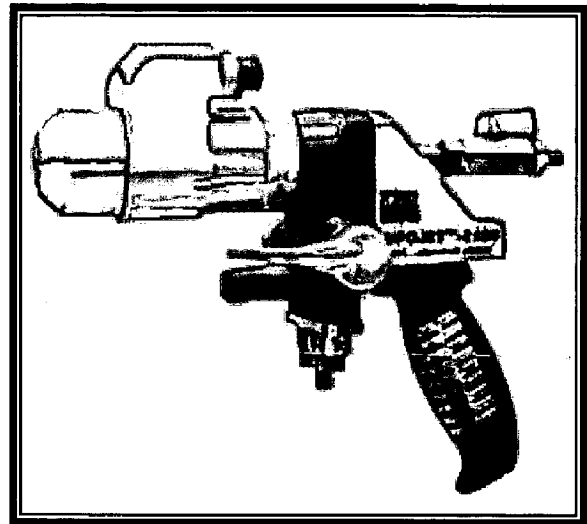
For measuring porosity, the HVOF coated specimens were polished to reveal the coating microstructure. A 'PMP3 Inverted Metallurgical Microscope' made in Japan, alongwith Image Analyser using Dewinter Material Plus 1.01 software based on ASTM (American Society for Testing and Materials) B276 was used to determine the porosity values. The computer analysis system determines the pore area size in the view field by converting the pore areas (grey-level areas) into a background colour such as red while the rest of the microstructure remains in its original colour. The area of one feature is numerically related to the total area of the picture, as the program counts the number of one colour type pixels (red) and sets that as a ratio of the total number of pixels in the picture (total area). Ten values of porosity have been measured for each coating. Average values of the porosity for each coating have been reported in Chapter 5.

4.4.4 Metallographic Studies

For obtaining cross-section microstructures of the as-sprayed coatings, the specimens were prepared as explained in section 4.4.1. Thereafter, cross-section microstructures of the coatings were obtained by a Axiovert 200 MAT Inverted Optical Microscope (Carl Zeiss



HVOF Hijet 9600



HVOF Hipojet 2100

Fig. 4.1 High velocity oxy-fuel systems used in the current research.

Ltd, Germany), interfaced with imaging software Zeiss AxioVision Release 4.1, Germany. The surface morphologies of the coatings were also studied on the same microscope. Cross-section microstructures as well as surface morphologies of the specimens have been reported in Chapter 5 of the present study.

4.4.5 Measurement of Microhardness

As-sprayed specimens were sectioned, mounted and polished as explained in Section 4.4.1 in order to measure the microhardness of the coatings as well as the substrate across the cross-section,. The microhardness was measured by a Miniload 2 Microhardness Tester (Leitz, Wetzlar, Germany), fitted with a Vickers pyramidal diamond indenter. A load of 15 grams (147.1 mN) load was used for penetration and the hardness value was calculated from the relation $H_v = 1854.4 \times F/d^2$ (Where F is load in grams and d is the mean penetrated diameter in μm). Average of five measurements is reported as a hardness value and these microhardness values are presented in Chapter 5.

4.4.6 X-Ray Diffraction (XRD) Analysis

XRD analysis was performed on both the feedstock powders as well as HVOF coated specimens to identify the various phases present on their surfaces. Diffraction patterns were obtained by a Bruker AXS D-8 Advance Diffractometer (Germany) with CuK_α radiation and nickel filter at 20 mA under a voltage of 35 kV. The specimens were scanned with a scanning speed of 1 Kcps in 2θ range of 10° to 110° and the intensities were recorded at a chart speed of 1 cm/min with $2^\circ/\text{min}$ as Goniometer speed. The relative intensities of all the peaks have been calculated by assuming height of the most prominent peak as 100%. The diffractometer interfaced with Bruker DIFFRAC^{plus} X-Ray diffraction software provides 'd' values directly on the diffraction pattern. These 'd' values were then used for identification of various phases with the help of inorganic ASTM X-Ray diffraction data cards.

4.4.7 Scanning Electron Microscopy (SEM) and Energy Dispersive X-Ray (EDAX) Analysis

4.4.7.1 Surface Morphology/EDAX Analysis

Surface morphologies of the feedstock powders and coated specimens were studied with the help of a Scanning Electron Microscope (LEO 435VP, Leo Electron Microscopy Ltd., Cambridge, UK, Resolution of 4.0 nm) with an aim to understand the structure of the coatings and to identify inclusions, unmelted and partially melted particles, pores etc. Surface EDAX analysis was carried out for the coated specimens at Central Research Facilities (CRF), Indian Institute of Technology, Kharagpur (India) on a Scanning Electron Microscope (JSM-5800, JEOL, New York, Resolution-5 nm), fitted with an EDAX attachment (Model-6841, Oxford, UK). The equipment could directly indicate the

elements or phases (oxides) present along with their compositions (weight %) based on built-in EDAX software, which is a patented product of Oxford ISIS300. The EDAX analysis was done at some selected areas considered to be representatives of the coating structure, so that the obtained data could be useful to understand the formation of desired compositions in the coatings. SEM morphologies of the feedstock powders as well as SEM/EDAX analysis for the coated specimens have been reported in Chapter 5.

4.4.7.2 Cross-Section analysis

BSEI/EDAX analysis along the cross-sections of some coated specimens, prepared as explained in Section 4.4.1, was carried out at Inter University Consortium (IUC) for Department of Atomic Energy (DAE) Facilities, Indore (India). The equipment consisted of a Scanning Electron Microscope of JEOL with EDAX attachment of Oxford model Flex Scan 520, England make. The BSE images were taken and the EDAX analysis was performed to ascertain elemental composition (weight %) at different points. The data could be used to identify the presence of various elements across the cross-section of the coatings.

4.4.8 Electron Probe Micro Analyser (EPMA)

To obtain cross-sectional analysis of the different elements present in the coatings, the specimens were cut along the cross-section, mounted and polished in accordance with the procedure already discussed in section 4.4.1. The polished specimens were coated with carbon before performing the EPMA analysis. In this analysis, first BSE image of representative area of the specimen was recorded and, thereafter elemental X-ray mapping was carried out for that area. The selected area has three regions i.e. substrate, coating and some epoxy region. X-ray mappings were obtained for all the elements of the substrate and the coatings, but only those mappings are reported in Chapter 5 which indicates the presence of some element. EPMA analysis was done at Institute Instrumentation Centre (IIC), Indian Institute of Technology Roorkee, Roorkee (India) on a JXA-8600M microprobe.

4.5 HOT CORROSION STUDIES

4.5.1 Studies in Molten Salt (Na_2SO_4 -60% V_2O_5) Environment

4.5.1.1 Experimental Set-up

The hot corrosion experiments were carried out at 900 °C in a laboratory silicon carbide tube furnace, Digitech, India make. The furnace was calibrated to an accuracy of ± 5 °C using Platinum/Platinum-13% Rhodium thermocouple fitted with a temperature indicator of Electromek (Model-1551 P), India. The uncoated as well as the coated specimens were polished down to 1 μm alumina on a cloth polishing wheel machine to obtain similar condition of reaction before being subjected to the corrosion run. Thereafter the physical dimensions of the specimens were measured carefully with a

Sylvac digital vernier caliper (Swiss make, resolution 0.01), to evaluate their surface areas. Subsequently, the specimens were washed properly with acetone and dried in hot air to remove the moisture. During experimentation, alumina boats were used to perform the hot corrosion runs in the tube furnace. The alumina boats used for these studies were pre-heated at a constant temperature of 1200 °C for 8 h so that their weight would remain constant during the course of high temperature cyclic study. The weight of boat loaded with specimen was measured after each cycle during the corrosion run, and the spalled scale in the boat, if any, was also taken into consideration for the weight change measurements. Holding time in the furnace was one hour in still air after which the boat with specimen was taken out and cooled at the ambient temperature for 20 minutes. Thereafter weight of the boat along with specimen was measured and this constituted one cycle of the study. Fifty hot corrosion runs were performed for each coated and uncoated specimens. As hot corrosion studies were cyclic in this work, it creates dynamic conditions for corrosion testing of the specimens. An Electronic Balance Model CB-120 (Contech, Mumbai, India) with a sensitivity of 10^{-3} g was used to conduct the thermogravimetric studies. Visual observations were made after the end of each cycle with respect to colour, luster or any other physical aspect of the oxide scales during the course of corrosion runs. The reproducibility in the experiments was established by repeating the hot corrosion experiments for 10 cases.

4.5.1.2 Na_2SO_4 -60% V_2O_5 Salt Coating

The coated as well as the uncoated specimens were prepared for the studies as discussed in section 4.4.1. A salt mixture of Na_2SO_4 -60% V_2O_5 (wt%) was properly mixed in distilled water. After washing with acetone, the specimens were then heated in an oven up to 250 °C. The heating of the specimens was found necessary for the proper adhesion of the salt layer. Thereafter, a layer of Na_2SO_4 -60% V_2O_5 mixture was applied uniformly on the warm polished specimens with the help of a camel hair brush. The amount of the salt coating was kept in the range of 3.0 -5.0 mg/cm². The salt coated specimens as well as the alumina boats were then kept in the oven for 3-4 hours at 100 °C. Thereafter they were weighed before exposing to the hot corrosion tests.

4.5.1.3 Hot Corrosion Runs

The uncoated as well as coated specimens, after application of the salt coating, were subjected to the hot corrosion in the silicon carbide tube furnace at 900 °C for 50 cycles as discussed in section 4.5.1.1. In the tube furnace, the silicon carbide heating rods were fitted around the outer surface of the high alumina refractory tube and specimens were kept inside the tube.

4.5.2 Studies in Industrial Environment

The HVOF coated as well as uncoated superalloy specimens were exposed to the platen superheater zone of the coal fired boiler of Stage-II at Guru Nanak Dev Thermal Plant, Bathinda, Punjab (India). This zone was selected for the present study as many breakdowns occurred in this power plant due to hot corrosion degradation of the platen superheater tubes of the coal fired boilers. A hole of 01 mm diameter was drilled in all the specimens to hang them in the boiler for experimentation. The coated as well as uncoated specimens were polished down to 1 μ m alumina on a cloth polishing wheel machine to obtain similar conditions of reaction on the surface of all the specimens. The physical dimensions of the specimens were measured with a Sylvac digital vernier caliper (Swiss make, resolution 0.01), to evaluate their surface areas. To measure the thickness loss during experimentations, the average thickness of each specimen (average of 10 measurements) was measured using Sylvac micrometer screw gauge (Swiss make, resolution 0.001), before exposing them to the boiler environment. The coated as well as uncoated specimens were then hanged with the help of a stainless steel wire through the soot blower dummy points at 34.5 m height from the base of the boiler. The specimens were exposed to the combustion environment for 10 cycles. Each cycle consisted of 100 hours heating followed by 1 hour cooling at ambient conditions. The temperature was measured at regular intervals during the study and the average temperature was about 900 °C with variation of ± 10 °C. After the end of each cycle the specimens were visually observed for any change in the surface texture and weight of the specimens were measured subsequently using an Electronic Balance Model CB-120 (Contech, Mumbai, India, and sensitivity 10^{-3} g). The chemical analysis of the flue gas and ash present inside the boiler is given in Table 4.4. The average volumetric flow of the flue gases was 122.44 m³/sec. The SO_x and NO_x values of the flue gases were 280.53 mg/m³ and 1166.67 μ g/m³, respectively. The analysis of flue gases showed presence of 12.2 % CO₂ and 7% O₂.

4.6 ANALYSIS OF CORROSION PRODUCTS

All the specimens exposed to the hot corrosion studies in the laboratory as well as in the boiler environments were analysed for characterisation of the corrosion products. XRD, SEM, surface and cross-section EDAX, measurement of scale thickness and EPMA analysis were performed to examine the surface and cross-section of the corroded specimens.

4.6.1 Visual Observations

After every hot corrosion run, surface scale of each specimen was visually examined for any change in colour, luster, adherence-spalling tendency, and growth and development

of cracks in the coatings/oxide scales etc. After the completion of 50 cycles (each cycle of 1 hr heating and 20 minutes cooling) in laboratory and 10 cycles (each cycle of 100 hrs heating and 1 hr cooling) in case of industrial environment, the specimens were examined carefully and then their macrographs were taken. The physical conditions of the exposed surface like colour, spalled scale, disintegration of the coating etc. if any can be seen from these macrographs. The macrographs of the specimens after exposure to the molten salt and industrial environments are shown in chapters 6 and 7, respectively. The macrographs were obtained on a Stemi 2000C Stereo Microscope (Carl Zeiss Jena GmbH, Germany), fitted with a Sony Cyber-Shot DSC-S85 Digital Still Camera.

Table 4.4: Chemical analysis of ash and flue gases inside the boiler.

Ash		Flue Gases	
Constituent	Wt. %age	Volumetric flow = 122.44 m ³ /sec	
		Constituent	Value relative to flue gases
Silica	52.65	SO _x	280.53 mg/m ³
Fe ₂ O ₃	5.35	NO _x	1166.67 µg/m ³
Al ₂ O ₃ -Fe ₂ O ₃ /Al ₂ O ₃	31.06	CO ₂	12.2
Calcium oxide	1.57	O ₂	7.0
Magnesium oxide	1.50	40% excess air was supplied to the boiler for the combustion of coal.	
SO ₃	0.29		
Na ₂ O	0.39		
K ₂ O	1.25		
Ignition loss	4.81		

4.6.2 Thermogravimetric Studies

The weight change values were measured at the end of each cycle with the aim to understand the kinetics of corrosion. In case of hot corrosion study in the molten salt environment, the spalled scale, if any, was included at the time of measurement of weight change to determine the total rate of corrosion. However in case of the specimens exposed to the industrial environment, the actual working conditions of the coal fired boiler in a thermal power plant, the spalled scale could not be collected and incorporated in the weight change. In this case the weight change consists of a weight gain owing to the formation of the oxide scales and a weight loss due to the suspected spalling and fluxing of the oxide scales. Therefore, the net weight change in the industrial environment represents the combined effects of these two processes. The weight change

data was plotted with respect to number of hours for each specimen and the plots have been presented in subsequent chapters 6, 7 and 8.

4.6.3 Evaluation of Corrosion Rate

In case of studies conducted in the platen superheat zone of the coal fired boiler, the weight change data could not be used for predicting the corrosion behaviour due to suspected spalling and ash deposition on the specimens. Further the weight change data might have also been affected by the erosion due to ash. In actual industrial environment the extent of corrosion was assessed by measuring:

- (i) the average scale thickness formed after 1000 hours of exposure to the boiler environment. The depth from the surface to scale-substrate interface is taken as the scale thickness;
- ii) the scale thickness lost due to spallation or possible evaporation during experimentation; and
- (iii) the depth of internal corrosion attack which is taken as the distance from the scale-substrate interface to the site up to which the corrosive species penetrated into the substrate.

The sum of the average scale thickness, scale thickness lost and depth of internal corrosion attack provide an estimate of the material depth affected by the hot corrosion and thereby of the remaining sound metal.

4.6.4 Measurement of Scale Thickness and Depth of Internal Attack

After exposure at 900 °C in the laboratory tube furnace and in industrial conditions, the corroded specimens were cut across the cross-section and polished as discussed in section 4.4.1. A Scanning Electron Microscope (LEO 435VP) with attached Robinson Back Scattered Detector (RBSD) was used to obtain the BSE Images at the areas where the scale thickness was observed to be the least. Average thickness of the scales and depth of internal attack were measured from the BSE images and the data has been presented in the subsequent chapters 6 and 7 of the present study.

4.6.5 Measurement of Scale Thickness Lost

The scale thickness lost due to the spallation or evaporation was assessed by finding the difference in thickness of the specimens before and after 1000 hours exposure to the actual working environment of the coal fired boiler. The thickness was measured using a Sylvac micrometer screw gauge (Swiss make, resolution 0.001) and every represented value was taken as the average of 10 measured values.

4.6.6 X-Ray Diffraction (XRD) Analysis

The different phases formed in the oxide scales of hot corroded specimens after 50 cycles in the laboratory study and 1000 hours in the actual environment of the coal fired boiler have been identified with the X-ray diffraction analysis as described in section 4.4.6.

4.6.7 SEM/EDAX Analysis

4.6.7.1 Surface Morphology

To identify the morphology and weight percentage of different phases formed at the surface, SEM/EDAX analysis of the corroded specimen was conducted at CRF, Indian Institute of Technology, Kharagpur (India). The details regarding the equipment have already been provided in section 4.4.7.1. The specimens were scanned under the microscope and the critical areas of interests were photographed with an aim to understand the morphology of the surface scale, micro cracks, voids etc. The EDAX analysis was performed on these identified areas of interest with an aim to identify the various corrosion products and their composition (weight %).

4.6.7.2 Cross-Section Analysis

To understand the formation of oxides and various other phases across the cross – section of corroded samples, the SEM/EDAX analysis for some of the selected specimens was carried out as explained in section 4.4.7.2. The cross-sectional BSE images were taken and the EDAX analysis was then performed to ascertain the elemental composition (weight %) at selected areas of interest in the scale, coating and substrate.

4.6.8 Electron Probe Micro Analyser (EPMA)

The corroded specimens were cut along the cross-section, mounted and polished as described in section 4.4.1. The EPMA analysis was carried out as already discussed in section 4.4.8. Some specimens were analysed at National Geophysical Research Institute (NGRI), Hyderabad (India), and Defense Metallurgical Research Laboratory, Hyderabad (India) using a Cameca SX100, 3 Wavelength Dispersive Spectrometer, made in France.

For carrying out the EPMA analysis, some critical areas of interest across the cross section of each corroded specimen were selected and then BSEI and elemental X-ray mappings were obtained at that particular area. The selected area includes three regions i.e. base specimen, coating/oxide scale and some epoxy region at the top of the scale. The X-ray mappings were obtained for all the elements present in the substrate, the coatings and the environment of study, but only those maps are reported in which an identified element has substantial concentration.

SUBSTRATE SUPERALLOYS AND CHARACTERISATION OF THE COATINGS

This chapter describes the substrate superalloys and characterization of the coatings for the properties relevant to high temperature corrosive environment applications. Various techniques such as optical microscopy, X-ray diffractometry (XRD), scanning electron microscopy/energy-dispersive analysis (SEM/EDAX), electron probe microanalysis (EPMA), and microhardness tester were used for metallographic examinations to observe cracks, voids, inclusions etc. and to evaluate the physical properties like porosity and microhardness of the as-sprayed coatings. The results are discussed at the end of this chapter.

5.1 FEEDSTOCK MATERIALS

5.1.1 SEM Analysis

SEM morphologies of Cr_3C_2 -NiCr, NiCrBSi and Stellite-6 feedstock powders are shown in Fig. 5.1. Cr_3C_2 -NiCr powder particles have irregular shapes, whereas NiCrBSi and Stellite-6 powders have spherical morphology. Particle size range for all the feedstock powders, as provided by the manufacturer, is given in Table 4.2.

5.1.2 XRD Analysis

The diffraction patterns for the Cr_3C_2 -NiCr, NiCrBSi and Stellite-6 powders, and Ni-20Cr wire used as feedstock alloys in the present investigation are shown in Fig 5.2 on reduced scale. The various phases identified in the feedstock alloys are presented in Table 5.1. The principal phase consisting of Ni-based fcc (face-centered cubic) for the Cr_3C_2 -NiCr and NiCrBSi powders and Ni-20Cr wire, and Co-based fcc for Stellite-6 powder indicates the formation of solid solution. In Cr_3C_2 -NiCr powder presence of Cr_3C_2 as a major phase has also been noted.

Table 5.1: Major and minor phases identified by XRD analysis of the feedstock alloys.

Description	Major phases	Minor phases
Cr_3C_2 -NiCr powder	γ -Ni solid solution, Cr_3C_2	----
NiCrBSi powder	γ -Ni solid solution	Cr_7C_3
Stellite-6 powder	γ -Co solid solution	M_7C_3
Ni-20Cr wire	γ -Ni solid solution	Cr

5.2 SUBSTRATE SUPERALLOYS

The optical microstructures of the substrate superalloys under study are shown in Fig. 5.3. The microstructures of the superalloys have been characterized by comparing them with those of similar international Standard superalloys given in Metals Handbook (1972) and ASM Handbook (1995). The microstructures of Superni 75 and Superni 718, Figs. 5.3 (a) and (d) respectively, have a nickel-rich γ -solid solution matrix. Carbide particles are dispersed in the gamma matrix of Superni 75 and Superni 718 mainly along the grain boundaries. The microstructures of Superni 600 and Superni 601, Figs. 5.3 (b) and (c), have Ni-Cr-Fe solid solution in which carbides are presents in the grains and along the grain boundaries. Twin boundaries are also visible in the structure of superalloys. In the case of Superni 601 superalloy, $M_{23}C_6$ carbides also precipitate as continuous streaks to form thick black boundary envelopes (ASM Handbook, 1995). The microstructure of the Superfer 800H consists of a solid solution matrix in which some of the grains are delineated by particles of precipitated carbides at the grain boundaries and by twinning lines (Metals Handbook, 1972).

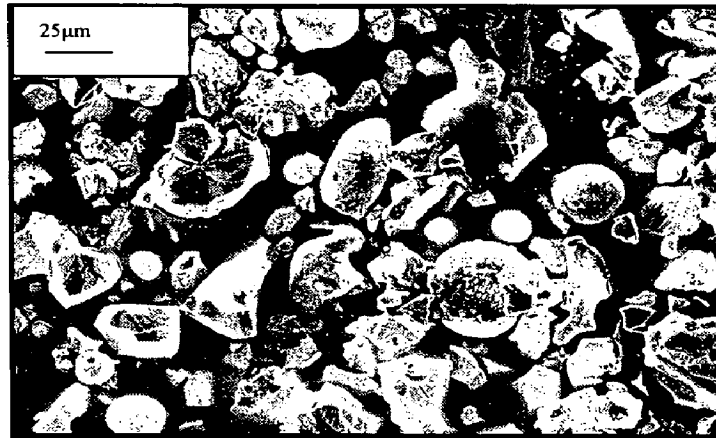
5.3 COATED SUPERALLOYS

5.3.1 Visual Examinations

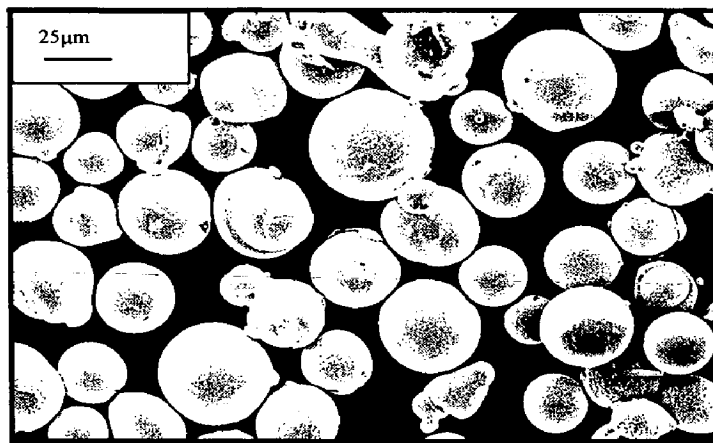
Optical macrographs for the as-sprayed specimens are shown in Fig. 5.4. It can be observed that as-sprayed Cr_3C_2 -NiCr coating have dull deep grey appearance, whereas NiCrBSi coating indicates the existence of shining silver grey colour. Stellite-6 and Ni-20Cr coatings show the shining grey and light grey appearances, respectively. Visual observations indicate that as-sprayed NiCrBSi, Stellite-6 and Ni-20Cr coatings have smooth surfaces, whereas the Cr_3C_2 -NiCr coating has rough surface. Further all the coatings were found to be free from surface cracks. Surface roughness of all the coatings had been measured with surface recorder (SE-1200, Kosaka Lab, Ltd., Japan, Resolution 0.008 μ m) and values were found to be in the range of 4-6 μ m.

5.3.2 Measurements of Coating Thicknesses

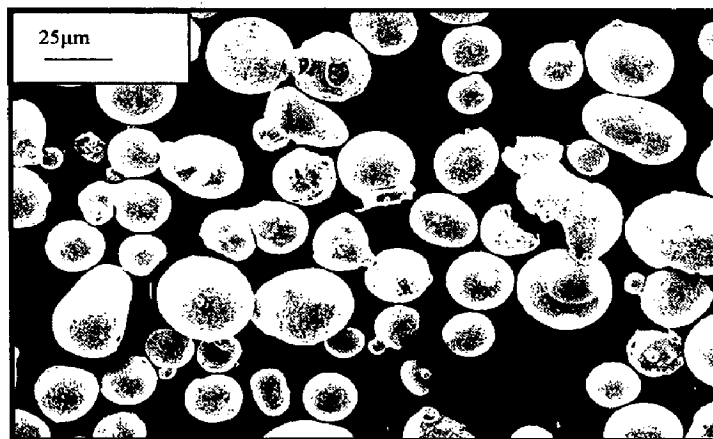
The coating thickness was measured from the Back Scattered Electron Images (BSEI) obtained along cross-section of the coated specimens and the average thickness of each coating is reported in Table 5.2. The thickness of the coating was measured for all the coated specimens. However, only one BSE image for each coating is shown in Fig. 5.5. The coating thickness on other substrate superalloys was noted to be in the same range (260-290 μ m).



(a)



(b)



(c)

Fig. 5.1 SEM of different coating powders: (a) $\text{Cr}_3\text{C}_2\text{-NiCr}$ powder, (b) NiCrBSi Powder, (c) stellite-6 powder.

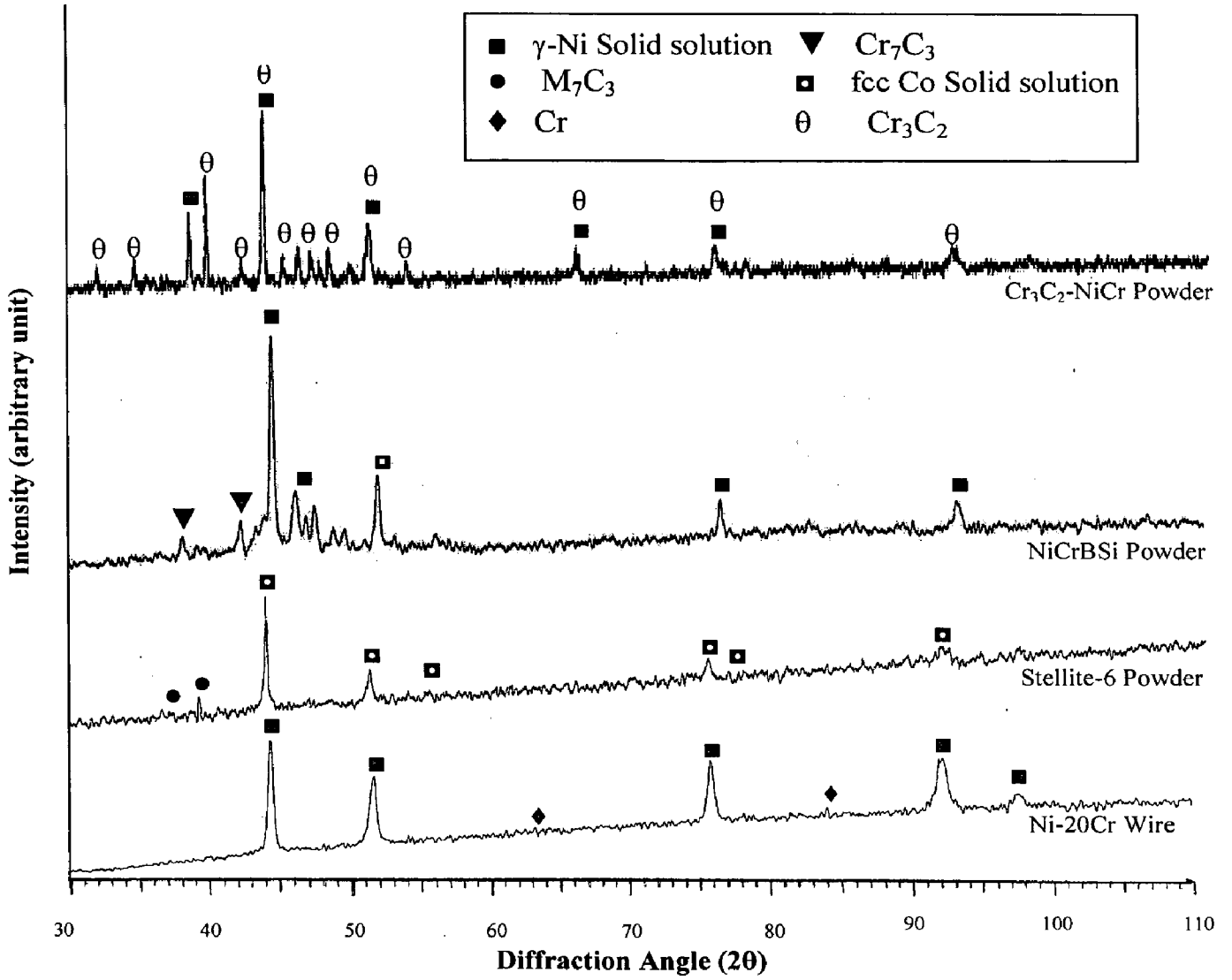


Fig. 5.2 X-ray diffraction patterns for the HVOF feedstock materials.

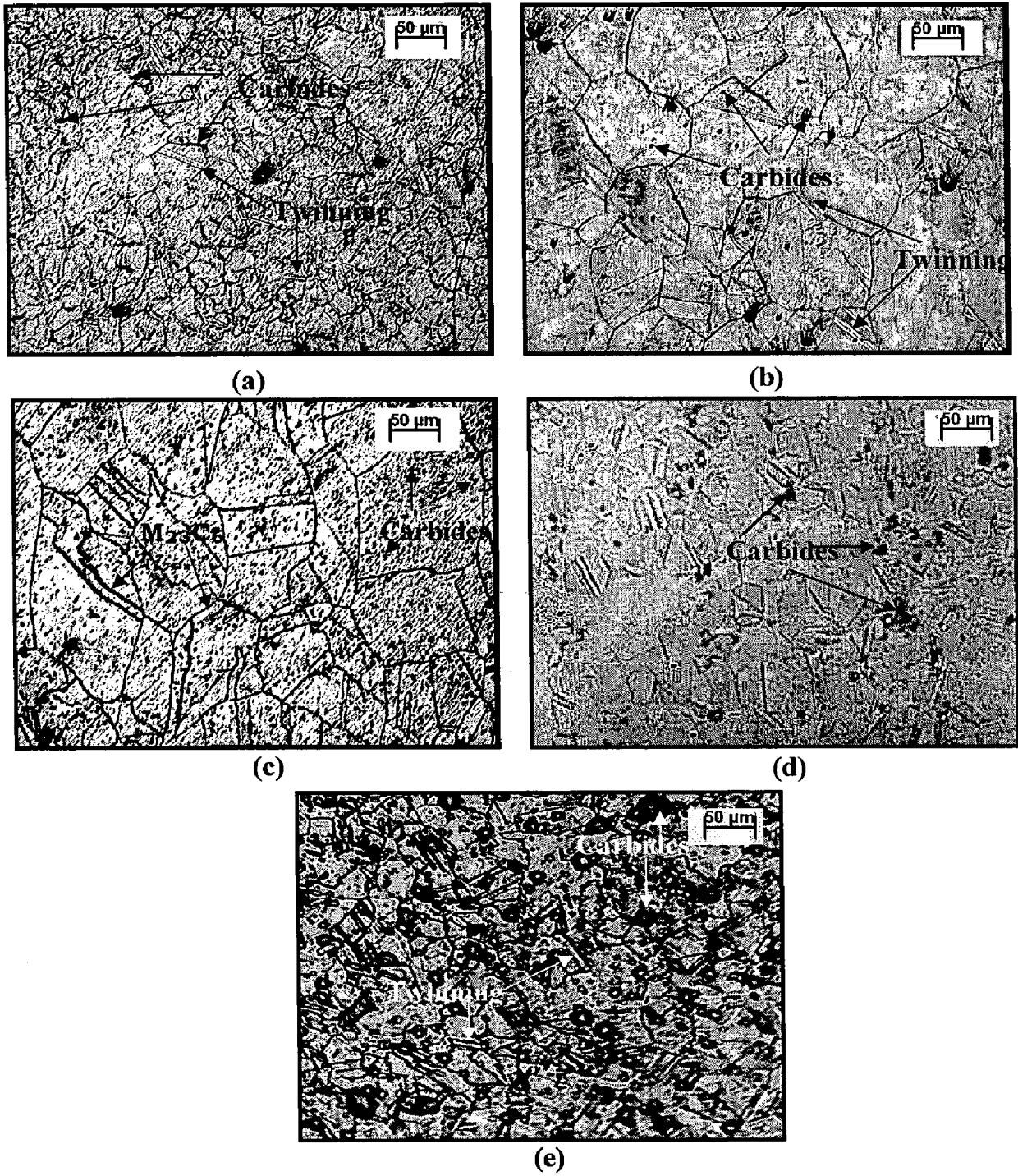


Fig. 5.3 Optical micrographs of the substrate superalloys:
 (a) Superni 75 (b) Superni 600 (c) Superni 601
 (d) Superni 718 (e) Superfer 800H.

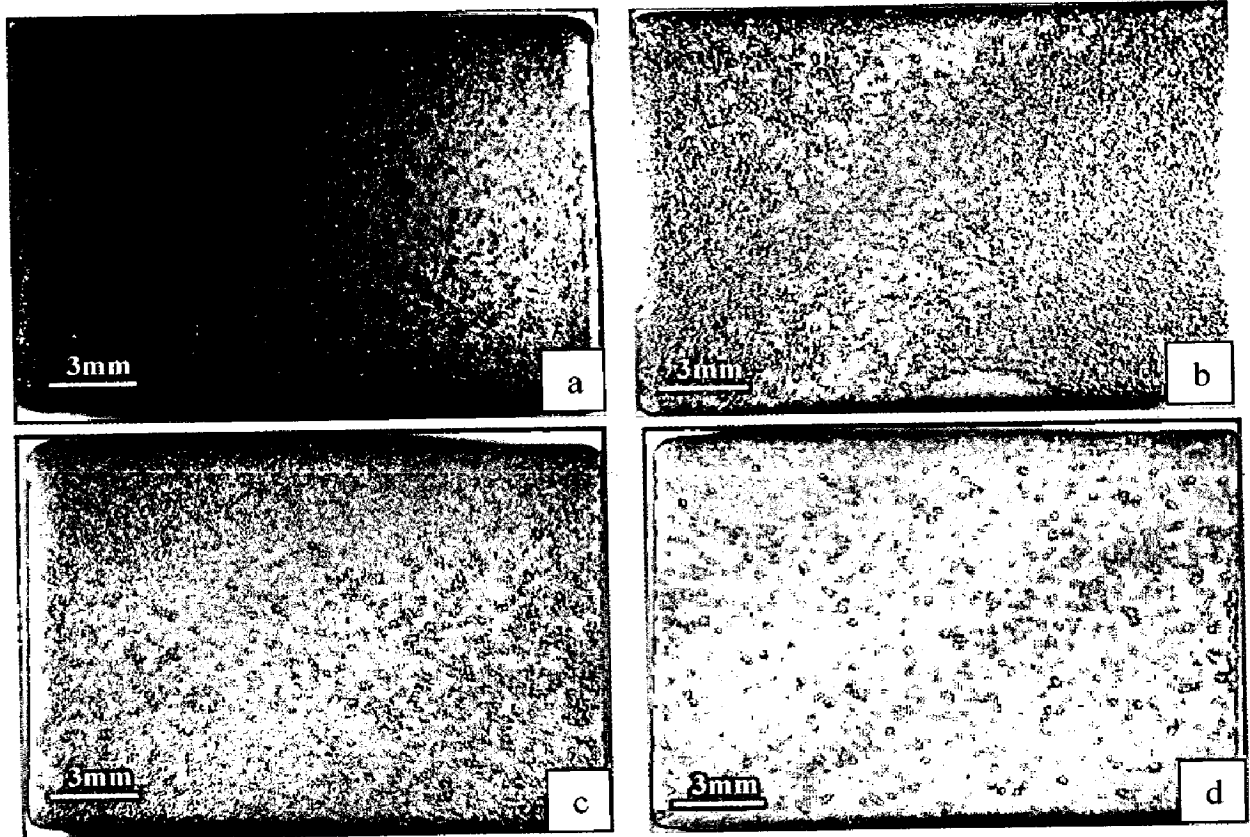


Fig. 5.4 Optical macrographs of as-sprayed specimens with:
(a) Cr_3C_2 -NiCr coating (b) NiCrBSi coating
(c) Stellite-6 coating (d) Ni-20Cr coating.

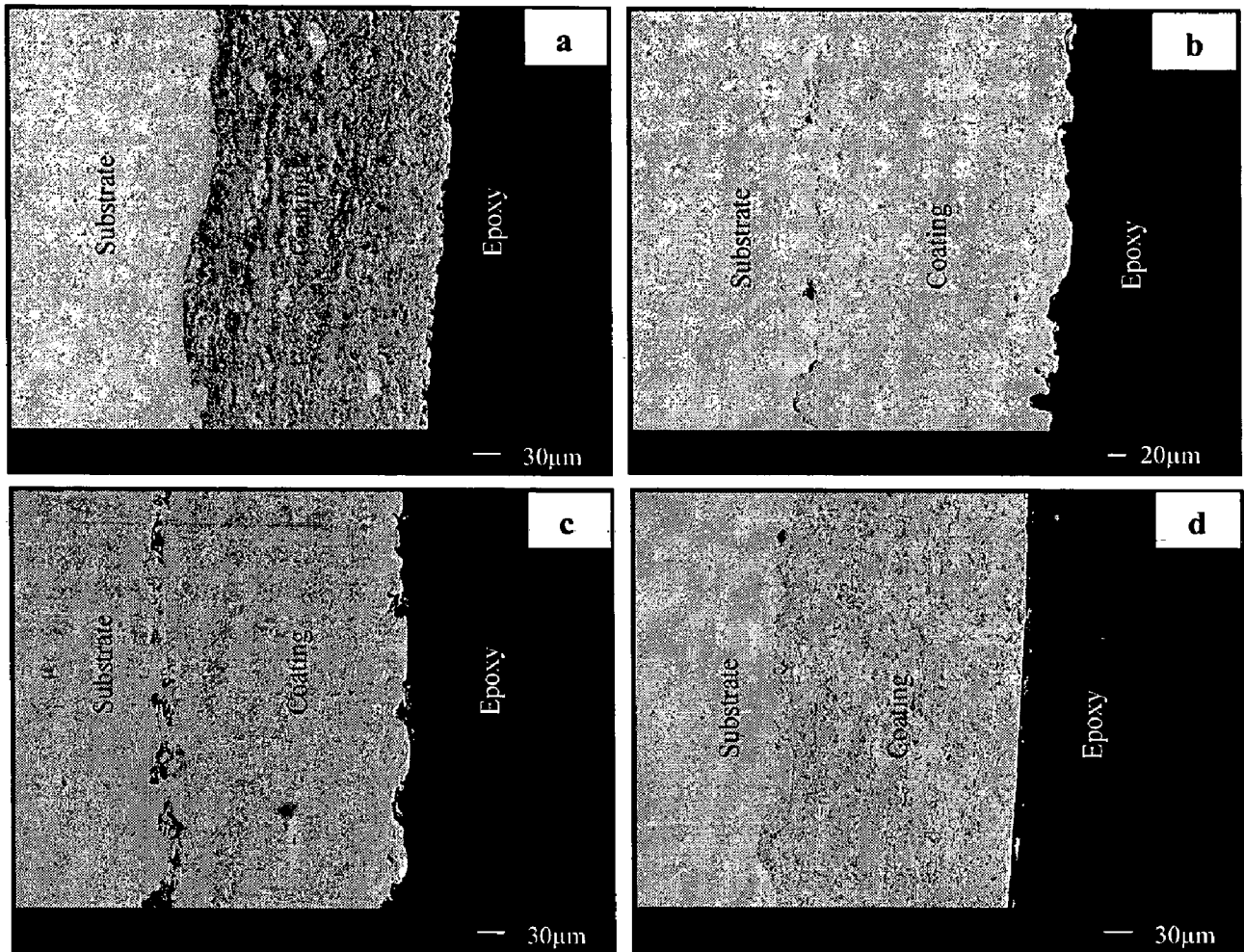


Fig. 5.5 BSEI micrographs showing cross-section morphologies of different HVOF coatings on Superni 75 superalloy: (a) Cr₃C₂-NiCr coating (b) NiCrBSi coating (c) Stellite-6 coating (d) Ni-20Cr coating.

Table 5.2: Average coating thickness and porosity of the HVOF coatings.

HVOF coatings	Average Coating Thickness (μm)	Porosity (%age)
$\text{Cr}_3\text{C}_2\text{-NiCr}$	290	< 1.5%
NiCrBSi Powder	285	< 1.5 %
Stellite-6 Powder	298	<2%
Ni-20Cr wire	259	<1%

5.3.3 Porosity Analysis

Porosity or voids in the coating microstructure is an important issue in thermal spraying, as due to this physical property corrosion resistance of different thermal spraying coatings may differ. The porosity of the HVOF sprayed coatings has been identified by PMP3 inverted metallurgical microscope with stereographic imaging and then the porosity was evaluated with the help of software as described in chapter 4. Average porosity of the as-sprayed coatings is found to be less than 2%. The porosity values of different HVOF sprayed coatings used in the current study are reported in Table 5.2.

5.3.4 Microhardness Measurements

The hardness of the coatings has been measured along the cross-section of coated superalloys. Figures 5.6 and 5.7 show the microhardness profiles along the cross-section of the coatings as a function of distance from the coating-substrate interface. In the substrate, the hardness of Superni 75, Superni 601 and Superni 718 superalloys is found to be in the range 310 to 400 Hv, whereas Superni 600 and Superfer 800H superalloys showed hardness in the range 250 to 285 Hv.

As indicated by the microhardness profiles, $\text{Cr}_3\text{C}_2\text{-NiCr}$ (Fig. 5.6a) coating has the maximum values of hardness of about 950 Hv, followed by Stellite-6 (Fig. 5.7a) and NiCrBSi (Fig. 5.6b) coatings. Ni-20Cr coating has the least hardness with a maximum value of the order of 630 Hv (Fig. 5.7b). Further, an increase in hardness of the substrate has been observed near the coating-substrate interface in all the profiles shown in Fig. 5.6 and 5.7.

Standard deviations of hardness for all the coatings deposited on different superalloys have been found in the range of 16.7-23.4, except Ni-20Cr coated Superni 601 which has a relatively more standard deviation of 31.9.

5.3.5 Metallographic studies of the Coatings

5.3.5.1 Surface Microstructures

Optical micrographs showing surface morphologies of the HVOF coatings are shown in Fig. 5.8 to 5.11. It can be observed from the microstructures that coatings in general have dense and nearly uniform structures possessing very few pores and voids. Contents of un-melted particles are found to be very less. Further, all the coatings appeared to be free from surface cracks. In general, each particular coating deposited on different superalloys appeared to have almost similar microstructures.

5.3.5.1(a) Cr_3C_2 -NiCr Coating

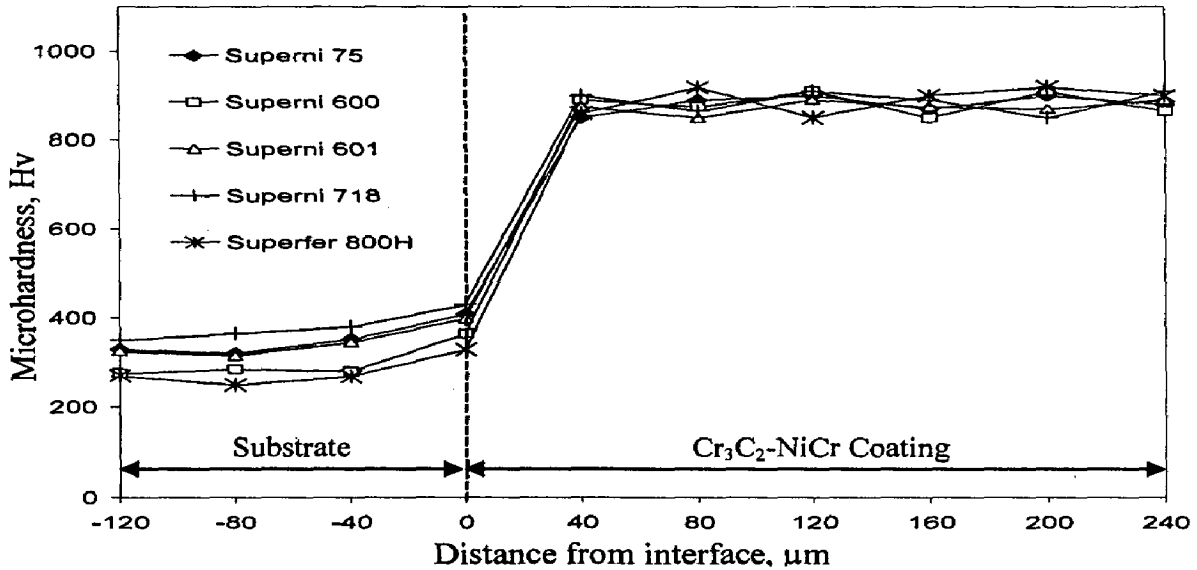
Figure 5.8 shows the optical micrographs for the Cr_3C_2 -NiCr coating on different superalloys selected for the present study. The flat splats of irregular shape are almost uniformly distributed in the coating. White globules which are disbursed throughout the structure appeared to be the melted regions. Some limited voids and un-melted particles are also visible in the structure of the coatings. Un-melted particles are identified in the coating by their shape, size and surface morphology.

5.3.5.1(b) NiCrBSi Coating

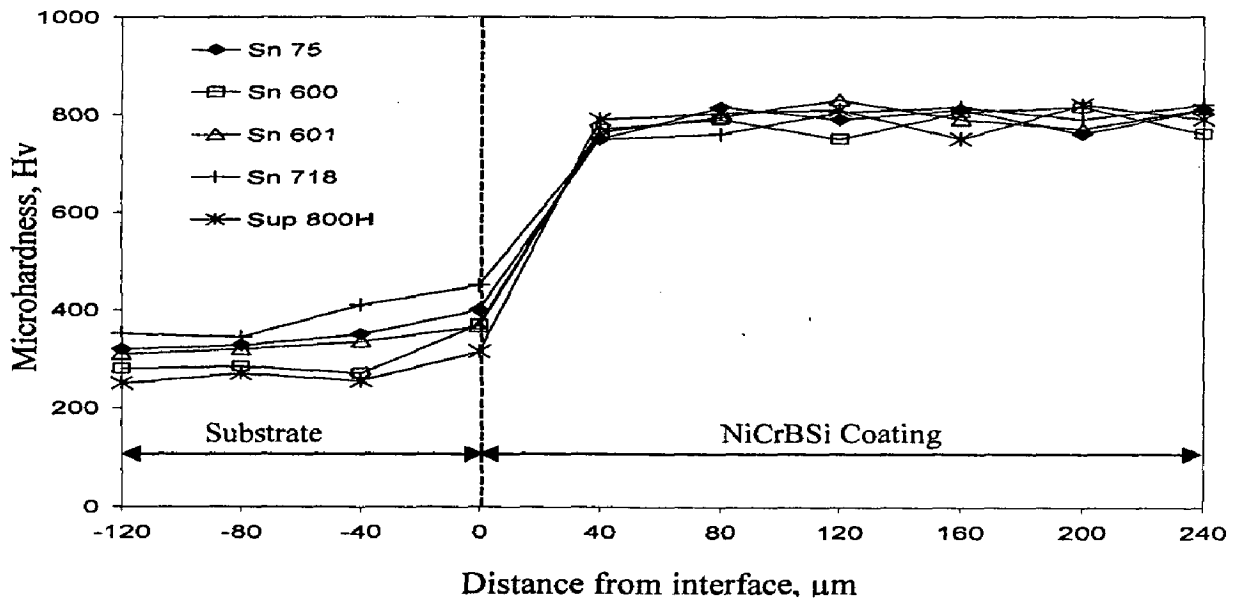
Optical micrographs showing surface morphologies of NiCrBSi coating on different substrates are shown in Fig. 5.9. Small and nearly round contrast black spots in the coating structure have been identified as porosity through stereographic imaging on optical microscope and dark black streaks are the inclusions. Thin light grey colour stringers seen in the microstructure at the splat boundaries are presumably the oxides (Fig. 5.9b). Dark black stringers around the grain boundaries are carbides of M_xC_y type. The uniform microstructure of the coating indicates that a high proportion of the feedstock powder has been fully melted prior to impacting the substrate.

5.3.5.1(c) Stellite-6 Coating

Figure 5.10 shows optical micrographs presenting surface morphologies of Stellite-6 coated superalloys. Structure of the as-sprayed Stellite-6 coating mainly consists of fcc cobalt-rich metallic matrix, as also reported by Kong et al. (2003), in which large melted droplets provide matrix dispersed with light and dark coloured phases. Some M_xC_y particles are present in an alpha (fcc) matrix (Metals Handbook, 1972). These M_xC_y carbides have shown their presence mostly at the locations near the splat boundaries (Fig.5.10 candd). Some limited voids and unmelted particles are also seen in the structure.

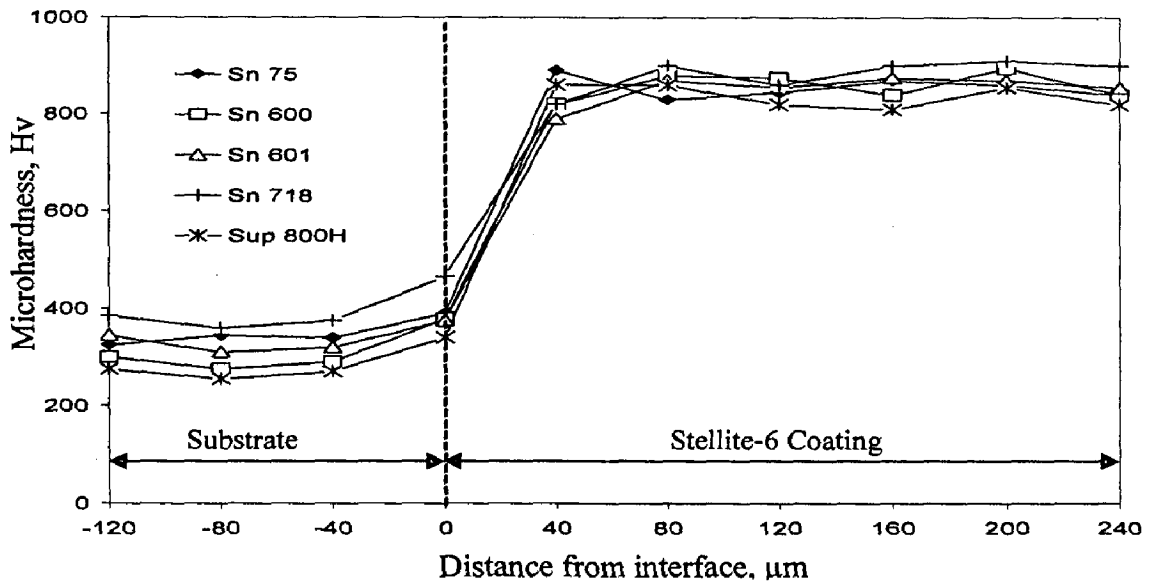


(a)

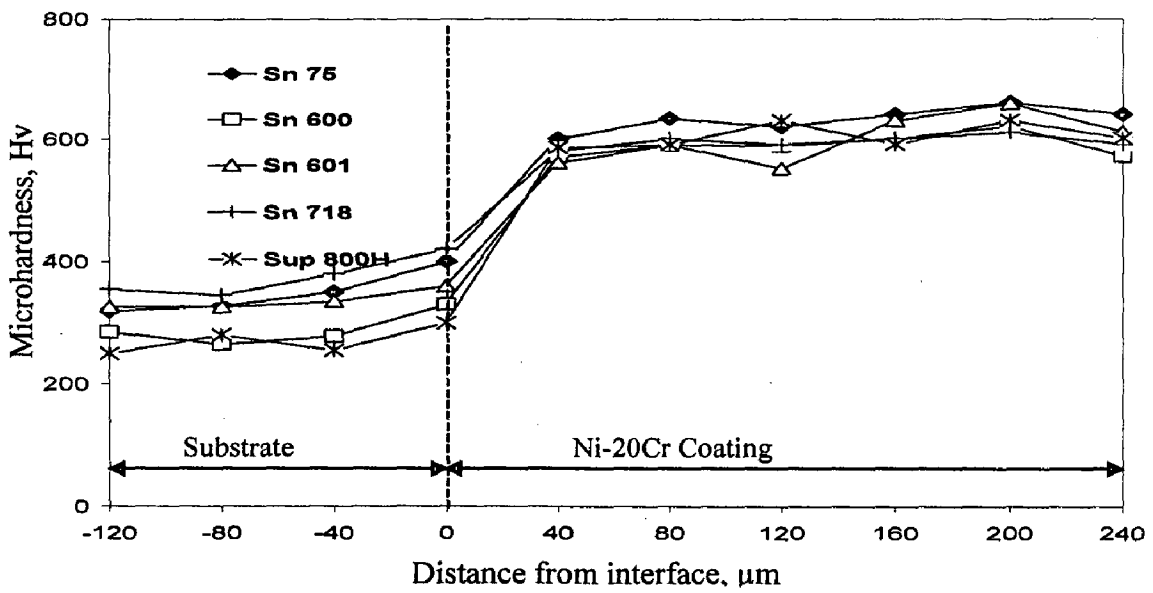


(b)

Fig. 5.6 Microhardness profiles of HVOF sprayed coatings for different superalloys along the cross section : (a) Cr₃C₂-NiCr coating, (b) NiCrBSi coating.



(a)



(b)

Fig. 5.7 Microhardness profiles of HVOF sprayed coatings for different superalloys along the cross section: (a) Stellite-6 coating, (b) Ni-20Cr coating.

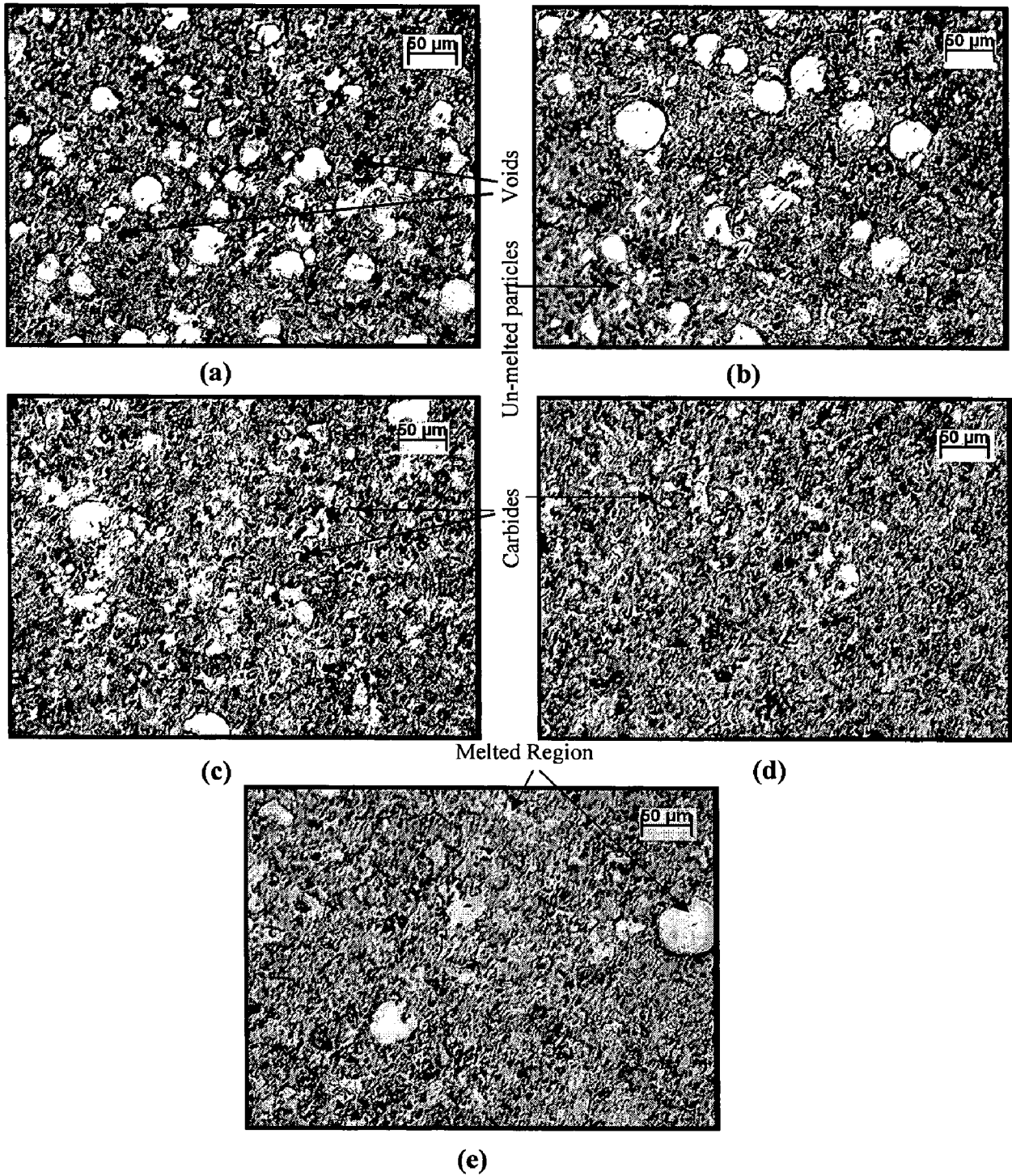


Fig. 5.8 Optical micrographs showing surface morphology of HVOF sprayed $\text{Cr}_3\text{C}_2\text{-NiCr}$ coating on substrate superalloys:
 (a) Superni 75 (b) Superni 600 (c) Superni 601
 (d) Superni 718 (e) Superfer 800H.

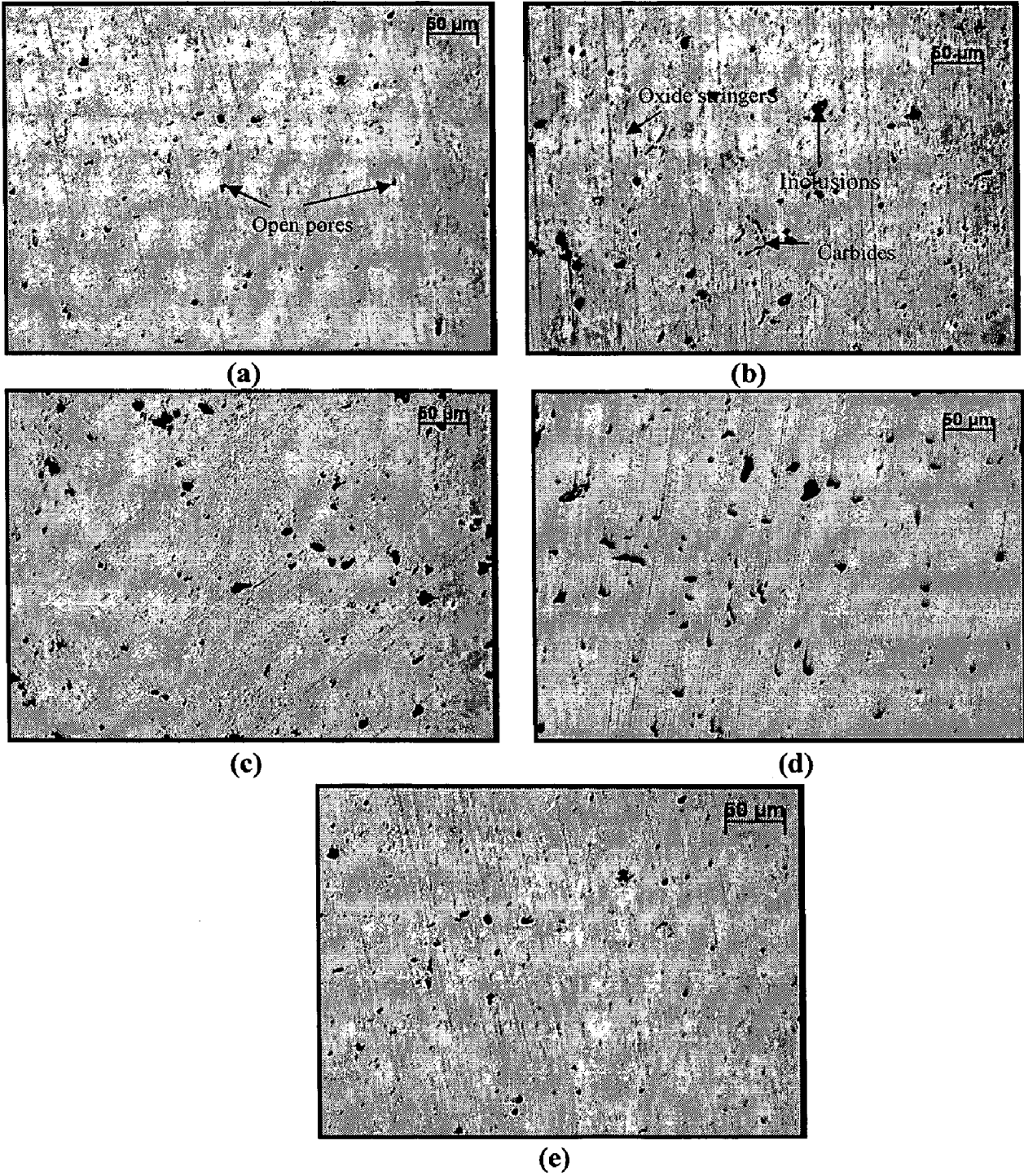


Fig. 5.9 Optical micrographs showing surface morphology of HVOF sprayed NiCrBSi coating on substrate superalloys:
 (a) Superni 75 (b) Superni 600 (c) Superni 601
 (d) Superni 718 (e) Superfer 800H.

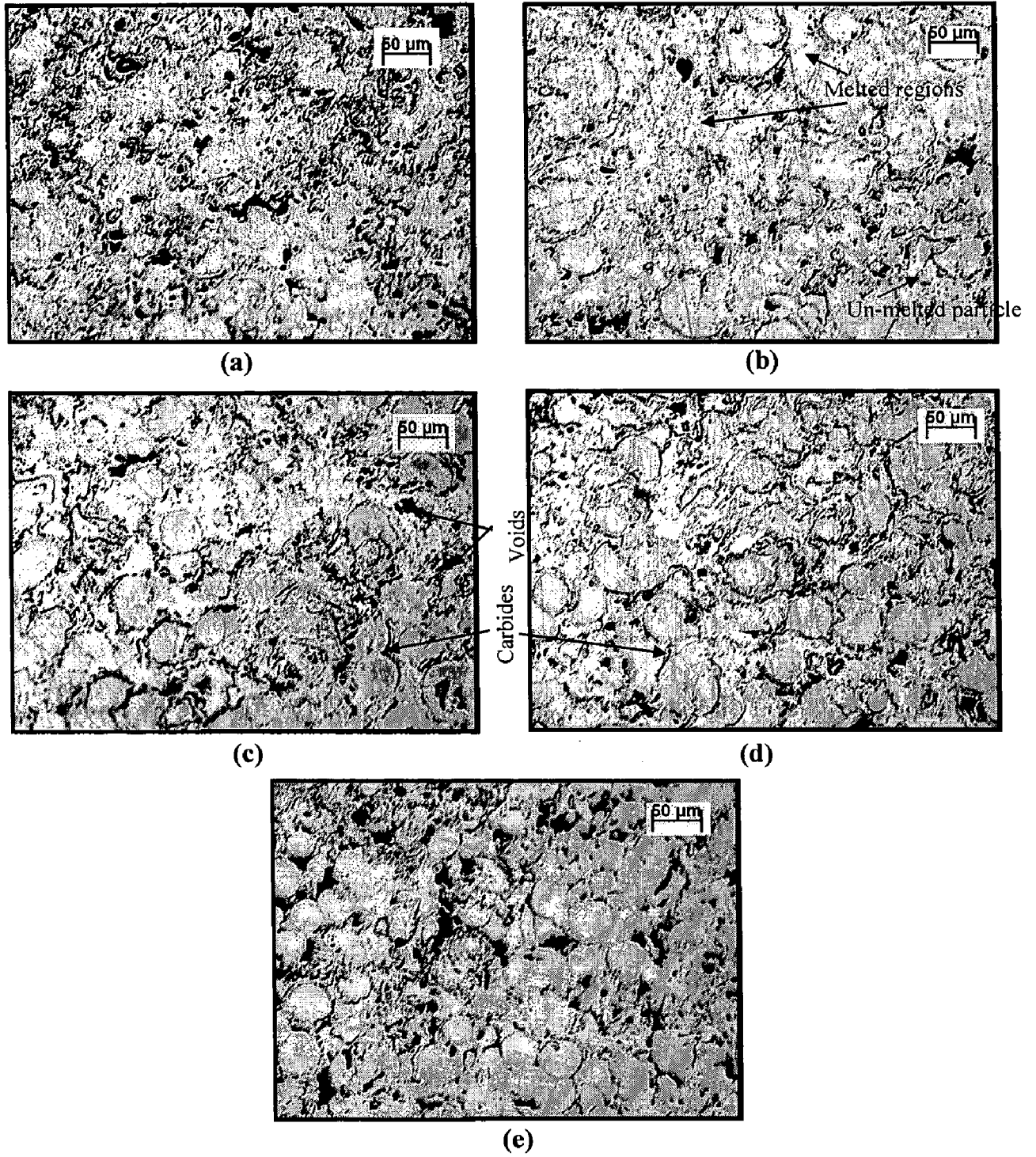


Fig. 5.10 Optical micrographs showing surface morphology of HVOF sprayed Stellite-6 coating on substrate superalloys:
 (a) Superni 75 (b) Superni 600 (c) Superni 601
 (b) Superni 718 (e) Superfer 800H.

5.3.5.1(d) Ni-20Cr wire Coating

Optical micrographs showing surface morphologies of Ni-20Cr wire coating on different substrates are shown in Fig. 5.11. The microstructure of Ni-20Cr coating using wire as feedstock material is found to be homogeneous and uniform with very little contents of voids and pores. The irregular shaped flat splats formed in the as-sprayed coating are found to be uniformly distributed and observed to be smallest in size amongst the coatings under study.

5.3.5.2 Cross-Section Microstructures

Optical micrographs showing cross-section microstructures of the coatings are shown in Fig.5.12. As microstructures of a particular coating on different substrates are almost alike, cross-section micrographs of all the coatings on one superalloy have been reported and others are not shown. As is evident from the micrographs, the coatings have lamellar flat splat structure typical of that observed in HVOF coatings. The coatings were deposited on stationary substrates by moving the HVOF gun and the required thickness of the coatings have been obtained by varying number of passes. This led to the development of lamellar structure of the coatings. All the coatings have dense structures with the porosity (less than 2%) randomly distributed in the coatings. The dark spots in the coatings, or islands at the coatings substrate interface, are mostly inclusions. Oxides, which are formed due to the oxidation of in-flight particles, have appeared in the microstructure in the form of intersplat lamellae oriented parallel to the substrate surface. Black dark stringers around the splat boundaries in case of Cr₃C₂-NiCr, NiCrBSi and Stellite-6 coatings are indications of the presence of carbides.

Cr₃C₂-NiCr coatings have comparatively fine grain microstructure with white globules disbursed throughout the structure. Microstructure of NiCrBSi coating consists of relatively large size molten metal droplets. The splat size of the Stellite-6 coating appears to be larger as compared to that in the Cr₃C₂-NiCr and Ni-20Cr wire coatings. Ni-20Cr coating has a comparatively finest grain structure amongst all the coatings, and voids, pores and inclusions are negligible.

5.3.6 XRD Analysis

X-ray diffractograms for the Cr₃C₂-NiCr, NiCrBSi, Stellite-6 and Ni-20Cr as-sprayed coatings are shown in Fig. 5.13 to 5.16 respectively on reduced scales. The major and minor phases formed in the as-sprayed coatings are presented in Table 5.3. The presence of Ni-based fcc as principal phase for as-sprayed Cr₃C₂-NiCr, NiCrBSi and Ni-20Cr coatings; and Co-based fcc for Stellite-6 coating signifies the formation of solid solution matrix.

Table 5.3: Major and minor phases identified by XRD analysis of the as-sprayed coatings.

Description	Major phases	Minor phases
Cr ₃ C ₂ -NiCr coating	γ-Ni solid solution	Cr ₇ C ₃
NiCrBSi coating	γ-Ni solid solution	Cr ₇ C ₃ , Ni ₃ B, NiCr ₂ O ₄
Stellite-6 coating	γ-Co solid solution	CoNiO ₂
Ni-20Cr coating	γ-Ni solid solution	Cr

5.3.7 SEM Analysis

SEM morphologies for the HVOF sprayed Cr₃C₂-NiCr, NiCrBSi, Stellite-6, and Ni-20Cr coatings on the different substrate superalloys are shown in Fig. 5.17 to 5.20. In general, micrographic features indicate that the coatings are homogeneous and massive, and free of cracks. Very limited un-melted particles are observed in the structures of the coatings. These un-melted particles may stick to surface due to the high impact during HVOF spraying. The coatings show the existence of some oxide stringers/inclusions and very limited open pores. Further some localized areas having higher densities of open pores can be seen in some of the micrographs. Surface morphologies revealed that all the coatings have mostly crystalline structures. The Cr₃C₂-NiCr and Ni-20Cr coatings have small size splats, Fig. 5.17 and Fig. 5.20 respectively; whereas the splats are very coarse for the Stellite-6 coatings (Fig. 5.19). Medium sized splats are observed in the case of NiCrBSi coatings (Fig. 5.18).

5.3.8 EDAX Analysis

5.3.8.1 Surface Analysis

EDAX analysis of the coatings was done at some selected areas of interest, as shown in SEM micrographs (Figs. 5.21 and 5.22). In these micrographs, the regions marked 'M' indicates the melted region, whereas 'P' represents the partially melted regions.

In the case of Cr₃C₂-NiCr coating, one can see melted, partially melted and black areas (Fig. 5.21a). Partially melted areas have a composition of 69% chromium and 30% nickel, which is close to the powder composition. Black area in the coating is found to be rich in nickel. In the case of NiCrBSi coating, there are globular melted particles in the matrix of partially melted layer (Fig 5.21b). These melted particles have nearly the same composition as that of the starting powder. Boron element of the coating could not be detected. In partially melted areas, the amount of nickel is slightly less and silicon has increased as compared to the melted areas. In the case of Stellite-6 coating, there is an indication of Co-rich splats surrounded by partially melted zone having nearly the same composition as that of the matrix (Fig. 5.22a). In case of Ni-20Cr coated superalloy surface, the melted regions have a composition similar to that of the wire, with some partially melted dendritic zones where the nickel is present in slightly higher amounts and chromium is depleted in comparison to the melted region (Fig. 5.22b).

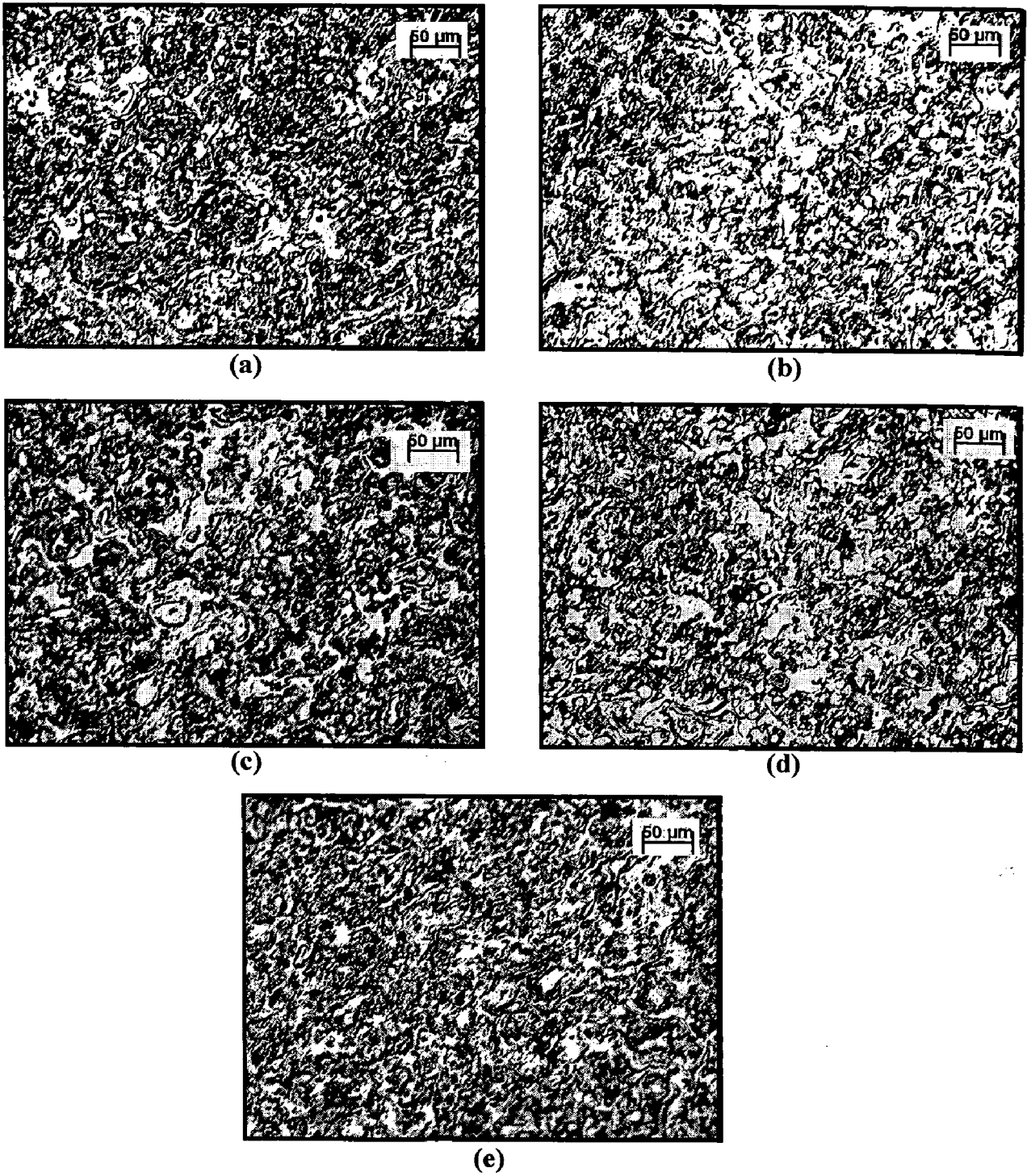


Fig. 5.11 Optical micrographs showing surface morphology of HVOF sprayed Ni-20Cr coating on substrate superalloys:
 (a) Superni 75 (b) Superni 600 (c) Superni 601
 (d) Superni 718 (e) Superfer 800H.

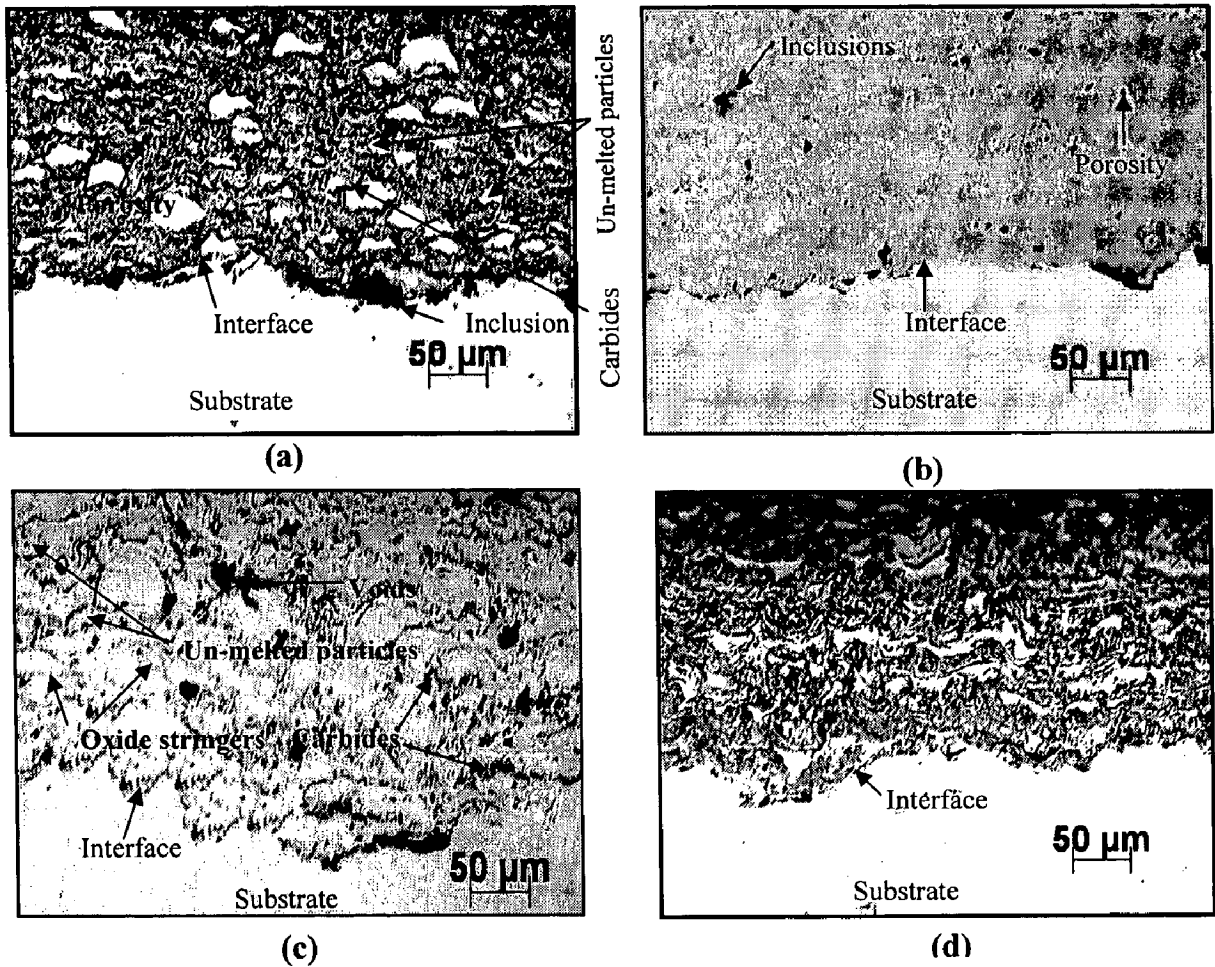


Fig.5.12 Optical micrographs showing cross-section microstructures of different coatings on superfer 800H superalloy:
 (a) Cr₃C₂-NiCr coating (b) NiCrBSi coating
 (c) Stellite-6 coating (d) Ni-20Cr coating.

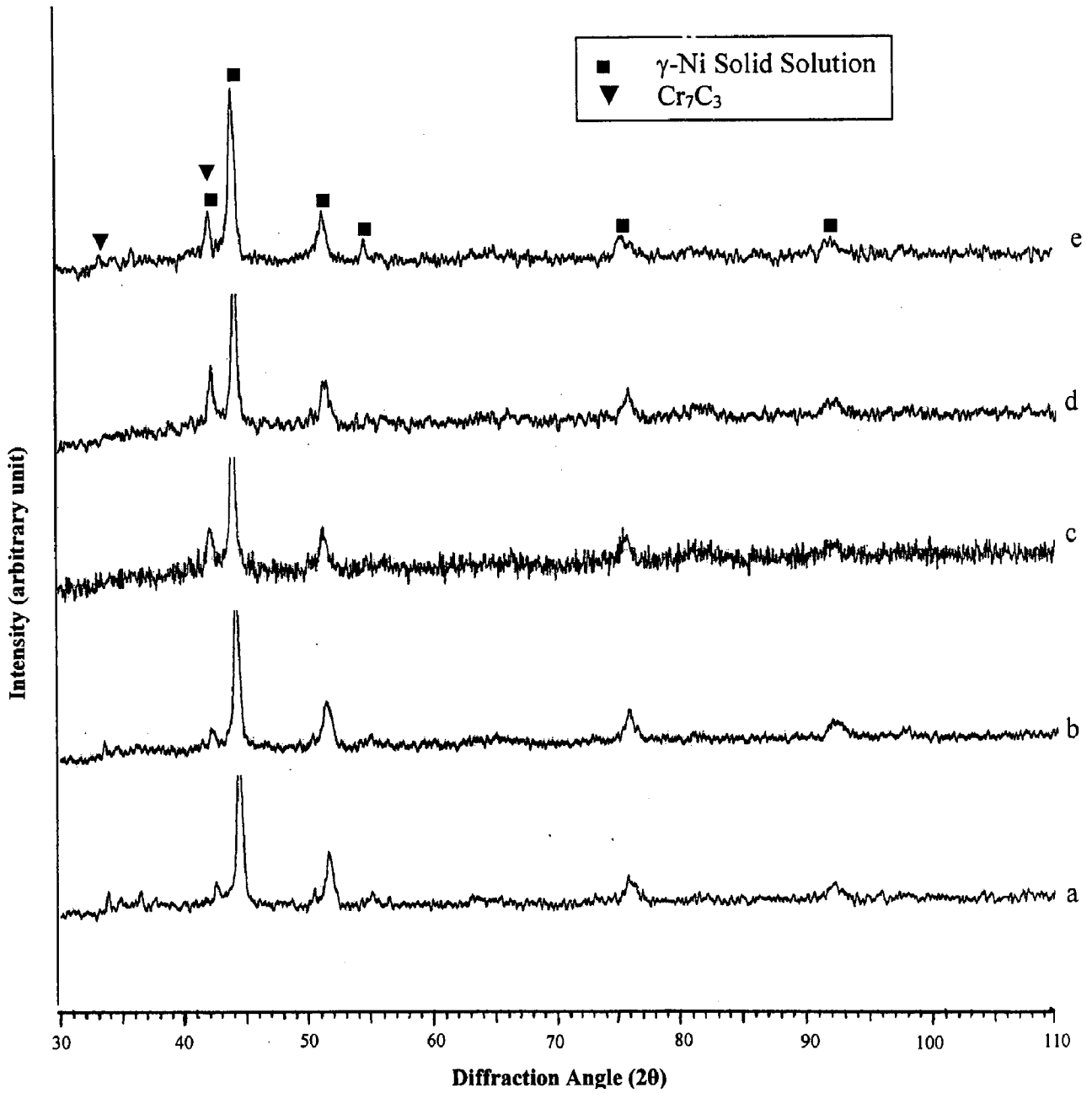


Fig.5.13 X-ray diffractions for the Cr_3C_2 -NiCr coatings on different superalloy:
 (a) Superni 75 (b) Superni 600 (c) Superni 601
 (d) Superni 718 (e) Superfer 800H.

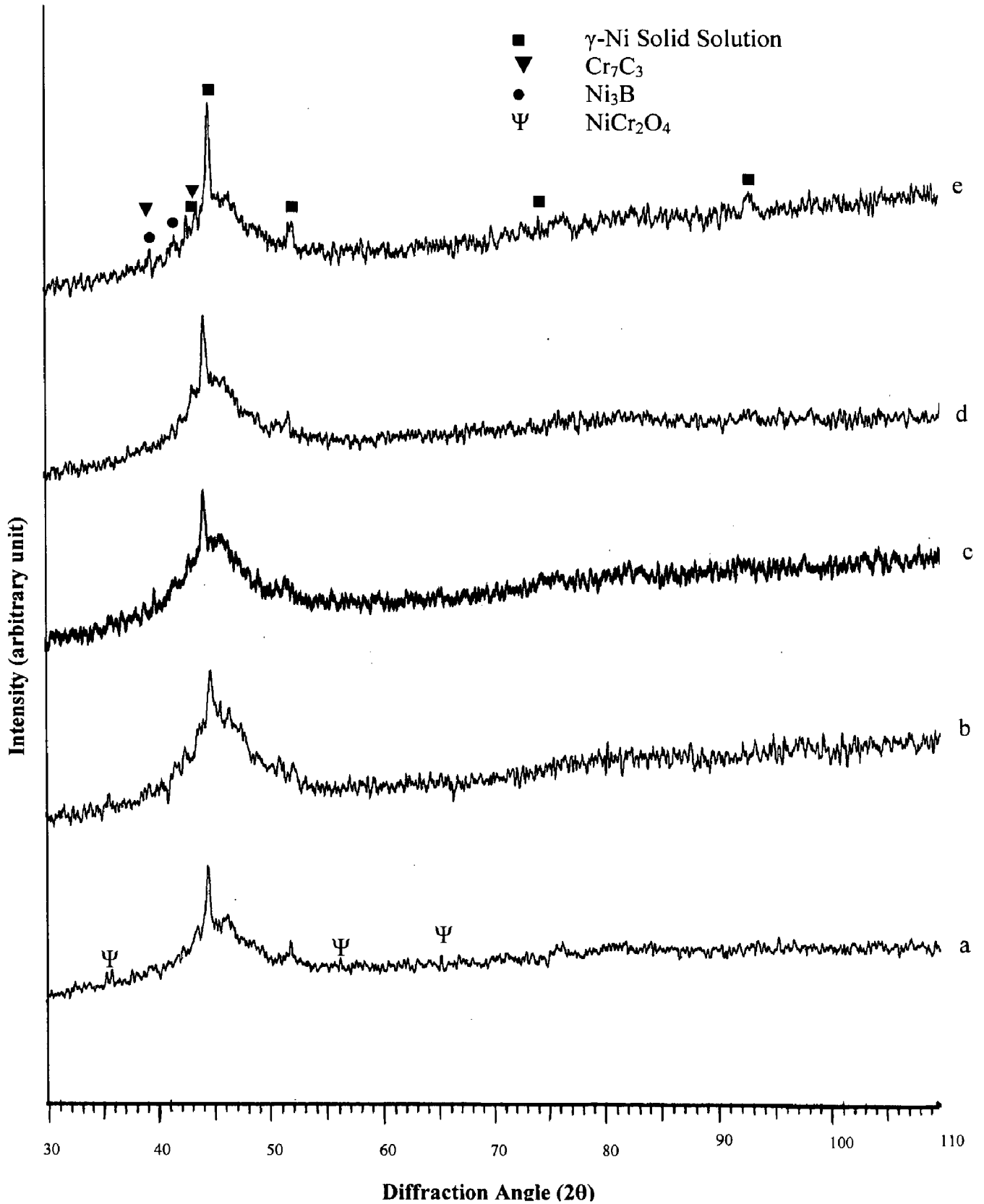


Fig.5.14 X-ray diffractions for the NiCrBSi coatings on different superalloy:
 (a) Superni 75 (b) Superni 600 (c) Superni 601
 (d) Superni 718 (e) Superfer 800H.

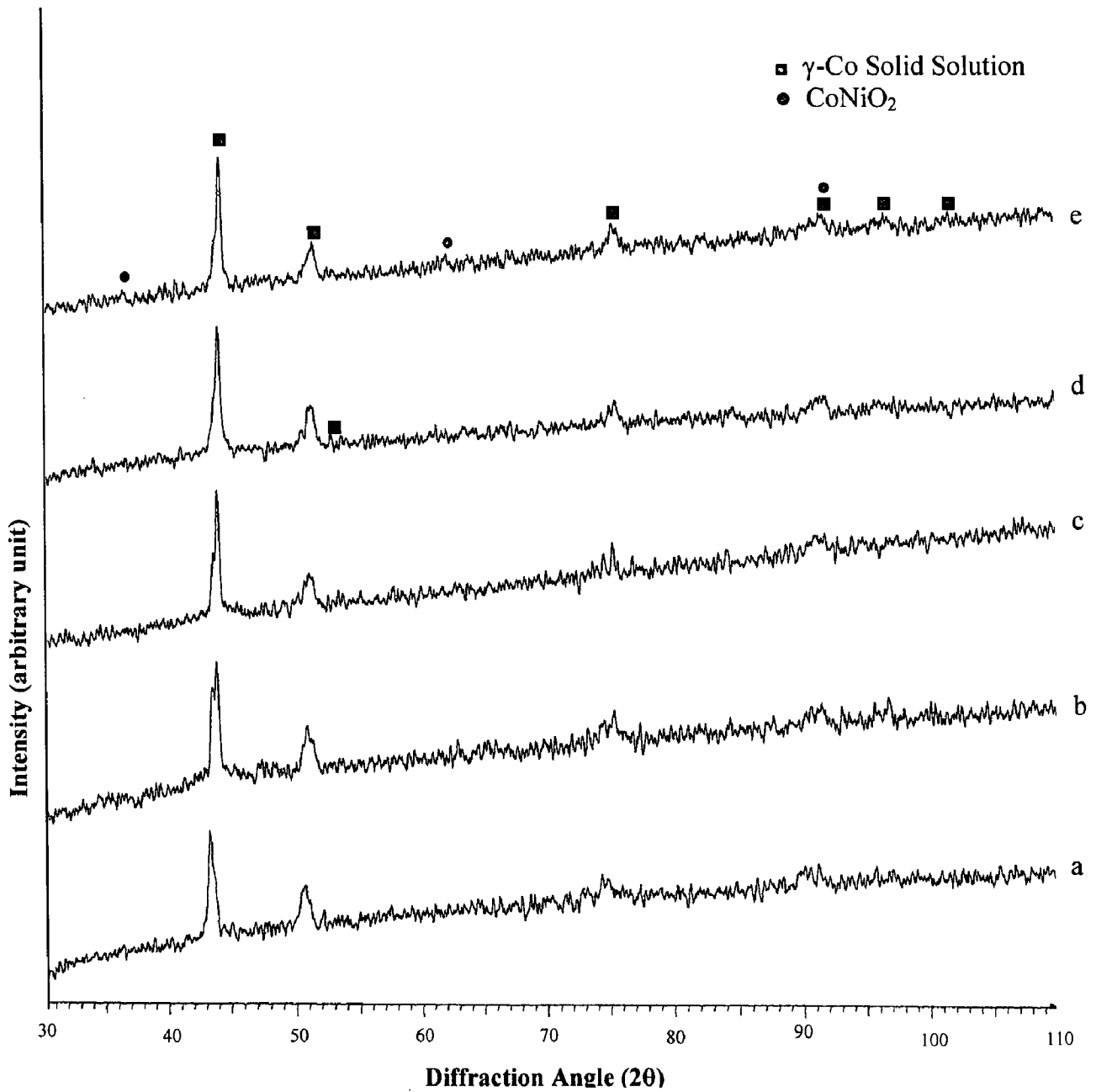


Fig.5.15 X-ray diffractions for the Stellite-6 coatings on different superalloy:
 (a) Superni 75 (b) Superni 600 (c) Superni 601
 (d) Superni 718 (e) Superfer 800H.

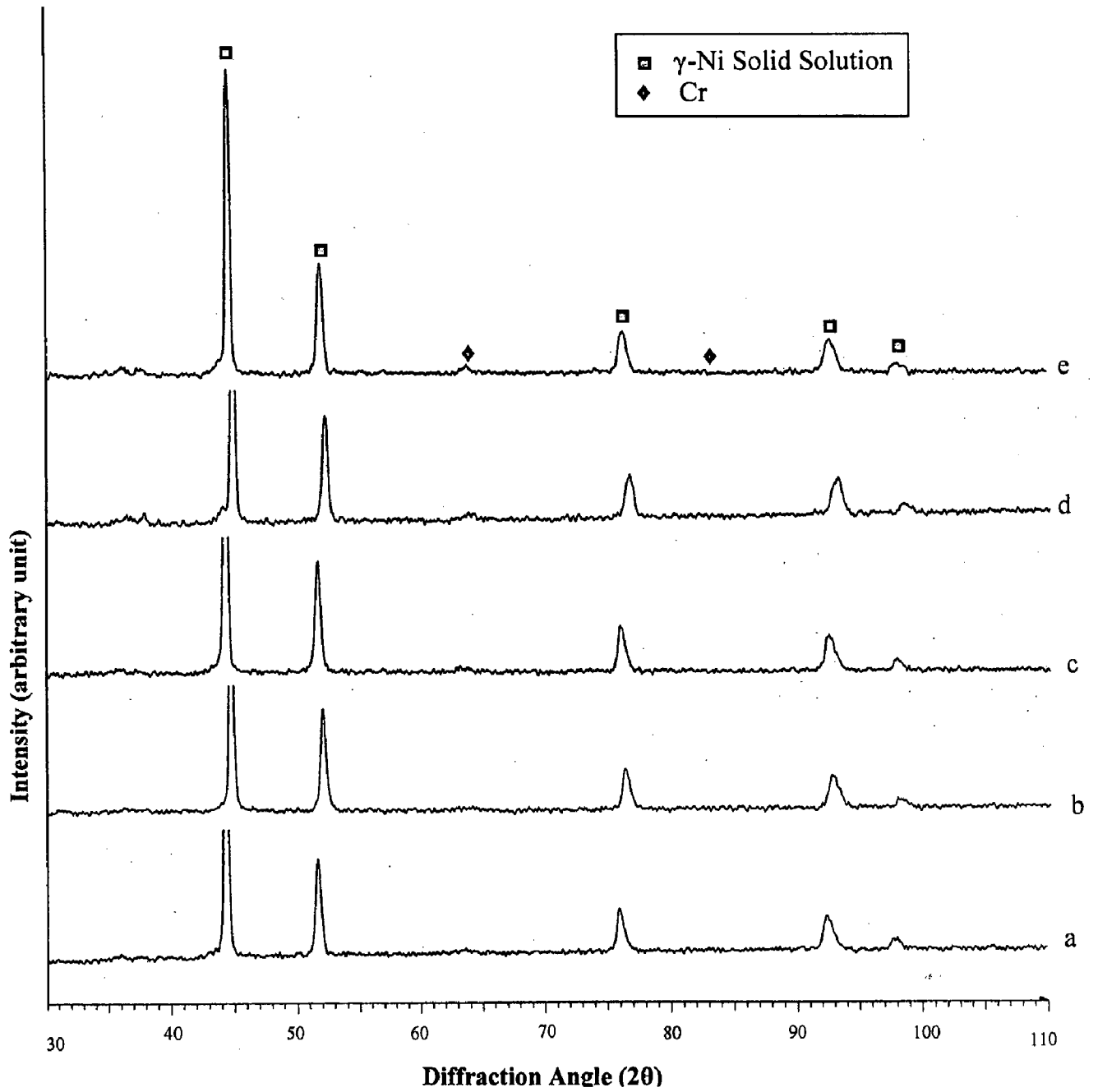


Fig.5.16 X-ray diffractions for the Ni-20Cr wire coatings on different superalloy:
 (a) Superni 75 (b) Superni 600 (c) Superni 601
 (d) Superni 718 (e) Superfer 800H.

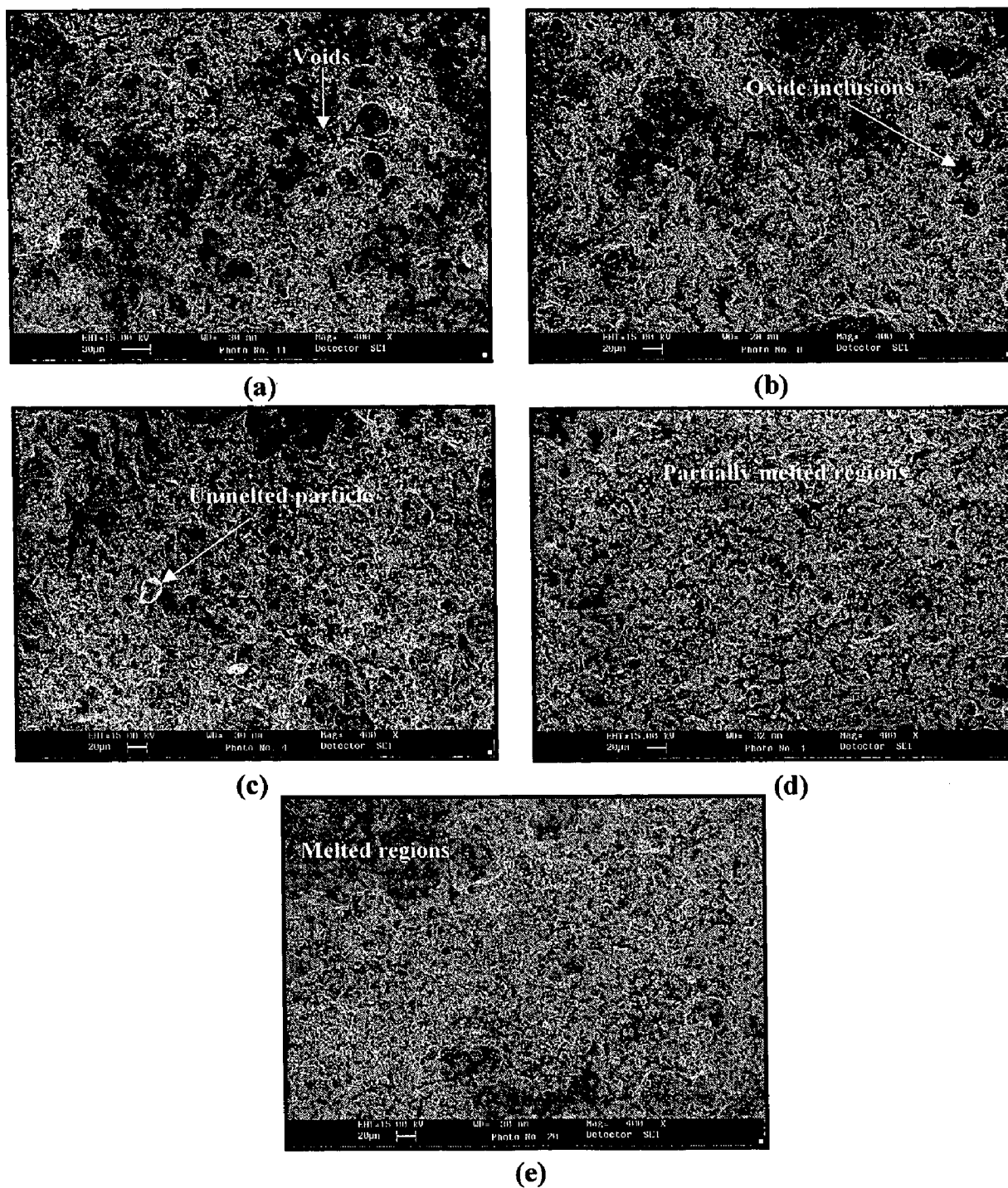


Fig. 5.17 SEM micrographs showing surface morphology of HVOF sprayed $\text{Cr}_3\text{C}_2\text{-NiCr}$ coating on substrate superalloys:
 (a) Superni 75 (b) Superni 600 (c) Superni 601
 (d) Superni 718 (e) Superfer 800H.

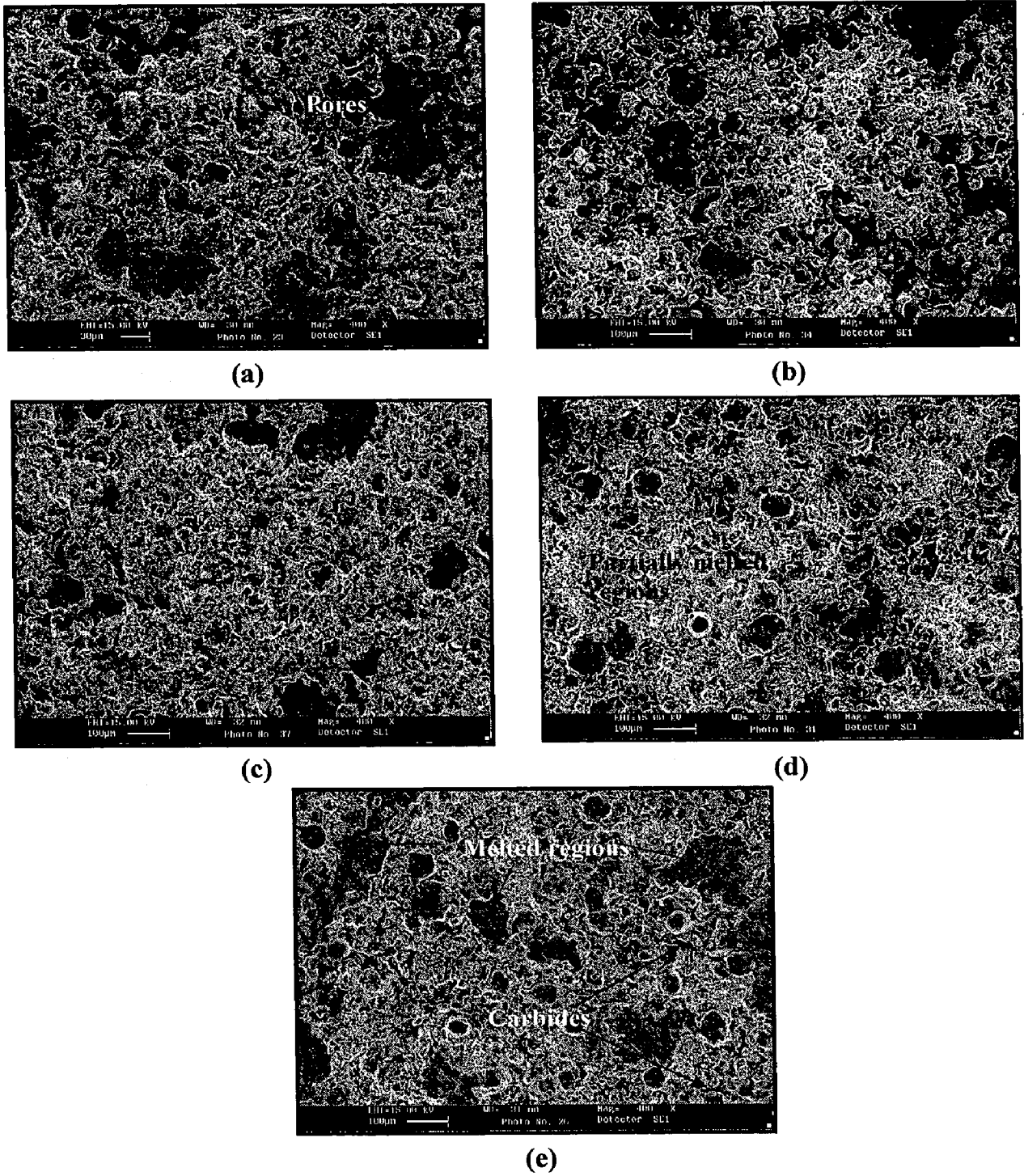
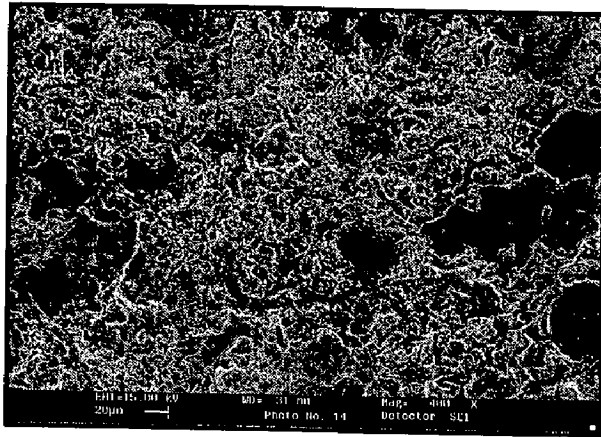
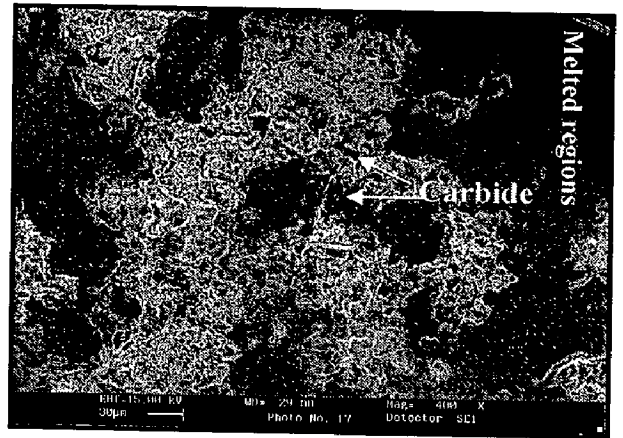


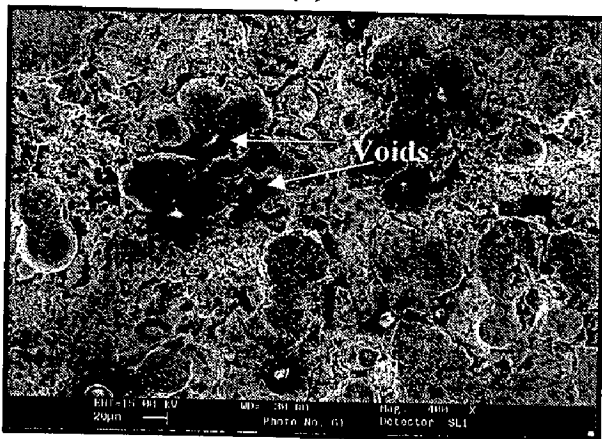
Fig. 5.18 SEM micrographs showing surface morphology of HVOF sprayed NiCrBSi coating on substrate superalloys:
 (a) Superni 75 (b) Superni 600 (c) Superni 601
 (d) Superni 718 (e) Superfer 800H.



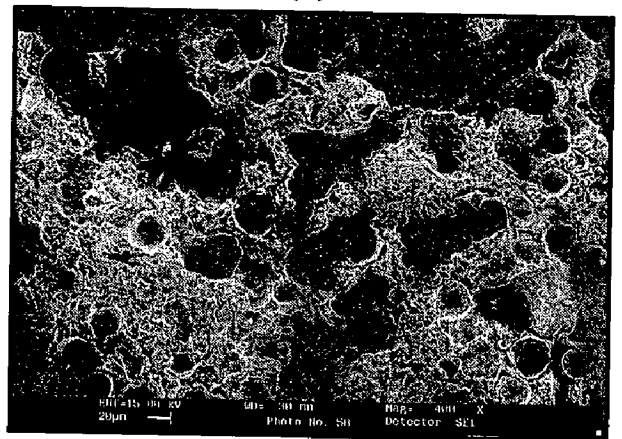
(a)



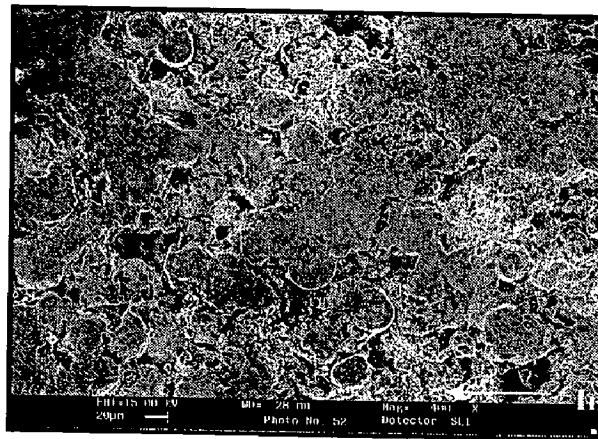
(b)



(c)

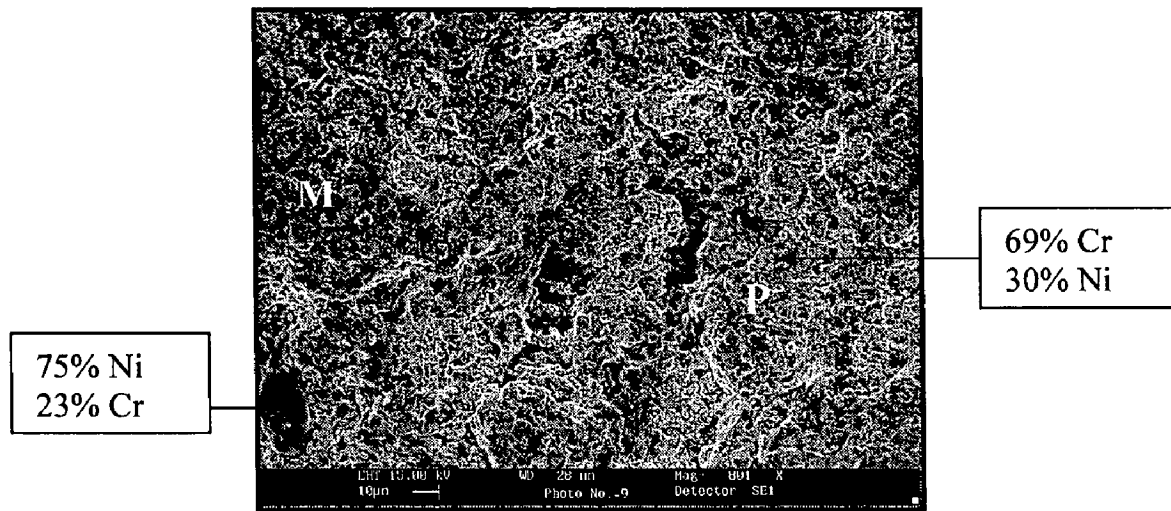


(d)

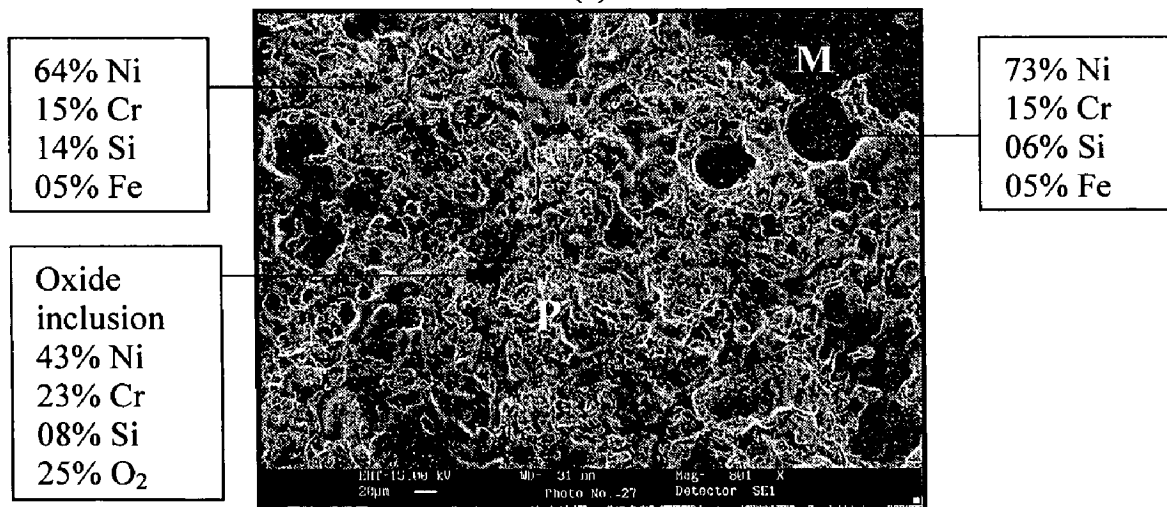


(e)

Fig. 5.19 SEM micrographs showing surface morphology of HVOF sprayed Stellite-6 coating on substrate superalloys:
 (a) Superni 75 (b) Superni 600 (c) Superni 601
 (d) Superni 718 (e) Superfer 800H.



(a)



(b)

Fig. 5.21 SEM/EDAX analysis of the HVOF sprayed coatings showing elemental composition (wt%) at selected points:
 (a) $\text{Cr}_3\text{C}_2\text{-NiCr}$ Coating (b) NiCrBSi Coating.

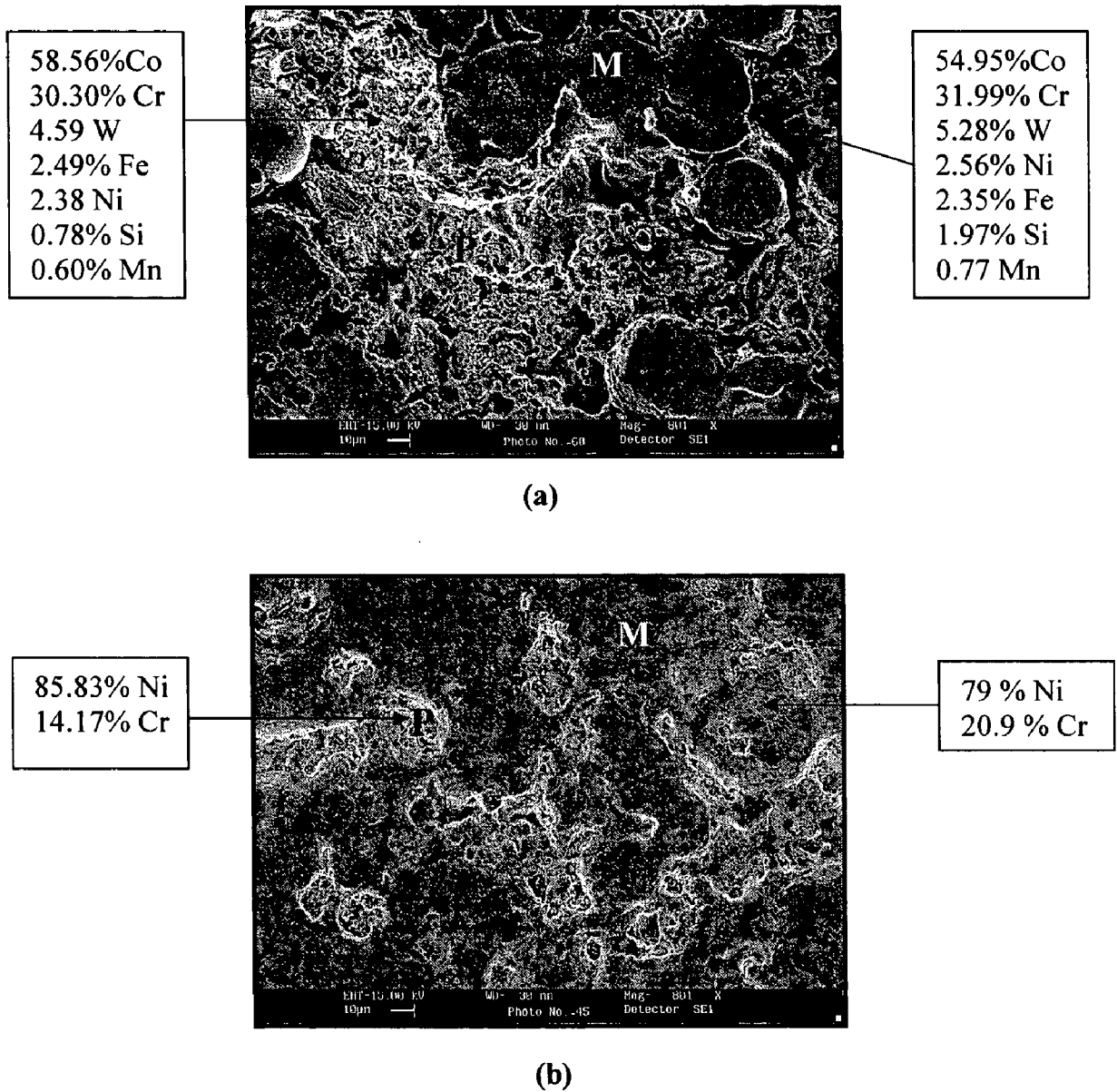


Fig. 5.22 SEM/EDAX analysis of the HVOF sprayed coatings showing elemental composition (wt%) at selected points:
 (a) Stellite-6 coating (b) Ni-20Cr coating.

5.3.8.2 Cross-Section Analysis

BSE images were obtained at the cross-section of the coated superalloys and EDAX analysis was performed at some selected areas of interest to ascertain elemental composition (weight %) at different points across the coatings. Figure 5.23a shows that at Point 1 in the substrate near the coating-substrate interface of $\text{Cr}_3\text{C}_2\text{-NiCr}$ coated Superfer 800H, there is slight decrease in weight percentage of iron (from 43.9% to 41.49%) while nickel has increased a little more (from 32% to 35.6%) than the nominal substrate composition. This indicates a limited diffusion of iron from the substrate to the coating and that of nickel from the coating to the substrate. BSEI and EDAX analyses at Points 2 and 4 show that the contrast phase is the matrix having composition similar to that of powder. White phase at Point 3 is found to be nickel-rich splat. In the case of NiCrBSi coated superalloy, elemental weight percentage analysis revealed negligible diffusion across the coating-substrate interface (Fig. 5.23b). Oxide inclusions of aluminum oxide have been found at the coating-substrate interface (Point 2) where all other elements are absent. EDAX results at Point 3 and 4 revealed that the composition of the coating is similar to the powder composition.

EDAX analysis of the Stellite-6 coated superalloys (Point 1) also shows very little diffusion of iron and nickel across the coating-substrate interface (Fig. 5.23c). Black areas at the coating-substrate interface (Point 2) are again observed to be the inclusions of aluminium oxide, where all other elements are found to be absent. Further, analysis at Point 3 shows that the light grey phase comprises of cobalt-rich splats with substantial amounts of chromium. At Point 4, the weight percentage of chromium has increased (from 28% to 30.57%) whereas that of cobalt decreased (from 59.8% to 12.97%). The existence of little oxygen at this point indicates the presence of oxide stringers which appear in the microstructure in the form of intersplat lamellae oriented parallel to the substrate surface. Similar analysis of the Ni-20Cr wire coating reveals that the white phase (Point 3) consists of nickel rich-splats, whereas contrast phase (Point 4) is the matrix having composition similar to that of feedstock wire (Fig. 5.23d).

5.3.9 EPMA Analysis

The X-ray mappings for the HVOF sprayed $\text{Cr}_3\text{C}_2\text{-NiCr}$, NiCrBSi, Stellite-6 and Ni-20Cr coatings are shown in Fig. 5.24 to 5.27, which indicate the presence of basic elements of the feedstock materials in the respective coatings.

The elemental mappings for the $\text{Cr}_3\text{C}_2\text{-NiCr}$ coating (Fig. 5.24) show that the nickel-rich splats are present in the chromium-rich matrix. Elemental map of Fe shows diffusion from the substrate to coating in trace amounts. Inclusions exclusively of aluminum appeared at the coatings-substrate interface. Similar analysis of the NiCrBSi coating (Fig. 5.25) shows that in addition to the presence of basic elements of the coatings, aluminum diffused across the coatings. Aluminium also forms clusters at the top of the coating as well as at the coating-substrate interface.

The EPMA analysis for the Stellite-6 coating (Fig. 5.26) indicates that the coating primarily consists of cobalt and chromium along with silicon. Nickel shows its presence in the form of thin stringers. Iron is present as thin discontinuous streaks at the coating-substrate interface. Small amount of titanium has diffused from the substrate to the coatings. Cross-sectional BSE image of the as-sprayed Ni-20Cr coating (Fig. 5.27) shows a typical lamellar structure consisting of mainly Ni-rich splats with chromium mainly present at the splat boundaries. Iron and manganese have shown marginal diffusion whereas silicon and aluminum diffused significantly from the substrate to coating. Aluminum has also shown its tendency to concentrates in pockets at the coating-substrate interface.

5.4 DISCUSSION

All the superalloys under study have a solid solution matrix. The carbides are invariably present in all the superalloys. In addition to the solid solution hardening, strength of the Ni-base superalloys also depends on the mechanism of precipitation hardening. Keeping in view the role of various alloying elements, carbides MC, M_7C_3 and M_{23}C_6 have the possibility of formation by precipitation in the superalloys under study. Among them, M_{23}C_6 has the strongest possibility of formation in all the cases, as it is mainly promoted by Cr (ASM Handbook, 1995). Further, M_{23}C_6 carbide has a tendency to precipitate at the grain boundaries. The possible carbides in case of Fe-based superalloy Superfer 800H are M_{23}C_6 and MC. Some large globules seen in Fig. 5.3 (e) indicate the presence of MC (TiC) phase.

Thick coatings have better corrosion resistances (Heath et al., 1997), but self-disintegration of thicker coatings restricts the thickness of the coatings. Therefore, it was decided to deposit 250-300 μm thick HVOF coatings in the present study, to ensure integrity of the coatings (Singh, 2003A). The coating thicknesses, as measured along the cross-section for some randomly selected samples, have been found in the desired range of 250-300 μm (Table 5.2).

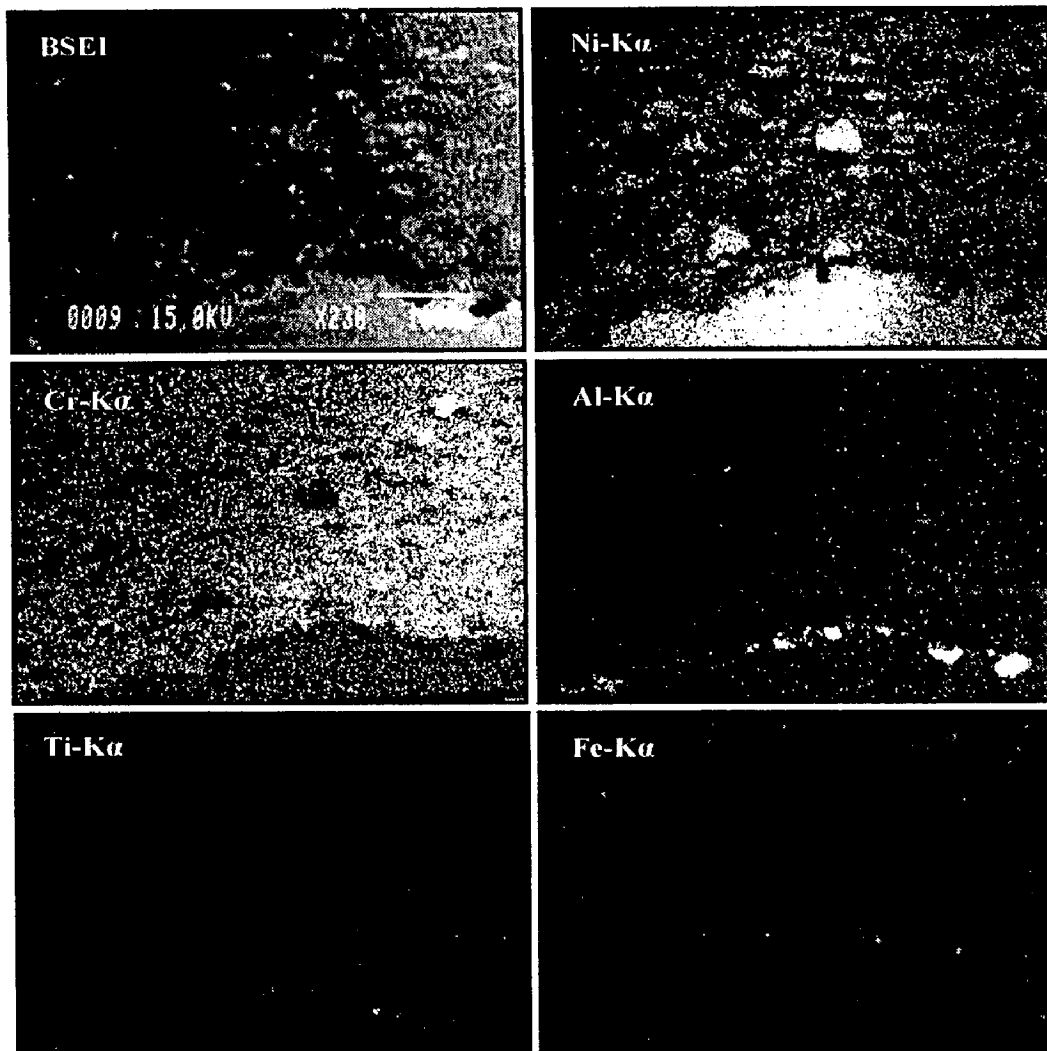


Fig. 5.24 Composition image (BSEI) and X-ray mappings at the cross-section of the as-sprayed $\text{Cr}_3\text{C}_2\text{-NiCr}$ coating on Superni 75 superalloy.

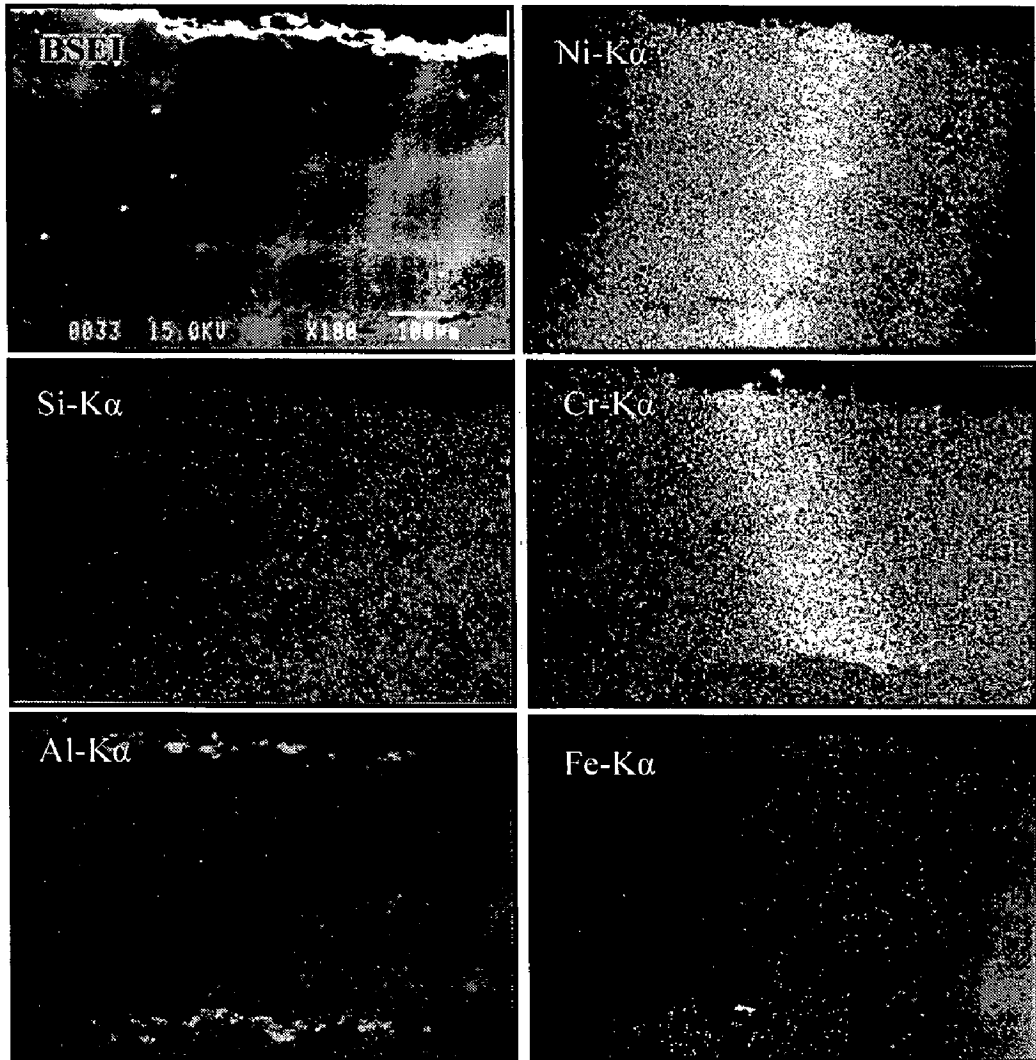


Fig. 5.25 Composition image (BSEI) and X-ray mappings at the cross-section of as-sprayed NiCrBSi coating on Superni 601 superalloys.

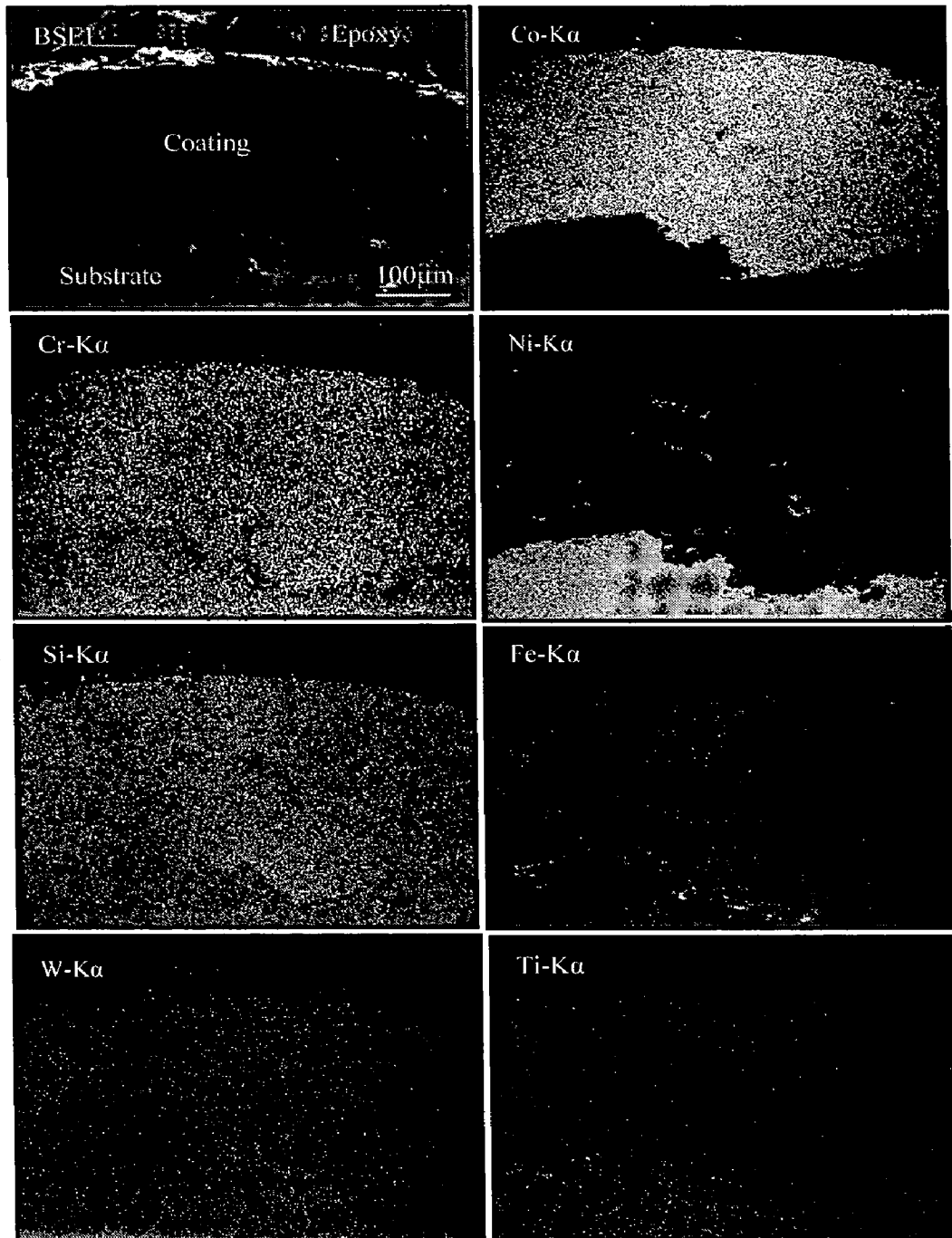


Fig. 5.26 Composition image (BSEI) and X-ray mappings at the cross-section of the as-sprayed Stellite-6 coating on Superni 75 superalloys.

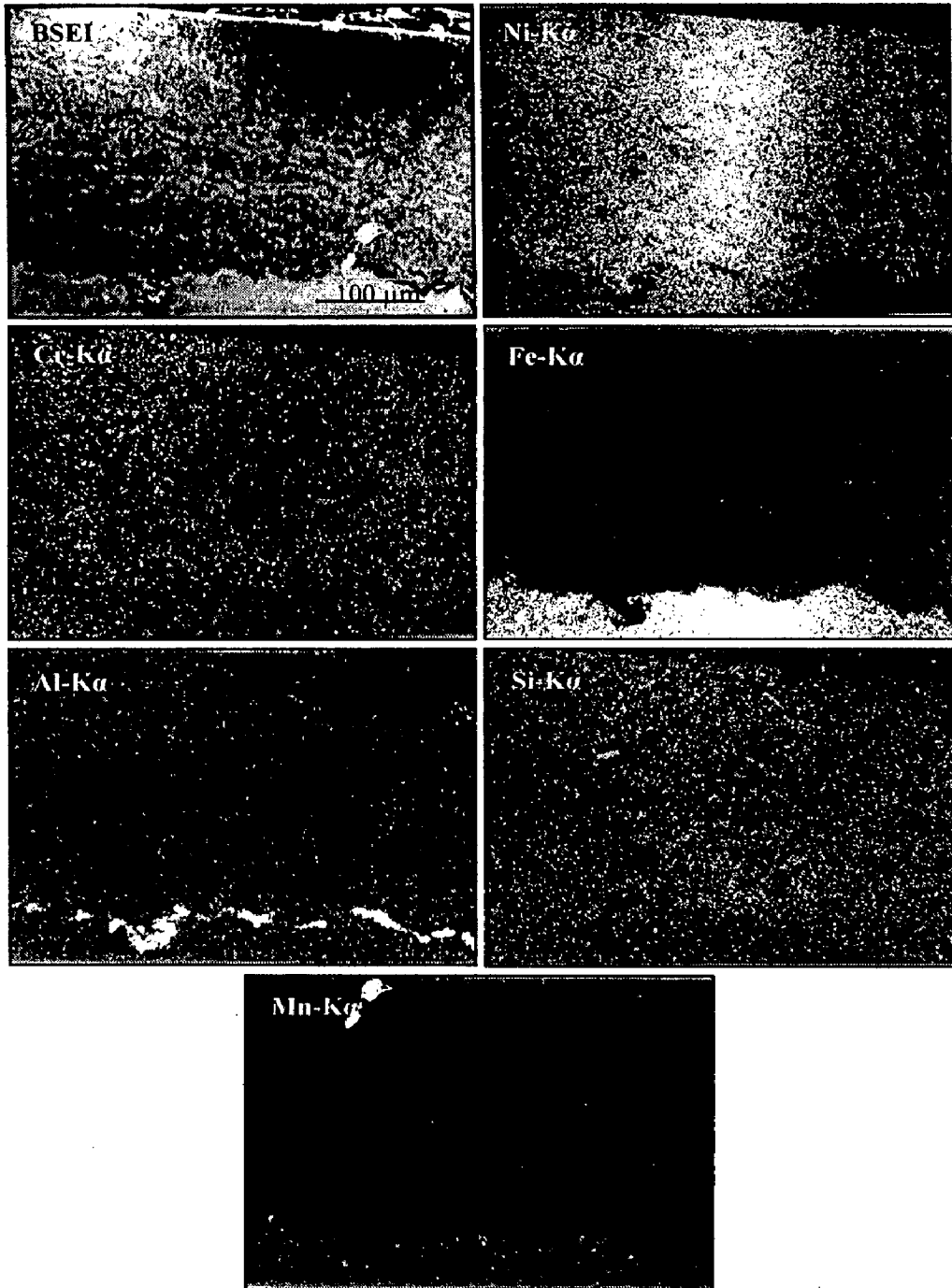


Fig. 5.27 Composition image (BSEI) and X-ray mappings at the cross-section of the as-sprayed Ni-20Cr coating on Superfer 800H superalloy.

HVOF coatings have a relatively smooth as-sprayed finish (surface roughness 4-6, Fig. 5.4) due to the high impact energy inflicted upon the impinging particles, which causes better mechanical bonding of the sprayed particles thus forming homogenous structures, thereby requiring less finishing as compared to other thermal spraying processes.

The coatings have very less porosity (up to 2%). Porosity is one of the most important properties of the coatings for higher temperatures applications in corrosive environments, as porosities are the preferential corrosion paths through which the corrosive species can penetrate the coatings to reach the substrate and may cause rapid corrosion attack. Dense coatings provide better corrosion resistance (Zhao et al., 2004A; Zhao et al., 2005B). The low value of porosity of the as-sprayed HVOF coatings might be due to high kinetic energy of the powder particles. As a result, there may be an excellent joining of flat disc particles with the substrate and with an interlayer, and thus the coatings produced are very dense. The measured values of the porosity are in close agreement with the findings of Helali and Hashmi (1992); Gil and Staia (2002); Guilemany et al. (2002); Suegama et al. (2002 and 2004); Miguel et al. (2003); Aalamialeagha et al. (2003); Planche et al. (2005); and are reported by the author in his earlier publication (Sidhu et al, 2006B, 2006D and 2006G).

Hardness is the most frequently quoted mechanical property of the coatings (Tucker, 1994). It may affect the erosion-corrosion degradation behavior of the coatings. Two very interesting observations have been made after detail examination of the microhardness profiles shown in Figs 5.6 and 5.7. Firstly, all the substrates near the coating-substrate interface have shown higher hardness compared to the core substrates. The reason for this increased hardness near the coating-substrate interface is attributed to the work hardening effect of sandblasting on the substrate prior to the coating process as observed by Sundararajan et al. (2004B). This increase in hardness is also contributed by the high speed impact of the coating droplets during HVOF spraying as reported by Hidalgo et al. (1997 and 2000); Singh (2003A); and Sidhu et al. (2004 and 2005A). The author has reported this increase in hardness phenomenon in his earlier publications (Sidhu et al., 2006B, 2006D and 2005E). Second interesting observation is that the microhardness of the coatings under study has been found to be much higher than the substrate superalloys. The higher hardness values of the coatings is attributed to the higher impact velocity resulting in high density and cohesive strength of the individual splats, Verdon et al. (1998) and Hawthorne et al. (1999). Some difference in the hardness

values of each coating, along the cross section of each substrate, has also been noticed. This difference in hardness values of the coatings is due to the presence of porosity, un-melted, melted and partially melted particles, and oxide inclusions as revealed by the cross section micrographs of the coatings shown in Fig. 5.12. The measured values of microhardness of HVOF coatings under study are found to be in good agreement with the findings of Vuoristo et al. (1994); Gil and Staia (1999); Lee and Min (2000); Wang and Lee (2000); Miguel et al. (2003); Zhao et al. (2004B); and Planche et al. (2005). Some difference in the microhardness values of each coating on different substrates is due to minor diffusion of elements from the substrate to coating as indicated by EDAX and EPMA analysis reported under section 5.3.8.1 and 5.3.9, respectively.

From the cross-section micrographs of the coatings on different substrates shown in Fig. 5.5 and 5.12, it can be inferred that the coatings have nearly uniform dense structures and exhibit characteristic splatlike, layered morphologies due to the deposition and re-solidification of molten or semi-molten droplets. The long axis of the impacted splats are oriented parallel to the substrate surface. Micrographs show that a high proportion of the feedstock powders/wire is fully or partially melted prior to impact on the substrate, as very less number of un-melted particles are observed in the microstructures. Further, the coatings possess some voids and oxide inclusions that are typical characteristic of the HVOF sprayed coatings. No significant difference is observed between the microstructure of the individual coating deposited on different substrates. Microstructures observed in the present study are almost analogous with the findings of HVOF sprayed coatings by Dent et al. (2001); Kong et al. (2003); Sundararajan et al. (2003A and 2003B); and Zhao et al. (2004B).

SEM/EDAX analysis shown in Fig. 5.21 and Fig. 5.22 indicate that HVOF coatings under study meet the required composition. The regions marked 'M' in these micrographs (Fig. 5.22) which appear featureless, have formed from the impact of fully molten feedstock droplets. Subsequently, these droplets solidified at a high cooling rate, which has been proposed by Moreau et al. (1991) to be typically around 10^7 Ks^{-1} for splat solidification. Such a high cooling rate would result in the formation of a microcrystalline structure (Kong et al., 2003). These micro-crystalline grains have solidified directly from the melt by heterogeneous nucleation on pre-existing grains of oxide (Dent et al., 2001).

The presence of some contrast stringers, where EDAX analysis has shown the existence of small quantity of oxygen (Point 4 of Fig. 5.23C), are the oxide phase. It

indicates that some limited oxidation has occurred at the surface of in-flight particles or at the coating surface, prior to the deposition of the next layer. Similar findings of formations of oxides in the HVOF coatings have also been reported by Dent et al. (2001) and Kong et al. (2003). Some oxide inclusions are also detected in SEM/EDAX analysis (Fig. 5.21b).

Some inclusions are found to be present invariably in all the coatings at the coating substrate interface. EDAX analysis has shown the presence of aluminum and oxygen at these places, which indicates that these inclusions are aluminium oxide (refer Fig 5.23b and 5.23c). The EPMA elemental maps also indicate that the islands of alumina are present at the scale-substrate interface (Fig. 5.24), which do not match with the elements of substrate alloy or coating powders. There is a possibility that some alumina powder might have been retained during polishing of the specimens. Similar islands of aluminium oxides due to retained alumina powder during polishing were reported by Sundararajan et al. (2003A).

XRD analysis shows that Cr_3C_2 phase which is present in the Cr_3C_2 -NiCr powder (Fig 5.2) is absent in the HVOF sprayed Cr_3C_2 -NiCr coating (Fig. 5.13). This is due to the decarburization of Cr_3C_2 during spraying in HVOF process. As a result Cr_7C_3 phase is formed in the as-sprayed Cr_3C_2 -NiCr coating as has been reported in the literature by Barbezat et al. (1993) and Vuoristo et al. (1994) also. Formation of phases in the HVOF sprayed Cr_3C_2 -NiCr coating/powder similar to the present study have also been reported by Vuoristo et al. (1994); Guilemany et al. (1997B) and Murthy and Venkataraman, (2004). In case of as-sprayed NiCrBSi coating, the XRD peak around 44° is found to be very broad, suggesting the formation of an amorphous matrix (Fig. 5.14). The phases similar to as-sprayed NiCrBSi coating in the present study have also been revealed by Dent et al. (2001); Modi and Calla (2001); Miguel et al. (2003) and Planche et al. (2005) for HVOF sprayed NiCrBSi/NiCrBC coatings.

The M_7C_3 carbide phase, which is present in Stellite-6 alloy powder (Fig. 5.2), is not present in the Stellite-6 coating obtained by HVOF process as revealed by the XRD analysis (Fig. 5.15). Its formation in the deposits is suppressed by the high cooling rates (around 10^7 Ks^{-1}) occurring during splat solidification (Moreau et al., 1991). Very similar results have been obtained by Kong et al. (2003). The XRD analysis for the Stellite-6 and NiCrBSi coatings have shown the presence of very small intensity peaks of spinel oxide CoNiO_2 and NiCr_2O_4 , respectively. Similar findings of the presence of oxide phases in HVOF coatings have been reported by Dent et al. (2001); Kong et al. (2003); Zhang et al. (2003).

Both the Ni-20Cr feedstock wire and after the spray, Ni-20Cr coatings showed the formation of γ -Ni solid solution as a principal phase along with very low intensity peaks of chromium (Fig. 5.2 and 5.16). It indicates that the HVOF sprayed Ni-20Cr coatings did not undergo any change in their phases and compositions as compared to the feedstock wire. Similar XRD analysis for HVOF sprayed Ni-20Cr coating has been reported by Sundararajan et al. (2003A). The X-ray diffraction results for all the as-sprayed coatings are well supported by SEM/EDAX and EPMA results.

Based on the results of XRD, SEM/EDAX, EPMA, optical microscopy and microhardness testing, the HVOF sprayed Ni-20Cr wire coating has been found to be technically viable and effective alternative to HVOF sprayed Ni-20Cr powder coating reported by Ak et al. (2003). Figures 5.28 and 5.29 depict the SEM micrographs of HVOF sprayed Ni-20Cr coatings using Ni-20Cr powder (as reported by AK et al., 2003) and Ni-20Cr wire (used in the present investigation), as feedstock alloys, respectively. It is evident from the SEM micrographs that the coating obtained using Ni-20Cr powder as feedstock alloy (Fig. 5.28) has more porosity as compared to the coating obtained using Ni-20Cr wire (Fig. 5.29).

EDAX (Fig. 5.23) as well as EPMA results (Fig.5.24 to Fig. 5.27) for the HVOF sprayed coatings under study indicated that there exist inter-diffusion of various elements between the substrate and coatings, which may effect the hot corrosion behaviour of any particular coating on different substrates. Aluminium and silicon are found to be the most vulnerable element to the diffusion phenomenon. Ni, Fe, Ti, and Mn are some other elements which are prone to minor diffusion. The diffusion of elements between the substrate and coating can have a major influence on coating performance for higher temperature applications (Nicholls, 2000; Sundararajan et al., 2005).

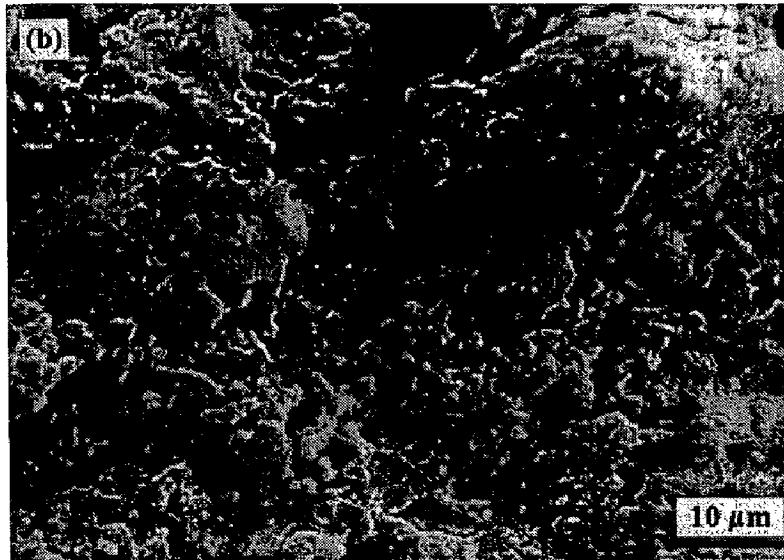


Fig. 5.28 SEM micrograph of HVOF sprayed coating reported by Ak et al. (2003), using Ni-20Cr powder as feedstock alloy.

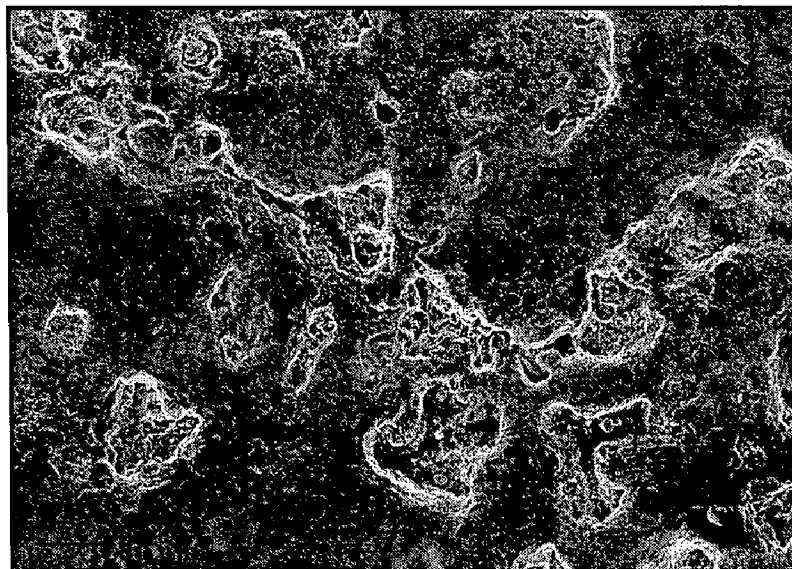


Fig. 5.29 SEM micrograph of HVOF sprayed coating using Ni-20Cr wire as feedstock alloy.

Chapter 6

HOT CORROSION STUDIES IN MOLTEN SALT ENVIRONMENT

This chapter describes the hot corrosion behaviour of the HVOF coated as well as uncoated superalloys in an aggressive environment of molten salt (Na_2SO_4 -60% V_2O_5) at 900 °C under cyclic conditions. Thermogravimetric technique was used to understand the kinetics of corrosion. The specimens were visually examined at the end of each cycle during the course of study. The different phases and their distribution in the hot corroded specimens were analysed with the help of XRD, SEM/EDAX and EPMA. The parabolic rate constants and scale thickness values have been evaluated after 50 cycles of exposure.

6.1 RESULTS AND DISCUSSION

6.1.1 Visual Examination

6.1.1.1 Bare Superalloys

The macrographs for base superalloys Superni 75, 600, 601, 718 and Superfer 800H after hot corrosion at 900 °C for 50 cycles in Na_2SO_4 -60% V_2O_5 environment are shown in Fig. 6.1. During first cycle of the study, light brownish grey and light black colour scales were noticed on the surfaces of nickel- and iron-based superalloys, respectively. Subsequently, the colour of scale turned to dark brownish grey on Ni-based superalloys and black in the case of Fe-based superalloy. The Superni 75 superalloy showed a very little amount of spallation of the scale which was mainly confined to edges and corners, and the scales was found to be relatively intact as compared with other superalloys (Fig. 6.1a). In the case of Superni 600 the scale indicated a tendency to crack from the 8th cycle onward resulting in the peeling as well as spallation of the scale at many locations.

A fragile scale appeared on the surface of uncoated Superni 601 superalloy during the earlier cycles and cracks developed in the scale were confined mostly to the edges. At the end of 10th cycle, cracks developed even on the top surface of the scale (Fig. 6.2) resulting intensive spalling as can be seen in Fig. 6.1c. Intensive spalling and sputtering (disintegration of the scale accompanied by cracking sound during cooling) of the scale was observed during hot corrosion study of Superni 718 superalloy from 6th cycles onwards. During 17th cycle, the spalling and sputtering of the

scale was so intensified that the corrosion products even started falling outside the boat. Heavy sputtering of the scale continued during cooling period of the cycles and reintroduction of the sample into the furnace. This superalloy had shown maximum spalling and sputtering of the scale among all the superalloys studied in the present research work (Fig 6.1d).

In the case of iron based superalloy Superfer 800H, micro spalling of the scale had started from the third cycle onwards which intensified as the period of study progressed. Sputtering of the corrosion products was also spotted during 8th cycle and heavy sputtering was observed after 12th cycle onwards. Sputtering continued while the sample was getting cooled at the end of each cycle and while keeping the boat inside the furnace. This affected the total weight gained by the bare superalloy and the actual weight gain might be more than what was observed. The surface of the specimen, which turned shining black colour during early cycles, became rough with progress of the study and contained uniformly distributed pores on the scale surface.

6.1.1.2 HVOF Coated Superalloys

The macrographs for the HVOF sprayed Cr_3C_2 -NiCr, NiCrBSi, Stellite-6 and Ni-20Cr coated superalloys hot corroded in Na_2SO_4 -60% V_2O_5 environment at 900 °C for 50 cycles are shown in Figs. 6.3 to 6.6.

The Cr_3C_2 -NiCr coated superalloys indicated some superficial minor cracks at the edges and corners of some specimens during experimentations. The marginal spalling from these regions, mostly confined to the outer layers of the coating, was observed during early cycles (Fig. 6.3). The colour of the scale was dark grey during the first 2-3 cycles which turned to blackish green with the progress of the study. The Cr_3C_2 -NiCr coated Superni 75 and Superni 601 superalloys were having relatively smoother surfaces as compared to other substrates. After the 30th cycle of study, the spallation of the scale was not observed in any of coated superalloys. However, only in case of Cr_3C_2 -NiCr coated Superfer 800H, the coating had broken from one corner of the specimen during the last cycle (Fig.6.3e).

In the scales of NiCrBSi coated superalloys, shining yellowish tinges were observed on dark black background during earlier cycles of the study. Subsequently, the colour of the scale became reddish brown (rust colour) after few cycles. Compact and dense continuous scale gradually developed on all the coated superalloys and no spallation of the scale was noticed even at the corners or edges (Fig. 6.4).

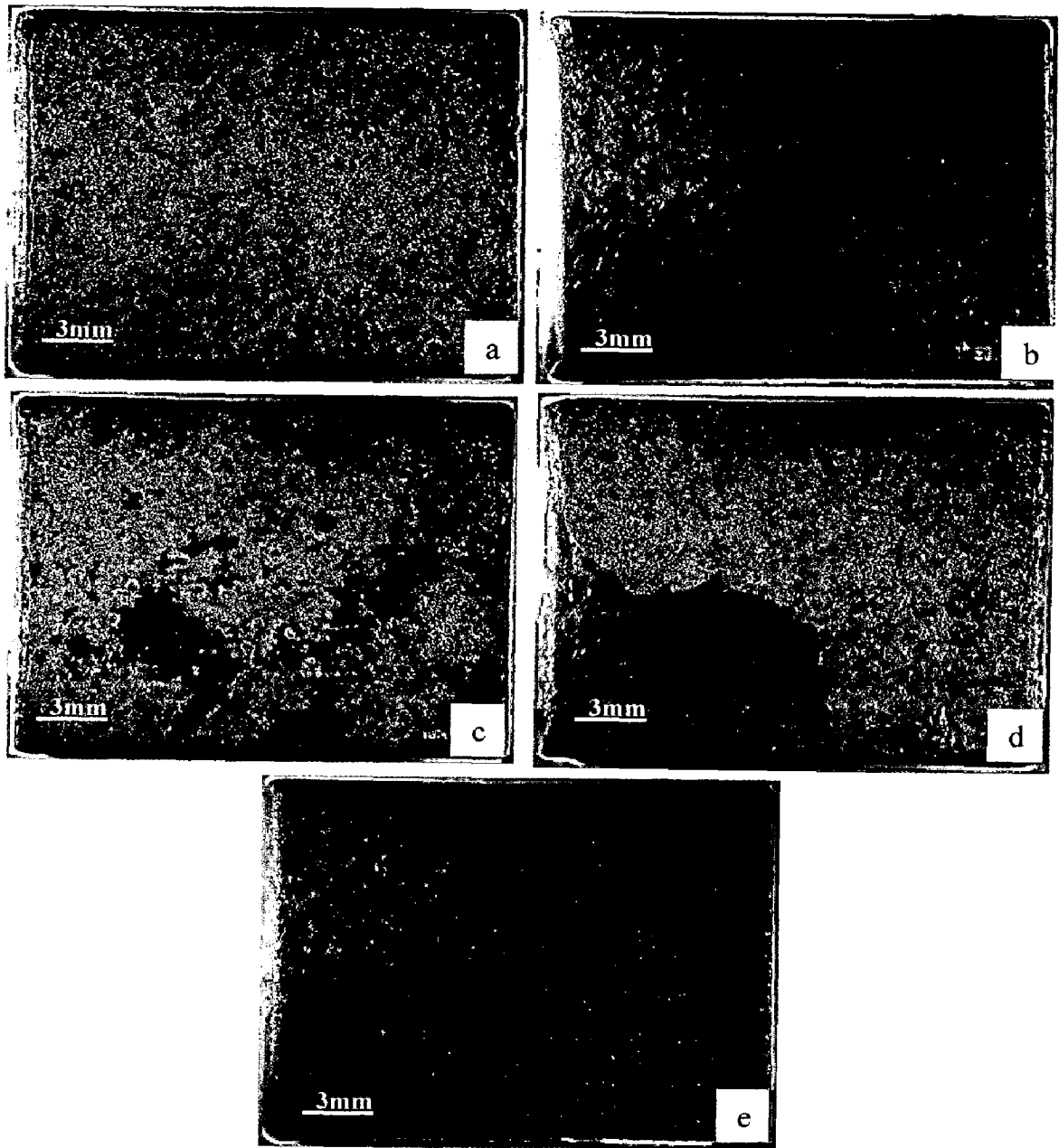


Fig. 6.1 Macrographs of the bare superalloys subjected to hot corrosion in $\text{Na}_2\text{SO}_4\text{-60\%V}_2\text{O}_5$ environment at 900 °C for 50 cycles:
(a) Superni 75 (b) Superni 600 (c) Superni 601
(d) Superni 718 (e) Superfer 800H.

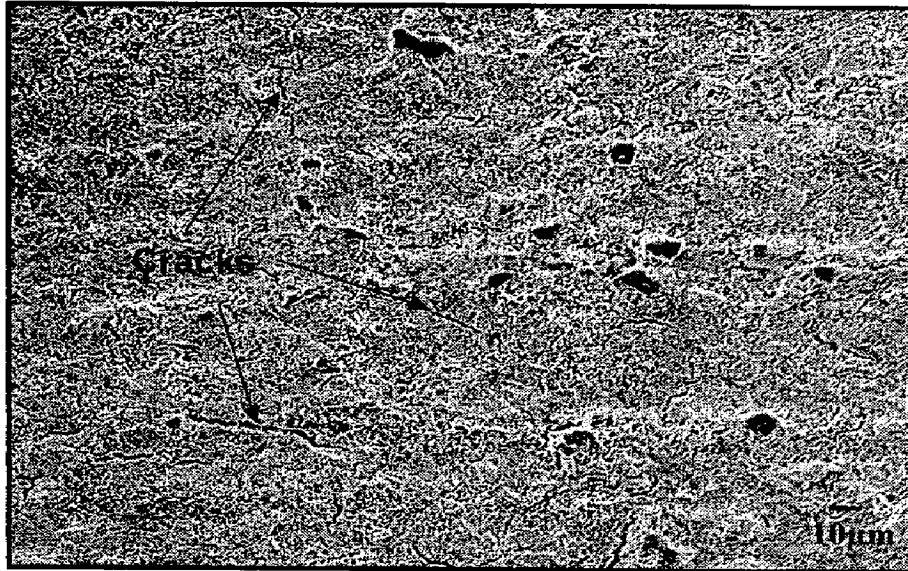


Fig. 6.2 Cracks developed in the scale of uncoated superalloy Superni 601 subjected to hot corrosion in Na_2SO_4 -60% V_2O_5 environment at 900 °C after 10th cycles.

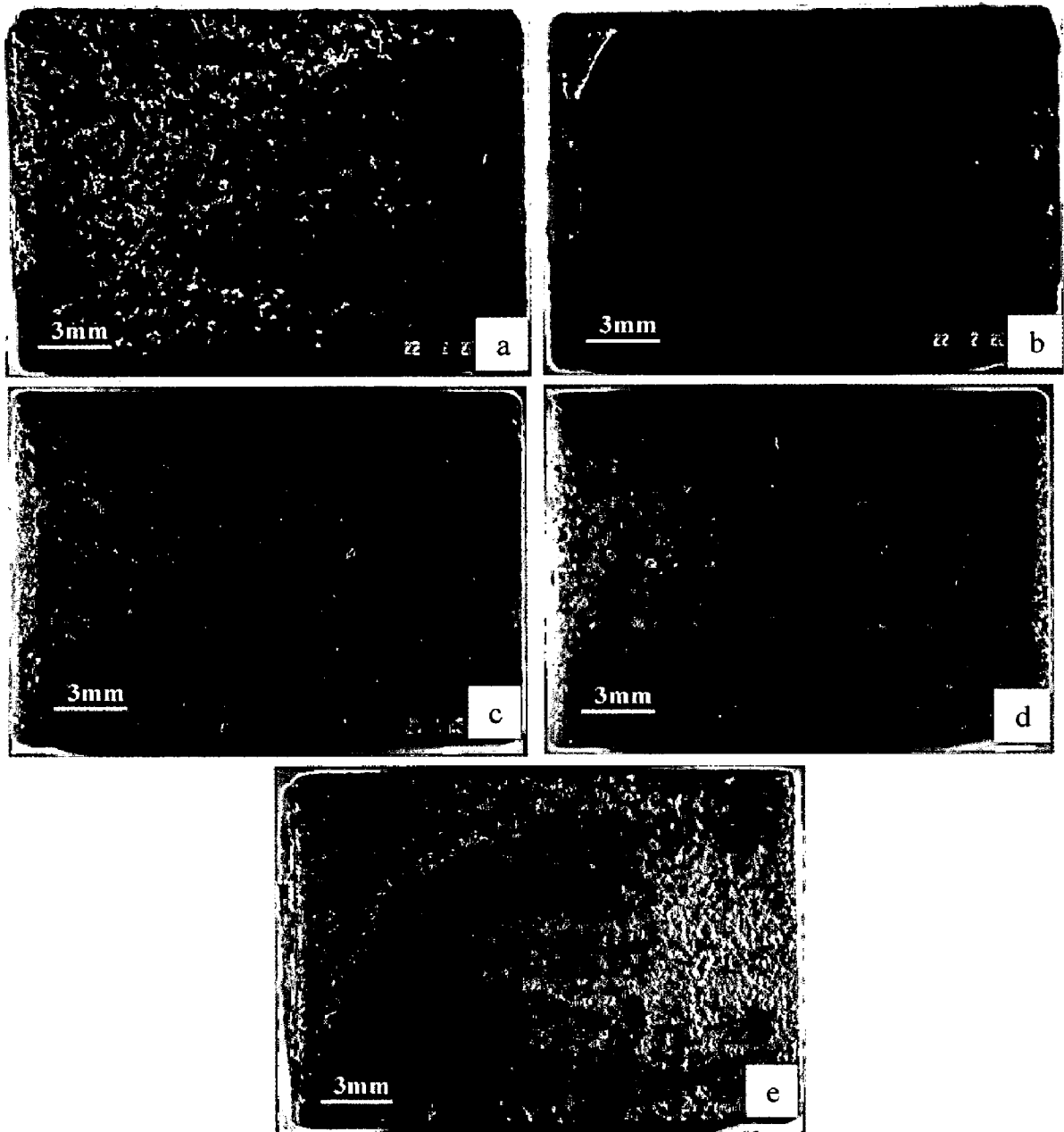


Fig. 6.3 Macrographs of the $\text{Cr}_3\text{C}_2\text{-NiCr}$ coated superalloys subjected to hot corrosion in $\text{Na}_2\text{SO}_4\text{-60\%V}_2\text{O}_5$ environment at 900°C for 50 cycles:
(a) Superni 75 (b) Superni 600 (c) Superni 601
(d) Superni 718 (e) Superfer 800H.

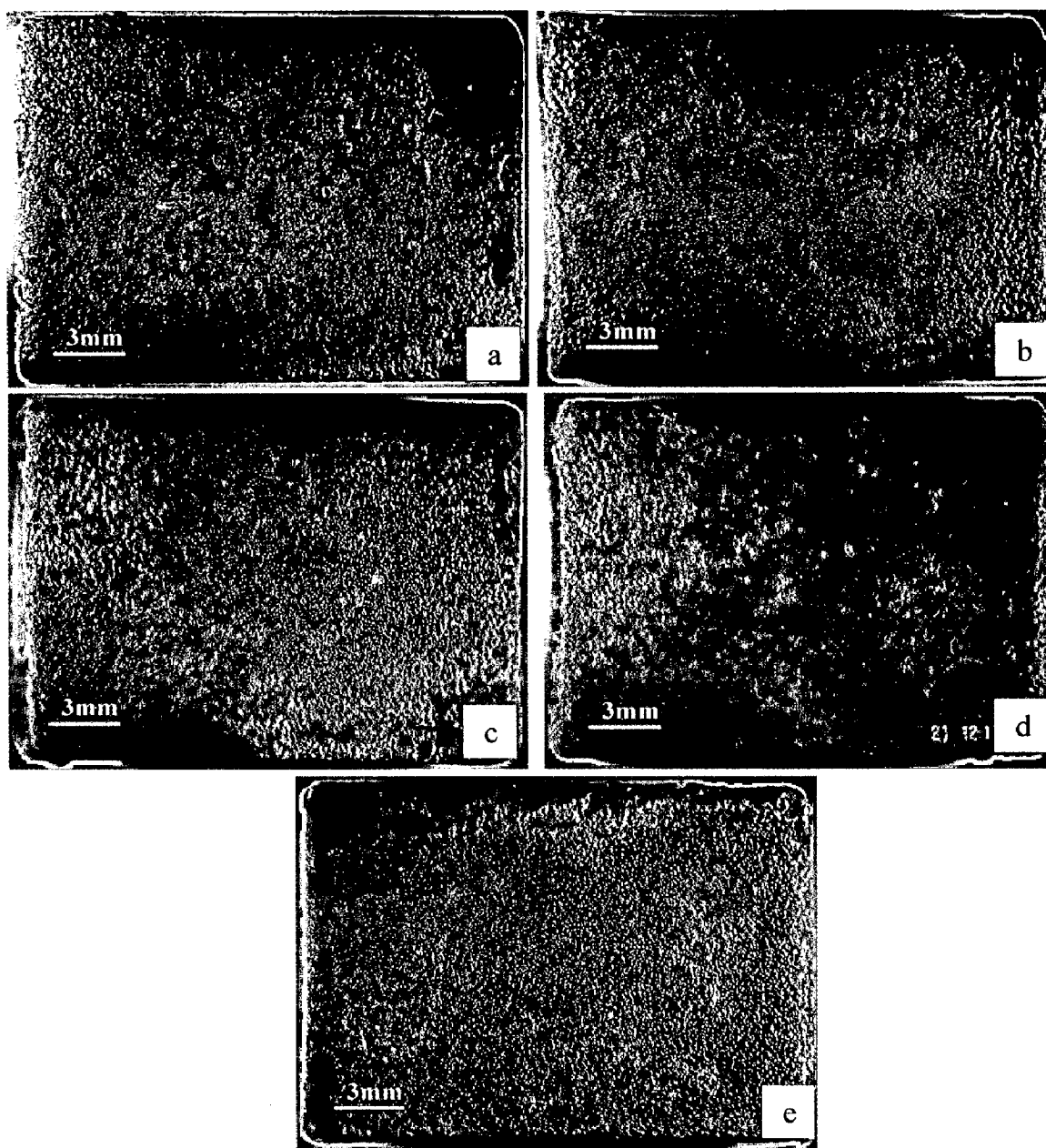


Fig. 6.4 Macrographs of the NiCrBSi coated superalloys subjected to hot corrosion in $\text{Na}_2\text{SO}_4\text{-60}\%\text{V}_2\text{O}_5$ environment at $900\text{ }^\circ\text{C}$ for 50 cycles:
 (a) Superni 75 (b) Superni 600 (c) Superni 601
 (d) Superni 718 (e) Superfer 800H.

Colour of the oxide scale for all the Stellite-6 coated superalloys was black after the first cycle which turned to dark grey during 7th to 9th cycles, and subsequently showed the formation of silver grey patches on the dark greenish/brownish grey background (Fig. 6.5). Invariably all the Stellite-6 coated superalloys have shown some spalling and peeling from 6th cycle onwards in the form of blackish powdered particles. Green colour areas were observed from where spallation of scale had occurred. Green colour patch is clearly visible in case of coated Superni 75 superalloy (Fig 6.5a). Stellite-6 coating has shown a comparatively higher extent of spallation amongst all the coatings especially for Superni 600, Superni 718 and Superfer 800H substrates.

In the case of Ni-20Cr coating, a blackish grey scale was formed after first cycle which gradually turned to dark black during next few cycles. After 15th cycle, a very shining silver grey scale appeared for all the Ni-20Cr coated superalloys, except the Superni 75 on which dark grey scale appeared (Fig 6.6). In general, the scales were found to be smooth and intact. Only some minor spallation of the scales was noted in Ni-20Cr coated superalloys near the edges, except for Ni-20Cr coated Superni 601 substrate where this minor spallation was observed on the surface also (Fig. 6.6c).

6.1.2 Hot Corrosion of Bare and Coated Superni 75

6.1.2.1 Corrosion Kinetics

Thermogravimetric data for the hot corroded bare and coated Superni 75 is compiled in the form of a graph between weight gain per unit area expressed in mg/cm² versus time expressed in number of cycles and is shown in Fig 6.7. The figure shows that all the coatings on Superni 75 have relatively higher weight gain during the early cycles of the study, and thereafter the weight gain is nearly gradual. The overall weight gains after 50 cycles of hot corrosion for bare Superni 75, Cr₃C₂-NiCr-, NiCrBSi-, Stellite-6- and Ni-20Cr-coated Superni 75 are found to be 12.015, 7.481, 8.699, 9.902 and 7.121 mg/cm², respectively. Evidently the bare superalloy gains the maximum weight during the course of study. From the weight gain data it can be inferred that all the coatings deposited on Superni 75 have provided necessary protection against hot corrosion. Amongst the HVOF coatings, Ni-20Cr coating has shown the highest hot corrosion resistance under the given conditions followed by Cr₃C₂-NiCr, NiCrBSi and Stellite-6 coatings. The Ni-20Cr coating reduced the weight gain of Superni 75 by around 41%. The hot corrosion resistance in terms of weight gain of Cr₃C₂-NiCr and Ni-20Cr coated Superni 75 is almost found to be similar, whereas Stellite-6 coated Superni 75 has shown minimum resistance. Figure 6.8 shows the cumulative weight gain/ unit area for all cases.

Further, the weight gain square (mg²/cm⁴) data were plotted as a function of time (number of cycles) as shown in Fig. 6.9 to establish the rate law for the hot

corrosion. The plots show observable deviations from the parabolic rate law for bare Superni 75, while the coated Superni 75 follow parabolic rate law. The parabolic rate constant k_p was calculated by a linear least-square algorithm function in the form of $(\Delta W/A)^2 = k_p \cdot t$, where $\Delta W/A$ is the weight gain per unit surface area (mg/cm^2), t is the hot corrosion time in seconds. The parabolic rate constant, k_p , for bare Superni 75, calculated on the basis of 50 cycles data, is found to be $9.716 \times 10^{-10} \text{ g}^2 \text{ cm}^{-4} \text{ s}^{-1}$. The values of k_p for $\text{Cr}_3\text{C}_2\text{-NiCr}$, NiCrBSi , Stellite-6 and Ni-20Cr coated Superni 75 are found to be 2.997, 4.216, 5.238, and $2.213 \times 10^{-10} \text{ g}^2 \text{ cm}^{-4} \text{ s}^{-1}$, respectively.

6.1.2.2 Scale Thickness Measurement

Scale thickness was measured from the SEM back scattered images taken across the cross-section of bare and coated Superni 75 superalloys after subjecting to hot corrosion for 50 cycles at 900°C (Fig. 6.10). These micrographs were taken at the locations where the scale thickness was the least. The scale thickness was taken as the distance from the surface to the site up to which the oxygen has penetrated into the bare/coated superalloys. The average scale thickness value for bare Superni 75 is found to be $108 \mu\text{m}$, and that for $\text{Cr}_3\text{C}_2\text{-NiCr}$, NiCrBSi , Stellite-6 and Ni-20Cr coated Superni 75 are 268, 280, 303 and $255 \mu\text{m}$, respectively.

6.1.2.3 X-ray Diffraction Analysis

The diffraction patterns for the bare and coated Superni 75 after subjecting to hot corrosion for 50 cycles at 900°C are shown in Fig. 6.11. Only the main phases are indicated in the XRD spectrum. The various phases identified with the XRD analysis are presented in Table 6.1. Cr_2O_3 and NiCr_2O_4 are the common major phases invariably formed during hot corrosion of all the coatings deposited on Superni 75. Whereas SiO_2 and CoO are the other major phases produced on NiCrBSi and Stellite-6 coated Superni 75 respectively, while NiO formed on $\text{Cr}_3\text{C}_2\text{-NiCr}$ and Ni-20Cr coated Superni 75.

Table 6.1: Major and minor phases identified by XRD analysis of the hot corroded bare and coated Superni 75.

Description	Major phases	Minor phases
Uncoated Superni 75 superalloy	NiO , Fe_2O_3 , NiCr_2O_4 , $\text{Ni}(\text{VO}_3)_2$, and FeV_2O_4	Cr_2O_3 , FeS , FeV , and TiO_2
$\text{Cr}_3\text{C}_2\text{-NiCr}$ coated	Cr_2O_3 , NiO , and NiCr_2O_4	Fe_2O_3
NiCrBSi coated	SiO_2 , Cr_2O_3 , NiCr_2O_4 , and Fe_2O_3	----
Stellite-6 coated	CoO , Cr_2O_3 , CoCr_2O_4 , and NiCr_2O_4	Fe_2O_3 , and NiO
Ni-20Cr coated	NiO , Cr_2O_3 , and NiCr_2O_4	Fe_2O_3 , and TiO_2

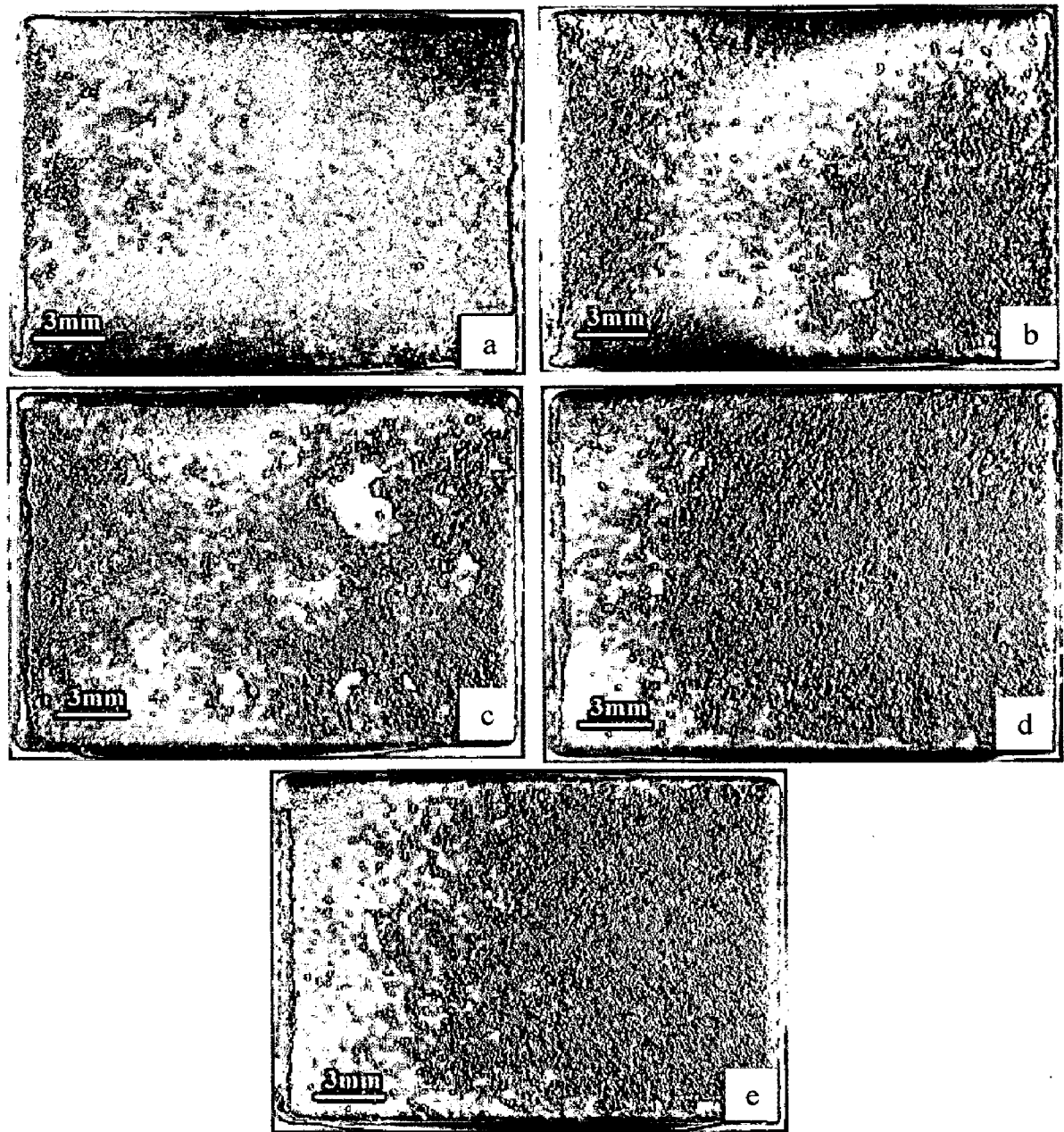


Fig. 6.6 Macrographs of the Ni-20Cr coated superalloys subjected to hot corrosion in Na_2SO_4 -60% V_2O_5 environment at 900 °C for 50 cycles:

- (a) Superni 75 (b) Superni 600 (c) Superni 601
(d) Superni 718 (e) Superfer 800H.

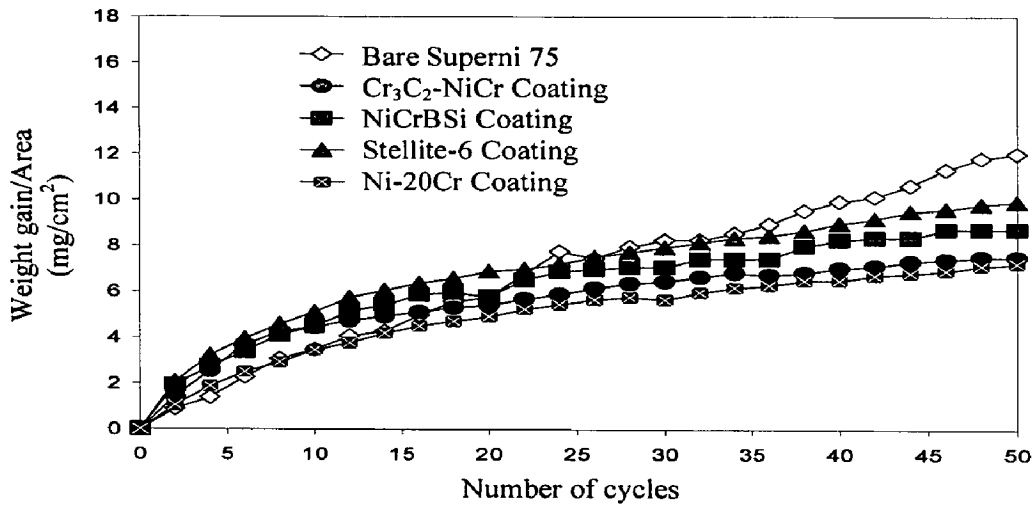


Fig. 6.7 Weight gain vs. number of cycles plot for the coated and uncoated Superni 75 subjected to hot corrosion for 50 cycles in Na_2SO_4 -60% V_2O_5 environment at 900 °C.

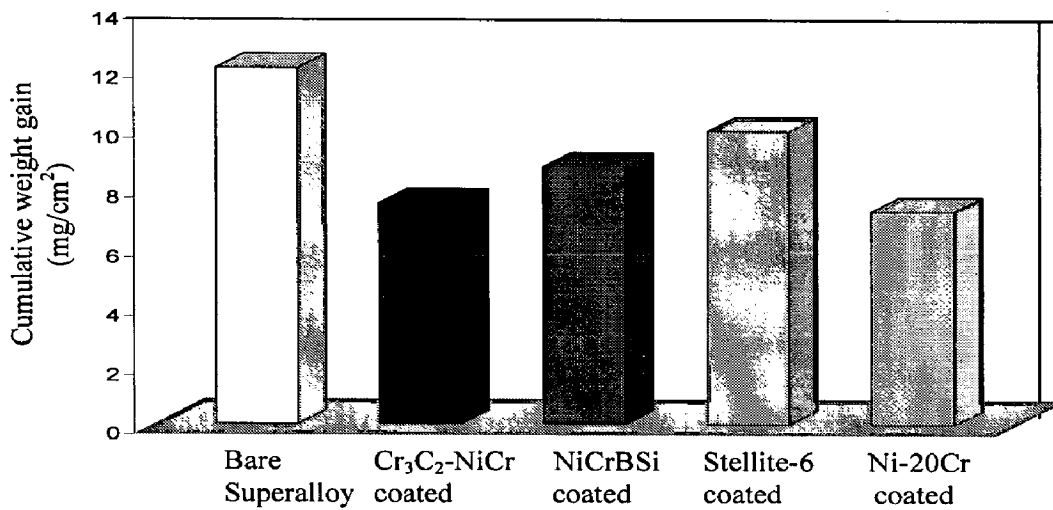


Fig.6.8 Bar charts showing cumulative weight gain per unit area for the coated and uncoated Superni 75 subjected to hot corrosion for 50 cycles in Na_2SO_4 -60% V_2O_5 environment at 900 °C.

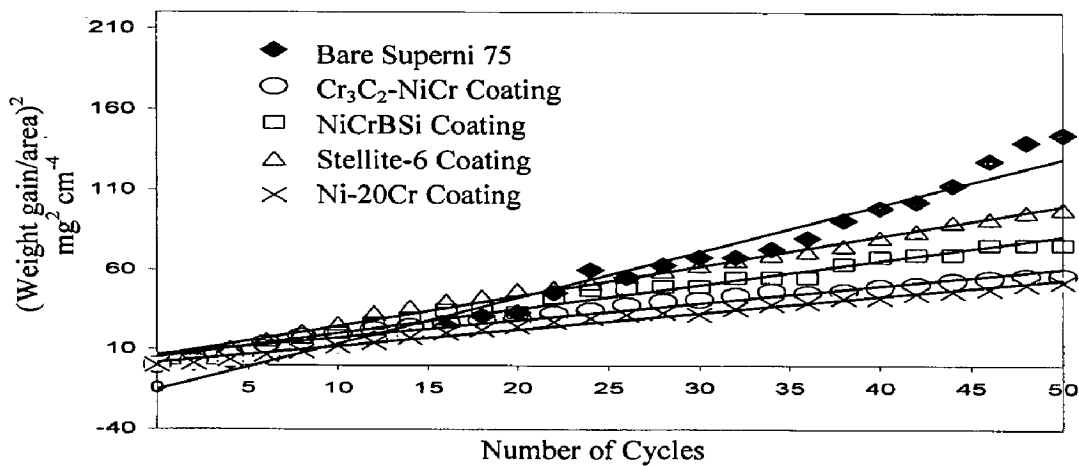


Fig. 6.9 $(\text{Weight gain/area})^2$ vs. number of cycles plot for the coated and uncoated superalloy Superni 75 subjected to hot corrosion for 50 cycles in Na_2SO_4 -60% V_2O_5 environment at 900 °C.

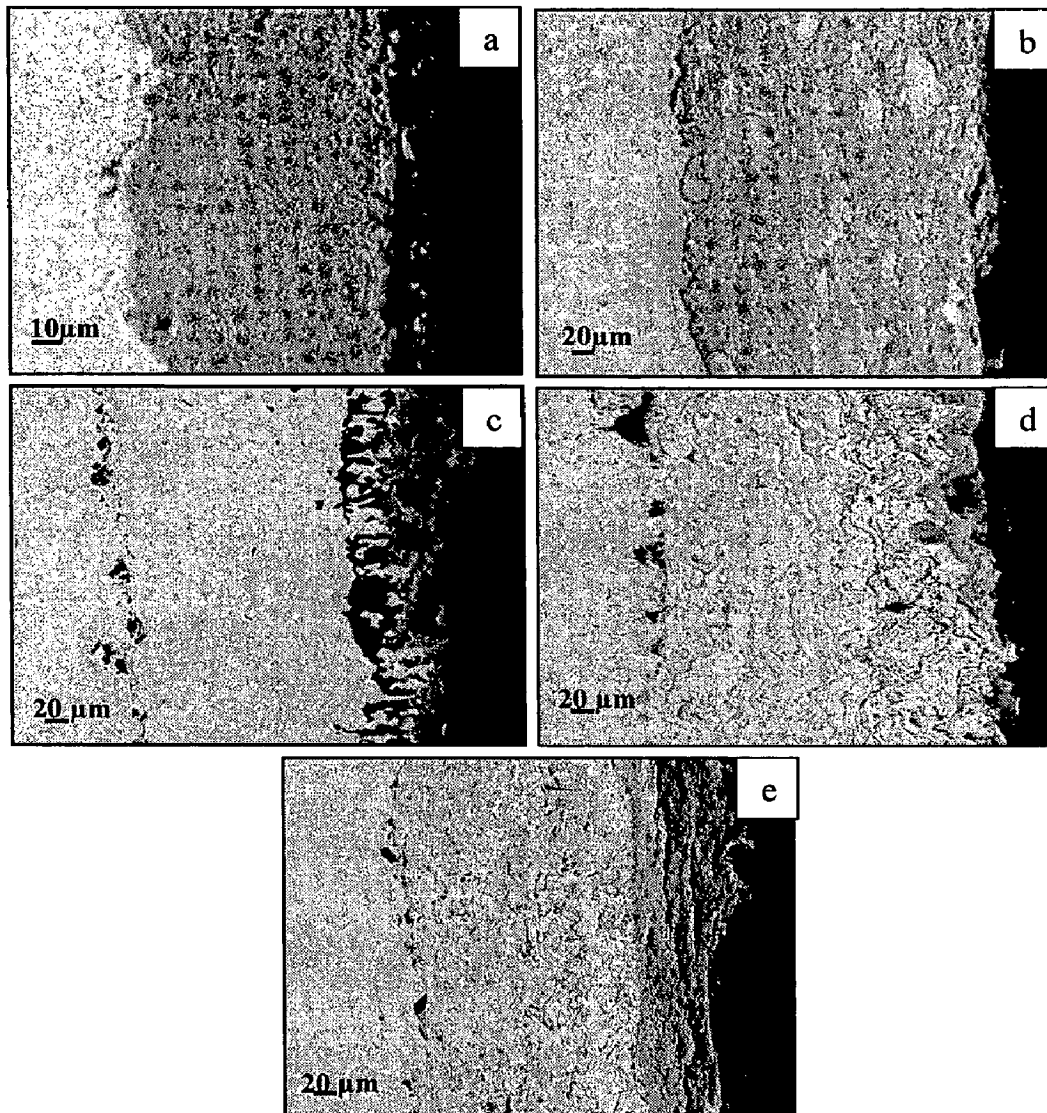


Fig. 6.10 SEM back scattered images for the bare and HVOF coated Superni 75 superalloy subjected to hot corrosion in $\text{Na}_2\text{SO}_4\text{-60\%V}_2\text{O}_5$ environment at $900\text{ }^\circ\text{C}$ for 50 cycles: (a) Bare superalloy (b) $\text{Cr}_3\text{C}_2\text{-NiCr}$ coated (c) NiCrBSi coated (d) Stellite-6 coated (e) Ni-20Cr coated.

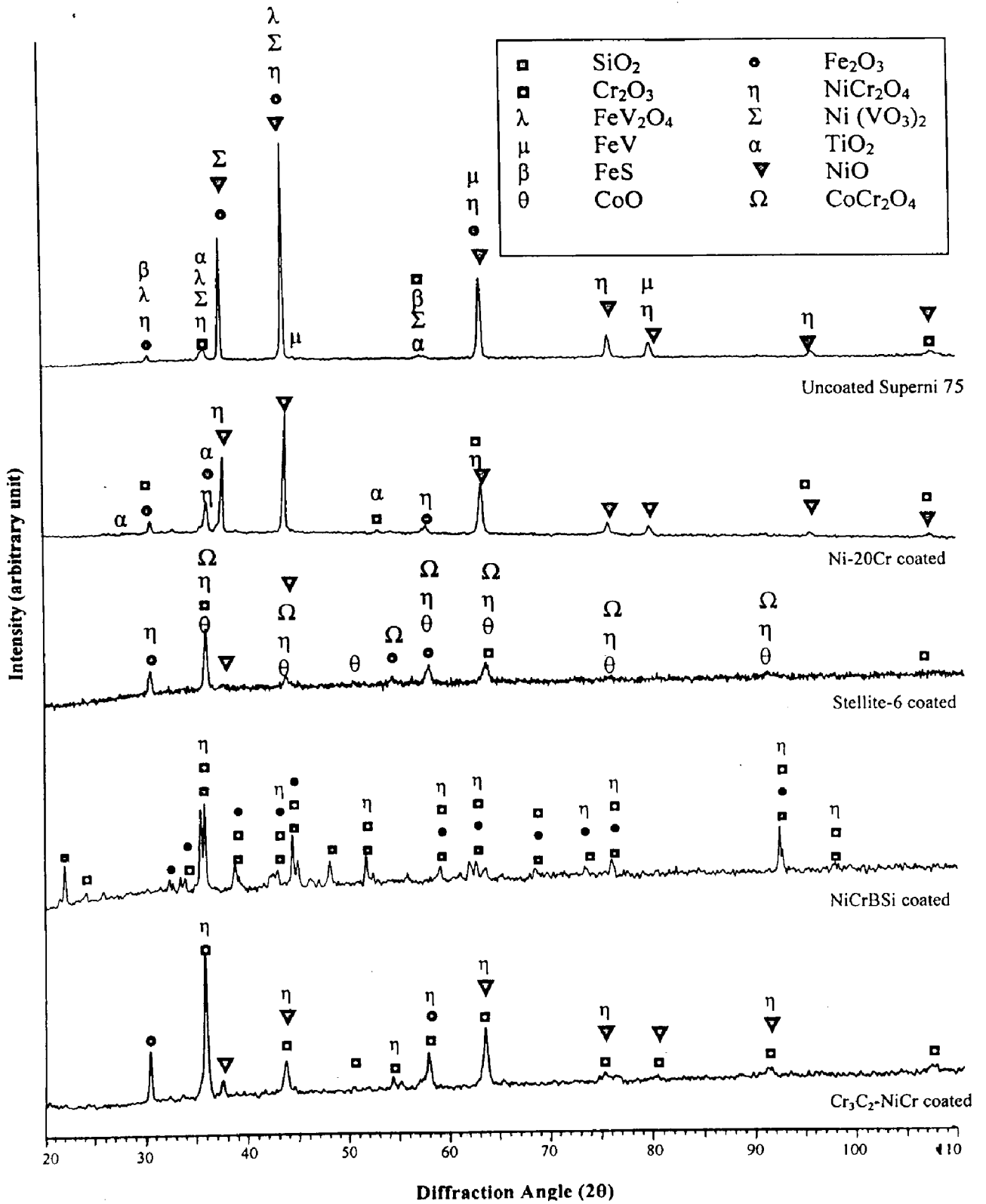


Fig. 6.11 X-ray diffraction patterns for the bare and coated superalloy Superni 75 subjected to hot corrosion in Na₂SO₄-60%V₂O₅ environment at 900 °C for 50 cycles.

6.1.2.4 SEM/EDAX Analysis

(a) Surface Analysis

SEM micrographs showing surface morphologies and EDAX analysis of the corroded bare and coated Superni 75 are given in Fig. 6.12. Figure 6.12a shows that the scale formed on bare Superni 75 is fragile. The cracks as well as spalled regions are clearly visible in the surface scale. Evidently, the corroded scale has a tendency for spalling. The EDAX results show that the oxides, both on the surface scale and in subscale, are rich in nickel. The uppermost scale, which has relatively more Fe_2O_3 and slightly less Cr_2O_3 and NiO than the sub scale regions, has shown the tendency for spalling.

In general, the oxide scale formed on the surface of all the coatings deposited on Superni 75, is nearly uniform and continuous (Figs. 6.12b to 6.12e). The surface oxides of corroded NiCrBSi and Ni-20Cr coatings are relatively coarse and rough as compared to that on the Cr_3C_2 -NiCr and Stellite-6 coatings. The EDAX analysis of hot corroded Cr_3C_2 -NiCr coated Superni 75 shows Cr_2O_3 and NiO as principal phases along with small percentage of Fe_2O_3 and V_2O_5 phases (Fig. 6.12b). The scale of NiCrBSi coated specimens consists of silica-rich globules uniformly dispersed in the white phase matrix where silica has decreased and NiO, Cr_2O_3 and Fe_2O_3 have increased (Fig. 6.12 c). EDAX results of the hot corroded Stellite-6 coated superalloy (Fig. 6.12d) indicated CoO and Cr_2O_3 as the main phases along with small amounts of SiO_2 , NiO, Fe_2O_3 , and WO_3 , while the scale of Ni-20Cr coated superalloy is enriched with NiO along with small weight percentages of Fe_2O_3 , TiO_2 , Cr_2O_3 and Na_2O (Fig. 6.12e).

The presence of oxides of Ti and Fe in the surface oxide layers (Fig. 6.12e) reveals that these elements have diffused from the substrate to the uppermost part of the scale during hot corrosion of the specimen.

(b) Cross-Section Analysis

BSEI and elemental variation across the cross-section of bare and HVOF coated Superni 75 corroded in molten salt at 900°C are shown in Fig. 6.13. A continuous and adherent oxide scale is formed after 50 cycles of hot corrosion as can be seen from Fig. 6.13a. EDAX analysis at Point 1 shows the existence of some amount of oxygen indicating the penetration behaviour of oxide scale into the substrate. At Point 2, the concentration of Cr and O is high and Ni has decreased substantially, whereas at Point 3 and 4 amount of Ni is relatively more. Quantity of oxygen has also increased at Points 3 and 4. Therefore it can be inferred that the scale has relatively more oxides of Ni in its upper region, while lower portion of the scale is rich with oxides of Cr.

EDAX analysis of corroded NiCrBSi coated Superni 75 (Fig. 6.13b) shows that the corrosive species are not present at Point 1 which indicates that the substrate superalloy remain unaffected during the hot corrosion runs. Dark black phase present at the coating-substrate interface (Point 2) is found to be rich in Al and O and, therefore, is an inclusion of aluminium oxide as already discussed in section 5.4, as aluminium is neither present in the coating nor in the substrate. Major part of the NiCrBSi coating remained resistant to hot corrosion during the course of study as EDAX analysis has revealed the presence of only basic elements of the coating at Points 3 and 4. Dark contrast phase in the upper part of the scale (Point 5) is found to be rich in Cr and Si. The existence of oxygen at this point leads to the formation of Cr- and Si-rich oxide scale. The white phase in this region of the scale (Point 6) consists of un-oxidised Ni-rich splats as oxygen is found to be absent at this region. The weight percentage of Cr and O increased appreciably at the top of scale (Point 7) whereas Ni decreased substantially signifying that light contrast phase at the top of scale might be rich with chromium oxide.

Cross-section EDAX analysis of the corroded Stellite-6 coated Superni 75 reveals (Fig. 6.13c) that the concentration of Cr and O increases in the uppermost part of the scale while the amount of Co decreases considerably suggesting the formation of Cr-rich outer oxide scale (Points 5 and 6). Un-oxidised Co-rich splats (Point 3) are uniformly dispersed in the scale as oxygen is absent at this region. Evidently the presence of oxygen at Point 4 indicates that the oxides are formed mainly at the splat boundaries. Presence of relatively high Ti and O and less Cr in the region of Point 2 suggests the formation of stringers of titanium oxide. At Point 1 in the substrate, Fe content decreased from 3 wt% to 0.15 wt% which indicates the diffusion of Fe from the substrate to the coating during hot corrosion of the Stellite-6 coated Superni 75.

6.1.2.5 EPMA Analysis

Elemental X-ray mappings at the cross-section of uncoated Superfer 75 superalloys after cyclic oxidation at 900 °C in Na₂SO₄-60%V₂O₅ environment for 50 cycles are shown in Fig. 6.14. The BSE image indicates the formation of a dense scale (about 78 μm thick) consisting mainly of nickel and chromium. Titanium and iron show their existence throughout the cross-section. The upper part of the scale is rich in nickel, whereas chromium forms a dense layer just above the scale-substrate interface. Traces of sodium and sulphur are present throughout the scale. The existence of vanadium in the scale indicates the possibility of formation of various vanadates.

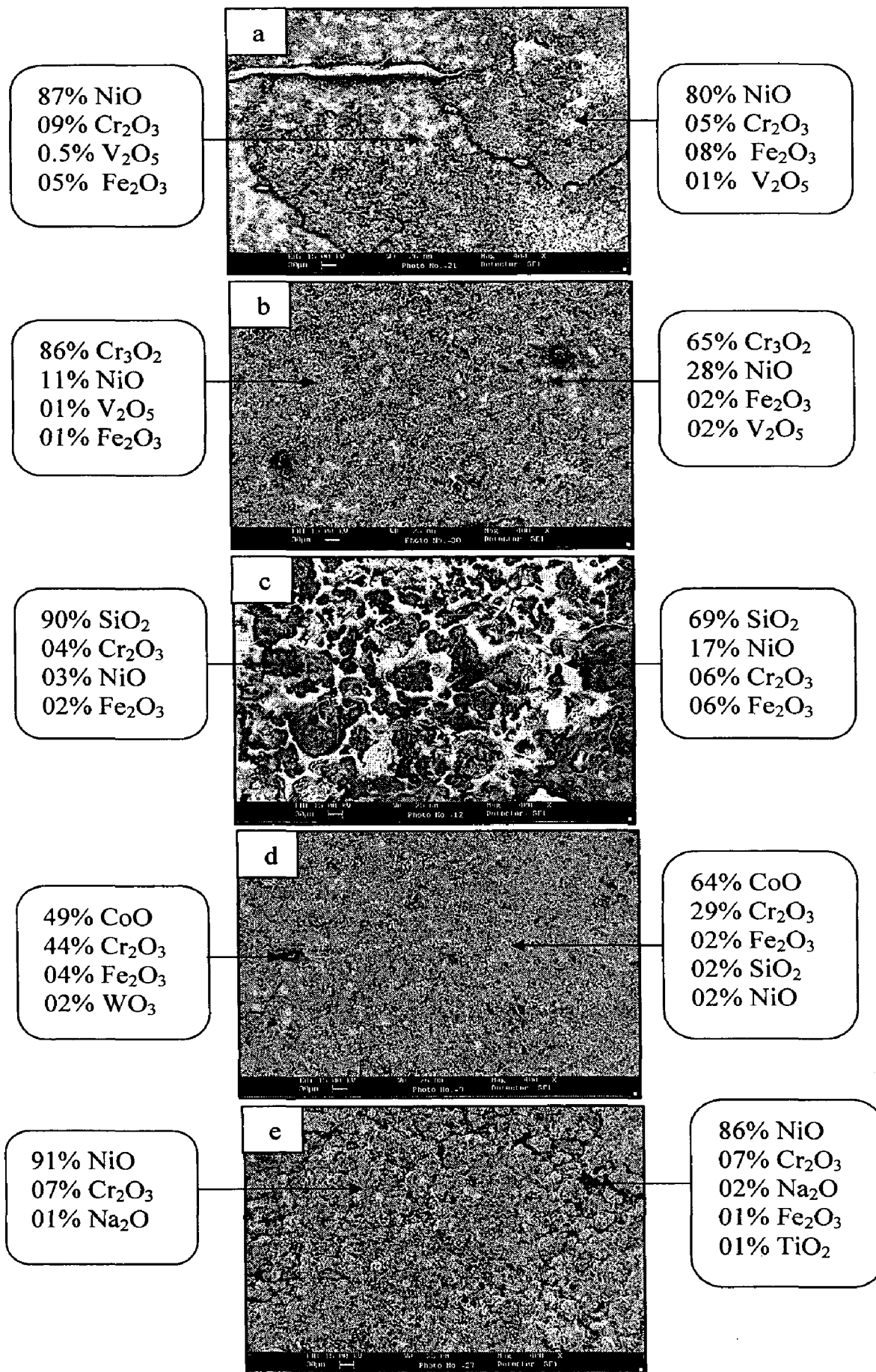


Fig.6.12 SEM/EDAX analysis showing elemental composition (wt.%) for the bare and coated Superni 75 subjected to hot corrosion in Na₂SO₄-60%V₂O₅ environment at 900 °C for 50 cycles: (a) Bare Superni 75 (b) Cr₃C₂-NiCr coated (c) NiCrBSi coated (d) Stellite-6 coated (e) Ni-20Cr coated.

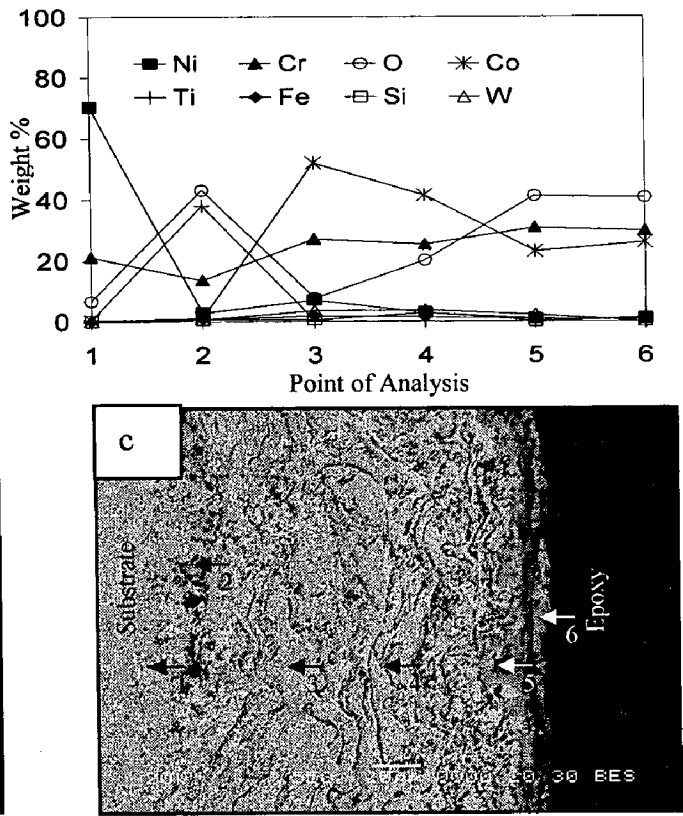
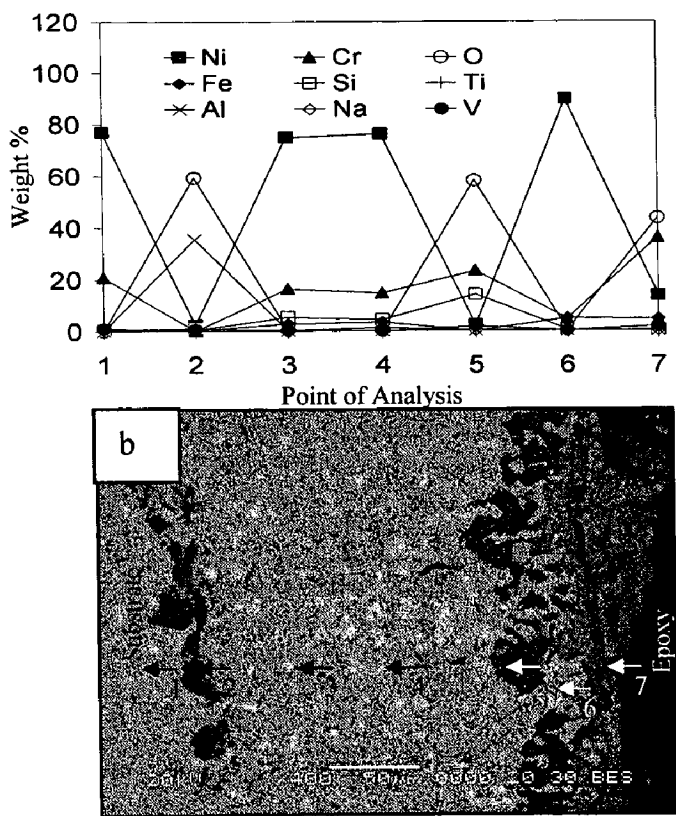
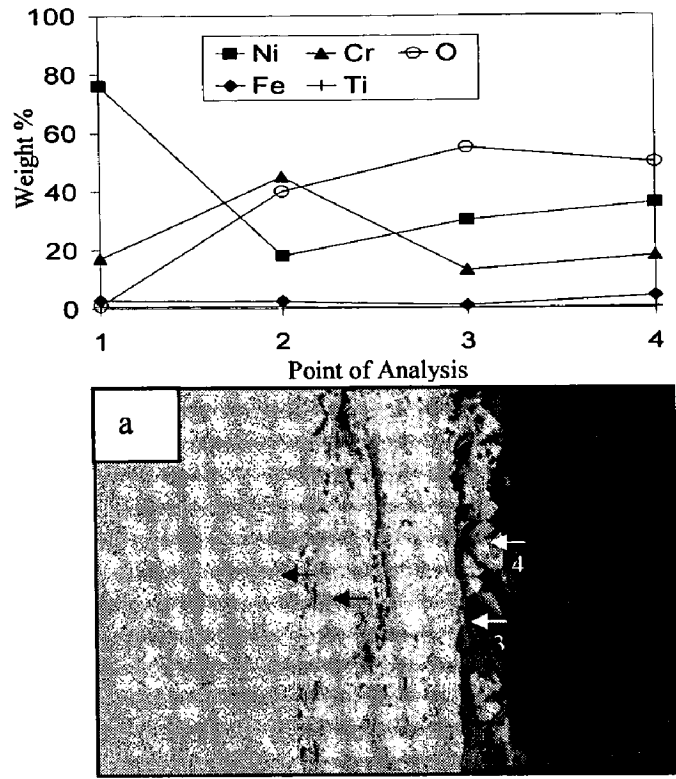


Fig 6.13 Oxide scale morphologies and variations of elemental composition across the cross section of HVOF coated Superni 75 superalloy hot corroded in Na_2SO_4 -60% V_2O_5 environment at 900 °C for 50 cycles (a) Bare Superni 75 (b) NiCrBSi coated (c) Stellite-6 coated.

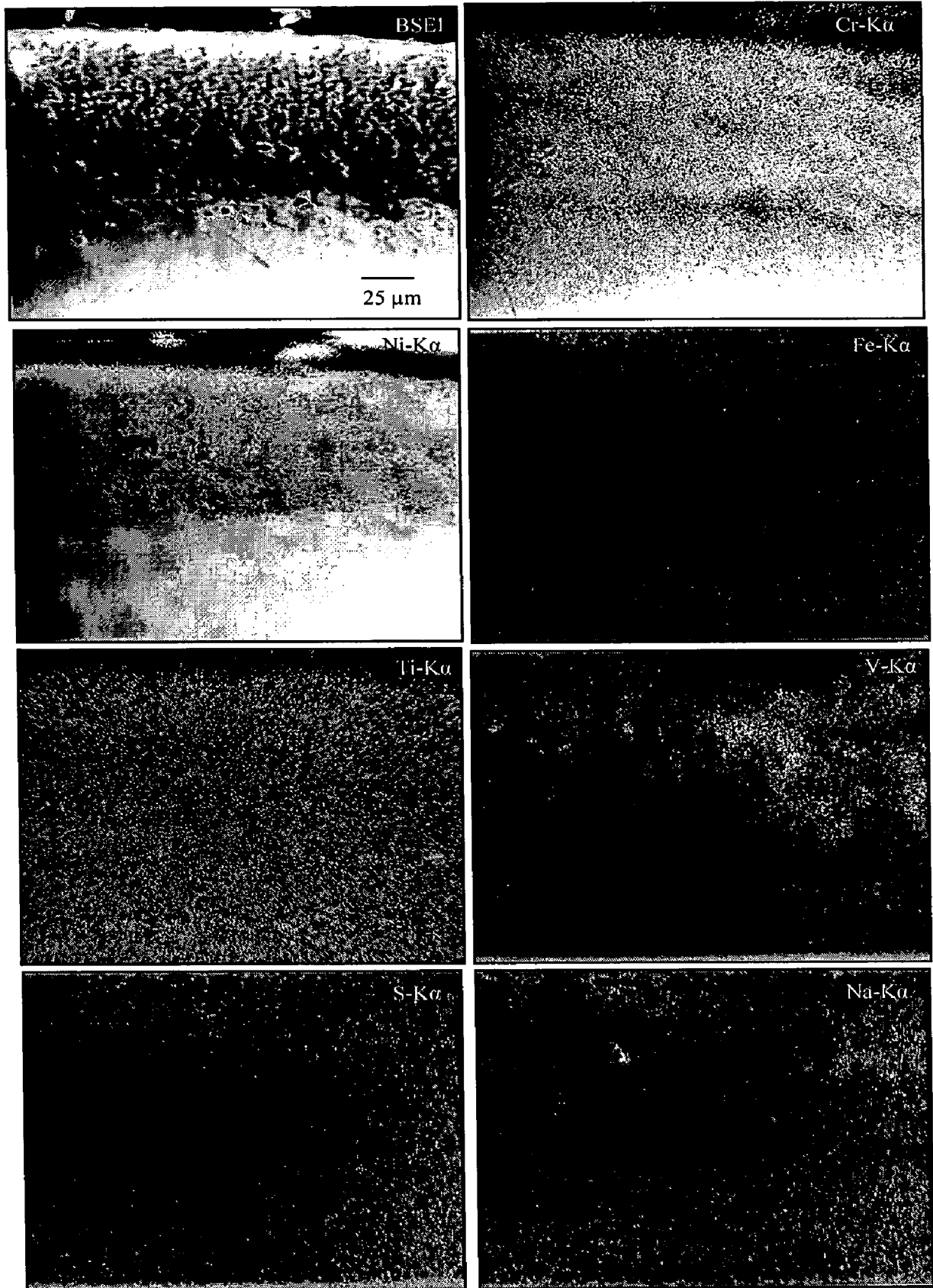


Fig. 6.14 Composition image (BSEI) and X-ray mappings of the cross-section of the bare Superni 75 subjected to hot corrosion at 900 °C in $\text{Na}_2\text{SO}_4\text{-60\%V}_2\text{O}_5$ environment for 50 cycles.

EPMA analyses of the scale formed on coated Superni 75 after hot corrosion in Na_2SO_4 -60% V_2O_5 environment at 900 °C for 50 cycles are shown in Figs. 6.15 to 6.18. Invariably in all the cases, sodium, vanadium and sulphur show their presence throughout the scale mainly at splat boundaries suggesting their penetration into the scale through the splat boundaries. Titanium and iron elements of the substrate superalloy, in general, have shown their presence by diffusion from the substrate to the scale, the extent of diffusion varying with the type of coating formed.

EPMA elemental maps of the corroded Cr_3C_2 -NiCr coated Superni 75 show that the scale has a lamellar structure and consists of Ni-rich splats with chromium mainly present at the splat boundaries (Fig. 6.15a). Similar analysis of the same specimen at some other cross-section using the oxygen detection crystal indicates (Fig. 6.15b) that the scale is rich with Cr_2O_3 . The Ni-rich splats of irregular size present throughout the scale are found to be mostly in an un-oxidised state, whereas chromium oxide is mainly formed at the boundaries of these splats. Evidently, the substrate is in the un-reacted state as the elemental mapping for O shows absence of oxygen underneath the scale-substrate interface thereby suggesting the excellent protection behaviour of the Cr_3C_2 -NiCr coating deposited on Superni 75.

X-ray mappings for NiCrBSi coated Superni 75 after 50 cycles of hot corrosion in molten salt environment at 900 °C (Fig. 6.16) indicate the formation of relatively dense scale consisting mainly of Ni, Cr and Si elements uniformly dispersed. Uppermost part of the scale is primarily rich in silicon. Chromium shows a tendency to form a thick band in the subscale region just below the top scale, thereby leaving a Cr-depleted band under it. Nickel-rich and Si-rich splats are present at an alternate position in the scale and Cr mostly exists at the splat boundaries. Titanium shows a tendency to form a thin discontinuous streak at the scale-substrate interface. Further, a thick layer of V can be seen in the upper part of the scale.

EPMA analysis at the cross-section of Stellite-6 coated Superni 75 shows the formation of Cr-rich thick layer in the topmost part of the scale, thereby leaving a Cr depleted band under it (Fig. 6.17). Cobalt and Si are observed to be relatively less in this Cr-rich topmost scale. Remaining part of the scale mostly consists of Co-rich splats with boundaries enriched in Cr and Si. Existence of Ni-rich areas in the vicinity of scale-substrate interface and its negligible amounts in the upper part of the scale indicates that Ni has diffused towards the interface during the course of study. Titanium forms thin streaks at the scale-substrate interface.

The scale formed on the Ni-20Cr coated Superni 75 has retained lamellar structure of the as-sprayed coating (Fig. 6.18). The X-ray maps indicate that the topmost part of the scale comprises mainly of chromium, nickel and oxygen, suggesting the formation of chromium and nickel oxides and their spinels. In the remaining part of the scale, chromium co-exists with oxygen at the boundaries of nickel-rich splats thus forming stringers of Cr_2O_3 at the splat boundaries. Diffusion of substrate elements such as iron and titanium is found to be negligible in this coating-substrate combination. The penetration of oxygen is restricted to scale-substrate interface indicating the excellent protection behavior of the Ni-20Cr coating. Titanium shows a tendency to cluster at the scale-substrate interface.

6.1.3 Hot Corrosion of Bare and Coated Superni 600

6.1.3.1 Corrosion Kinetics

The weight gain plots for the bare and coated Superni 600 are shown in Fig. 6.19. It can be inferred from the plots that the necessary protection against hot corrosion is provided by the HVOF coatings under study, as the weight gain values for the coated Superni 600 are smaller than those for bare Superni 600. The cumulative weight gain/unit area values are given in Fig. 6.20. The Ni-20Cr coating provides the best protection and successfully reduces the weight gain by 55% of that gained by bare Superni 600. The Cr_3C_2 -NiCr and NiCrBSi coatings show almost comparable weight gain per unit area, thus providing similar hot corrosion resistance to Superni 600 under the given conditions. In terms of weight gain, the Stellite-6 coating has shown minimum resistance. All the coatings deposited on Superni 600 follow the parabolic behaviour up to 50 cycles as can be inferred from the square of weight change (mg^2/cm^4) vs. number of cycle plots shown in Fig. 6.21, whereas the bare Superni 600 shows visible deviation from the parabolic rate law. The parabolic rate constants (k_p in $10^{-10} \text{ g}^2 \text{ cm}^{-4} \text{ s}^{-1}$) for the bare Superni 600 is calculated as 13.7, whereas for Cr_3C_2 -NiCr, NiCrBSi, Stellite-6 and Ni-20Cr coated Superni 600, values of k_p are 3.72, 4.84, 8.15 and 3.05, respectively.

6.1.3.2 Scale Thickness Measurement

The BSE images across the smallest cross-section of corroded bare and coated Superni 600 are shown in Fig. 6.22. The average scale thickness as measured from these micrographs for bare Superni 600 superalloy is found to be 65 μm , and that for Cr_3C_2 -NiCr, NiCrBSi, Stellite-6 and Ni-20Cr coated Superni 600 are 257, 289, 317 and 244 μm , respectively.

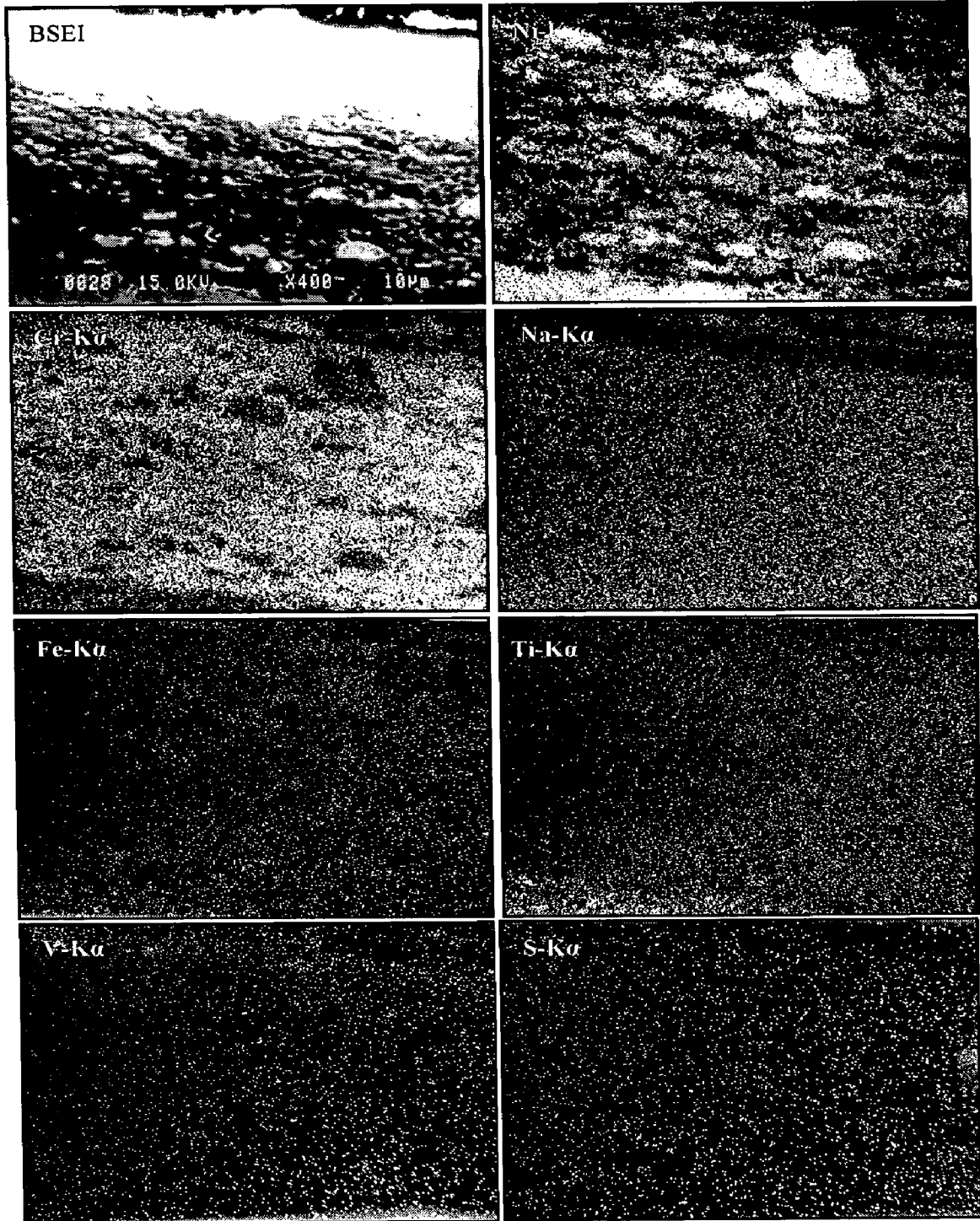


Fig. 6.15a Composition image (BSEI) and X-ray mappings of the cross-section of the $\text{Cr}_3\text{C}_2\text{-NiCr}$ coated Superalloy subjected to hot corrosion at 900°C in $\text{Na}_2\text{SO}_4\text{-60\%V}_2\text{O}_5$ environment for 50 cycles.

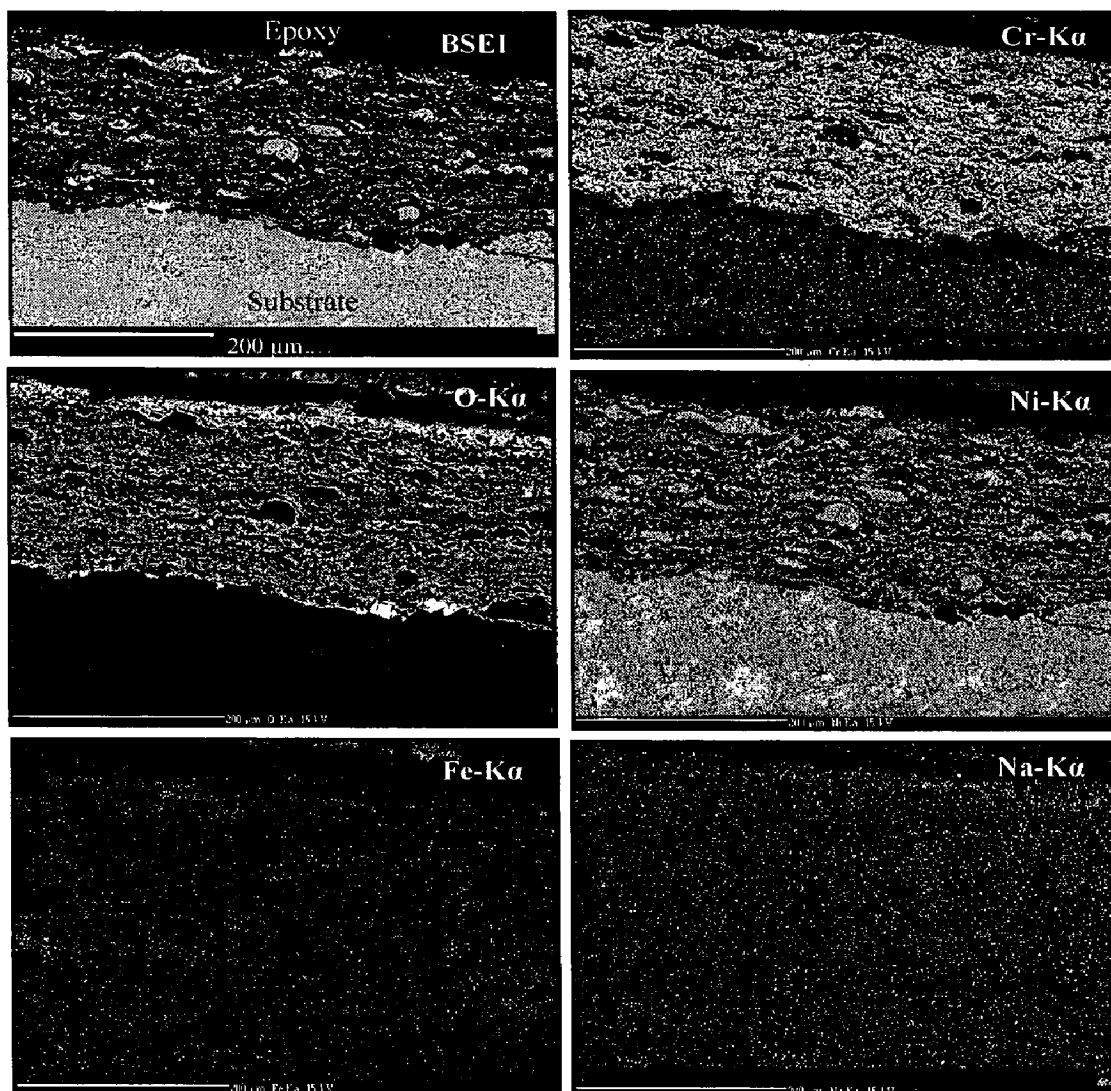


Fig. 6.15b Composition image (BSEI) and X-ray mappings, using oxygen detection crystal, of the cross-section of the $\text{Cr}_3\text{C}_2\text{-NiCr}$ coated Superni 75 superalloy subjected to hot corrosion at 900 °C in $\text{Na}_2\text{SO}_4\text{-60}\%\text{V}_2\text{O}_5$ environment for 50 cycles.

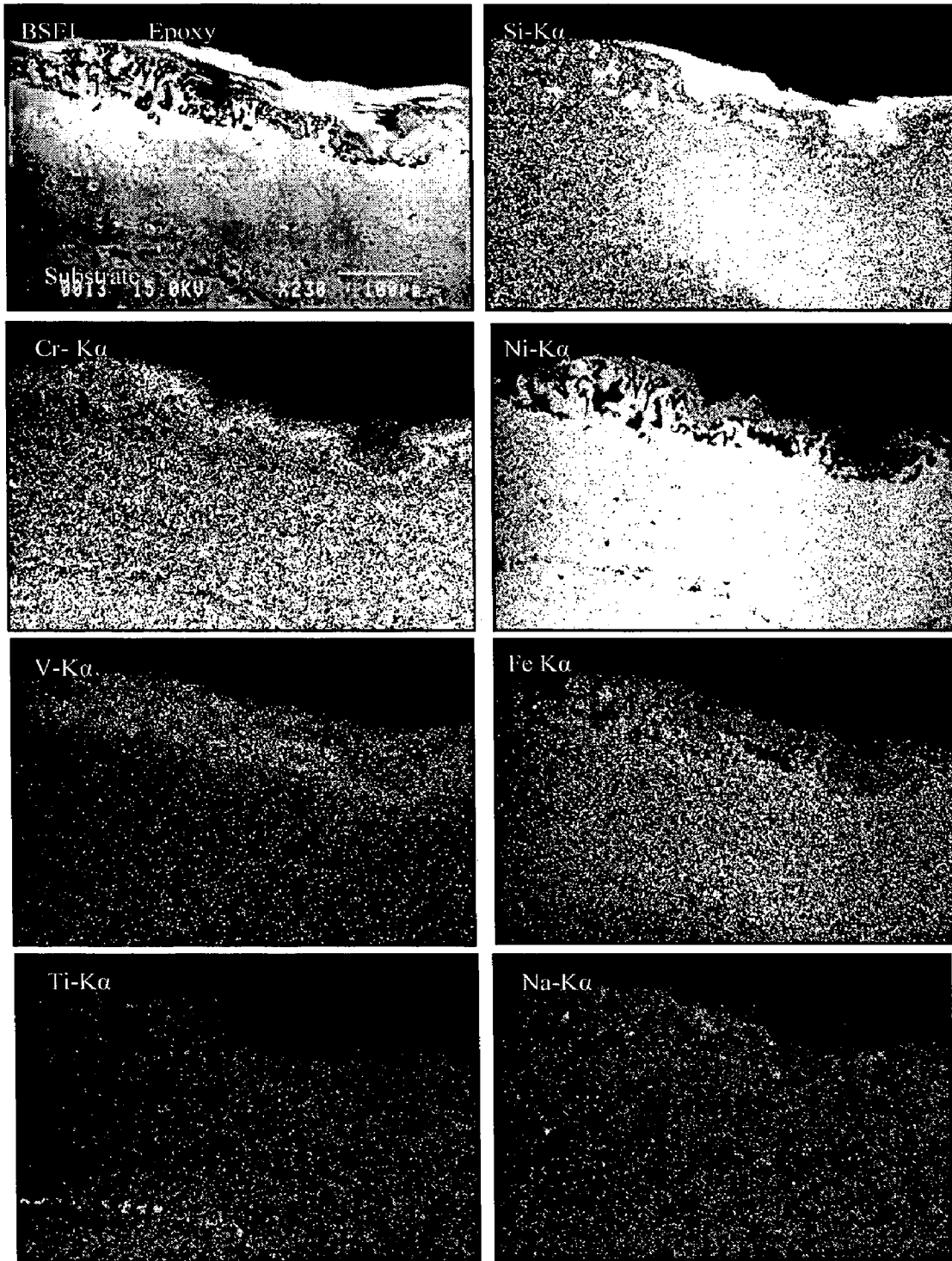


Fig. 6.16 Composition image (BSEI) and X-ray mappings of the cross-section of the NiCrBSi coated Superni 75 superalloy subjected to hot corrosion at 900 °C in Na_2SO_4 -60% V_2O_5 environment for 50 cycles.

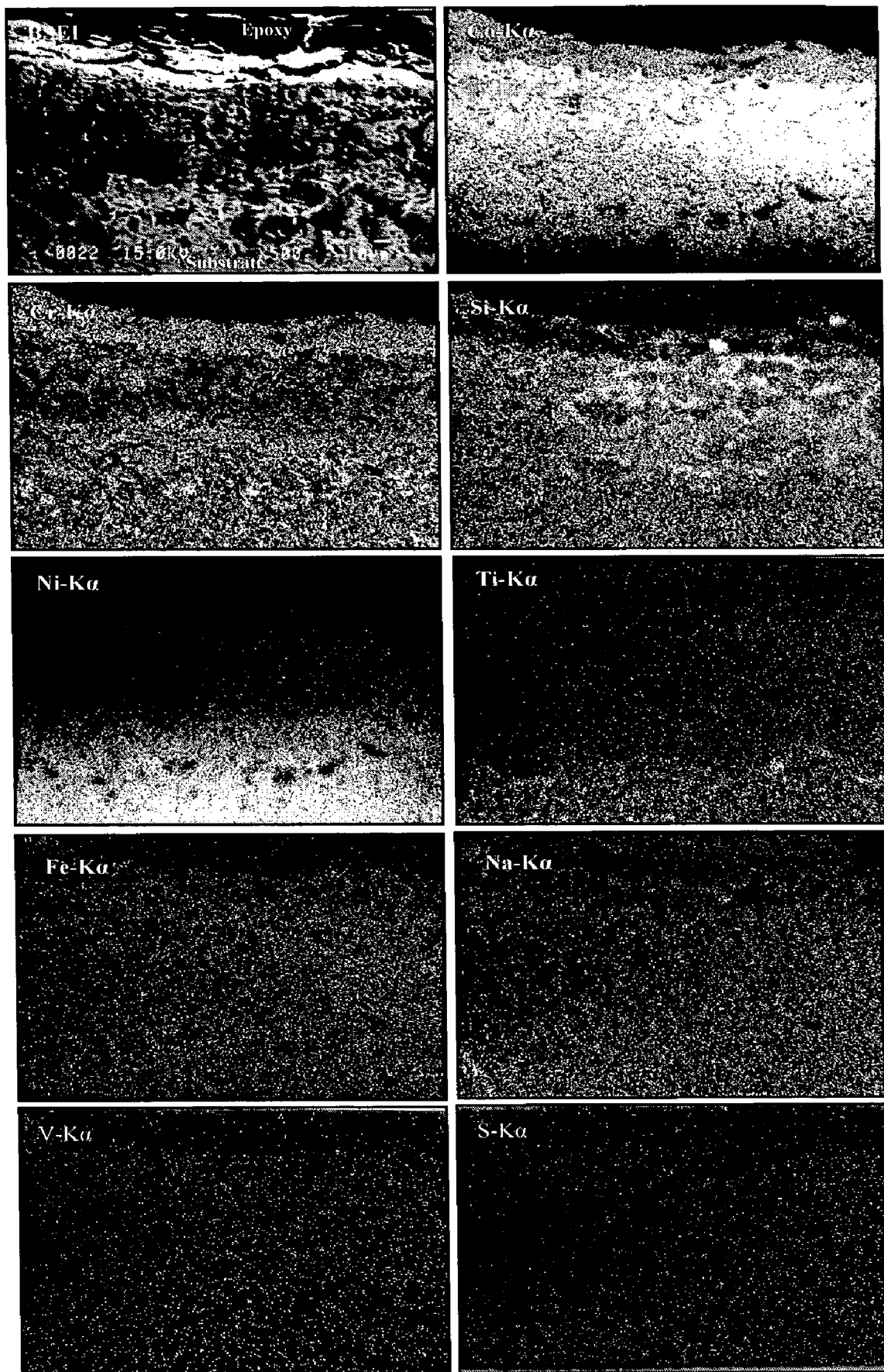


Fig. 6.17 Composition image (BSEI) and X-ray mappings of the cross-section of the Stellite-6 coated Superni 75 superalloy subjected to hot corrosion at 900 °C in Na₂SO₄-60%V₂O₅ environment for 50 cycles.

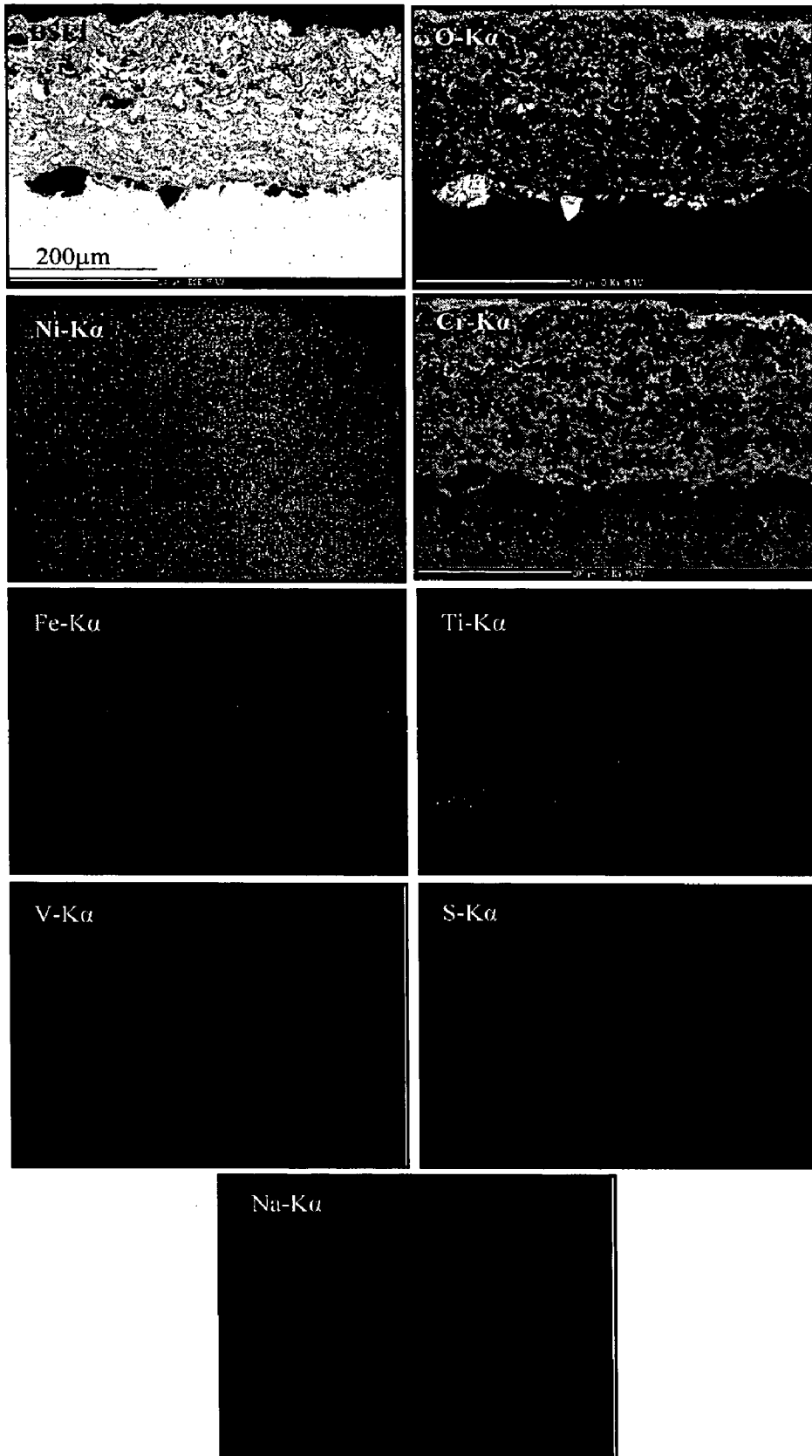


Fig. 6.18 Composition image (BSEI) and X-ray mappings of the cross-section of the Ni-20Cr coated Superni 75 superalloy subjected to hot corrosion at 900 °C in Na_2SO_4 -60% V_2O_5 environment for 50 cycles.

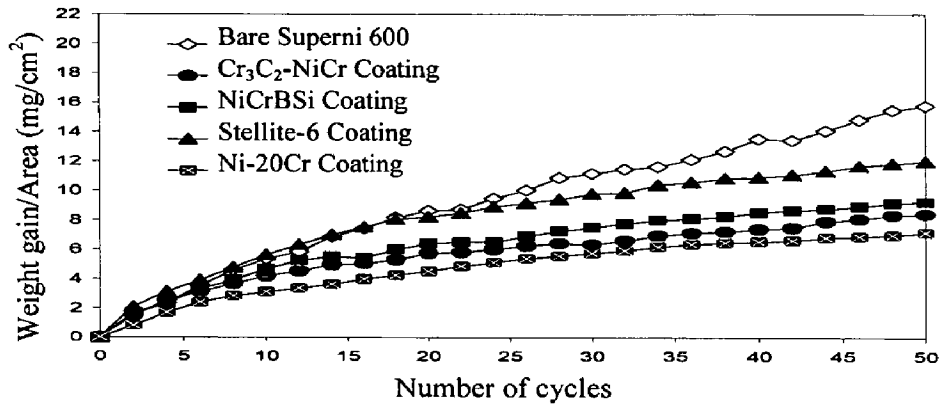


Fig. 6.19 Weight gain vs. number of cycles plot for the coated and uncoated Superni 600 subjected to hot corrosion for 50 cycles in Na_2SO_4 -60% V_2O_5 environment at 900 °C.

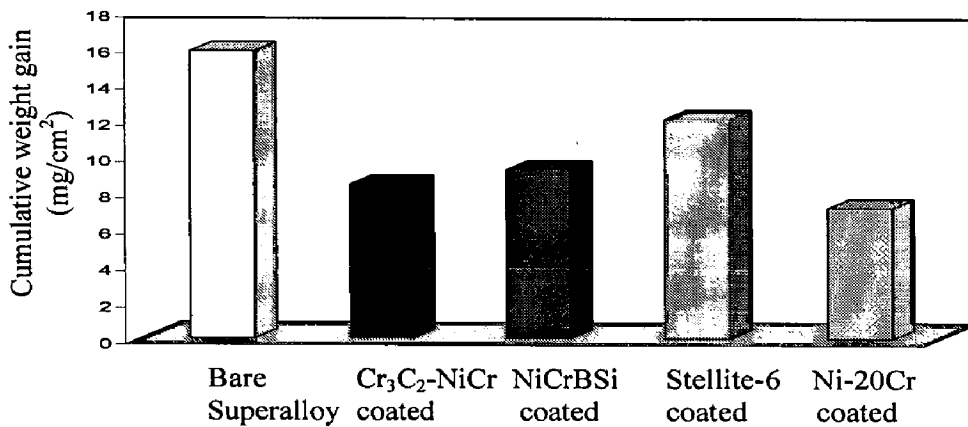


Fig. 6.20 Bar charts showing cumulative weight gain per unit area for the coated and uncoated Superni 600 subjected to hot corrosion for 50 cycles in Na_2SO_4 -60% V_2O_5 environment at 900 °C.

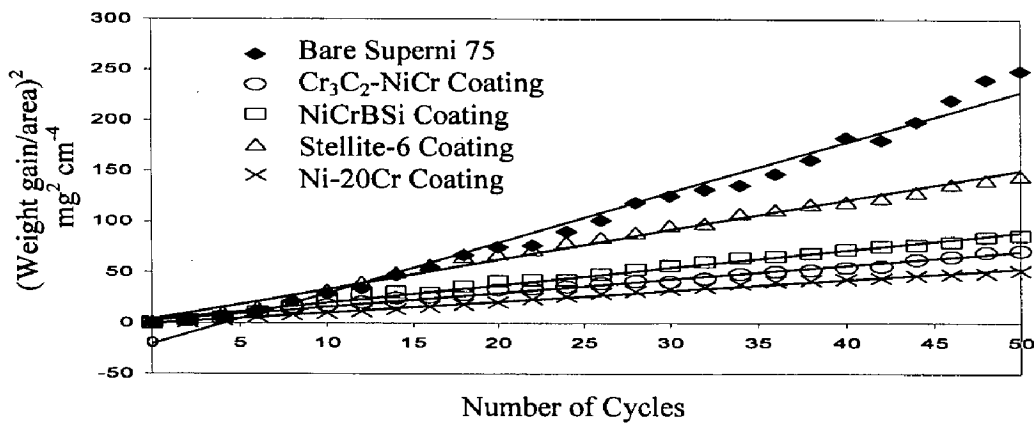


Fig. 6.21 $(\text{Weight gain/area})^2$ vs. number of cycles plot for the coated and uncoated superalloy Superni 600 subjected to hot corrosion for 50 cycles in Na_2SO_4 -60% V_2O_5 environment at 900 °C.

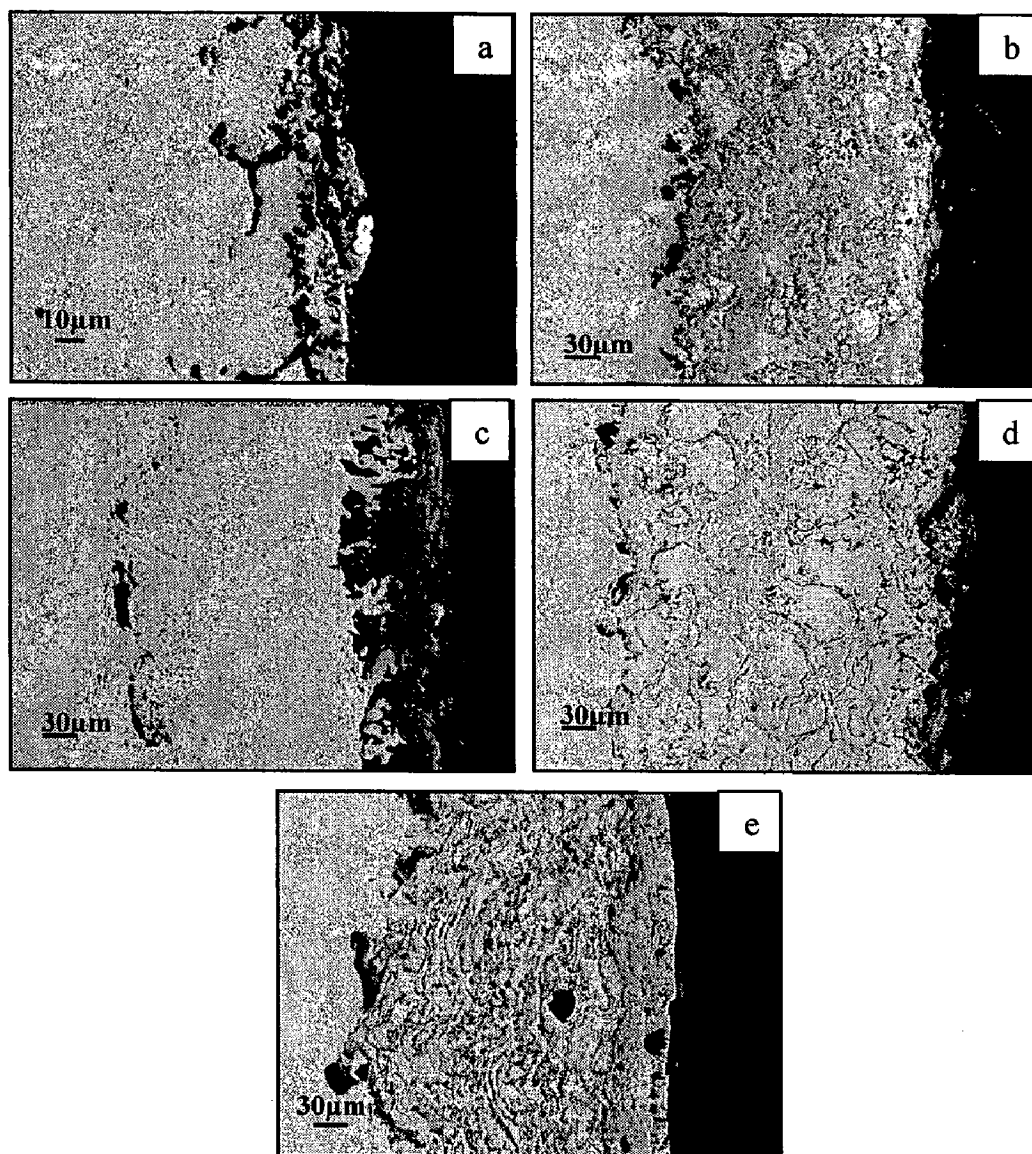


Fig. 6.22 SEM back scattered images for the bare and HVOF coated Superni 600 superalloy subjected to hot corrosion in $\text{Na}_2\text{SO}_4\text{-60\%V}_2\text{O}_5$ environment at $900\text{ }^\circ\text{C}$ for 50 cycles: (a) Bare superalloy (b) $\text{Cr}_3\text{C}_2\text{-NiCr}$ coated (c) NiCrBSi coated (d) Stellite-6 coated (e) Ni-20Cr coated.

6.1.3.3 X-ray Diffraction Analysis

The XRD profiles for the scale of bare and coated Superni 600 after exposure to molten salt environment for 50 cycles are shown in Fig. 6.23. The major and minor phases present in the surface scale of the specimens are given in Table 6.2.

The existence of Fe_2O_3 phase on the surface of corroded $\text{Cr}_3\text{C}_2\text{-NiCr}$, Stellite-6 and Ni-20Cr coated Superni 600, respectively, indicates the diffusion of Fe from the substrate during hot corrosion of the specimens. Presence of MnO_2 phase in the corroded Stellite-6 and $\text{Cr}_3\text{C}_2\text{-NiCr}$ coated alloy indicates minor diffusion of Mn also from the substrate.

Table 6.2: Major and minor phases identified by XRD analysis of the hot corroded bare and coated Superni 600.

Description	Major phases	Minor phases
Uncoated Superni 600 superalloy	NiO, Fe_2O_3 , NiCr_2O_4 , $\text{Ni}(\text{VO}_3)_2$, FeV, and FeV_2O_4	CrVO_4
$\text{Cr}_3\text{C}_2\text{-NiCr}$ coated	Cr_2O_3 , NiO, NiCr_2O_4 , Fe_2O_3 , and $\text{Ni}(\text{VO}_3)_2$	MnO_2
NiCrBSi coated	SiO_2 , Cr_2O_3 , NiCr_2O_4 , Fe_2O_3 , and $\text{Ni}(\text{VO}_3)_2$	-----
Stellite-6 coated	CoO, Cr_2O_3 , CoCr_2O_4 , NiCr_2O_4 , Fe_2O_3 , and NiO	MnO_2
Ni-20Cr coated	NiO, NiCr_2O_4 , Fe_2O_3 , and $\text{Ni}(\text{VO}_3)_2$	Cr_2O_3

6.1.3.4 SEM/EDAX Analysis

(a) Surface Analysis

SEM micrographs along with EDAX analysis at some selected sites of interest of the corroded bare and coated Superni 600 are shown in Fig.6.24. The micrograph of the bare Superni 600 shows noticeable presence of cracks as well spalling in the scale (Fig. 6.24a). This may be due to the fluxing action of the molten salt on the oxide scale, as is indicated by the SEM images of bare superalloy (Figs. 6.22a and 6.24a). The EDAX analysis of the scale formed on bare superalloy shows NiO to be the predominant phase, which is porous due to reprecipitation by fluxing action. Besides NiO, small amounts of Cr_2O_3 , Fe_2O_3 and V_2O_5 are also found to be present in the scale.

The surface scale developed on $\text{Cr}_3\text{C}_2\text{-NiCr}$, Stellite-6 and Ni-20Cr coated Superni 600 is homogeneous and continuous, whereas compact scale is formed on NiCrBSi coated Superni 600 in which irregular size globules are packed together. The $\text{Cr}_3\text{C}_2\text{-NiCr}$ coated Superni 600 has Cr_2O_3 and NiO as principal phases along with small quantities of MnO and V_2O_5 (Fig. 6.24b). The globules present in the scale of NiCrBSi coated superalloy are found to be mainly rich in SiO_2 , while the oxides of Cr, Fe, Ni and V are

also found to be present in small amounts (Fig.6.24c). The scale formed on the Stellite-6 coated Superni 600 has CoO and Cr₂O₃ as main phases along with minor quantity of NiO, Fe₂O₃, MnO and WO₃ (Fig. 6.24d). Nickel oxide is detected as the principal phase in the scale of Ni-20Cr coated Superni 600 together with little quantity of Cr₂O₃, Fe₂O₃ and V₂O₅ phases (Fig. 6.24e).

The existence of Fe₂O₃ the surface scale of most of HVOF coated Superni 600 and that of MnO in some cases Fe₂O₃ indicates that these elements have diffused from the substrate to the uppermost part of the scale during hot corrosion of the specimens.

(b) Cross-Section Analysis

EDAX point analysis was carried out at different locations along the cross-section of the corroded bare and HVOF coated Superni 600 and the results are given in Fig. 6.25. A non-uniform oxide scale with variable thickness is formed on bare Superni 600 (Fig. 6.25a). The presence of about 30% (wt%) oxygen at Point 1 indicates that the oxygen has penetrated through the oxide scale formed on the surface of bare Superni 600. The EDAX analysis shows that the contrast grey phase (Point 2) mainly consists of Cr, and the presence of Ni is much lower as compared to the bare alloy. The existence of significant quantity of oxygen (40%) points out the possibility that this gray phase is rich in Cr₂O₃. The absence of oxygen at Point 3 and its presence at Point 1 shows that the growth of oxide scale is irregular. The dark black phase present in the subscale (Point 4) comprises of chromium, nickel and oxygen. The top surface of the scale (Point 5) contains mainly oxides of Ni, Cr and Fe.

BSE image shows that a continuous, adherent and compact oxide scale is formed on the NiCrBSi coated Superni 600 (Fig. 6.25b). EDAX analysis of the substrate near the coating-substrate interface (Point 1) shows the absence of oxygen and other corrosive species indicating the excellent protection behaviour of the coating. EDAX analysis shows the presence of alumina inclusion at the coating-substrate interface (Point 2) and its origin has already been discussed in section 5.4. Except the top surface of about 100 μm, the remaining portion of the coating is observed to be similar to the structure of as-sprayed conditions (Fig. 5.5b). EDAX analysis also shows the absence of oxygen in this region (Point 3). Top surface of the coating showed drastic changes in the structure. The featureless white appearance of the as-coated coating is transformed into a new grey phase with the formation of irregular grain shaped structure underneath. The dark black phase in the upper part of the scale (Point 6) is found to be rich in Si, Ni and O, suggesting the formation of oxides of Si and Ni. The white grains (Point 5) underneath the upper part of the scale are Ni-rich splats which are in an un-oxidised state due to absence of oxygen at

this point. EDAX analysis shows that the light grey phase formed at the boundaries of these splats (Point 4) consists of mainly Si, Ni, Cr and oxygen. The wt% of Si increases at this point to 35% while wt% of Ni decreases to 25% (being 4.8 wt% Si and 72 wt% Ni in the coating alloy). The presence of oxygen, about 36 wt%, indicates that this light grey phase is rich in silicon oxide.

BSE image of corroded Ni-20Cr coated Superni 600 (Fig. 6.25c) shows the formation of a homogeneous, continuous and adherent oxide scale, about 45 μm thick. The remaining portion of the coating has maintained its lamellar and flat splat structure. The light grey layer in the upper part of the scale (Point 5) is found to be rich in nickel oxide. The white phase (Point 2) is identified as un-oxidised Ni-rich splats which are uniformly spread in the scale, and oxides are formed mainly at the boundaries of these Ni-rich splats. EDAX analyses at Points 3 and 4 show that these oxide stringers formed at splat boundaries are mainly rich in chromium oxide. Therefore, the coating contains chromium oxide uniformly distributed in a Ni-based matrix. A little amount of oxygen has found near the scale-substrate interface (Point 1) suggests that some oxygen penetrated during initial cycles of hot corrosion runs. Iron and manganese elements of the substrate are present across the scale. Diffusion of Fe (4.2 wt%) is found to be more than that of Mn (1.3 wt%) near the coating substrate interface (Point 2).

6.1.3.5 EPMA Analysis

BSE images and EPMA elemental mappings for the uncoated and coated Superni 600 after cyclic hot corrosion at 900 °C in Na_2SO_4 -60% V_2O_5 environment for 50 cycles are shown in Figs. 6.26 to 6.30.

The BSE image shows that the oxide scale formed on the bare Superni 600 is penetrating into the substrate (Fig. 6.26). The scale is spongy and consists mainly of chromium and nickel along with significant amount of iron. Chromium forms a thick band just above the scale-substrate interface thereby leaving a chromium depleted layer underneath. The oxide scale penetrates along the grain boundaries and consists of chromium-rich stringers. Vanadium penetrates through the scale and at most of the places it coexists with nickel, iron and chromium indicating the formation of various vanadates.

The scale formed on the Cr_3C_2 -NiCr coated Superni 600 exhibits dense structure with layered morphology in which Cr is present at boundaries of Ni-rich splats (Fig. 6.27). The elemental maps for Cr, Ni, Fe and O show that the scale formed is rich in Cr_2O_3 with small amount of NiO and Fe_2O_3 . The Ni-rich splats remain mostly in an un-oxidised state. The Cr, Ni and O co-exist at some places suggesting the formation of NiCr_2O_4 . Iron diffused outward up to the surface of the scale. It is very interesting to

note that concentration of Cr remains the same throughout the scale and it did not get reduced by diffusion. In the O elemental map, its higher concentration is noticed at the interface. These islands do not match with the elements present both in the substrate and coating. These islands are identified as aluminium oxides possibly due to the incorporation of alumina powder during polishing as already discussed under section 5.4. The S penetrates through the coating and reaches up to the scale-substrate interface.

X-ray mappings for the corroded NiCrBSi coated Superni 600 (Fig. 6.28) indicate the formation of a scale consisting of mainly silicon, nickel and chromium. Iron and sodium are also present throughout the scale. Silicon forms a thick band in the uppermost part of the scale, whereas chromium forms a thick band in the subscale area just below the top scale thereby leaving a chromium depleted layer underneath. Nickel-rich splats are present in the subscale containing chromium and silicon at the splat boundaries. Iron shows a relatively higher concentration near the scale-substrate interface indicating its diffusion from the substrate to the coating. Manganese also diffused up to the surface of the scale. The presence of vanadium and sulphur below the top scale indicates that they have penetrated along the splat boundaries.

The topmost layer of the scale formed on Stellite-6 coated Superni 600 mainly consists of chromium and oxygen which indicates that this thin layer is rich in chromium oxide (Fig. 6.29). Some amounts of Fe and Co also exist in this region and form their oxides. Just under this layer, there is an intermediate band enriched in cobalt-rich splats which are oxidized mostly at the boundaries. In the remaining part, the scale has a lamellar splat structure. The presence of oxygen, chromium and silicon indicates that the oxides of chromium and silicon are formed mostly at the splat boundaries and the cobalt-rich splats are found to be in the un-reacted state. Sulphur penetrates through the scale and reaches to the vicinity of scale-substrate interface.

BSE image for the corroded Ni-20Cr coated Superni 600 (Fig. 6.30) shows the formation of a thin featureless layer in the upper part of the scale, whereas the rest of the coating retains lamellar structure. X-ray map reveals that this continuous, compact and adherent topmost scale is rich in nickel. Underneath of topmost layer, the chromium is present at the boundaries of nickel-rich splats. Iron diffuses from the substrate into the scale and diffusion is significant near the substrate-scale interface. Manganese also diffuses from the substrate up to surface of the scale. The presence of sodium, sulphur and vanadium throughout the scale indicate the penetrating behaviour of these corroding species through the coating.

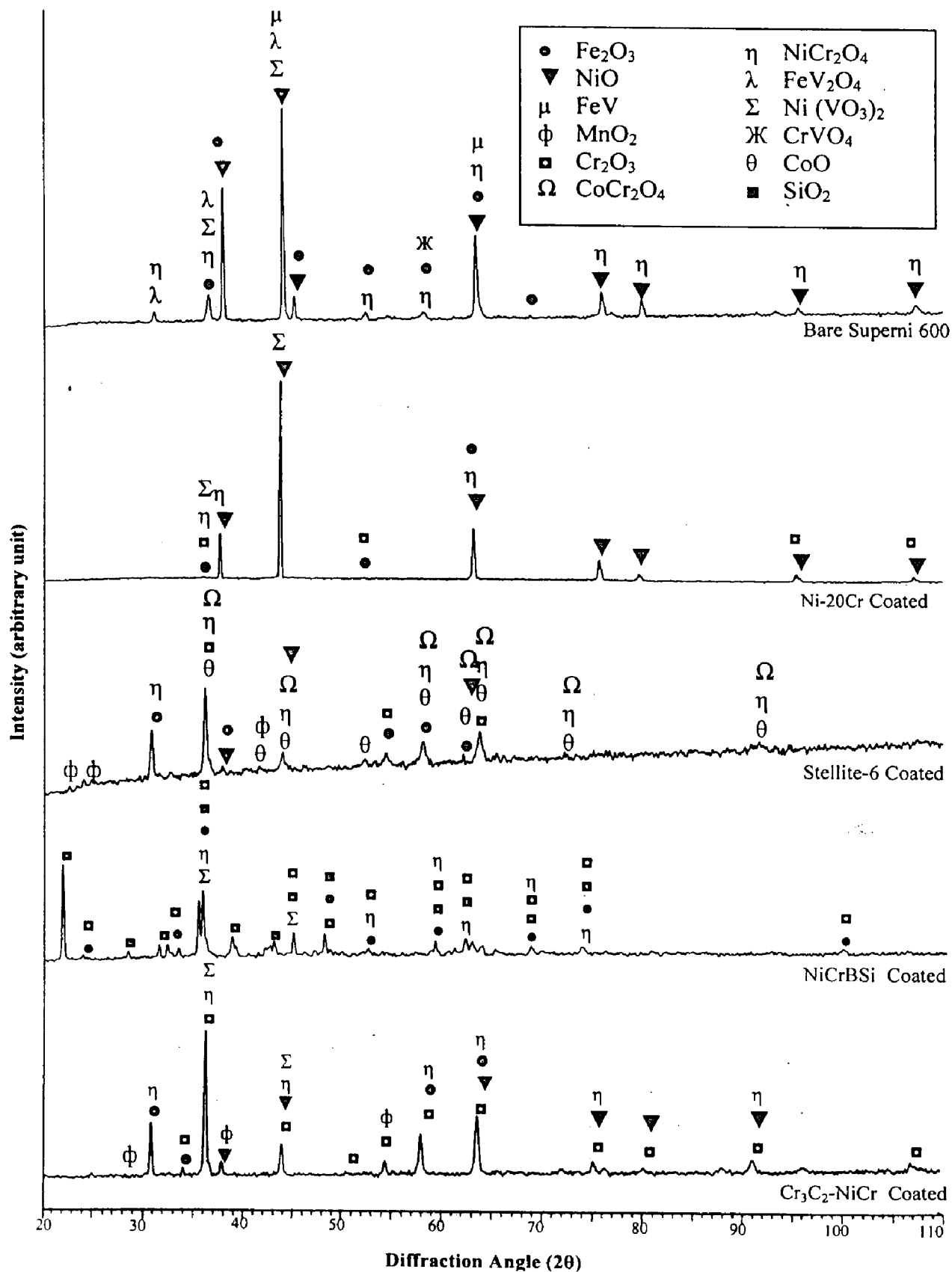


Fig. 6.23 X-ray diffraction patterns for the bare and coated superalloy Superni 600 subjected to hot corrosion in Na₂SO₄-60%V₂O₅ environment at 900 °C for 50 cycles.

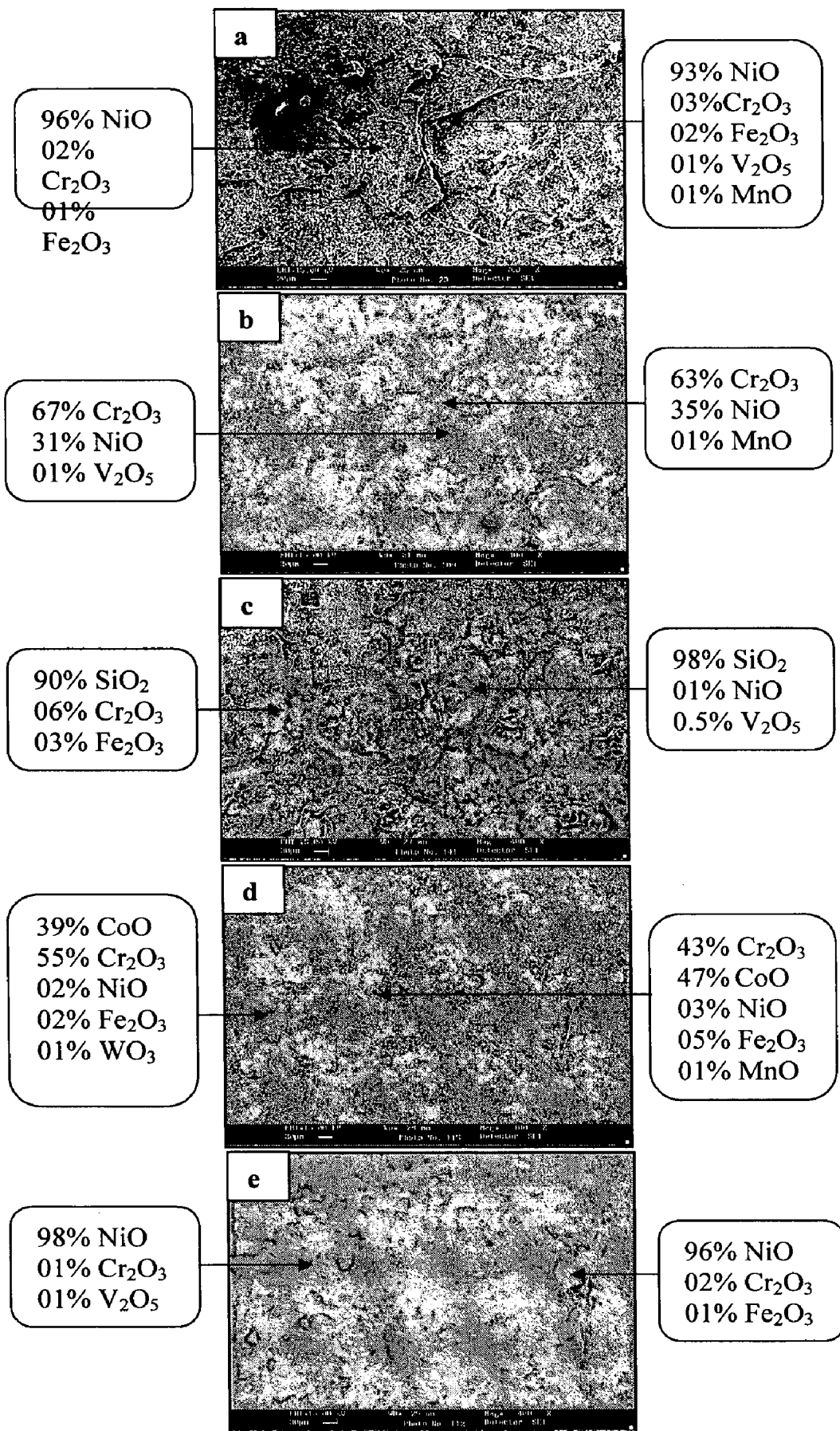


Fig.6.24 SEM/EDAX analysis showing elemental composition (wt.%) for the bare and coated Superni 600 subjected to hot corrosion in Na₂SO₄-60%V₂O₅ environment at 900 °C for 50 cycles: (a) Bare Superni 600 (b) Cr₃C₂-NiCr coated (c) NiCrBSi coated (d) Stellite-6 coated (e) Ni-20Cr coated.

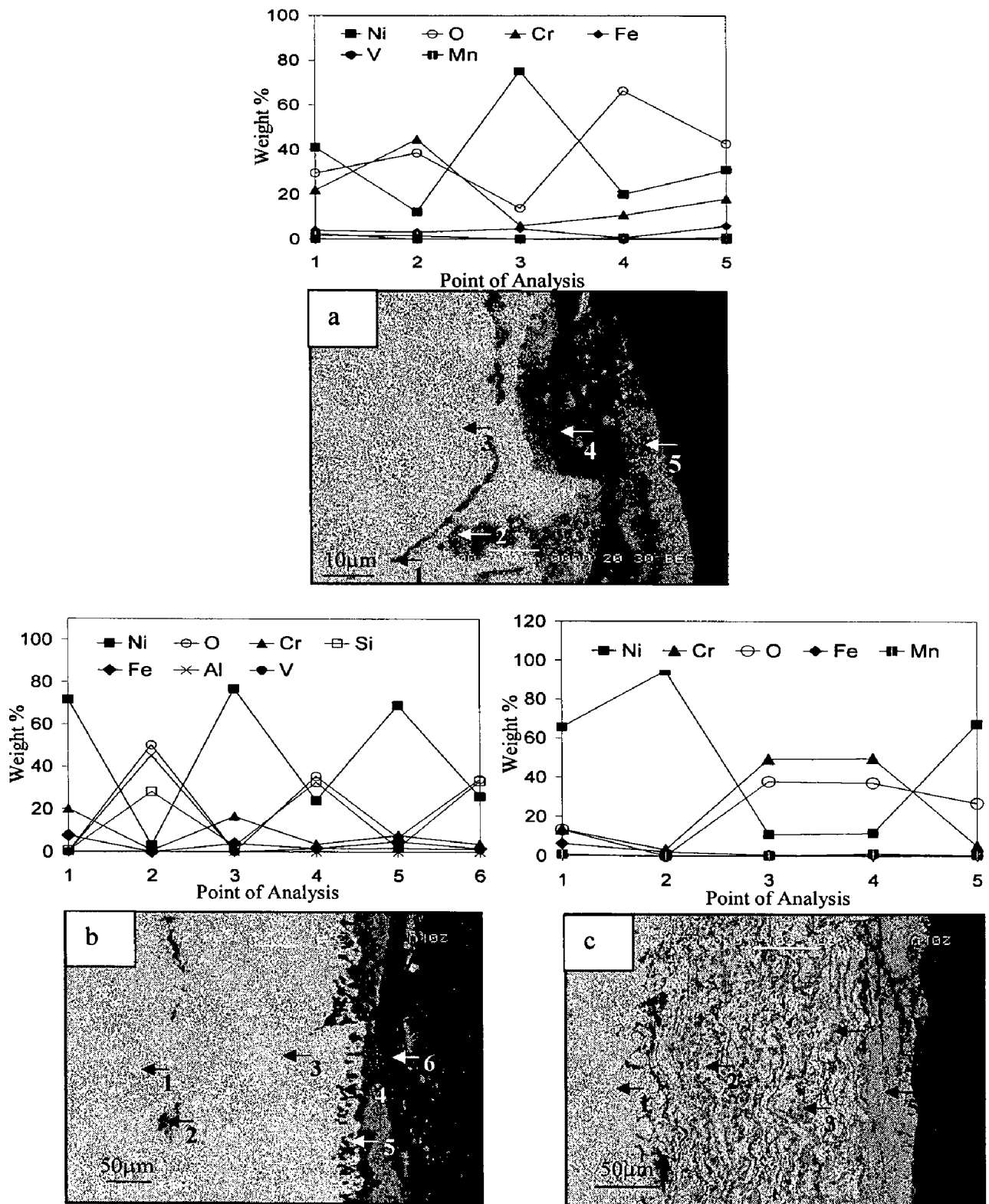


Fig 6.25 Oxide scale morphologies and variations of elemental composition across the cross section of uncoated and coated Superni 600 hot corroded in $\text{Na}_2\text{SO}_4\text{-60\%V}_2\text{O}_5$ environment at $900\text{ }^\circ\text{C}$ for 50 cycles: (a) Bare Superni 600 (b) NiCrBSi coated (c) Ni-20Cr coated.

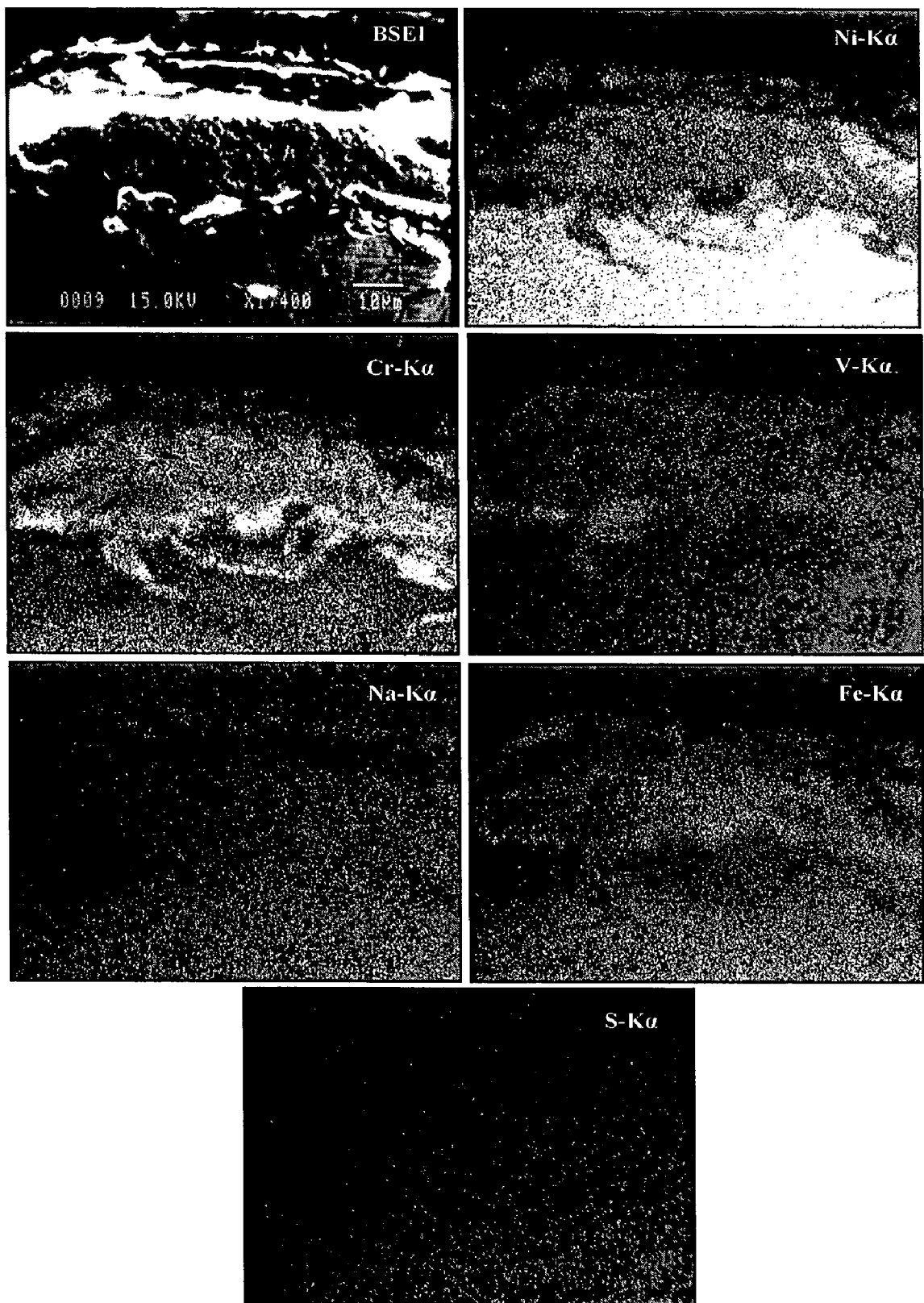


Fig. 6.26 Composition image (BSEI) and X-ray mappings of the cross-section of the bare Superni 600 subjected to hot corrosion at 900 °C in Na_2SO_4 -60% V_2O_5 environment for 50 cycles.

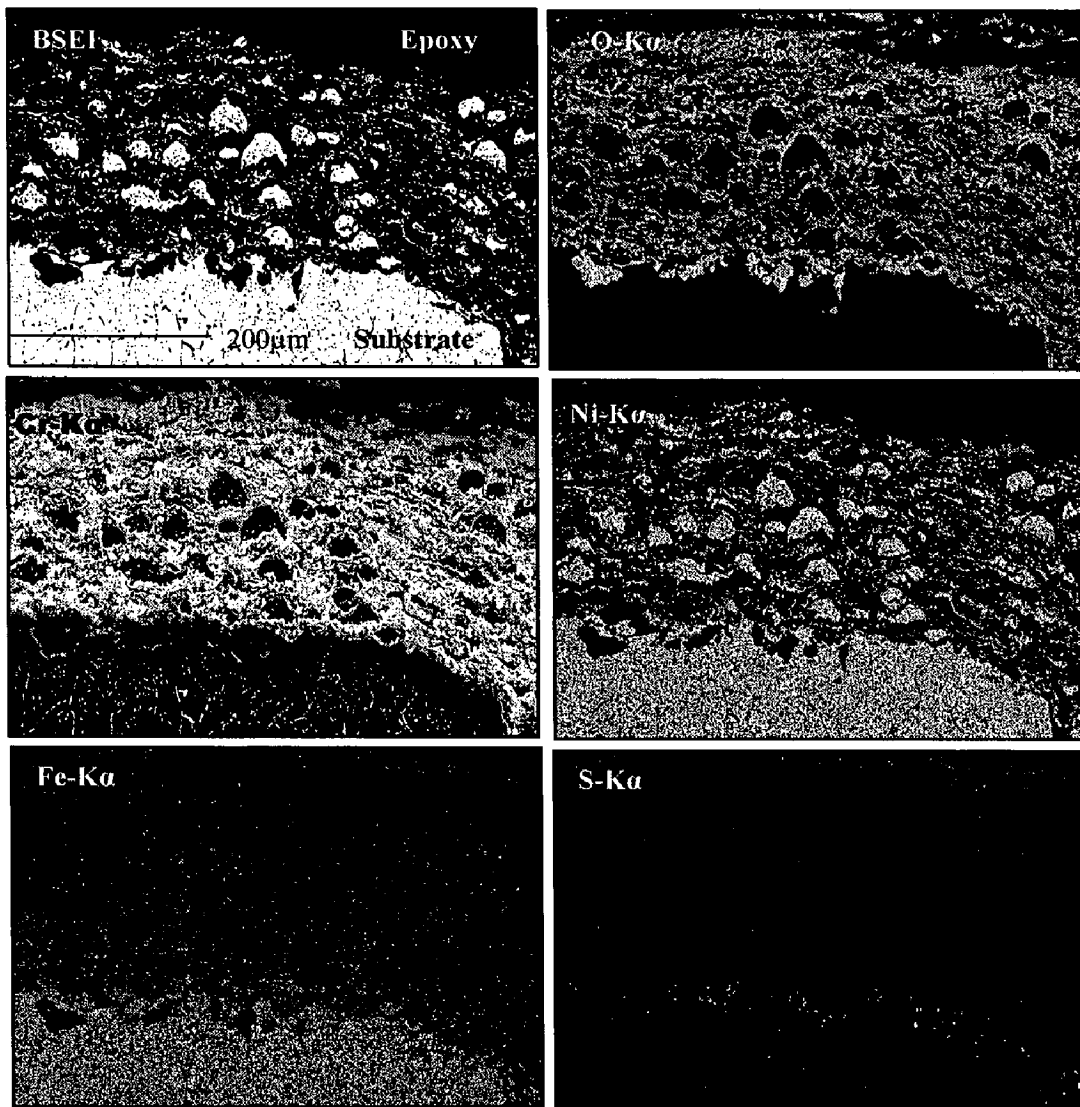


Fig. 6.27 Composition image (BSEI) and X-ray mappings of the cross-section of the $\text{Cr}_3\text{C}_2\text{-NiCr}$ coated Superni 600 superalloy subjected to hot corrosion at 900°C in $\text{Na}_2\text{SO}_4\text{-60\%V}_2\text{O}_5$ environment for 50 cycles.

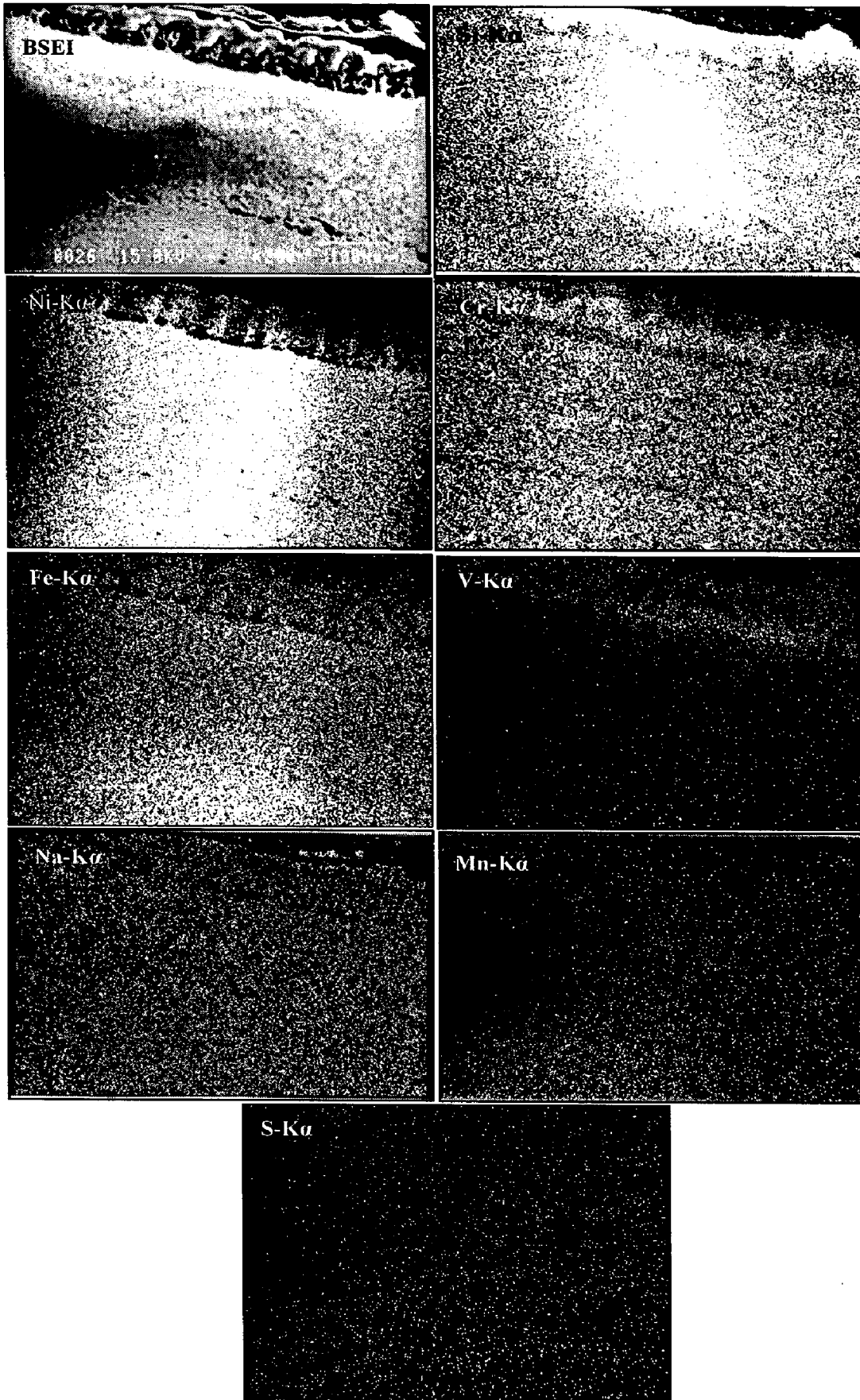


Fig. 6.28 Composition image (BSEI) and X-ray mappings of the cross-section of the NiCrBSi coated Superni 600 superalloy subjected to hot corrosion at 900 °C in Na₂SO₄-60%V₂O₅ environment for 50 cycles.

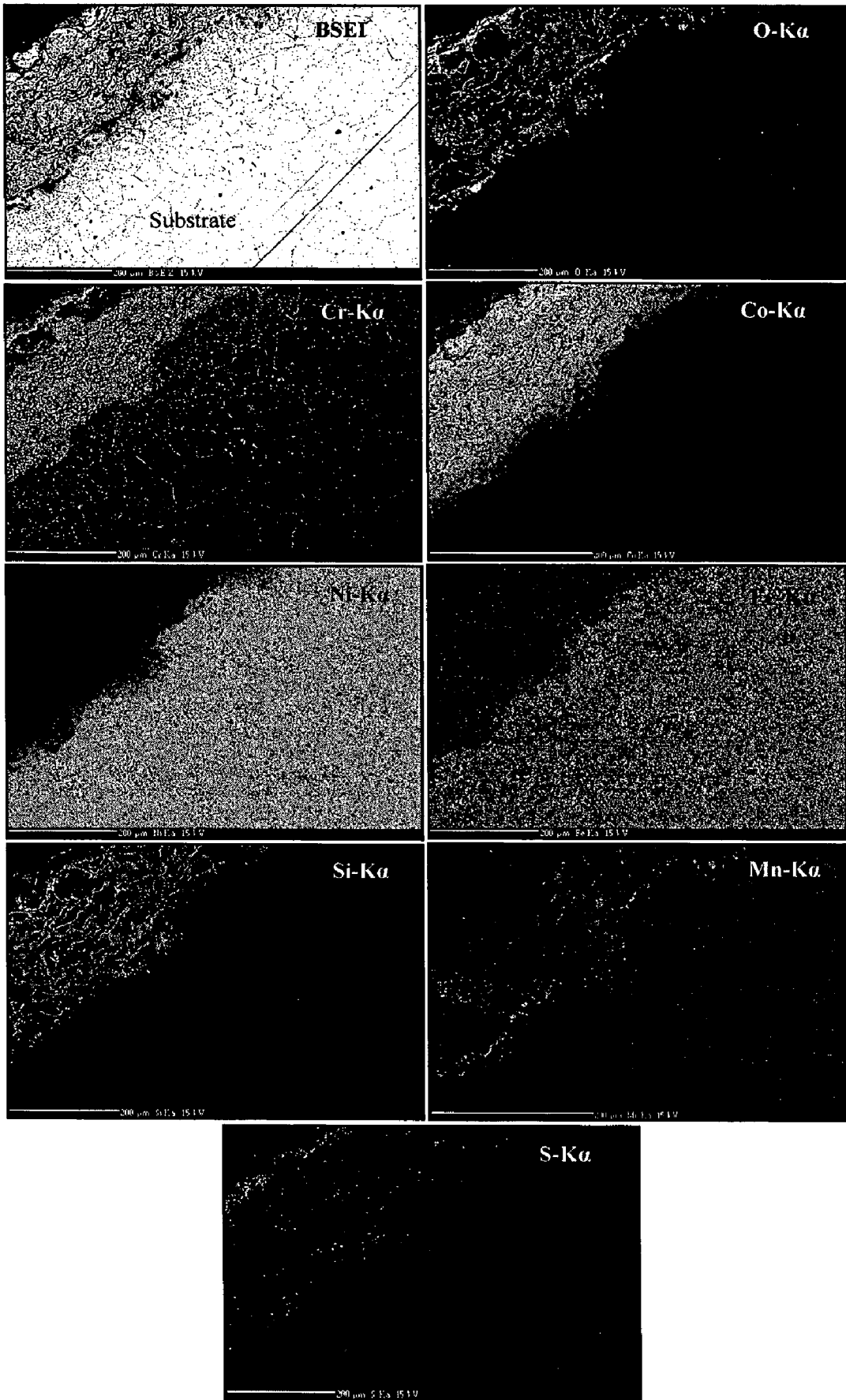


Fig. 6.29 Composition image (BSEI) and X-ray mappings of the cross-section of the Stellite-6 coated Superni 600 superalloy subjected to hot corrosion at 900 °C in Na₂SO₄-60%V₂O₅ environment for 50 cycles.

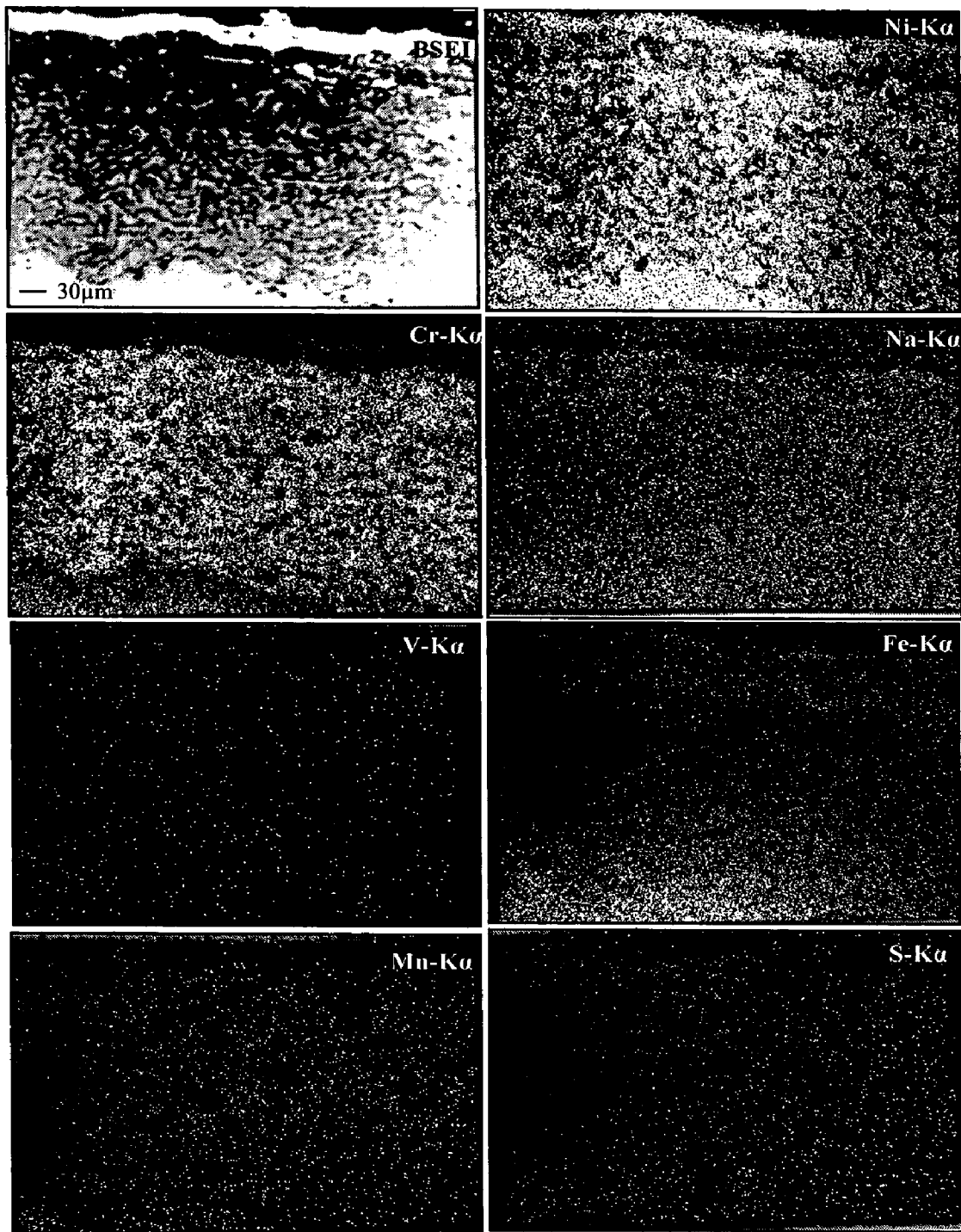


Fig. 6.30 Composition image (BSEI) and X-ray mappings of the cross-section of the Ni-20Cr coated Superni 600 superalloy subjected to hot corrosion at 900 °C in Na_2SO_4 -60% V_2O_5 environment for 50 cycles.

6.1.4 Hot Corrosion of Bare and Coated Superni 601

6.1.4.1 Corrosion Kinetics

All the four coatings deposited on Superni 601 show a better hot corrosion resistance as compared to the bare Superni 601 in the given molten salt environment (Fig. 6.31) and follow a parabolic behaviour (Fig. 6.33). The bare Superni 601 shows a sub-parabolic behaviour and a maximum weight gain. Intensive spalling was observed from the surface of the bare Superni 601 during the cooling period of the cycles.

The Ni-20Cr coated Superni 601 shows a minimum weight gain which is only 25% of the weight gained by the bare alloy. The Stellite-6 coated Superni 601 reveals a higher weight gain, which is approximately 1.5 times of the weight gained by the Ni-20Cr coated Superni 601 and 40% of the weight gained by the bare Superni 601. The Cr₃C₂-NiCr coating on Superni 601 stands second highest in hot corrosion resistance, followed by NiCrBSi coating. Figure 6.32 shows the cumulative weight gain/unit area for the bare and coated Superni 601.

Figure 6.33 shows (weight gain/area)² vs. number of cycles plot. It can be observed from the graph that the coated Superni 601 followed a parabolic rate law in all the cases. Thus it can be inferred that the coatings provide the necessary protection to bare Superni 601 in the given molten salt environment and act as diffusion barriers to the corroding species. The bare Superni 601 shows some deviations from the parabolic rate law. The parabolic rate constants (k_p in $10^{-10} \text{ g}^2 \text{ cm}^{-4} \text{ s}^{-1}$) for the bare Superni 601 is calculated as 33.586, whereas k_p values for Cr₃C₂-NiCr, NiCrBSi, Stellite-6 and Ni-20Cr coated Superni 601 are 4.703, 4.626, 6.213, and 3.089, respectively.

6.1.4.2 Scale Thickness Measurement

The BSE images across the smallest cross-section of corroded bare and coated Superni 601 are shown in Fig. 6.34. The average scale thickness value measured from these BSE images for bare Superni 601 is found to be 138 μm , and that for Cr₃C₂-NiCr, NiCrBSi, Stellite-6 and Ni-20Cr coated Superni 601 are 270, 317, 337, and 247 μm , respectively.

6.1.4.3 X-ray Diffraction Analysis

Figure 6.35 shows the XRD spectra for the scale formed on bare and coated Superni 601. The major and minor phases identified with the XRD analysis are given in Table 6.3.

Table 6.3: Major and minor phases identified by XRD analysis of the hot corroded bare and coated Superni 601.

Description	Major phases	Minor phases
Uncoated Superni 601	NiO, Fe ₂ O ₃ , NiCr ₂ O ₄ , Ni(VO ₃) ₂ , and FeV ₂ O ₄	SiO ₂ , and CrVO ₄
Cr ₃ C ₂ -NiCr coated	Cr ₂ O ₃ , NiO, NiCr ₂ O ₄ , and Fe ₂ O ₃	Ni(VO ₃) ₂ , MnO, and Al ₂ O ₃
NiCrBSi coated	SiO ₂ , Cr ₂ O ₃ , NiCr ₂ O ₄ , and NiO	Fe ₂ O ₃ , Al ₂ O ₃ , and Ni(VO ₃) ₂
Stellite-6 coated	CoO, CoCr ₂ O ₄ , and NiCr ₂ O ₄	Fe ₂ O ₃
Ni-20Cr coated	NiO, NiCr ₂ O ₄ , Fe ₂ O ₃ , Al ₂ O ₃ , and Ni(VO ₃) ₂	Cr ₂ O ₃

The existence of Al₂O₃, and Fe₂O₃ phases on the surface of Cr₃C₂-NiCr, NiCrBSi and Ni-20Cr coated Superni 601 and that MnO on Cr₃C₂-NiCr coated Superni 601 indicates the outward diffusion of Al, Mn and Fe from the substrate to the coating during hot corrosion of the specimens.

6.1.4.4 SEM/EDAX Analysis

(a) Surface Analysis

The scale formed on the uncoated Superni 601 (Fig. 6.36a) has a rough surface with uniform pitting throughout. Evidently cracks were developed in the scale. Black spots are regions from where spalling of the scale has occurred. The EDAX analysis of the scale shows Fe₂O₃ to be the predominant phase, with substantial amounts of NiO and Cr₂O₃. Small amounts of SiO₂, MnO and Al₂O₃ are also present in the scale of bare Superni 601.

All the coatings deposited on Superni 601 show the formation of uniform oxide scale without having any crack (Fig. 6.36). The EDAX analysis of Cr₃C₂-NiCr coated specimen shows Cr₂O₃ as principal phase along with NiO and Fe₂O₃. The scale formed on NiCrBSi coated superalloy has a nodular appearance with SiO₂ as the principal phase and black areas rich in NiO and Fe₂O₃. EDAX analysis of the corroded Stellite-6 coated Superni 601 reveals CoO and Cr₂O₃ as the main phases with small amounts of NiO, Fe₂O₃, and MnO, whereas the Ni-20Cr coating forms a fine grain continuous scale consisting of mainly Cr₂O₃ and NiO. The presence of Fe (Figs. 6.36b and 6.36e), Mn (Figs. 6.36 c and 6.36d) and Si (Fig. 6.36e) in the scale of corroded specimens indicate the diffusion of these elements from the substrate to the coating during hot corrosion runs, as these elements do not exist in the composition of the coating alloys.

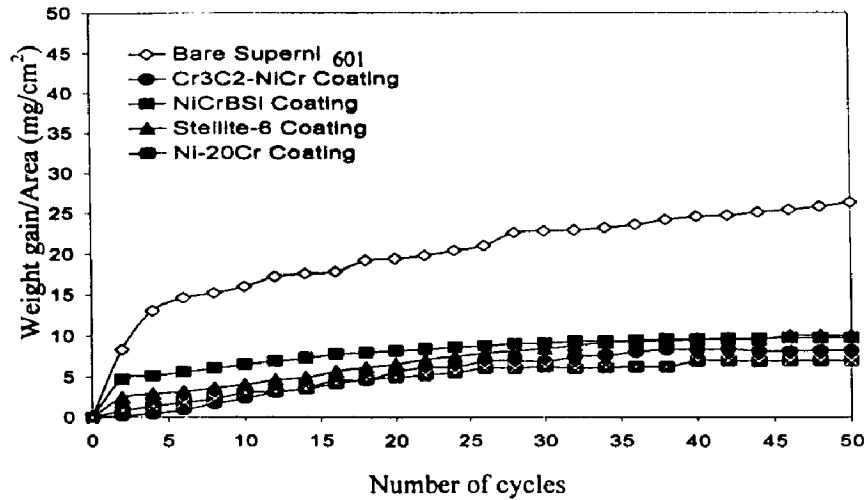


Fig. 6.31 Weight gain vs. number of cycles plot for the coated and uncoated Superni 601 hot corroded for 50 cycles in Na₂SO₄-60%V₂O₅ environment at 900 °C.

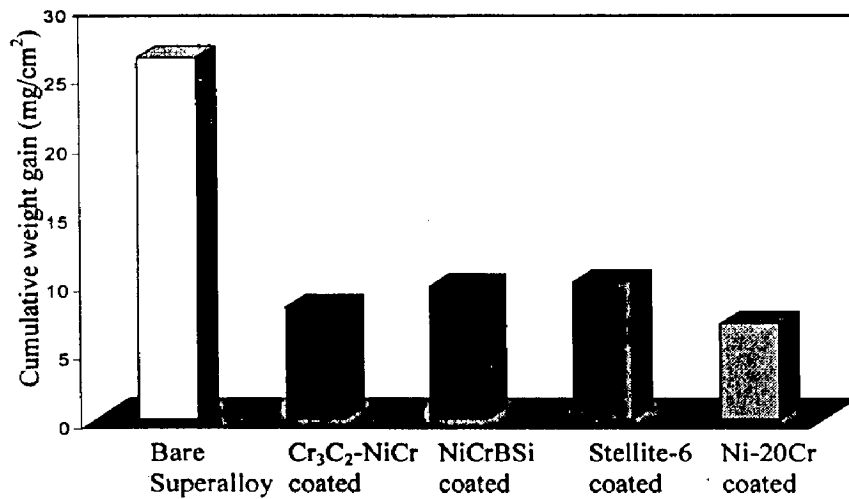


Fig.6.32 Bar charts showing cumulative weight gain per unit area for the coated and uncoated Superni 601 subjected to hot corrosion for 50 cycles in Na₂SO₄-60%V₂O₅ environment at 900 °C.

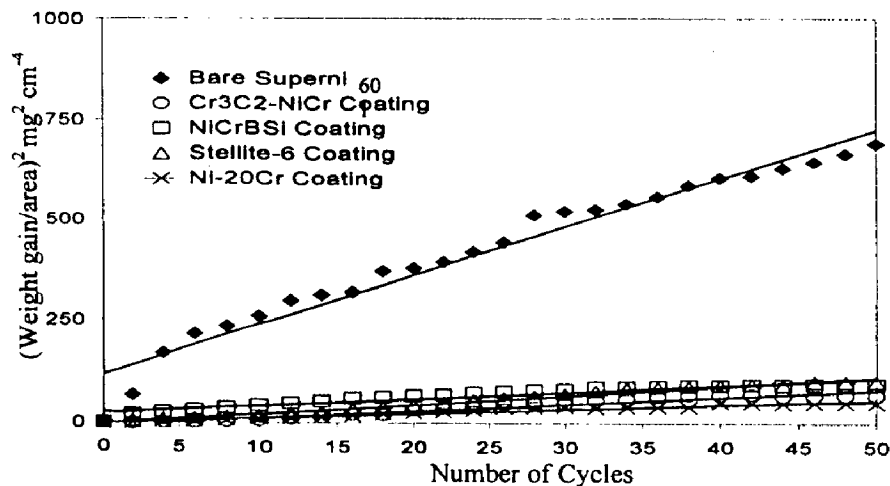


Fig. 6.33 (Weight gain/area) ² vs. number of cycles plot for the coated and uncoated Superni 601 hot corroded for 50 cycles in Na₂SO₄-60%V₂O₅ environment at 900 °C.

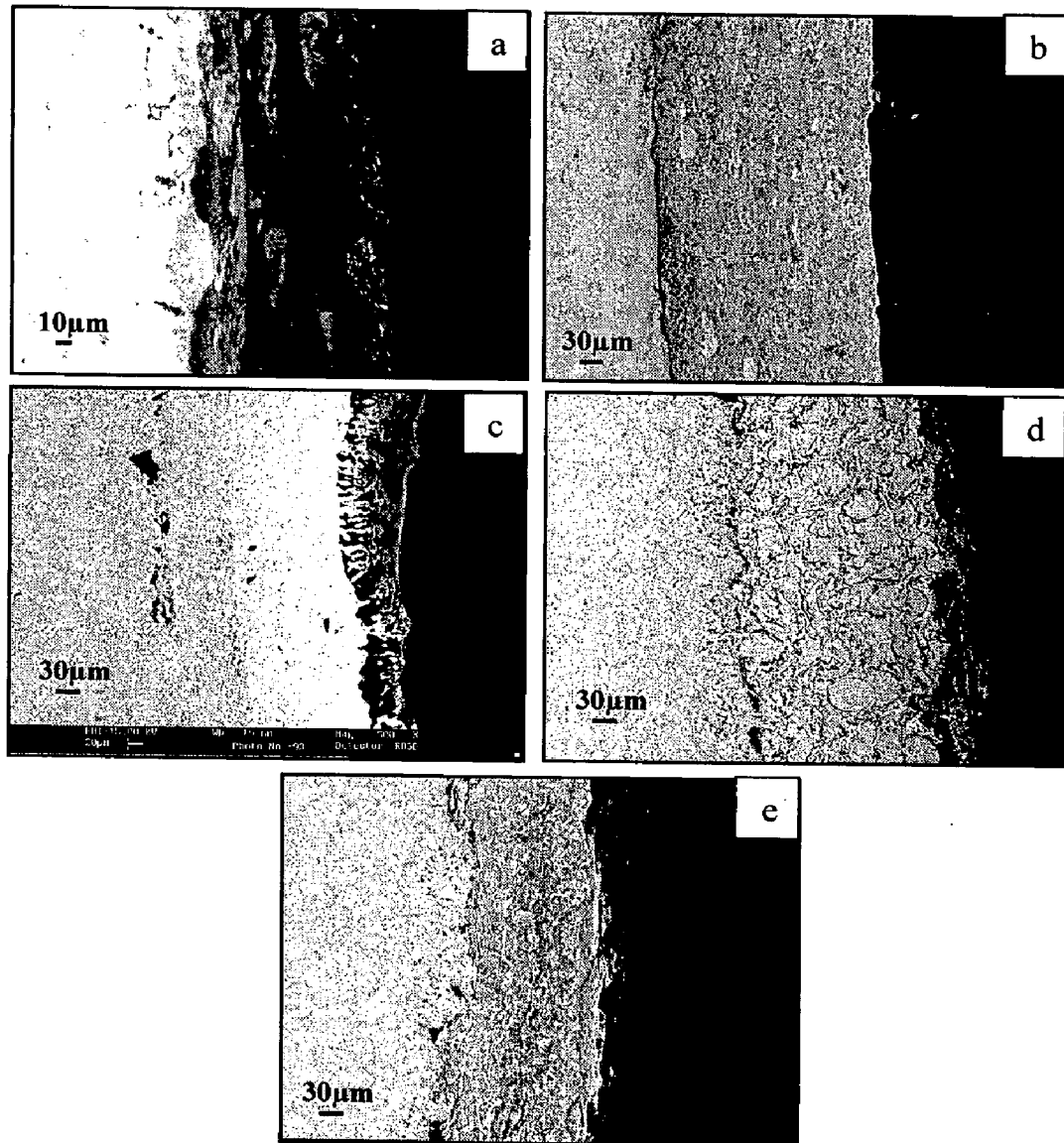


Fig. 6.34 SEM back scattered images for the bare and HVOF coated Superni 601 subjected to hot corrosion in Na_2SO_4 -60% V_2O_5 environment at 900 °C for 50 cycles: (a) Bare superalloy (b) Cr_3C_2 -NiCr coated (c) NiCrBSi coated (d) Stellite-6 coated (e) Ni-20Cr coated.

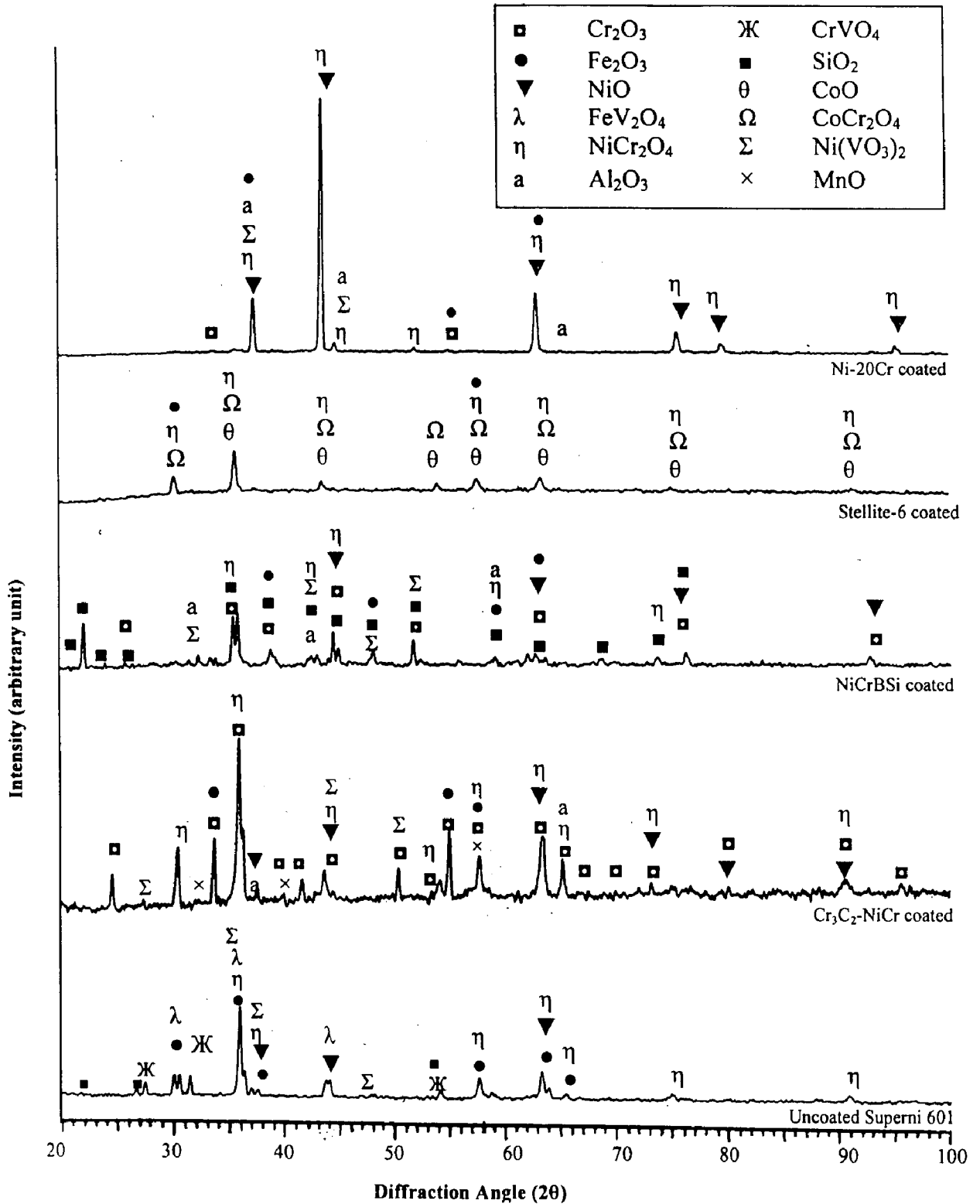


Fig. 6.35 X-ray diffraction patterns for the bare and coated Superni 601 subjected to hot corrosion in Na₂SO₄-60%V₂O₅ environment at 900 °C for 50 cycles.

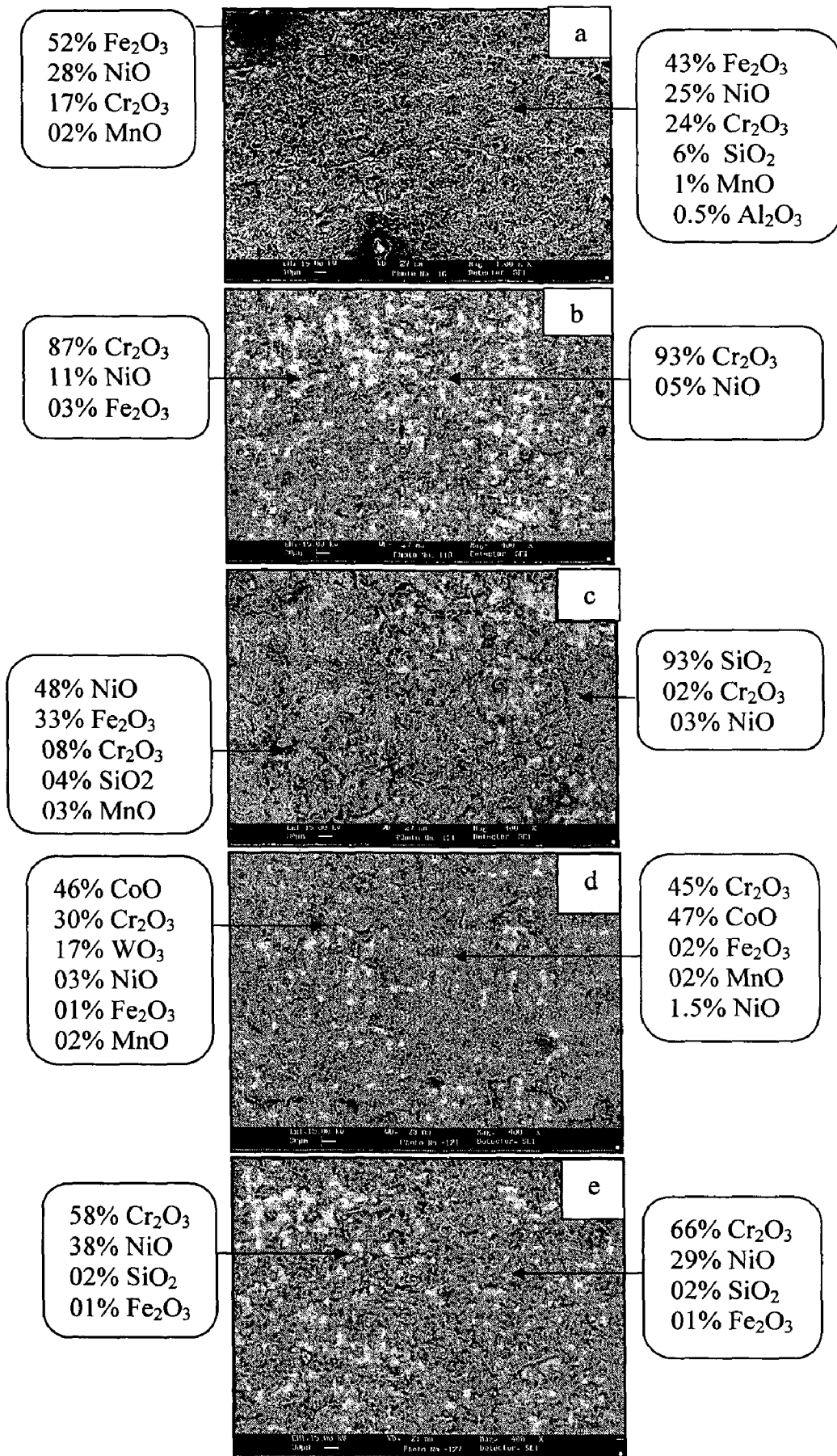


Fig. 6.36 SEM/EDAX analysis showing elemental composition (wt.%) for the bare and coated Superni 601 subjected to hot corrosion in Na₂SO₄-60%V₂O₅ environment at 900 °C for 50 cycles: (a) Bare Superni 601 (b) Cr₃C₂-NiCr coated (c) NiCrBSi coated (d) Stellite-6 coated (e) Ni-20Cr coated.

(b) Cross-Section Analysis

Figure 6.37 shows the BSE images and EDAX analysis at some selected point of interest across the cross-section of coated Superni 601 corroded in molten salt environment for 50 cycles at 900 °C. There is no indication of scale initiation at the interface or delamination of the coating. EDAX analysis shows the absence of oxygen near the coating-substrate interface (Point 1 of Fig. 6.37a). Therefore, it can be inferred that Cr₃C₂-NiCr coating acts as a diffusion barrier to the oxygen. The light grey phase (Points 2 and 4) consists of mainly chromium and oxygen with significant decrease in nickel. The white area (Point 3) in the scale is detected as Ni-rich splat. Upper part of the scale (Point 5) consists of mainly chromium oxide as EDAX analysis shows the presence of 35 wt% of Cr and 65 wt% of O. The presence of Mn (1.2 wt%) at Point 4 shows its diffusion from the substrate to coating.

BSE image of the corroded Stellite-6 coated Superni 601 is shown in Fig. 6.37b. The dense Stellite-6 coating observed in the as-sprayed conditions (Fig. 5.23c) is transformed into a featureless appearance at the top most part of the scale (Point 5 of Fig. 6.37b). The splat (Point 3) is rich in Co and Cr, with relatively lesser amount of O, indicating that the splats present in the scale are mostly in un-oxidised state. EDAX analysis shows that oxides of chromium and silicon are formed at the splat boundaries (Point 4). The topmost part of the scale (Point 5) is found to be rich in chromium oxide. Higher concentration of oxygen and aluminium is noticed corresponding to the black phase at the interface (Point 2). Therefore, these islands (black phase at the interface) are of aluminium oxides possibly due to the incorporation of alumina powder as already discussed in section 5.4.

The scale formed on a Ni-20Cr coated Superni 601 has a lamellar structure consisting of Ni-rich splats in mainly un-reacted state (Point 2 of Fig. 6.37c) and chromium oxide at the splat boundaries (Points 3 and 4). The presence of Mn, Si and Fe at these points indicates their outward diffusion from the substrates to the coating through the splat boundaries. The subscale (Point 5) comprises of mainly nickel and oxygen along with chromium. The top surface of the scale (Point 6) contains Ni and Cr along with 56 wt% O, suggesting the formation of oxides of Ni and Cr and their spinels. The existence of Fe (0.87 wt%) and Si (2.1 wt%) at Point 6 reveals their diffusion to the surface. The absence of oxygen at Point 1 shows that the substrate Superni 601 is in un-oxidised state.

6.1.4.5 EPMA Analysis

BSEI and EPMA elemental mappings for the uncoated and coated Superni 601 after cyclic oxidation at 900 °C in Na₂SO₄-60%V₂O₅ environment for 50 cycles are shown in Figs. 6.38 to 6.42.

An EPMA analysis of the corroded bare Superni 601 is shown in Fig. 6.38. The upper part of the scale contains high concentration of Al-rich clusters along with Cr, Ni and Fe. The Cr diffuses from the substrate to form Cr-rich middle layer of the scale thereby leaving a Cr-depleted layer. In this Cr-rich layer Ni and Fe are also present. Stringers of aluminium are seen penetrating into the substrate. Vanadium is mainly present in the upper part of the scale. Elemental maps show that vanadium coexists in the scale along with Ni, Fe and Cr. Thus the formation of various vanadates is obvious.

Elemental X-ray mappings for the corroded Cr₃C₂-NiCr coated Superni 601 (Fig 6.39) show the formation of Cr-rich scale in which elongated irregular shaped Ni-rich splats are uniformly distributed. Small amounts of Al and Mn diffused from the substrate to the coatings along the splat boundaries and also formed thick and thin streaks at the scale-substrate interface, respectively. Diffusion of iron from the substrate to the coating along the splat boundaries is also evident. However, diffusion of Fe in this coating is relatively less than that noted in Ni-20Cr coated Superni 601 (Fig. 6.42). This can be attributed to the formation of continuous streaks of Al at the interface, which might have acted as barrier to the outward diffusion of Fe. Sodium, vanadium and sulphur are present throughout the scale along the splat boundaries, thereby indicating ingress of the same from the molten salt environment.

X-ray mappings of corroded NiCrBSi coated Superni 601 are shown in Fig. 6.40. Elemental map for O indicates that only upper part of the coating is oxidized forming thick oxide layer consisting of two bands. The topmost band consists mainly of SiO₂, as silicon and oxygen co-exist in their respective micrographs. In the underlying band which is just below the topmost band, oxygen is found to be absent and nickel-rich splat are present. At the boundaries of these splats oxygen co-exists along with chromium and silicon. Therefore, it can be inferred that the underlying band consists of unoxidised nickel-rich splats encircled by oxides of mainly chromium and silicon. The elemental map for Cr shows the depletion of Cr just beneath the underlying band. The diffused Cr has formed a thick chromium oxide layer in the underlying band. Aluminium co-exists with oxygen along the coating-substrate interface. The formation of streaks of aluminium oxide at the interface might be partly attributed to the reason already discussed in section 5.4, and partly to the diffusion of aluminium from the substrate. Presence of vanadium, sulphur and sodium below the top scale indicates that they have penetrated along the splat boundaries. Elemental maps show that Ni and V co-exist in the oxide layer suggesting the possibility of formation of nickel vanadates.

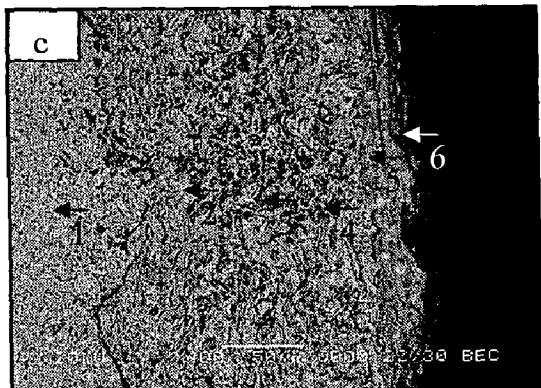
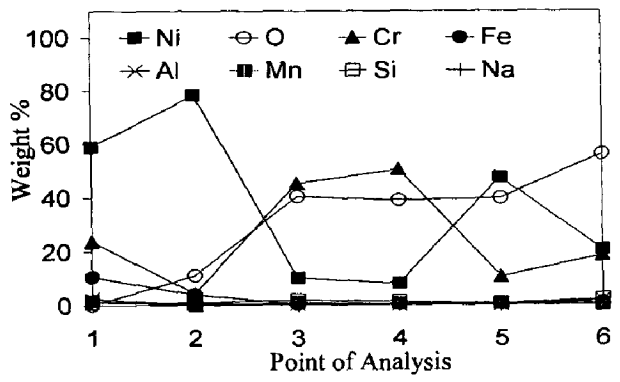
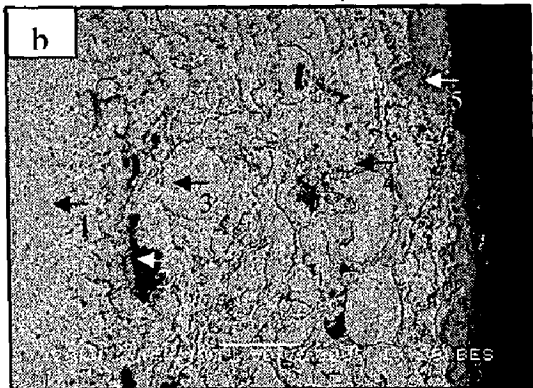
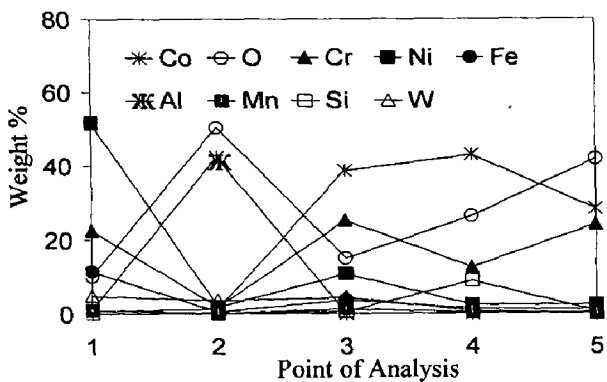
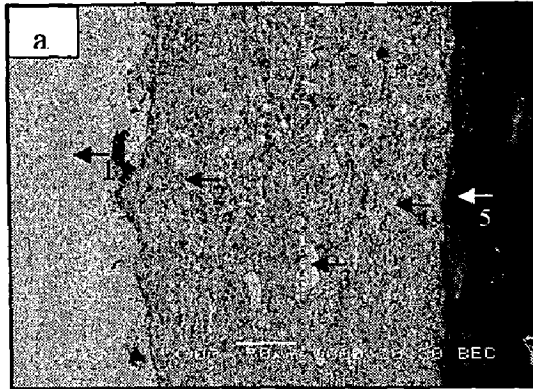
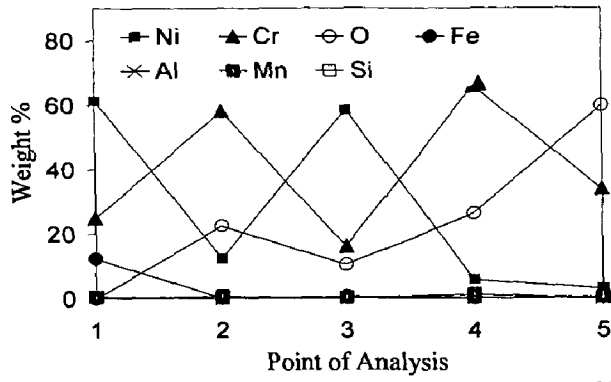


Fig 6.37 Oxide scale morphologies and variations of elemental composition across the cross section of HVOF coated Superni 601 hot corroded in Na_2SO_4 -60% V_2O_5 environment at 900 °C for 50 cycles: (a) Cr_3C_2 -NiCr coated (b) Stellite-6 coated (c) Ni-20Cr coated.

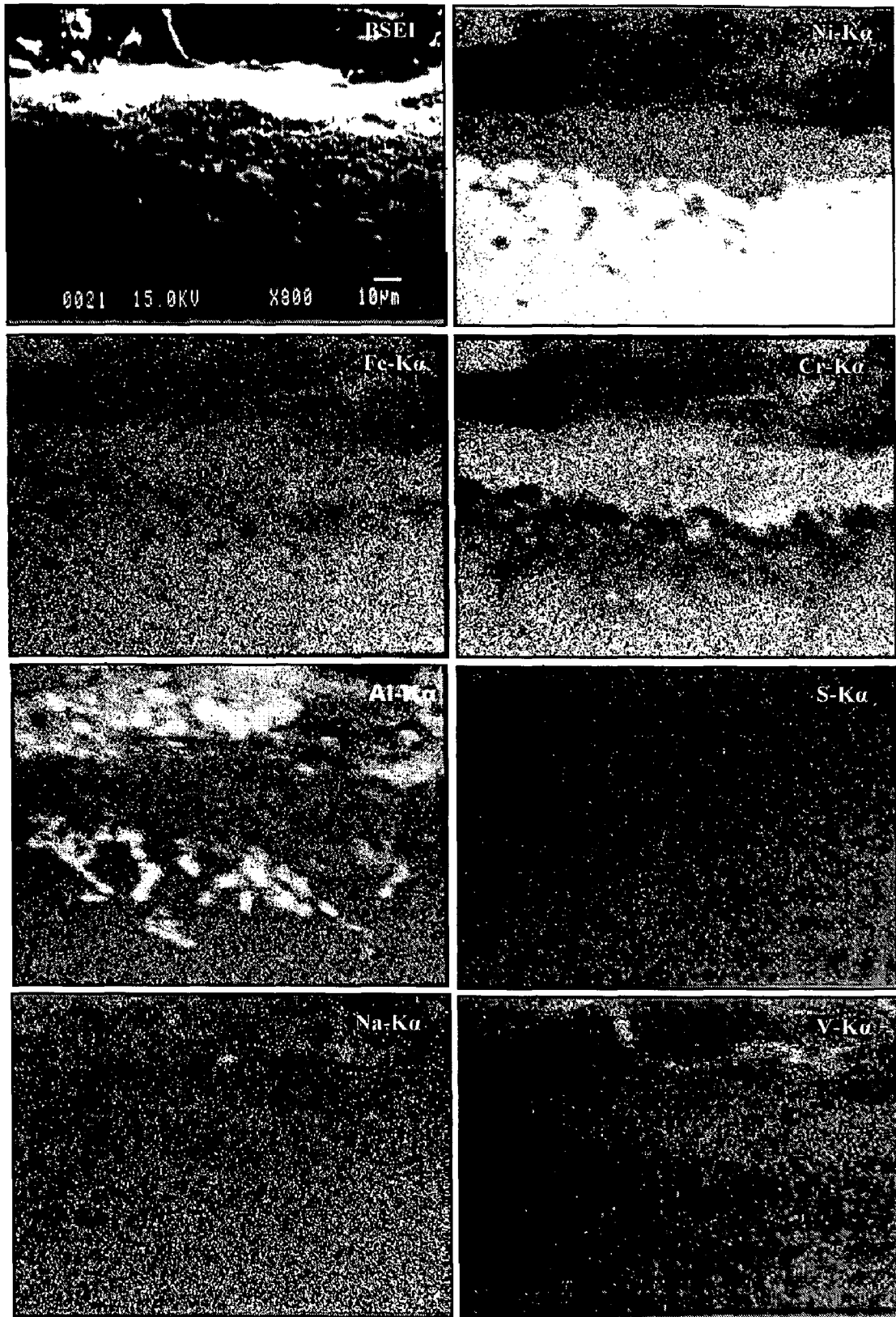


Fig. 6.38 Composition image (BSEI) and X-ray mappings of the cross-section of the bare Superni 601 subjected to hot corrosion at 900 °C in Na₂SO₄-60%V₂O₅ environment for 50 cycles.

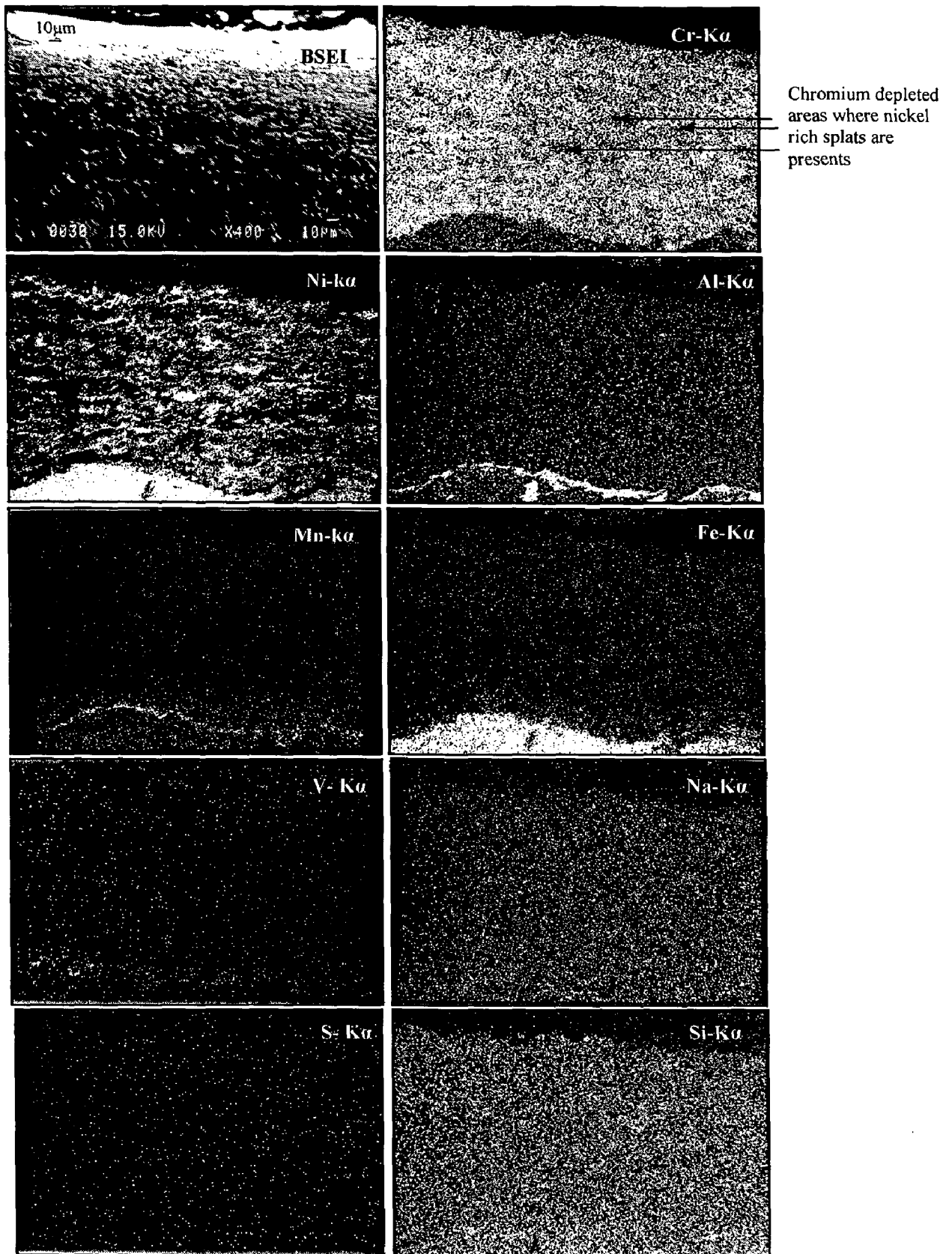


Fig. 6.39 Composition image (BSEI) and X-ray mappings of the cross-section of the $\text{Cr}_3\text{C}_2\text{-NiCr}$ coated Superni 601 subjected to hot corrosion at $900\text{ }^\circ\text{C}$ in $\text{Na}_2\text{SO}_4\text{-60\%V}_2\text{O}_5$ environment for 50 cycles.

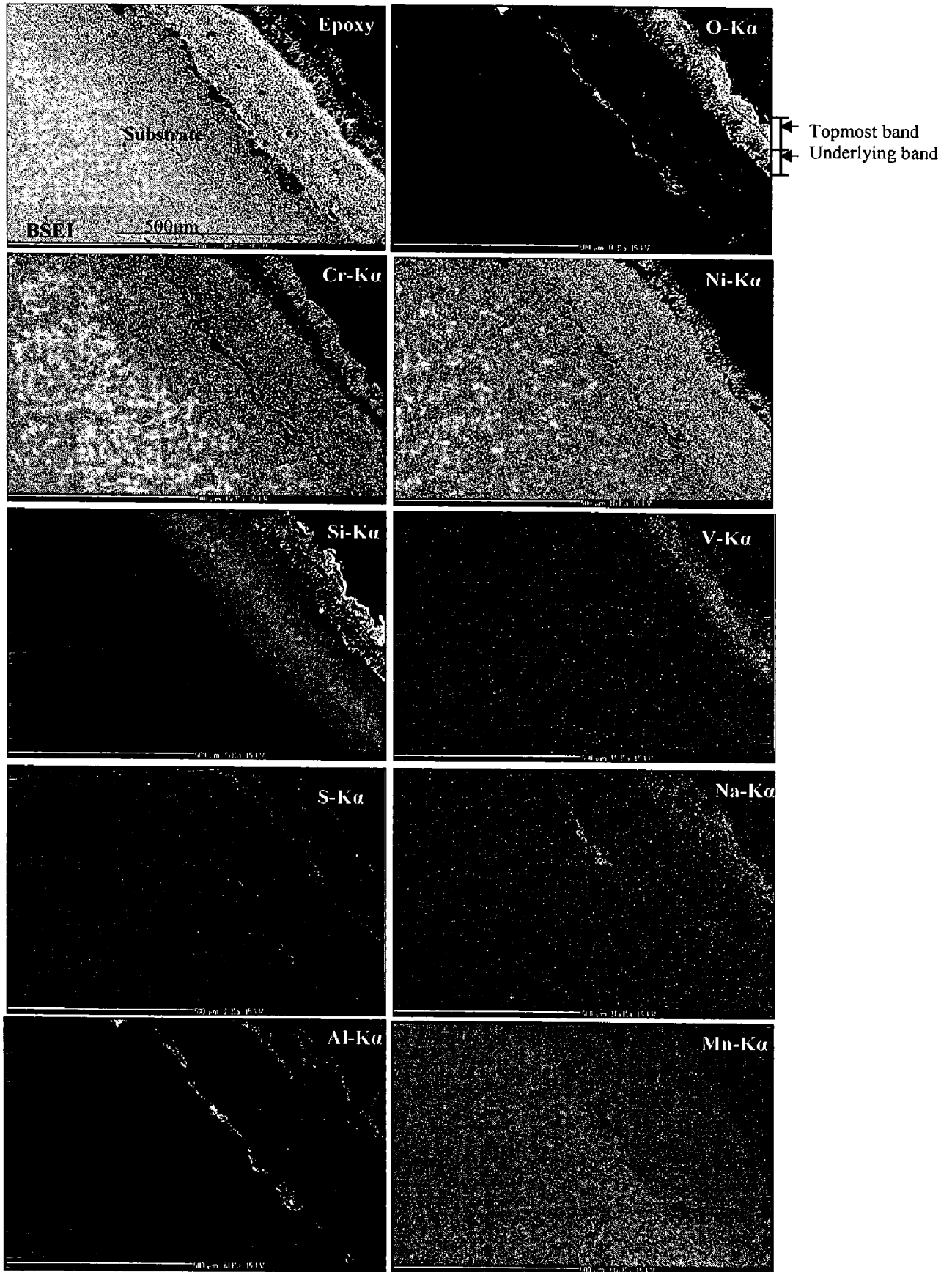


Fig. 6.40 Composition image (BSEI) and X-ray mappings of the cross-section of the NiCrBSi coated Superni 601 subjected to hot corrosion at 900 °C in Na₂SO₄-60%V₂O₅ environment for 50 cycles.

A similar analysis of the Stellite-6 coated Superni 601 (Fig. 6.41) indicates a massive scale consisting mainly of chromium and cobalt, along with Si, Ni and Fe. Iron and nickel show higher concentration in topmost part of the scale, whereas Cr-rich layer is formed in the sub-scale. Beneath this Cr-rich layer, a Co-rich thick band is present in which Cr has relatively low concentration. This can be attributed to diffusion of Cr from underneath to form oxide in the subscale. Silicon and chromium form stringers at the boundaries of Co-rich splats. Higher concentration of Ni and Fe in the lower part of the scale suggests the inward diffusion of nickel towards the scale-substrate interface and outward diffusion of iron from the substrate.

The BSE image and EPMA analysis along the cross-section of corroded Ni-20Cr coated Superni 601 (Fig. 6.42) show the formation of a scale consisting of Ni-rich splats with chromium present along the splat boundaries. Elemental mappings show the outward diffusion of Fe, Al, Mn, and Si from the substrate to the surface of the scale. There is an under layer, just below the topmost layer which is mainly rich in nickel and is depleted of chromium. The diffusion of iron from the substrate to the scale is very intensive near the scale-substrate interface. Aluminium forms thick streaks at the topmost layer of the scale as well as at the scale-substrate interface, whereas silicon shows a tendency to form small streaks at the splat boundaries.

6.1.5 Hot Corrosion of Bare and Coated Superni 718

6.1.5.1 Corrosion Kinetics

The weight gain plots for the bare and coated Superni 718 subjected to the given molten salt environment are given in Fig 6.43. The cumulative weight gain for the bare Superni 718 could be measured accurately up to 16th cycles only with some spalling/sputtering, beyond which intense spalling and sputtering made it difficult to measure the overall weight gain. The value of weight gain up to 16th cycles is found as 8.35 mg/cm². The values of overall weight gain after 50 cycles of hot corrosion for the Cr₃C₂-NiCr, NiCrBSi, Stellite-6 and Ni-20Cr coated Superni 718 are found to be 8.14, 11.81, 10.83 and 4.72 mg/cm² respectively and are shown in Fig. 6.44.

The maximum hot corrosion resistance to the Superni 718 at 900 °C is provided by the Ni-20Cr coating, whereas NiCrBSi coating showed least resistance among the coating studied. The weight gain of Ni-20Cr coated Superni 718 after 50 cycles of exposure is about 60% less than that of the NiCrBSi coated Superni 718. In terms of weight gain, the Cr₃C₂-NiCr coating is the second highest hot corrosion resistance coating to Superni 718, followed by Stellite-6 coating.

The weight gain data reveals that the bare Superni 718 underwent accelerated oxidation, whereas coatings are found to be successful in protecting the superalloys from accelerated oxidation to a considerable extent in the given molten salt environment. All the coatings on Superni 718 have nearly followed the parabolic behaviour up to 50 cycles as can be inferred from square of weight change (mg^2/cm^4) vs. time (number of cycles) plots shown in Fig. 6.45. The parabolic rate constants (k_p in $10^{-10} \text{ g}^2 \text{ cm}^{-4} \text{ s}^{-1}$) for the Cr_3C_2 -NiCr, NiCrBSi, Stellite-6, and Ni-20Cr coated Superni 718 after 50 cycles of hot corrosion are evaluated as 3.77, 3.31, 6.94 and 1.44, respectively.

6.1.5.2 Scale Thickness Measurement

The BSE images across the cross-section of bare and coated Superni 718 after hot corrosion for 50 cycles at 900°C are shown in Fig. 6.46. The average scale thickness values obtained from the smallest cross-section for bare Superni 718; and Cr_3C_2 -NiCr, NiCrBSi, Stellite-6 and Ni-20Cr coated Superni 718 are 86; and 244, 311, 288 and 222 μm , respectively.

6.1.5.3 X-ray Diffraction Analysis

XRD profiles for the scale of bare and coated Superni 718 are shown in Fig 6.47 and the major and minor phases detected with XRD analysis are listed in Table 6.4.

Table 6.4: Major and minor phases identified by XRD analysis of the hot corroded bare and coated Superni 718.

Description	Major phases	Minor phases
Uncoated Superni 718 superalloy	NiO, Cr_2O_3 , Fe_2O_3 , NiCr_2O_4 , $\text{Ni}(\text{VO}_3)_2$, TiO_2 , FeV_2O_4 , FeV, and FeS	-
Cr_3C_2 -NiCr coated	Cr_2O_3 , NiO, NiCr_2O_4 , $\text{Ni}(\text{VO}_3)_2$, and Fe_2O_3	SiO_2 , and Al_2O_3
NiCrBSi coated	SiO_2 , Cr_2O_3 , NiO, NiCr_2O_4 , and Fe_2O_3	MnO_2 , and Al_2O_3
Stellite-6 coated	Cr_2O_3 , Fe_2O_3 , NiO, CoCr_2O_4 , and NiCr_2O_4	MnO_2
Ni-20Cr coated	NiO	Cr_2O_3 , and NiCr_2O_4

6.1.5.4 SEM/EDAX Analysis

(a) Surface Analysis

SEM micrographs and EDAX analysis of the corroded bare and coated Superni 718 are given in Fig.6.48. The surface morphology of the bare Superni 718 (Fig. 6.48a) provides evidence of spalling and sputtering of the oxide scale visually observed during cooling period of the hot corrosion cycles. The scale is spongy. The black areas are the

regions where from the spalling of the scale has occurred. EDAX analysis shows that the surface scale contains oxides of mainly nickel, iron and chromium with little amount of titanium, aluminium, manganese and vanadium.

The surface morphology of the coated Superni 718 after 50 cycles of hot corrosion show the formation of regular, incessant, adherent and homogeneous scales, with negligible spalling symptoms. EDAX analysis shows that the scale developed on the surface of Cr₃C₂-NiCr coated Superni 718 is rich in chromium oxide (93-95 wt%), along with very little amount of nickel oxide (Fig. 6.48b). The presence of little amounts of oxides of Fe, Al, Mn and Si shows outward diffusion of these elements to surface of the scale. Micrograph of corroded NiCrBSi coated Superni 718 (Fig. 6.48c) indicates the formation of dense, compact and relatively massive scale. EDAX analysis of the scale shows SiO₂ as the major phase. In addition, Fe₂O₃, Cr₂O₃, V₂O₅, Na₂O, and Al₂O₃ are also present in small amounts. The globules present in the scale also have SiO₂ as the predominant phase with substantial amounts of NiO and Cr₂O₃.

EDAX results of the corroded Stellite-6 coated Superni 718 (Fig. 6.48d) indicate CoO and Cr₂O₃ as the main phases along with small amounts of NiO, Fe₂O₃, Al₂O₃ and WO₃ phases, while the scale of Ni-20Cr coated superalloy is found to be enriched in NiO with very little amount of Cr₂O₃ (Fig. 6.48e). The scale formed on Stellite-6 coated Superni 718 is relatively rough and also shows some indications of spalling, whereas a very shining and dense oxide scale appears on the surface of corroded Ni-20Cr coated Superni 718. Evidently, aluminium diffused outward from the substrate to the coating during the hot corrosion of the specimens (Figs.6.48c and 6.48d). EDAX analysis shows the presence of un-reacted salt also on the surface of specimens (Figs.6.48a and 6.48c).

(b) Cross-Section Analysis

Absence of gap or crack at the scale-substrate interface indicates that the scale formed on the coated Superni 718 is adherent (Fig. 6.49). EDAX analysis of corroded Cr₃C₂-NiCr coated Superni 718 (Fig. 6.49a) at Point 1 shows the presence of only basic elements of the substrate. The absence of corrosive species at this point indicates that the substrate superalloy remained unaffected during the hot corrosion runs. In the dark black phase at the scale-substrate interface (Point 2), Al increased substantially (24 wt%). The reasons for increase in Al at the interface have already been discussed under section 6.1.4.5. The white phase (Point 3) in the scale is identified as Ni-rich splat surrounded by the Cr-rich areas (Point 4). The presence of oxygen at Point 4 indicates that this grey phase is chromium oxide. EDAX analysis has detected 77 wt% of Cr and 20 wt% of O at Point 5. Thus, it can be inferred that the subscale (Point 5) is rich in chromium oxide. The topmost part of the scale (Point 6), containing mainly Cr and Ni along with about 60 wt% of O, is

rich in oxides of Cr and Ni and their spinels. EDAX analysis at Point 1 shows that amount of Ni increases from 52 wt% to 60 wt%, whereas amount of Fe decreases from 18.5 wt% to 14 wt%. This indicates the inward diffusion of Ni from the coating to substrate and outward diffusion of Fe from substrate to coating. Iron has diffused up to Point 4.

Figure 6.49b shows the BSE image across the cross-section of the scale formed on NiCrBSi coated Superni 718. The upper part of the as-sprayed coating, about 90 μm thick, as shown in Fig. 5.5, has changed significantly after exposure to molten salt environment. The white featureless appearance of the as-sprayed coating is transformed into a dark grey phase at the top surface with black patches and grain shaped structure underneath. EDAX analysis at Point 1 indicates that the coating has protected the substrate from the corrosive species. The black phase at the interface (Point 2) is detected as exclusively the oxides of aluminium. The absence of oxygen at Points 3 and 4 indicates that only upper part of the coating has oxidized. The grey phase in the subscale (Point 5) contains more chromium and oxygen, whereas amount of Ni has decreased indicating the possibility of chromium oxide formation. The black patch at Point 6 has almost equal amount of Cr and Si, whereas dark black dense phase at the topmost part of the scale (Point 7) is found to be rich in Si. The O is also present at Points 7. Thus it can be inferred that upper part of the coating is dominated by the oxides of silicon.

6.1.5.5 EPMA Analysis

BSE images and EPMA elemental mappings for the uncoated and coated Superni 718 after cyclic hot corrosion in Na_2SO_4 -60% V_2O_5 environment at 900 °C for 50 cycles are shown in Figs. 6.50 to 6.54.

The scale formed on bare Superni 718 consists of different layers (Fig. 6.50). The uppermost layer is found to be rich in nickel, along with some amount of Cr, Fe, Ti, Al and Mo. Below this top layer, there exist a thin middle layer mainly rich in iron. Beneath this iron-rich layer, another layer rich in Cr is formed. The Ti and Al show their presence in the penetrating zone of the scale in the form of clusters. The Al, Si, Mo and Ti are present throughout the scale cross-section. Some globules of Si can be seen in the upper part of the scale.

The scale formed on the Cr_3C_2 -NiCr coated Superni 718 after 50 cycles of hot corrosion has maintained layered morphology except uppermost scale of 20-30 μm (Fig. 6.51). The uppermost part of the scale consists of mainly Cr, Ni and Fe. The remaining part of the scale consists of Ni-rich flat splats with chromium at the splat boundaries. Iron shows outward diffusion from the substrate up to surface of the scale. Aluminium and titanium elements of the substrate form thick and thin continuous streaks at the interface. High density dots for vanadium can be seen in the upper part of the scale.

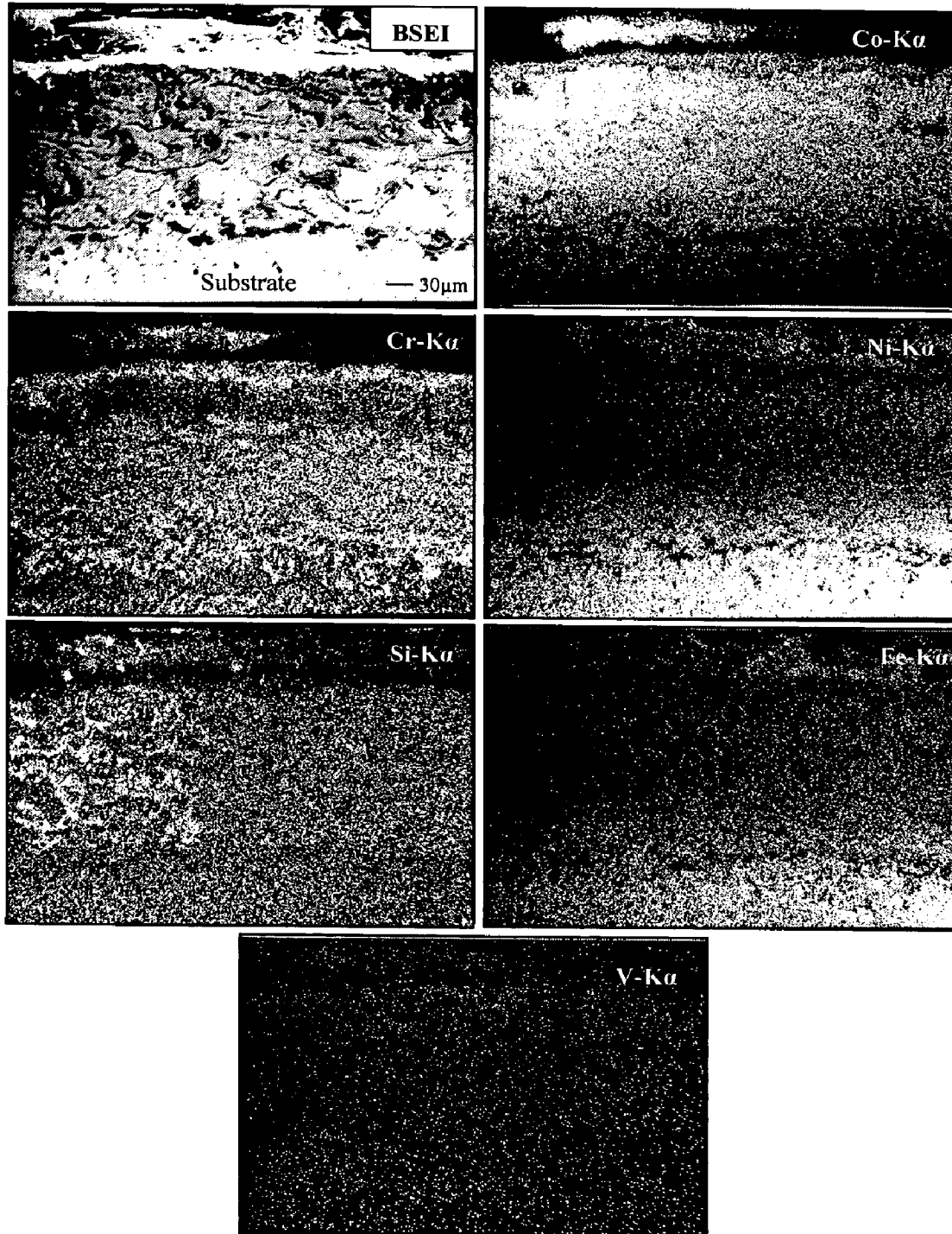


Fig. 6.41 Composition image (BSEI) and X-ray mappings of the cross-section of the Stellite-6 coated Superni 601 subjected to hot corrosion at 900 °C in Na_2SO_4 -60% V_2O_5 environment for 50 cycles.

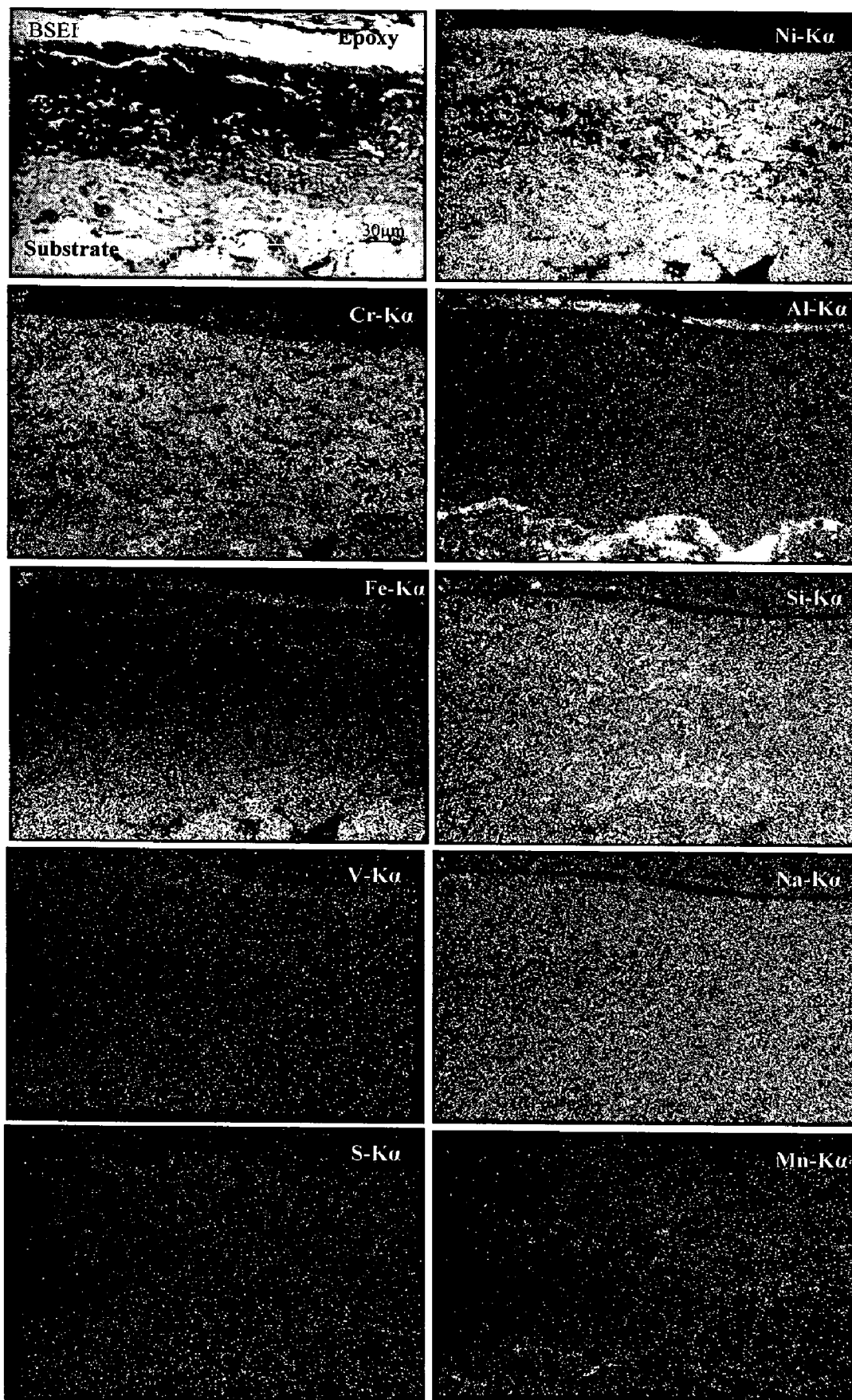


Fig. 6.42 Composition image (BSEI) and X-ray mappings of the cross-section of the Ni-20Cr coated Superni 601 subjected to hot corrosion at 900 °C in Na₂SO₄-60%V₂O₅ environment for 50 cycles.

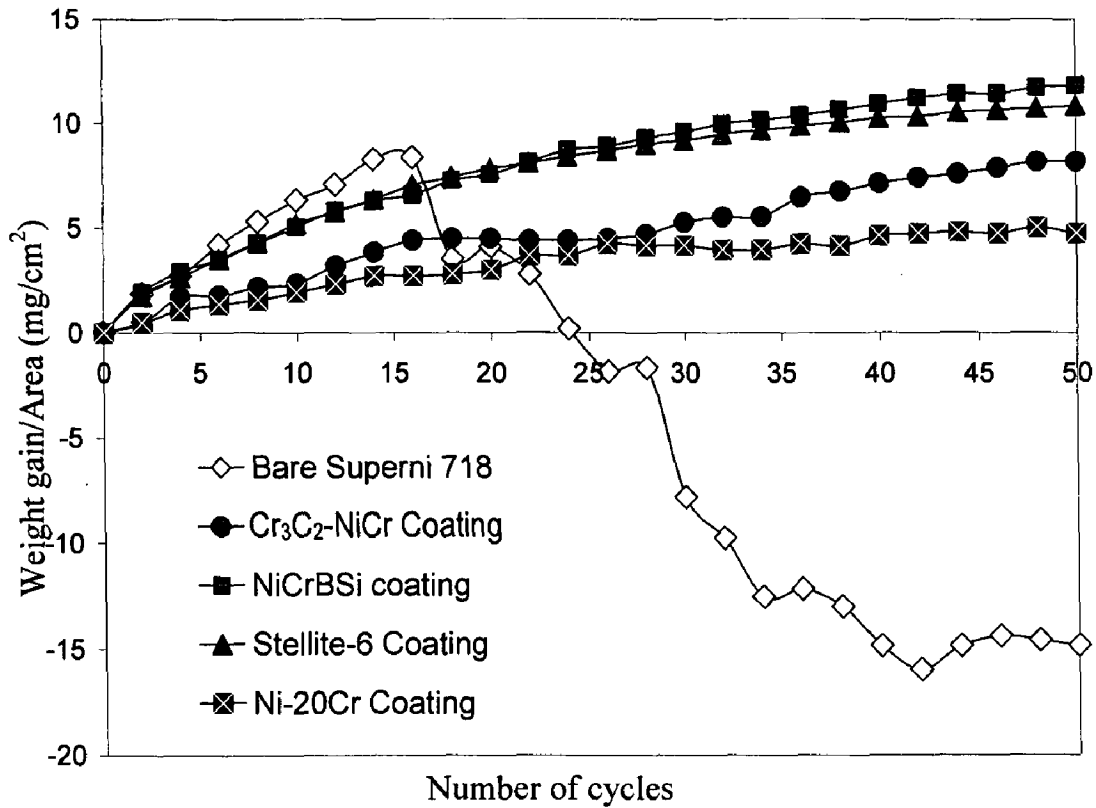


Fig. 6.43 Weight gain vs. number of cycles the plot for coated and uncoated Superni 718 subjected to hot corrosion for 50 cycles in Na_2SO_4 -60% V_2O_5 environment at 900 °C.

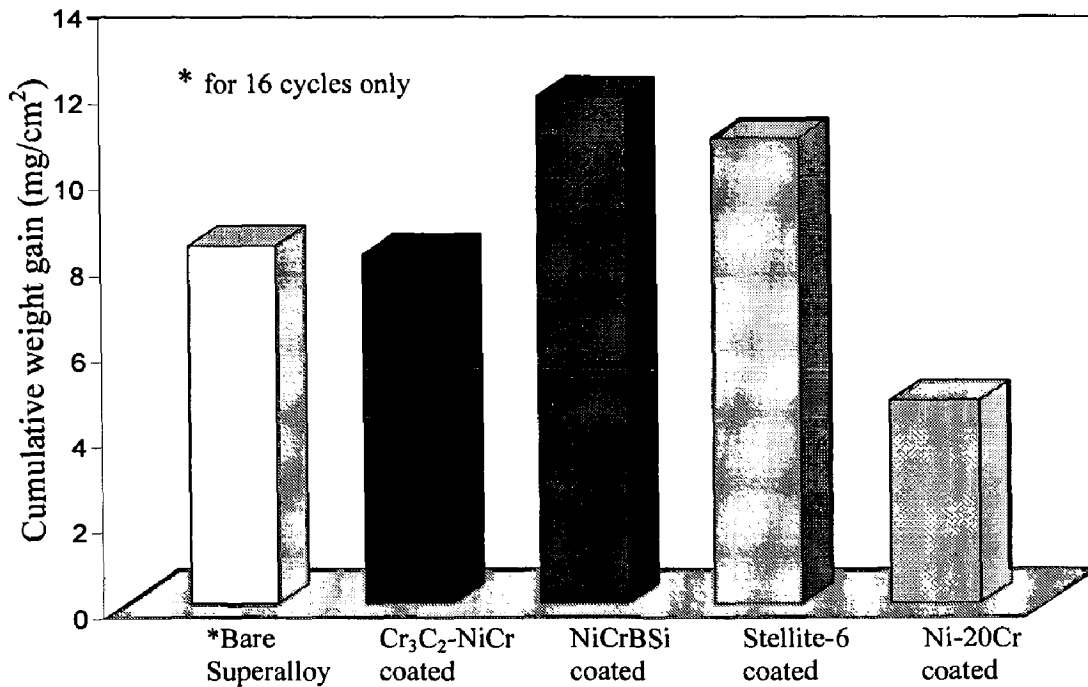


Fig. 6.44 Bar charts showing cumulative weight gain per unit area for the coated and uncoated Superni 718 subjected to hot corrosion for 50 cycles in Na_2SO_4 -60% V_2O_5 environment at 900 °C.

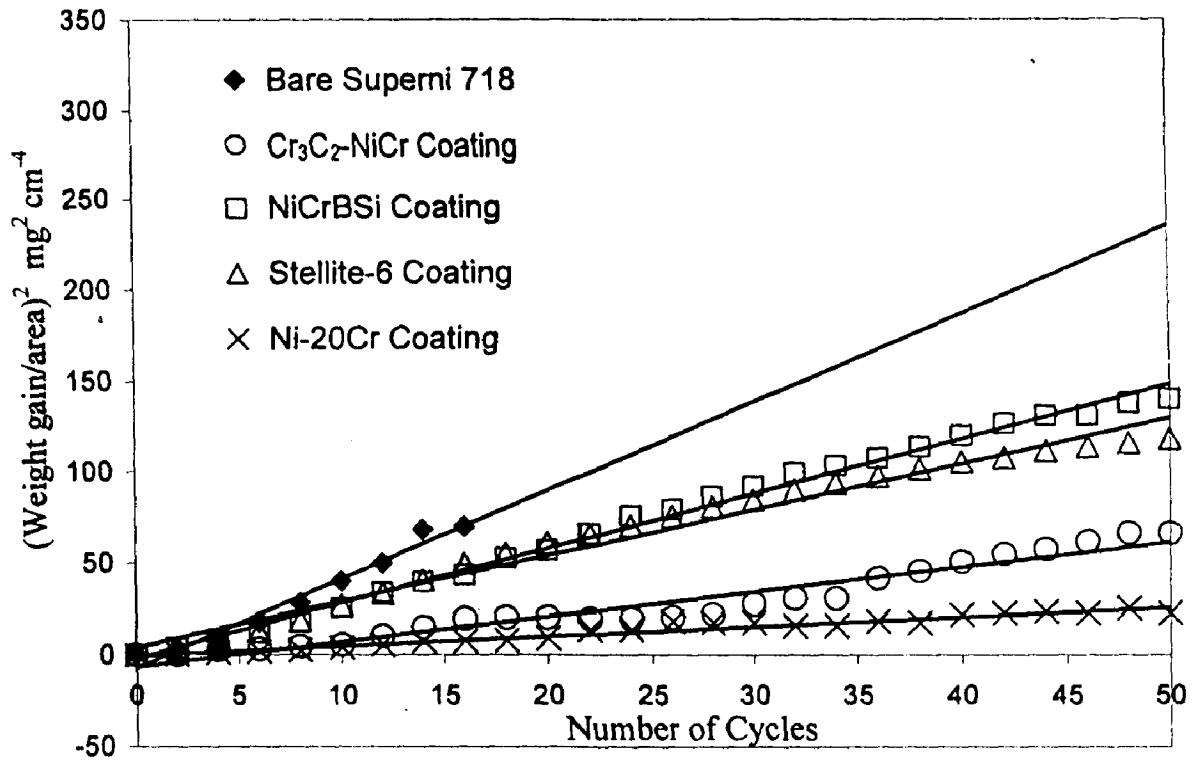


Fig. 6.45 $(\text{Weight gain/area})^2$ vs. number of cycles plot for the coated and uncoated Superni 718 subjected to hot corrosion for 50 cycles in Na_2SO_4 -60% V_2O_5 environment at 900 °C.

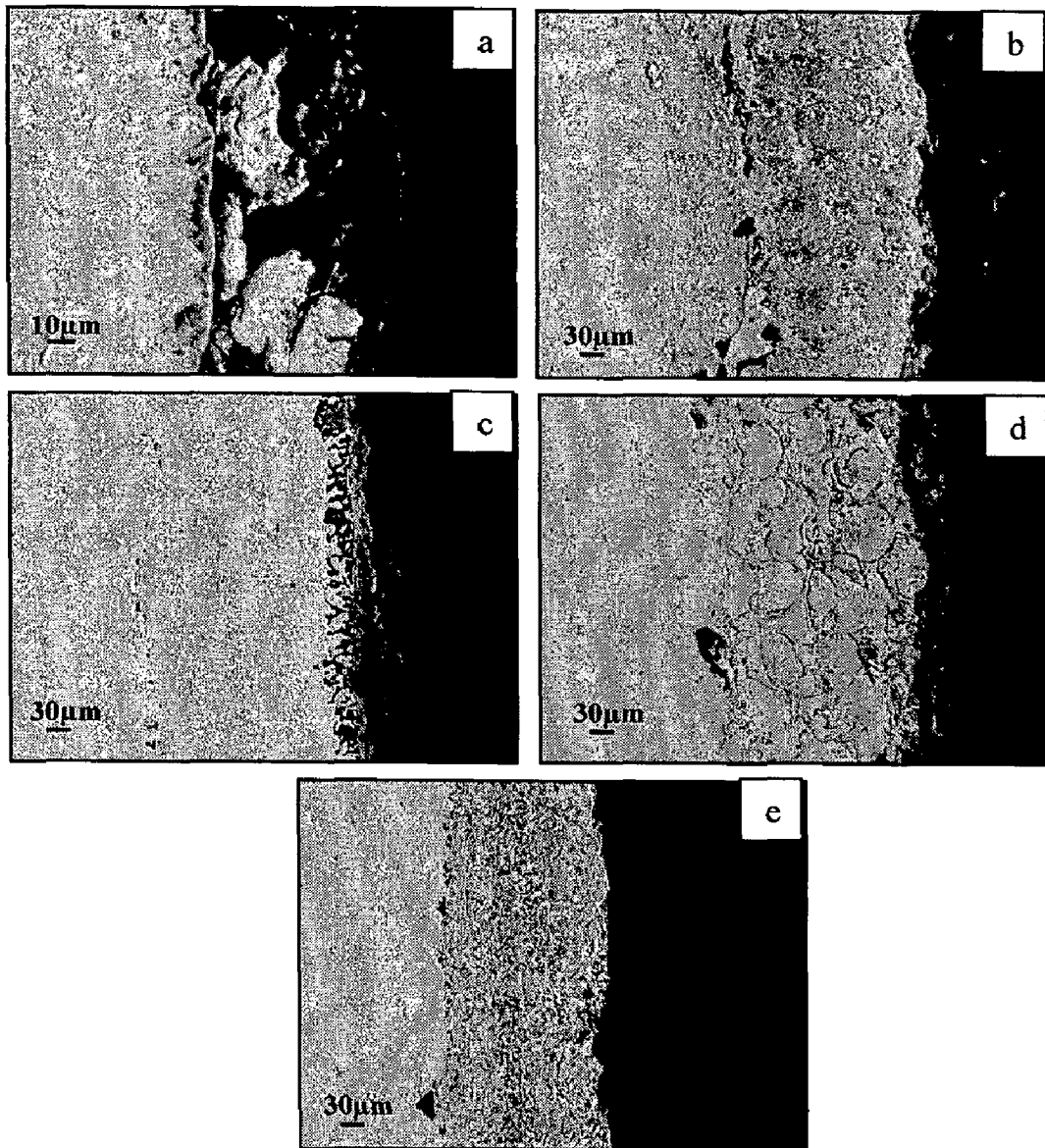


Fig. 6.46 SEM back scattered images for the bare and HVOF coated Superni 718 subjected to hot corrosion in Na_2SO_4 -60% V_2O_5 environment at 900 °C for 50 cycles: (a) Bare superalloy (b) Cr_3C_2 -NiCr coated (c) NiCrBSi coated (d) Stellite-6 coated (e) Ni-20Cr coated.

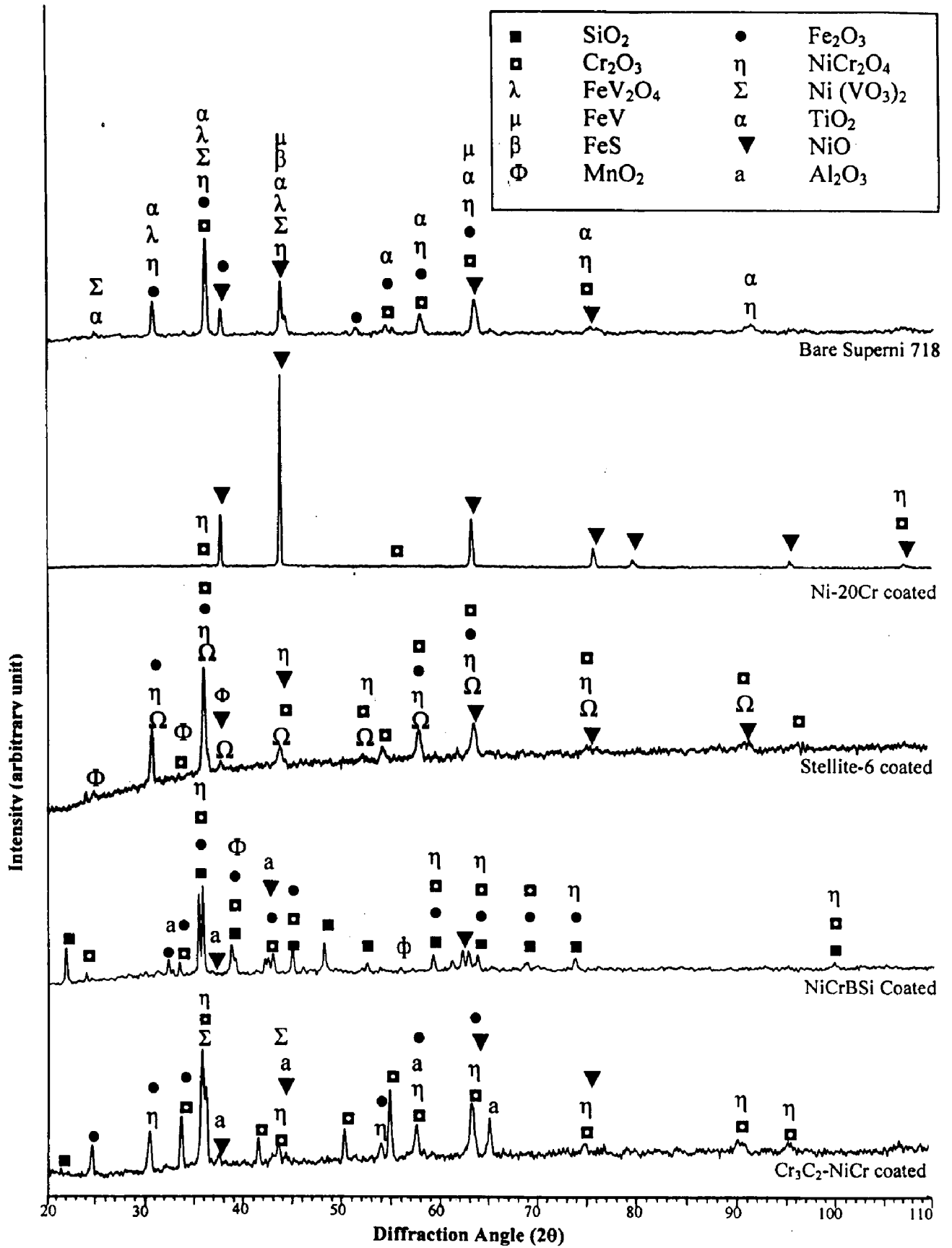


Fig. 6.47 X-ray diffraction patterns for the bare and coated Superni 718 subjected to hot corrosion in Na₂SO₄-60%V₂O₅ environment at 900 °C for 50 cycles.

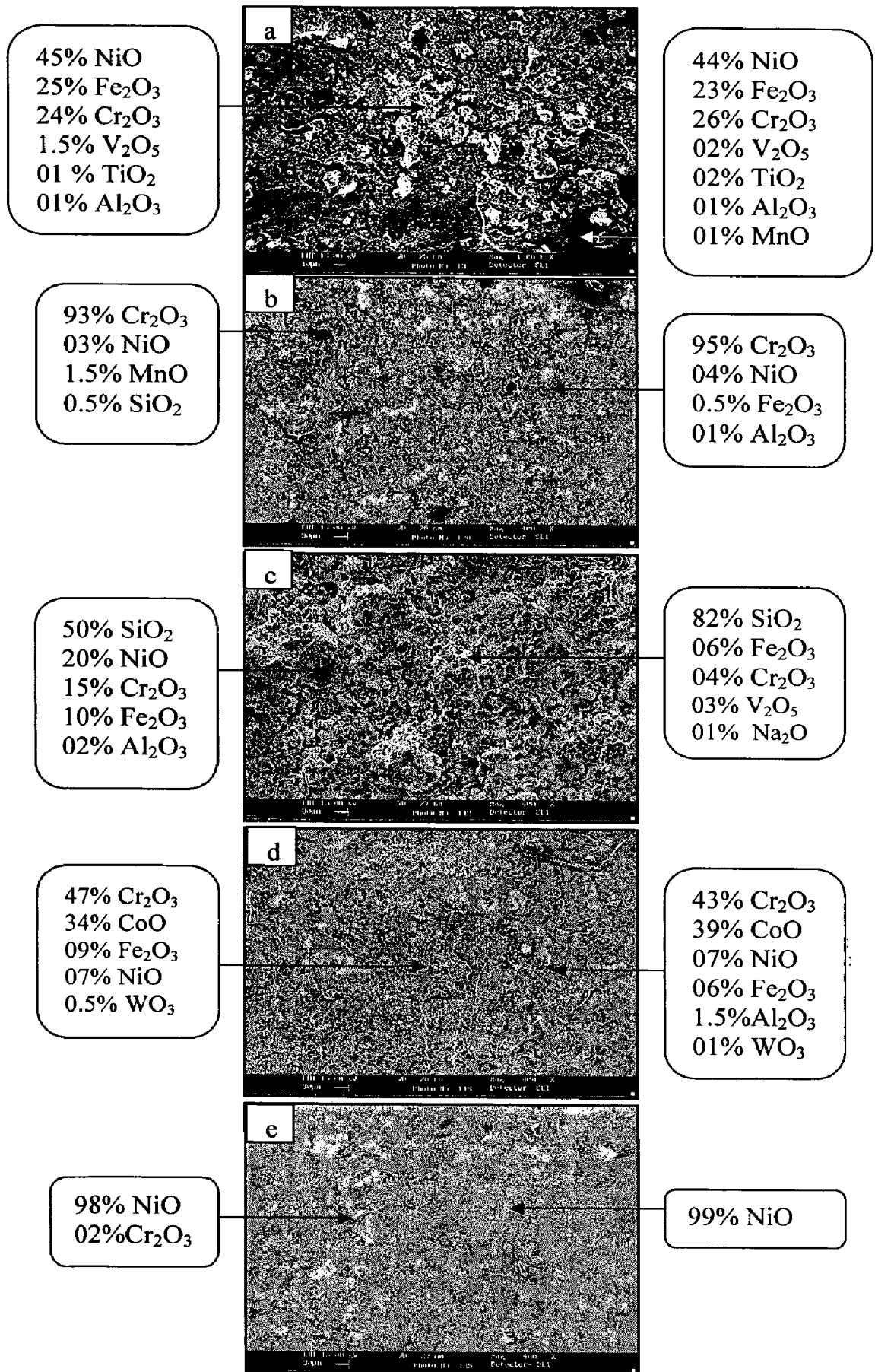


Fig.6.48 SEM/EDAX analysis showing elemental composition (wt.%) for the bare and coated Superni 718 subjected to hot corrosion in Na₂SO₄-60%V₂O₅ environment at 900 °C for 50 cycles: (a) Bare Superni 718 (b) Cr₃C₂-NiCr coated (c) NiCrBSi coated (d) Stellite-6 coated (e) Ni-20Cr coated.

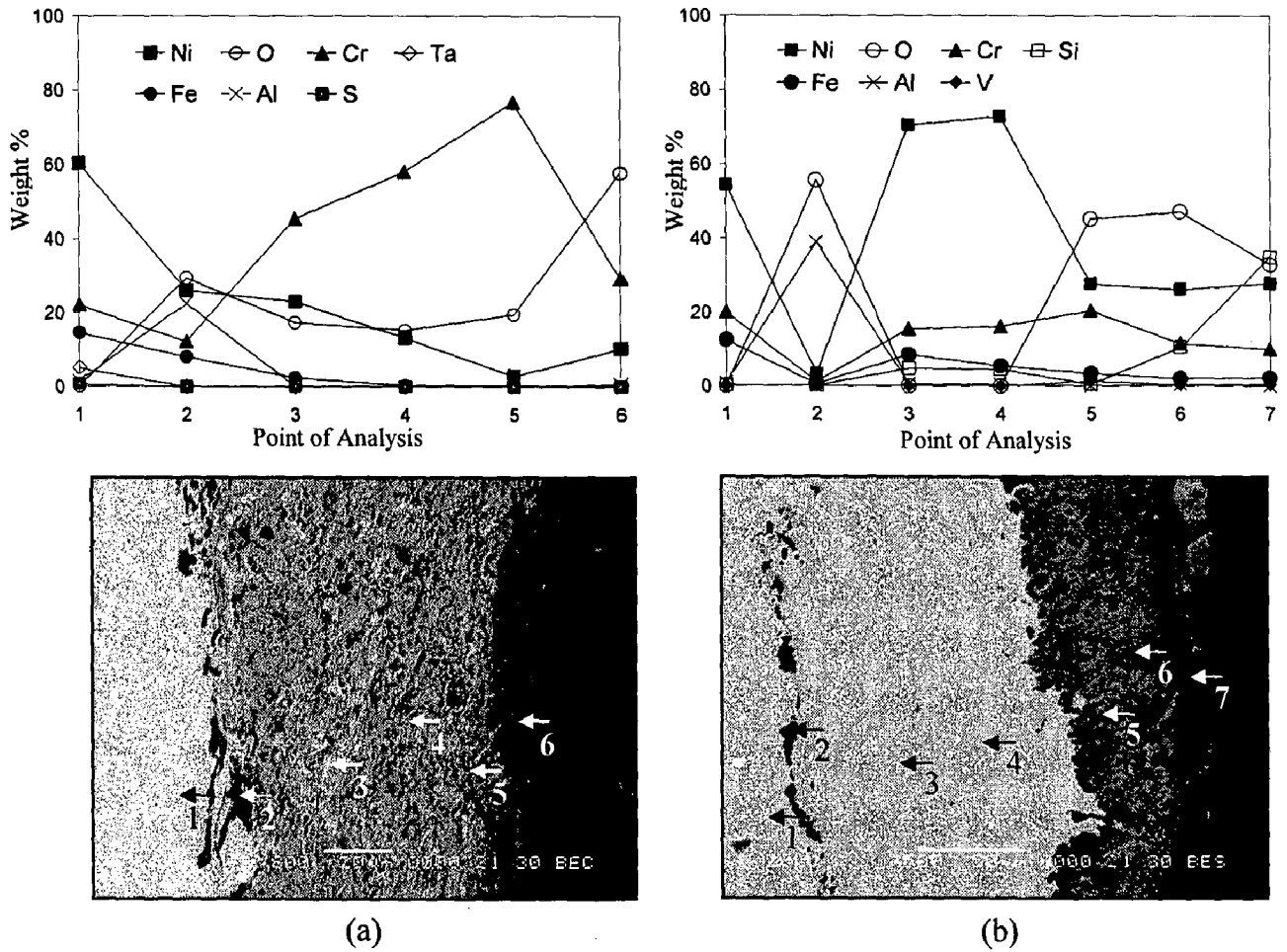


Fig 6.49 Oxide scale morphologies and variations of elemental composition across the cross section of HVOF coated Superni 718 hot corroded in $\text{Na}_2\text{SO}_4\text{-60}\%\text{V}_2\text{O}_5$ environment at $900\text{ }^\circ\text{C}$ for 50 cycles: (a) $\text{Cr}_3\text{C}_2\text{-NiCr}$ coated (b) NiCrBSi coated.

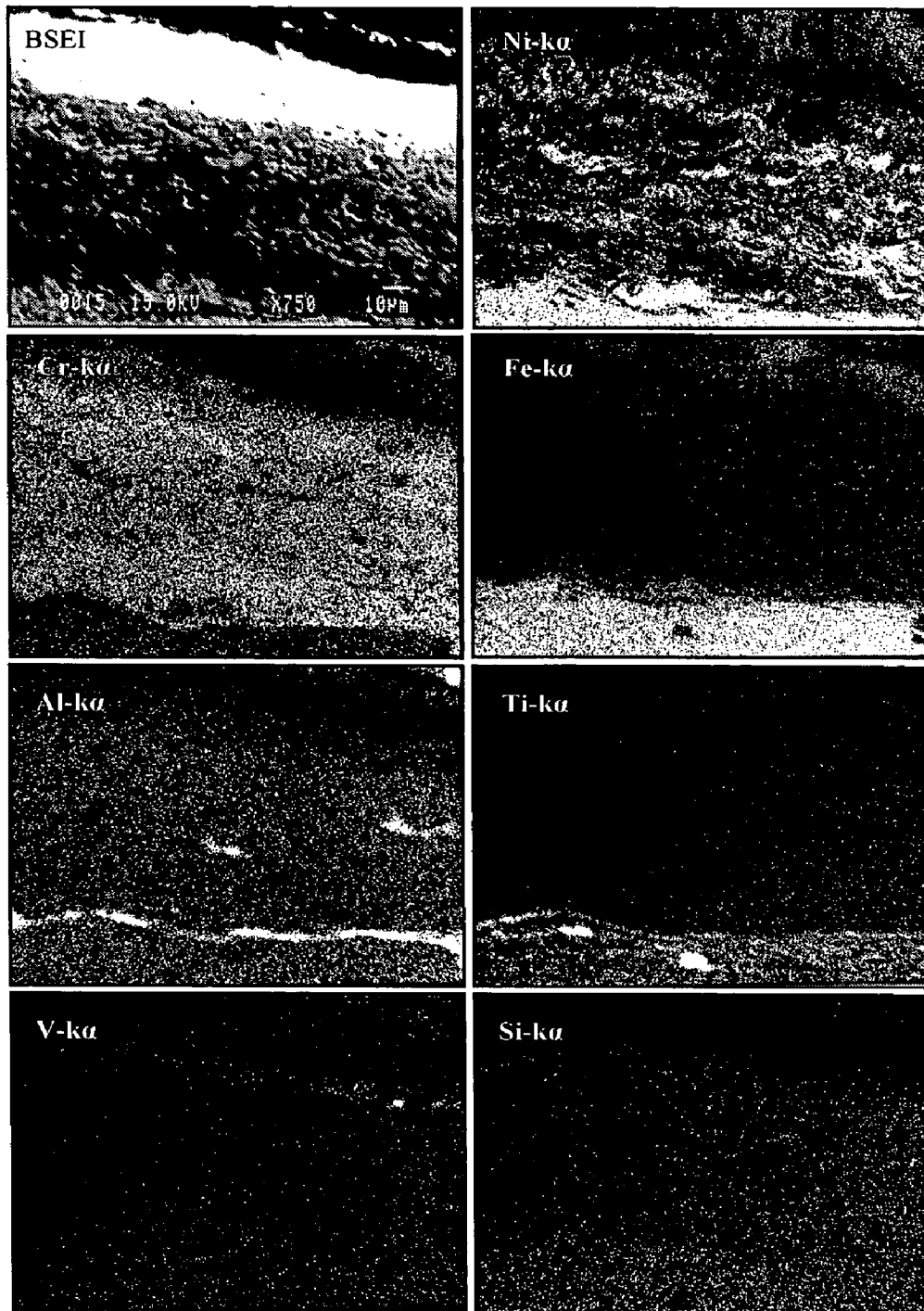


Fig. 6.51 Composition image (BSEI) and X-ray mappings of the cross-section of the $\text{Cr}_3\text{C}_2\text{NiCr}$ coated Superni 718 subjected to hot corrosion at $900\text{ }^\circ\text{C}$ in $\text{Na}_2\text{SO}_4\text{-}60\%\text{V}_2\text{O}_5$ environment for 50 cycles.

EPMA analysis at the cross-section of corroded NiCrBSi coated Superni 718 (Fig. 6.52) indicates the formation of a dense scale about 110 μm thick rich in nickel, silicon and chromium, along with some amounts of iron and aluminium. The topmost layer of the scale is rich in silicon. The nickel-rich splats present in the scale contain silicon and chromium at the splat boundaries. Chromium shows a tendency to diffuse towards the upper part of the scale and forms a thick band in the subscale region, and thereby leaves a chromium depleted band underneath. The presence of aluminium throughout the scale and the formation of a nearly continuous thick streak of aluminium exclusively at the coating-substrate interface, reflects the possibility of its outward diffusion from the substrate. Nickel diffuses from the coating to the substrate as indicated by the thick layer of nickel just below the coating-substrate interface. Existence of higher concentration of iron above the scale-substrate interface also reflects its outward diffusion tendency from the substrate. Traces of sodium, sulphur and vanadium are also present throughout the scale, thereby indicating ingress of the same across the splat boundaries. The titanium and molybdenum have also diffused from the substrate to the coating.

BSE image and elemental mappings for the corroded Stellite-6 coated Superni 718 show the formation of thick layer of nickel, about 35 μm , in the outermost part of the scale (Fig. 6.53). High intensity dots of iron and some traces of chromium also coexist with nickel in this layer of the scale. Just beneath of this layer, Cr forms a thick continuous layer thereby leaving a Cr-depleted area underneath. In the remaining part of the scale, Cr and Si show a tendency to form thick stringers at the boundaries of Co-rich splats. Traces of Ni and Fe are present throughout the scale. Titanium and aluminium also diffused from the substrate to the coating and form almost continuous thin streaks at the scale-substrate interface.

BSE image at the cross-section of corroded Ni-20Cr coated Superni 718 (Fig. 6.54) shows the formation of about 45 μm thick featureless layer in the upper part of the scale, whereas rest of the coating retains lamellar structure of as-sprayed coating. This compact and adherent topmost scale is found to be rich in nickel. In the remaining part chromium is present at the boundaries of Ni-rich splats. Chromium shows a tendency to form thick bands in the sub-scale, central portion and just above the scale-substrate interface. Iron, aluminium, titanium and silicon diffused from the substrate into the scale. Diffusion of iron is significant near the scale-substrate interface.

6.1.6 Hot Corrosion of Bare and Coated Superfer 800H

6.1.6.1 Corrosion Kinetics

Thermogravimetric data for the hot corroded bare and coated Superfer 800H is shown in Fig. 6.55. The HVOF coated Superfer 800H shows a much lower weight gain compared to the uncoated Superfer 800H in the given molten salt environment. The Ni-

20Cr coating on Superfer 800H shows the lowest weight gain among all the coatings under study. Its weight gain is approximately 1/11th of the weight gained by the uncoated superalloy. The Cr₃C₂-NiCr coating is the second lowest in weight gain, which is less than 1/5th of that indicated by the uncoated superalloy. The weight gained by NiCrBSi coating is little more than 1/5th and that gained by Stellite-6 coating is little less than 1/4th of the weight gain shown by the bare Superfer 800H. Figure 6.56 shows the cumulative weight gain/ unit area for all coatings under study.

From the weight gain data it can be inferred that necessary protection against hot corrosion is provided by all the coatings. The Ni-20Cr coating has provided the best protection, whereas the Cr₃C₂-NiCr and NiCrBSi coatings showed almost similar resistance to hot corrosion. The Stellite-6 coating has provided the least resistance to hot corrosion among all the coatings.

All the coatings have followed the parabolic behaviour up to 50 cycles (Fig 6.57). The parabolic rate constant, k_p , for bare Superfer 800H calculated on the basis of 50 cycles data is found to be $106.668 \times 10^{-10} \text{ g}^2 \text{ cm}^{-4} \text{ s}^{-1}$, where k_p for Cr₃C₂-NiCr, NiCrBSi, Stellite-6 and Ni-20Cr coated Superfer 800H are 5.363, 4.131, 6.308, and $1.180 \times 10^{-10} \text{ g}^2 \text{ cm}^{-4} \text{ s}^{-1}$, respectively.

6.1.6.2 Scale Thickness Measurement

The SEM back scattered images across the cross-section of corroded bare and coated Superfer 800H are shown in Fig. 6.58. The average scale thickness value measured from these micrographs for bare Superfer 800H is found to be 84 μm , and that for Cr₃C₂-NiCr, NiCrBSi, Stellite-6 and Ni-20Cr coated Superfer 800H are 280, 306, 313, and 300 μm , respectively.

6.1.6.3 X-ray Diffraction Analysis

The diffraction patterns for the bare and coated Superfer 800H after hot corrosion for 50 cycles at 900 °C are shown in Fig. 6.59. The various phases identified with the XRD analysis are presented in Table 6.5.

Table 6.5: Major and minor phases identified by XRD analysis of the hot corroded bare and coated Superfer 800H after 50 cycles.

Description	Major phases	Minor phases
Uncoated Superfer 800H superalloy	Fe ₂ O ₃ , NiO, NiFe ₂ O ₄ , FeV ₂ O ₄ , NiS, CrS, and FeS	Cr ₂ O ₃
Cr ₃ C ₂ -NiCr coated	NiO, Cr ₂ O ₃ , NiCr ₂ O ₄ , and Fe ₂ O ₃	----
NiCrBSi coated	NiO, Cr ₂ O ₃ , NiCr ₂ O ₄ , Fe ₂ O ₃ , and SiO ₂	----
Stellite-6 coated	CoO, Cr ₂ O ₃ , and CoCr ₂ O ₄	----
Ni-20Cr coated	NiO, and Cr ₂ O ₃	NiCr ₂ O ₄

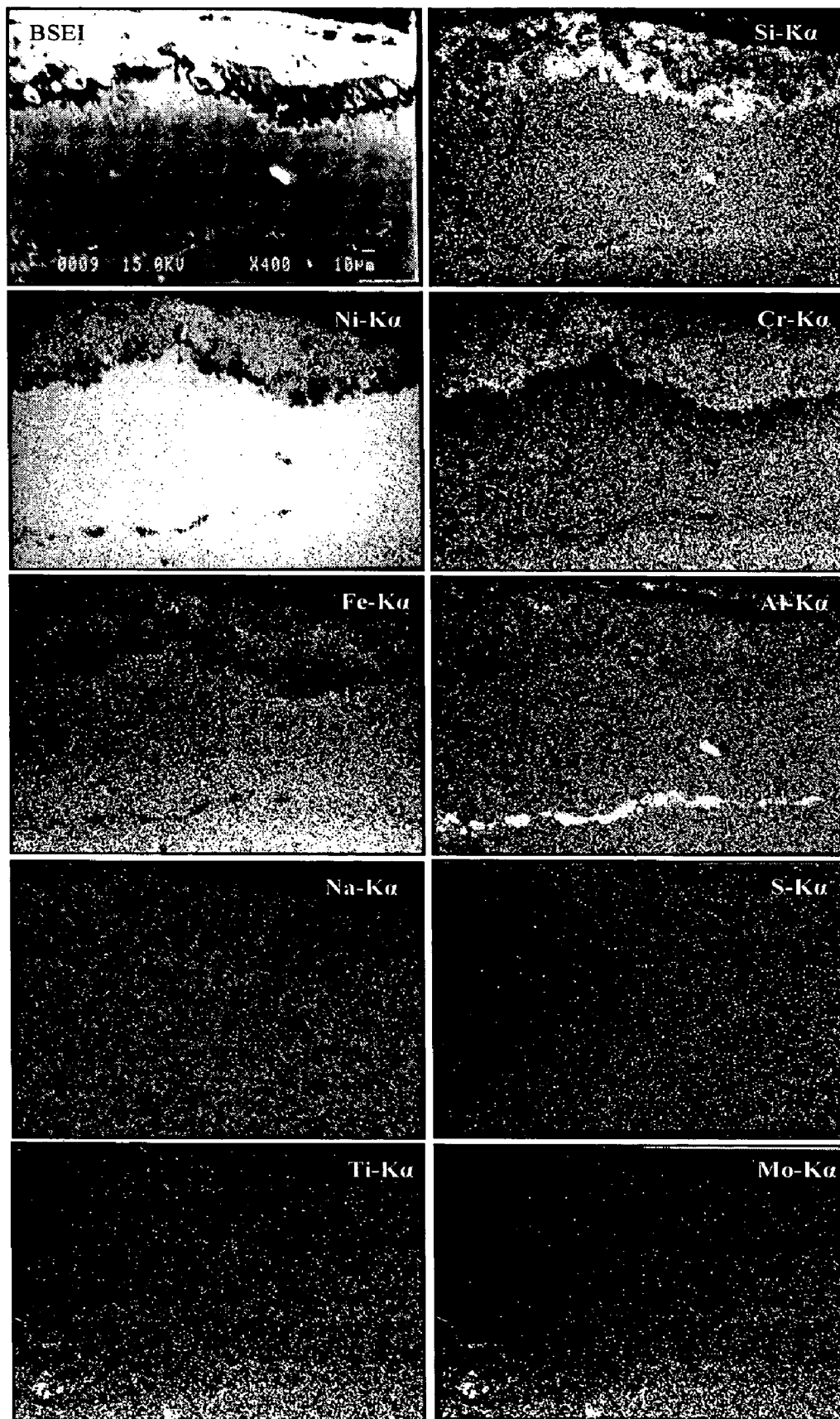


Fig. 6.52 Composition image (BSEI) and X-ray mappings of the cross-section of the NiCrBSi coated Superni 718 subjected to hot corrosion at 900 °C in Na_2SO_4 -60% V_2O_5 environment for 50 cycles.

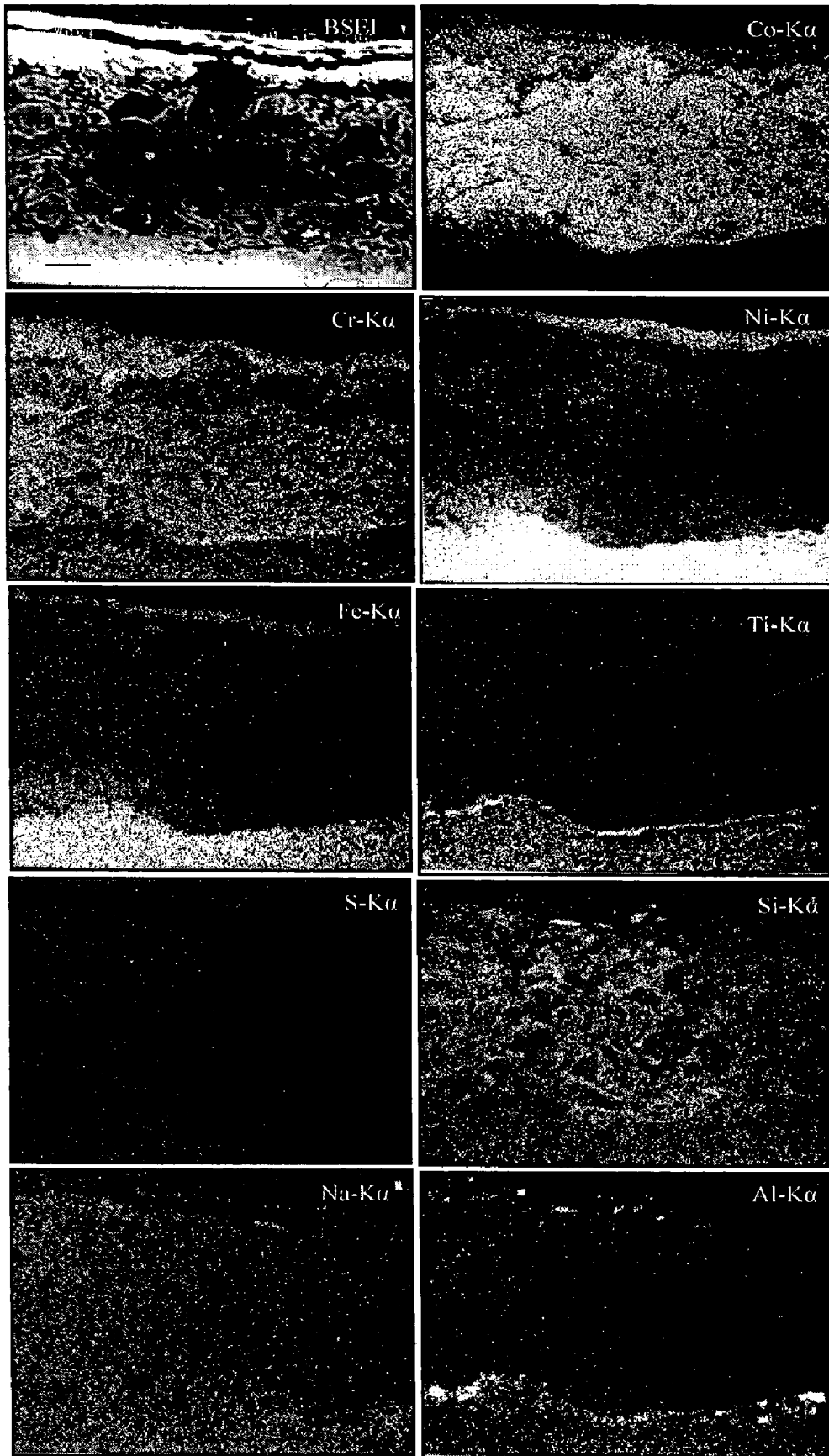


Fig. 6.53 Composition image (BSEI) and X-ray mappings of the cross-section of the Stellite-6 coated Superni 718 subjected to hot corrosion at 900 °C in Na_2SO_4 -60% V_2O_5 environment for 50 cycles.

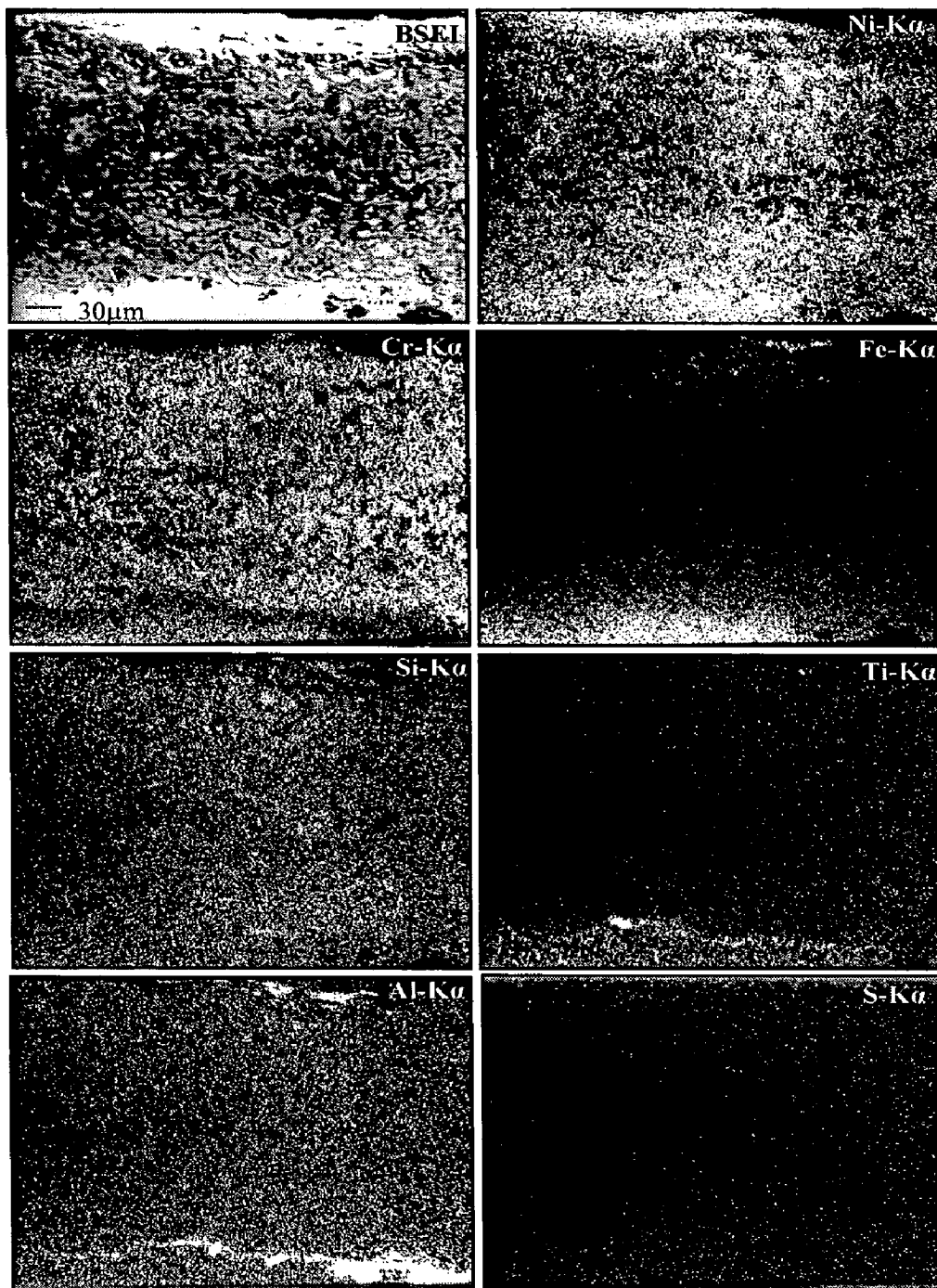


Fig. 6.54 Composition image (BSEI) and X-ray mappings of the cross-section of the Ni-20Cr coated Superni 718 subjected to hot corrosion at 900 °C in Na₂SO₄-60%V₂O₅ environment for 50 cycles.

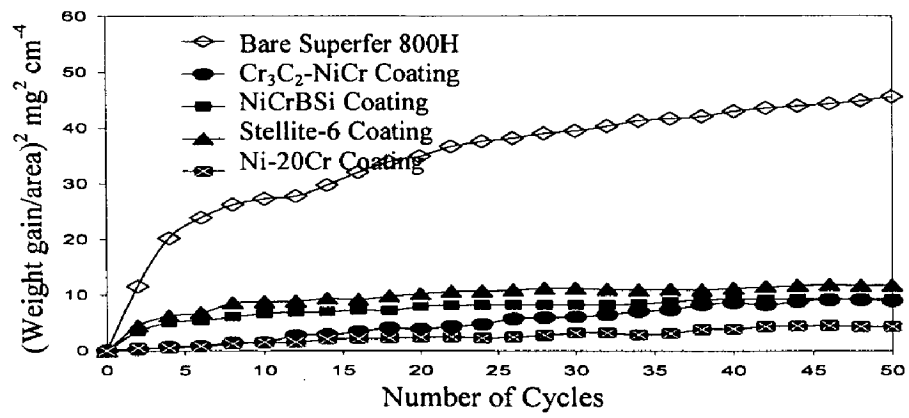


Fig. 6.55 Weight gain vs. number of cycles plot for the coated and uncoated Superfer 800H hot corroded for 50 cycles in Na₂SO₄-60%V₂O₅ environment at 900 °C.

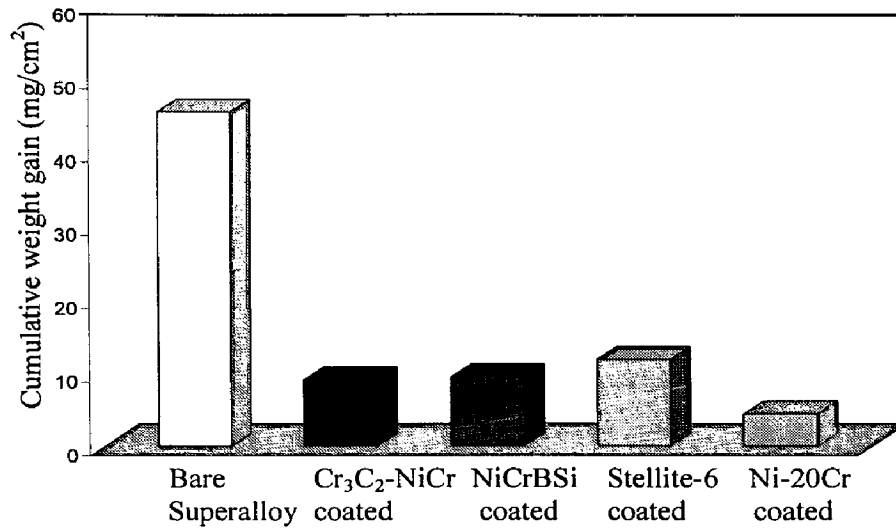


Fig. 6.56 Bar charts showing cumulative weight gain per unit area for the coated and uncoated Superfer 800H hot corroded for 50 cycles in Na₂SO₄-60%V₂O₅ environment at 900 °C.

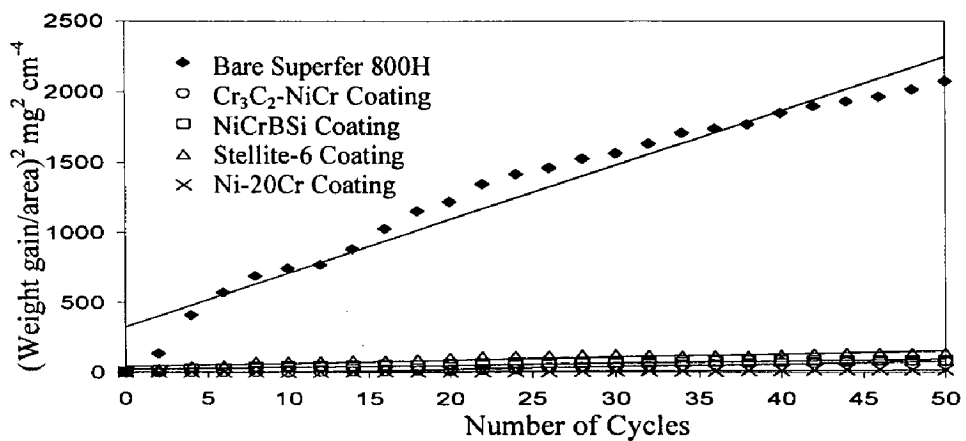


Fig. 6.57 (Weight gain/area)² vs. number of cycles plot for the coated and uncoated Superfer 800H hot corroded for 50 cycles in Na₂SO₄-60%V₂O₅ environment at 900 °C.

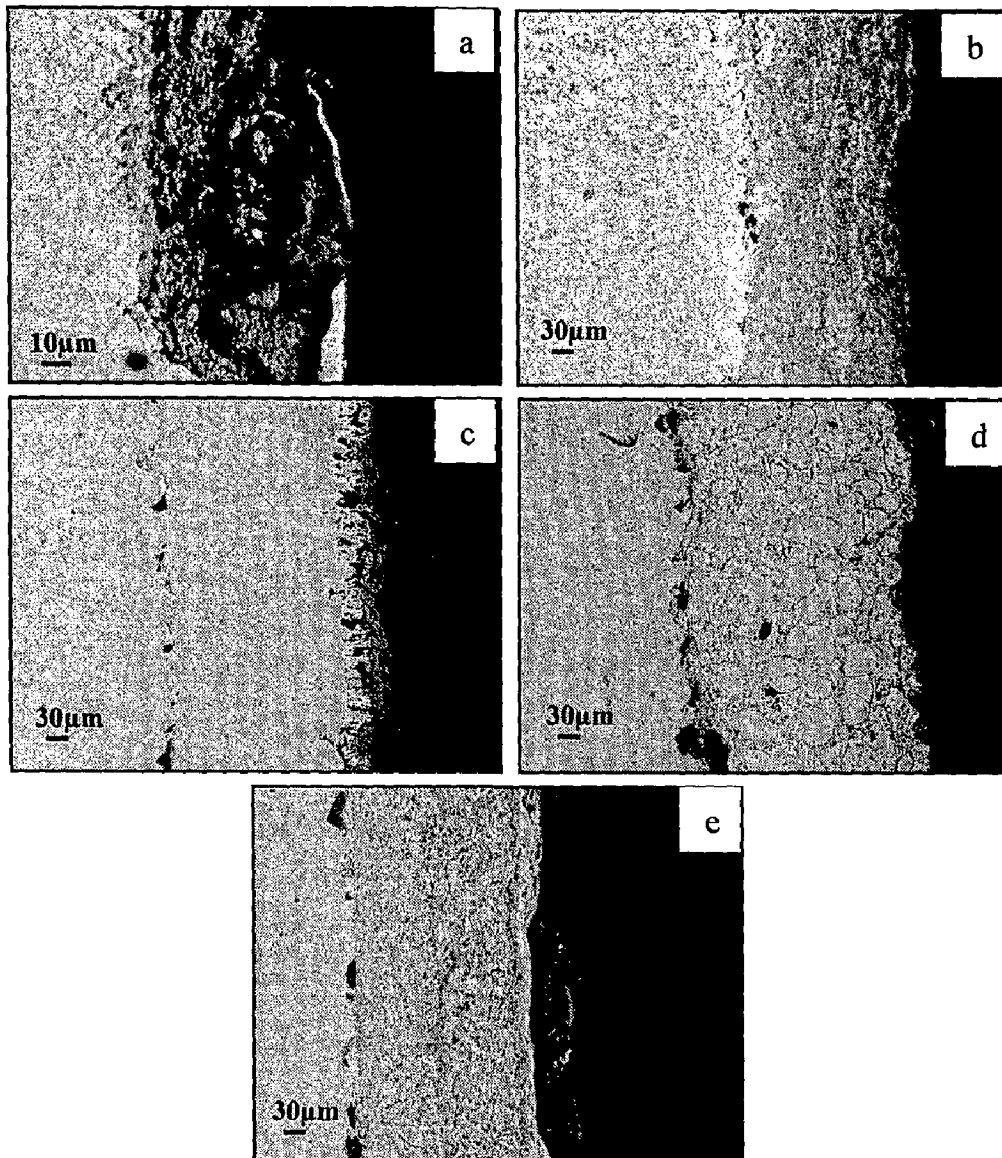


Fig. 6.58 SEM back scattered images for the bare and HVOF coated Superfer 800H subjected to hot corrosion in Na₂SO₄-60%V₂O₅ environment at 900 °C for 50 cycles: (a) Bare superalloy (b) Cr₃C₂-NiCr coated (c) NiCrBSi coated (d) Stellite-6 coated (e) Ni-20Cr coated.

while the Ni content increased from 32 wt% to 37.8 wt% which indicates the diffusion of Fe from the substrate to the coating and Ni from the coating to substrate during hot corrosion of the HVOF sprayed Cr₃C₂-NiCr coating. EDAX results also indicate the diffusion of small amounts of Si, Al and Mn from the substrate to the scale.

The uppermost part of the scale of corroded Stellite-6 coated Superfer 800H has relatively higher concentration of Cr and O, whereas the amount of Co decreased considerably indicating the formation of Cr-rich outer oxide scale (Point 5 in Fig. 6.61b). The EDAX analysis shows the formation of Cr₂O₃ (Point 4) at the boundaries of unoxidised Co-rich splats (Point 3). The presence of O and V at Point 4 indicates that these species penetrate into the coatings across the splat boundaries. Existence of Mn (1.2 wt%) at the uppermost part of the scale shows its diffusion from the substrate to the coating during hot corrosion of the superalloy.

In case of Ni-20Cr coated Superfer 800H, the dark black phase at the coating substrate interface (Point 2 in Fig. 6.61c), which is rich in Al and O, is an inclusion of aluminium oxide as already discussed in section 5.4. White phase in the scale of Ni-20Cr coated Superfer 800H consists of Ni-rich flat splats (Point 3) and contrast grey phase at the boundaries of these splats (Point 4) is found to be rich in Cr and O where the concentration of Ni has decreased substantially. The upper part of the scale mainly consists of Cr and Ni along with O (Point 6), whereas the subscale at Point 5 shows relatively more Ni concentration. The appearance of green colour patches after spallation, as shown in Fig. 6.61(c), is due to the presence of this Ni-rich oxide in the subscale. Significant amount of Fe is also present in the topmost part of the scale (Point 6) indicating its outward diffusion from the substrate.

6.1.6.5 EPMA Analysis

Elemental X-ray mappings at the cross-section of uncoated and coated Superfer 800H after cyclic hot corrosion in Na₂SO₄-60%V₂O₅ environment at 900 °C for 50 cycles are shown in Fig. 6.62 to Fig. 6.66.

Besides intensive spallation of the scale during each cooling period of the cycle, the BSE image of bare Superfer 800H (Fig. 6.62) shows the penetration of oxide scale up to a thickness of 124µm after 50 cycles of hot corrosion in the given molten salt environment. The upper part of the scale which is rich in Fe and Cr also contains Si, Ni, Al, and Mn. The Cr forms a thin streak at the lower part of the scale with a relatively higher concentration, thereby leaving a Cr-depleted layer underneath. In this Cr-depleted layer, the Ni forms a dense continuous band. At some other places in the scale there are small streaks containing Cr, Al and Si. Traces of V are present in the scale.

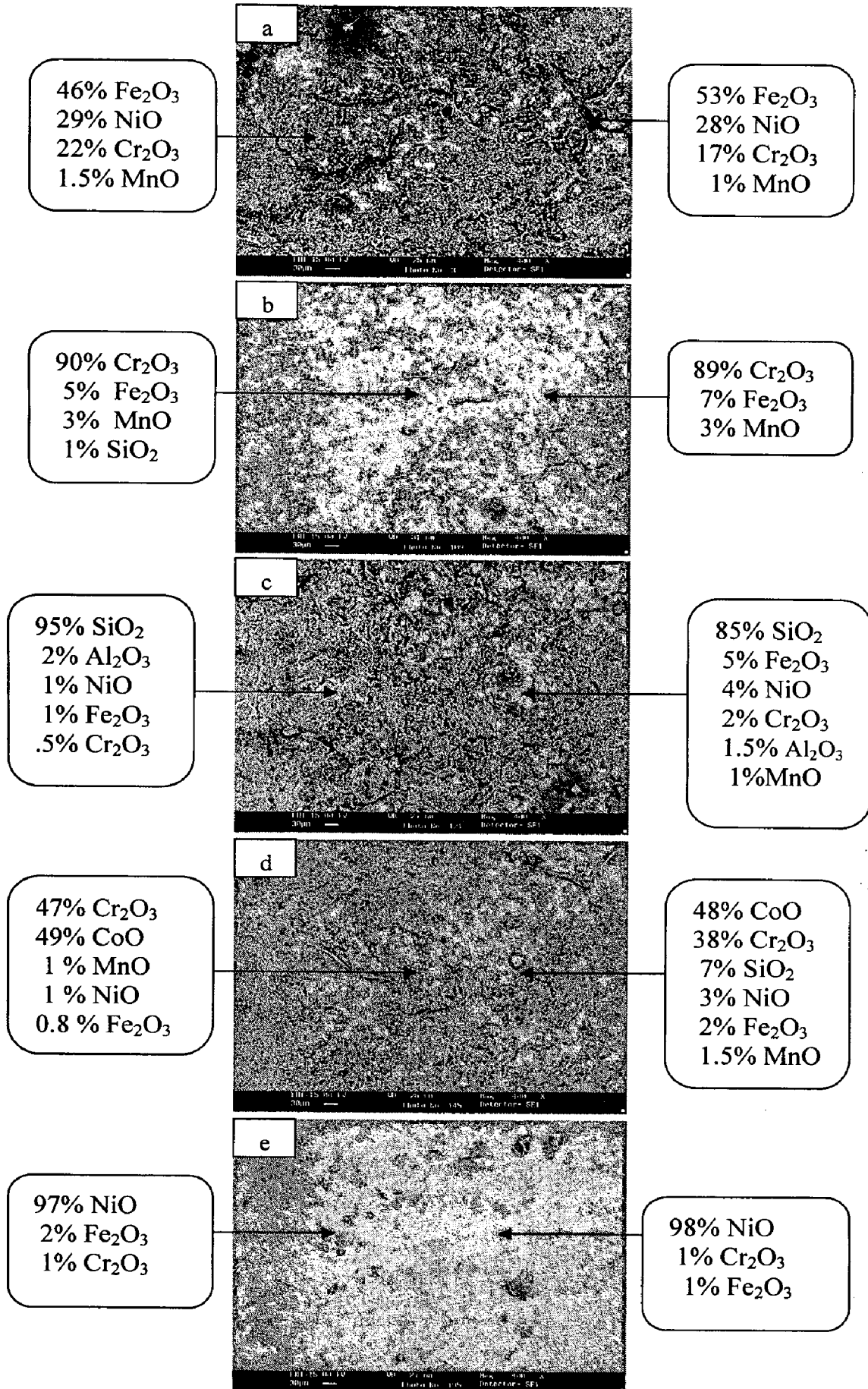


Fig.6.60 SEM/EDAX analysis showing elemental composition (wt.%) for the bare and coated Superfer 800H subjected to hot corrosion in Na₂SO₄-60%V₂O₅ environment at 900 °C for 50 cycles: (a) Bare Superfer 800H (b) Cr₃C₂-NiCr coated (c) NiCrBSi coated (d) Stellite-6 coated (e) Ni-20Cr coated.

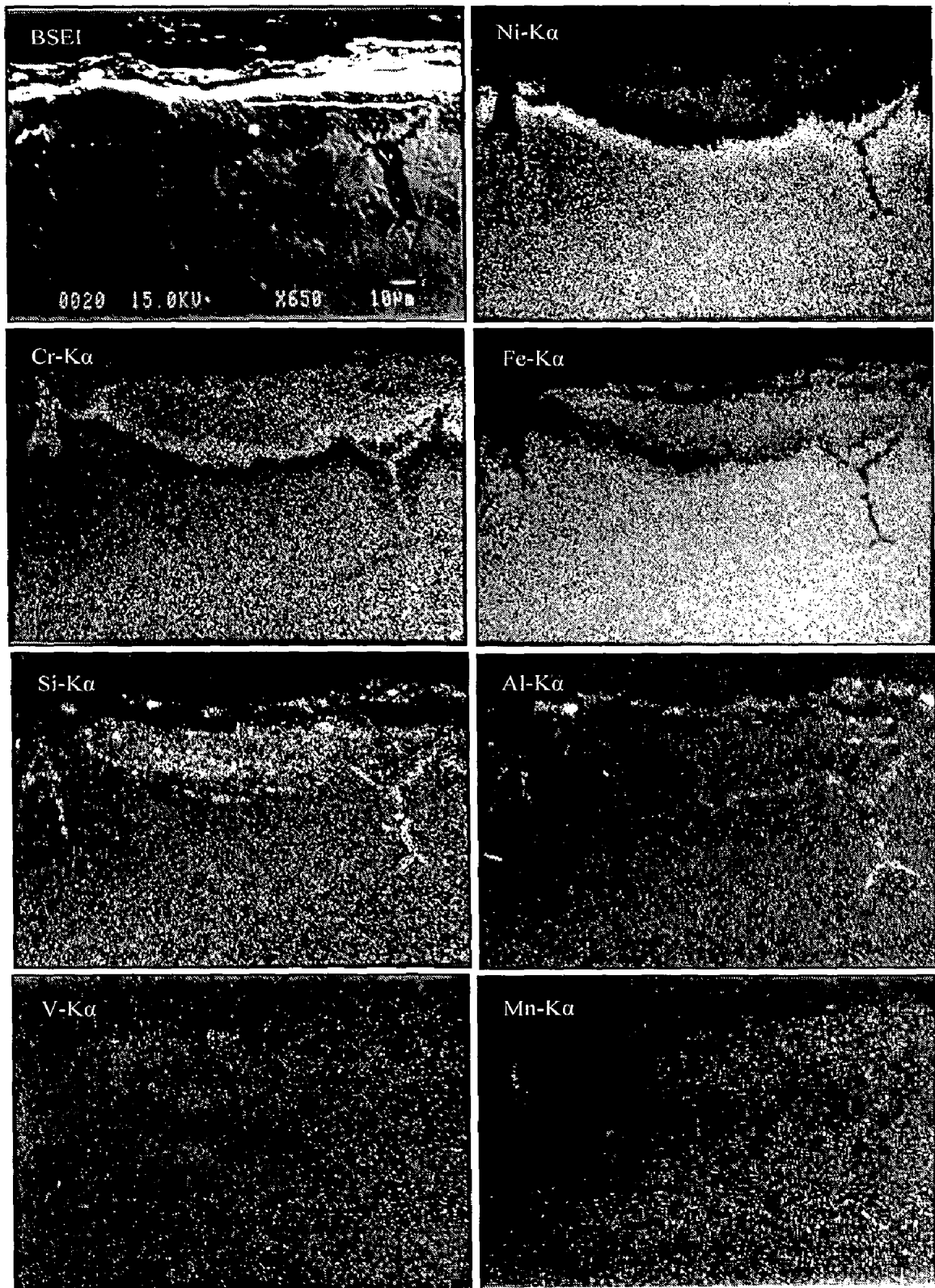


Fig. 6.62 Composition image (BSEI) and X-ray mappings of the cross-section of the bare Superfer 800H subjected to hot corrosion at 900 °C in Na_2SO_4 -60% V_2O_5 environment for 50 cycles.

In general, the presence of sodium, vanadium and sulphur in the scale formed on all the coatings deposited on Superfer 800H suggests that these corrosive species penetrate into the coatings through the splat boundaries (Figs. 6.63 to 6.66). Some elements of the substrate such as Si, Mn, Ti, Al, and Fe show their diffusion from the substrate to the scale, but the extent of diffusion varies depending on types of coatings. Invariably in all the cases, diffused Fe is found to be present in higher concentration at the top of scales.

In the case of Cr₃C₂-NiCr coated Superfer 800H (Fig. 6.63), the scale has a lamellar structure in which chromium is mainly present at the boundaries of Ni-rich splats. Silicon, manganese and titanium diffused from the substrate to form prominent thin streaks at the scale-substrate interface. Diffusion of Fe in this coating is found to be relatively less as compared to that in other coatings deposited on Superfer 800H. EPMA analysis for the corroded NiCrBSi coated Superfer 800H (Fig. 6.64) indicates the formation of dense scale with Ni, Cr and Si uniformly dispersed. Topmost part of the scale has more amounts of silicon. Diffusion of iron is found to be higher in this case especially just above the scale-substrate interface. Further a layer of V can be seen in the upper part of the scale. Aluminium tends to cluster at the scale-substrate interface where other elements are depleted.

Similar analysis of Stellite-6 coated Superfer 800 H (Fig. 6.65) shows that the scale is mainly rich in chromium and cobalt along with some amount of nickel. The upper layer of the scale has higher concentration of nickel and the second layer, just below of upper layer, has higher amount of chromium and cobalt. The remaining part of the scale consists of Co-rich splats and globules, with chromium mainly present at their boundaries. The existence of Fe-rich areas above the scale-substrate interface and higher concentration of Fe in the topmost scale indicate that the extent of outward diffusion of Fe from the substrate in this coating-substrate system is high. Aluminium shows its presence in the form of clusters, mainly at the scale-substrate interface where all other elements are found depleted of. The formation of these islands of aluminium at the interface is partly attributed to diffusion from the substrate and partly due to alumina powder retained during polishing of the specimen, as discussed earlier under section 5.4. Manganese shows a tendency to form thin streaks in the scale as well as at the scale-substrate interface.

EPMA analysis for the corroded Ni-20Cr coated Superfer 800H (Fig. 6.66) indicated that the scale has a lamellar structure and is rich in nickel and chromium. Careful observations show that the scale consists of Ni-rich splats with chromium at the splat boundaries. The upper part of the scale is found to be rich in nickel along with some amounts of iron and chromium. The extent of outward diffusion of Fe from the substrate above the scale-substrate interface is found to be high in this coating-substrate system. The chromium rich thick bands are formed in the sub-scale, central portion and

just above the scale-substrate interface of the oxidized coating. Titanium and aluminium show their tendency to form streaks at the scale-substrate interface.

6.2 SUMMARY OF RESULTS

Results as obtained after hot corrosion of uncoated and coated superalloys in the given molten salt environment are summarised in Table 6.6. These tabulated results are ready reference to compare the hot corrosion behaviour of coated and uncoated superalloys.

Table 6.6: Summary of the results for uncoated and coated superalloys exposed to molten salt ($\text{Na}_2\text{SO}_4\text{-60\%V}_2\text{O}_5$) at 900°C for 50 cycles.

Base super-alloy	Coating	Weight gain mg/cm^2	Scale thickness μm	$k_p \times 10^{-10} \text{ g}^2\text{cm}^{-4}\text{s}^{-1}$	Major XRD phases	Minor XRD phases	Remarks
Superni 75	Uncoated	12.01	108	9.716	NiO, Fe_2O_3 , NiCr_2O_4 , $\text{Ni}(\text{VO}_3)_2$, and FeV_2O_4	Cr_2O_3 , FeS, FeV, and TiO_2	Light brownish grey scale formed during 1 st cycle subsequently turned to dark grey. Scale is irregular, and has a tendency for spallation.
	Cr_3C_2 -NiCr coated	7.48	268	2.997	Cr_2O_3 , NiO, and NiCr_2O_4	Fe_2O_3	Dark grey scale appeared during the first 2-3 cycles turned to blackish green with the progress of the study. Surface scale is continuous and adherent. Scale has maintained good contact with the substrate.
	NiCrBSi coated	8.69	280	4.216	SiO_2 , Cr_2O_3 , NiCr_2O_4 , and Fe_2O_3	-----	Reddish brown colour compact and dense continuous scale is formed without any spallation even at the corners or edges. Sound contact between the coating and the base alloy is maintained after total exposure of 50 cycles.

	Stellite-6 coated	9.90	303	5.238	CoO, Cr ₂ O ₃ , CoCr ₂ O ₄ , and NiCr ₂ O ₄	Fe ₂ O ₃ , and NiO	Dark blackish grey scale formed during cyclic exposures showed some spallation in the powder form. The coating found to be integral with the base alloy after exposure. Green colour patches appear in the surface scale from where spallation has occurred.
	Ni-20Cr coated	7.21	255	2.213	NiO, Cr ₂ O ₃ , and NiCr ₂ O ₄	Fe ₂ O ₃ , and TiO ₂	The dark grey colour surface scale is found to be smooth and intact. Contact between the coating and the base alloy is found to be excellent during and after the cyclic hot corrosion runs.
Superni 600	Uncoated	15.77	65	13.710	NiO, Fe ₂ O ₃ , NiCr ₂ O ₄ , Ni(VO ₃) ₂ , FeV, and FeV ₂ O ₄	CrVO ₄	Fragile dark grey scale is formed. Cracks developed in the scale from 8 th cycle onward, resulting in spallation and peeling of the scale up to the end of study.
	Cr ₃ C ₂ -NiCr coated	8.42	257	3.720	Cr ₂ O ₃ , NiO, NiCr ₂ O ₄ , Fe ₂ O ₃ , and Ni(VO ₃) ₂	MnO ₂	Intact blackish green scale indicated minor spalling from the edges and corners. Coating maintained integrity with the substrate after total exposure of 50 cycles.
	NiCrBSi coated	9.25	289	4.841	SiO ₂ , Cr ₂ O ₃ , NiCr ₂ O ₄ , Fe ₂ O ₃ , and Ni(VO ₃) ₂	-----	Reddish brown colour irregular size globules, rich in SiO ₂ , are uniformly dispersed in the surface scale. The scale is compact and adherent. Sound contact between the coating and the base alloy is maintained after exposures.

	Stellite-6 coated	12.03	317	8.150	CoO, Cr ₂ O ₃ , CoCr ₂ O ₄ , NiCr ₂ O ₄ , Fe ₂ O ₃ , and NiO	MnO ₂	Scale showed some spallation in the powder form. The coating found to be adherent with base alloy after exposures.
	Ni-20Cr coated	7.16	244	3.05	NiO, NiCr ₂ O ₄ , Fe ₂ O ₃ , and Ni(VO ₃) ₂	Cr ₂ O ₃	A very shining silver grey scale is formed after 15 th cycle of the study. The surface scale is smooth and intact. The scale maintained continuity and adherence with the base alloy during cyclic exposures.
Superni 601	Uncoated	26.23	138	33.586	NiO, Fe ₂ O ₃ , NiCr ₂ O ₄ , Ni(VO ₃) ₂ , and FeV ₂ O ₄	SiO ₂ , and CrVO ₄	Fragile and uneven dark grey scale has number of cracks. Cracks developed at the edges during 1 st cycle. After 10 th cycle, the scale spalled from the surface which continued up to the end of study.
	Cr ₃ C ₂ -NiCr coated	8.18	270	4.703	Cr ₂ O ₃ , NiO, NiCr ₂ O ₄ , and Fe ₂ O ₃	Ni(VO ₃) ₂ , MnO, and Al ₂ O ₃	Smoother, continuous and adherent scale formed; minor spallation occurred from the edges and corners; integrity between the coating and base alloy preserved after corrosion runs.
	NiCrBSi coated	9.70	317	4.626	SiO ₂ , Cr ₂ O ₃ , NiCr ₂ O ₄ , and NiO	Fe ₂ O ₃ , Al ₂ O ₃ , and Ni(VO ₃) ₂	Reddish brown colour dense, compact and continuous scale is formed; scale maintained excellent integrity with the base alloy without any spalling.
	Stellite-6 coated	10.01	337	6.213	CoO, CoCr ₂ O ₄ , and NiCr ₂ O ₄	Fe ₂ O ₃	Scale showed some spallation in the powder form, no adherence loss is observed at the coating-substrate interface after total 50 cycles of exposure.

	Ni-20Cr coated	6.97	247	3.089	NiO, NiCr ₂ O ₄ , Fe ₂ O ₃ , Al ₂ O ₃ , and Ni(VO ₃) ₂	Cr ₂ O ₃	Shining silver grey colour continuous and adherent oxide scale is formed. Contact between coating and base alloy is found to be excellent during and after the cyclic exposures.
Superni 718	Uncoated	8.35* *Up to 16th cycle only	86	-	NiO, Cr ₂ O ₃ , Fe ₂ O ₃ , NiCr ₂ O ₄ , Ni(VO ₃) ₂ , TiO ₂ , FeV ₂ O ₄ , FeV, and FeS	---	Fragile and uneven scale with intensive spalling and sputtering occurred from 6 th cycle onward, which further intensified after 17 th cycle.
	Cr ₃ C ₂ -NiCr coated	8.14	244	3.77	Cr ₂ O ₃ , NiO, NiCr ₂ O ₄ , Ni(VO ₃) ₂ , and Fe ₂ O ₃	SiO, and Al ₂ O ₃	Homogeneous and regular blackish green scale is formed with little spalling from the edges and corners. Coating found to be adherent with the substrate during and after exposures.
	NiCrBSi coated	11.81	311	3.31	SiO ₂ , Cr ₂ O ₃ , NiO, NiCr ₂ O ₄ , and Fe ₂ O ₃	MnO ₂ , and Al ₂ O ₃	Compact, dense, continuous and relatively massive reddish brown colour oxide scale is formed. The coating maintained good contact with the base alloy during cyclic hot corrosion runs.
	Stellite-6 coated	10.83	288	6.94	Cr ₂ O ₃ , Fe ₂ O ₃ , NiO, CoCr ₂ O ₄ , and NiCr ₂ O ₄	MnO ₂	Scale showed some spallation in the powder form. Sound contact between the coating and the base alloy is maintained during and after exposures.
	Ni-20Cr coated	4.72	222	1.44	NiO	Cr ₂ O ₃ , and NiCr ₂ O ₄	A smooth and very shining silver grey scale formed during cyclic exposures is found to be adherent and intact. No indication of any adherence loss between the coating and the substrate alloy is observed.

Superfer 800H	Uncoated	45.53	84	106.668	Fe ₂ O ₃ , NiO, NiFe ₂ O ₄ , FeV ₂ O ₄ , NiS, CrS, and FeS	Cr ₂ O ₃	Black colour irregular scale is formed with a tendency for spallation. Micro spalling of the scale started from 3 rd cycle, which intensified after 12 th cycle onwards and continued till the end of study.
	Cr ₃ C ₂ - NiCr coated	8.93	280	5.363	NiO, Cr ₂ O ₃ , NiCr ₂ O ₄ , and Fe ₂ O ₃	----	Minor spallation of the scale occurred during the cyclic study. The coating has broken from one corner of the specimen during last cycle of the study.
	NiCrBSi coated	9.3	306	4.131	NiO, Cr ₂ O ₃ , NiCr ₂ O ₄ , Fe ₂ O ₃ , and SiO ₂	----	Reddish brown colour granular scale formed during cyclic exposures is found to be compact, regular and adherent. Sound contact between the coating and base alloy is maintained after exposure.
	Stellite-6 coated	11.72	313	6.308	CoO, Cr ₂ O ₃ ,and CoCr ₂ O ₄	----	The oxide scale showed some spallation in the form of powder particles from 6 th cycle onwards. The coating found to be integral with the base alloy during and after the hot corrosion exposures.
	Ni-20Cr coated	4.33	300	1.180	NiO, and Cr ₂ O ₃	NiCr ₂ O ₄	A uniform, homogeneous and continuous oxide scale is formed on this coated superalloy. The coating maintained excellent contact with the base alloy during and after cyclic exposures to the molten salt environment.

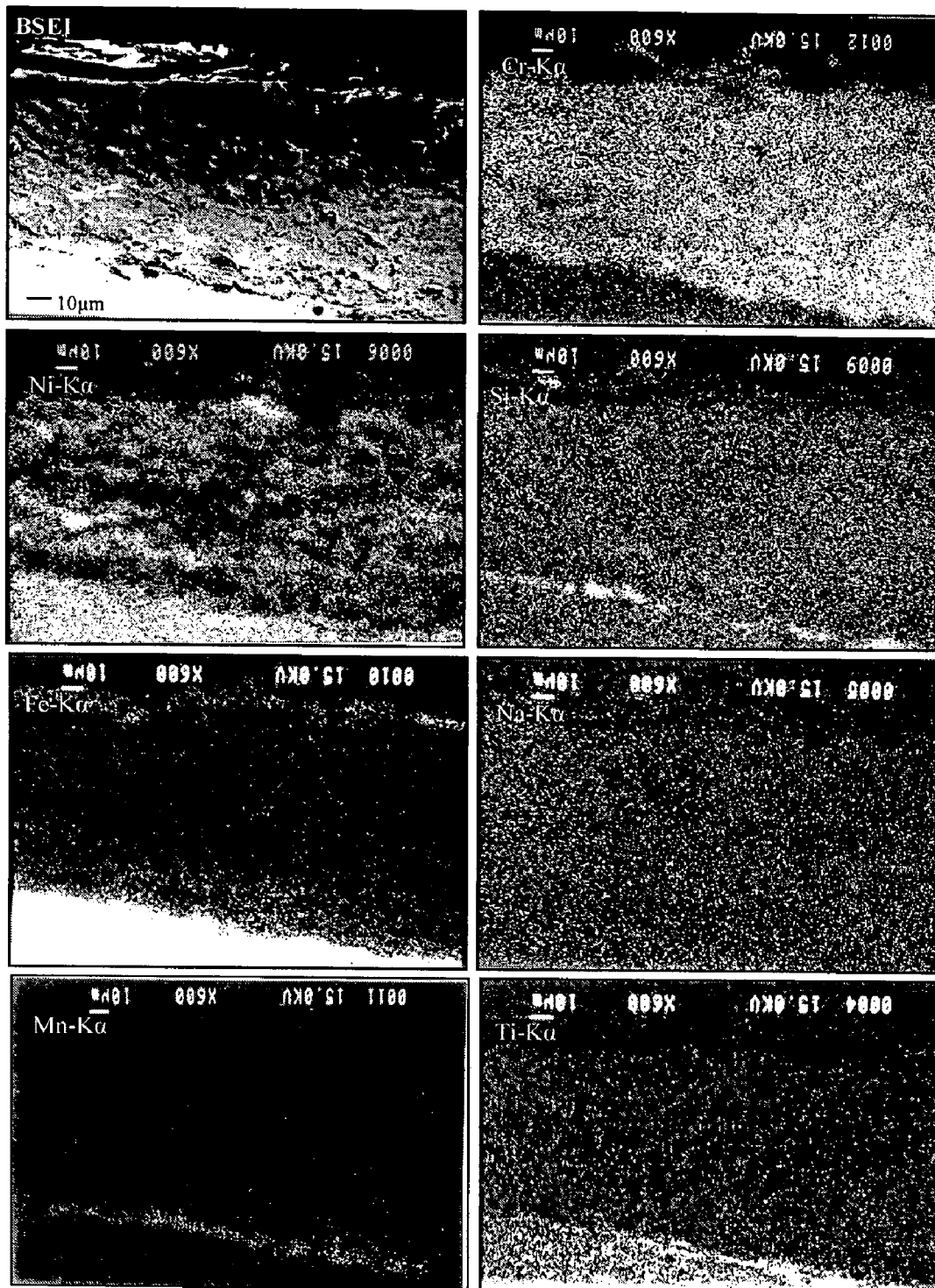


Fig. 6.63 Composition image (BSEI) and X-ray mapping of the cross-section of the $\text{Cr}_3\text{C}_2\text{-NiCr}$ coated Superfer 800H subjected to hot corrosion at $900\text{ }^\circ\text{C}$ in $\text{Na}_2\text{SO}_4\text{-60\%V}_2\text{O}_5$ after 50 cycles.

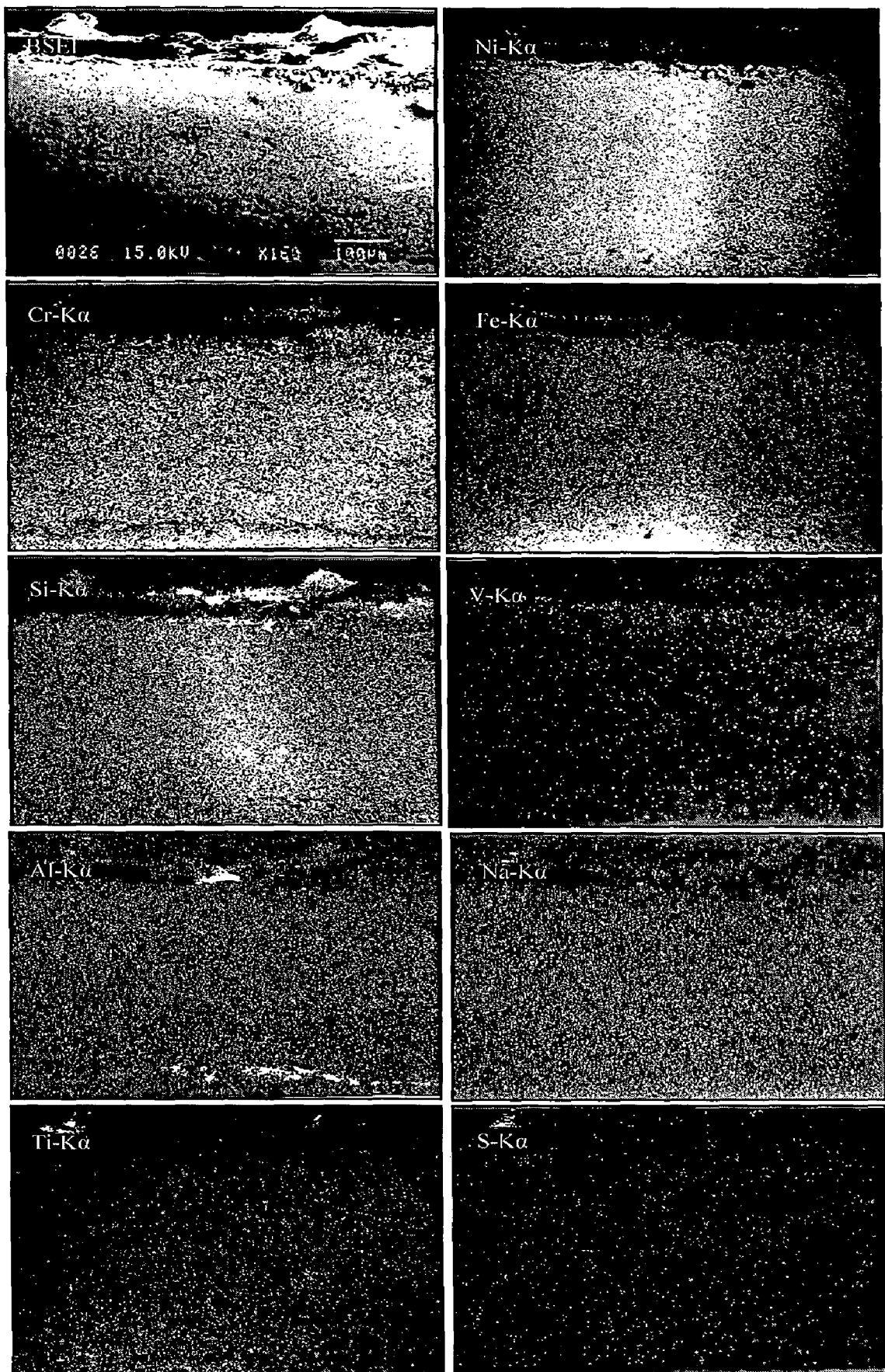


Fig. 6.64 Composition image (BSEI) and X-ray mapping of the cross-section of the NiCrBSi coated Superfer 800H subjected to hot corrosion at 900 °C in Na_2SO_4 -60% V_2O_5 after 50 cycles.

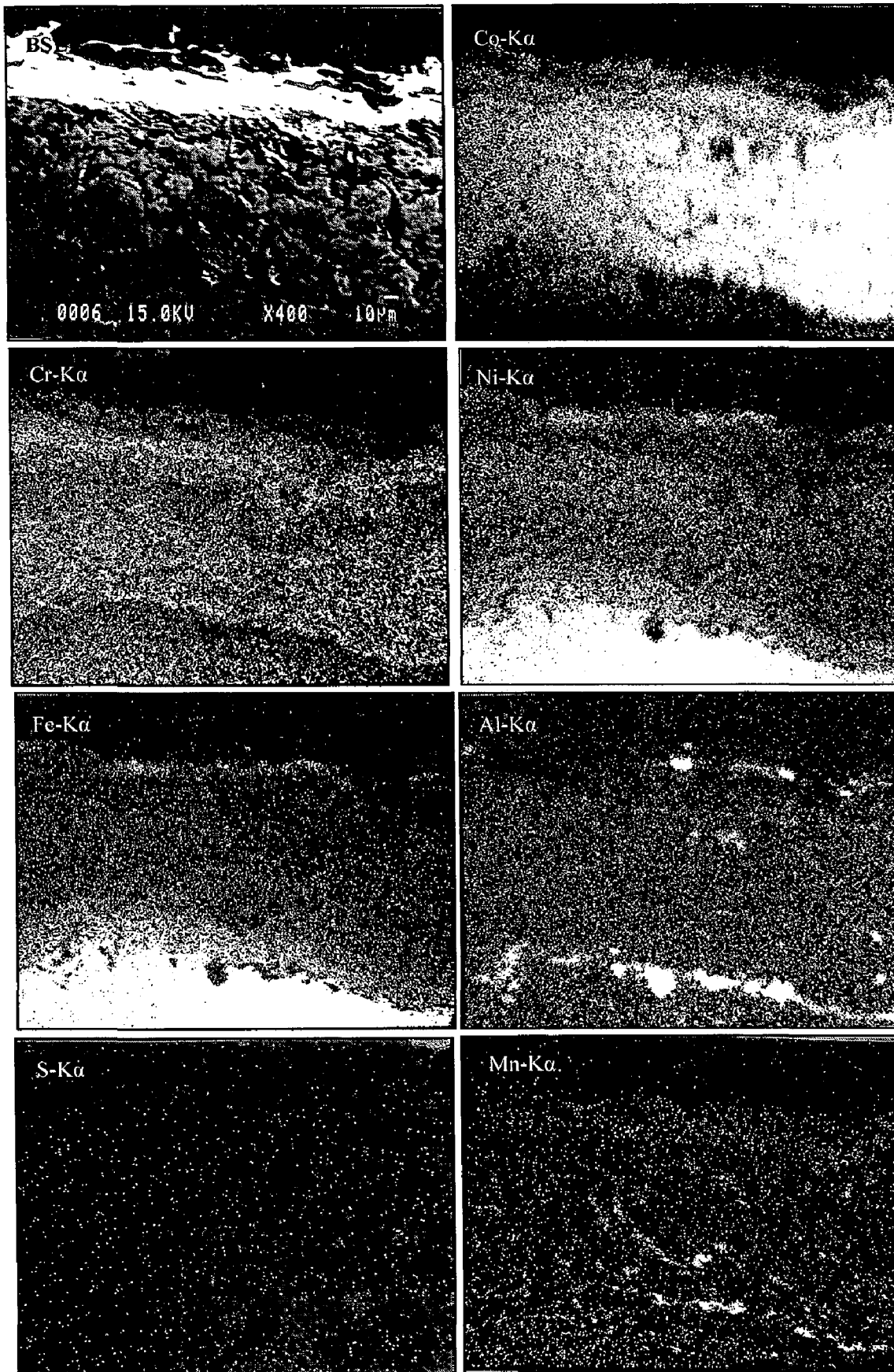


Fig. 6.65 Composition image (BSEI) and X-ray mapping of the cross-section of the Stellite-6 coated Superfer 800H subjected to hot corrosion at 900 °C in Na_2SO_4 -60% V_2O_5 after 50 cycles.

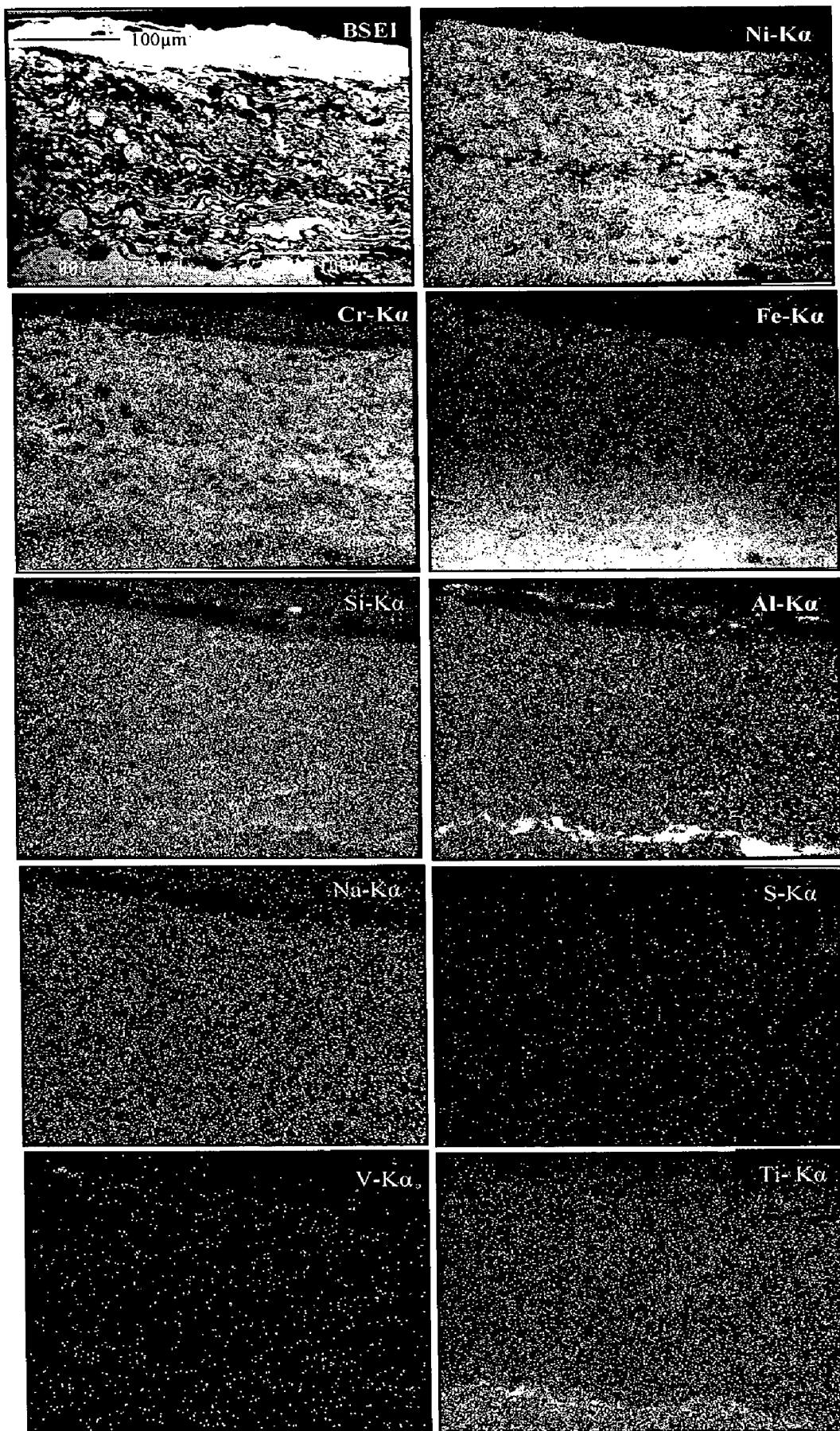


Fig. 6.66 Composition image (BSEI) and X-ray mapping of the cross-section of the Ni-20Cr coated Superfer 800H subjected to hot corrosion at 900 °C in Na_2SO_4 -60% V_2O_5 after 50 cycles.

6.3 COMPREHENSIVE DISCUSSION

6.3.1 Uncoated Superalloys

In comparison to HVOF coated superalloys, the uncoated superalloys in general show accelerated oxidation in Na_2SO_4 -60% V_2O_5 environment at 900 °C and oxide scale penetrates deeply into the substrates. The Ni-based superalloy Superni 718 was worst affected by the hot corrosion attack in the given molten salt environment. SEM micrographs of the corroded bare superalloys noticeably show the presence of cracks and spallation tendency of the scale (Figs. 6.22a, 6.34a, 6.46a, and 6.58a). These SEM images of bare superalloys indicate the fluxing action of the molten salt under the thermal cyclic test conditions at 900 °C. The surface oxide scale formed on the bare superalloys is irregular and porous due to reprecipitation by fluxing action (Figs. 6.12a, 6.24a and 6.60a).

On the basis of thermogravimetric data it is concluded that the Ni-based Superni 75 offers maximum resistance and Fe-base superalloy Superfer 800H offers least resistance to hot corrosion amongst the superalloys Superni 75, 600, 601 and Superfer 800H. The weight gain values for Superni 718 could not be measured for 50 cycles due to intensive sputtering and spalling of the scale. Therefore weight gain data for Superni 718 can not be compared with others (the data is available only for 16 cycles). In terms of the cumulative weight gain for 50 cycles (Fig. 6.67), the hot corrosion resistance of the superalloys under study can be arranged in the following order:

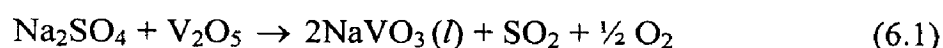
Superni 75 > Superni 600 > Superni 601 > Superfer 800H

The superior corrosion resistance of Ni-based superalloys can be attributed to the development of thick layer of nickel oxide, and to the formation of nickel vanadates. The oxides of nickel are more protective than the oxides of iron formed dominantly during the hot corrosion of Fe-based superalloy. Moreover, in comparison to the Fe-based superalloy Superfer 800H, a relatively thick and dense protective layer of chromium oxide is formed on the Ni-based superalloys. The formation of $\text{Ni}(\text{VO}_3)_2$ in case of Ni-based superalloys acts as a diffusion barrier for the oxidizing species (Seierstein and Kofstad, 1987).

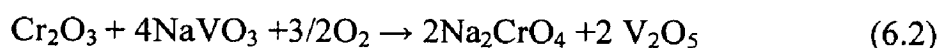
Amongst the Ni-based superalloys, the Superni 75 and Superni 600 performed relatively better than Superni 601 under the given conditions. The comparatively less corrosion resistance shown by Superni 601 is due to the presence of lower amounts of $\text{Ni}(\text{VO}_3)_2$ as revealed by XRD analysis. Further, the formation of a compact, continuous, and adherent scale in the case of Superni 75 (Figs. 6.10a and 6.14) provides better resistance to hot corrosion as compared to the scale formed on Superni 600 (Figs. 6.22a and 6.26).

Invariably all the superalloys under study showed some deviations from the parabolic rate law of oxidation during the 50 cycles of hot corrosion. This is attributed to the intensive spalling and sputtering of the oxide scale. In the case of Superni 718, the spalling and sputtering was so intensive that it became impossible to evaluate the overall weight gain up to 50 cycles. The parabolic rate constants (k_p in $10^{-10} \text{g}^2 \text{cm}^{-4} \text{s}^{-1}$) for uncoated Superni 600, Superni 601 and Superfer 800H subjected to hot corrosion in the given molten salt environment at 900 °C for 50 hours under cyclic conditions are found to be 13.7, 33.586 and 106.668 respectively, whereas these values for the same alloys cyclic oxidized in air at same temperature for same number of cycles are reported to be as 0.061, 0.161 and 0.088, respectively (Singh, 2005E). Similarly under the same conditions, the value of k_p ($10^{-10} \text{g}^2 \text{cm}^{-4} \text{s}^{-1}$) for Superni 75 hot corroded in molten salt environment is calculated as 9.716, while this alloys oxidized in air showed transition in parabolic rate constant from 0.016 to 0.0217 after 16th cycle as reported by Singh (2005E). From this data it can be inferred that the uncoated Ni- and Fe-based superalloys under study showed lesser resistance to the given molten salt environment in comparison to the air oxidation.

The rate of weight gain for uncoated superalloys increases continuously, although the rate of increase is high during the initial period of exposure (Fig 6.68). This high rate of increase in weight gain during initial period can partially be attributed to the formation of NaVO_3 . In the temperature range of 900 °C, the Na_2SO_4 -60% V_2O_5 interact to form NaVO_3 having a melting point of 610 °C as proposed by Kolta et al., (1972)



This NaVO_3 acts as a catalyst and also as an oxygen carrier to the base alloy, which leads to rapid oxidation of the basic elements of the superalloys to form the protective oxide scale during the earlier stages of hot corrosion. Further, the oxide of nickel combines with the oxides of chromium and iron to form spinels NiCr_2O_4 and NiFe_2O_4 , respectively. The rapid increase in weight gain during initial hours has also been reported by Gitanjali (2003) while studying the hot corrosion behaviour of nickel-based superalloys in the same environment and at the same temperature. Slower increase in weight gain during the subsequent cycles is probably due to the growth of oxides, and simultaneous dissolution of Cr_2O_3 in the molten salt because of the following reaction (Seiersten and Kofstad, 1987 ; Swaminathan et al., 1993):



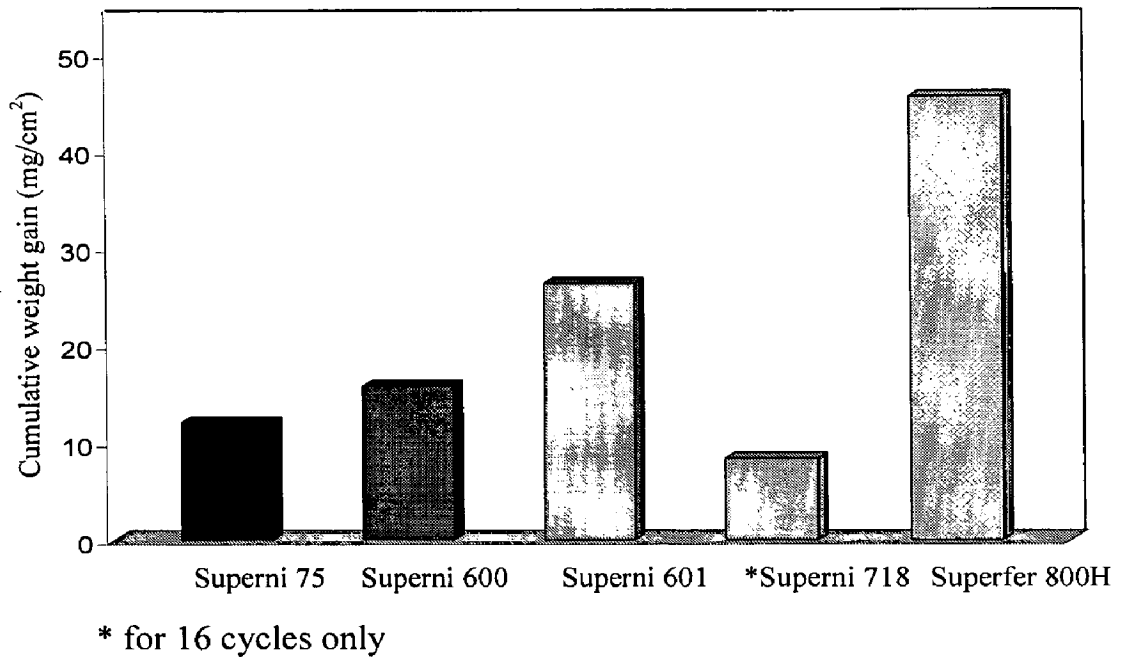


Fig. 6.67 Bar charts showing cumulative weight gain per unit area for uncoated superalloys hot corroded for 50 cycles in $\text{Na}_2\text{SO}_4\text{-60\%V}_2\text{O}_5$ environment at 900°C .

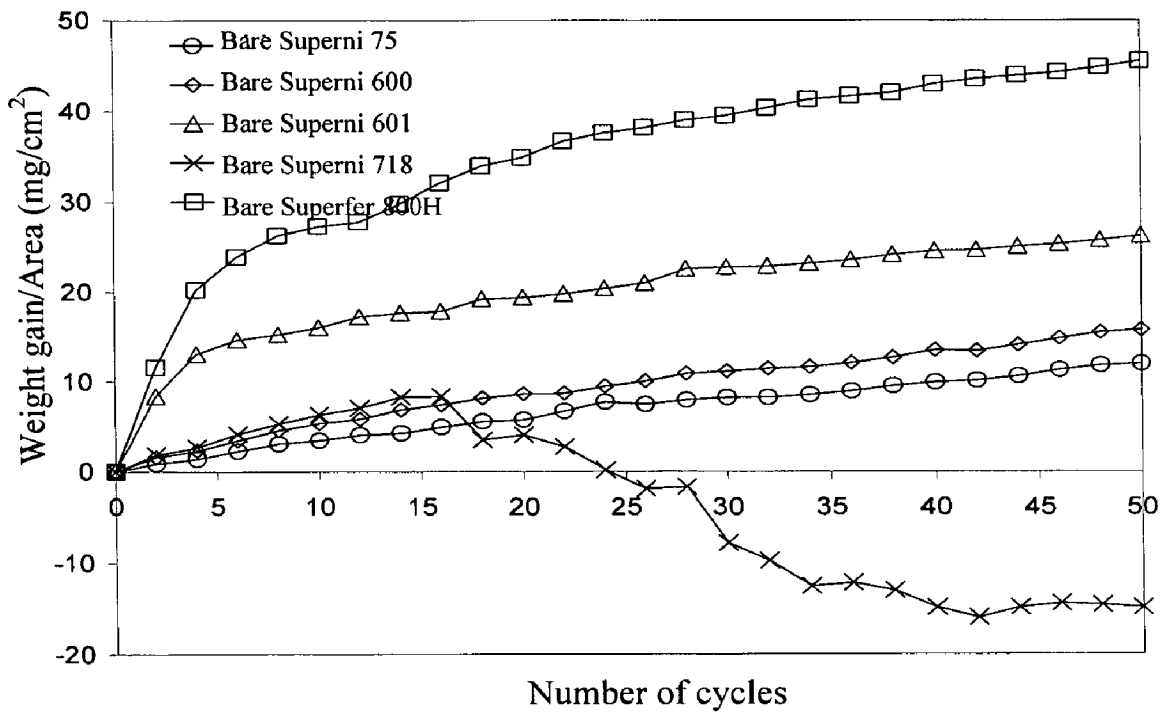
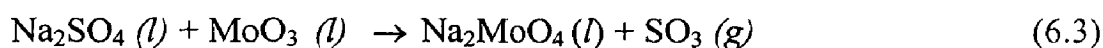


Fig. 6.68 Weight gain vs. number of cycles plot for uncoated superalloys subjected to hot corrosion for 50 cycles in $\text{Na}_2\text{SO}_4\text{-60\%V}_2\text{O}_5$ environment at 900°C .

This Na_2CrO_4 gets evaporated as a gas (Fryburg et al., 1984). After a period of high oxidation rate, the slow rate of oxidation with the further progress of study can also be ascribed to the slower growth rate of chromia scale (Seal et al., 2000). Furthermore, the formation of nickel vanadate or iron-vanadate in the scales with the progress of study has also contributed to slower oxidation rate as these vanadates are capable of decreasing the short circuit diffusion of ions as suggested by Swaminathan et al., (1993) and Tiwari and Prakash (1997). Based on the EPMA analysis with the support of SEM, XRD, EDAX (surface/cross-section) analyses, the possible mechanism governing the corrosion process for superalloy Superni 600 in the environment of Na_2SO_4 -60% V_2O_5 is shown in Fig. 6.69.

In addition to the above mentioned mechanism, the intensive spalling and sputtering of the scale of Superni 718 can be ascribed to the presence of higher amount of molybdenum (3.05%). The molybdenum forms MoO_3 , which according to Peters et al. (1976) reacts with Na_2SO_4 to form a low melting point phase Na_2MoO_4 by the following reaction:



This might have caused alloy induced acidic fluxing and accelerated spalling of the scale. Identical findings have also been reported by Pettit and Meier (1985), Misra (1986), Shih et al. (1989) and Singh (2005E).

The surface XRD analysis indicates the formation of Fe_2O_3 and NiO as common main phases in the surface scales of all the Ni- and Fe-based superalloys. Further, the spinel NiCr_2O_4 and vanadates of nickel and iron are present in the surface scale of Ni-base superalloys, whereas Fe-base superalloy forms spinel NiFe_2O_4 and iron vanadates. The XRD analysis shows the formation of sulfides of iron/nickel in the surface scale of Superni 718 and Superfer 800H, despite never sputtering and spallation of the scale of these superalloys during hot corrosion study. This indicates that the corrosive species of the molten salt environment penetrated deeply and caused the internal sulfidation of the substrate superalloys (Figs. 6.47 and 6.59). These X-ray diffraction results are well supported by SEM/EDAX and EPMA results.

6.3.2 HVOF Coated Superalloys

In general, the HVOF coatings under study showed protective behaviour in the given molten salt environment at 900 °C under cyclic conditions and performed better than the bare superalloys selected for the present research work. The results of the present investigation show that due to selective oxidation property of chromium and

silicon, Cr_2O_3 and SiO_2 , formed along the boundaries of nickel-rich and cobalt-rich splats and in pores, have blocked the passages and enabled the coatings to develop barriers against the penetration and diffusion of corrosive species. Additionally, very low porosity and the flat splat structure of the coatings have also contributed in developing hot corrosion resistance at higher temperatures, since corrosive species mostly propagate along the splat boundaries and through the pores and voids. Due to dense and flat splat structure of the coatings, the distance from the coating surface to coating-substrate interface along splat boundaries is highly increased which enables the coatings to develop resistance against hot corrosion.

6.3.2.1 Cr_3C_2 -NiCr Coating

The weight gain data for the HVOF Cr_3C_2 -NiCr coated superalloys shows that the coating is successful in reducing the overall weight gain (Fig. 6.70). The parabolic rate constants for the uncoated superalloys are found to be greater than those for the coated superalloys and all the coated superalloys showed parabolic oxidation behaviour for the total 50 cycles of study in the given environment. The weight gain data for the bare Superni 718 could be measured up to 16th cycles only due to intensive spalling and sputtering of the scale. However, the cumulative weight gain per unit area of coated Superni 718 for 50 cycles (8.14 mg/cm^2) is found to be less than the corresponding value for 16 cycles of uncoated Superni 718 (8.35 mg/cm^2). Hence, it can be inferred that the necessary protection is provided by the Cr_3C_2 -NiCr coating to the Ni- and Fe-based superalloys in the given molten salt environment. The minor deviations from the parabolic rate law as shown by the coated specimens in the present study were also reported by Choi et al. (2002) and Liu et al. (1998). This minor scatter in data is attributed to the formation and rapid growth of inhomogeneous oxides during hot corrosion process as suggested by Choi et al. (2002). The relative hot corrosion rates for the Cr_3C_2 -NiCr coated superalloys based on the thermogravimetric data, although not very significantly apart, can be arranged in the following order:

Superfer 800H > Superni 600 > Superni 601 > Superni 718 > Superni 75

In general, the weight gain of the coated specimens is relatively high during the first few cycles of hot corrosion, but subsequent increase in weight is gradual. The initial high oxidation rate of the coated specimens might be ascribed to the rapid formation of oxides at the splat boundaries and within open pores due to the penetration of the oxidizing species. These oxides once formed, block the pores and splat boundaries, and act as diffusion barriers to the further ingress of oxidizing species. As a consequence, the

growth of the oxides is confined mainly to the surface of the specimens. Therefore, a steady state of oxidation has been reached with the progress of exposure time.

The presence of Cr_2O_3 , NiO , and NiCr_2O_4 surface oxides, as detected by XRD analysis, has contributed to the hot corrosion resistance of Cr_3C_2 -NiCr coated superalloys. The presence of these phases is further confirmed by EDAX analysis as well as by EPMA analysis. The EPMA analysis shows the formation of thick and dense Cr_2O_3 -rich scale (Figs. 6.15b and 6.27). These oxides, particularly Cr_2O_3 , partially inhibit oxidation of the substrate alloys by blocking the diffusion of reacting species towards the substrate alloys, as has been suggested by Nicoll and Wahl (1983), Stroosnijder et al. (1994) and Toma et al. (1999). Presence of the spinel NiCr_2O_4 in the oxide scales also helps to develop oxidation resistance as these spinel phases usually have much smaller diffusion coefficients for the cations and anions than those in their parent oxides (Chatterjee et al., 2001). The author has reported the formation of these phases in earlier publications (Sidhu et al., 2006C, 2006E and 2006F).

The difference in performance of this coating on different substrates can be attributed to the diffusion of substrate elements. Substrate elements diffuse up to top of the scale and form less protective oxides as has been indicated by XRD/EDAX/ EPMA analysis. Shifler (2004) also reported that high-temperature coatings on various superalloy substrates behaved differently during 1000 hours of exposure in a hot corrosion environment at 899°C . He reported that differences in chemical compositions between a coating and a substrate alloy can lead to inter-diffusion between these materials which can modify the oxidation and corrosion resistance of the coating.

The relatively lower hot corrosion resistance of this coating on Superfer 800H might be due to the diffusion of substrate elements such as Fe, Ti and Mn. Diffusion of iron reached up to top of the scale where it is oxidized to form a thin layer of less protective iron oxide (Fig. 6.63). The better performance of the coated Superni 75 is due to the formation of a thick layer of more protective chromium oxide in the topmost part of the scale instead of Fe_2O_3 . The diffusion of iron is relatively less in this case (Fig. 6.15b).

It can be seen from the EPMA analysis of the coated superalloys that there is minor diffusion of basic elements from the substrate during earlier cycles of the study. This indicates that the coating has been successful in acting as a reservoir for the formation of protective oxides/spinels, and consequently increases the service life of the substrate superalloys. Moreover, it is clear from the back scattered images for the coated superalloys subjected to hot corrosion for 50 cycles that the substrates have not been affected by internal oxidation and the coatings appear to be integral with the substrates.

This is further confirmed by the cross-sectional EDAX analysis which shows that the oxygen has not penetrated into the substrate superalloys (Figs. 6.37a, 6.49a and 6.61a). Further, it is obvious from the oxygen maps of Cr₃C₂-NiCr coated superalloys that the base superalloys have not undergone internal oxidation (Figs. 6.15b and 6.27).

The scales formed on the coated specimens were intact with no or very little spallation. In fact, all the coatings under study viz. Cr₃C₂-NiCr, NiCrBSi, Stellite-6 and Ni-20Cr maintained their continuous surface contact with the base superalloys, when subjected to molten salt induced corrosion at 900 °C under cyclic conditions. During cooling periods of the thermal cycles, some minor spallation was observed at or near the edges and corners of the coated superalloys in the form of tiny flakes. This is due to the development of superficial cracks along or near the edges and corners, which resulted in minor spalling of the coating from/near the edges, the extent of which is insignificant in context of the overall surface area of the specimens. These spalled flakes came out from the outer layers of the coatings. This phenomenon has been observed in most of the cases. This tendency is attributed to the differential thermal expansion coefficient values of the oxide scale, coatings, and the base superalloys (Table A.2) (Rapp et al., 1981B and Liu et al., 2001). The stress concentration factor at the sharp edges of the specimens has also contributed to this minor spalling. It is pertinent to mention here that the edges of the specimens were deliberately kept sharp to create severe conditions for the accelerated testing of the coated specimens. In actual design, the sharp edges and corners are avoided to eliminate stress concentration. Minor spallation was also observed in areas of local convex curvature. Reporting the occurrence of similar observations, Strawbridge et al. (1997) attributed spallation to the development of out-of-plane tensile stresses in the region of convex curvature during cooling.

EPMA analysis of the Cr₃C₂-NiCr coated superalloys (Figs. 6.15a and 6.39) indicates that sulphur has penetrated into the scales, and in some cases it has also penetrated up to the substrate alloys (Fig. 6.27), and co-exists with Cr forming CrS. The oxidation of this CrS might yield a protective scale of Cr₂O₃ as reported by Khanna and Jha (1998). The diffusion of vanadium is confined mainly to the surface scale. However, once the splat boundaries and pores present in the coating are blocked due to formation of oxides, the transportation of the reacting species towards the base alloy is stopped. Based on the EPMA analysis along with the results of SEM, XRD, and EDAX (surface/cross-section) analyses, the schematic representation of the probable hot corrosion mode for the Cr₃C₂-NiCr coated Superni 75 is shown in Fig. 6.71.

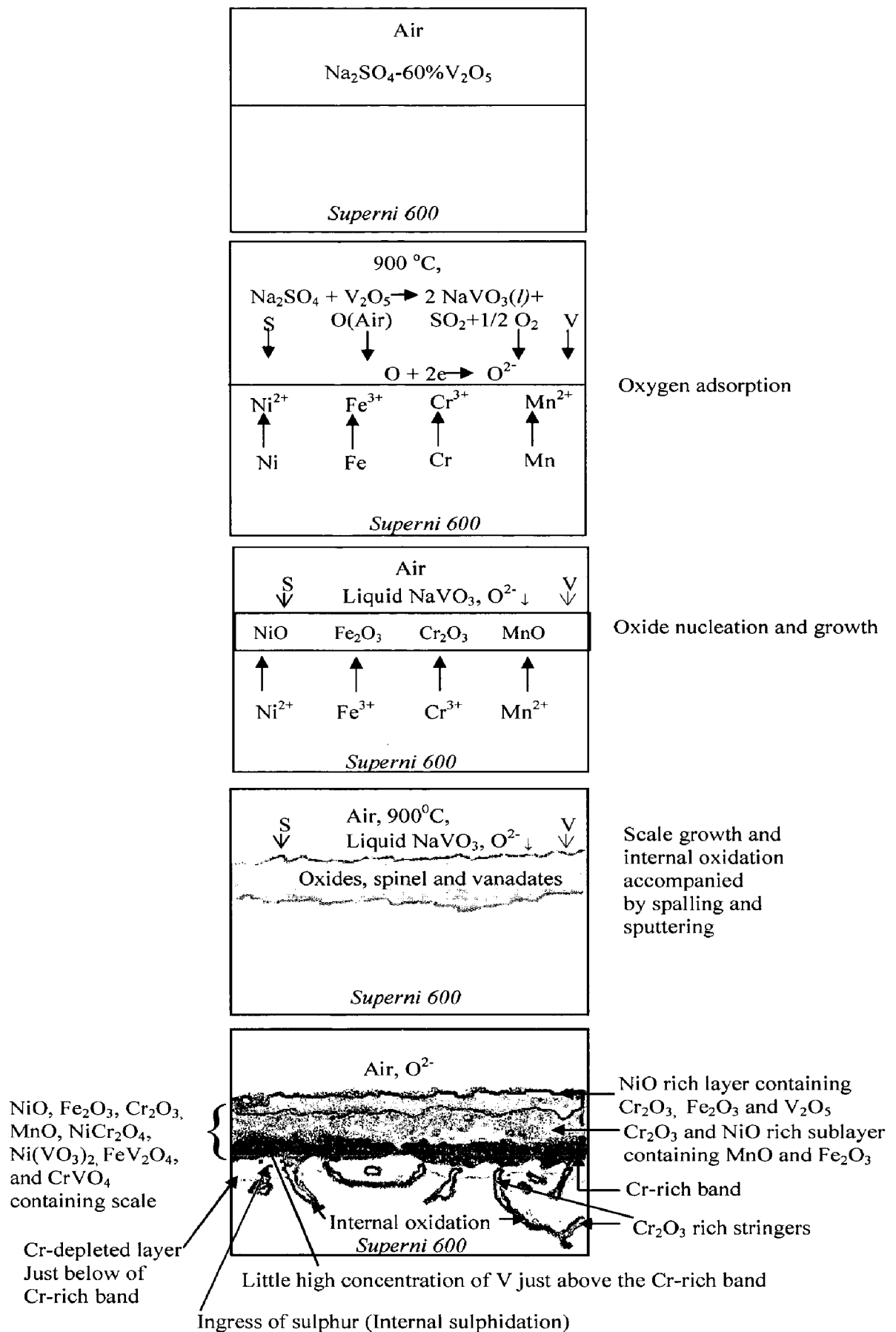
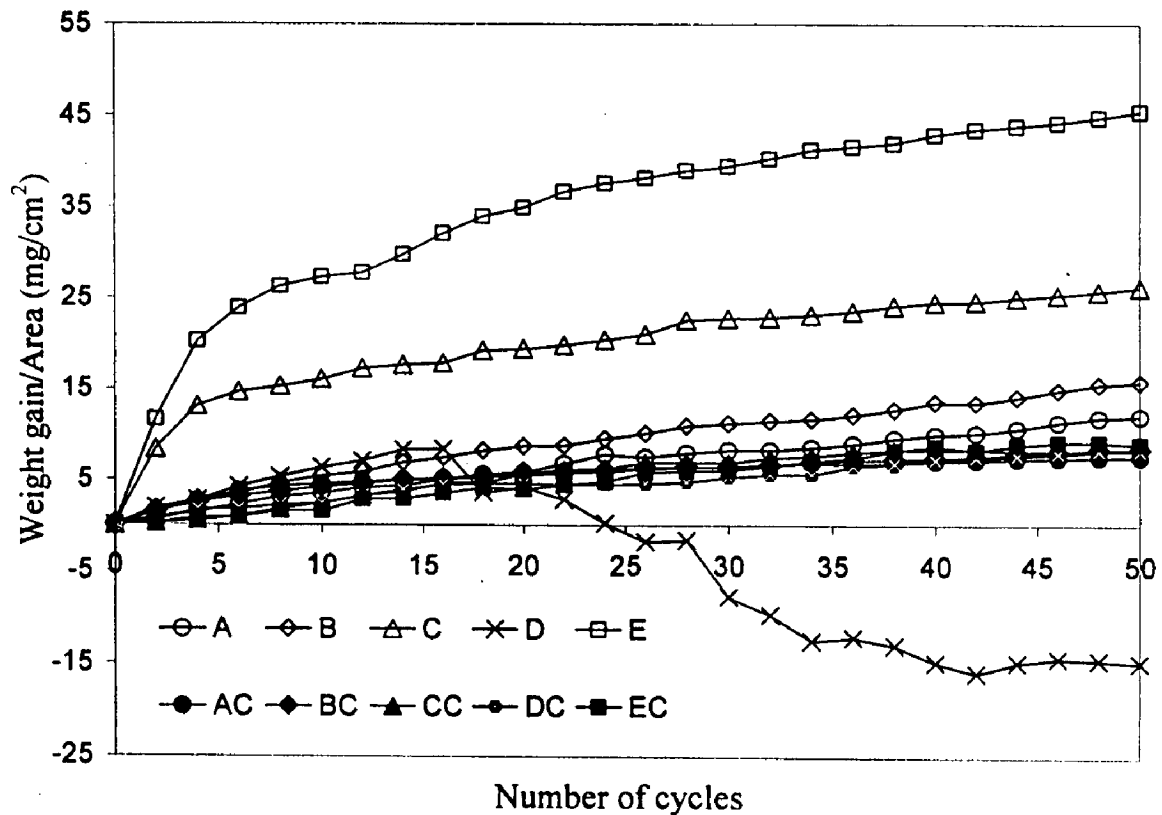


Fig. 6.69 Schematic diagram showing probable hot corrosion mechanism for the uncoated Superni 600 exposed to Na₂SO₄-60%V₂O₅ environment at 900 °C for 50 cycles.



- | | | | |
|-----|--------------------|------|---------------------------|
| A : | Bare Superni 75 | AC : | HVOF coated Superni 75 |
| B : | Bare Superni 600 | BC : | HVOF coated Superni 600 |
| C : | Bare Superni 601 | CC : | HVOF coated Superni 601 |
| D : | Bare Superni 718 | DC : | HVOF coated Superni 718 |
| E : | Bare Superfer 800H | EC : | HVOF coated Superfer 800H |

Fig. 6.70 Weight gain vs. number of cycles plot for the uncoated and Cr₃C₂-NiCr coated superalloys subjected to hot corrosion for 50 cycles in Na₂SO₄-60%V₂O₅ environment at 900 °C.

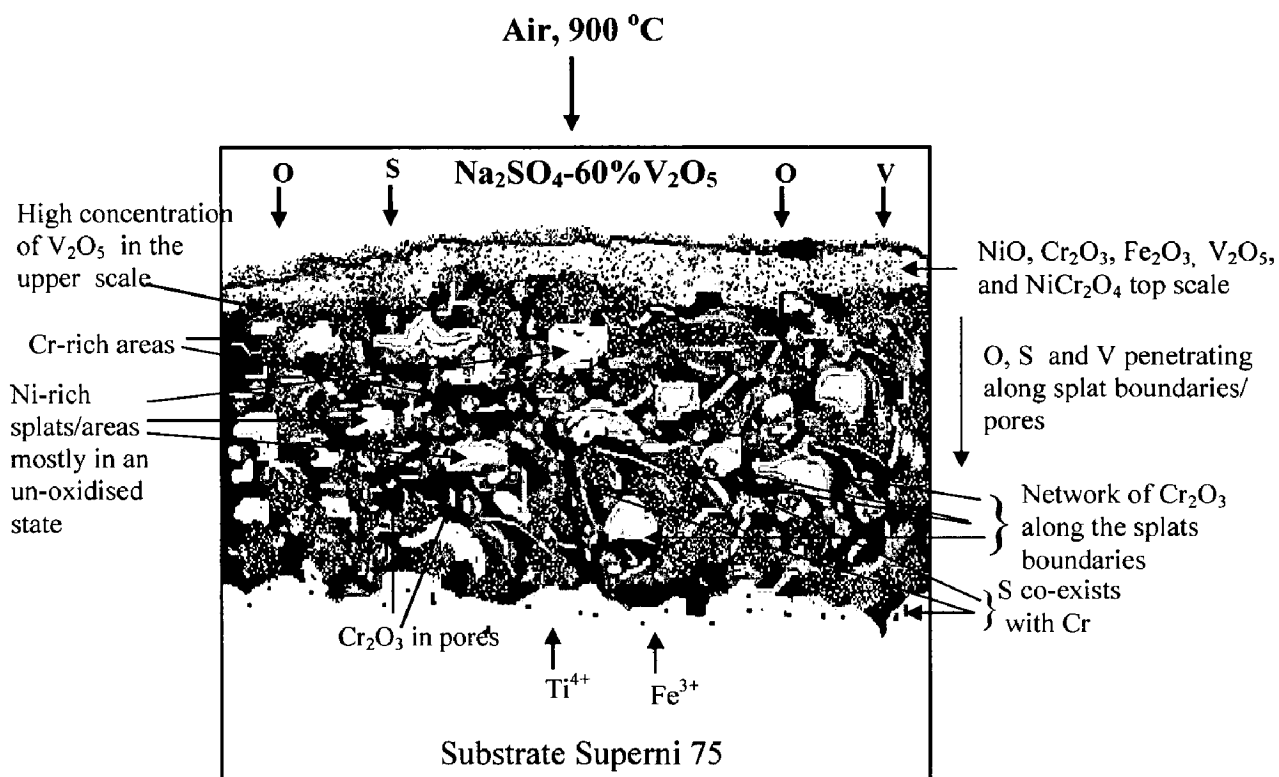


Fig. 6.71 Schematic diagram showing possible hot corrosion mode for the Cr₃C₂-NiCr coated Superni 75 exposed to Na₂SO₄-60%V₂O₅ environment at 900 °C for 50 cycles.

6.3.2.2 NiCrBSi Coating

In the given molten salt environment, the NiCrBSi coating oxidised up to 100-120 μm from top surface of the scale and the remaining portion appears similar to the structure of as-sprayed coating. The cross-section EDAX analysis (Figs. 6.13b, 6.25b and 6.49b) and EPMA analysis (Fig. 6.40) show the absence of oxygen and other corrosive species in the substrate near the coating-substrate interface. Therefore, it is concluded that the NiCrBSi coating provides necessary protection to the substrate superalloys in the given molten salt environment. The formation of two thick oxide layers in the scale, the uppermost one rich in silicon oxides and the sub-layer rich in chromium oxide might have contributed for the hot corrosion resistance of this coating as can be seen in the EPMA analysis shown in Fig. 6.40.

The NiCrBSi coating reduces the weight gain of Superni 75, Superni 600, Superni 601, and Superfer 800H; and their parabolic rate constants are found to be lower than respective uncoated superalloys for 50 cycles of hot corrosion study. The cumulative weight gain per unit areas of NiCrBSi coated Superni 718 for 16 cycles (6.58 mg/cm^2) is found to be less than the corresponding value of uncoated Superni 718 (8.35 mg/cm^2). Further these coated superalloys follow the parabolic rate law of oxidation up to 50 cycles. Therefore, it can be inferred that NiCrBSi coated superalloys showed better hot corrosion resistance than the uncoated superalloys. Hot corrosion behaviour of the NiCrBSi coated specimens in terms of overall weight gain after 50 cycles, is noted as:

Superni 718 > Superni 601 > Superfer 800H > Superni 600 > Superni 75

The better hot corrosion resistance of coated Superni 75 can be attributed to the presence of a thick layer of silicon in the top scale, and chromium-rich layer in the sub-scale, Fig. 6.16. The cross-section EDAX analysis (Fig. 6.13b) shows that these elements are oxidised to form SiO_2 and Cr_2O_3 , which are the protective oxides against the corrosive species (Stroosnijder et al., 1994). While the relatively low corrosion resistance of the coated Superni 718 is due to the formation of discontinuous layer of silicon in the top-scale as well as due to the presence of relatively low concentration of chromium in the sub-scale (Fig. 6.52). The diffusion of various elements from the substrate such as Mo and Ti might have a detrimental effect on the hot corrosion resistance of NiCrBSi coated Superni 718. The titanium diffused considerably into the coating as it has a higher

affinity towards oxygen and is considered unfavourable to the corrosion resistance (Li and Gleeson, 2004). The molybdenum has diffused to the surface and oxidised in the presence of Na_2SO_4 to form low melting point Na_2MoO_4 , which has high solubility for protective oxides (Pettit and Meier, 1985).

The XRD analysis reveals the presence of SiO_2 and Cr_2O_3 as the main protective phases along with NiO and NiCr_2O_4 in the surface scale of the hot corroded NiCrBSi coated superalloys. The EDAX and EPMA analysis further support the formation of these phases. The author has reported the formation of these phases in earlier publications (Sidhu et al., 2006A, 2006C, 2006D, and 2006E).

The surface scales formed on NiCrBSi coated superalloys have been observed to be dense and compact, and show no indication of any spallation/ sputtering or peeling off during the course of study (Figs. 6.12c, 6.24c, 6.36c, 6.48c and 6.60c). Further, the scales maintained their good contact with the substrate superalloys after 50 cycles of study as is apparent from the BSEI micrographs shown in Figures 6.16, 6.28, 6.40, 6.52 and 6.64. Wang et al. (2004) have reported that the addition of Si and B can promote the selective oxidation of the protective scale-forming elements resulting in the formation of a continuous scale in the initial corrosion stage and improve the adherence of the outer scale to the coating in the subsequent hot corrosion process. Therefore, the behaviour of the NiCrBSi coating is in good agreement with the findings of Wang et al. (2004).

The vanadium is present mostly in the upper part of the scale (Figs. 6.16, 6.28, 6.40 and 6.64) and co-exists with nickel suggesting the possibility of the formation of nickel-vanadates. The XRD analysis confirms the formation of $\text{Ni}(\text{VO}_3)_2$ (Figs. 6.23 and 6.35). The $\text{Ni}(\text{VO}_3)_2$ formed also acts as a diffusion barrier for the oxidizing species (Seierstein and Kofstad, 1987). Sulphur penetrates into the scale and co-exists mostly with Cr forming CrS . The oxidation of this CrS yields a protective scale of Cr_2O_3 as discussed under section 6.3.2.1. On the basis of the results of EPMA, SEM, XRD, and EDAX (surface/cross-section) analyses, schematic representation of the possible hot corrosion mode for the NiCrBSi coated Superni 601 subjected to molten salt environment for 50 cycles at 900°C is shown in Fig. 6.72.

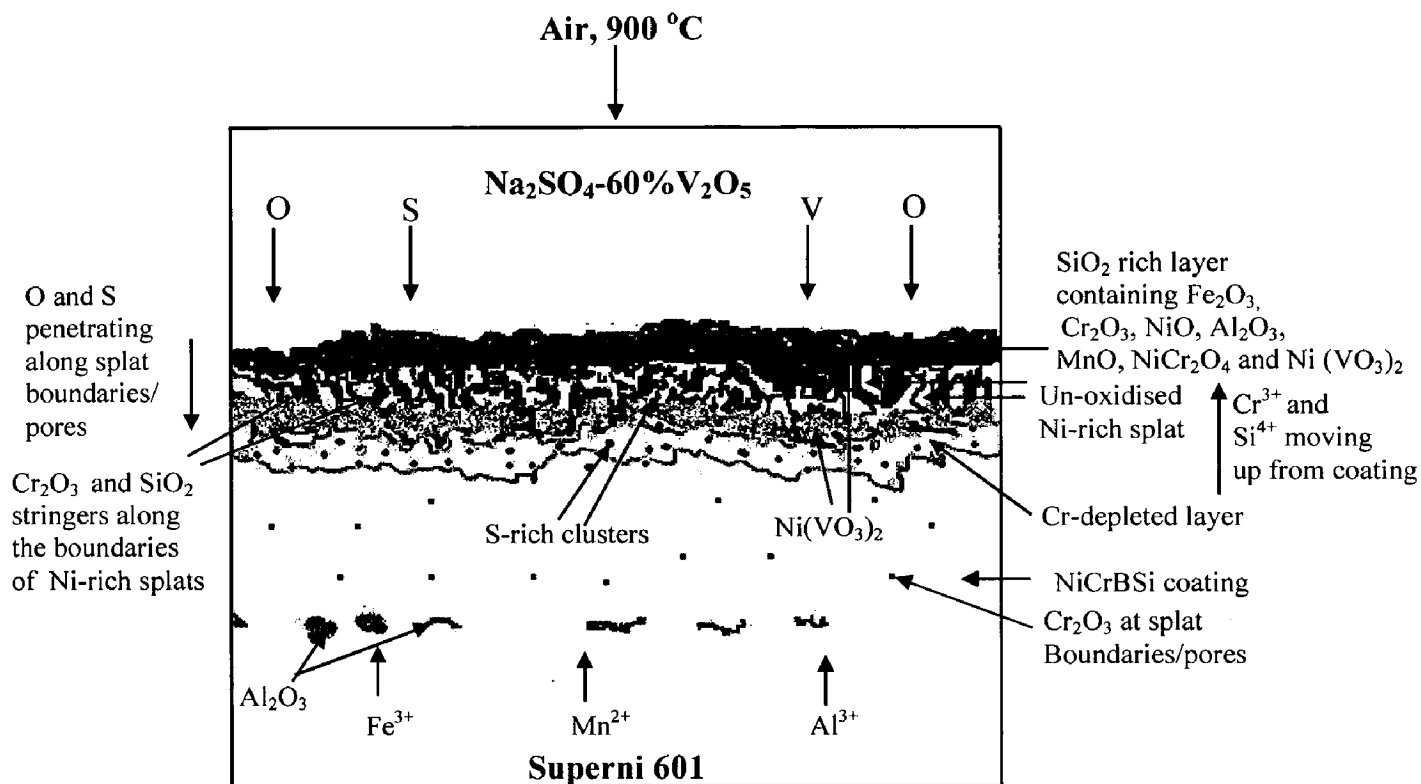


Fig. 6.72 Schematic diagram showing possible hot corrosion mode for the NiCrBSi coated Superni 601 exposed to $\text{Na}_2\text{SO}_4\text{-}60\%\text{V}_2\text{O}_5$ environment at 900 °C for 50 cycles.

6.3.2.3 *Stellite-6 Coating*

The hot corrosion resistance of the Stellite-6 coated superalloys based upon the overall weight gain after 50 cycles of study, although not significant apart, can be arranged in the following order (Fig. 6.73):

Superni 75 > Superni 601 > Superni 718 > Superni 600 > Superfer 800H

The results show that the parabolic rate constants for the uncoated Superni 75, Superni 600, Superni 601, and Superfer 800H are greater than those for the coated superalloys. All the Stellite-6 coated superalloys follow parabolic rate law of oxidation up to 50 cycles with an exception of Superni 718, which has shown slight deviations after 44 cycles. In case of coated Superni 718, the cumulative weight gain per unit area for 16 cycles (7.03 mg/cm^2) is found to be less than the corresponding value for the uncoated Superni 718 (8.35 mg/cm^2). Further the partially oxidised coating has successfully maintained its integrity on all the substrate superalloys under study as can be seen from the back-scattered images reported in Figs. 6.10d, 6.17, 6.22d, 6.29, 6.41, 6.46d, and 6.53. Hence, it can be inferred that the Stellite-6 coating provided the necessary protection to the Ni- and Fe-based superalloys in the given molten salt environment. The minor deviations from the parabolic rate law in some cases can be attributed to the formation and rapid growth of inhomogeneous oxides, and their dissolution due to the fluxing action of the molten salt.

The hot corrosion resistance of Stellite-6 coating and its tendency to act like a diffusion barrier to the degrading species can be attributed to the formation of oxides of chromium and silicon at the boundaries of Co-rich splats as revealed by cross-section EDAX analysis (Fig. 6.37b). These Co-rich splats mostly remain in un-oxidised state. The elemental maps for Cr, Si, and O (Fig. 6.29) further confirm that the splat boundaries are blocked by Cr_2O_3 and SiO_2 .

Additionally, the better hot corrosion resistance shown by Stellite-6 coated Superni 75 can be attributed to the formation of homogeneous and continuous thick band of chromium in the topmost part of the scale (Fig. 6.17), whereas relatively less resistance of coated Fe-based Superfer 800H is due to the formation of a porous layer of nickel in the topmost scale (Fig. 6.65). The NiO present in the surface scale is porous due to reprecipitation by fluxing action of molten salt $\text{Na}_2\text{SO}_4\text{-60\%V}_2\text{O}_5$ at 900°C under thermal cyclic test conditions. Further, the NiO is less protective than chromium oxide.

The XRD analysis revealed the formation of oxides of mainly cobalt and chromium, along with the spinels of cobalt-chromium and nickel-chromium, which are reported to be protective in nature against corrosion. Formation of these phases

has also been confirmed by EDAX analysis, and EPMA. As proposed by Luthra (1985) formation of spinel CoCr_2O_4 blocks the diffusion activities through the cobalt oxide (CoO) thereby suppressing the further formation of this oxide. He further opined that increase in the growth of CoCr_2O_4 and Cr_2O_3 , in competition with CoO and Co_3O_4 formation, increases the corrosion resistance of alloys. The formation of most of these phases has also been reported by Sidhu (2006I) while studying the plasma sprayed Stellite-6 coating in the same molten salt environment for the same number of cycles at the same temperature.

The vanadium and sulphur show their existence in the scale similar way as has already been discussed in Section 6.3.2.1. Manganese and iron elements of the substrate diffuse into the scale, and iron reaches up to top of the scale (Figs. 6.53 and 6.65).

The parabolic rate constants (k_p) for the HVOF sprayed Stellite-6 coating on Superni 75, Superni 600, Superni 601, Superni 718 and Superfer 800H have been found as 5.23, 8.1, 6.21, 6.94, and $6.3 \times 10^{-10} \text{ g}^2 \text{ cm}^{-4} \text{ s}^{-1}$ respectively, whereas these values for argon shrouded plasma sprayed Stellite-6 coatings on the same superalloys hot corroded in the same environment at same temperature for same number of cycles has been reported by Singh (2005E) as 26.92, 43.26, 42.36, 30.38 and $50 \times 10^{-10} \text{ g}^2 \text{ cm}^{-4} \text{ s}^{-1}$ respectively. Therefore HVOF sprayed Stellite-6 coating performed better than argon shrouded plasma sprayed Stellite-6 coating in the given molten salt environment.

Fig. 6.74 shows probable mode of corrosion phenomena for the Stellite-6 coated Superni 600.

6.3.2.4 Ni-20Cr Coating

The Ni-20Cr coating has provided the best hot corrosion resistance to the superalloys amongst all the coatings under study. Thermogravimetric data shows that the weight gain values for the Ni-20Cr coated specimens are much smaller than that of the bare superalloys (Fig. 6.75). The weight gain value (4.72 mg/cm^2) for Ni-20Cr coated Superni 718 after 50 cycles of hot corrosion is found to be much less than the weight gain value of bare Superni 718 measured after 16 cycles (8.35 mg/cm^2). As already discussed in section 6.3.1 due to heavy spalling and sputtering of the scale, the weight gain values for uncoated Superni 718 could not be measured after 16th cycles. The values of the parabolic rate constants, k_p , for the coated superalloys are found to be very less than their respective uncoated superalloys. Further, a continuous, compact and shining surface oxide scale is formed on the Ni-20Cr coated superalloys with negligible spallation (Figs. 6.24e, 6.36e, 6.48e and 6.60e). The BSE images show that the scale is adherent (Figs. 6.10e, 6.22e, 6.34e, 6.46e, 6.58e), and EDAX analysis reveals that the substrate is not affected by internal oxidation (Figs. 6.25c, 6.37c and 6.61c). Elemental

map for O also shows that penetration of oxygen is restricted up to scale-substrate interface (Fig. 6.18). Therefore, it can be inferred that the Ni-20Cr coating has imparted necessary hot corrosion resistance to the superalloys under study in the given molten salt environment at 900 °C.

The Ni-20Cr coating has shown a tendency to act as diffusion barriers to the corroding species as the parabolic rate law has been followed in all the cases. The parabolic rate constants (k_p in $10^{-10} \text{ g}^2\text{cm}^{-4}\text{s}^{-1}$) for HVOF sprayed Ni-20Cr coating on Superni 600, Superni 601, Superni 718 and Superfer 800H subjected to hot corrosion in molten salt environment ($\text{Na}_2\text{SO}_4\text{-60\%V}_2\text{O}_5$) at 900 °C for 50 cycles under cyclic conditions are found to be 3.0, 3.089, 1.44 and 1.180, respectively, whereas these values for the argon shrouded plasma sprayed Ni-20Cr coating deposited on the same superalloys hot corroded in the same molten salt environment under same conditions are 5.05, 4.72, 8.32, and 5.04 respectively as reported by Singh (2005E). Further k_p value for HVOF sprayed Ni-20Cr coating on Superni 75 subjected to hot corrosion in the above mentioned environment and conditions is found as $2.213 \times 10^{-10} \text{ g}^2\text{cm}^{-4}\text{s}^{-1}$, whereas argon shrouded plasma sprayed Ni-20Cr coated Superni 75 hot corroded in the same environment under the same conditions, as reported by Singh (2005E), has a inconsistency in the parabolic rate constant, which has value of $22.95 \times 10^{-10} \text{ g}^2 \text{ cm}^{-4} \text{ s}^{-1}$ up to first 16 cycles and then changes to $9.36 \times 10^{-10} \text{ g}^2 \text{ cm}^{-4} \text{ s}^{-1}$ for 17th to 38th cycle. This follows another transition to somewhat lower value of $4.49 \times 10^{-10} \text{ g}^2 \text{ cm}^{-4} \text{ s}^{-1}$ in the remaining cycles. Therefore, it can be inferred that the performance of HVOF sprayed Ni-20Cr coating deposited on different superalloys under study is either better or comparable to argon shrouded plasma sprayed Ni-20Cr coating deposited on the same alloys.

The hot corrosion resistance of the Ni-20Cr coated superalloys based upon the overall weight gain after 50 cycles of cyclic study can be arranged in the following order (Fig. 6.75):

Superfer 800H > Superni 718 > Superni 601 > Superni 600 > Superni 75

The Ni-20Cr coating performed best on Superfer 800H substrate as it has decreased the overall weight gain of the bare alloy by more than 90%. The better hot corrosion resistance of Ni-20Cr coated Superfer 800H and Superni 718 to the given environment is due to the formation of chromium-rich thick bands in the sub-scale, central portion and just above the scale-substrate interface of the corroded coating (Figs. 6.66 and 6.54), whereas the relatively low corrosion resistance of the Ni-20Cr coated Superni 75 is due to the absence of such Cr-rich bands in the scale (Fig. 6.18).

map for O also shows that penetration of oxygen is restricted up to scale-substrate interface (Fig. 6.18). Therefore, it can be inferred that the Ni-20Cr coating has imparted necessary hot corrosion resistance to the superalloys under study in the given molten salt environment at 900 °C.

The Ni-20Cr coating has shown a tendency to act as diffusion barriers to the corroding species as the parabolic rate law has been followed in all the cases. The parabolic rate constants (k_p in $10^{-10} \text{ g}^2\text{cm}^{-4}\text{s}^{-1}$) for HVOF sprayed Ni-20Cr coating on Superni 600, Superni 601, Superni 718 and Superfer 800H subjected to hot corrosion in molten salt environment ($\text{Na}_2\text{SO}_4\text{-60}\%\text{V}_2\text{O}_5$) at 900 °C for 50 cycles under cyclic conditions are found to be 3.0, 3.089, 1.44 and 1.180, respectively, whereas these values for the argon shrouded plasma sprayed Ni-20Cr coating deposited on the same superalloys hot corroded in the same molten salt environment under same conditions are 5.05, 4.72, 8.32, and 5.04 respectively as reported by Singh (2005E). Further k_p value for HVOF sprayed Ni-20Cr coating on Superni 75 subjected to hot corrosion in the above mentioned environment and conditions is found as $2.213 \times 10^{-10} \text{ g}^2\text{cm}^{-4}\text{s}^{-1}$, whereas argon shrouded plasma sprayed Ni-20Cr coated Superni 75 hot corroded in the same environment under the same conditions, as reported by Singh (2005E), has a inconsistency in the parabolic rate constant, which has value of $22.95 \times 10^{-10} \text{ g}^2 \text{ cm}^{-4} \text{ s}^{-1}$ up to first 16 cycles and then changes to $9.36 \times 10^{-10} \text{ g}^2 \text{ cm}^{-4} \text{ s}^{-1}$ for 17th to 38th cycle. This follows another transition to somewhat lower value of $4.49 \times 10^{-10} \text{ g}^2 \text{ cm}^{-4} \text{ s}^{-1}$ in the remaining cycles. Therefore, it can be inferred that the performance of HVOF sprayed Ni-20Cr coating deposited on different superalloys under study is either better or comparable to argon shrouded plasma sprayed Ni-20Cr coating deposited on the same alloys.

The hot corrosion resistance of the Ni-20Cr coated superalloys based upon the overall weight gain after 50 cycles of cyclic study can be arranged in the following order (Fig. 6.75):

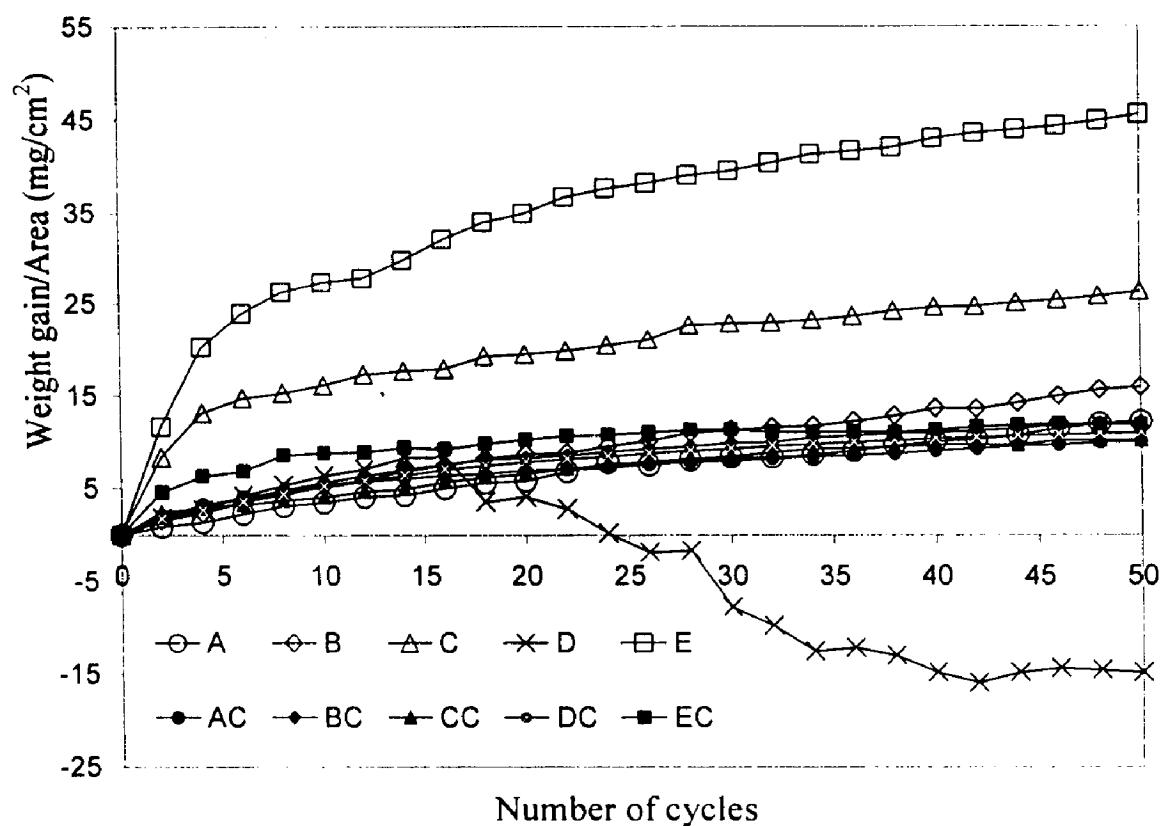
Superfer 800H > Superni 718 > Superni 601 > Superni 600 > Superni 75

The Ni-20Cr coating performed best on Superfer 800H substrate as it has decreased the overall weight gain of the bare alloy by more than 90%. The better hot corrosion resistance of Ni-20Cr coated Superfer 800H and Superni 718 to the given environment is due to the formation of chromium-rich thick bands in the sub-scale, central portion and just above the scale-substrate interface of the corroded coating (Figs. 6.66 and 6.54), whereas the relatively low corrosion resistance of the Ni-20Cr coated Superni 75 is due to the absence of such Cr-rich bands in the scale (Fig. 6.18).

Selective oxidation of chromium along the nickel-rich splats boundaries, as detected by cross-sectional EDAX analysis (Points 3 and 4 in Figs. 6.25c and 6.37c) and confirmed by EPMA analysis (Fig. 6.18), acts as diffusion barrier to the inward diffusion of corrosive species. Chromium has higher affinity for oxygen than nickel and forms more stable oxide. NiO is less stoichiometric oxide than Cr₂O₃ (Sundararajan et al., 2003A). This infers that the oxidation of Ni-Cr coating is solely based on the formation of Cr₂O₃. The better hot corrosion resistance of the coating can also be partly attributed to the uniform fine grain microstructure of as sprayed Ni-20Cr coating as reported by the author in his earlier publication (Sidhu et al., 2006G).

The formation of NiO, Cr₂O₃ and NiCr₂O₄ phases in the scale of Ni-20Cr coated superalloys, as revealed by the XRD analysis and supported by EDAX and EPMA analysis, indicates towards the protective nature of this coating. These results are consistent with the findings of Longa and Takemoto (1992) as they have also identified phases like Cr₂O₃, NiO and NiCr₂O₄ for NiCr flame sprayed coatings on steel substrates when oxidised in an environment of Na₂SO₄-85%V₂O₅ at 900°C.

The iron, titanium and aluminium have shown considerable diffusion into the coatings, as revealed by XRD/EDAX and EPMA analysis. Sulphur penetrates into the scale mainly along the splat boundaries and co-exists with chromium, whereas penetration of vanadium is mainly restricted to the upper layer of the scale similar to other coatings (Figs. 6.42 and 6.64). Based upon the results of cross-section EDAX analysis, along with the support of XRD, surface EDAX and EPMA, the proposed hot corrosion mode for the Ni-20Cr coated Superni 600 is shown in Fig. 6.76.



A :	Bare Superni 75	AC :	HVOF coated Superni 75
B :	Bare Superni 600	BC :	HVOF coated Superni 600
C :	Bare Superni 601	CC :	HVOF coated Superni 601
D :	Bare Superni 718	DC :	HVOF coated Superni 718
E :	Bare Superfer 800H	EC :	HVOF coated Superfer 800H

Fig. 6.73 Weight gain vs. number of cycles plot for the uncoated and Stellite-6 coated superalloys subjected to hot corrosion for 50 cycles in Na₂SO₄-60%V₂O₅ environment at 900 °C.

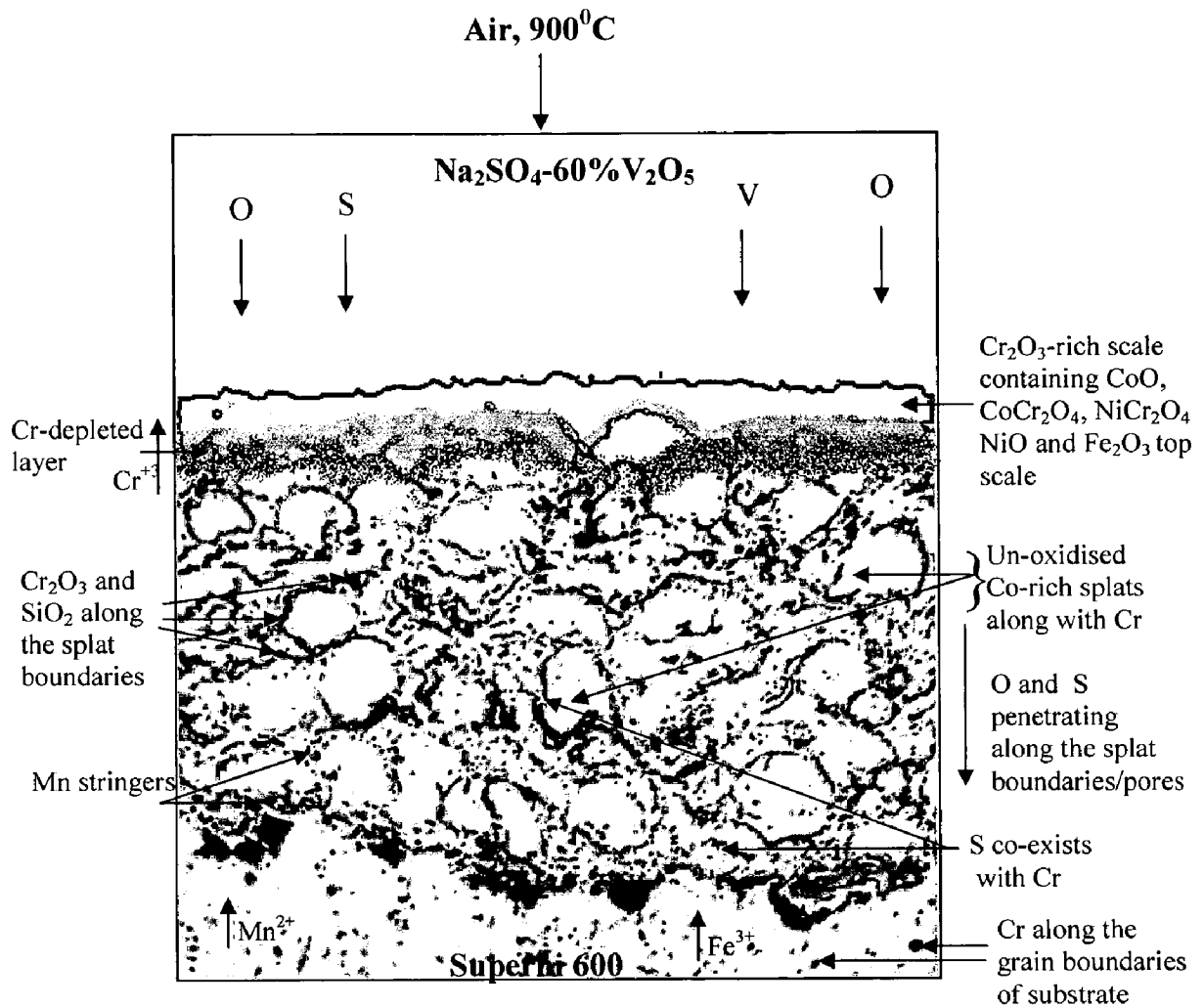
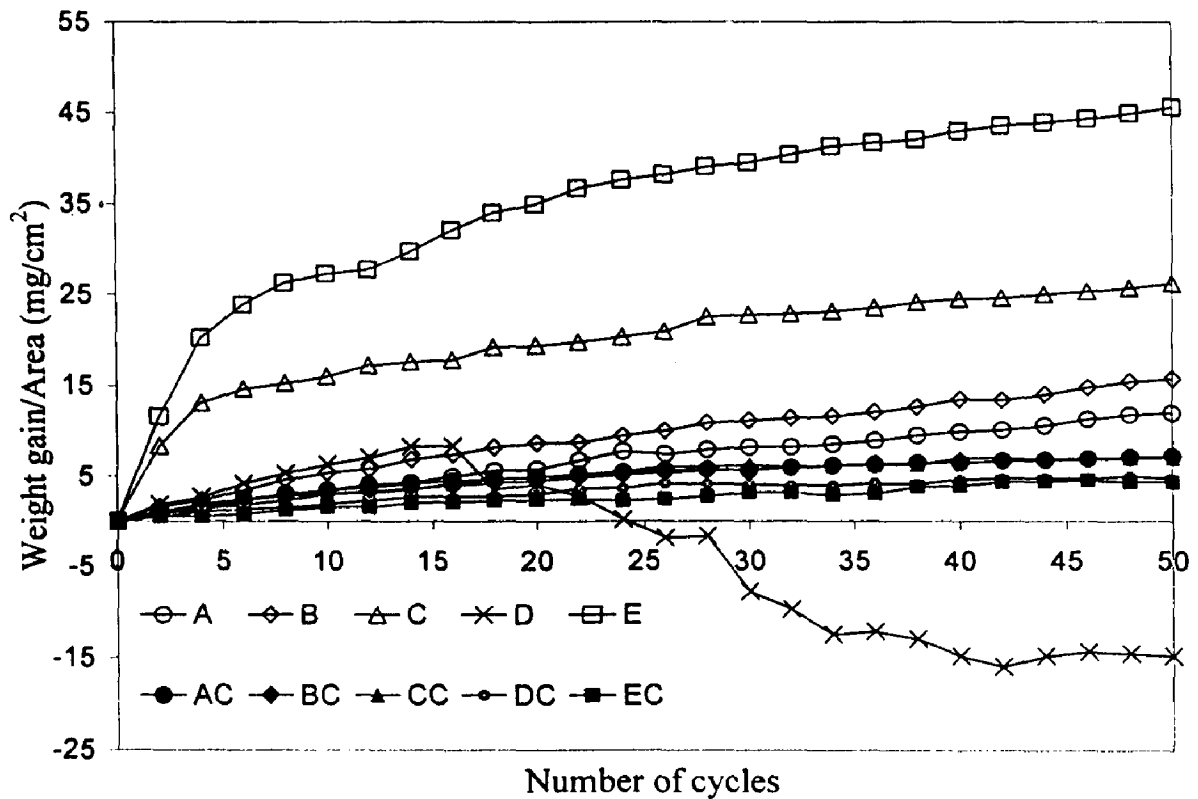


Fig. 6.74 Schematic diagram showing possible hot corrosion mode for the Stellite-6 coated Superalloy 600 exposed to Na₂SO₄-60%V₂O₅ at 900 °C for 50 cycles.



- | | | | |
|-----|--------------------|------|---------------------------|
| A : | Bare Superni 75 | AC : | HVOF coated Superni 75 |
| B : | Bare Superni 600 | BC : | HVOF coated Superni 600 |
| C : | Bare Superni 601 | CC : | HVOF coated Superni 601 |
| D : | Bare Superni 718 | DC : | HVOF coated Superni 718 |
| E : | Bare Superfer 800H | EC : | HVOF coated Superfer 800H |

Fig. 6.75 Weight gain vs. number of cycles plot for uncoated and Ni-20Cr coated superalloys subjected to hot corrosion for 50 cycles in Na₂SO₄-60%V₂O₅ environment at 900 °C.

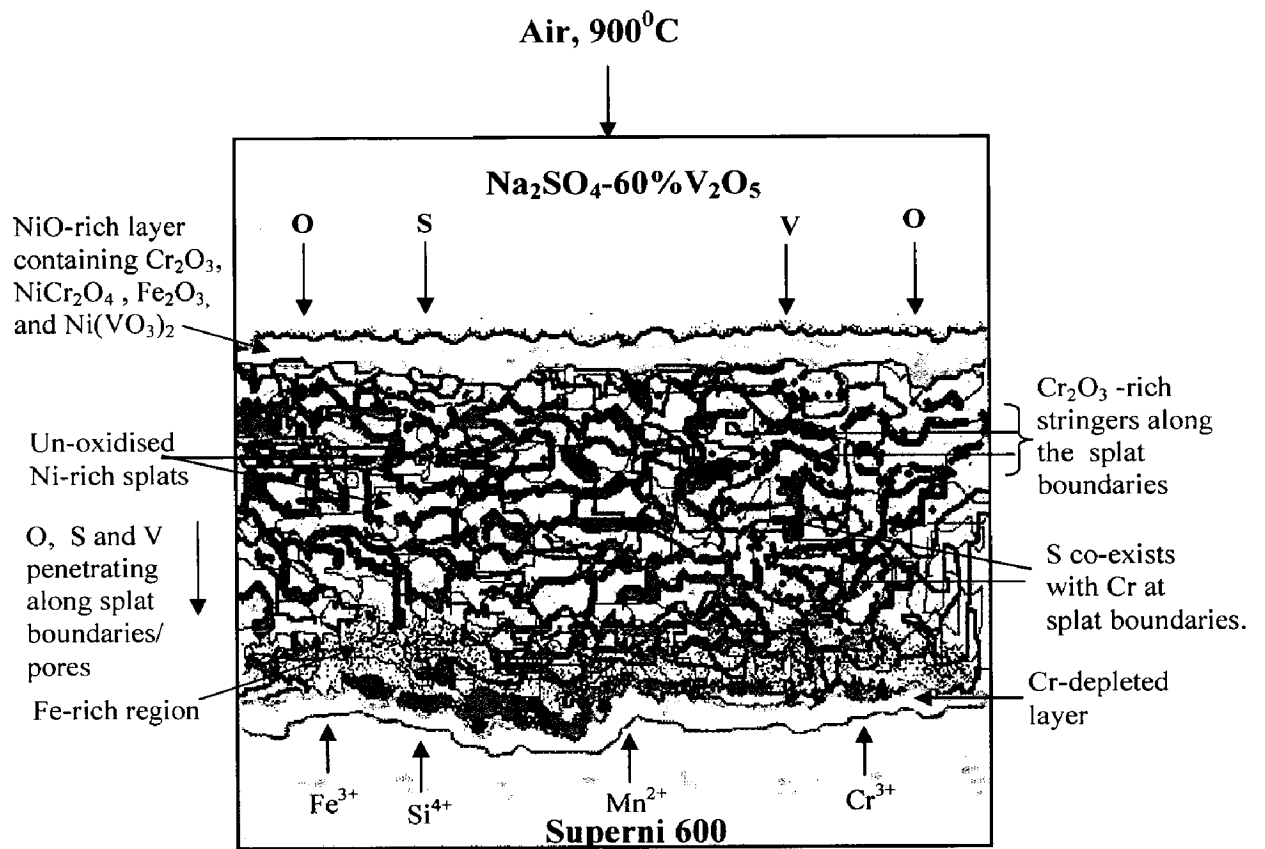


Fig. 6.76 Schematic diagram showing possible hot corrosion mode for the Ni-20Cr coated Superni 600 exposed to Na₂SO₄-60%V₂O₅ at 900 °C for 50 cycles.

CHAPTER 7

HOT CORROSION STUDIES IN INDUSTRIAL ENVIRONMENT

This chapter focuses on the study of hot corrosion behaviour of the HVOF coated and uncoated superalloys exposed to platen superheater zone of the coal fired boiler of a Guru Nanak Dev thermal Plant, Bathinda, Punjab. The specimens were kept in the platen superheater zone of the boiler where the gas temperature was $900^{\circ}\text{C}\pm 10^{\circ}\text{C}$. Experiments were performed for 10 cycles, each cycle consisting of 100 hrs exposure followed by 1 hr cooling at ambient temperature. The specimens were visually examined at the end of each cycle for any change in the colour, luster, spalling tendency and other physical changes of the scale if any.

Weight gain was measured at the end of each cycle. However in this environment the weight change data could not be of much use for predicting hot corrosion behaviour because of suspected spalling and ash deposition on the samples. Hence the extent of corrosion has been evaluated by measuring the thickness of the unreacted portion of the samples after the total exposure of 1000 hrs. The different phases and their distribution in the hot corroded specimens were analysed with the help of XRD, SEM/EDAX and EPMA.

7.1 RESULTS AND DISCUSSION

7.1.1 Visual Examination

7.1.1.1 *Bare Superalloys*

The macrographs for the substrate superalloys after 1000 hours exposure to platen superheater zone of the coal fired boiler are shown in Fig. 7.1. After exposure of 100 hrs, light grey scale appeared on the surfaces of Ni-based superalloys, whereas dark grey surface scale formed on the Fe-based superalloy. Subsequently, colour of the scale turned to brownish and light grey on the Ni- and Fe-based Superalloys, respectively. The Superni 75 and Superni 600 showed little spallation symptoms during the course of study, whereas spallation was noticed from the surface of Superni 601, Superni 718 and Superfer 800H. The surface of the specimens became gradually rough with the progress of study.

7.1.1.2 *HVOF Coated Superalloys*

The macrographs for the HVOF coated superalloys after exposure to boiler environment at 900°C are shown in Figs. 7.2 to 7.5. In general, the scales formed on all the coated superalloys have yellowish or reddish brown appearance after 1000 hours exposure.

The Cr₃C₂-NiCr coated specimens showed only minor spallation from the edges and corners. The coating remained intact on the surface except in coated Superfer 800H specimen (Fig. 7.2e). The Cr₃C₂-NiCr coated Superfer 800H showed the symptoms of minor spallation of the scale from edges after 3rd cycle, whereas coated Superni 601 indicated similar spallation from 5th cycle onward. The Cr₃C₂-NiCr coated Superni 75, Superni 600 and Superni 718 indicated little spallation during 6th to 7th cycles only. In the case of Cr₃C₂-NiCr coated Superfer 800H, heavy spallation and detachment of the coating was observed from 7th cycle onward which continued till the end of study (Fig. 7.2e). The scale colour of the Cr₃C₂-NiCr coated superalloy which was light grey after first cycle turned to brownish grey after 5th-6th cycles.

The dark grey scale formed on NiCrBSi coated superalloys during first cycle subsequently changed to yellowish appearance with green tinges on the surfaces of Superni 75, Superni 718 and Superfer 800H superalloys, whereas grey and brown colour scales were formed on Superni 600 and Superni 601 superalloys, respectively. Like Cr₃C₂-NiCr coated alloys, NiCrBSi coated superalloys also showed little spallation during experimentation in this environment. Greenish colour spots were formed on sites where from spallation of the scale has occurred, while in some cases shining silver colour areas were observed (Fig. 7.3b). Even after 1000 hours of exposure, the scale was intact and didn't show presence of any crack.

Grey colour scale formed on Stellite-6 and Ni-20Cr coated superalloys during first cycle turned to brownish grey on coated Superni 75, Superni 601, and Superni 718; and greenish grey on Superni 600 and Superfer 800H superalloys (Figs. 7.4 and 7.5). Invariably all the Stellite-6 and Ni-20Cr coated superalloys showed negligible spallation during experimentations. The greenish tinges were observed in the scale after second/third cycle of the study and thereafter, there was fading of green colour but slight greenish appearance remained up to the end of study. Uniform, intact and adherent scale formed on these coated superalloys after 1000 hours of exposure didn't show any crack or spallation tendency. Only minor spallation of the scale was observed near the edges of some specimens.

7.1.2 Hot Corrosion of Superalloys

The hot corrosion behaviour of bare and HVOF coated superalloys in the given environment has been assessed by evaluating the thermogravimetric data, and metal thickness loss corresponding to the combined effects of average thickness of scale, scale thickness lost due to spallation or evaporation and the depth of internal corrosion attack after 1000 hours exposure. The coated superalloys, in general, showed no scale thickness loss, whereas the average scale thickness loss for the bare Superni 75, Superni 600, Superni 601, Superni 718 and Superfer 800H was found to be 80, 101, 203, 194, and 248 μm , respectively.

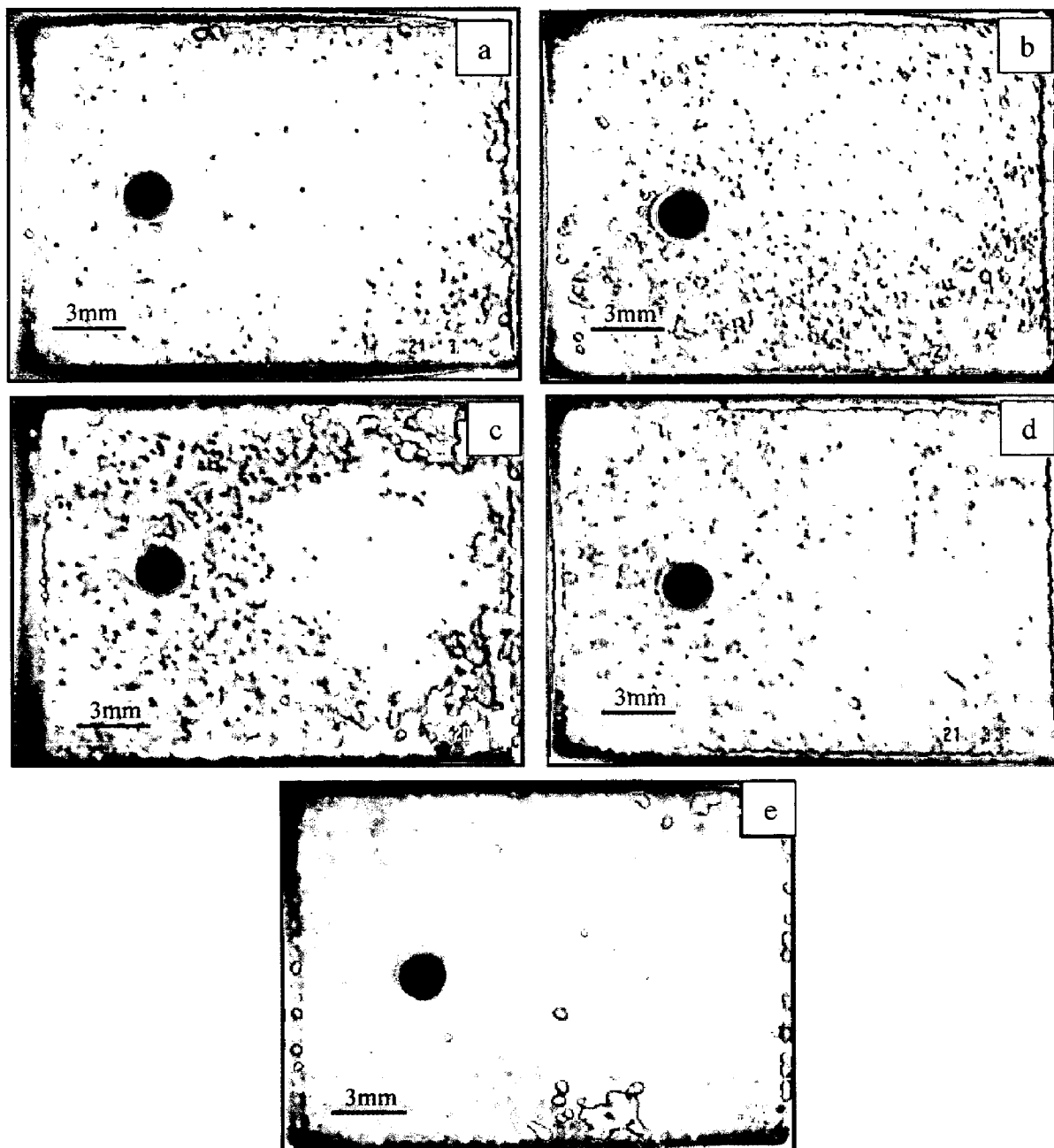


Fig. 7.1 Macrographs of the bare superalloys after 1000 hrs exposure to platen superheater zone of the coal fired boiler at 900 °C:
 (a) Superni 75 (b) Superni 600 (c) Superni 601
 (d) Superni 718 (e) Superfer 800H.

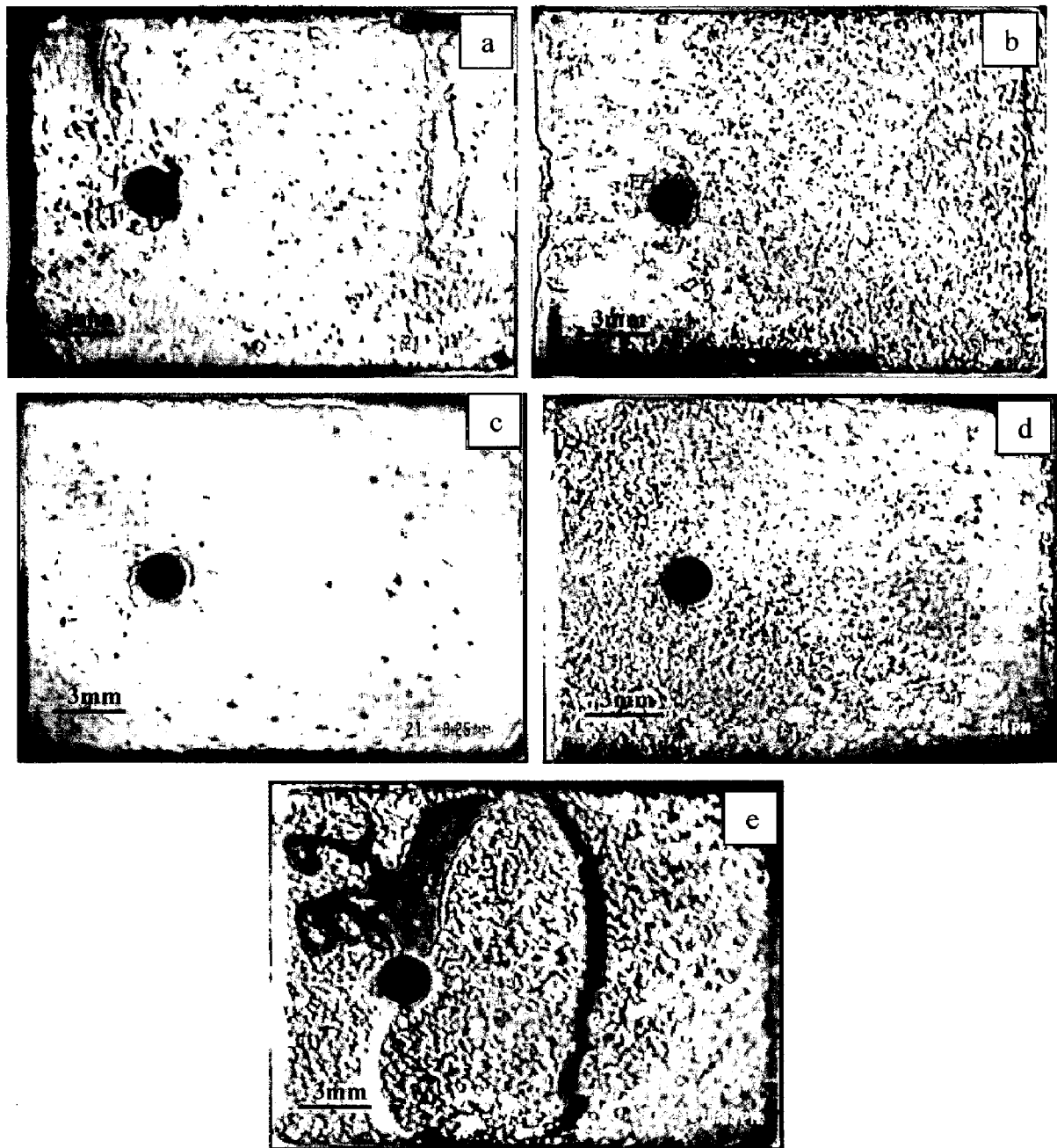


Fig. 7.2 Macrographs of the $\text{Cr}_3\text{C}_2\text{-NiCr}$ coated superalloys after 1000 hrs exposure to platen superheater zone of the boiler at $900\text{ }^\circ\text{C}$:
 (a) Superni 75 (b) Superni 600 (c) Superni 601
 (d) Superni 718 (e) Superfer 800H.

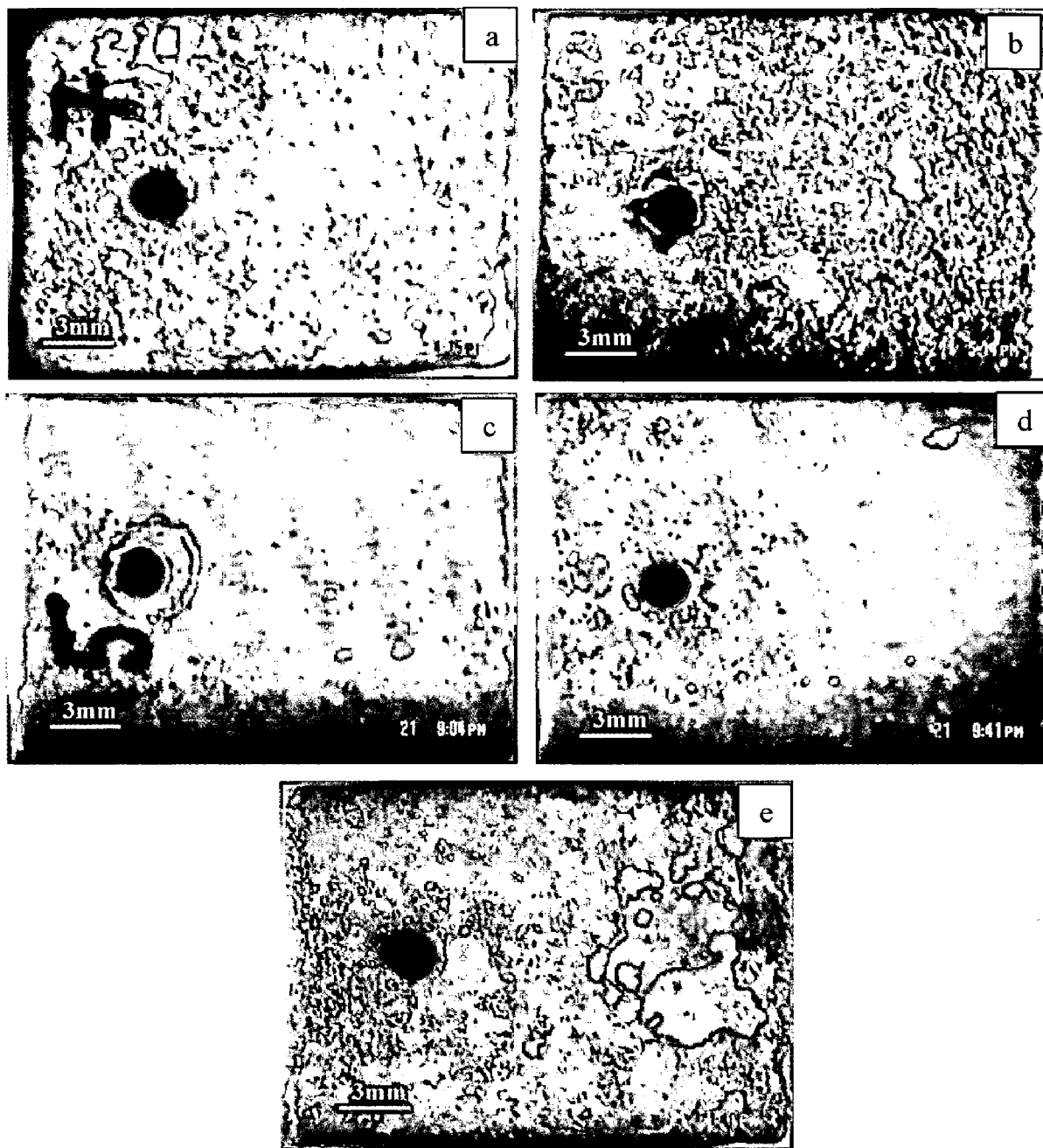


Fig. 7.3 Macrographs of the NiCrBSi coated superalloys after 1000 hrs exposure to platen superheater zone of the boiler at 900 °C:
 (a) Superni 75 (b) Superni 600 (c) Superni 601
 (d) Superni 718 (e) Superfer 800H.

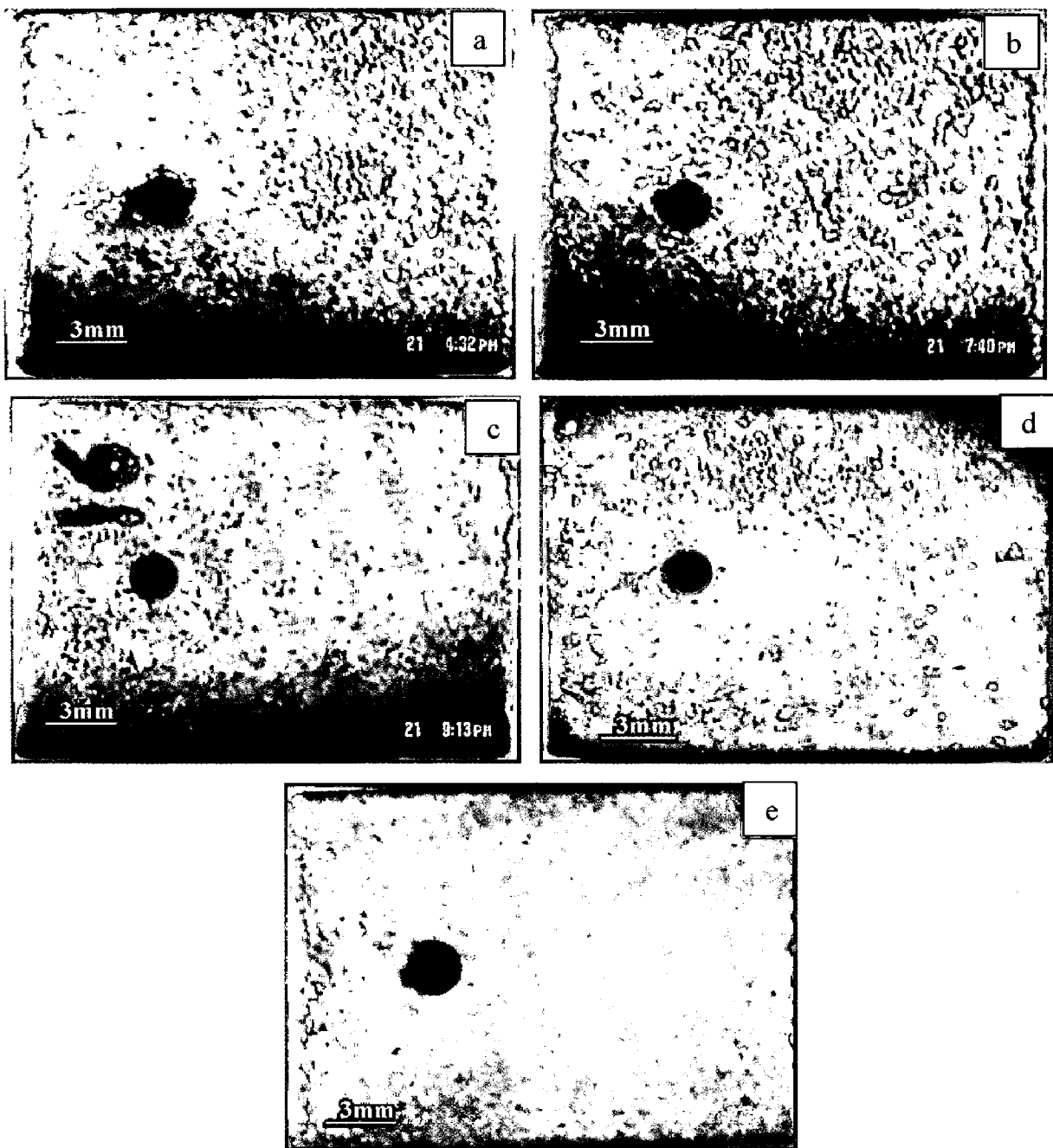


Fig. 7.4 Macrographs of the Stellite-6 coated superalloys after 1000 hrs exposure to platen superheater zone of the boiler at 900 °C:
 (a) Superni 75 (b) Superni 600 (c) Superni 601
 (d) Superni 718 (e) Superfer 800H.

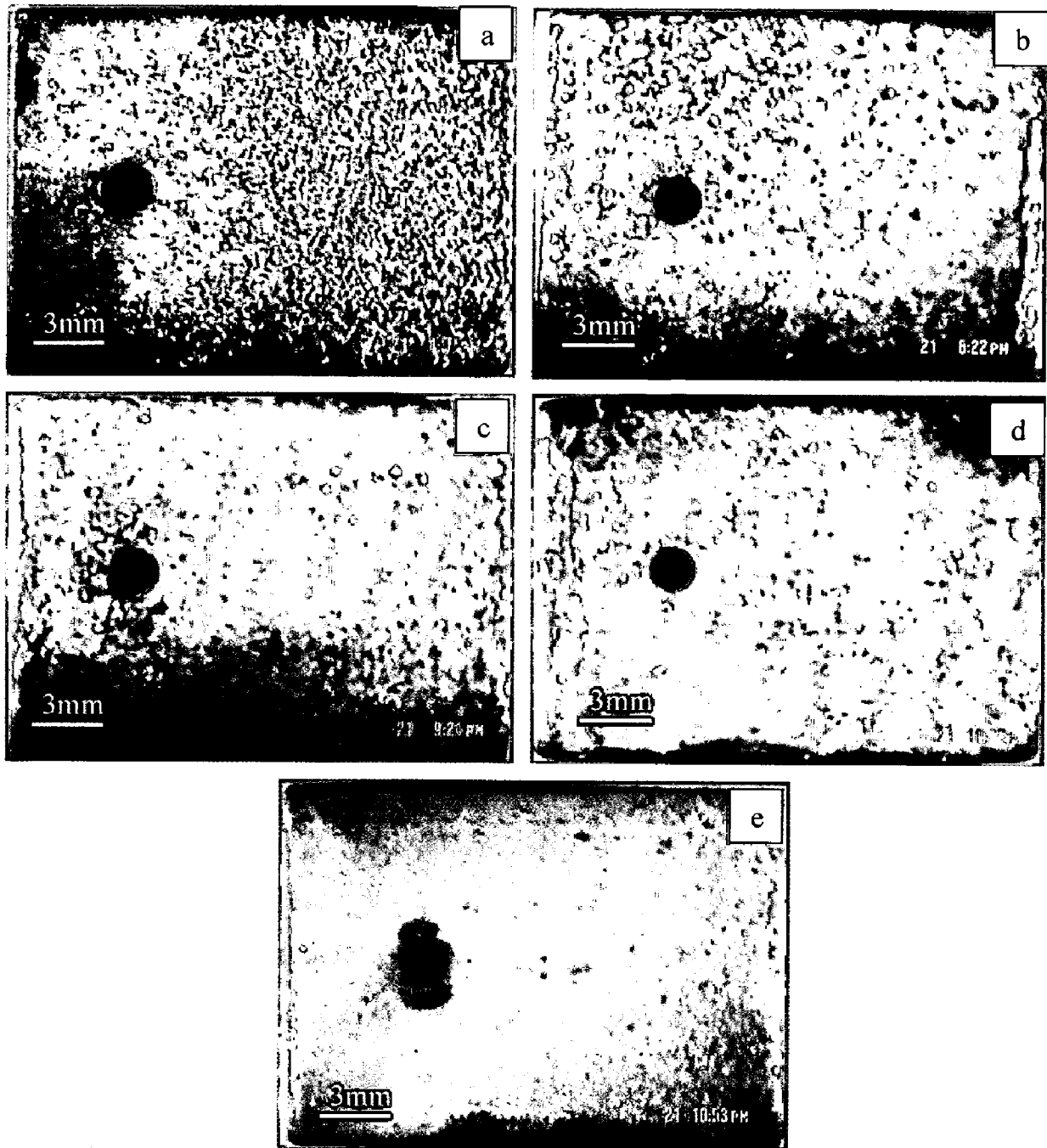


Fig. 7.5 Macrographs of the Ni-20Cr coated superalloys after 1000 hrs exposure to platen superheater zone of the boiler at 900 °C:
 (a) Superni 75 (b) Superni 600 (c) Superni 601
 (d) Superni 718 (e) Superfer 800H.

7.1.3 Hot Corrosion of Bare and Coated Superni 75

7.1.3.1 Corrosion Kinetics

The weight change per unit area (mg/cm^2) versus time plots for 1000 hours exposure of bare and coated Superni 75 to the boiler environment are shown in Fig. 7.6. The weight change consists of weight gain owing to the formation of the oxide scale and weight loss due to the suspected spalling and fluxing of the oxide scale. The net weight change of the specimens in the given environment represents the combined effects of these two processes.

The Ni-20Cr coated Superni 75 shows the lowest weight gain and the Cr_3C_2 -NiCr coated superalloy shows the highest weight gain, which is about 40% more than that gained by the former. The Stellite-6 coating is the second lowest in weight gain, while the weight gain of NiCrBSi coating is almost comparable to Stellite-6 coating. Figure 7.7 shows $(\text{weight change}/\text{area})^2$ vs. time plots. It can be observed from the graph that the Stellite-6 and Ni-20Cr coated Superni 75 follow a parabolic rate law, whereas Cr_3C_2 -NiCr and NiCrBSi coated Superni 75 show some deviation from the parabolic rate law. The weight change plot for the bare alloy indicates significant deviation from the parabolic rate law, suggesting that spallation of the scale might have occurred. Thus it can be inferred that the coatings provide the necessary protection to bare Superni 75 in the given environment and act as diffusion barriers to the corroding species. The parabolic rate constants (k_p in $10^{-12} \text{ g}^2 \text{ cm}^{-4} \text{ s}^{-1}$) for the Cr_3C_2 -NiCr, NiCrBSi, Stellite-6 and Ni-20Cr coated Superni 75 are found to be as 11.36, 8.88, 8.50, and 4.16, respectively. The parabolic rate constants for the bare superalloys could not be calculated as it did not follow the parabolic rate law.

7.1.3.2 Average Scale Thickness and Depth of Internal Attack

The BSE images across the cross-section of scales formed on bare and coated Superni 75 are shown in Fig. 7.8. The average scale thickness for bare Superni 75 is found to be 40 μm , and that for Cr_3C_2 -NiCr, NiCrBSi, Stellite-6 and Ni-20Cr coated Superni 75 are 340, 325, 293, and 209 μm , respectively. Coated superalloys show no internal corrosion attack, whereas the bare Superni 75 shows internal corrosion attack up to 8 μm from the scale-substrate interface. The average scale thickness, scale thickness lost (reported under section 7.1.2) and depth of internal corrosion attack for bare and coated Superni 75 are given in Fig. 7.9.

7.1.3.3 X-ray Diffraction Analysis

The diffraction patterns for the corroded bare and coated Superni 75 are shown in Fig. 7.10. The various phases identified with the XRD analysis at the surface of corroded specimens are presented in Table 7.1. The presence of Al_2O_3 and SiO_2 phases indicates the interaction of ash deposits with the oxide scale formed on the surface of the specimens.

Table 7.1: Major and minor phases identified by XRD analysis for the bare and coated Superni 75 hot corroded in actual boiler environment.

Description	Major phases	Minor phases
Uncoated Superni 75 superalloy	Cr ₂ O ₃ , Fe ₂ O ₃ , Al ₂ O ₃ , and SiO ₂	FeS
Cr ₃ C ₂ -NiCr coated	Cr ₂ O ₃ , Fe ₂ O ₃ , Al ₂ O ₃ , and NiCr ₂ O ₄	SiO ₂
NiCrBSi coated	Cr ₂ O ₃ , Fe ₂ O ₃ , and NiCr ₂ O ₄	NiO, and Al ₂ O ₃
Stellite-6 coated	Cr ₂ O ₃ , Fe ₂ O ₃ , CoCr ₂ O ₄ , and NiCr ₂ O ₄	CoO
Ni-20Cr coated	Cr ₂ O ₃ , Al ₂ O ₃ , SiO ₂ , and Fe ₂ O ₃	----

7.1.3.4 SEM/EDAX Analysis

7.1.3.4(A) Surface Analysis

The SEM micrographs showing surface morphology of the scale formed on bare and coated Superni 75 are given in Fig. 7.11.

The black areas present on the surface of uncoated Superni 75 indicate that little spallation of the scale has occurred (Fig. 7.11a). The EDAX analysis shows that the white phase of the scale consists mainly of SiO₂, Al₂O₃, Fe₂O₃ and some amounts of TiO₂, Cr₂O₃, SO₃, CaO, and K₂O. It is inferred that the composition of the white phase is almost similar to ash composition along with some other oxides of the scale. The spalled regions are found to be rich in Fe₂O₃, with SiO₂ and Al₂O₃ markedly decreased relative to white phase.

In general, continuous granular scales rich in silica and alumina are formed on the coated Superni 75 without indication of any crack. The uniform and adherent surface scales formed on NiCrBSi and Stellite-6 coated Superni 75 also contain significant amount of Cr₂O₃ (Figs. 7.11c and 7.11d) along with some amounts of NiO/CoO, TiO₂, Fe₂O₃. The EDAX analysis of the white region indicates the interaction of ash deposits with the oxides formed in the scale. The EDAX analysis of Cr₃C₂-NiCr and Ni-20Cr coated specimens show the presence of ash deposits in the surface scale as the composition of these deposits is similar to ash composition, along with very little amounts of Cr₂O₃, NiO and TiO₂ (Figs. 7.11b and 7.11e). The presence of TiO₂ in the surface scale indicates its outward diffusion from the substrate, whereas presence of Fe₂O₃ in the surface scale is due to diffusion from the substrate and partly due to interaction with ash (Figs. 7.11b, 7.11d and 7.11e).

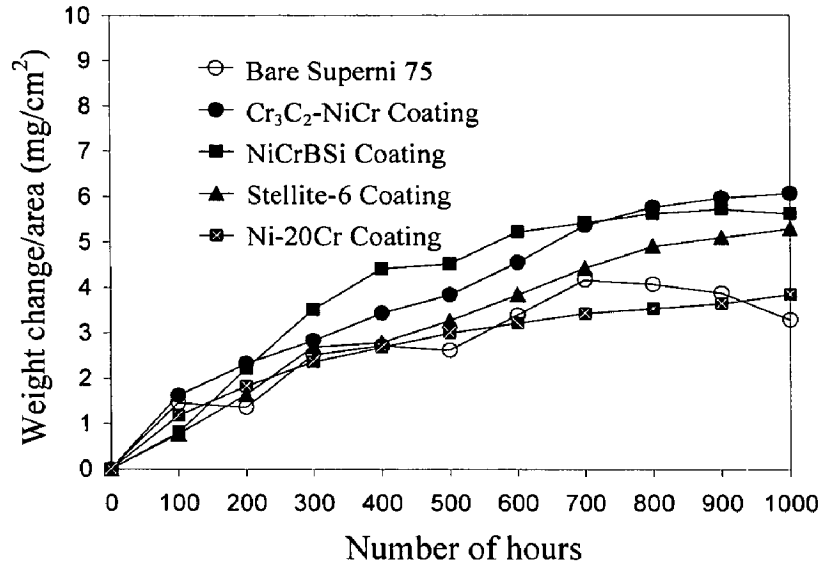


Fig. 7.6 Weight change vs. time plots for the coated and uncoated Superni 75 subjected to 1000 hrs cyclic exposure to platen superheater zone of the coal fired boiler at 900 °C.

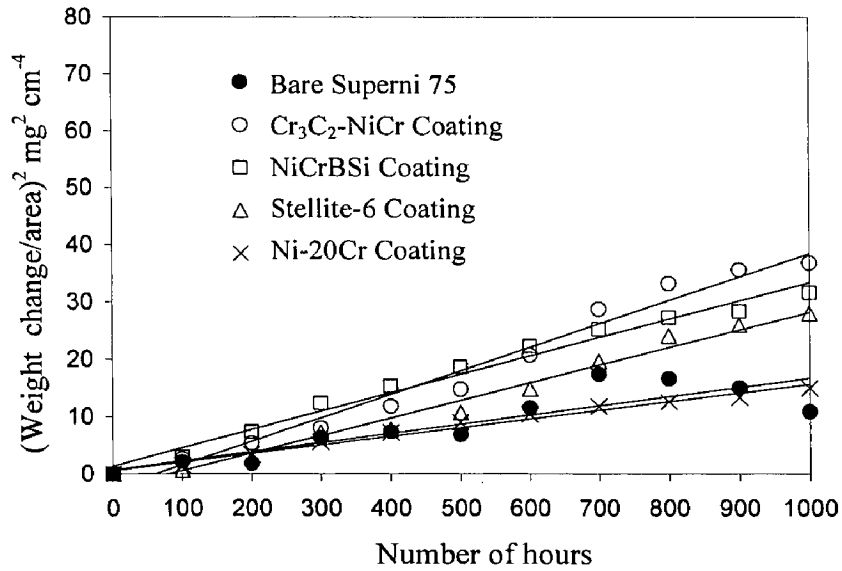


Fig. 7.7 (Weight change/area)² vs. time plots for the coated and uncoated superalloy Superni 75 subjected to 1000 hrs cyclic exposure to platen superheater zone of the coal fired boiler at 900 °C.

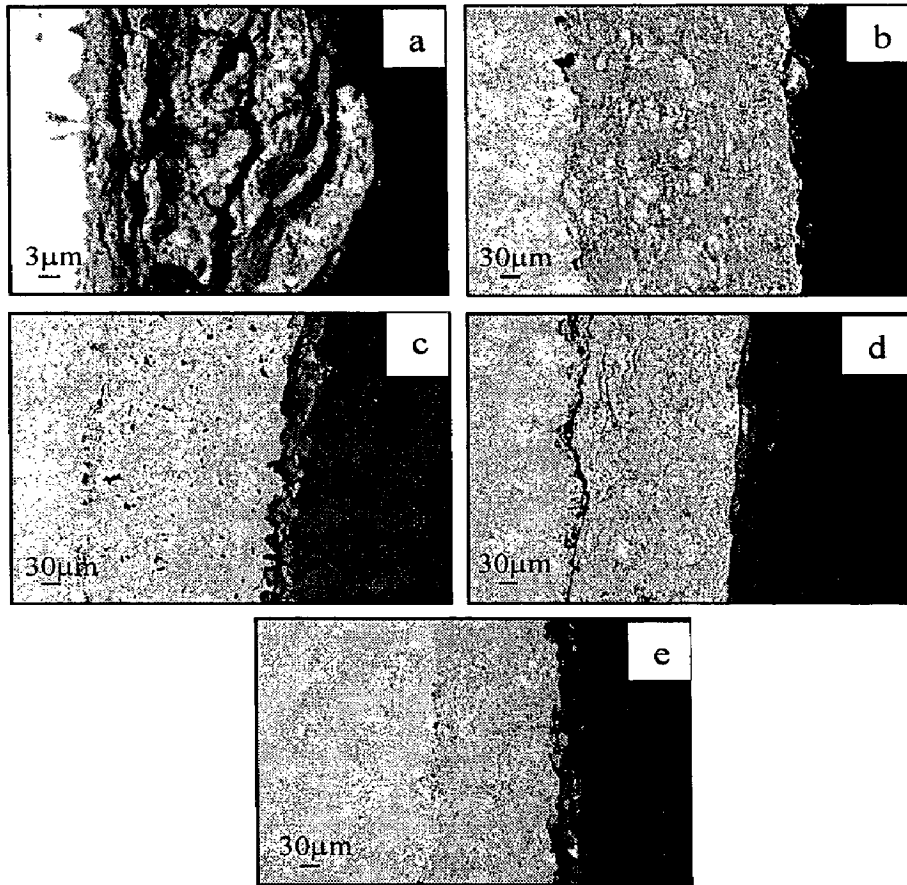


Fig. 7.8 BSE images for the bare and HVOF coated Superni 75 after 1000 hrs exposure to platen superheater zone of the coal fired boiler at 900 °C: (a) Bare superalloy (b) Cr₃C₂-NiCr coated (c) NiCrBSi coated (d) Stellite-6 coated (e) Ni-20Cr coated.

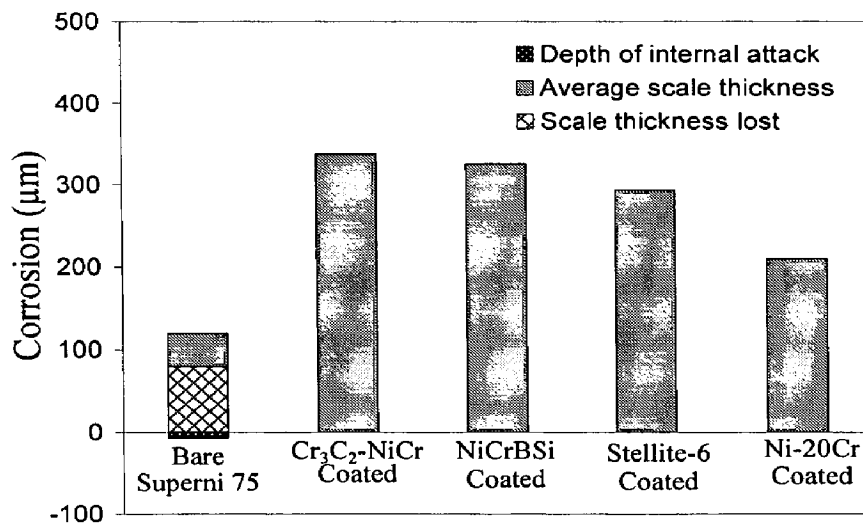


Fig. 7.9 Bar charts indicating the extent of corrosion for the bare and HVOF coated Superni 75 after 1000 hrs exposure to the coal fired boiler at 900 °C.

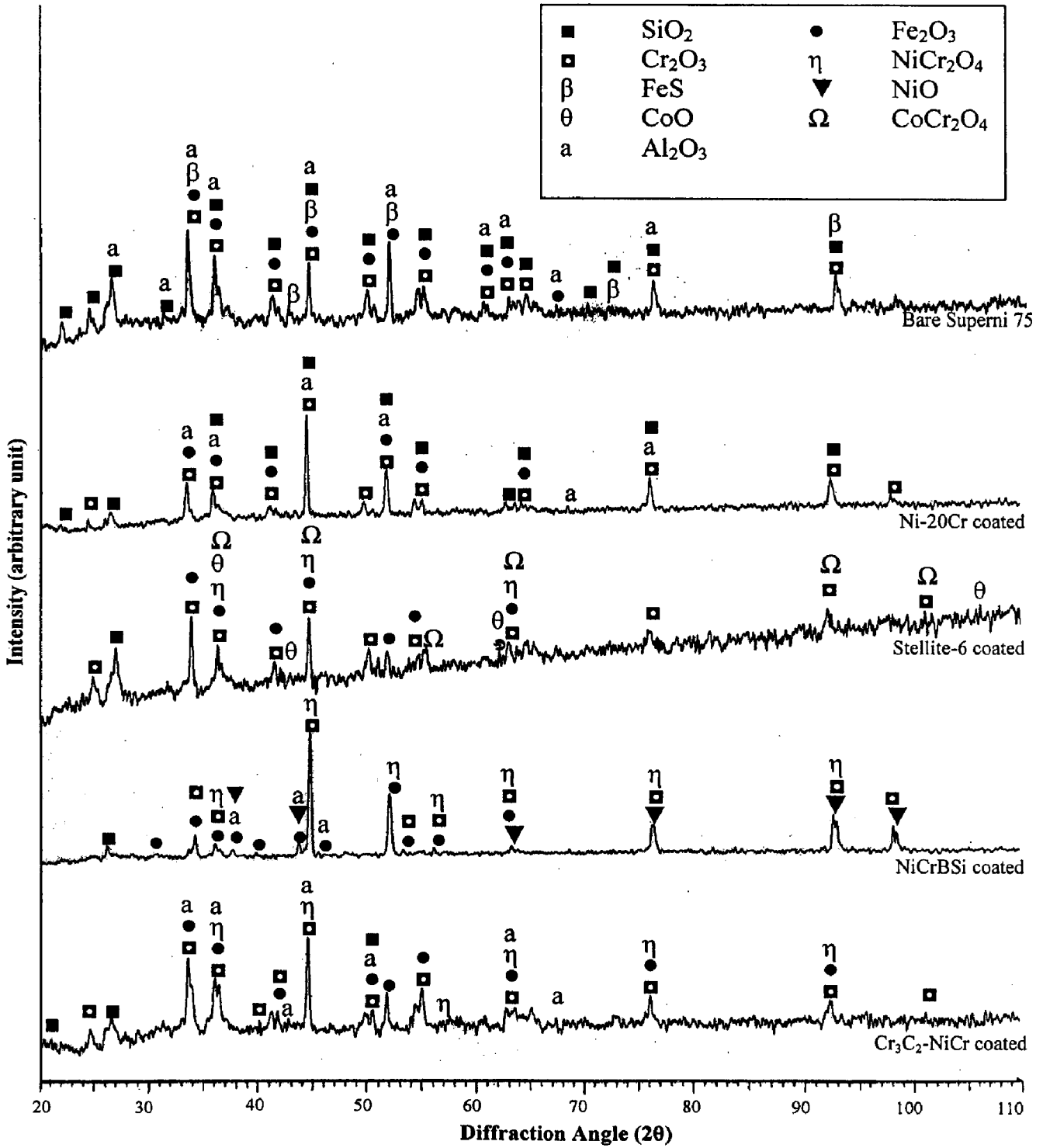


Fig. 7.10 X-ray diffraction patterns for the bare and coated superalloy Superni 75 after 1000 hrs exposure to platen superheater zone of the coal fired boiler at 900 °C.

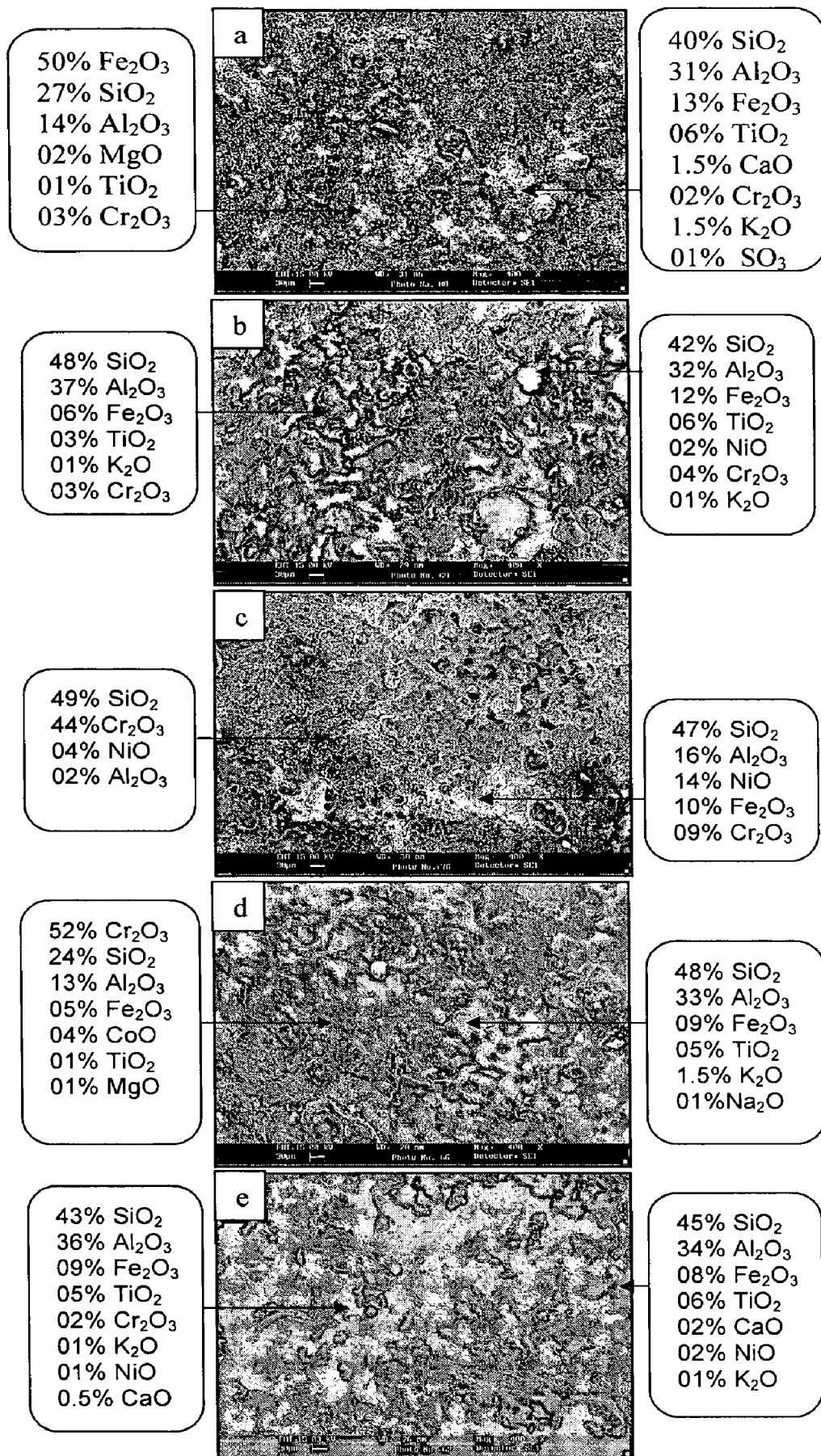


Fig. 7.11 SEM/EDAX analysis showing elemental composition (wt.%) for the bare and coated Superni 75 after 1000 hrs exposure to platen superheater zone of the coal fired boiler at 900 °C: (a) Bare Superni 75 (b) Cr₃C₂-NiCr coated (c) NiCrBSi coated (d) Stellite-6 coated (e) Ni-20Cr coated.

7.1.3.4(B) Cross-Section Analysis

The BSE images and EDAX analysis at some selected point of interest across the cross-section of corroded uncoated and NiCrBSi coated Superni 75 are shown in Fig. 7.12.

About 45 μm thick corrosion scale formed on the bare Superni 75 has a duplex structure (Fig. 7.12a). The inner layer is continuous and adherent with the substrate, whereas adherence loss can be seen in the intermediate zone of the outer layer. EDAX analysis indicated that the inner layer (Point 3) contains mainly chromium, nickel and oxygen with small amounts of iron, titanium, and sulphur; and the outer layer (Points 4 and 5) exhibit presence of silicon, aluminium and oxygen rich zones which indicate the interaction of ash with the outer scale. The Point 2 indicates the penetration of oxide scale into the substrate. However, as compared to other substrates, the internal attack in this substrate is confined to only a very limited extent. The EDAX analysis shows that this contrast grey phase (Point 2) consists mainly of Cr which has increased, whereas Ni has decreased substantially in this phase. The existence of significant quantity of oxygen (42 wt%) points out that this gray phase is rich in Cr_2O_3 . The substrate alloy contains small amounts of sulphur (1.0 wt%) at Point 1.

BSE image of the corroded NiCrBSi coated Superni 75 (Fig. 7.12b) gives no indication of adhesion loss of the scale. The EDAX analysis shows the absence of oxygen near the coating-substrate interface (Point 1). Therefore, it can be inferred that NiCrBSi coating develops a barrier to the penetration of oxygen. The thin contrast stringers at the scale-substrate interface (Point 2) are enriched rich in aluminium (34 wt%) and oxygen (40 wt%) along with 2.2 wt% titanium, whereas the amounts of Ni, Cr and Fe have decreased substantially. The white areas (Point 3 and 4) in the scales are found to be Ni-rich splats and absence of oxygen at these points suggests that these Ni-rich splats are in the unoxidised state. Black contrast spots (Point 5) are present at the splat boundaries throughout the coating. The featureless sub-scale layer (Point 6) is rich in chromium and oxygen suggesting the presence of mainly Cr_2O_3 . Some silicon and significant nickel are also present in these regions. The topmost part of the scale (Point 7) contains mainly of chromium, silicon and oxygen with little amount of nickel.

7.1.3.5 EPMA Analysis

BSE images and elemental X-ray maps for the uncoated and coated Superni 75 after cyclic exposure to the given environment are shown in Figs. 7.13 to 7.17.

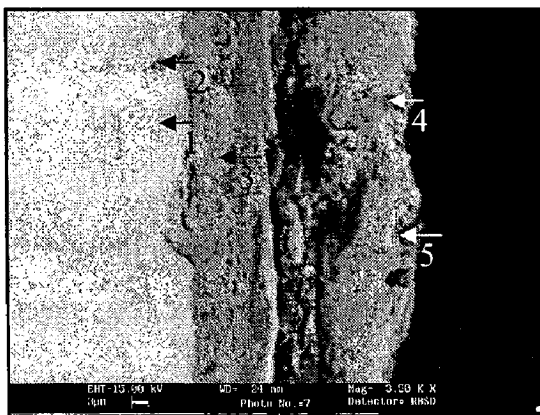
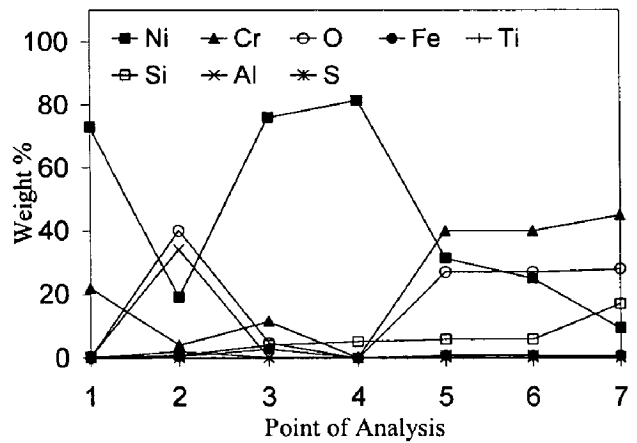
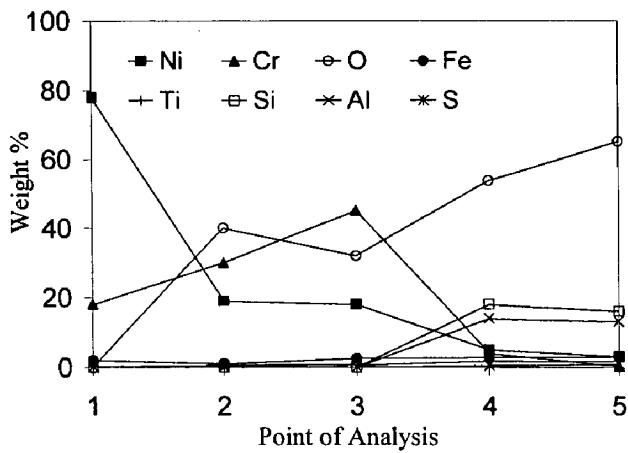
The BSE image of the bare Superni 75 shows severe internal attack as the oxide scale is penetrating deeply into the substrate to about 30 μm (Fig. 7.13). Elemental maps show that the ash particles of Al, Si, K and Ca form a thick layer in the topmost part of the scale. Underneath of these deposits, Fe forms a nearly continuous thin layer, whereas

Cr along with Ti forms a thick band. Titanium also shows a tendency to form clusters in the areas of internal attack, where Ni gets depleted.

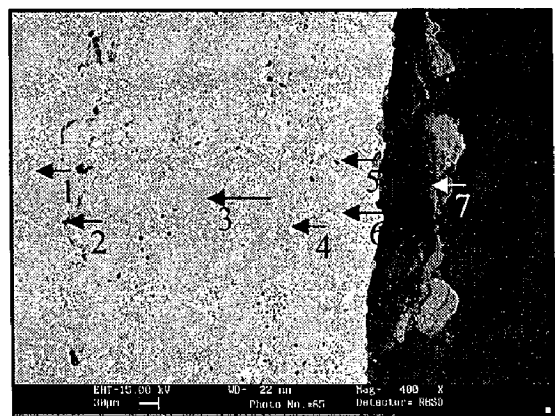
The Cr₃C₂-NiCr coated Superni 75 forms a continuous and adherent oxide scale after exposure to boiler environment for 1000 hours at 900 °C (Fig. 7.14). The upper half of the coating changed significantly as compared to lower half. The topmost layer of the scale is found to be enriched with oxides of chromium and iron. Chromium mostly co-exists with oxygen and forms thick network of Cr₂O₃ in the upper half of the coating just beneath of topmost layer. The Ni-rich splats present throughout the scale mostly remain in un-oxidised state whereas chromium forms oxide at their boundaries. The formation of a thick layer of iron at the topmost part of the scale is due to diffusion of iron from the substrate and partly due to ash deposition in the surface scale. Titanium shows a tendency to diffuse outward from the substrate due to its higher affinity towards oxygen and reaches up to the surface where it forms a continuous thick streak. Some islands of aluminium are present at the scale-substrate interface, where all other elements are found to be absent. The presence of oxygen at these places indicates that these islands are inclusions of aluminium oxide. The silicon, sulphur and potassium show their presence mainly in the surface scale. The penetration of oxygen is restricted up to the scale-substrate interface thereby indicating the protective nature of the coating.

X-ray mappings for the corroded NiCrBSi coated Superni 75 indicate that silicon and chromium form a thick and continuous layer in the topmost part of the scale (Fig. 7.15). Nickel is also present in the topmost scale in the form of a porous layer. The presence of aluminium and calcium in the surface scale provides evidence of interaction of ash with the scale. The sulphur penetrates along the splat boundaries and reaches up to the scale-substrate interface and co-exists with chromium forming CrS. The oxidation of this CrS yields a protective scale of Cr₂O₃ as suggested by Khanna and Jha (1998). Nickel-rich splats are present uniformly throughout the scale, and chromium and silicon are mostly present at their splat boundaries. The elemental mapping for iron shows a large amount of outward diffusion from the substrate to the coating.

A scale formed on Stellite-6 coated Superni 75 (Fig. 7.16) has a lamellar flat splat structure. The scale mainly consists of Co-rich splats with chromium mostly present at their boundaries. The presence of a continuous thick layer consisting of aluminium, calcium and iron in the topmost scale is an indication of the interaction of ash with the scale. Iron has also diffused from the substrate to reach the topmost scale. Significant amount of titanium diffused outward from the substrate and formed a thick layer in the topmost part of the scale. Sodium and sulphur are present throughout the scale indicating that they might have penetrated along the splat boundaries or through the open pores during the initial hours of exposure. But once the oxides are formed, they blocked the splat boundaries and pores and didn't allow these corrosive species to penetrate further.



(a)



(b)

Fig 7.12 Oxide scale morphologies and variations of elemental composition (wt%) across the cross section of bare and HVOF coated Superni 75 after 1000 hrs exposure to platen superheater zone of the coal fired boiler at 900 °C :
(a) Bare Superni 75 (b) NiCrBSi coated.

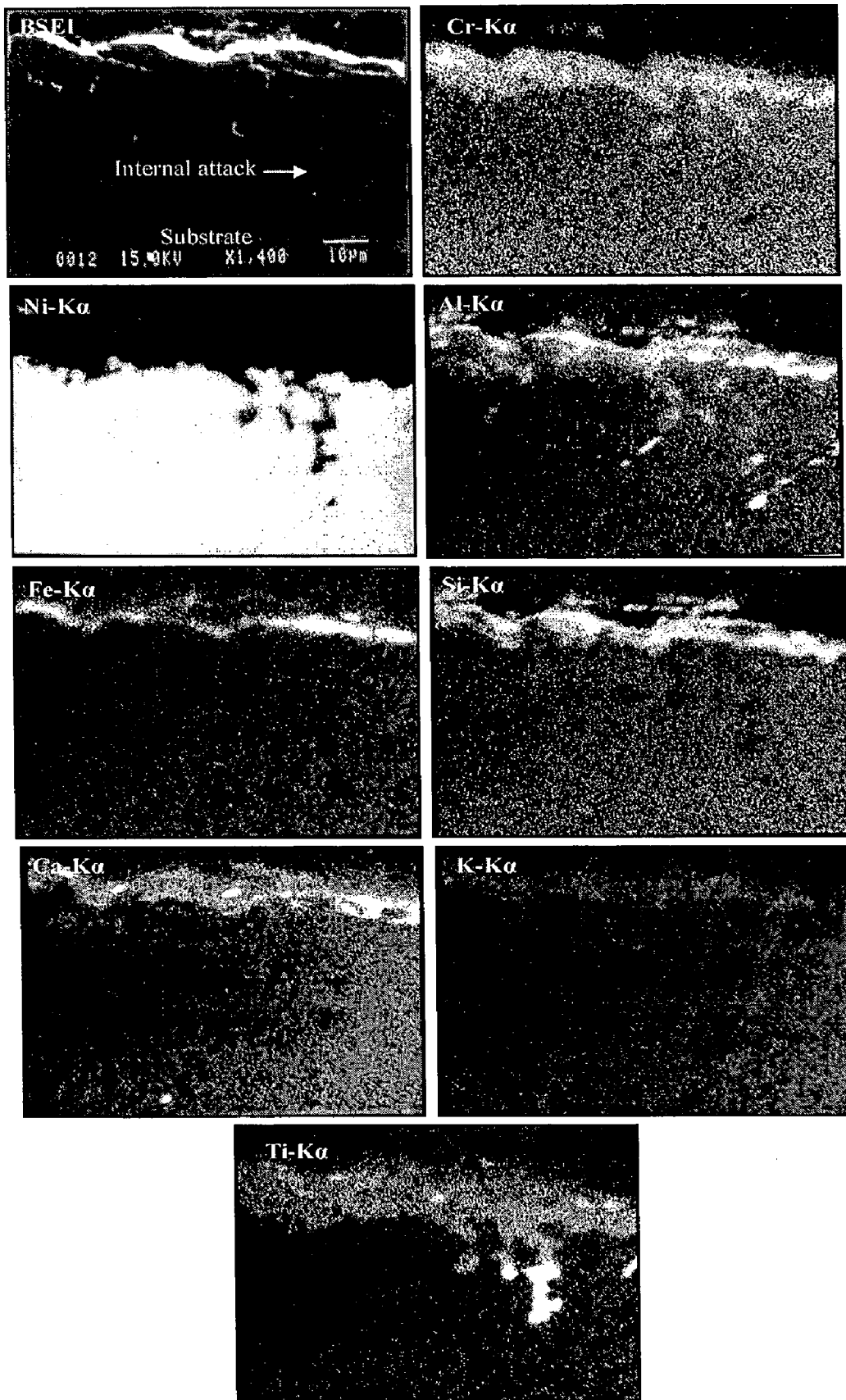


Fig. 7.13 Composition image (BSEI) and X-ray mappings across the cross-section of bare Superni 75 after 1000 hrs exposure to platen superheater zone of the coal fired boiler at 900 °C.

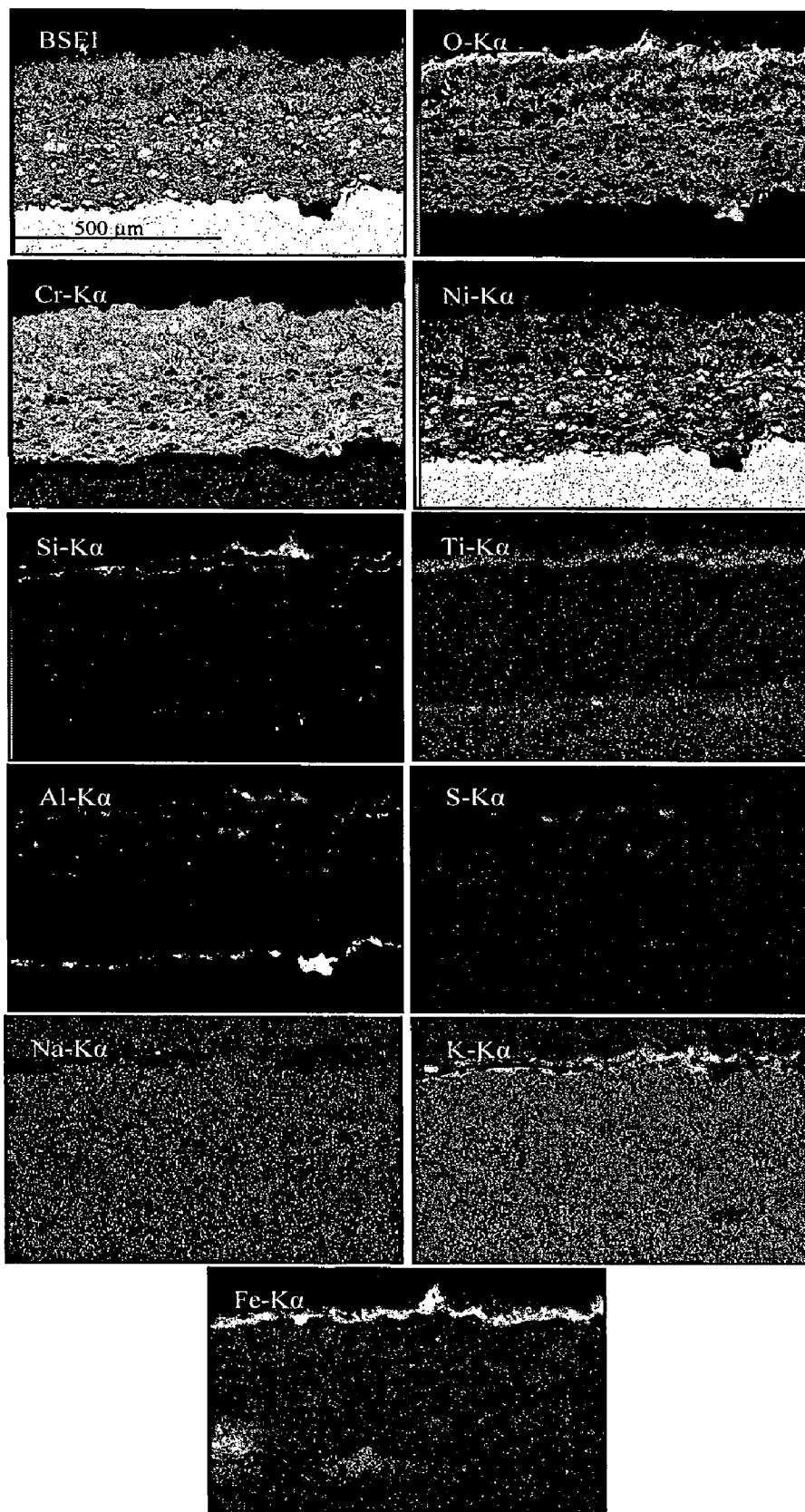


Fig. 7.14 Composition image (BSEI) and X-ray mappings across the cross-section of $\text{Cr}_3\text{C}_2\text{-NiCr}$ coated Superni 75 after 1000 hrs exposure to platen superheater zone of the coal fired boiler at 900 °C.

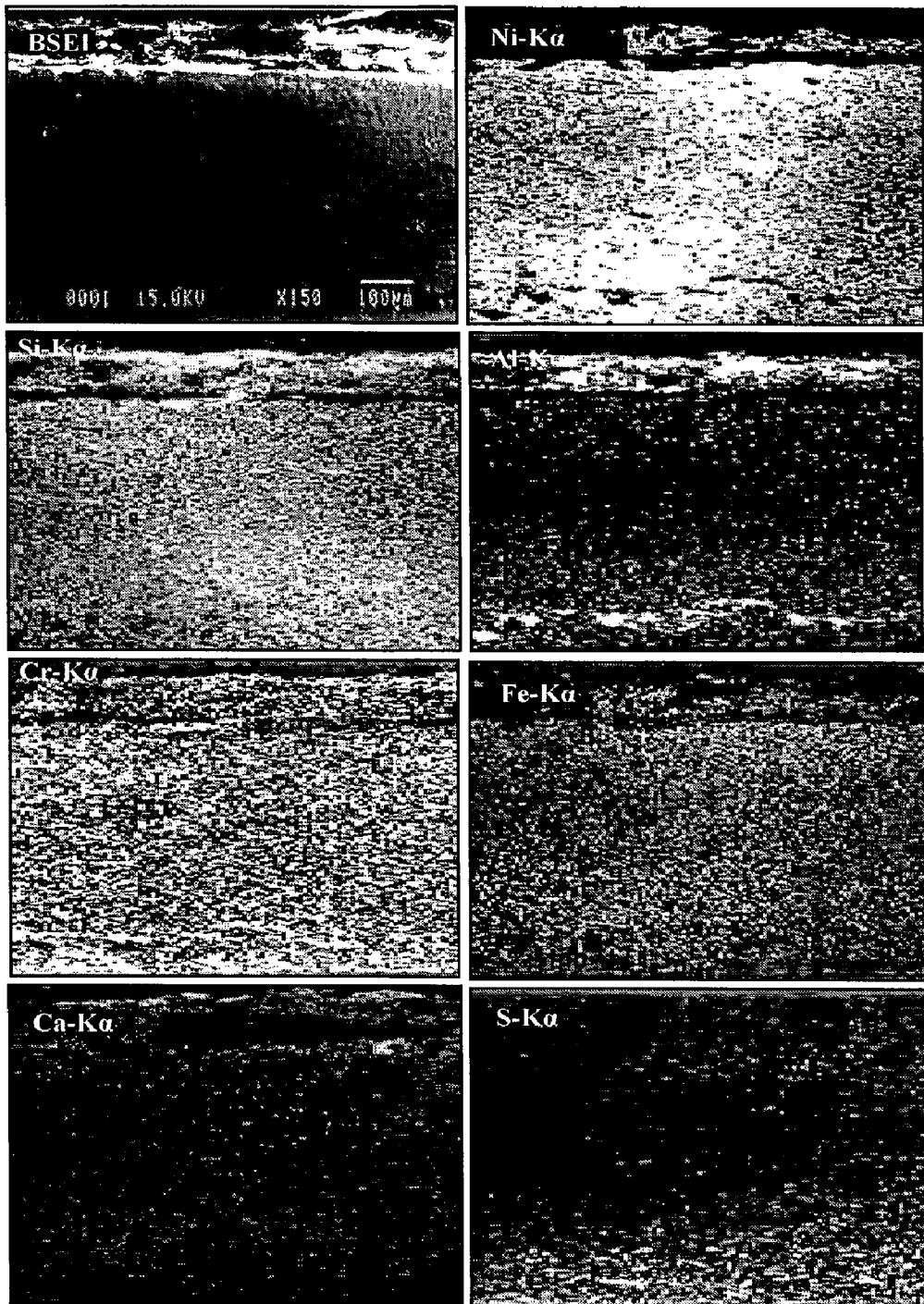


Fig. 7.15 Composition image (BSEI) and X-ray mappings across the cross-section of NiCrBSi coated Superni 75 after 1000 hrs exposure to platen superheater zone of the coal fired boiler at 900 °C.

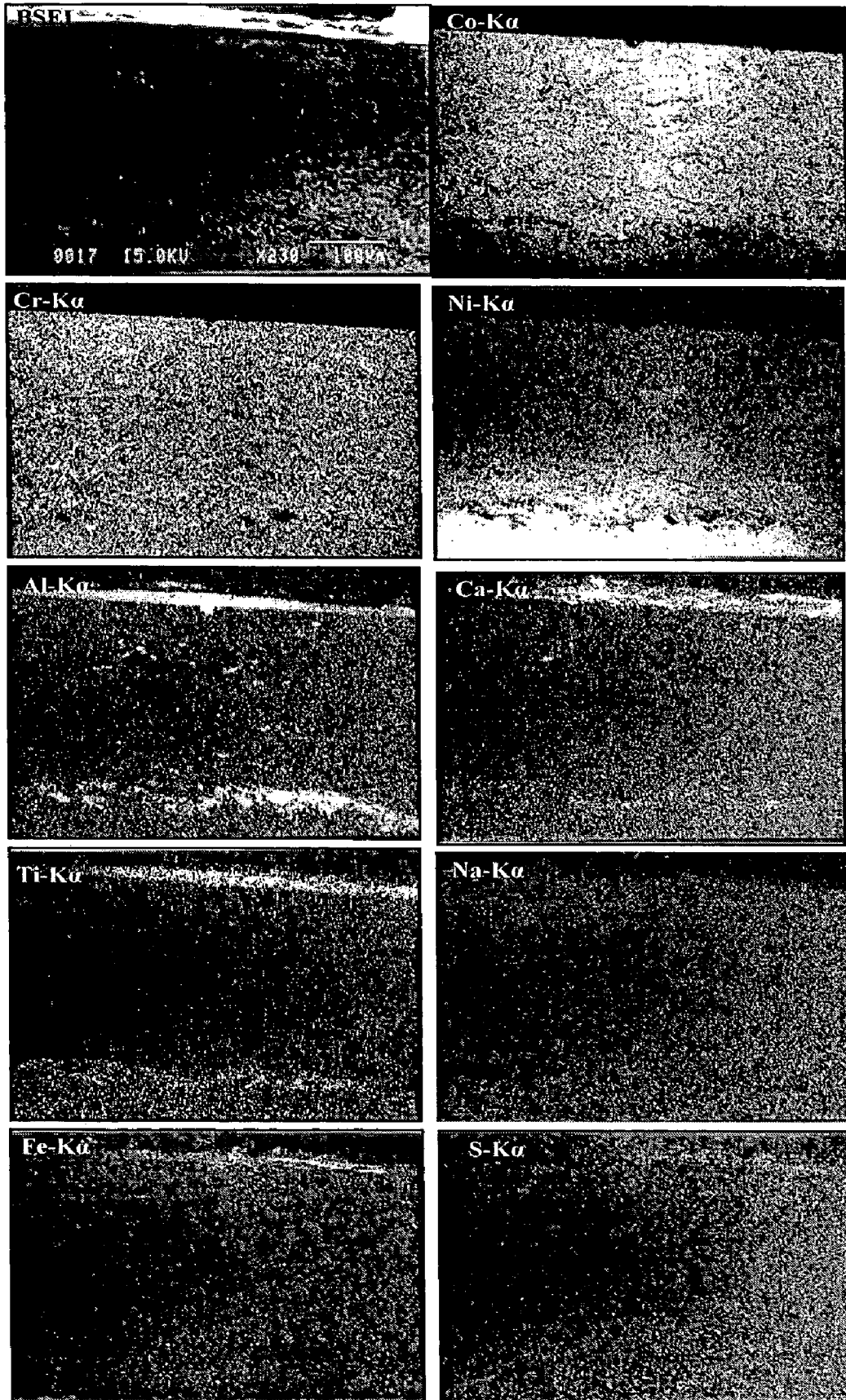


Fig. 7.16 Composition image (BSEI) and X-ray mappings across the cross-section of Stellite-6 coated Superni 75 after 1000 hrs exposure to platen superheater zone of the coal fired boiler at 900 °C.

The scale formed on the Ni-20Cr coated Superni 75 after 1000 hrs exposure to the given environment has a lamellar structure with elongated splats (Fig. 7.17). The elemental mappings for Cr, Ni and O show that Cr_2O_3 is mostly formed at the boundaries of Ni-rich splats, whereas Ni-rich splats generally remain un-oxidised. Chromium shows a tendency to form a Cr_2O_3 -rich thick network just above the scale-substrate interface. The elemental mappings for Si, Al, Fe, K, and Ca show the presence of high density dots at the topmost part of the scale indicating that ash particles of the boiler environment are interacting with the scale. Some corrosive species from the boiler environment penetrates into the scale and exist mostly at the splat boundaries. The exclusive islands of Al and O which co-exist at the scale-substrate interface are the inclusions of Al_2O_3 . In this coating-substrate system, diffusion of iron is found to be negligible. The absence of oxygen beneath the scale-substrate interface indicates that the Ni-20Cr coating effectively protects the substrate.

7.1.4 Hot Corrosion of Bare and Coated Superni 600

7.1.4.1 Corrosion Kinetics

The weight change plots for the bare and coated Superni 600 are shown in Fig. 7.18. After 1000 hours of cyclic exposure to boiler environment, the Ni-20Cr coating deposited on Superni 600 revealed the lowest weight gain, whereas the weight gain is highest for NiCrBSi coating. The Stellite-6 and Cr_3C_2 -NiCr coatings showed the second and third lowest weight gains. The bare Superni 600 showed a minimum weight gain than its coated counterpart due to spallation of the scale. Figure 7.19 shows (weight change/area)² verses time plots. It can be seen from the graph that all the coatings on Superni 600 follow a parabolic rate law with little deviations, whereas substrate Superni 600 shows considerable deviations from the parabolic rate law which has been attributed to spallation of the scale during experimentations. Therefore, it can be inferred that the coatings have provided the necessary protection to bare Superni 600 in the given environment. The parabolic rate constants (k_p in $10^{-12} \text{ g}^2 \text{ cm}^{-4} \text{ s}^{-1}$) for the Cr_3C_2 -NiCr, NiCrBSi, Stellite-6 and Ni-20Cr coated Superni 600 are found to be as 8.38, 9.36, 6.33, and 5.58, respectively.

7.1.4.2 Average Scale Thickness and Depth of Internal Attack

SEM back scattered micrographs along the cross-section of scale formed on bare and coated Superni 600 are shown in Fig. 7.20. The average scale thickness and depth of internal corrosion attack for bare Superni 600 are evaluated to be as about 18 μm and 34 μm , respectively. The average scale thickness for Cr_3C_2 -NiCr, NiCrBSi, Stellite-6 and Ni-20Cr coated Superni 600 is found to be as 310, 200, 275, and 205 μm , respectively. The BSEI micrographs show no internal corrosion attack for the Cr_3C_2 -NiCr and Stellite-6 coated Superni 600, whereas corrosive effects can be seen for NiCrBSi and Ni-20Cr coated Superni 600 to a depth of 120 and 60 μm , respectively. The corrosive species might have

penetrated through the splat boundaries of NiCrBSi and Stellite-6 coatings during the initial hours of exposure. Subsequently, oxide phases formed at the splat boundaries and in pores blocked the diffusion of corrosive species. The average scale thickness, scale thickness loss (reported under section 7.1.2) and depth of internal corrosion attack for bare and coated Superni 600 are given in Fig. 7.21. By considering the combined effects of average scale thickness, scale thickness lost and depth of internal corrosion attack, it is noted that the Ni-20Cr coating offers highest resistance to hot corrosion in the given environment, followed by Stellite-6 and Cr₃C₂-NiCr coatings respectively, whereas NiCrBSi coating offers least resistance. The Ni-20Cr and Stellite-6 coatings have shown almost similar resistance to the boiler environment.

7.1.4.3 X-ray Diffraction Analysis

The diffraction patterns for the bare and coated Superni 600 after exposure to boiler environment are shown in Fig. 7.22. The main phases detected with XRD analysis are presented in Table 7.2. The XRD analysis revealed the presence of phases like Al₂O₃ and SiO₂ which don't match with elements of either the substrate or the coating but they are matching with the main phases of ash composition suggesting the interaction of ash deposits with the outer layer of the scale.

Table 7.2: Major and minor phases identified by XRD analysis for the bare and coated Superni 600 after 1000 hrs exposure to actual environment of the coal fired boiler.

Description	Major phases	Minor phases
Uncoated Superni 600 superalloy	Cr ₂ O ₃ , Fe ₂ O ₃ , Al ₂ O ₃ , SiO ₂ , and FeS	NiS
Cr ₃ C ₂ -NiCr coated	Cr ₂ O ₃ , Fe ₂ O ₃ , Al ₂ O ₃ , SiO ₂ , NiO, and NiCr ₂ O ₄	MnO ₂
NiCrBSi coated	Cr ₂ O ₃ , Fe ₂ O ₃ , NiO, Al ₂ O ₃ , SiO ₂ , and NiCr ₂ O ₄	MnO ₂
Stellite-6 coated	Cr ₂ O ₃ , Fe ₂ O ₃ , CoCr ₂ O ₄ , and NiCr ₂ O ₄	CoO, MnO ₂ , and Al ₂ O ₃
Ni-20Cr coated	NiO, Fe ₂ O ₃ , Al ₂ O ₃ , Cr ₂ O ₃ , and NiCr ₂ O ₄	MnO ₂

7.1.4.4 SEM/EDAX Analysis

7.1.4.4(A) Surface Analysis

The SEM micrographs for the corroded bare and coated Superni 600 are shown in Fig. 7.23.

A fragile scale with number of cracks is formed on the surface of bare Superni 600 (Fig. 7.23a). The EDAX analysis shows that the surface scale has a composition almost similar to ash composition indicating the participation of condensed phases from the

boiler environment in the corrosion mechanism. The white phase of the scale is rich in silica, alumina and Fe_2O_3 , whereas dark grey phase has relatively higher amounts of iron oxide. It can be seen that the scale has a tendency for spallation.

A continuous and adherent granular scale is formed on the Cr_3C_2 -NiCr and Ni-20Cr coated Superni 600, whereas the scales formed on NiCrBSi and Stellite-6 coated superalloy are relatively massive. In general, all the coatings have formed compact scales without indications of any crack. The EDAX analysis of the surface scales formed on coated specimens also shows mainly the presence of ash deposits. The grains formed in the scale of Ni-20Cr coated specimen are found to be rich in nickel oxide. The presence of manganese oxide in the outermost layer of the scale formed on Cr_3C_2 -NiCr and Stellite-6 coated Superni 600 indicates its outward diffusion from the substrate (Figs. 7.23b and 7.23d).

7.1.4.4(B) Cross-Section Analysis

The BSE images and EDAX analysis at some selected point of interest across the cross-section of corroded Stellite-6 and Ni-20Cr coated Superni 600 are shown in Fig. 7.24. The scale formed on both the coated specimens is continuous and adherent, and has retained lamellar structure of the as-sprayed coatings. There is no indication of any crack in the scale. The EDAX analysis for both the coated specimens shows that manganese element of the substrate has diffused outward up to the surface.

The EDAX analysis of Stellite-6 coated Superni 600 (Fig. 7.24a) shows the presence of very little amount of oxygen at Point 1 just below the scale-substrate interface, indicating that only limited oxygen has penetrated during initial hours of the exposure. The EDAX results at Points 2 and 5 indicate the existence of Co-rich splats. The presence of chromium and oxygen at Points 3 and 4 suggests that chromium oxide is formed at the boundaries of these Co-rich splats due to the selective oxidation of the chromium. The topmost scale (Point 6) composed mainly of oxygen and chromium and, therefore, this region is rich in chromium oxide. The oxides formed at the boundaries of Co-rich splats and in the topmost layer of the coating blocked the penetration of degrading species to the substrate after initial hours of the exposure.

The absence of degrading species underneath the scale-substrate interface (Point 1 of Fig 7.24b) of Ni-20Cr coated Superni 600 is a symptomatic of the protective behaviour of this coating. The scale formed at Point 2 has enriched in chromium and oxygen and nickel has decreased significantly in this region. It implies that a thick layer of Cr_2O_3 is formed just above the scale-substrate interface. The white phase in the scale (Point 3) consists of Ni-rich splats surrounded by chromium oxide. Further, there is a possibility of solid-state reaction at the splat boundaries to form NiCr_2O_4 spinel. The scale formed at Points 4 and

5 mainly composed of nickel, chromium and oxygen indicating that the uppermost scale consists essentially of oxides of Ni and Cr.

7.1.4.5 EPMA Analysis

BSE images and elemental X-ray maps for the uncoated and coated Superni 600 after exposure to the given environment are shown in Figs. 7.25 to 7.29.

The BSE image shows that the scale formed on the bare Superni 600 penetrates into the substrate (Fig. 7.25). The EPMA analysis indicates that thick layers formed at the upper part of the scale consist of mainly aluminium, silicon, iron and sulphur along with potassium. The presence of Al, Si and Fe in the surface scale might be due to the formation of condensed phases from the boiler environment and partly due to diffusion from the substrate. High intensity X-ray dots of manganese are also present in this layer of the deposits. Just beneath of these deposits, a thick band of chromium is formed with little amounts of nickel.

The Cr₃C₂-NiCr coated Superni 600 forms a uniform, homogeneous and adherent oxide scale after 1000 hours of cyclic exposure to the boiler environment (Fig. 7.26). The elemental map for oxygen shows that the oxide scale has blocked the penetration of oxygen to the substrate, indicating protective characteristics of the coatings in the given environment. The topmost layer of the scale is enriched in silicon and oxygen with little amount of aluminium, suggesting that the topmost scale is rich in silica and alumina. Just beneath of this, a thin continuous and uniform Cr₂O₃-rich layer is formed. Elemental maps show that chromium and some amount of nickel co-exist with oxygen in the remaining part of the scale, thus forming Cr₂O₃ with some amounts of NiO and also NiCr₂O₄. The nickel-rich splats are mostly found in un-oxidised state. The sulphur and potassium, which penetrated from the corrosive media, are mostly present at the splat boundaries in traces.

The scale formed on the NiCrBSi coated Superni 600 mainly consists of Ni, Cr and Si with some amounts of Fe (Fig. 7.27). The islands of aluminium, silicon and iron are present in the topmost part of the scale. Aluminium also forms thick clusters at the scale-substrate interface at places where other elements are found to be absent. Similarly, silicon is present in high concentration in the vicinity of scale-substrate interface. Sulphur and potassium species of the corrosive environment are confined mainly to the upper part of the scale.

The elemental mappings for the Stellite-6 coated Superni 600 (Fig. 7.28) show that the scale mainly consists of Co-rich splats with Cr, Si and O co-existing at the splat boundaries/pores thereby suggesting that the oxides of silicon and chromium have sealed/plugged the splat boundaries/pores. Therefore, penetration of oxygen is restricted to scale-substrate interface as can be seen from the oxygen map. Chromium present in higher concentration just above the scale-substrate interface forms a thin streak of

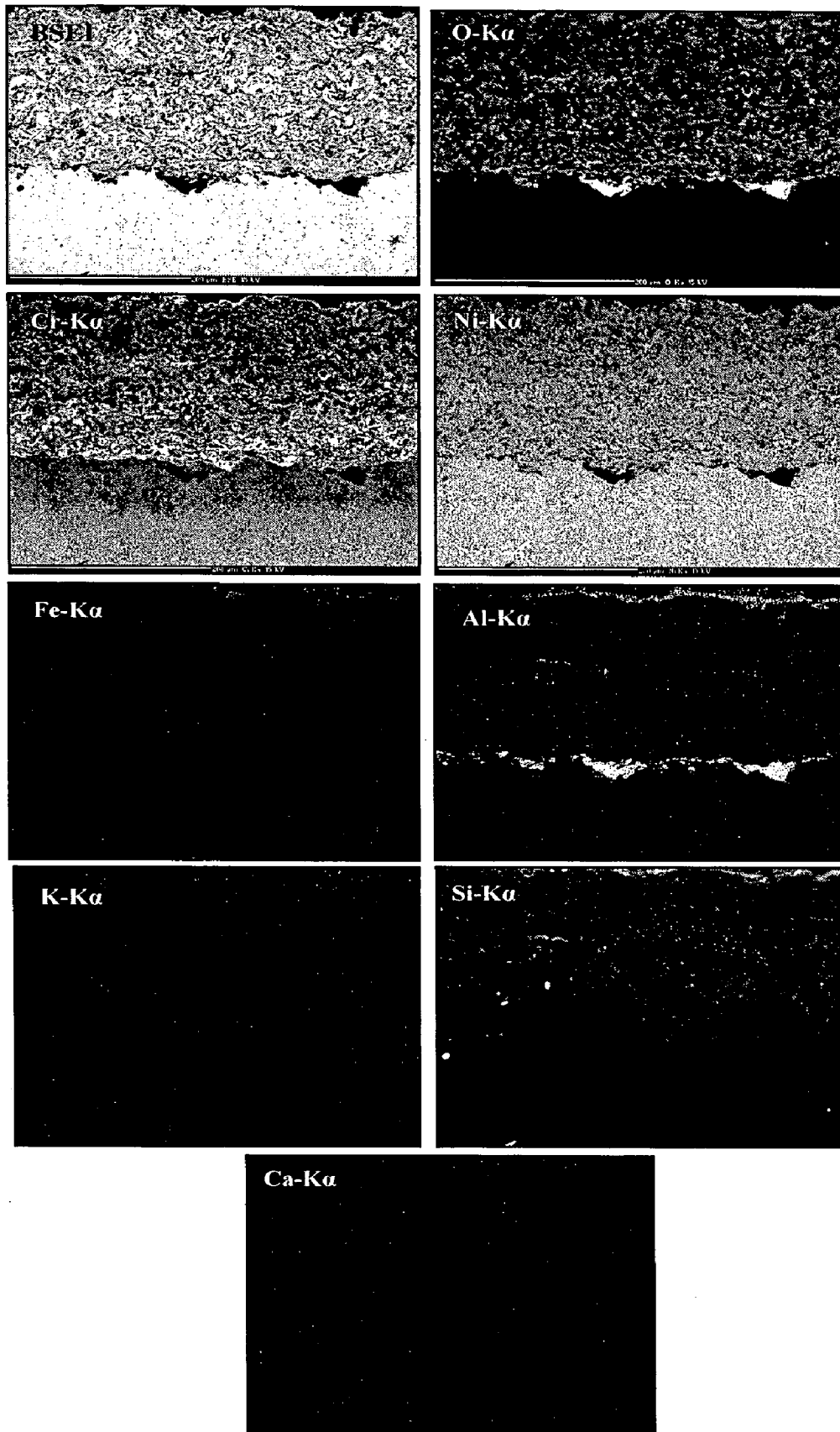


Fig. 7.17 Composition image (BSEI) and X-ray mappings across the cross-section of Ni-20Cr coated Superni 75 after 1000 hrs exposure to platen superheater zone of the coal fired boiler at 900 °C.

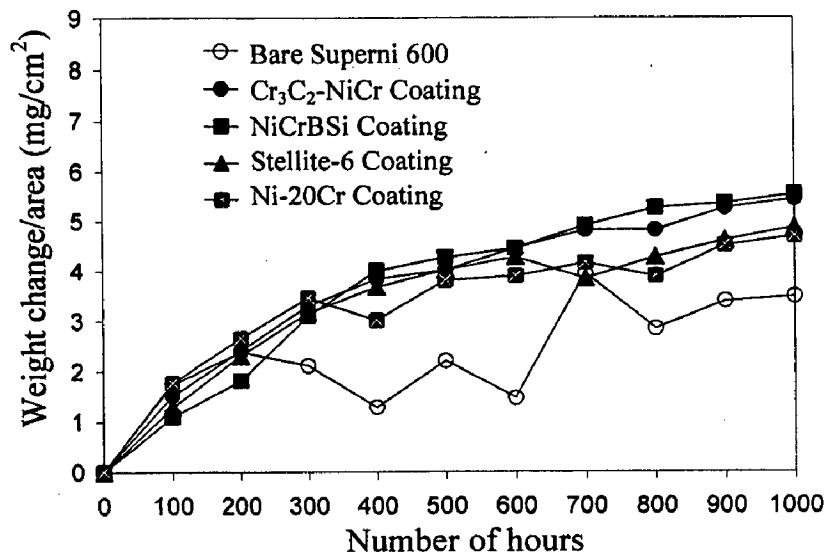


Fig. 7.18 Weight change vs. time plots for the coated and uncoated Superni 600 subjected to 1000 hrs cyclic exposure to platen superheater zone of the coal fired boiler at 900 °C.

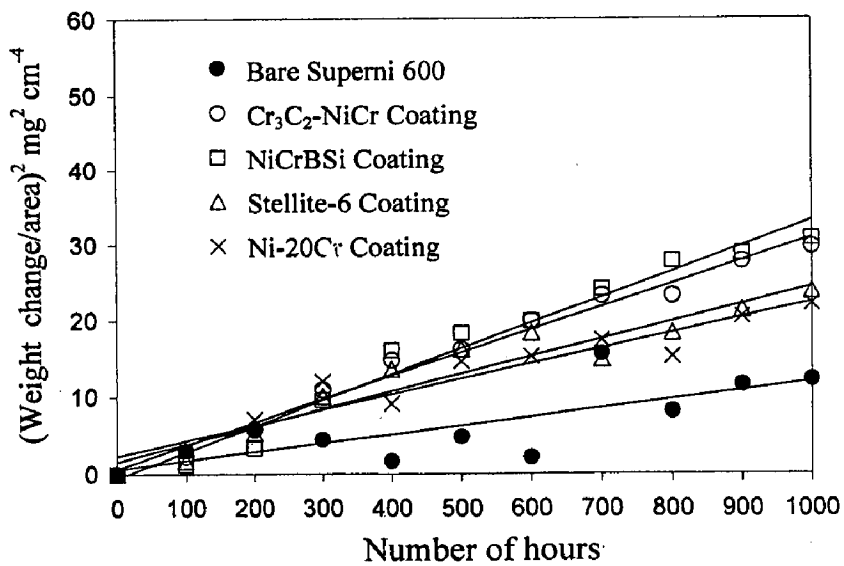


Fig. 7.19 (Weight change/area)² vs. time plots for the coated and uncoated Superalloy Superni 600 subjected to 1000 hrs cyclic exposure to platen superheater zone of the coal fired boiler at 900 °C.

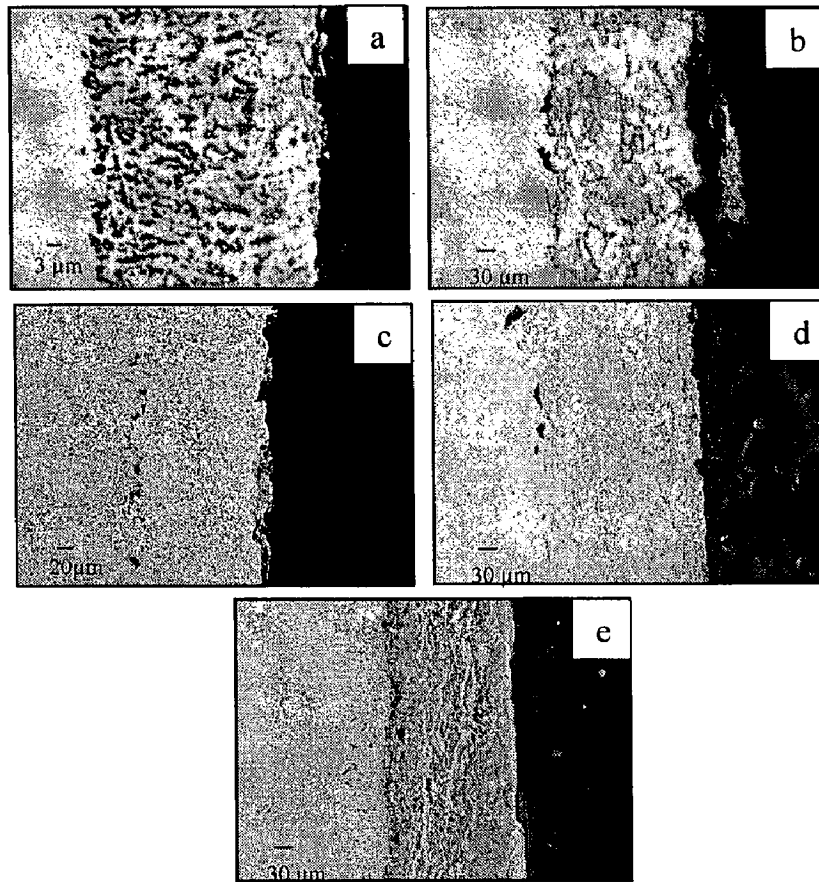


Fig. 7.20 BSE images for the bare and HVOF coated Superni 600 after 1000 hrs exposure to platen superheater zone of the coal fired boiler at 900 °C:
 (a) Bare superalloy (b) Cr₃C₂-NiCr coated (c) NiCrBSi coated
 (d) Stellite-6 coated (e) Ni-20Cr coated.

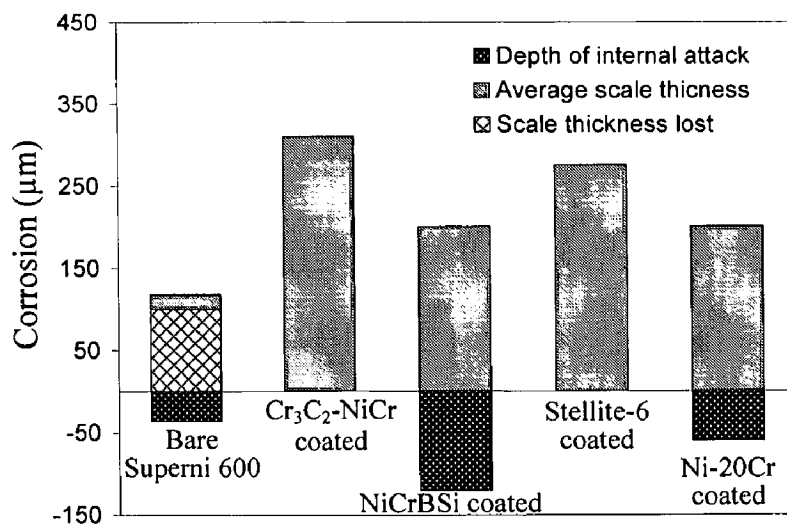


Fig. 7.21 Bar charts indicating the extent of corrosion for the bare and HVOF coated Superni 600 after 1000 hrs exposure to the coal fired boiler at 900 °C.

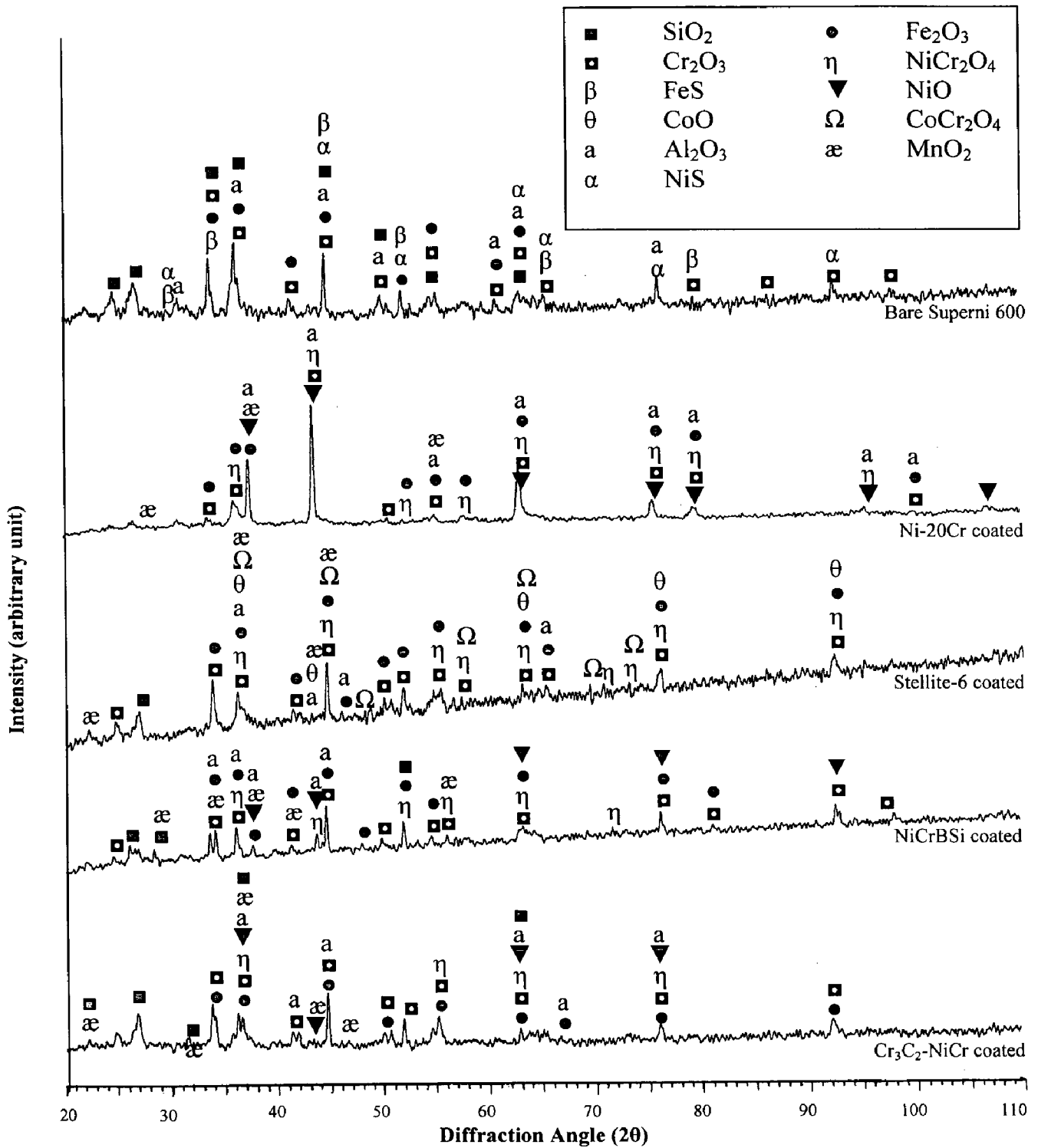


Fig. 7.22 X-ray diffraction patterns for the bare and coated superalloy Superni 600 after 1000 hrs exposure to platen superheater zone of the coal fired boiler at 900 °C.

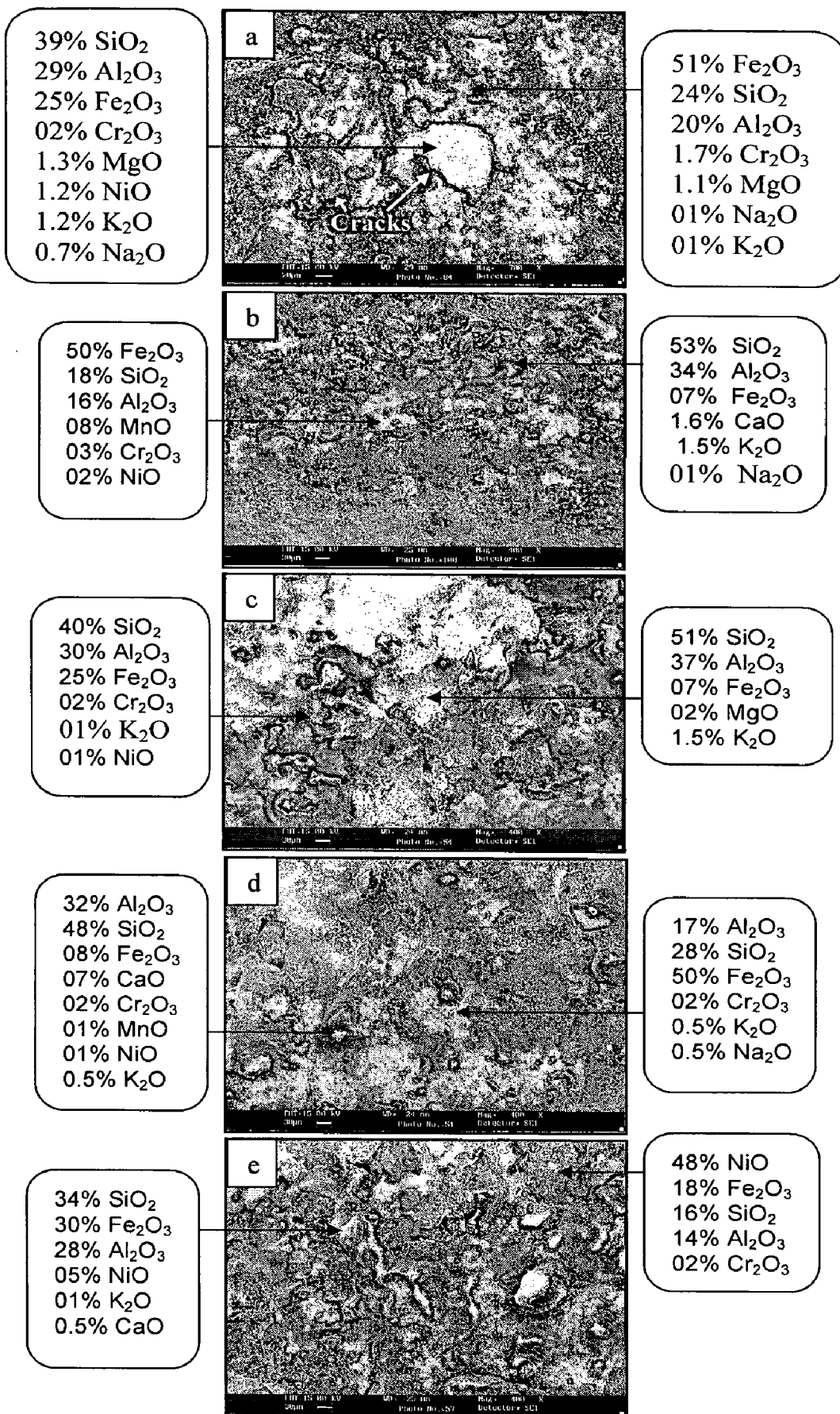


Fig. 7.23 SEM/EDAX analysis showing elemental composition (wt.%) for the bare and coated Superni 600 after 1000 hrs exposure to platen superheater zone of the coal fired boiler at 900 °C: (a) Bare Superni 600 (b) Cr₃C₂-NiCr coated (c) NiCrBSi coated (d) Stellite-6 coated (e) Ni-20Cr coated.

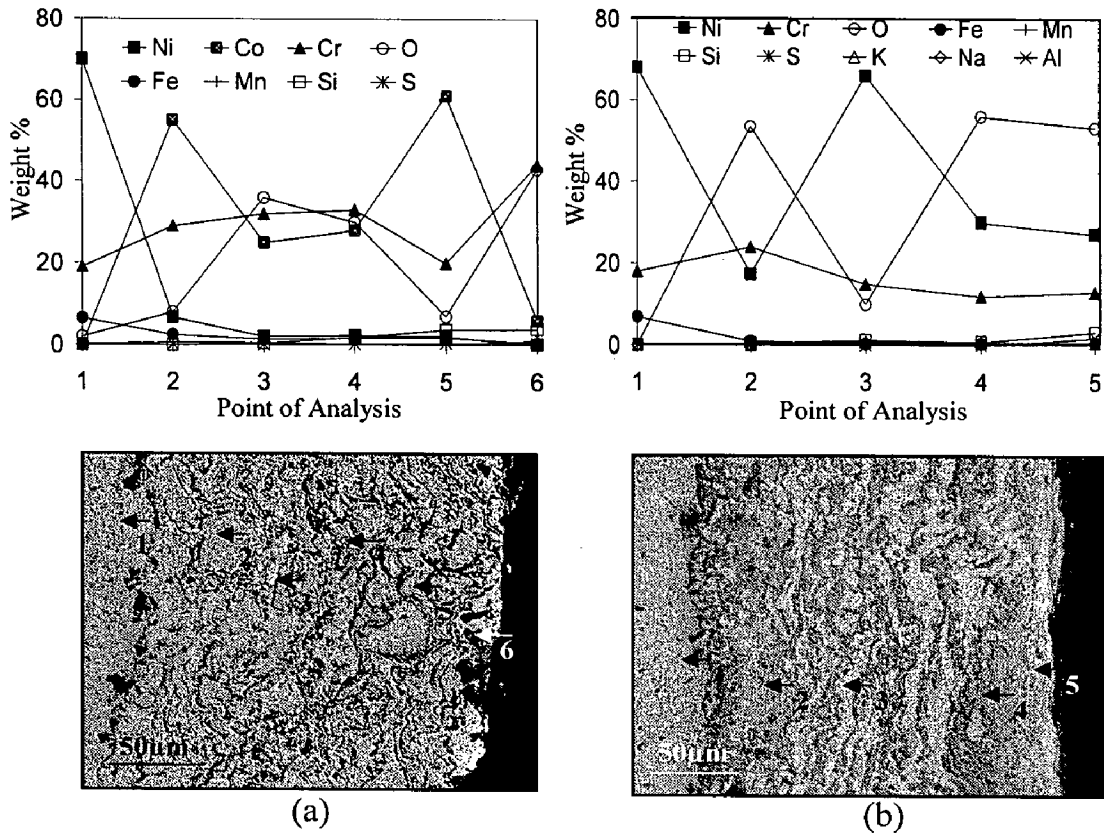


Fig 7.24 Oxide scale morphologies and variations of elemental composition (wt%) across the cross section of HVOF coated Superni 600 after 1000 hrs exposure to platen superheater zone of the coal fired boiler at 900 °C :
 (a) Stellite-6 coated (b) Ni-20Cr coated.

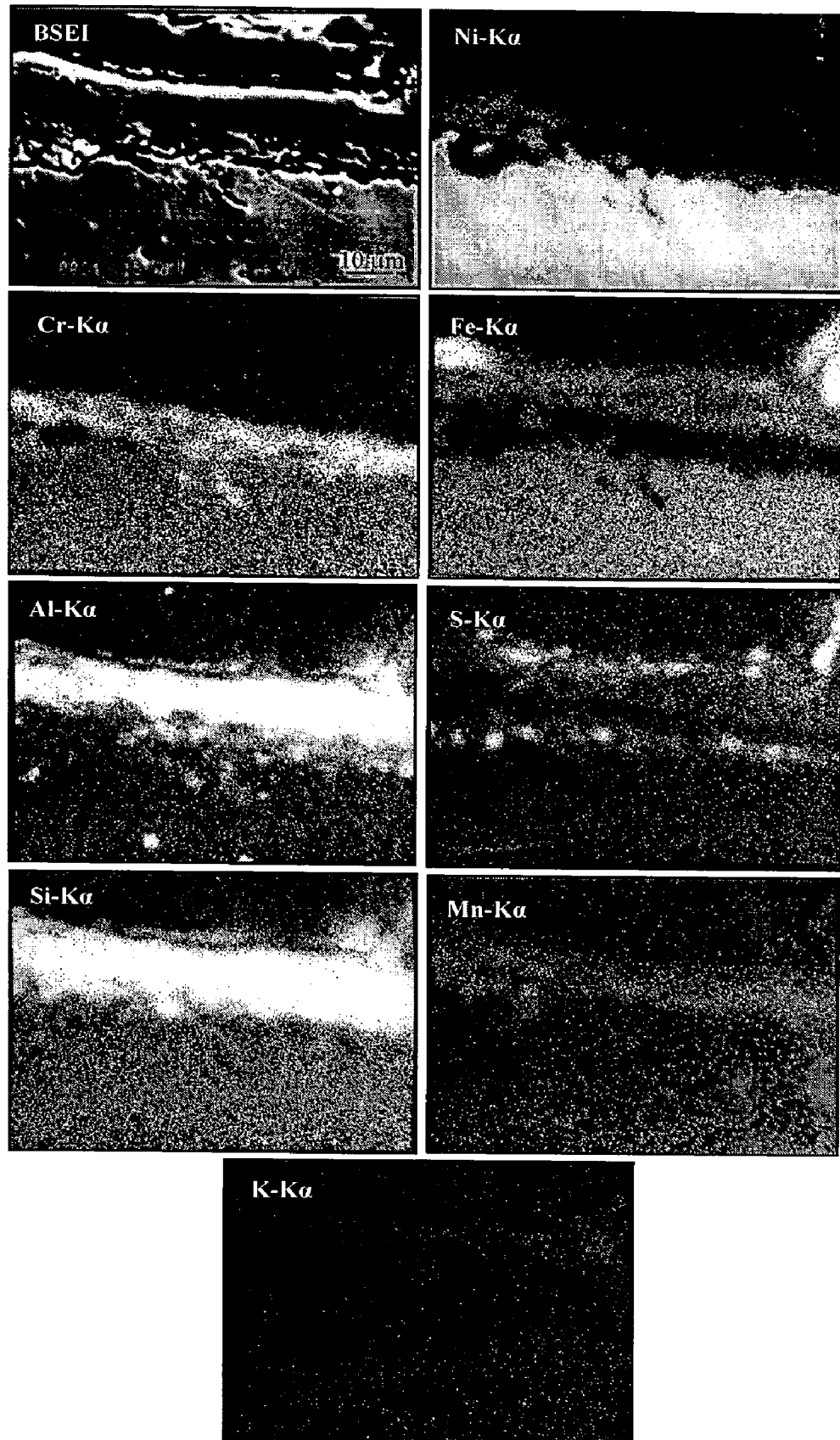


Fig. 7.25 Composition image (BSEI) and X-ray mappings across the cross-section of bare Superni 600 after 1000 hrs exposure to platen superheater zone of the coal fired boiler at 900 °C.

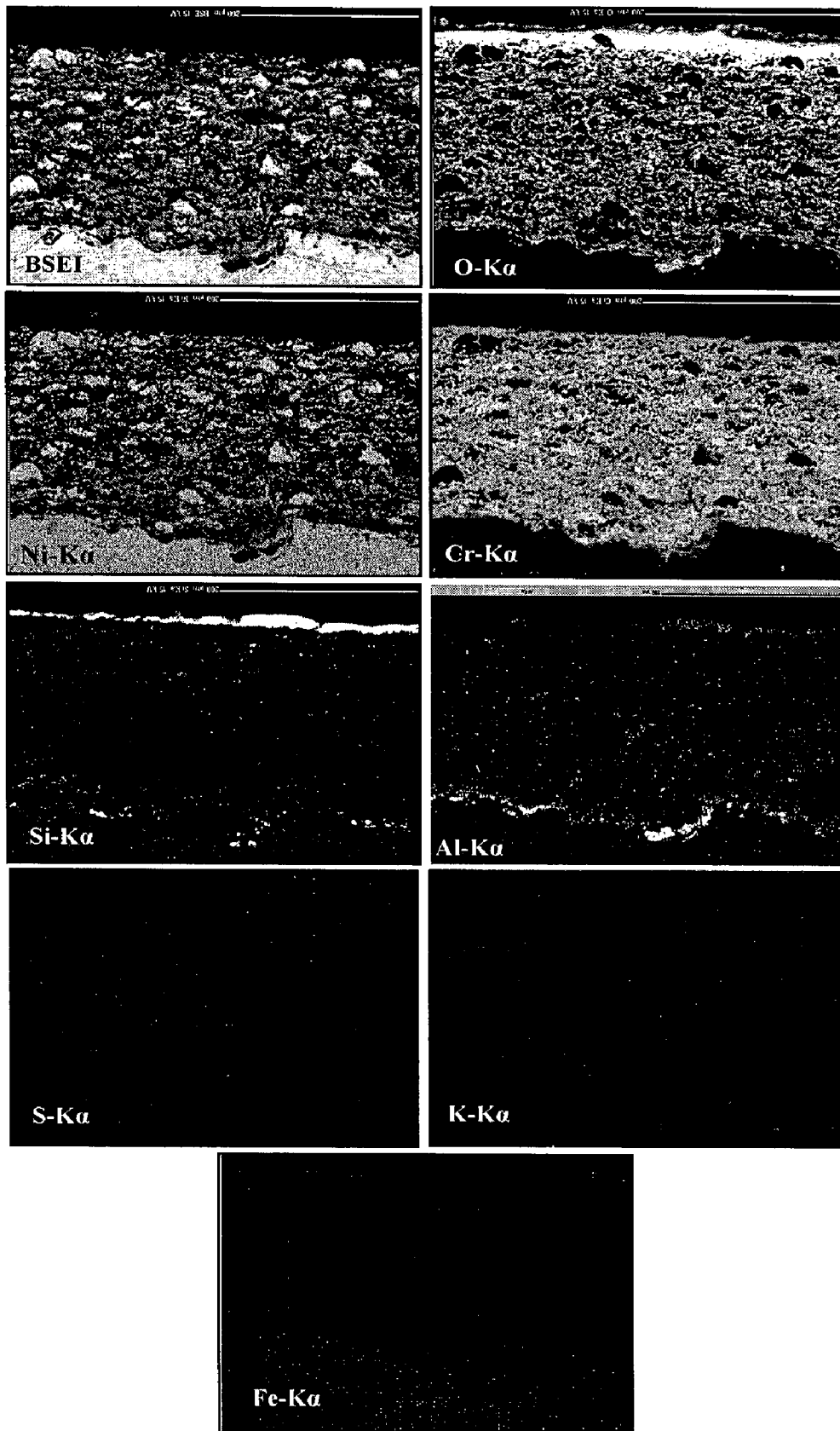


Fig. 7.26 Composition image (BSEI) and X-ray mappings across the cross-section of $\text{Cr}_3\text{C}_2\text{-NiCr}$ coated Superni 600 after 1000 hrs exposure to platen superheater zone of the coal fired boiler at 900°C .

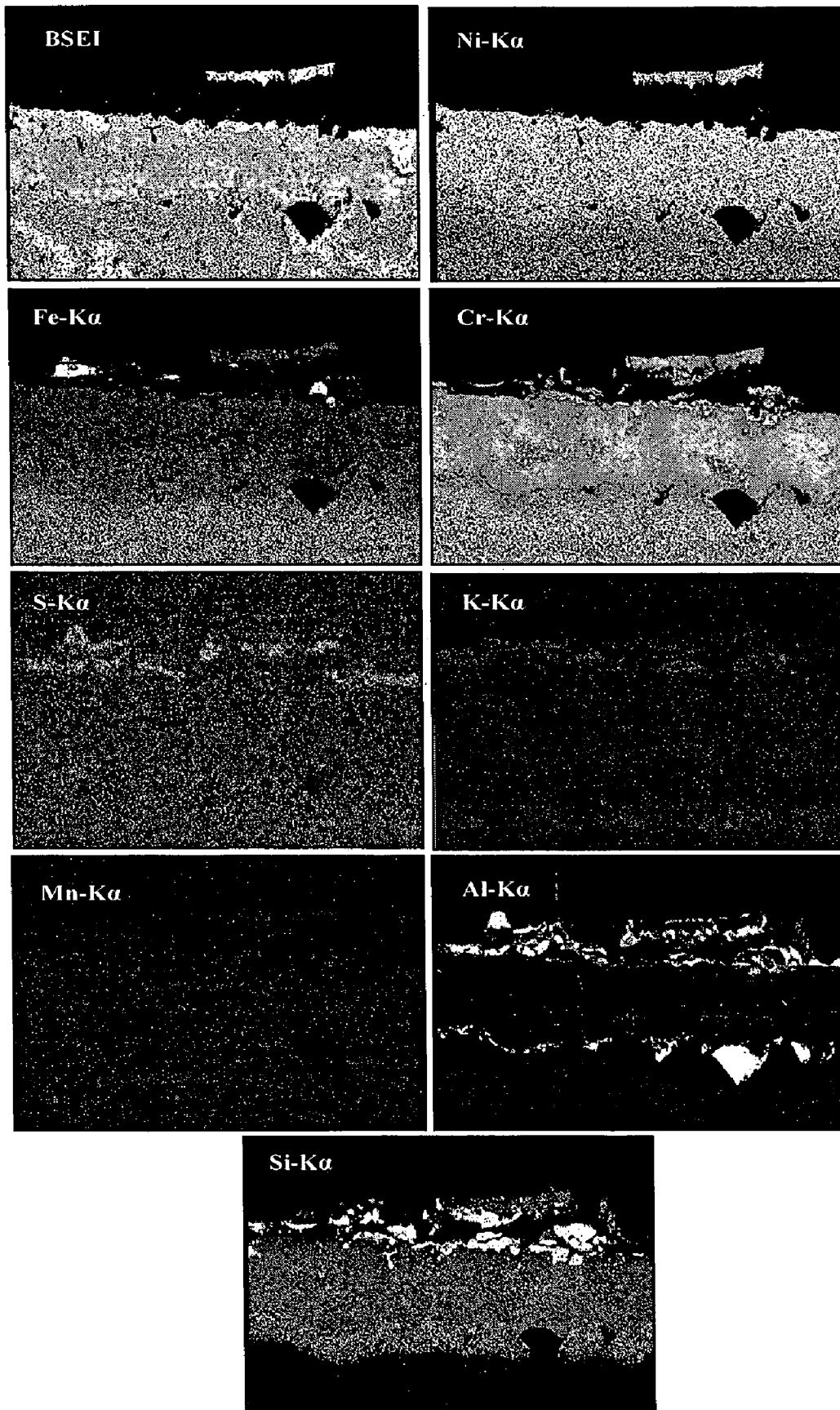


Fig. 7.27 Composition image (BSEI) and X-ray mappings across the cross-section of NiCrBSi coated Superni 600 after 1000 hrs exposure to platen superheater zone of the coal fired boiler at 900 °C.

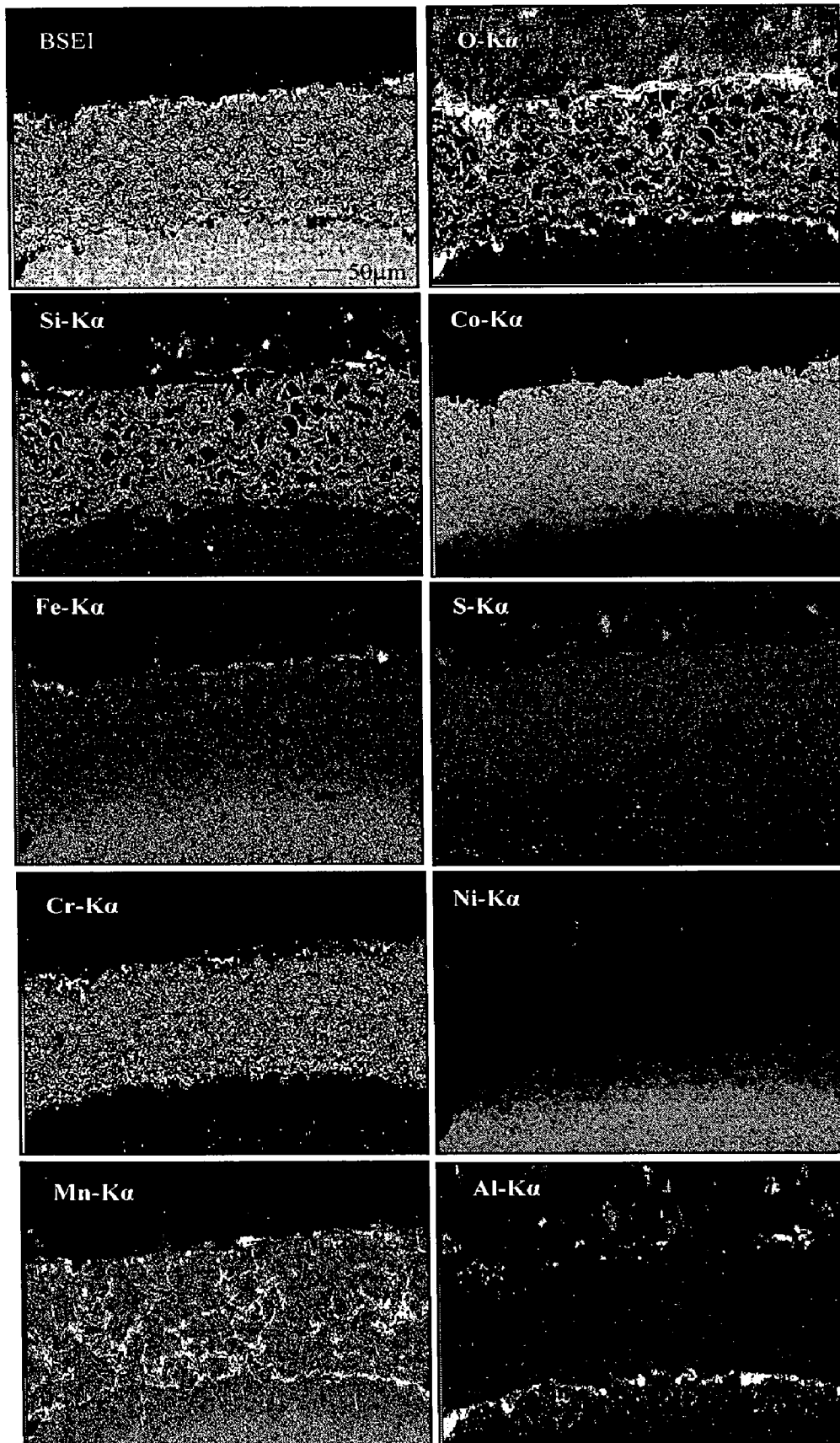


Fig. 7.28 Composition image (BSEI) and X-ray mappings across the cross-section of a Stellite-6 coated Superni 600 after 1000 hrs exposure to platen superheater zone of the coal fired boiler at 900 °C.

chromium oxide. Aluminium and manganese co-exist with O at the scale-substrate interface resulting in the formation of thin streaks of the oxides of aluminium and manganese. Manganese also forms thick streaks at the boundaries of most of the splats indicating its outward diffusion from the substrate. Some amount of cobalt seems to have diffused from the coating to the substrate. The presence of silicon, aluminium and iron in the topmost part of the scale is mainly due to ash deposition and partly due to diffusion from the substrate. Some traces of sulphur permeate into the substrate just below the scale-substrate interface.

The scale formed on Ni-20Cr coated Superni 600 consists of Ni-rich elongated splats with chromium mainly presents at the splat boundaries (Fig. 7.29). A chromium-rich band about 40 μm thick is formed just above the scale-substrate interface. The topmost layer of the scale is found to be rich in silicon, calcium, aluminium and iron indicating the interaction of the scale with ash. Iron and manganese diffused outwards from the substrate and have shown their higher concentration just above the scale-substrate interface.

7.1.5 Hot Corrosion of Bare and Coated Superni 601

7.1.5.1 Corrosion Kinetics

The weight change for the bare and coated Superni 601 during 1000 hours cyclic exposure to boiler environment is presented in Fig. 7.30.

The bare Superni 601 shows a relatively higher weight gain than Ni-20Cr and Stellite-6 coated specimens despite symptomatic spallation observed on the surface of bare alloy during cyclic study. The $(\text{weight change/area})^2$ verses time plot for bare alloy also indicates the suspected spallation behaviour of the scale (Fig. 7.31). Figure 7.31 shows that the HVOF coated Superni 601 in all the four cases follow nearly parabolic behaviour. Small deviations from the parabolic rate law may be due to minor superficial spallation from the upper layer of the coating. In general, all the coated specimens show a relatively higher weight gain during initials cycles, but subsequently the weight gain is moderate.

The Ni-20Cr and $\text{Cr}_3\text{C}_2\text{-NiCr}$ coatings on Superni 601 showed lowest and highest weight gain, respectively, amongst the coatings under study. The $\text{Cr}_3\text{C}_2\text{-NiCr}$ coated alloy gained 45% more weight than the Ni-20Cr coated alloy. The Stellite-6 and NiCrBSi coated Superni 601 stand second and third lowest in weight gain. The parabolic rate constants (k_p in $10^{-12} \text{ g}^2 \text{ cm}^{-4} \text{ s}^{-1}$) for the $\text{Cr}_3\text{C}_2\text{-NiCr}$, NiCrBSi, Stellite-6 and Ni-20Cr coated Superni 601 are found to be 13.19, 11.77, 4.69, and 4.13, respectively.

7.1.5.2 Average Scale Thickness and Depth of Internal Attack

The cross-sectional BSE images for the corroded bare and coated Superni 601 are shown in Fig. 7.32. The average scale thickness and depth of internal corrosion attack for

bare Superni 601 are found as 48 μm and 34 μm , respectively. The average scale thickness for Cr_3C_2 -NiCr, NiCrBSi, Stellite-6 and Ni-20Cr coated Superni 601 is found to be as 270, 390, 300, and 240 μm , respectively. The depth of internal corrosion for the Cr_3C_2 -NiCr, Stellite-6 and Ni-20Cr coated Superni 601 is measured as 140, 35 and 30 μm , respectively. The NiCrBSi coated alloy showed no internal corrosion. As explained in section 7.1.4.4 (B), the internal corrosion in case of other three coatings might be due to penetration of corrosive species during the initial hours of the exposure before the paths get sealed. The average scale thickness, scale thickness lost and depth of internal corrosion attack for bare and coated Superni 601 are given in Fig. 7.33. By considering the cumulative effects of average scale thickness, scale thickness lost (reported in section 7.1.2) and depth of internal attack, it is noted that the Ni-20Cr coating showed better resistance to the given environment followed by Stellite-6 and NiCrBSi coatings respectively, whereas the Cr_3C_2 -NiCr coating showed least resistance.

7.1.5.3 X-ray Diffraction Analysis

The diffraction patterns for the corroded bare and coated Superni 601 are shown in Fig. 7.34. The main phases identified with XRD analysis are given in Table 7.3.

Table 7.3: Major and minor phases identified by XRD analysis for the bare and coated Superni 601 after 1000 hrs exposure to actual environment of the coal fired boiler.

Description	Major phases	Minor phases
Uncoated Superni 601	Cr_2O_3 , Fe_2O_3 , Al_2O_3 , SiO_2 , NiS, and FeS	MnO_2
Cr_3C_2 -NiCr coated	Cr_2O_3 , Fe_2O_3 , Al_2O_3 , MnO_2 , and NiCr_2O_4	--
NiCrBSi coated	NiO, Fe_2O_3 , SiO_2 , and Al_2O_3	Cr_2O_3 , and NiCr_2O_4
Stellite-6 coated	Cr_2O_3 , Fe_2O_3 , Al_2O_3 , CoCr_2O_4 , and NiCr_2O_4	SiO_2
Ni-20Cr coated	NiO, Cr_2O_3 , and Al_2O_3	Fe_2O_3 , MnO_2 , and NiCr_2O_4

7.1.5.4 SEM/EDAX Analysis

7.1.5.4(A) Surface Analysis

The SEM/EDAX analysis for the bare and coated Superni 601 after 1000 hrs exposure to given environment is presented in Fig. 7.35.

The scale formed on bare Superni 601 appears to be fragile (Fig 7.35a). The black regions are indication of spallation of the scale during experimentations. The globules present in the scale consist of MnO_2 , Fe_2O_3 , SiO_2 , Al_2O_3 , Cr_2O_3 and NiO along with little amount of Na_2O and MgO. The outer scale (white phase) have a composition similar to

ash. Therefore it is inferred that the oxides of the scale are interacting with condensed phases of the ash.

A uniform and continuous scale is formed on the Cr₃C₂-NiCr and NiCrBSi coated Superni 601, whereas the scale formed on the Stellite-6 and Ni-20Cr coated superalloy shows the presence of large size distorted grains, Figs. 7.35b to 7.35e. In general, the EDAX analysis shows that the oxide scale formed on the surface of the specimens is interacting with the condensed phases of the ash. The scale formed on Ni-20Cr coating contains significant amounts of Cr₂O₃ and NiO, as compared to other coatings. The presence of manganese oxide in the surface scales indicates its outward diffusion from the substrate (Figs. 7.35b to 7.35d).

7.1.5.4(B) Cross-Sectional Analysis

The BSE images and EDAX analysis of the scale formed on Cr₃C₂-NiCr and NiCrBSi coated Superni 601 at some selected point of interest across the cross-section are shown in Figs. 7.36a and 7.36b, respectively. The scale appears to be adherent and free from cracks.

The EDAX analysis across the cross-section of both the corroded specimens (Point 1) shows the presence of very little amount of oxygen in the substrate just below the scale-substrate interface, indicating that a little amount of oxygen has penetrated along the splat boundaries or through the pores during initial hours of exposure. The white phase of the scales in both the coated specimens is identified as Ni-rich splat, which exists mostly in un-reacted state as little amount of oxygen is present in this phase. The presence of mainly chromium and oxygen at Points 3 in both the Figures and at Point 5 of Fig. 7.36(a) suggests the formation of chromium oxide in these regions due to selective oxidation of the chromium. The nickel has decreased considerably at some of these points. The topmost layers of both the specimens composed mainly of nickel, chromium and oxygen, which suggest that the oxides of nickel and chromium and their spinels have formed in the upper part of the scales.

7.1.5.5 EPMA Analysis

The BSE image for the bare Superni 601 shows the formation of approximately 70 µm thick porous scale which penetrates deeply into the substrate up to about 65 µm (Fig. 7.37). The scale mainly consists of Al, Cr, Ni, Si, and Mn. The presence of thick clusters of Al and Si in the scale is due to diffusion from the substrate as well as due to interaction with the ash. The presence of K and Na indicates that the condensed phases from the boiler environment are interacting with the oxide scale formed on the surface of the specimens. A little amount of Fe is also present in the scale.

The BSE image and EPMA elemental maps for the Cr₃C₂-NiCr coated Superni 601 shows the formation of a continuous, uniform, homogeneous and adherent scale

consisting of Ni-rich splats with chromium mostly at their splat boundaries (Fig. 7.38). Iron and manganese diffused outward from the substrate. Manganese and aluminium show a tendency to form thin and thick streaks at the scale-substrate interface, respectively. A continuous streak of Al is present at the scale-substrate interface, where all other elements are found to be absent.

The elemental mappings for NiCrBSi coated specimen shows the presence of a nearly continuous layer of silicon at the topmost part of the coating (Fig. 7.39). The oxygen also co-exists with silicon in this region indicating the formation of SiO_2 . A thin streak of Cr exists underneath of this silicon-rich layer as Cr_2O_3 . Elemental map for O shows that very limited oxygen has penetrated through pores or splat boundaries and co-exists with stringers of chromium and aluminium near the scale-substrate interface and forms their respective oxides. The absence of oxygen and other corrosive species below the scale-substrate interface shows protective behaviour of the coating in the given environment.

The Stellite-6 coated Superni 601 has retained a lamellar structure of the as-sprayed coating after 1000 hours exposure to given environment (Fig. 7.40). The scale mainly consists of Co-rich splats with high intensity dots of chromium and silicon mostly present at splats boundaries. The existence of islands of aluminium, iron and silicon with oxides of nickel and chromium at the topmost part of the scale indicates interaction between ash and scale. Manganese diffuses outward from the substrate and forms stringers at the splat boundaries. Aluminium forms a thin streak at the scale-substrate interface, whereas nickel shows higher concentrations just above the scale-substrate interface.

The scale formed on Ni-20Cr coated Superni 601 has a layered structure consisting mainly of Ni-rich splats with Cr and O mostly present as Cr_2O_3 at the splat boundaries (Fig. 7.41). The Ni-rich splats appear to be in the un-oxidised as O is generally found to be absent at these sites. The elemental map for iron shows very less diffusion of iron from the substrate in this coating-substrate system. The formation of a thin streak of iron oxide in the surface scale of this coating might be due to interaction with ash. Aluminium forms a continuous thick streak at the scale-substrate interface and also shows a tendency of outward diffusion. The presence of some islands rich in Al in the topmost layer of the scale is due to outward diffusion from the substrate and/or due to interaction with ash. The penetration of oxygen is restricted to the scale-substrate interface. The S, K and Na corrosive species of the boiler environment show higher concentration in the topmost layer of the scale.

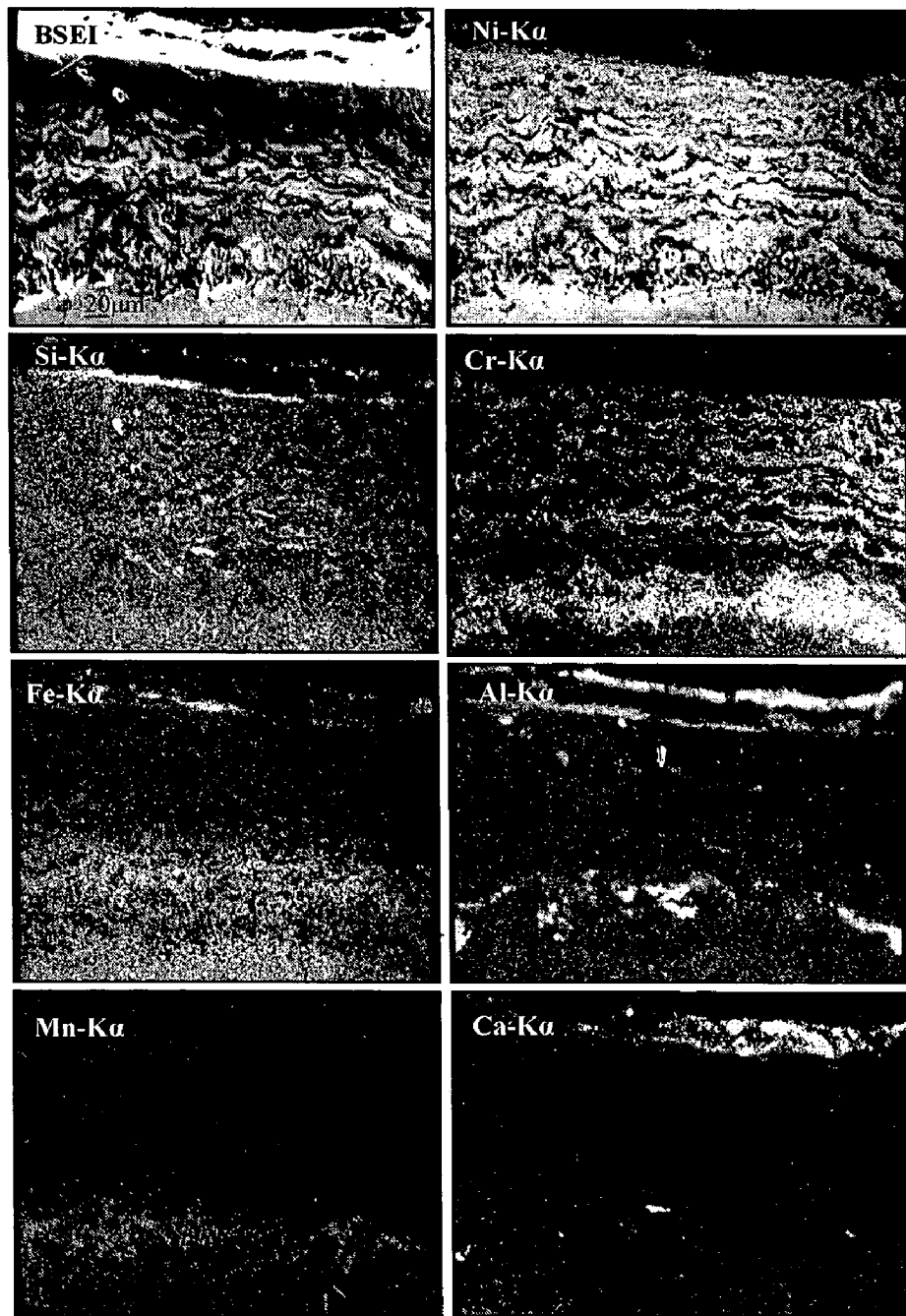


Fig. 7.29 Composition image (BSEI) and X-ray mappings across the cross-section of Ni-20Cr coated Superni 600 after 1000 hrs exposure to platen superheater zone of the coal fired boiler at 900 °C.

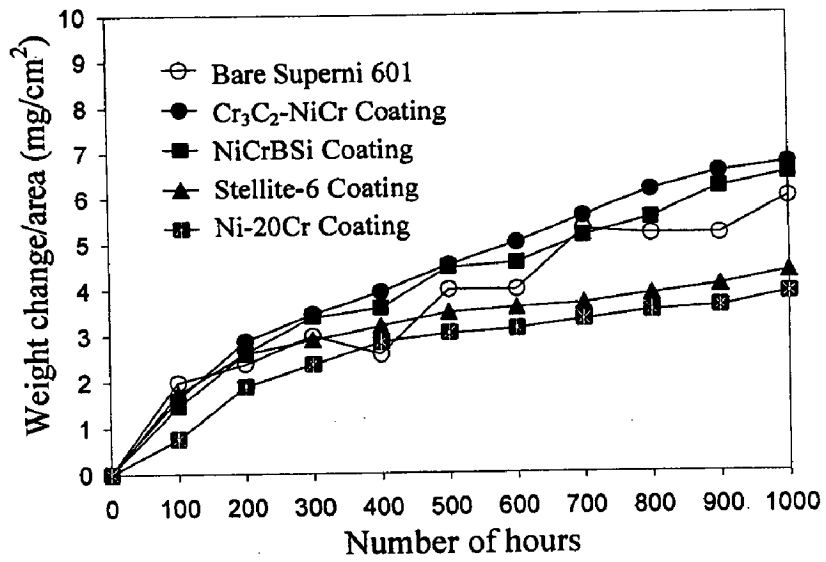


Fig. 7.30 Weight change vs. time plots for the coated and uncoated Superni 601 subjected to 1000 hrs cyclic exposure to platen superheater zone of the coal fired boiler at 900 °C.

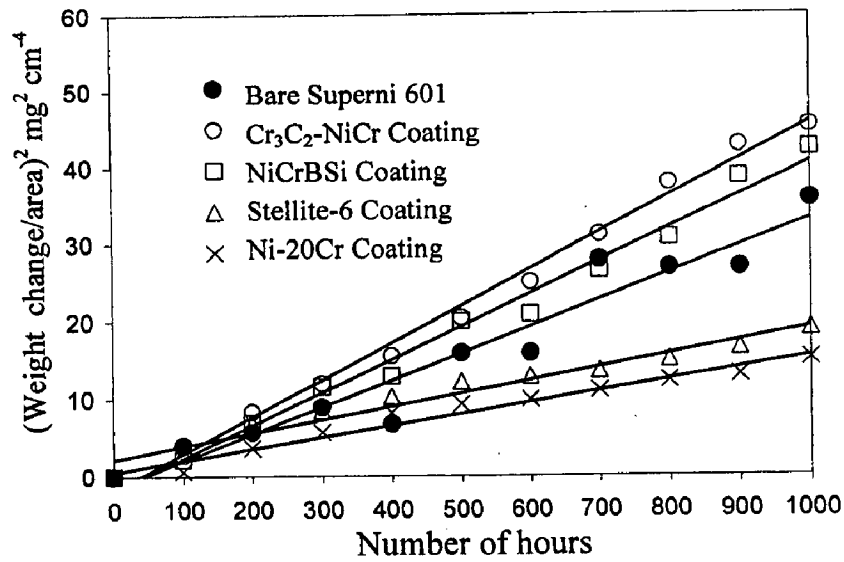


Fig. 7.31 (Weight change/area)² vs. time plots for the coated and uncoated Superalloy Superni 601 subjected to 1000 hrs cyclic exposure to platen superheater zone of the coal fired boiler at 900 °C.

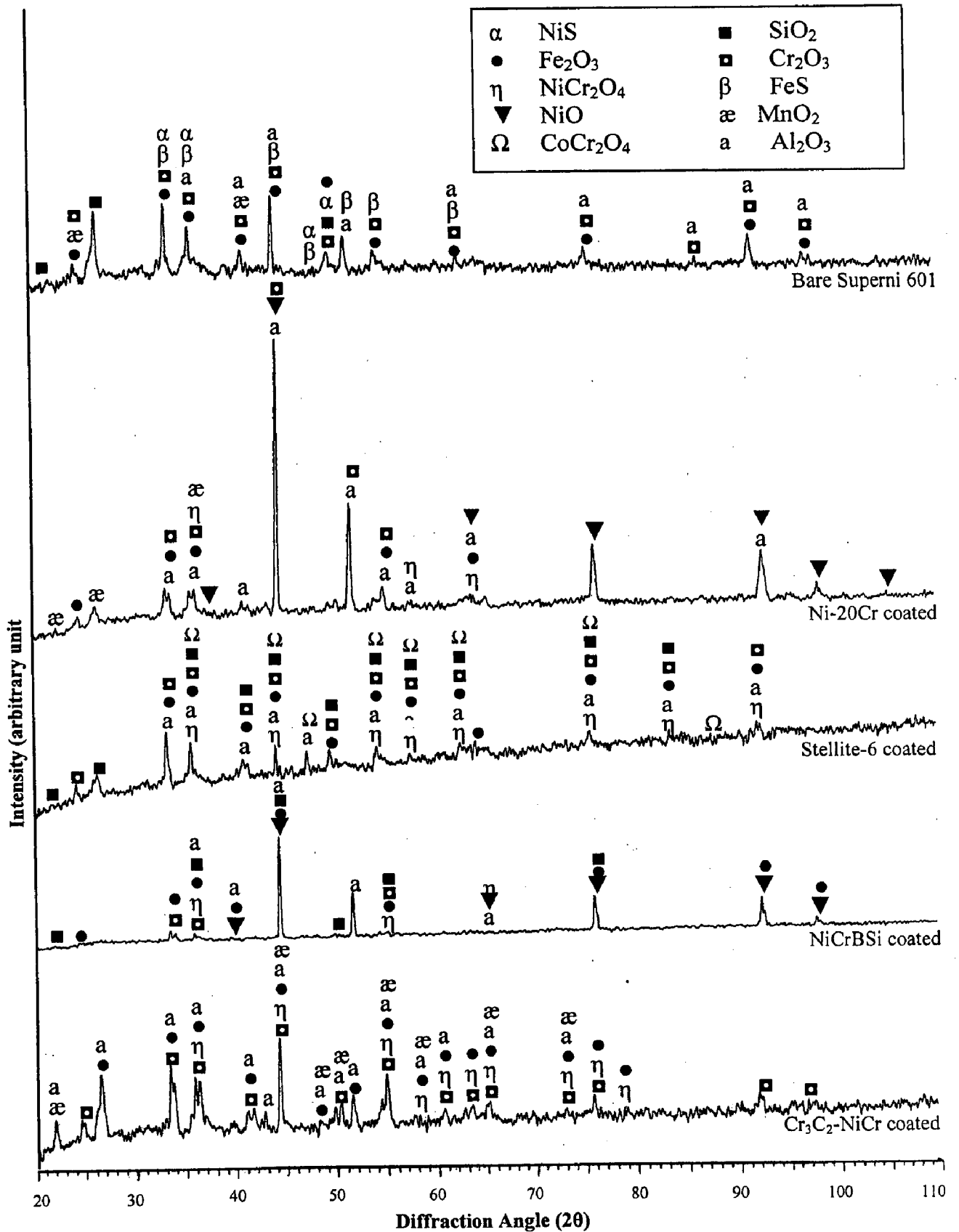


Fig. 7.34 X-ray diffraction patterns for the bare and coated superalloy Superni 601 after 1000 hrs exposure to platen superheater zone of the coal fired boiler at 900 °C.

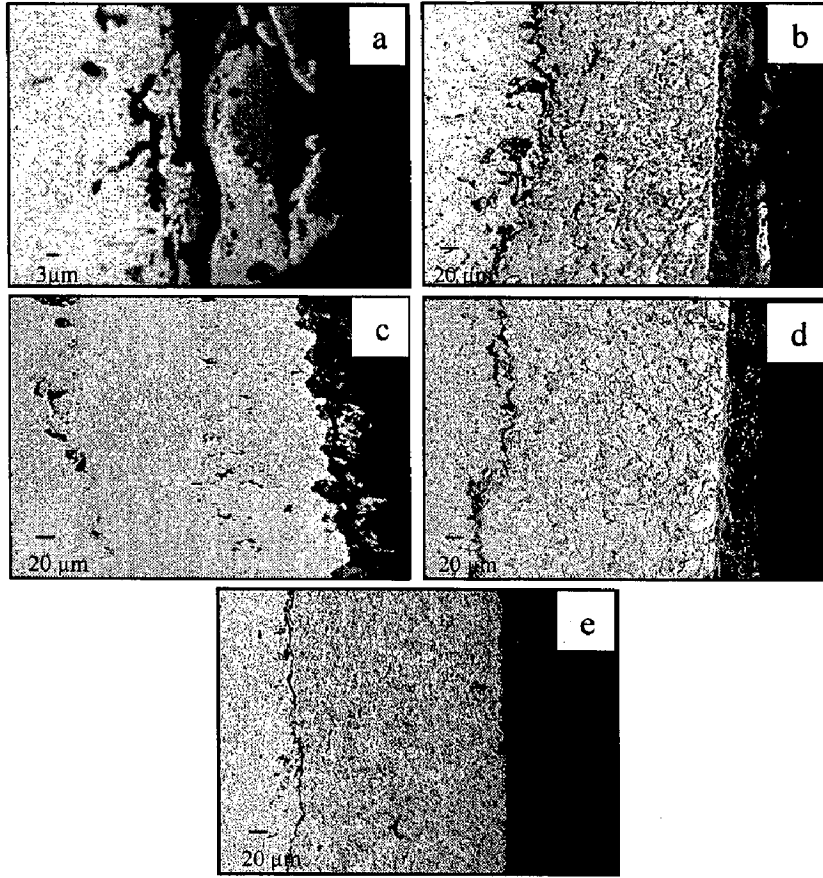


Fig. 7.32 BSE images for the bare and HVOF coated Superni 601 after 1000 hrs exposure to platen superheater zone of the coal fired boiler at 900 °C:
 (a) Bare superalloy (b) Cr₃C₂-NiCr coated (c) NiCrBSi coated
 (d) Stellite-6 coated (e) Ni-20Cr coated.

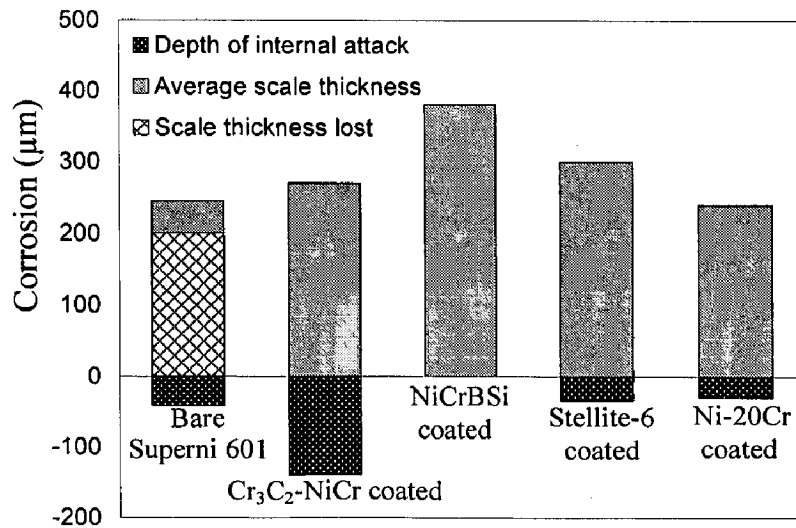


Fig. 7.33 Bar charts indicating the extent of corrosion for the bare and HVOF coated Superni 601 after 1000 hrs exposure to the coal fired boiler at 900 °C.

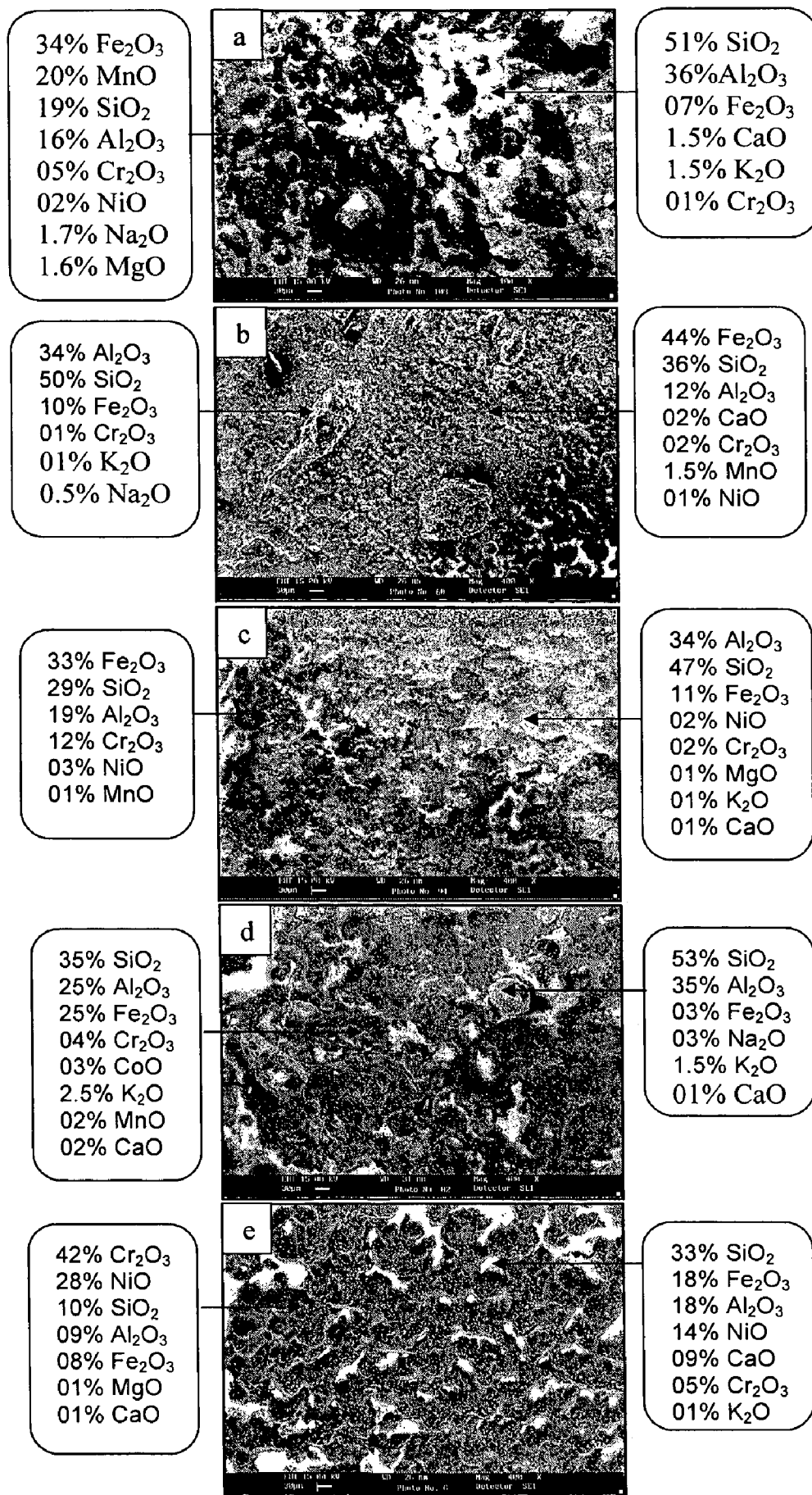


Fig. 7.35 SEM/EDAX analysis showing elemental composition (wt.%) for the bare and coated Superni 601 after 1000 hrs exposure to platen superheater zone of the coal fired boiler at 900 °C: (a) Bare Superni 601 (b) Cr₃C₂-NiCr coated (c) NiCrBSi coated (d) Stellite-6 coated (e) Ni-20Cr coated

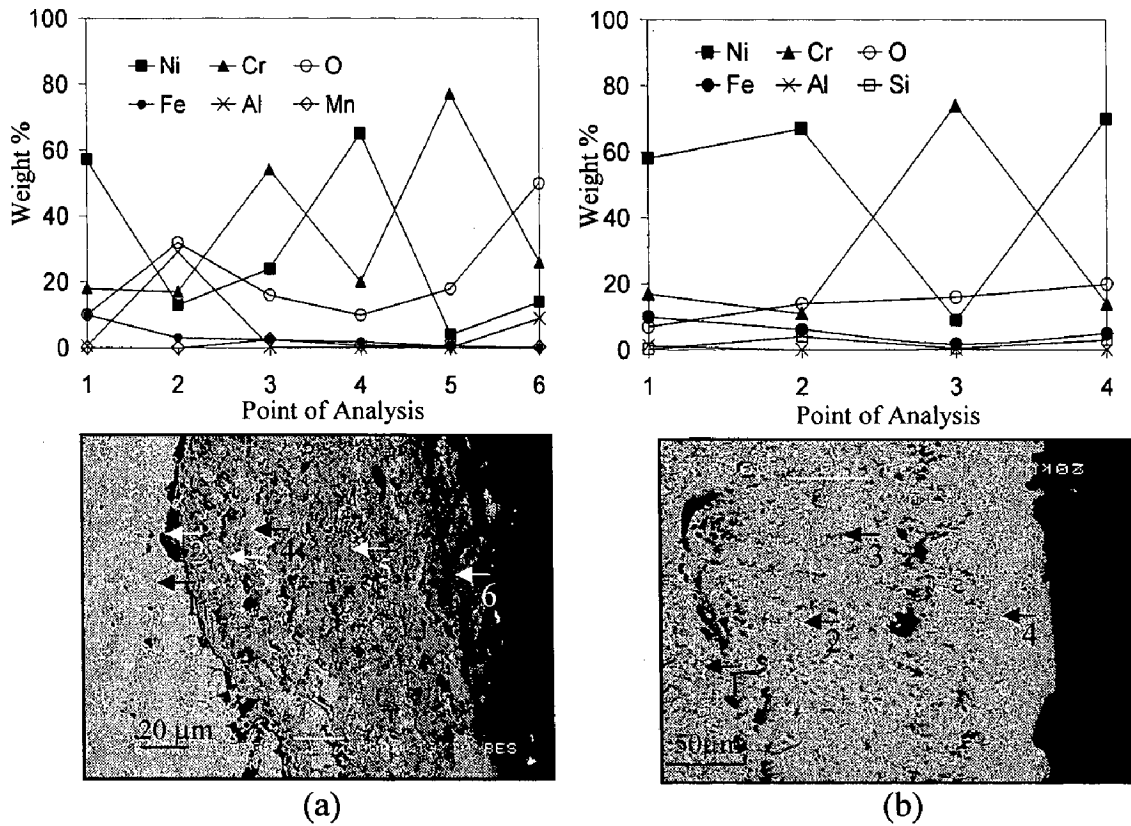


Fig 7.36 Oxide scale morphologies and variations of elemental composition (wt%) across the cross section of HVOF coated Superni 601 after 1000 hrs exposure to platen superheater zone of the coal fired boiler at 900 °C :
 (a) Cr₃C₂-NiCr coated (b) NiCrBSi coated

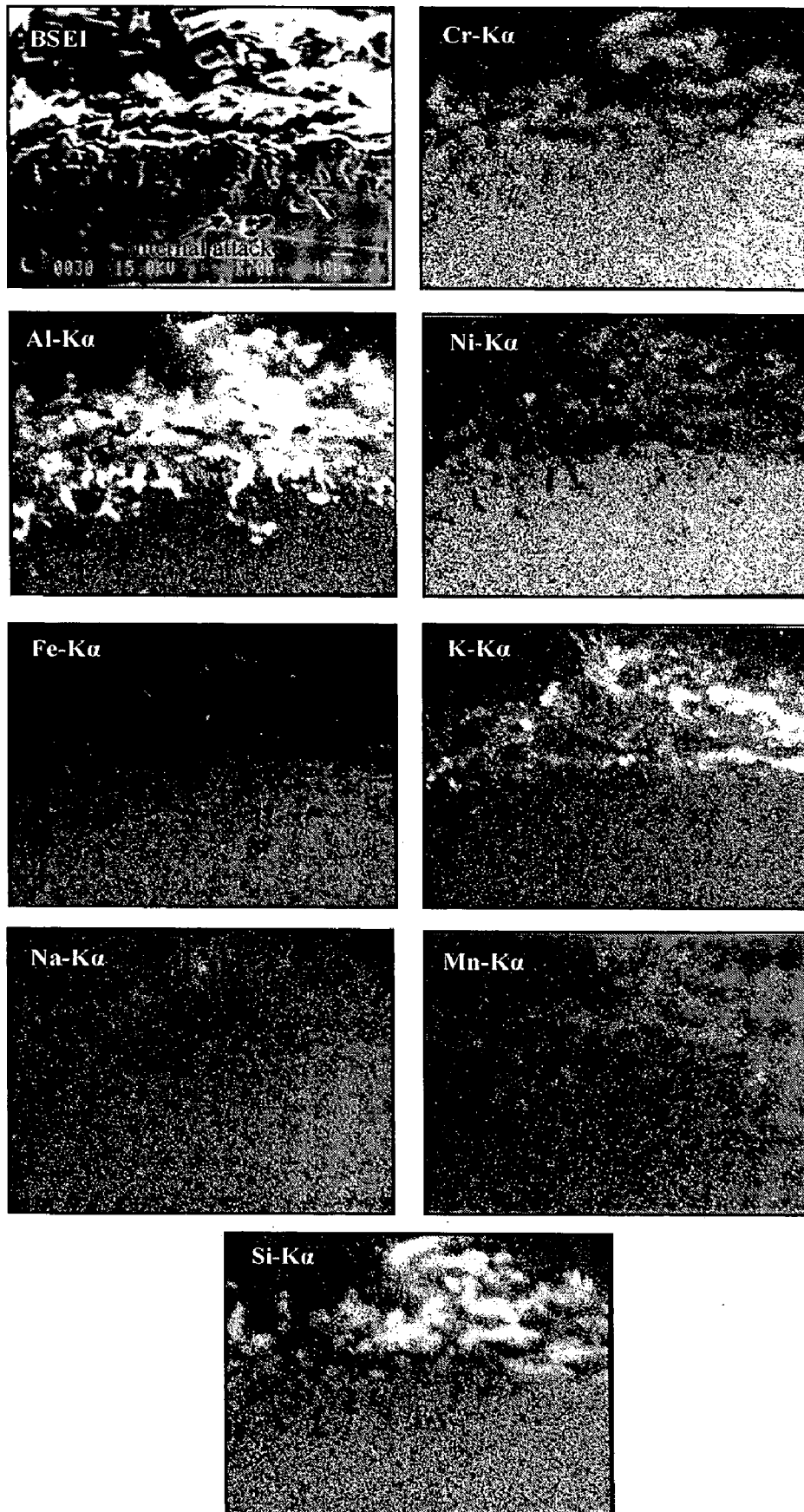


Fig. 7.37 Composition image (BSEI) and X-ray mappings across the cross-section of bare Superni 601 after 1000 hrs exposure to platen superheater zone of the coal fired boiler at 900 °C.

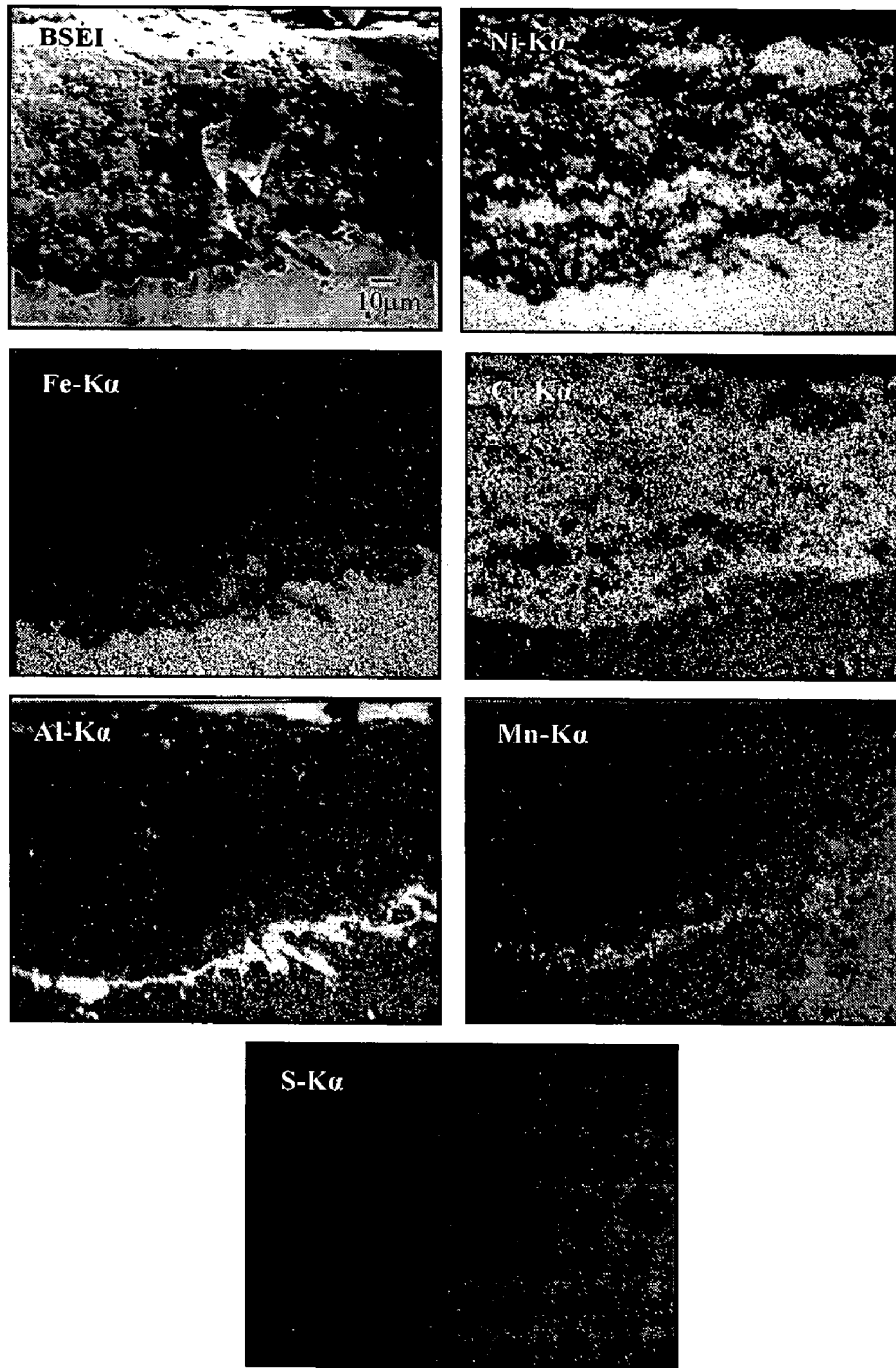


Fig. 7.38 Composition image (BSEI) and X-ray mappings across the cross-section of $\text{Cr}_3\text{C}_2\text{-NiCr}$ coated Superni 601 after 1000 hrs exposure to platen superheater zone of the coal fired boiler at 900 °C.

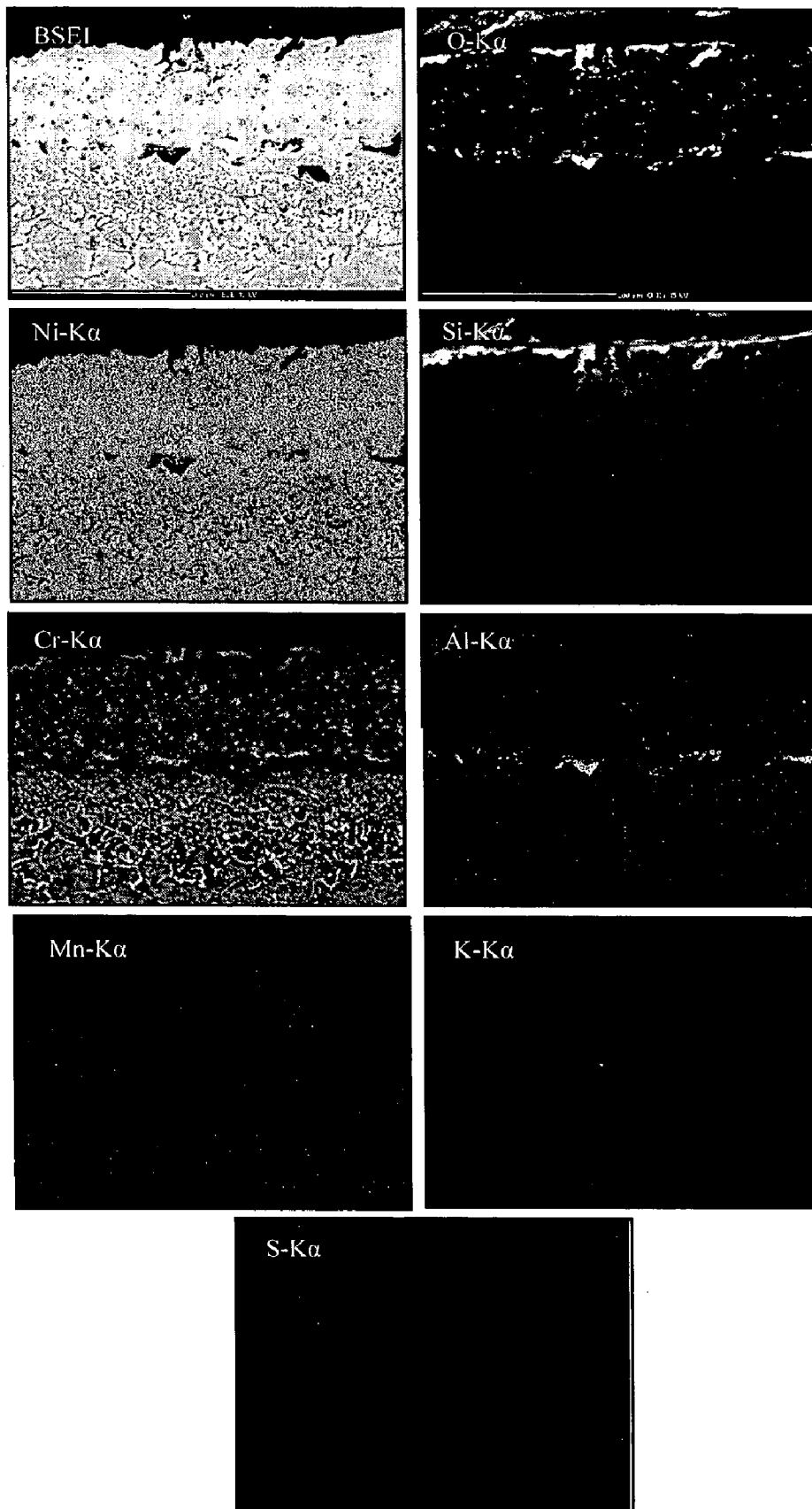


Fig. 7.39 Composition image (BSEI) and X-ray mappings across the cross-section of NiCrBSi coated Superni 601 after 1000 hrs exposure to platen superheater zone of the coal fired boiler at 900 °C.

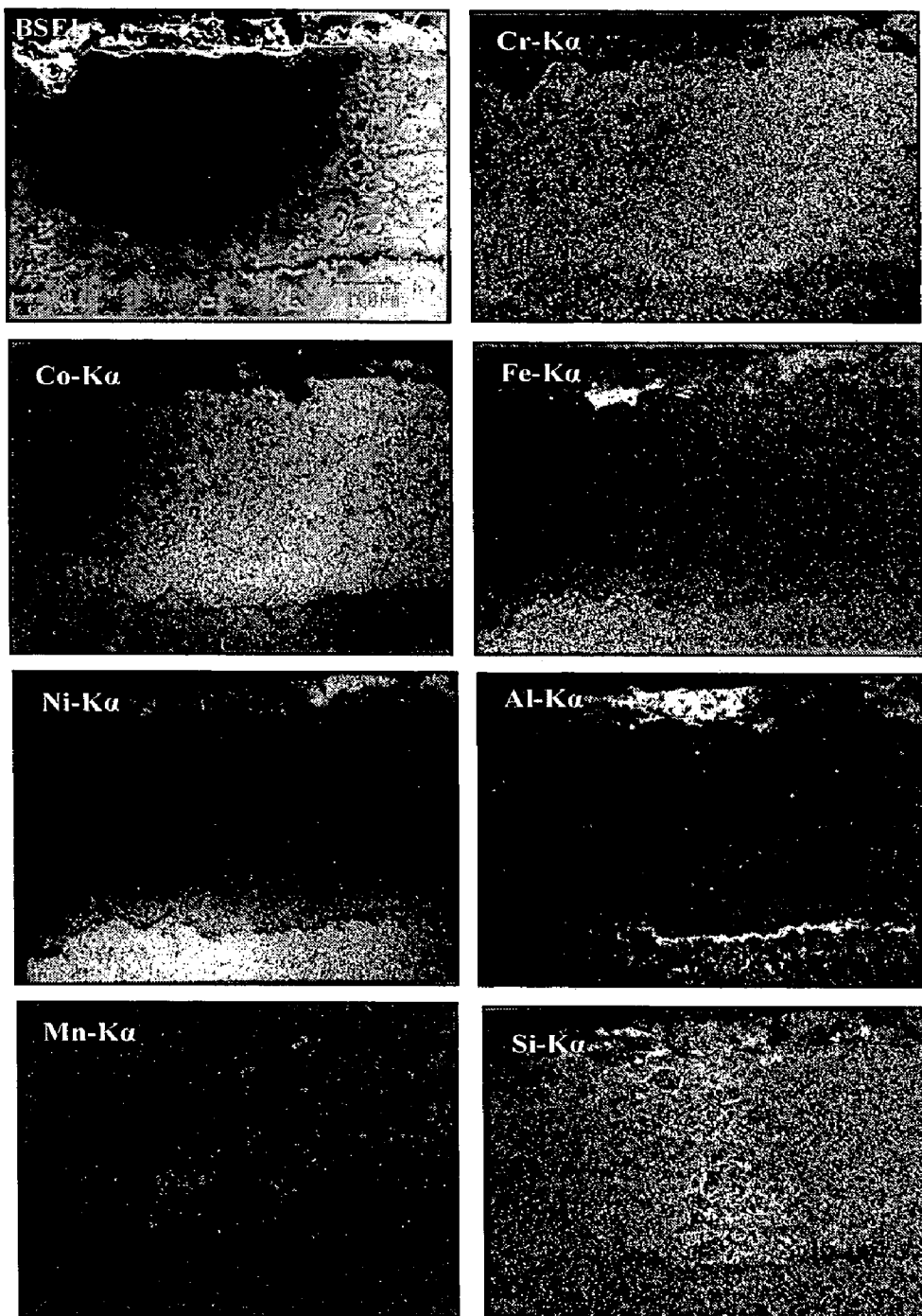


Fig. 7.40

Composition image (BSEI) and X-ray mappings across the cross-section of Stellite-6 coated Superni 601 after 1000 hrs exposure to platen superheater zone of the coal fired boiler at 900 °C.

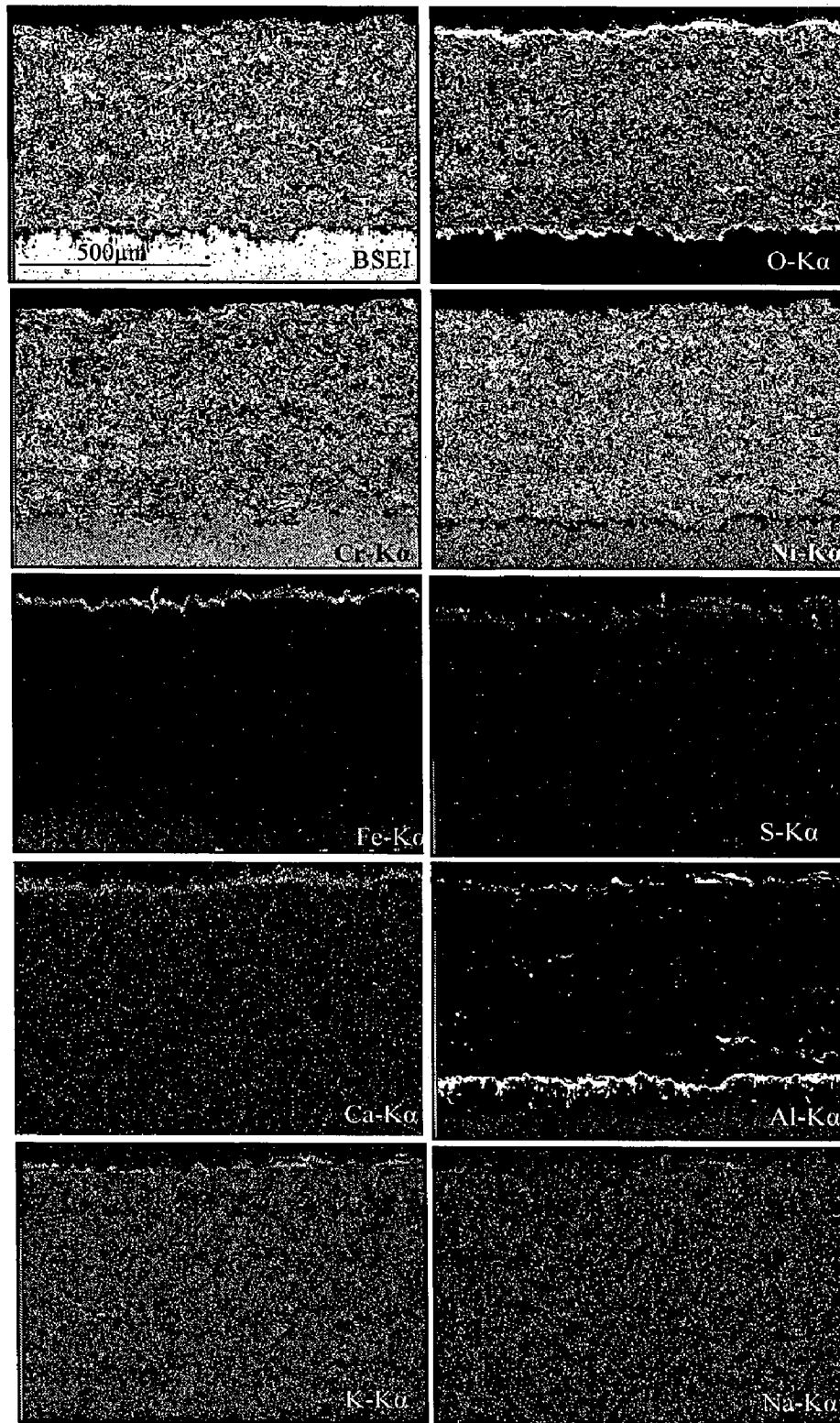


Fig. 7.41 Composition image (BSEI) and X-ray mappings across the cross-section of Ni-20Cr coated Superni 601 after 1000 hrs exposure to platen superheater zone of the coal fired boiler at 900 °C.

7.1.6 Hot Corrosion of Bare and Coated Superni 718

7.1.6.1 Corrosion Kinetics

The weight change plots for the bare and coated Superni 718 are shown in Fig. 7.42. The weight gain plot for bare alloy is irregular in shape (Fig. 7.42) and weight gain square curve shows considerable deviations from the parabolic rate law signifying large amount of suspected spallation of the scale formed on bare Superni 718 (Fig. 7.43). However the HVOF coated specimens follow a nearly parabolic rate law, and thus show their tendency to develop diffusion barriers to the corroding species. Similar to other HVOF coated substrates, the coated specimens of Superni 718, in general, show a relatively higher weight gain rate during initial cycles, which subsequently becomes moderate.

The Cr₃C₂-NiCr and Ni-20Cr coating have provided almost similar protection to Superni 718. They have provided higher corrosion resistance as compared to the other two coatings. The NiCrBSi coating showed highest weight gain, which is about 50% more than that gained by Ni-20Cr coated superalloy. The parabolic rate constants k_p for the Cr₃C₂-NiCr, NiCrBSi, Stellite-6 and Ni-20Cr coated Superni 718 are found to be: 2.77, 16.13, 13.80, and $4.44 \times 10^{-12} \text{ g}^2\text{cm}^{-4}\text{s}^{-1}$, respectively.

7.1.6.2 Average Scale Thickness and Depth of Internal Attack

The average scale thickness and depth of internal corrosion attack for bare Superni 718, as measured from the BSEI shown in Fig. 7.44, are found to be 49 μm and 12 μm , respectively. The average scale thickness for Cr₃C₂-NiCr, NiCrBSi, Stellite-6 and Ni-20%Cr coated Superni 718 is found to be: 270, 462, 340, and 230 μm , respectively. The coated alloy showed no indication of internal corrosion attack. The average scale thickness, scale thickness lost (reported in section 7.1.2) and depth of internal corrosion attack for bare and coated Superni 718 are given in Fig. 7.45. In terms of metal depth affected by the corrosion, Ni-20Cr coating deposited on Superni 718 showed better resistance to the boiler environment, followed by Cr₃C₂-NiCr and Stellite-6 coatings. The NiCrBSi coating showed relatively least resistance amongst all the coatings.

7.1.6.3 X-ray Diffraction Analysis

The XRD results for the bare and coated Superni 718 after exposure to boiler environment are shown in Fig. 7.46. The main phases identified with XRD analysis are given in Table 7.4.

7.1.6.4 SEM/EDAX Analysis

7.1.6.4(A) Surface Analysis

The SEM/EDAX results for the bare and coated Superni 718 after 1000 hrs exposure to given environment are shown in Fig. 7.47.

A massive scale formed on the bare Superni 718 has a spallation tendency as is evident from the SEM micrograph shown in Fig. 7.47a. The EDAX analysis shows the presence of condensed phases (white colour) from the surrounding atmosphere of the coal fired boiler interacting with the scale formed on the bare Superni 718. The dark grey phase from where spallation of the scale has occurred is found to be rich in iron Fe_2O_3 , SiO_2 and Al_2O_3 , along with some amounts of TiO_2 (8%), Cr_2O_3 (4%), Ta_2O_5 (01%) and Na_2O (01%). The Na, K and S present in the boiler environment form low melting point compound such as alkali-iron trisulphates as discussed in section 7.3.1, which are molten at the superheater zone of the boiler. These molten compounds cause fluxing of the scale, as is visible from the surface morphology of SEM micrograph shown in Fig. 7.47a.

Table 7.4: Major and minor phases identified by XRD analysis for the bare and coated Superni 718 after 1000 hrs exposure to actual environment of the coal fired boiler.

Description	Major phases	Minor phases
Uncoated Superni 718	Cr_2O_3 , Fe_2O_3 , Al_2O_3 , SiO_2 , and FeS	MnO_2
Cr_3C_2 -NiCr coated	Cr_2O_3 , Fe_2O_3 , NiO, Al_2O_3 , SiO_2 , and NiCr_2O_4	-
NiCrBSi coated	Cr_2O_3 , Fe_2O_3 , NiO, Al_2O_3 , SiO_2 , and NiCr_2O_4	MnO_2
Stellite-6 coated	Cr_2O_3 , Fe_2O_3 , NiO, Al_2O_3 , CoCr_2O_4 , and NiCr_2O_4	CoO, and SiO_2
Ni-20Cr coated	Cr_2O_3 , NiO, Fe_2O_3 , Al_2O_3 , and NiCr_2O_4	MnO_2 , TiO_2 , and SiO_2

A compact and adherent scale is formed on the HVOF coated Superni 718 without indication of any crack (Figs. 7.47 b to 7.47d). In general, the EDAX analysis of the surface scale of coated specimens indicates the presence of deposits of boiler environment with composition similar to ash, along with Cr_2O_3 and/or NiO. The presence of aluminium, silicon and iron in the surface scales is partly attributed to diffusion from the substrate and partly due to the deposited ash. The NiCrBSi and Stellite-6 coated superalloy show the presence of higher amounts of Cr_2O_3 , whereas Ni-20Cr coated superalloy showed relatively higher amounts of NiO. The presence of MnO (Figs. 7.47c and 7.47e), TiO_2 (Figs. 7.47b, 7.47d, and 7.47e), Ta_2O_5 (Fig. 7.47b) and MoO_3 (Fig. 7.47c) in the uppermost layer of the scale indicates their outward diffusion from the substrate.

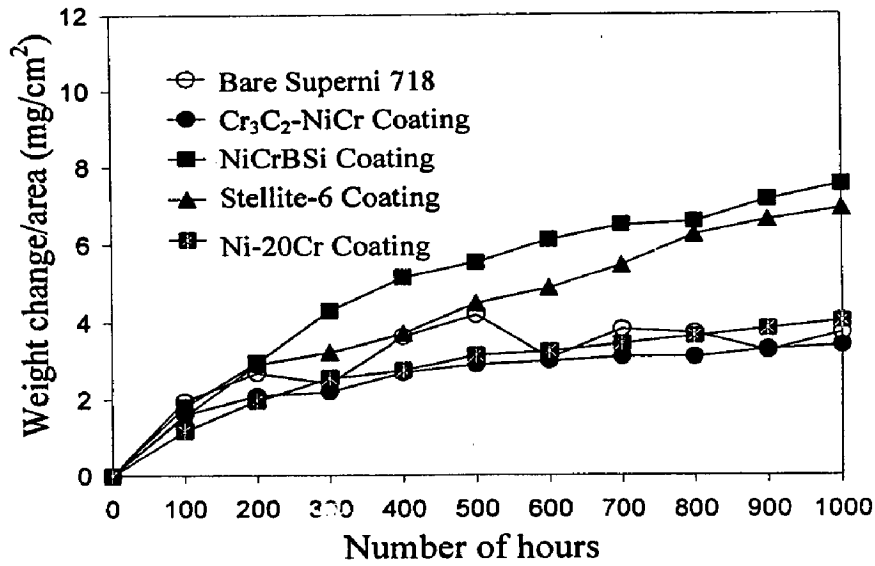


Fig. 7.42 Weight change vs. time plots for coated and uncoated Superni 718 subjected to 1000 hrs cyclic exposure to platen superheater zone of the coal fired boiler at 900 °C.

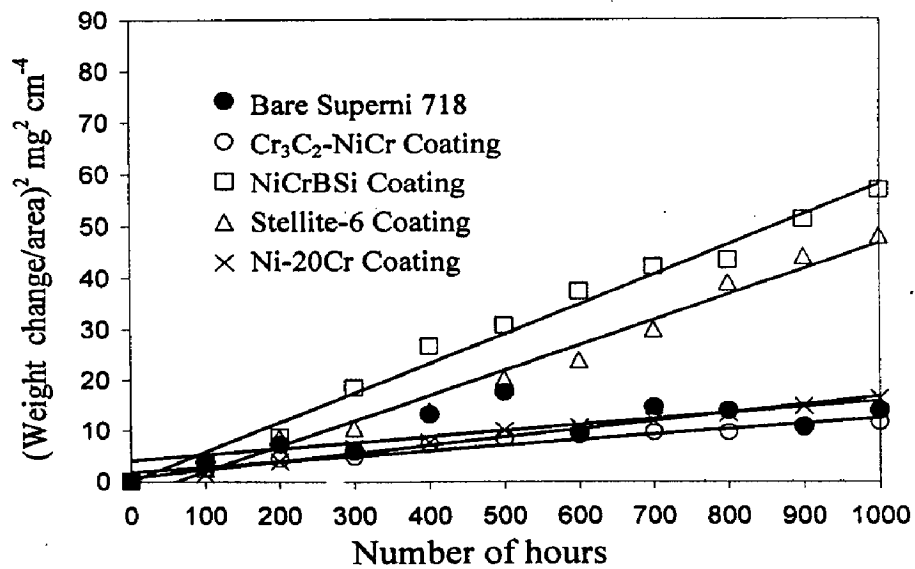


Fig. 7.43 (Weight change/area)² vs. time plots for coated and uncoated Superni 718 subjected to 1000 hrs cyclic exposure to platen superheater zone of the coal fired boiler at 900 °C.

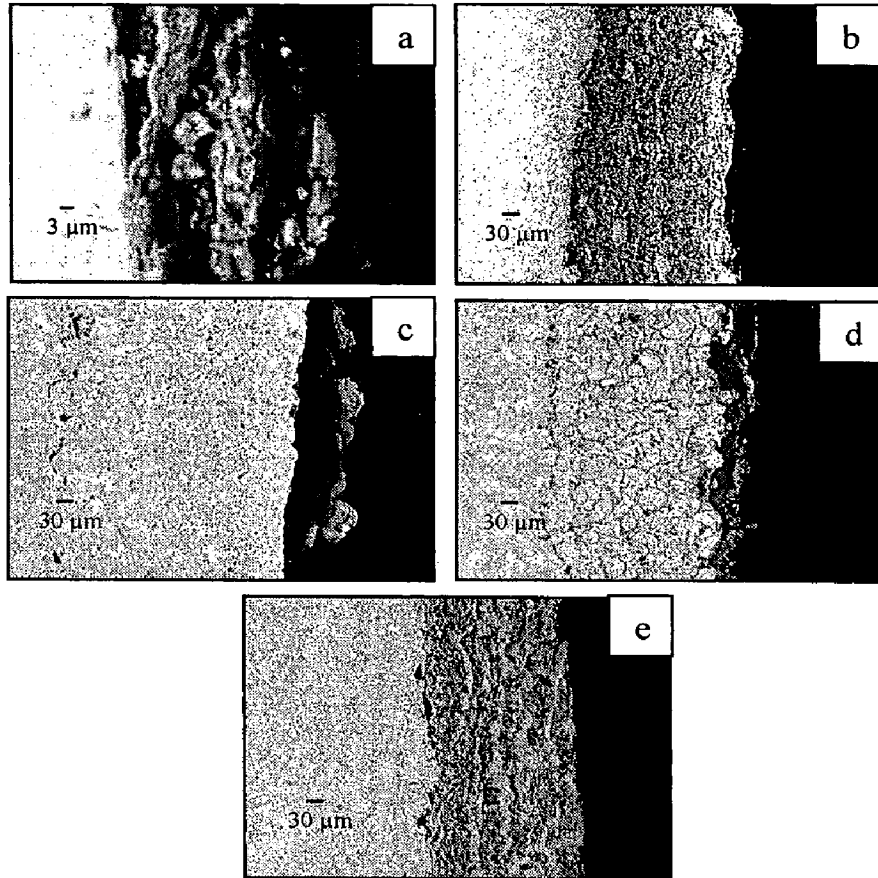


Fig. 7.44 BSE images for the bare and HVOF coated Superni 718 after 1000 hrs exposure to platen superheater zone of the coal fired boiler at 900 °C: (a) Bare superalloy (b) Cr₃C₂-NiCr coated (c) NiCrBSi coated (d) Stellite-6 coated (e) Ni-20Cr coated.

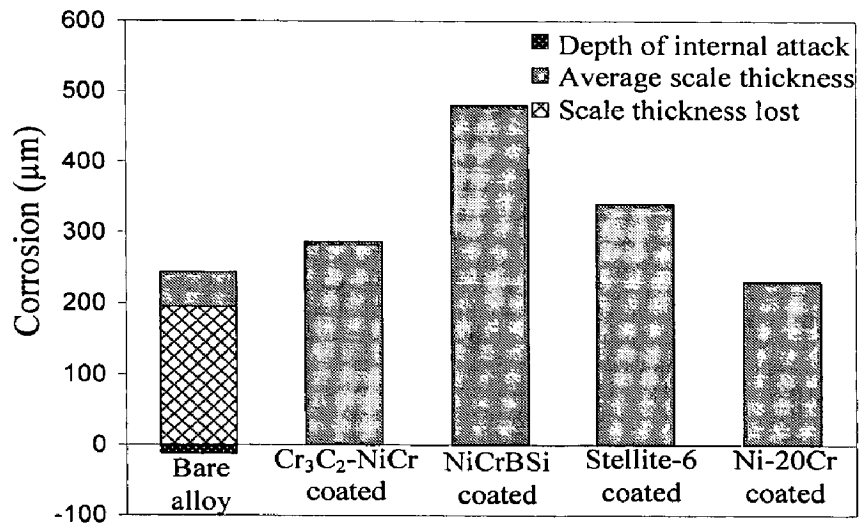


Fig. 7.45 Bar charts indicating the extent of corrosion for the bare and HVOF coated Superni 718 after 1000 hrs exposure to the coal fired boiler at 900 °C.

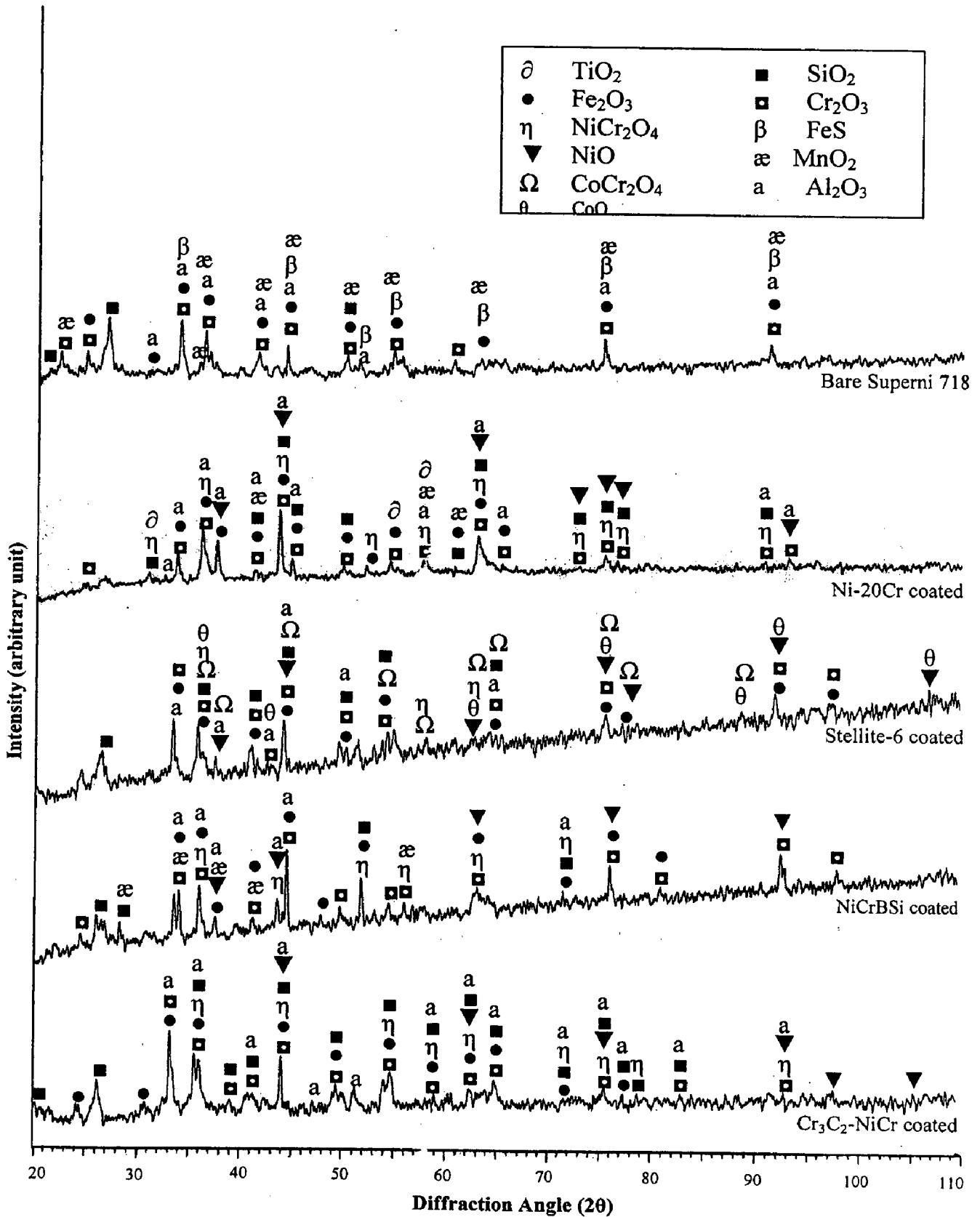


Fig. 7.46 X-ray diffraction patterns for the bare and coated superalloy Superni 718 after 1000 hrs exposure to platen superheater zone of the coal fired boiler at 900 °C.

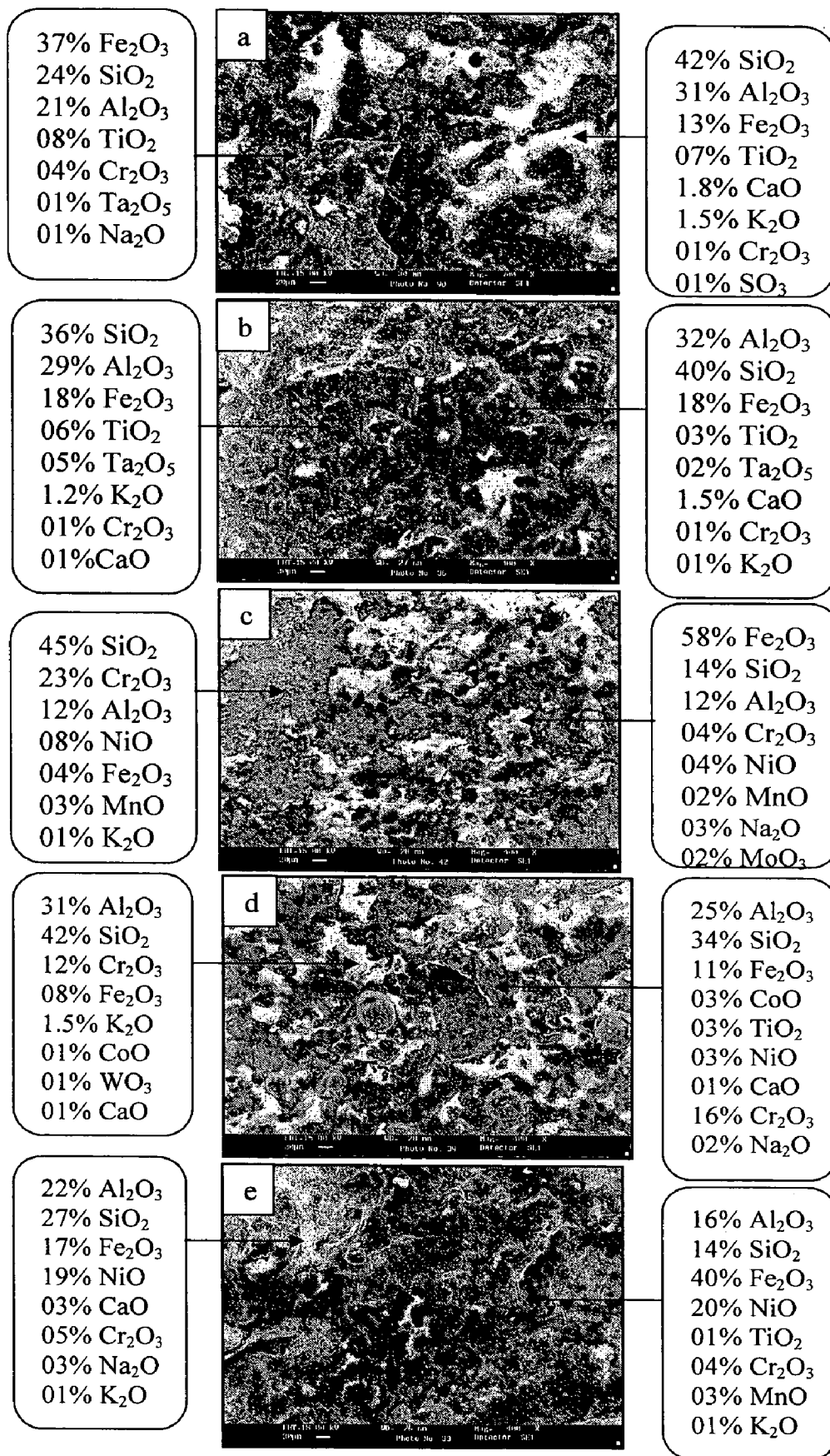


Fig. 7.47 SEM/EDAX analysis showing elemental composition (wt.%) for the bare and coated Superni 718 after 1000 hrs exposure to platen superheater zone of the coal fired boiler at 900 °C: (a) Bare Superni 718 (b) Cr₃C₂-NiCr coated (c) NiCrBSi coated (d) Stellite-6 coated (e) Ni-20Cr coated.

7.1.6.4(B) Cross-Section Analysis

The Figure 7.48 shows BSE image/EDAX analysis at some selected point of interest across the cross-section of corroded Ni-20Cr coated Superni 718. The lamellar structure scale formed on the coated alloy is adherent to the substrate and free from cracks. The oxide scale is protective as evident by the absence of degrading species beneath the scale-substrate interface (Point 1). The grey phase formed at Points 2 and 4 is found to be rich in chromium and oxygen and nickel has decreased significantly in these regions, whereas the white phase in the scale (Point 3) consists of Ni-rich splats. From the EDAX analysis of Points 2, 3 and 4, it can be inferred that the elongated Ni-rich splats are surrounded by mainly chromium oxide at the splat boundaries. The scale formed at Points 5 and 6 composed mainly of nickel, chromium and oxygen indicating the presence of oxides of Ni and Cr, and their spinels in the uppermost scale. The presence of lesser iron (14.1 wt%) at Point 1 and some amounts at Points 2 and 3 indicates outward diffusion of iron from the substrate. Similarly the presence of manganese (0.5 wt%) and titanium (2.0 wt%) in the surface scale indicates their outward diffusion from the substrate.

7.1.6.5 EPMA Analysis

The scale formed on the bare Superni 718 appears to be fragile and porous, and penetrates into the base substrate (Fig. 7.49). The elemental maps show that the scale consists mainly of Cr, Al, Si, and Ti with some amount of Fe in the topmost layer of the scale. Titanium forms a relatively thicker band than chromium. The Ta and Mo elements of the substrate diffused outward and reached almost to the uppermost part of the scale, whereas the presence of nickel in the scale is found to be negligible.

The EPMA analysis across the cross-section of corroded Cr₃C₂-NiCr coated Superni 718, as shown in Fig. 7.50, indicates the formation of Cr₂O₃-rich thick network around the Ni-rich splats. The absence of oxygen corresponding to the position of Ni-rich splats shows that these Ni-rich splats mostly remain un-oxidized even after 1000 hours of exposure to boiler environment. The relative density of Cr-rich areas is more than the Ni-rich splats. The topmost layer of the scale is enriched in Al₂O₃ and SiO₂ along with some amounts of Fe₂O₃. The presence of iron, aluminium and silicon in the surface scale is due to outward diffusion from the substrate and partly due to the entrapped ash particles. The elemental maps show negligible outward diffusion of Mo and Ti from the substrate in this coating-substrate system. Sodium and potassium show their presence across the scale in traces. Aluminium forms a thin streak at the scale-substrate interface, where all other elements are found to be

absent. The presence of high intensity dots of oxygen and aluminium at the scale-substrate interface indicates the formation of exclusively Al_2O_3 . The substrate superalloy is found to be free from the penetration of oxygen and other corrosive species, thereby indicating the protective behaviour of this coating-substrate system in the given conditions of study.

The NiCrBSi coated Superni 718 shows the formation of scale consisting mainly of Ni, Cr and Si with some amount of Fe (Fig. 7.51). The topmost part of the scale contains thick clusters of silicon and aluminium. Aluminium is also present in pockets at the scale-substrate interface at places where other elements are found to be absent. Potassium element of the corrosive environment is also present in traces.

The scale formed on Ni-20Cr coated Superni 718 has a lamellar structure in which chromium is mainly present at the boundaries of Ni-rich splats (Fig. 7.52). The elemental maps show that chromium co-exists with oxygen indicating the formation of Cr_2O_3 . Further the absence of oxygen in the scale corresponding to the sites of the splats indicates that these Ni-rich splats are mostly in the unoxidised state. The nickel co-exists with oxygen at the topmost part of the scale and forms a thin streak of NiO. The thin layer just below of this NiO-rich topmost scale is found to be rich in Cr_2O_3 with some amount of NiO. A thick network of Cr_2O_3 is formed in the central portion of the scale. The formation of Cr-depleted layer just below the scale-substrate interface reveals the outward diffusion of chromium from the substrate alloy. The substrate elements such as Ti, and Mn showed negligible diffusion in this coating-substrate system and, therefore, their element maps are not shown, whereas Si diffused from the substrate and is seen along the splat boundaries. The K and Na corrosive species are present in traces mainly in the topmost layer of the scale. A thin streak of Al is formed at scale-substrate interface. The absence of oxygen just below the scale-substrate interface indicates that the Ni-20Cr coating is effective in imparting hot corrosion resistance to the Superni 718 in the given environmental conditions.

7.1.7 Hot Corrosion of Bare and Coated Superfer 800H

7.1.7.1 Corrosion Kinetics

The weight change plots for the bare and coated Superfer 800H are shown in Fig. 7.53. The bare alloy showed higher weight gain as compared to coated specimens. The Ni-20Cr coated Superfer 800H showed lowest weight gain among all the coatings under study. Therefore, it provides maximum resistance to hot corrosion in the given environment. Its weight gain is about 35% less of that gained by the uncoated superalloy.

The Stellite-6 coating showed second lowest weight gain, whereas NiCrBSi coated alloy showed highest weight gain among all the coatings deposited on Superfer 800H superalloy. The weight gain of Cr₃C₂-NiCr coating could not be measured up to 1000 hours due to heavy spallation and detachment of the coating after 700 hours of the study.

The weight gain square (mg^2/cm^4) data plotted as a function of time is shown in Fig. 7.54 to establish the rate law for the hot corrosion. It can be observed from the graph that all the coatings have followed nearly parabolic behaviour up to 10 cycles and, therefore, thus they show a tendency to develop diffusion barriers to the corroding species. The weight gain square curve for the bare alloy shows considerable deviations from parabolic rate law signifying large amount of suspected spallation of the scale during experimentations. From the weight gain data it can be inferred that necessary protection against hot corrosion has been provided by all the coatings. The Ni-20Cr and Stellite-6 coatings provided the best protection to the Fe-based Superfer 800H superalloy, whereas the NiCrBSi coatings showed relatively least resistance to hot corrosion.

The parabolic rate constants (k_p in $10^{-12} \text{ g}^2 \text{ cm}^{-4} \text{ s}^{-1}$) for the Cr₃C₂-NiCr, NiCrBSi, Stellite-6 and Ni-20%Cr coated Superfer 800H are found as 6.22 (up to 700 hrs only), 11.61, 9.88, and 5.25, respectively.

7.1.7.2 Average Scale Thickness and Depth of Internal Attack

The combined effects of average scale thickness and internal corrosion attack for the bare; and Cr₃C₂-NiCr, NiCrBSi, Stellite-6 and Ni-20Cr coated superalloy are found to be 95; and 369, 380, 302 and 275 μm , respectively. The coated specimens show no scale thickness loss. The value of scale thickness loss in bare alloy is 248 μm as reported under section 7.1.2. Figure 7.56 indicates the average scale thickness, scale thickness lost and depth of internal corrosion attack for the bare and coated Superfer 800H as measured from the BSE images shown in Fig. 7.55. On comparing the relative performance of each coating, the Ni-20Cr coating deposited on Superfer 800H showed best resistance to the given environment followed by Stellite-6 and Cr₃C₂-NiCr coatings, respectively. The NiCrBSi coating showed relatively least resistance amongst all the coatings.

7.1.7.3 X-ray Diffraction Analysis

The diffraction patterns for the corroded bare and coated Superfer 800H are shown in Fig. 7.57. The main phases identified with the XRD analysis at the surface of corroded specimens are presented in Table 7.5.

Table 7.5: Major and minor phases identified by XRD analysis for the bare and coated Superfer 800H after 1000 hrs exposure to actual environment of the coal fired boiler.

Description	Major phases	Minor phases
Uncoated Superfer 800H	Cr ₂ O ₃ , NiO, Fe ₂ O ₃ , SiO ₂ , FeS, and NiFe ₂ O ₄	Al ₂ O ₃ , NiS, and MnO ₂
Cr ₃ C ₂ -NiCr coated	Cr ₂ O ₃ , Fe ₂ O ₃ , Al ₂ O ₃ , and NiCr ₂ O ₄	MnO ₂
NiCrBSi coated	Cr ₂ O ₃ , Fe ₂ O ₃ , Al ₂ O ₃ , SiO ₂ , and NiCr ₂ O ₄	NiO, and MnO
Stellite-6 coated	Cr ₂ O ₃ , Fe ₂ O ₃ , Al ₂ O ₃ , SiO ₂ , CoCr ₂ O ₄ , and NiCr ₂ O ₄	CoO
Ni-20Cr coated	Cr ₂ O ₃ , NiO, Fe ₂ O ₃ , Al ₂ O ₃ , SiO ₂ , and NiCr ₂ O ₄	MnO ₂

7.1.7.4 SEM/EDAX Analysis

7.1.7.4(A) Surface Analysis

SEM micrographs and EDAX analysis of the bare and coated Superfer 800H after 1000 hrs exposure to given environment are shown in Fig. 7.58.

The surface morphology of the bare Superfer 800H clearly shows the existence of black regions from where the spallation of the scale has occurred (Fig. 7.58a). The EDAX analysis shows that the white phase of the scale has a composition almost similar to that of ash along with some amounts of MnO and Cr₂O₃, whereas the spalled region contains relatively higher amount of Cr₂O₃ (29 wt%) along with some amounts of NiO and TiO₂. The spalled region has relatively lower amounts of SiO₂, Al₂O₃, Fe₂O₃, and MnO.

A uniform, compact, adherent and nearly homogeneous scale is formed on the HVOF coated Superfer 800H without indication of any crack or voids (Figs. 7.58b to 7.58d). The EDAX analysis of the grey phase of the scale of Cr₃C₂-NiCr coated alloy shows the presence of mainly Cr₂O₃, along with NiO and other oxides, whereas white phase has a composition almost similar to that of ash but contains little amounts of Cr₂O₃ (4 wt%) and TiO₂ (2 wt%) also. The scales formed on NiCrBSi, Stellite-6 and Ni-20Cr coated specimens are found to be rich in mainly Al₂O₃, SiO₂, and Fe₂O₃. The dark grey globules present in the scales formed on Stellite-6 and Ni-20Cr coatings contain higher percentage of Fe₂O₃ and lower content of SiO₂. The presence of MnO and TiO₂ in the uppermost layer of the scale of the coated specimens indicates their outward diffusion tendencies from the substrate.

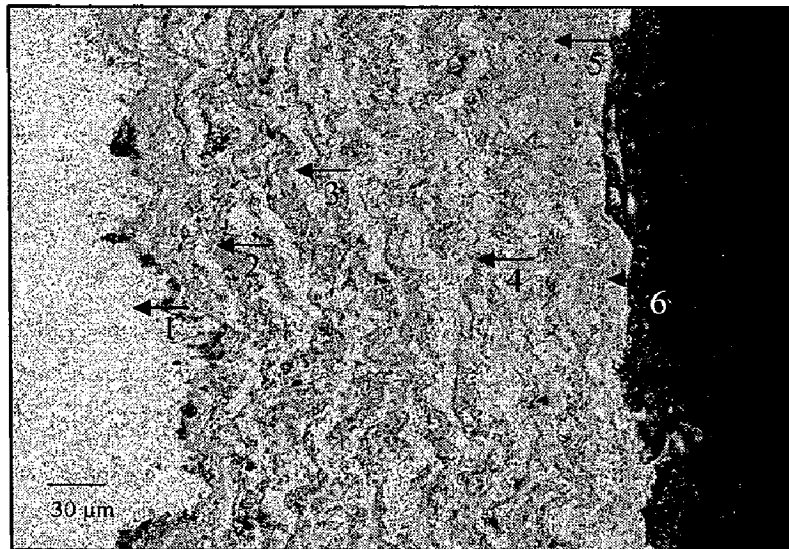
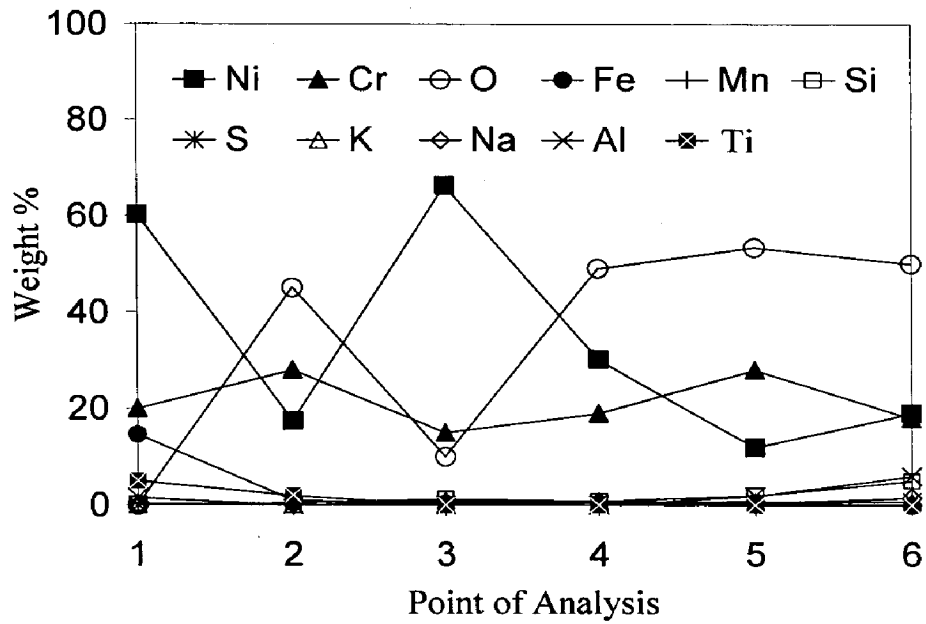


Fig 7.48 Oxide scale morphology and variations of elemental composition (wt%) across the cross section of Ni-20Cr coated Superni 718 after 1000 hrs exposure to platen superheater zone of the coal fired boiler at 900 °C.

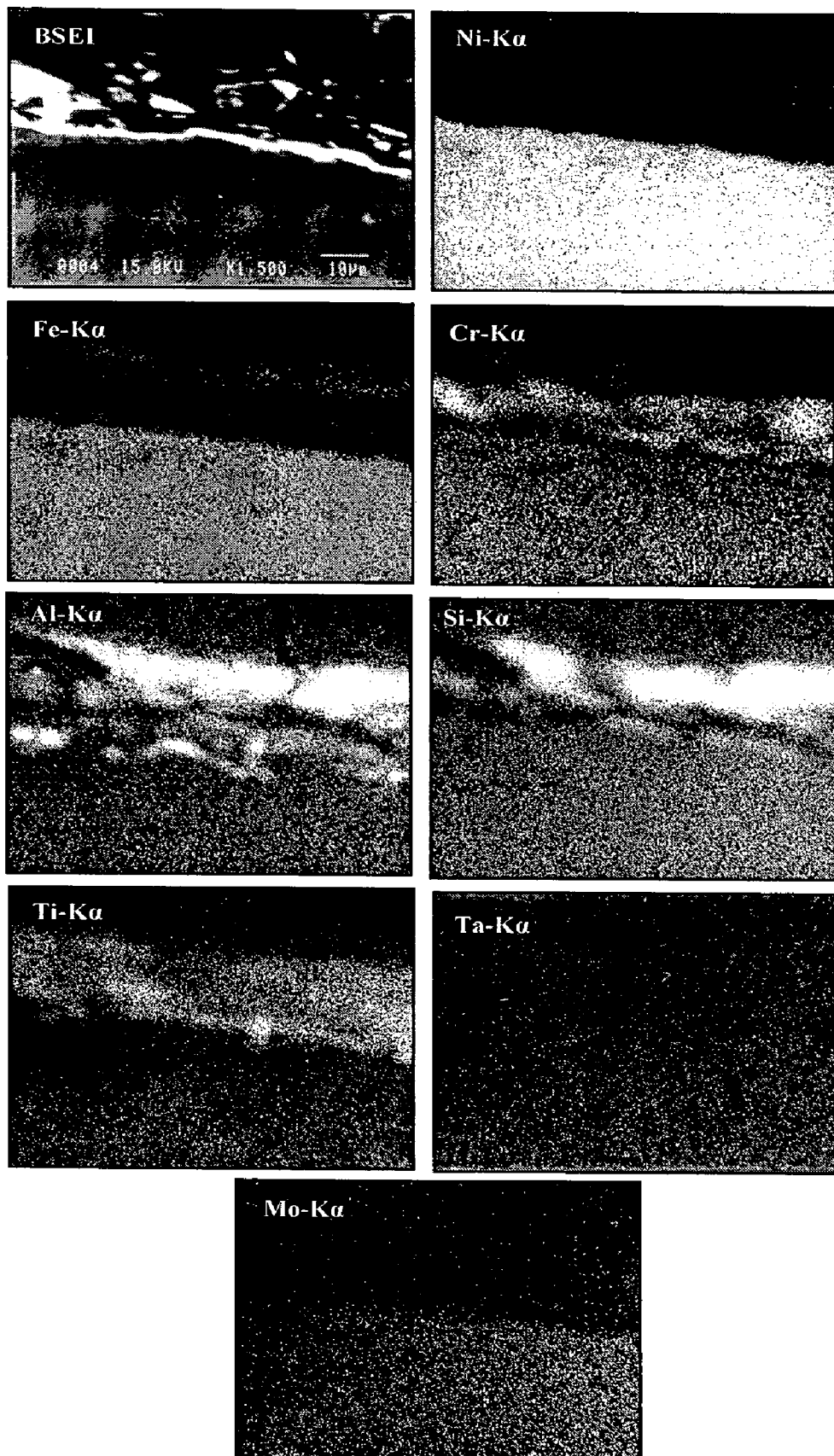


Fig. 7.49 Composition image (BSEI) and X-ray mappings across the cross-section of bare Superni 718 after 1000 hrs exposure to platen superheater zone of the coal fired boiler at 900 °C.

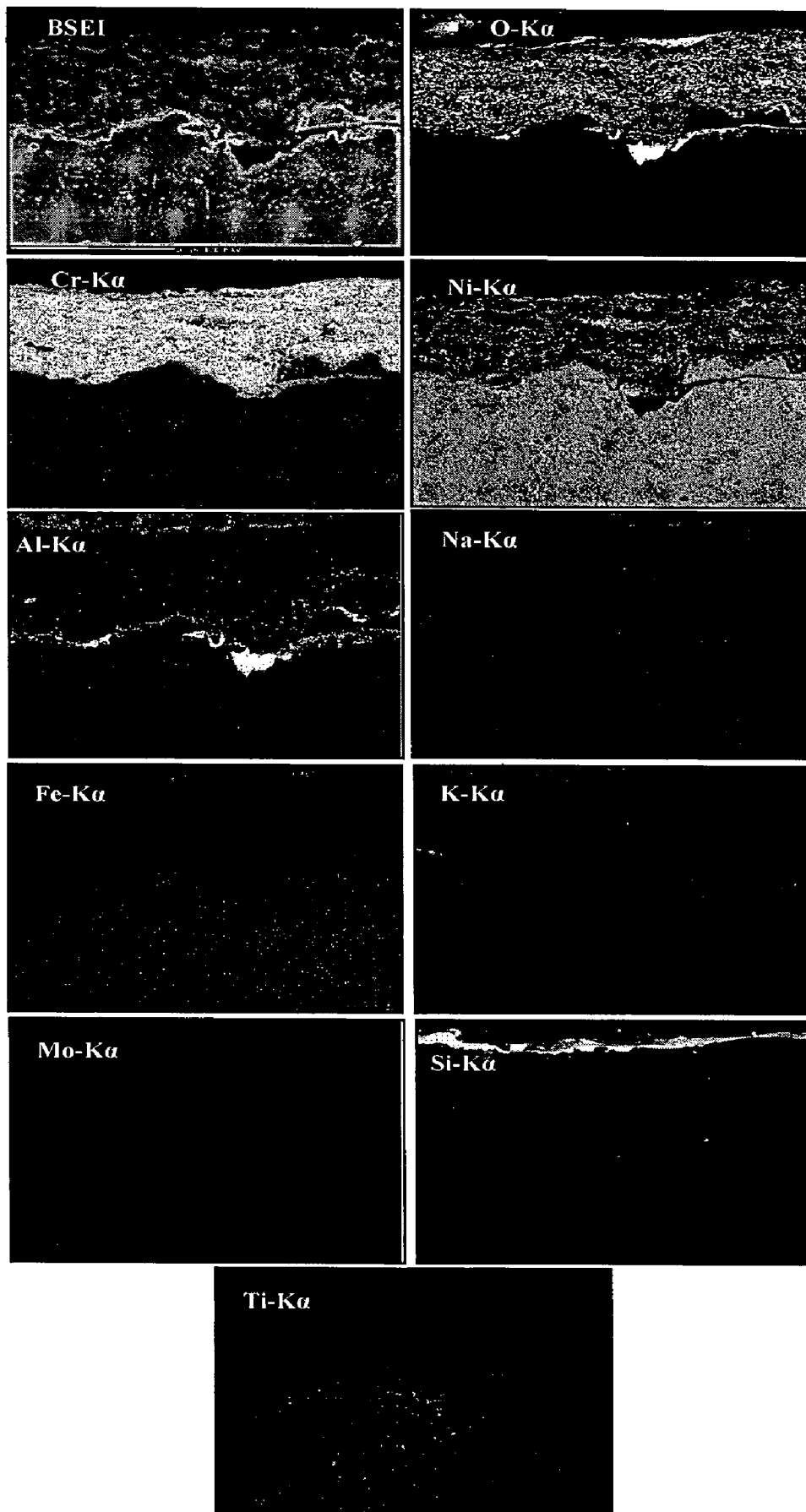


Fig. 7.50 Composition image (BSEI) and X-ray mappings across the cross-section of Cr_3C_2 -NiCr coated Superni 718 after 1000 hrs exposure to platen superheater zone of the coal fired boiler at 900 °C.

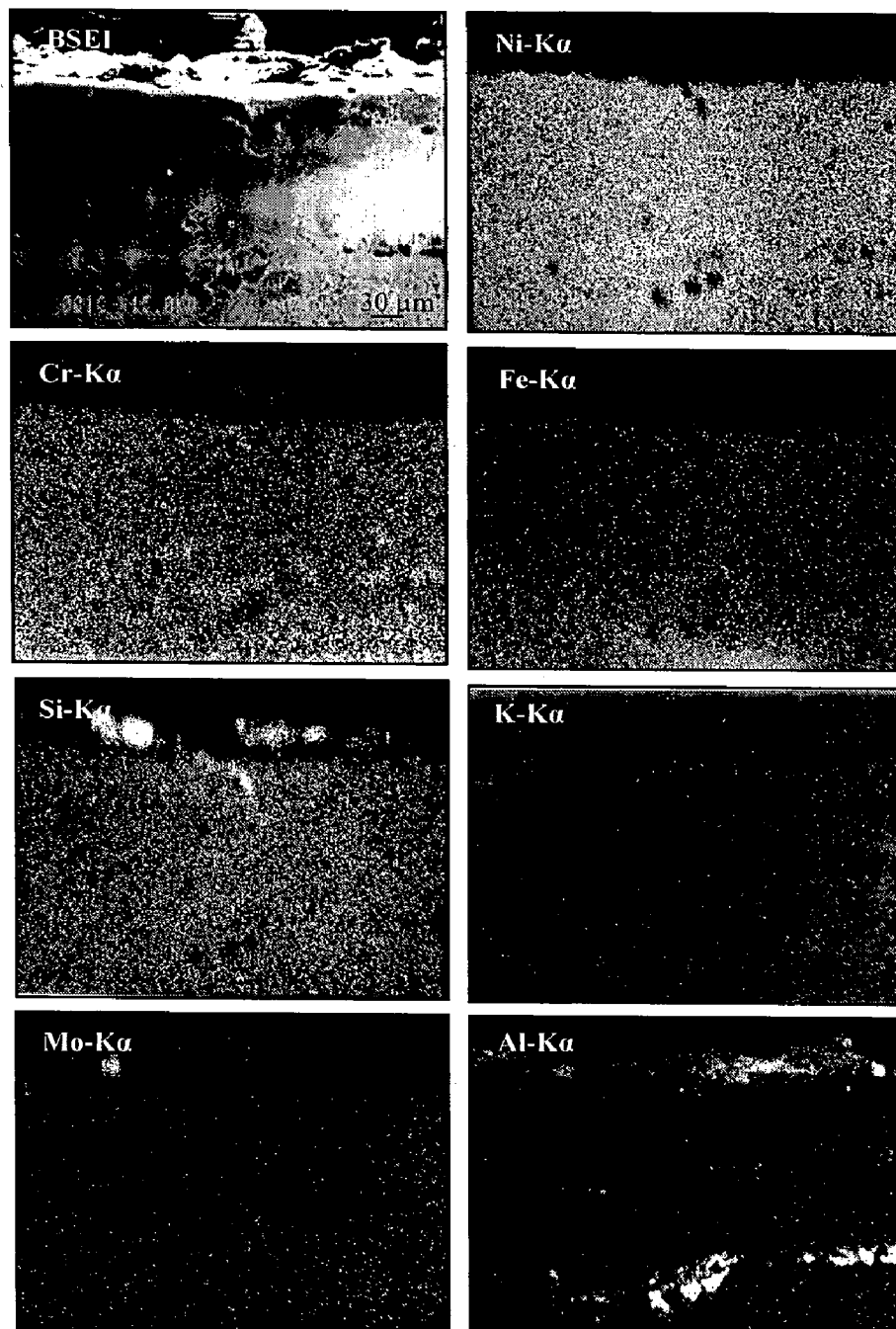


Fig. 7.51 Composition image (BSEI) and X-ray mappings across the cross-section of NiCrBSi coated Superni 718 after 1000 hrs exposure to platen superheater zone of the coal fired boiler at 900 °C.

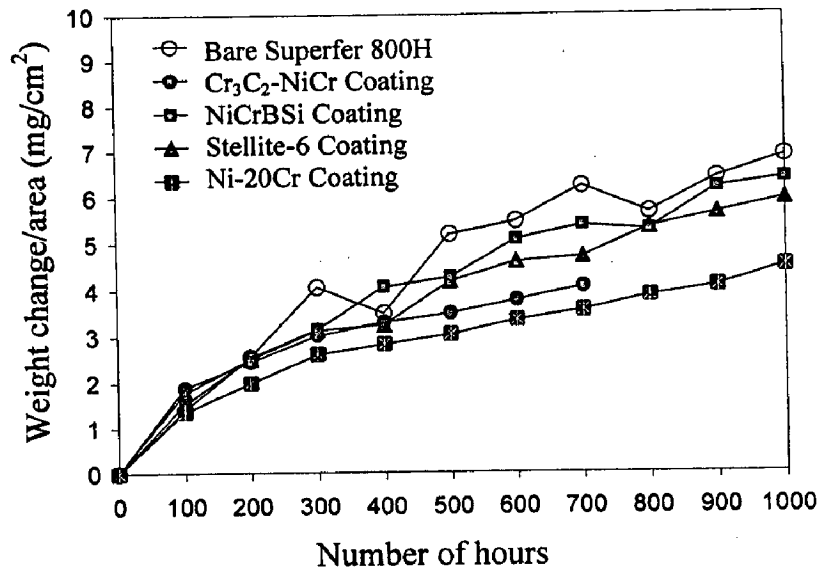


Fig. 7.53 Weight change vs. time plots for the coated and uncoated Superfer 800H subjected to 1000 hrs cyclic exposure to platen superheater zone of the coal fired boiler at 900 °C.

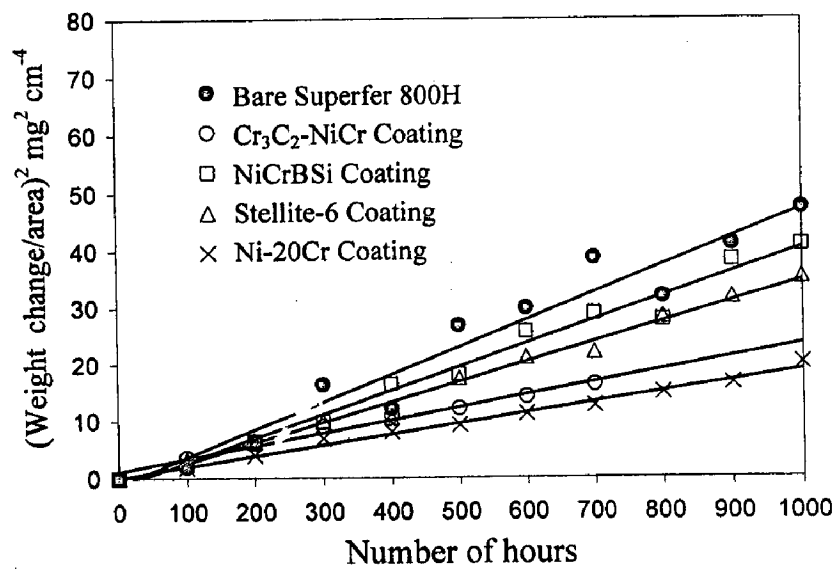


Fig. 7.54 (Weight change/area)² vs. time plots for the coated and uncoated Superfer 800H subjected to 1000 hrs cyclic exposure to platen superheater zone of the coal fired boiler at 900 °C.

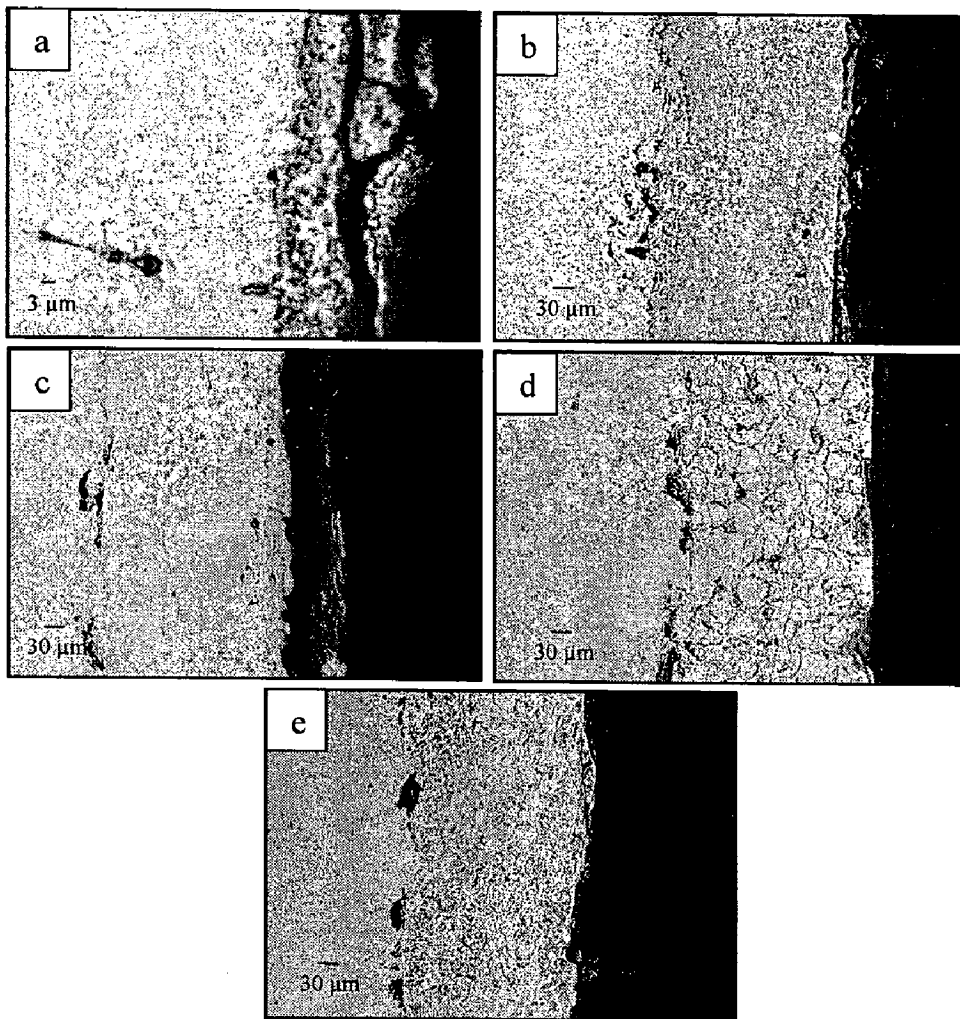


Fig. 7.55 BSE images for the bare and HVOF coated Superfer 800H after 1000 hrs exposure to platen superheater zone of the coal fired boiler at 900 °C:
 (a) Bare superalloy (b) Cr₃C₂-NiCr coated (c) NiCrBSi coated
 (d) Stellite-6 coated (e) Ni-20Cr coated.

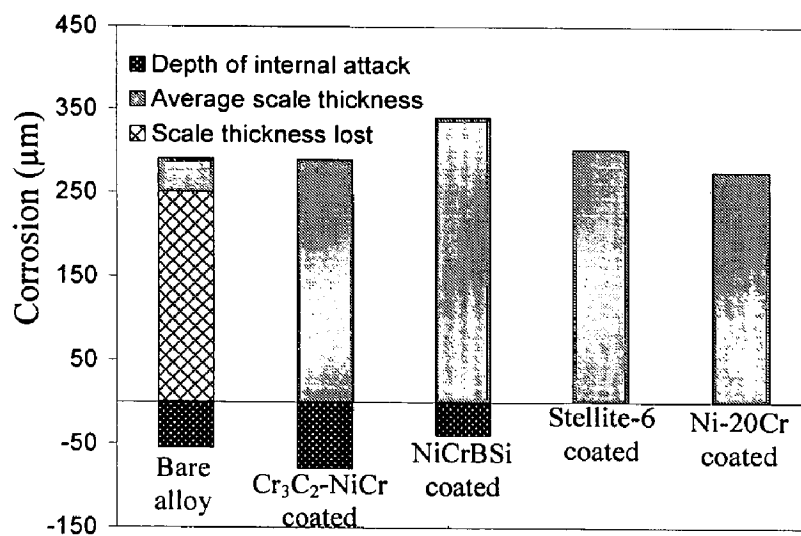


Fig. 7.56 Bar charts indicating the extent of corrosion for the bare and HVOF coated Superfer 800H after 1000 hrs exposure to the coal fired boiler at 900 °C.

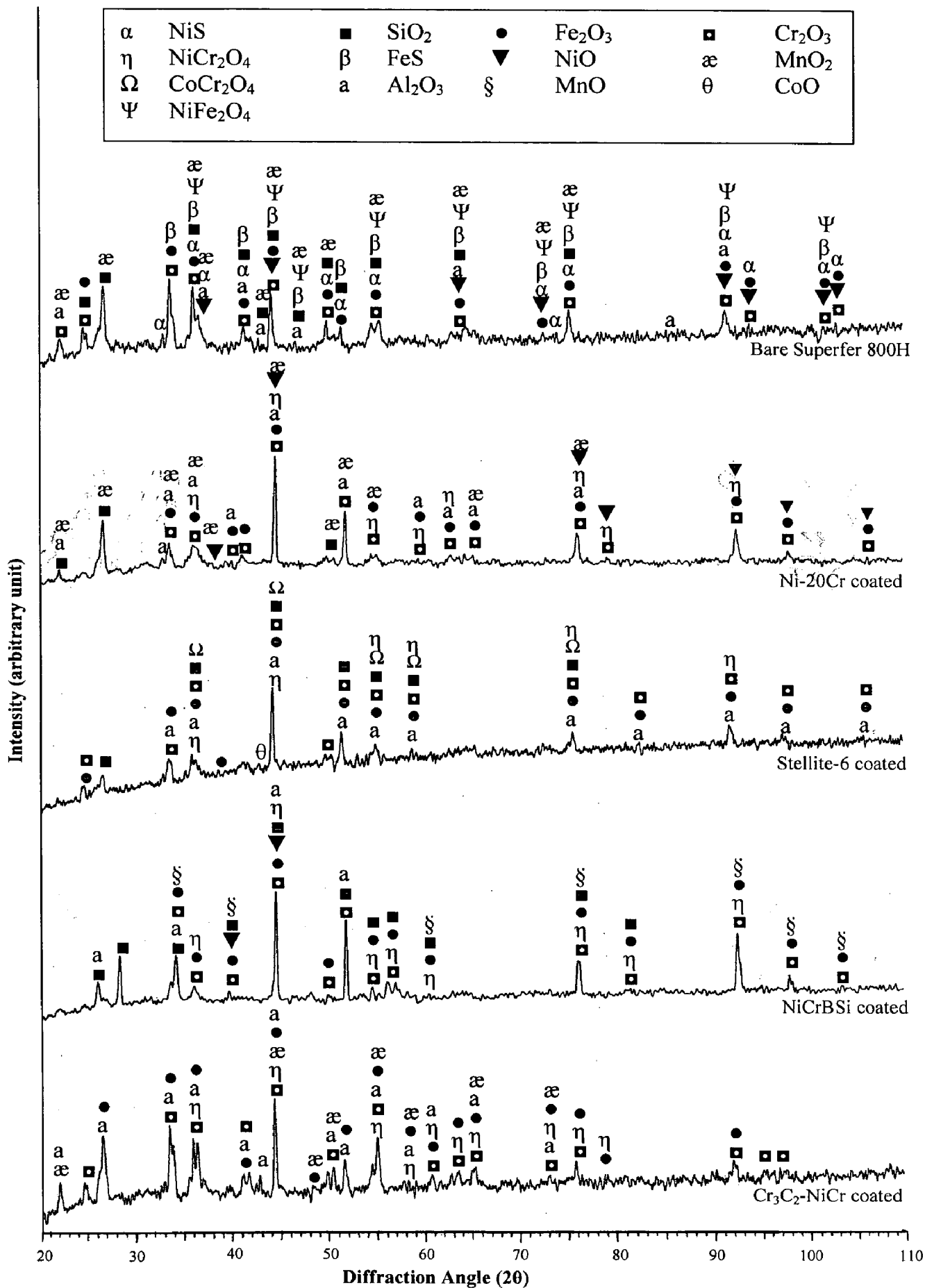


Fig. 7.57 X-ray diffraction patterns for the bare and coated Superfer 800H after 1000 hrs exposure to platen superheater zone of the coal fired boiler at 900 °C.

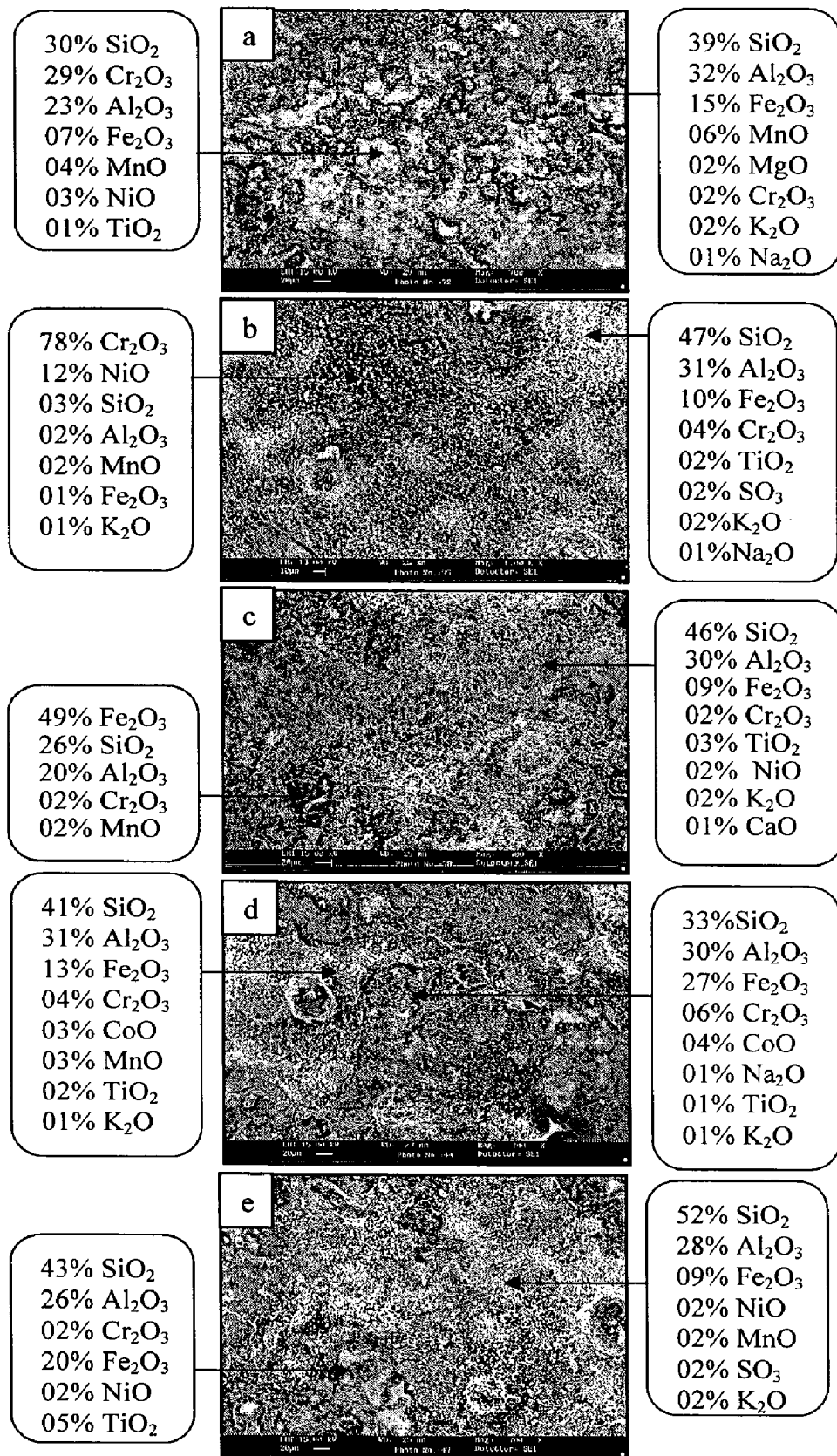


Fig. 7.58 SEM/EDAX analysis showing elemental composition (wt.%) for the bare and coated Superfer 800H after 1000 hrs exposure to platen superheater zone of the coal fired boiler at 900 °C: (a) Bare Superfer 800H (b) Cr₃C₂-NiCr coated (c) NiCrBSi coated (d) Stellite-6 coated (e) Ni-20Cr coated .

7.1.7.4(B) Cross-Section Analysis

Figure 7.59 shows the BSEI/EDAX analysis at some selected point of interest across the cross-section of the scales formed on bare and Stellite-6 coated Superfer 800H.

The EDAX analysis reveals the presence of 40 wt% of oxygen at Point 1 suggesting that the oxide scale formed on the bare Superfer 800H penetrates to about 35 μm into the substrate (Fig. 7.59a). The analysis at Point 2 indicates the presence of basic elements of the substrate. At Point 3, the scale comprises of manganese, aluminium, iron and oxygen. The outer layer of the scale (Points 4 and 5) mainly consists of aluminium, silicon and oxygen along with little amount of iron. The substrate alloy contains small amounts of sulphur (0.5 wt%) at Point 1..

The EDAX analysis of Stellite-6 coated Superfer 800H (Fig. 7.59b) reveals the presence of very little amount of oxygen at Point 1 indicating that this oxygen has penetrated to the substrate during initial hours of the exposure. The EDAX results at Points 2 and 4 indicate the existence of Co-rich splats. Further, the EDAX study reveals the presence of high wt% of chromium, silicon and oxygen at Points 3 and 5. Therefore, it can be inferred that the oxides of chromium and silicon are formed at the boundaries of these Co-rich splats due to the selective oxidation of the chromium. The topmost scale (Point 6) is mainly composed of oxygen and chromium indicating the formation of chromium oxide.

7.1.7.5 EPMA Analysis

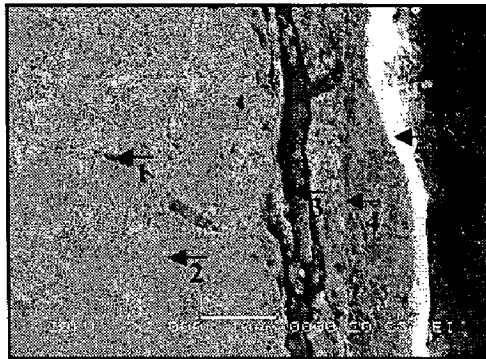
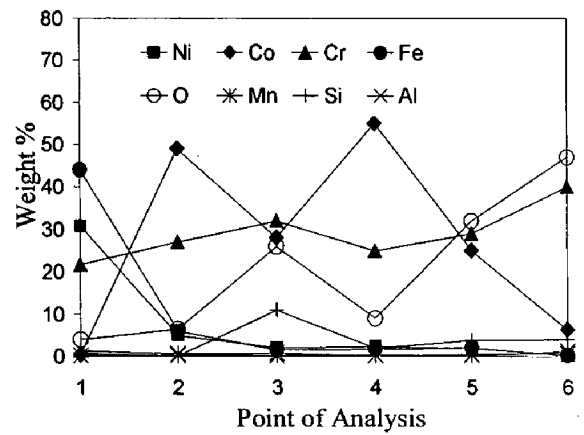
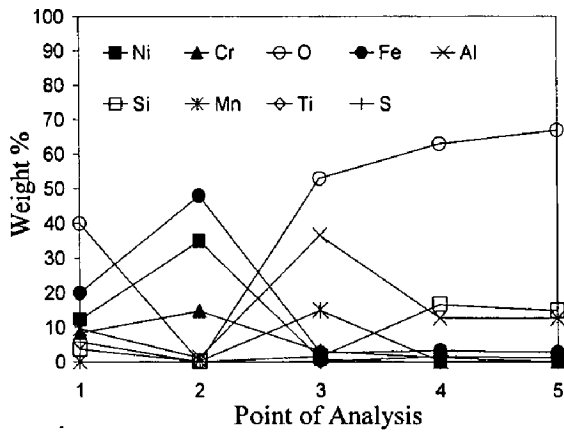
The EPMA analysis of the bare Superfer 800H after exposure to given environment shows that the topmost part of the scale mainly consists of Al, Si, Fe, Ti, Na, and S indicating the participation of ash in the corrosion mechanism (Fig. 7.60). Chromium along with titanium forms a band of about 7 μm thickness just below the topmost scale. The presence of nickel in the scale is found to be negligible.

The scale formed on the Cr_3C_2 -NiCr coated Superfer 800H consists of Ni-rich splats surrounded by the network of chromium (Fig. 7.61). The topmost part of the scale comprises of Si, Al, Fe and K. At the scale-substrate interface, manganese forms nearly a continuous band whereas Al and Si show their presence in the form of discontinuous streaks. It indicates that these elements have diffused from the substrates. The presence of high intensity dots of iron above the scale-substrate interface shows its outward diffusion from the substrate.

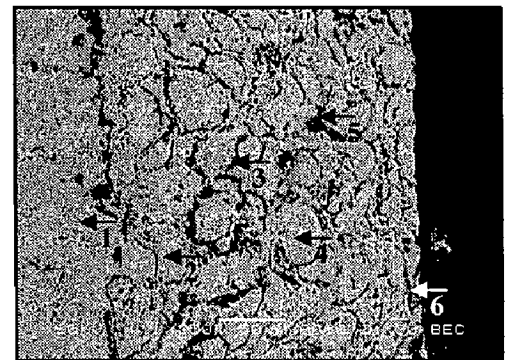
BSE image and EPMA elemental mappings for the corroded Stellite-6 coated Superfer 800H are shown in Fig.7.62. The elemental mappings show that Cr, Si and O

co-exist at the boundaries of Co-rich splats suggesting the formation of Cr_2O_3 and SiO_2 at these boundaries. A thin and continuous streak of Cr_2O_3 is formed just above the scale-substrate interface, thereby leaving a chromium depleted areas underneath. Aluminium forms a nearly continuous streak as well as some clusters at the scale-substrate interface. The presence of oxygen at these places indicates the formation of Al_2O_3 . These clusters of Al_2O_3 are mostly present at the places where all other elements are absent. Sodium and sulphur show their presence in traces throughout the scale, whereas relatively higher concentration of sodium exists in the topmost part of the scale. The cobalt diffused from the coating to the substrate, whereas Mn and Ti show minor diffusion from the substrate to the coating.

The BSEI image of Ni-20Cr coated Superfer 800H shows the formation of a continuous and adherent scale with lamellar structure consisting mainly of nickel and chromium (Fig. 7.63). Chromium is present mainly at the boundaries of Ni-rich splats. Thick and dense bands of silicon and aluminium are formed at to topmost part of the scale. A high amount of Al is also present at the scale-substrate interface, where almost all other elements are found to be absent. The iron, titanium, silicon and aluminium diffused from the substrate to the coating. The diffusion of iron appears to be highest just above the scale-substrate interface, whereas titanium forms a thick band at the topmost part of the scale.



(a)



(b)

Fig 7.59 Oxide scale morphologies and variations of elemental composition (wt%) across the cross section of bare and HVOF coated Superfer 800H after 1000 hrs exposure to platen superheater zone of the coal fired boiler at 900 °C :
 (a) Bare Superfer 800H (b) Stellite-6 coated.

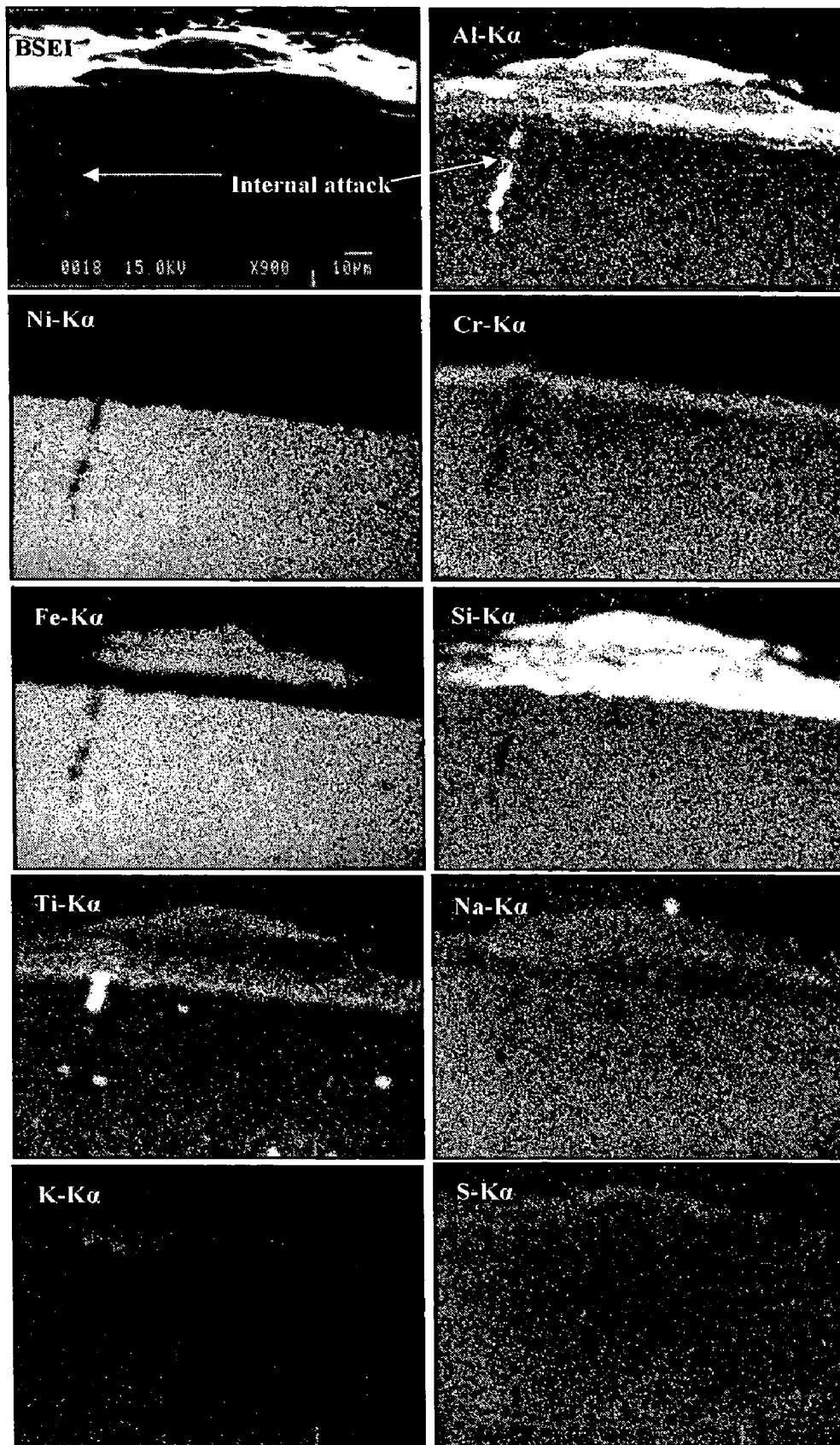


Fig. 7.60 Composition image (BSEI) and X-ray mappings across the cross-section of the bare Superfer 800H after 1000 hrs exposure to platen superheater zone of the coal fired boiler at 900 °C.

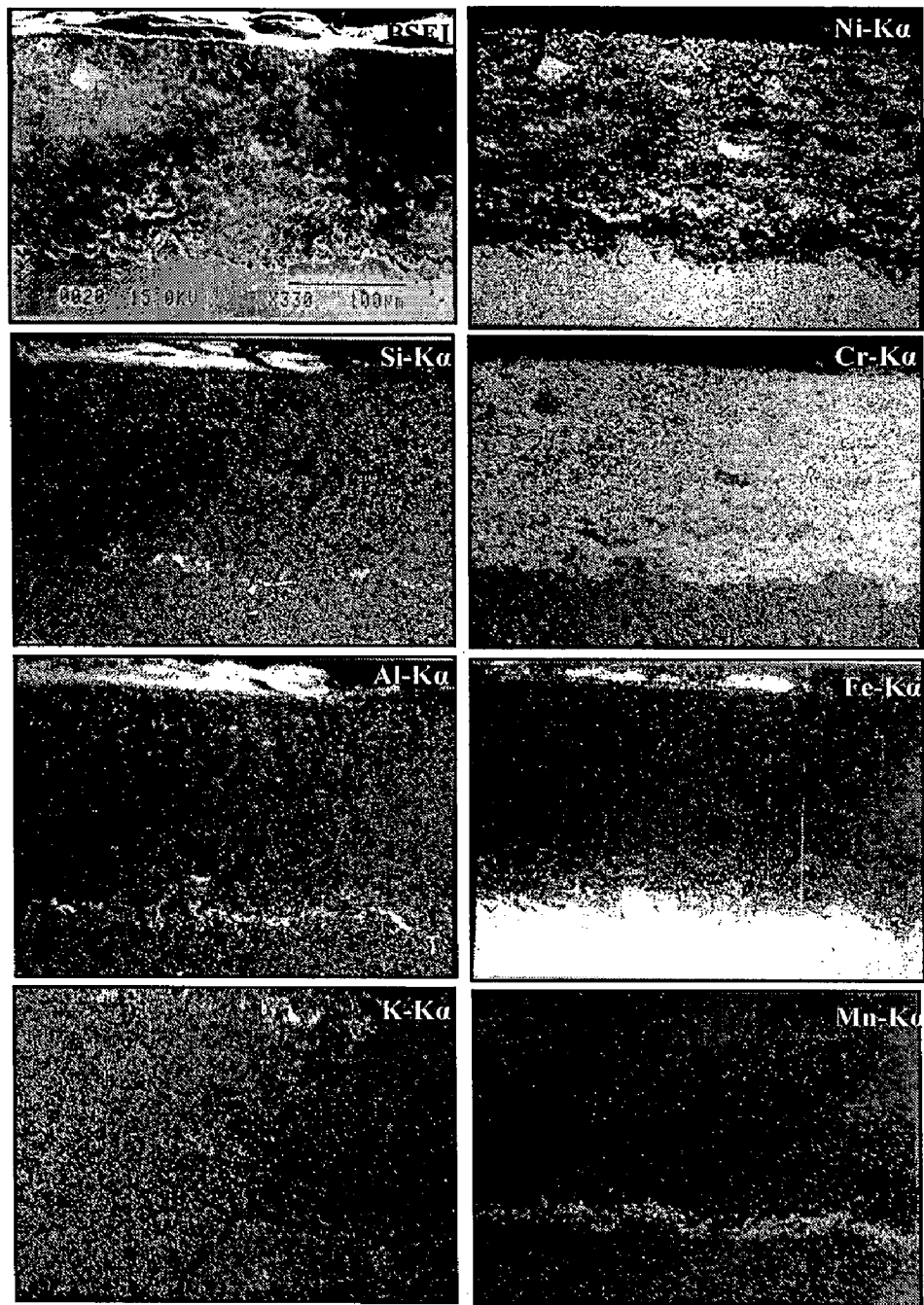


Fig. 7.61 Composition image (BSEI) and X-ray mappings across the cross-section of $\text{Cr}_3\text{C}_2\text{-NiCr}$ coated Superfer 800H after 1000 hrs exposure to platen superheater zone of the coal fired boiler at 900 °C.

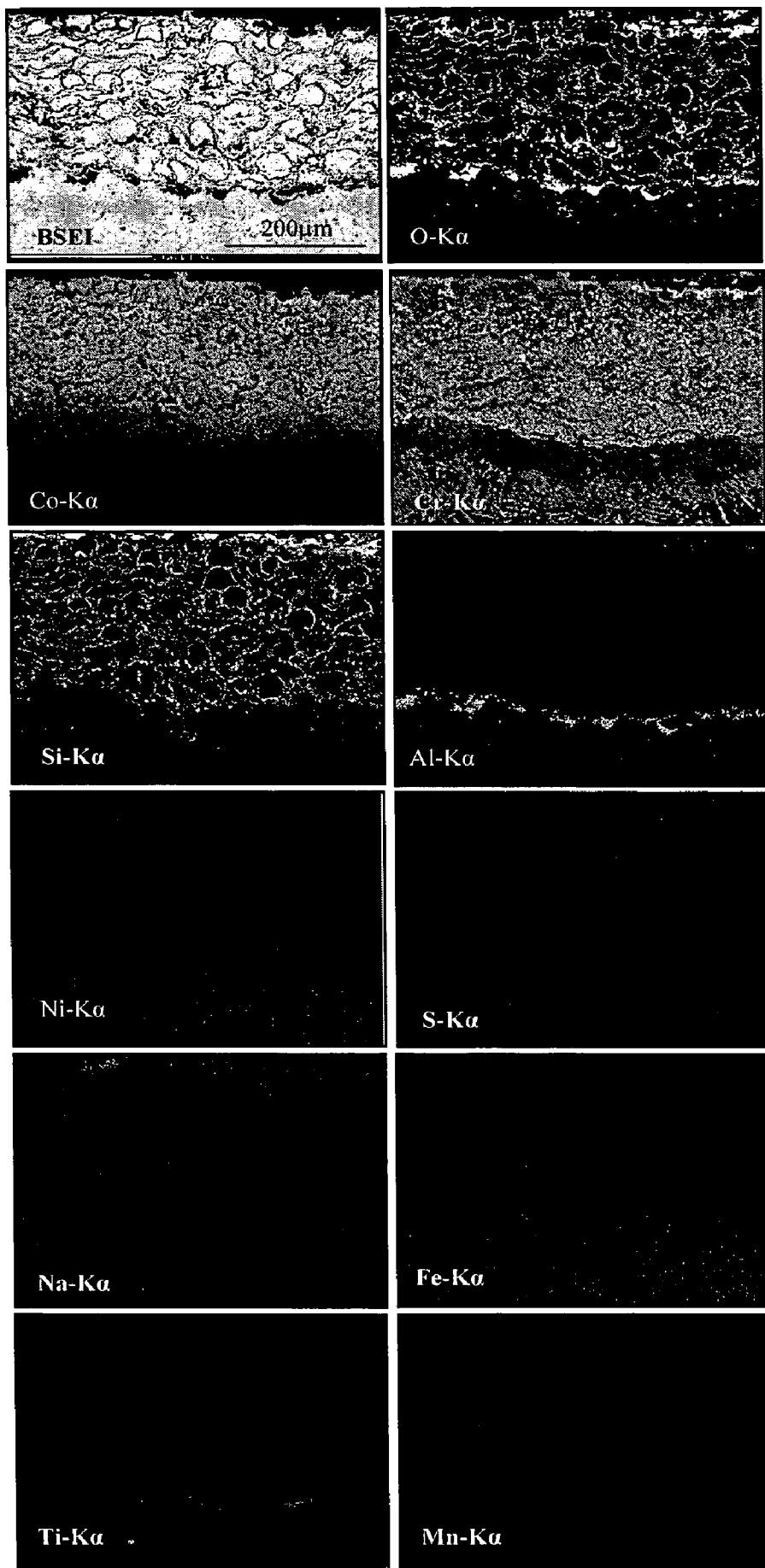


Fig. 7.62

Composition image (BSEI) and X-ray mappings across the cross-section of Stellite-6 coated Superfer 800H after 1000 hrs exposure to platen superheater zone of the coal fired boiler at 900 °C.

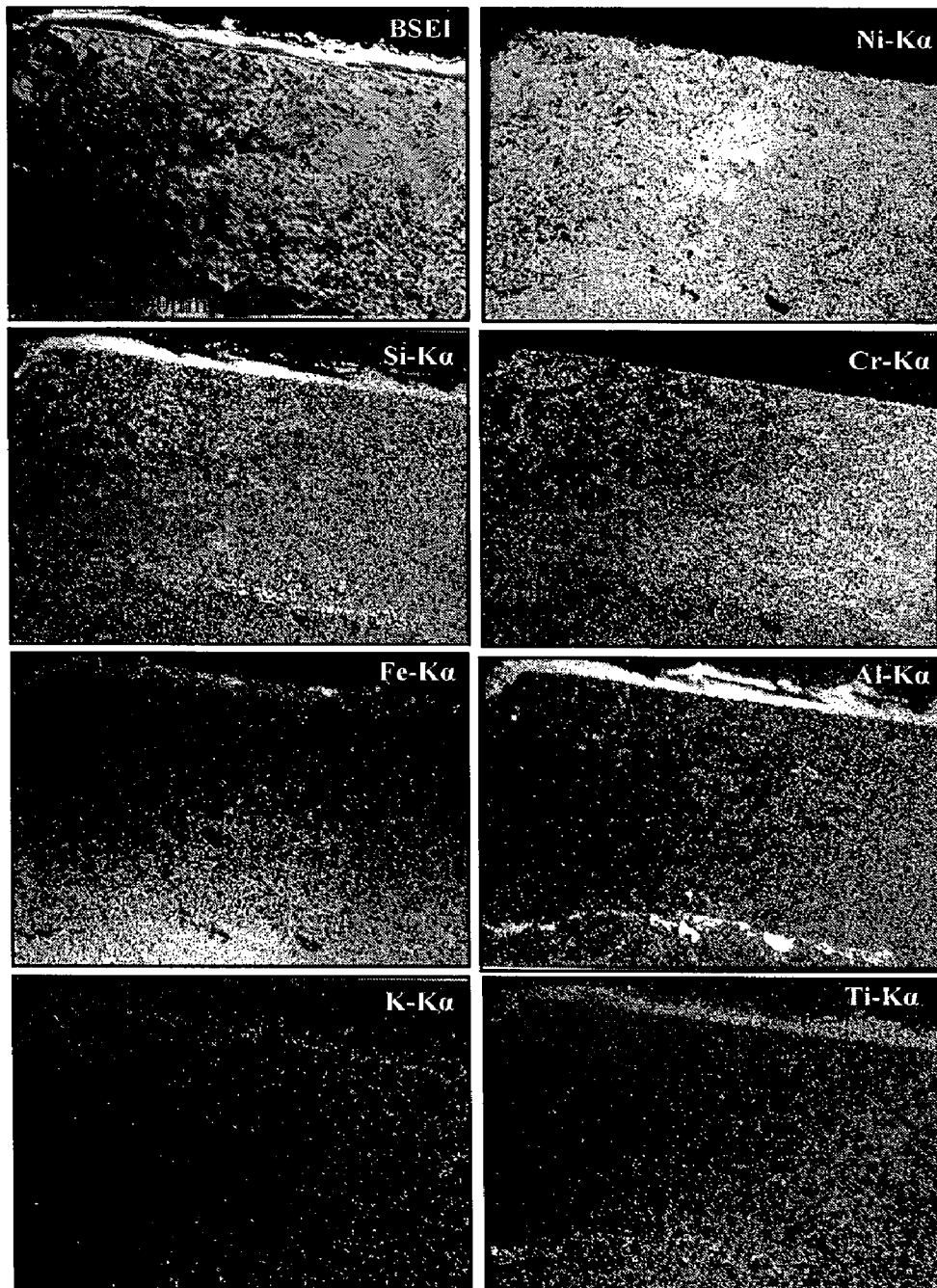


Fig. 7.63 Composition image (BSEI) and X-ray mappings across the cross-section of Ni-20Cr coated Superfer 800H after 1000 hrs exposure to platen superheater zone of the coal fired boiler at 900 °C.

7.2 SUMMARY OF RESULTS

Results obtained after 1000 hours exposure of uncoated and coated superalloys to the platen superheater zone of the coal fired boiler at 900 ± 10 °C are summarised in Table 7.6:

Table 7.6: Summary of the results for uncoated and coated superalloys exposed to platen superheater zone of the coal fired boiler at around 900 °C for 1000 hours.

Base super-alloy	Coating	Weight gain mg/cm ²	$k_p \times 10^{-12}$ g ² cm ⁻⁴ s ⁻¹	Extent of corrosion µm	Major XRD phases	Minor XRD phases	Remarks
Superni 75	Uncoated	3.29	-----	148	Cr ₂ O ₃ , Fe ₂ O ₃ , Al ₂ O ₃ , and SiO ₂	FeS	Brownish grey irregular scale is formed with little spallation. Internal attack observed.
	Cr ₃ C ₂ -NiCr coated	6.06	11.36	340	Cr ₂ O ₃ , Fe ₂ O ₃ , Al ₂ O ₃ , and NiCr ₂ O ₄	SiO ₂	Yellowish grey scale is formed which indicated minor spallation from the edges and corners. Coating remained intact and no internal attack observed.
	NiCrBSi coated	6.62	8.88	325	Cr ₂ O ₃ , Fe ₂ O ₃ , and NiCr ₂ O ₄	NiO, and Al ₂ O ₃	Yellowish scale with green tinges appeared. Scale maintained good contact with the substrate without indicating any crack, or internal corrosion attack.
	Stellite-6 coated	5.28	8.50	293	Cr ₂ O ₃ , Fe ₂ O ₃ , CoCr ₂ O ₄ , and NiCr ₂ O ₄	CoO	Brownish grey scale formed during cyclic exposures showed negligible spallation, no crack or internal attack noted. The coating found to be integral with the base alloy after exposure.

	Ni-20Cr coated	3.64	4.16	209	Cr ₂ O ₃ , Al ₂ O ₃ , SiO ₂ , and Fe ₂ O ₃	----	Reddish brown scale found to be regular, continuous and adherent; indicated negligible spallation, and free from cracks and internal corrosion attack. Coating maintained excellent contact with the substrate.
Superni 600	Uncoated	3.49	-----	153	Cr ₂ O ₃ , Fe ₂ O ₃ , Al ₂ O ₃ , SiO ₂ , and FeS	NiS	Fragile brownish grey scale formed. Cracks developed in the scale and indicated tendency for spallation. Internal attack noted.
	Cr ₃ C ₂ -NiCr coated	5.44	8.38	310	Cr ₂ O ₃ , Fe ₂ O ₃ , Al ₂ O ₃ , SiO ₂ , NiO, and NiCr ₂ O ₄	MnO ₂	Brownish grey granular scale formed on this coated alloy is continuous and adherent, indicated very little spallation only from the edges and corners, and no internal corrosion attack observed. Coating maintained integrity with the substrate.
	NiCrBSi coated	5.54	9.36	320	Cr ₂ O ₃ , Fe ₂ O ₃ , NiO, Al ₂ O ₃ , SiO ₂ , and NiCr ₂ O ₄	MnO ₂	Greenish grey scale indicated negligible spallation. Some internal attack noted. Coating maintained good contact with the base alloy.
	Stellite-6 coated	4.87	6.33	275	Cr ₂ O ₃ , Fe ₂ O ₃ , CoCr ₂ O ₄ , and NiCr ₂ O ₄	CoO, MnO ₂ , and Al ₂ O ₃	Greenish grey scale indicated negligible spallation tendency or internal corrosion attack. Sound contact exists between the coating and substrate.
	Ni-20Cr coated	4.69	5.58	265	NiO, Fe ₂ O ₃ , Al ₂ O ₃ , Cr ₂ O ₃ , and NiCr ₂ O ₄	MnO ₂	Light greenish scale, indicated no spallation and minor internal corrosion attack, and maintained excellent contact with the base alloy.

Superni 601	Uncoated	5.97	-----	285	Cr ₂ O ₃ , Fe ₂ O ₃ , Al ₂ O ₃ , SiO ₂ , NiS, and FeS	MnO ₂	Fragile and irregular scale formed on this alloy has cracks, and indicated significant spallation and internal corrosion attack.
	Cr ₃ C ₂ - NiCr coated	6.72	13.19	410	Cr ₂ O ₃ , Fe ₂ O ₃ , Al ₂ O ₃ , MnO ₂ , and NiCr ₂ O ₄	--	Yellowish brown scale formed on this coated superalloy is uniform, continuous and adherent; some spallation occurred from the edges and corners; integrity between the coating and base alloy is preserved after corrosion runs.
	NiCrBSi coated	6.50	11.77	390	NiO, Fe ₂ O ₃ , SiO ₂ , and Al ₂ O ₃	Cr ₂ O ₃ , and NiCr ₂ O ₄	Reddish brown colour dense, homogeneous and continuous scale is formed. Scale maintained excellent integrity with the base alloy without indicating any internal corrosion attack, and showed very little spalling from edges.
	Stellite-6 coated	4.35	4.69	335	Cr ₂ O ₃ , Fe ₂ O ₃ , Al ₂ O ₃ , CoCr ₂ O ₄ , and NiCr ₂ O ₄	SiO ₂	Brownish grey scale showed negligible spallation. No adherence loss is observed at the coating-substrate interface. Minor internal attack noted.
	Ni-20Cr coated	3.88	4.13	270	NiO, Cr ₂ O ₃ , and Al ₂ O ₃	Fe ₂ O ₃ , MnO ₂ , and NiCr ₂ O ₄	Brownish grey granular scale is formed, showed negligible spallation and little internal corrosion attack. Contact between the coating and base alloy is found to be excellent during and after the cyclic exposures.
Superni 718	Uncoated	3.72	-----	255	Cr ₂ O ₃ , Fe ₂ O ₃ , Al ₂ O ₃ , SiO ₂ , and FeS	MnO ₂	Uneven scale is formed with a tendency for spalling. Cracks in the scale and internal corrosion attack are noted during experimentations.

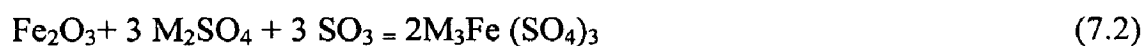
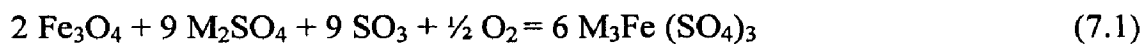
	Cr ₃ C ₂ - NiCr coated	3.40	2.77	270	Cr ₂ O ₃ , Fe ₂ O ₃ , NiO, Al ₂ O ₃ , SiO ₂ , and NiCr ₂ O ₄	-	Homogeneous and regular brownish grey granular scale is formed with little spalling from the edges and corners. Coating found to be adherent with the substrate without indicating any internal corrosion attack.
	NiCrBSi coated	7.54	16.13	462	Cr ₂ O ₃ , Fe ₂ O ₃ , NiO, Al ₂ O ₃ , SiO ₂ , and NiCr ₂ O ₄	MnO ₂	A continuous, dense and adherent scale formed on this coated superalloy indicated no internal corrosion attack. The coating maintained good contact with the base alloy during cyclic exposures.
	Stellite-6 coated	6.93	13.80	340	Cr ₂ O ₃ , Fe ₂ O ₃ , NiO, Al ₂ O ₃ , CoCr ₂ O ₄ , and NiCr ₂ O ₄	CoO and SiO ₂	Sound contact between the coating and the base alloy is maintained and no internal corrosion attack observed. Scale is adherent and free from cracks.
	Ni-20Cr coated	4.03	4.44	230	Cr ₂ O ₃ , NiO, Fe ₂ O ₃ , Al ₂ O ₃ , and NiCr ₂ O ₄	MnO ₂ , TiO ₂ , and SiO ₂	A brownish scale formed during cyclic exposures is found to be adherent, continuous and intact. Coating maintained excellent contact with the base superalloy without indicating any internal corrosion attack.
Superfer 800H	Uncoated	6.87	-----	343	Cr ₂ O ₃ , NiO, Fe ₂ O ₃ , SiO ₂ , FeS, and NiFe ₂ O ₄	Al ₂ O ₃ , NiS, and MnO ₂	Light grey colour fragile and irregular scale formed on this superalloy indicated heavy spallation and considerable internal corrosion attack.
	Cr ₃ C ₂ - NiCr coated	4.05* *up to 700 hours only	6.22* *up to 700 hours only	369	Cr ₂ O ₃ , Fe ₂ O ₃ , Al ₂ O ₃ , and NiCr ₂ O ₄	MnO ₂	The scale, having greenish appearance, indicated significant spallation. The coating maintained sound contact with the substrate after cyclic exposures.

NiCrBSi coated	6.39	11.61	380	Cr ₂ O ₃ , Fe ₂ O ₃ , Al ₂ O ₃ , SiO ₂ , and NiCr ₂ O ₄	NiO, and MnO	Yellowish scale with green tinges formed on this coated superalloy maintained good contact with the substrate and is free from cracks.
Stellite-6 coated	5.93	9.88	302	Cr ₂ O ₃ , Fe ₂ O ₃ , Al ₂ O ₃ , SiO ₂ , CoCr ₂ O ₄ , and NiCr ₂ O ₄	CoO	A regular and adherent scale with greenish appearance is formed without indicating any internal corrosion attack. The coating found to be integral with the base alloy during and after the hot corrosion exposures.
Ni-20Cr coated	4.48	5.25	275	Cr ₂ O ₃ , NiO, Fe ₂ O ₃ , Al ₂ O ₃ , SiO ₂ , and NiCr ₂ O ₄	MnO ₂	The scale is continuous, homogenous, dense and adherent and indicated no internal corrosion attack. The coating maintained excellent contact with the substrate during and after cyclic exposures.

7.3 COMPREHENSIVE DISCUSSION

7.3.1 Uncoated Superalloys

The XRD (Figs. 7.10, 7.22, 7.34, 7.46 and 7.57) and EDAX analysis (Figs. 7.11a, 7.23a, 7.35a and 7.58a) show the presence of ash deposition on the surface of the specimens. The interaction of ash with the oxide scales is further supported by EPMA analysis (Figs. 7.13, 7.25, 7.37, 7.49 and 7.60). The interaction of ash (Na₂O, K₂O etc.) with the boiler gas (SO₂, SO₃, O₂ etc.) results in the formation of alkali sulphates (K₂SO₄, Na₂SO₄). These alkali sulphates react with iron oxides (present in the scale or in the ash itself), in presence of SO₃ in the gas, to form alkali-iron trisulphates (Na,K)₃Fe(SO₄)₃ according to the following reactions.



Where M = Na or K

These alkali-iron trisulphates are molten at the operating temperature of the boiler due to their low melting temperatures: 624 °C for Na₃Fe(SO₄)₃, 618 °C for K₃Fe(SO₄)₃

and 552 °C for the mixed compound $(\text{Na,K})_3\text{Fe}(\text{SO}_4)_3$ (Srivastava et al., 1997; Weulersse-Mouturat et al., 2004). These molten compounds can flux the scale or react with the metal to form internal sulphides as per reaction given below:



Therefore, these alkali-iron trisulphates are responsible for the degradation of superheater in the coal-fired plants.

The XRD analysis shows the presence of sulfides in the surface scale. The BSE images of the bare alloys (Figs. 7.8a, 7.32a, 7.44a, and 7.55a) indicate the fluxing action of the molten salt and spallation tendency of the scale. The oxides scales formed on the surface of bare superalloys are irregular, fragile and non-adherent due to the reprecipitation by fluxing action (Figs. 7.23a, 7.35a, 7.47a and 7.58a). The oxide scales are less protective as internal corrosion attack to a depth of 55-75 μm has been observed (Figs. 7.20a and 7.55a). The $(\text{weight change/area})^2$ versus time plots also show significant deviations from the parabolic rate law (Fig. 7.64b) indicating spallation occurred from the surface of the bare specimens during experimentations. Such alkali-iron trisulphates were not identified in the scale, which may be due to their low content (Weulersse-Mouturat et al., 2004).

On the basis of thermogravimetric data shown in Fig 7.64a and material depth affected by the corrosion (Fig. 7.65), it can be inferred that the Ni-based Superni 75 provides maximum resistance and Fe-base Superfer 800H provides least resistance to hot corrosion amongst the given superalloys. On the basis of this data, the hot corrosion resistance of the superalloys under study can be arranged in the following order:

Superni 75 > Superni 600 > Superni 718 > Superni 601 > Superfer 800H

Comparatively higher hot corrosion resistance of Superni 75 and Superni 600 can be attributed to the formation of thick band of chromium as revealed by X-ray mappings (Figs. 7.13 and 7.25), whereas the presence of relatively discontinuous chromium layer for the Superni 601 and Superni 718 is responsible for their lesser hot corrosion resistance (Figs. 7.37 and 7.49). The lowest hot corrosion resistance of iron based superalloy Superfer 800H as compared to nickel base superalloys is due to the formation of thin irregular layer of chromium oxide (Fig. 7.60).

The presence of manganese leads to the formation of porous layer of chromium on Superni 601, Superni 718 and Superfer 800H superalloys. EPMA analysis shows that the concentration of Mn in the scale is much higher than in the alloy, indicating selective oxidation of Mn (Fig. 7.37). The selective oxidation of Mn produces voids in the alloy substrate due to the outward diffusion of manganese (Duh and Wang, 1990). Stott et al.

(1989A) and Marasco et al. (1991) reported that the diffusion of Mn across the chromium oxide scale causes detrimental effect on the oxidation resistance of the alloy. The relatively lesser resistance of Superni 601, Superni 718 and Superfer 800H alloys is in consistent with the reports of Stott et al. (1989A) and Marasco et al. (1991).

Overall analysis of the substrate specimens indicates that accelerated corrosion by alkali salt deposit (hot corrosion) is the main degradation mode of boiler tubes in the platen superheater zone of the coal fired boiler selected for the present study. The presence of ash deposits on the surface of almost all specimens is an indication of negligible erosion mode of degradation in this particular zone of the boiler.

Based on the results of EPMA, XRD, Surface and X-section EDAX analyses, the schematic diagram showing the probable hot corrosion mechanism for the uncoated superalloy exposed to 1000 hours in the actual environment of the coal fired boiler at 900 °C is shown in Fig. 7.66.

7.3.2 HVOF Coated Superalloys

In general, the coated specimens have shown better hot corrosion resistance than the bare substrate in the actual industrial environment of the coal fired boiler. The experiment results indicate that in addition to surface oxides, the splat boundaries of the coatings are also very active in developing hot corrosion resistance in comparison with the rest of the regions. Oxygen diffuses along the splat boundaries of the HVOF coatings and gets consumed due to oxidation of the coating elements present at the splat boundaries.

7.3.2.1 Cr_3C_2 -NiCr Coating

This coating proved to be effective in imparting the necessary protection to all the Ni-based superalloys and has shown little or marginal spallation during the cyclic study. The BSE images of the coated Superni 75, Superni 600 and Superni 718 show no indications of any internal corrosion attack (Figs. 7.8b, 7.20b and 7.44b). Oxygen elemental maps for these coated superalloys confirm that the permeation of oxygen is restricted to scale-substrate interface and substrate superalloys indicate no sign of oxidation (Figs. 7.14, 7.26 and 7.50). The partially oxidised coating is in intimate contact with the substrate for all the cases as is evident from the respective BSEI micrographs shown in Figures 7.8b, 7.20b, and 7.44b. Only in case of coated Superni 601 specimen, some internal corrosion attack has been observed due to penetration of the oxygen during initial hours of the exposure. Therefore, it is concluded that the Cr_3C_2 -NiCr coating has provided necessary protection to all the Ni-based superalloys in the coal fired boiler environment. The iron-based superalloy Superfer 800H suffered sever corrosion attack.

The spallation from the surface of the specimen as well as presence of cracks in the surface scale can be seen in Fig. 7.2e.

The partial oxidation of the coating at the splat boundaries has been noted in all cases. Penetration of the scale into the substrates, in case of coated Superni 601, has also been observed (Fig. 7.68). It is due to the formation of discontinuous scale and porosity in the coating. Identical findings have been reported by Belzunce et al. (2001) where they observed internal oxidation during the earlier stages of the study and suggested the penetration of oxidising species into the coatings through the open pores until all the accessible internal surfaces got oxidised. Niranatlumpong et al. (2000) also opined that internal oxidation takes place due to porosity in the thermal spray coatings.

The weight gain curves for $\text{Cr}_3\text{C}_2\text{-NiCr}$ coated alloys followed nearly parabolic behaviour. Little deviation from the parabolic rate law is due to some minor spallation of the oxide scale. The weight gain of the coated specimens is relatively high during the first few cycles of hot corrosion, but subsequently increase in weight is gradual (Fig 7.67). The initial high weight gain of the coated specimens has been attributed to the rapid formation of oxides at the surface and splat boundaries, and within open pores due to the penetration of the oxygen (Figs. 7.14, 7.26, 7.36a and 7.50),

The relative hot corrosion resistance of this coating for various substrate alloys based on the combined effects of average scale thickness, scale thickness loss and internal corrosion attack (Fig. 7.68), can be arranged in the following sequence:

Superni 718 > Superni 600 \approx Superni 75 > Superni 601

The corrosion resistance for the $\text{Cr}_3\text{C}_2\text{-NiCr}$ coated Superfer 800H can not be compared with others as it was most severely attacked by the hot corrosion in the given environment and most of the coating got spalled or detached from the surface of the specimen during the course of study (Fig. 7.2e).

The maximum corrosion resistance of $\text{Cr}_3\text{C}_2\text{-NiCr}$ coated Superni 718 has been attributed to the formation of chromium oxide rich scale. Due to the formation of dense oxide of chromium around the Ni-rich splats, the diffusion of Mo, Ti and Fe substrate elements in this coating-substrate system is found to be negligible (Fig. 7.50). Hence the coating proved to be effective in providing the highest corrosion resistance to Superni 718. Relatively lower resistance of the coated Superni 601 amongst the coated Ni-based superalloys may be attributed to the absence of chromium rich band in the top scale. The diffusion of manganese, aluminium and iron from the substrate to the coating is visible in this coating-substrate system (Fig. 7.38).

Spallation of the oxide scale and detachment of the coatings on Superfer 800H during experimentation might be attributed to the development of thermal shocks due to differences in the thermal expansion coefficients of the coatings, substrate and oxide scale (Table A.2) as reported by Rapp et al. (1981B) and Liu et al.(2001). Moreover, there may be some stresses generated in the scale due to differences in specific volume of the oxides and the coating. Stresses can also develop with time as a result of mechanical/physical properties changes in the coating due to reaction with the corrosive environment as has been suggested by Heath et al. (1997). They further opined that due to stresses, cracks are formed in the scale and through these cracks the corrosive species reach the base metal quickly and cut its way under the coating to result in adhesion loss.

The main phases identified with XRD and EDAX analyses in the surface scale of all the Cr₃C₂-NiCr coated alloys are SiO₂, Al₂O₃, Fe₂O₃, Cr₂O₃, NiO and NiCr₂O₄ after 1000 hours exposure to the coal fired boiler environment. The cross-section EDAX analysis shows that the oxides of mainly chromium and nickel, and their spinels have been responsible for blocking the transport of degrading species through the Cr₃C₂-NiCr coatings. The EPMA analysis further supported the results of XRD and EDAX analysis.

The probable mode of corrosion phenomena for this coating in the given boiler environment is shown in Fig. 7.69.

7.3.2.2 NiCrBSi Coating

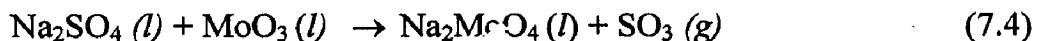
Although the weight change data as well as corrosion rate data show that NiCrBSi coating provides relatively less protection to the base alloys in the given boiler environment as compared to other coatings under study (Figs. 7.18, 7.21, 7.42, 7.45, 7.53 and 7.56), the coating has shown a tendency to act as a barrier to the inward diffusion of the corroding species as the parabolic rate law has been followed in all the cases. The BSE images show that the partially oxidised coating is in good contact and adherent to the substrates (Figs. 7.8c, 7.20c, 7.32c, 7.44c and 7.55c) and free from cracks.

The cross-sectional EDAX analysis of corroded NiCrBSi coated superalloys shows the absence of oxygen and other corrosive species in the substrate near the coating-substrate interface (Fig. 7.12b). The results of cross-sectional EDAX are further supported by EPMA analysis (Fig. 7.39). The internal corrosion attack in some NiCrBSi coated superalloys is due the penetration of little amount of oxygen through the coating to the substrate during initial period of exposure. However, with further exposure the oxidation of chromium along the splat boundaries and formation of oxide layer at the surface have blocked the penetration of oxygen (Fig. 7.36b). Therefore, it is concluded that the NiCrBSi coating has provided necessary protection to all the base alloys in the coal fired boiler environment.

The corrosion rate of the coated alloys based on the combined effects of average scale thickness, scale thickness loss and depth of internal corrosion attack is shown in Fig. 7.70. The degradation behaviour of all the coated alloys based on the corrosion rate can be arranged in the following sequence:

Superni 718 > Superni 601 > Superfer 800H > Superni 600 ≈ Superni 75

The superior corrosion resistance of NiCrBSi coated Superni 75 is due to the formation of a thin layer of chromium and silicon in topmost part of the scale as revealed by X-sectional EDAX (Fig. 7.12b) and confirmed by EPMA (Fig. 7.15). The absence of this layer in coated Superni 718 is the reason for its poor corrosion resistance amongst all the coated superalloys (Fig. 7.51). Elemental map for molybdenum shows its diffusion from the substrate to the coating surface (Fig. 7.51). EDAX analysis also shows the presence of molybdenum (2 wt%) in the surface scale of NiCrBSi coated Superni 718 (Fig. 7.47c). On oxidation, molybdenum forms MoO₃ which is liquid at 900 °C (M.P. 795°C). As already discussed in chapter 6, Section 6.3.1., the MoO₃, being an acidic oxide, further reacts with Na₂SO₄ to form a low melting point phase Na₂MoO₄ as per the following reaction:



This led to fluxing of the protective oxide scale. Identical findings have also been reported by Pettit and Meier (1985), Misra (1986), and Shih et al. (1989). Further, relatively better corrosion resistance of coated Superni 601 than coated Superni 718 is due to the presence of thin layer of silicon oxide along with streaks of chromium oxide at the topmost scale of coated Superni 601 (Fig. 7.39). The corrosion rate of the NiCrBSi coatings on different coating-substrate systems is further confirmed by the weight gain after 1000 hours of exposure in the given environment (Fig. 7.71).

The green colour patches observed on the surface of the exposed specimens (Fig. 7.3) is an indication for the formation of NiO, as reported by Bornstein et al. (1975). The XRD analysis reveals the presence of SiO₂, Al₂O₃, Fe₂O₃, Cr₂O₃, NiO and NiCr₂O₄ as main phases invariably formed on the surface scale of all the NiCrBSi coated specimens. The EDAX and EPMA analysis further support the formation of these phases. The detection of oxide phases of iron, aluminium and silicon in the surface scale of the exposed coating by XRD analysis is an indication of the presence of some ash deposits also. The EDAX and EPMA analysis further confirms the presence of ash deposits.

On the basis of the results of SEM, XRD, EDAX (surface/cross-section) and EPMA analyses, schematic representation of the possible hot corrosion mechanism for the NiCrBSi coated Superni 601 exposed to the coal fired boiler environment for 1000 hours at 900 °C is shown in Fig. 7.72.

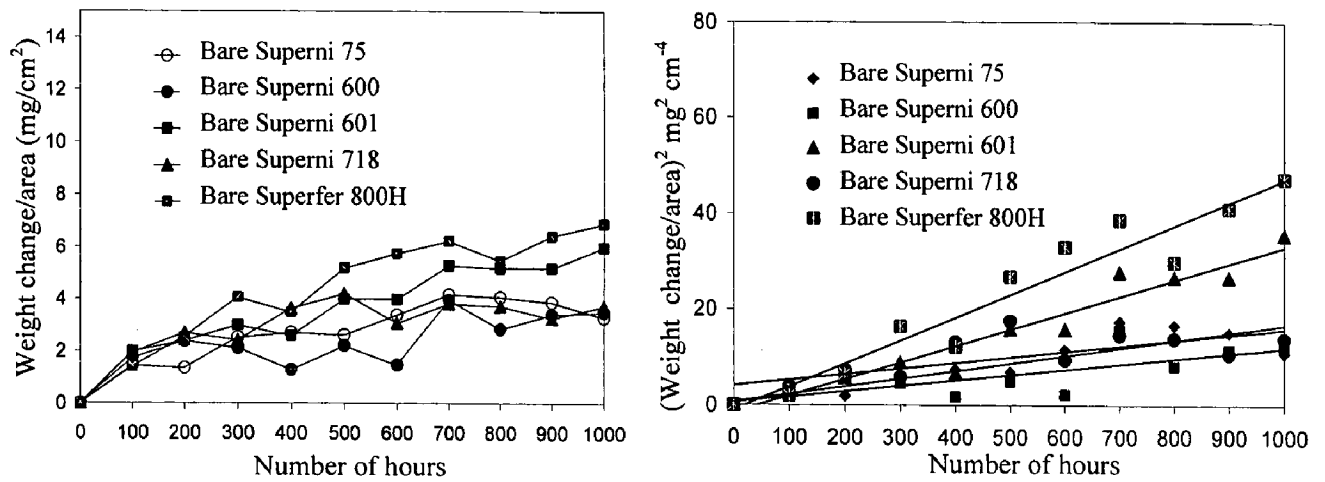


Fig. 7.64 (a) Weight change vs. time plots, and (b) $(\text{Weight change/area})^2$ vs. time plots, for the uncoated superalloys subjected to 1000 hrs cyclic exposure to platen superheater zone of the coal fired boiler at 900 °C.

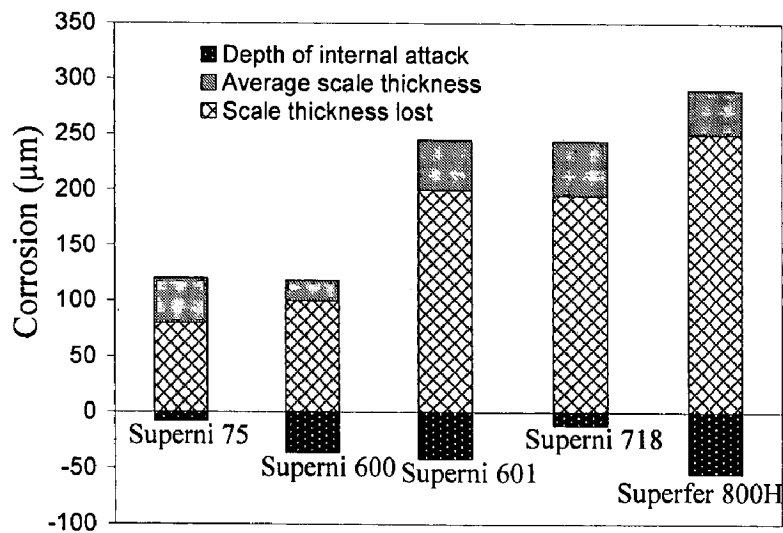


Fig. 7.65 Bar charts indicating the extent of corrosion for the bare superalloys after 1000 hrs exposure to the coal fired boiler at 900 °C.

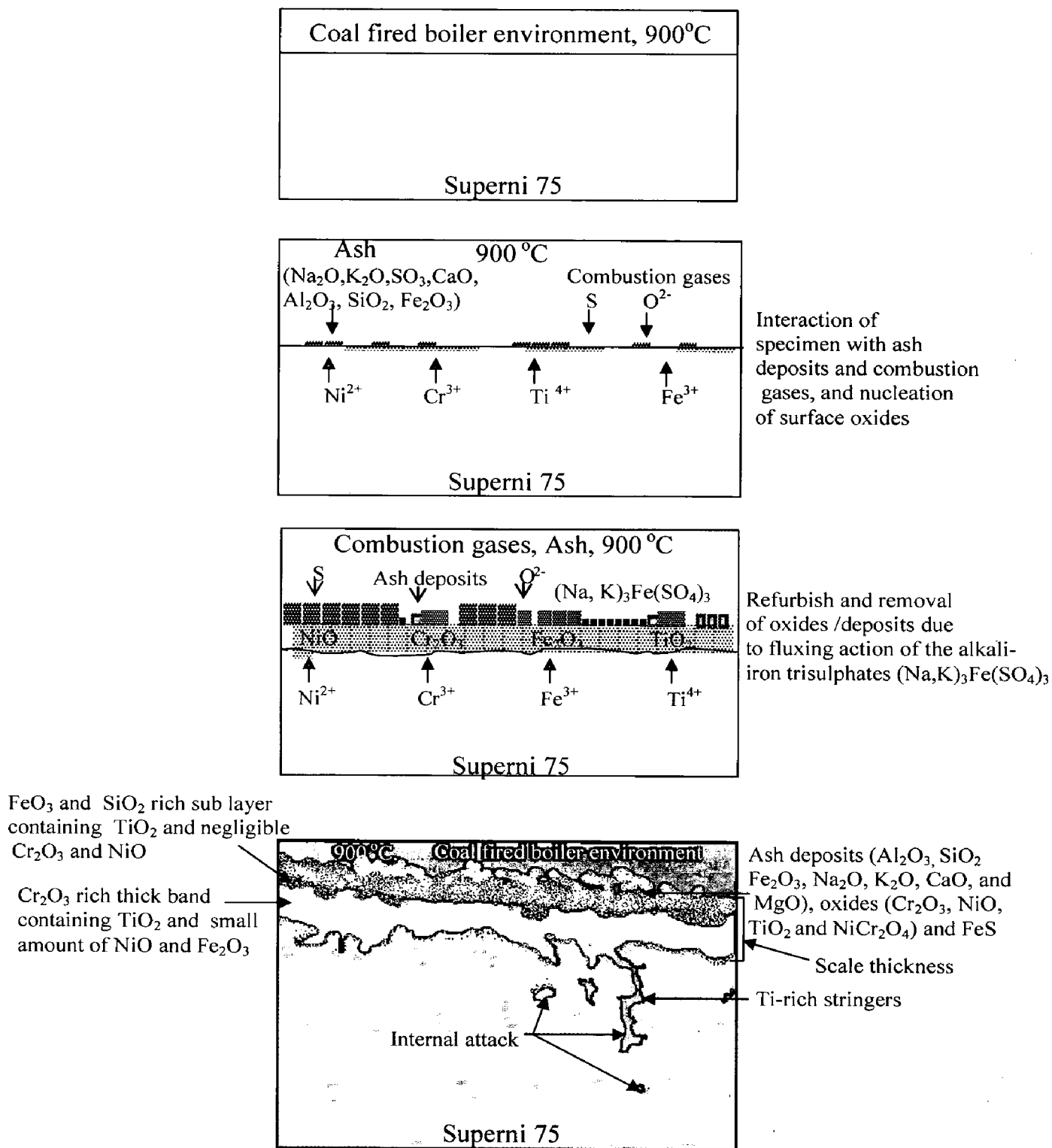


Fig. 7.66 Schematic diagram showing probable hot corrosion mechanism for the uncoated superalloy exposed to 1000 hours in the actual environment of the coal fired boiler at 900 °C.

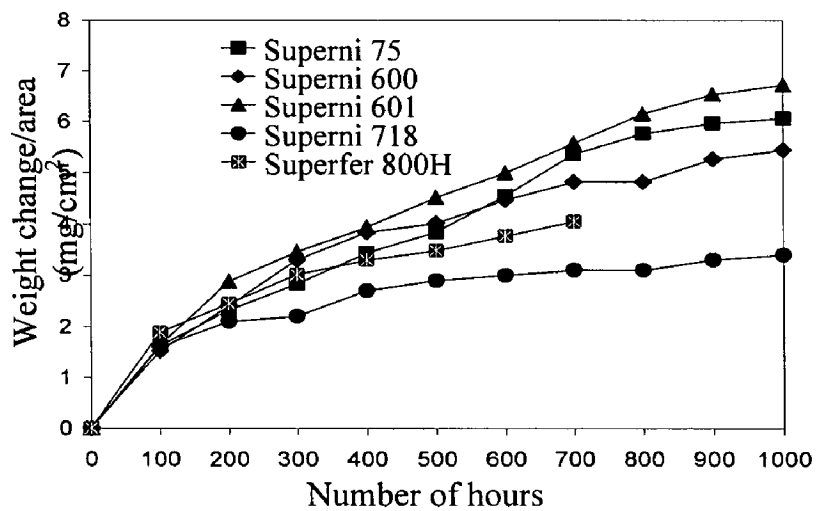


Fig. 7.67 Weight change vs. time plots for the $\text{Cr}_3\text{C}_2\text{-NiCr}$ coated superalloys subjected to 1000 hrs cyclic exposure to platen superheater zone of the coal fired boiler at 900 °C.

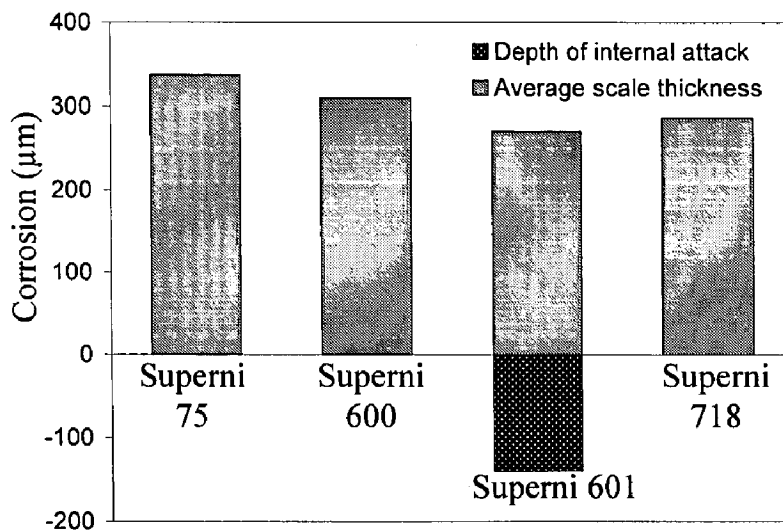


Fig. 7.68 Bar charts indicating the extent of corrosion for the $\text{Cr}_3\text{C}_2\text{-NiCr}$ coated superalloys after 1000 hrs exposure to the coal fired boiler at 900 °C.

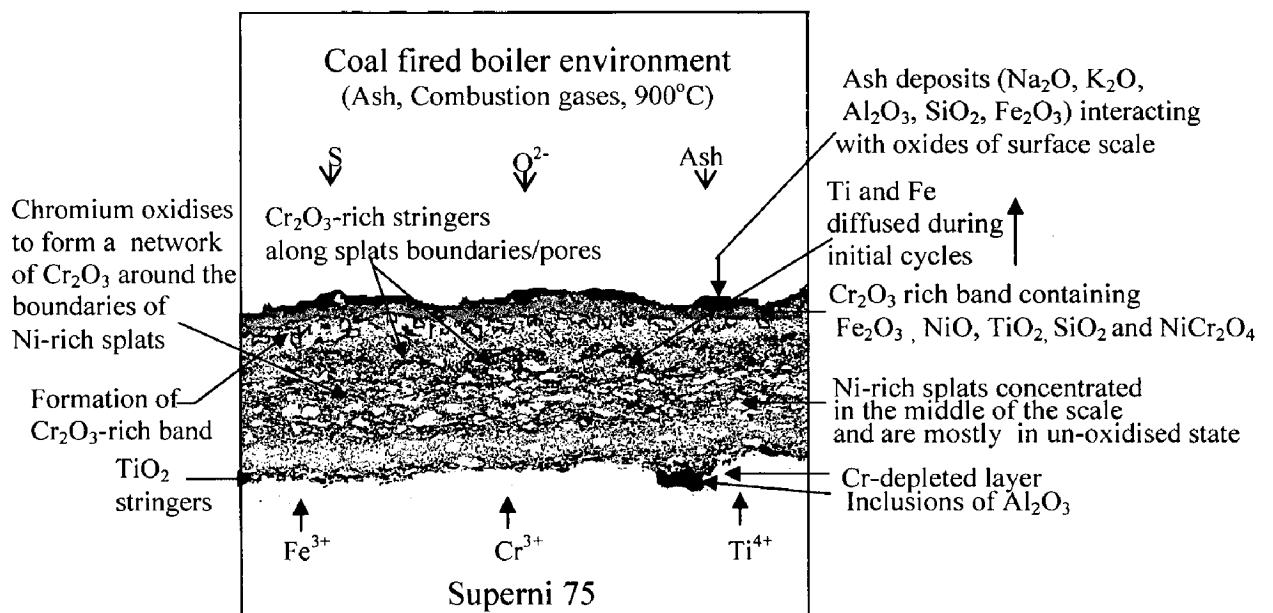


Fig. 7.69 Schematic diagram showing probable hot corrosion mode for the Cr₃C₂-NiCr coated superalloy exposed to 1000 hours in the actual environment of the coal fired boiler at 900 °C.

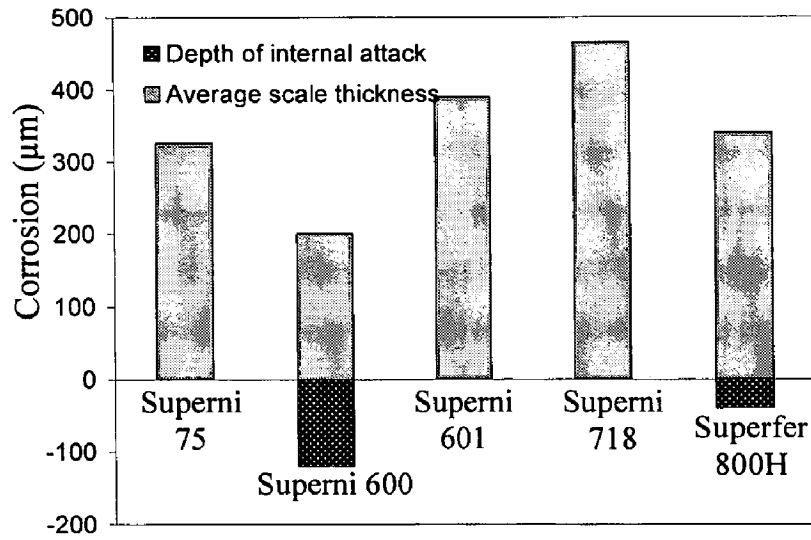


Fig. 7.70 Bar charts indicating the extent of corrosion for the NiCrBSi coated superalloys after 1000 hrs exposure to the coal fired boiler at 900 °C.

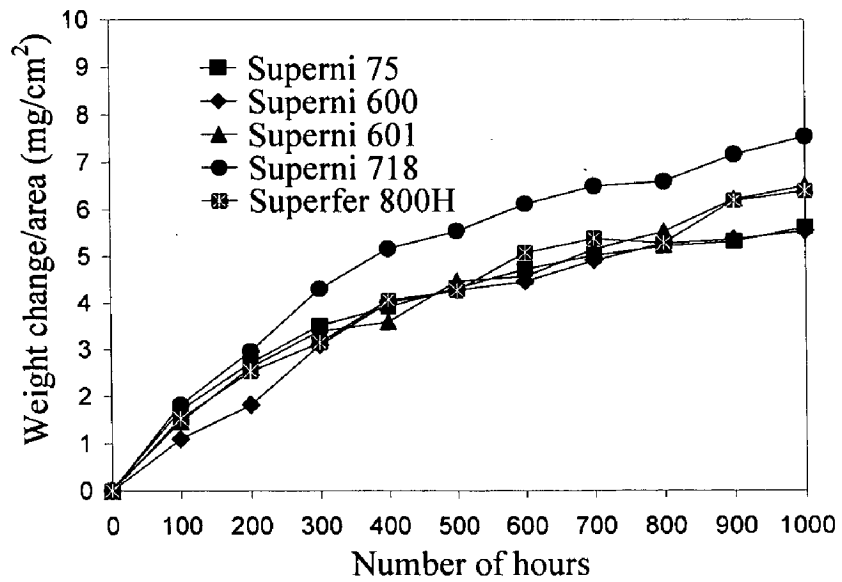


Fig. 7.71 Weight change vs. time plots for NiCrBSi coated superalloys subjected to 1000 hrs cyclic exposure to platen superheater zone of the coal fired boiler at 900 °C.

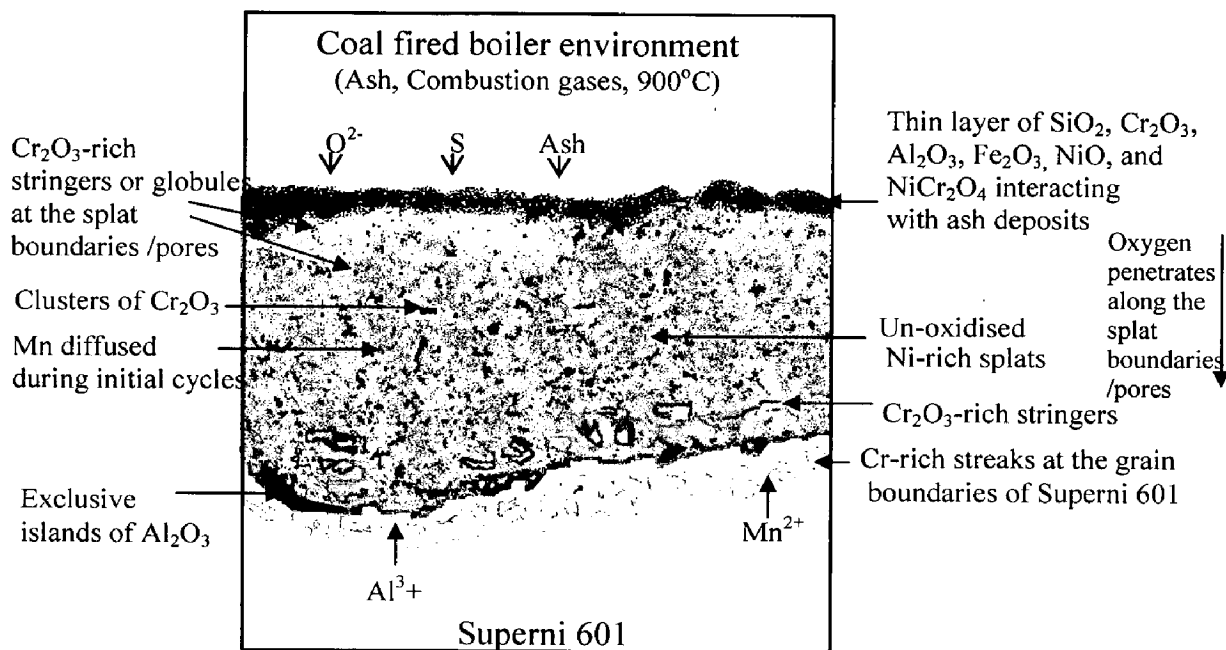


Fig. 7.72 Schematic diagram showing probable hot corrosion mode for the NiCrBSi coated superalloy exposed to 1000 hours in the actual environment of the coal fired boiler at 900 °C.

7.3.2.3 *Stellite-6 Coating*

This coating is found to be very effective in providing the necessary protection to both the Ni- and Fe-based superalloys in the actual working environment of the coal fired boiler. The coating remained intact without any indication of spalling during the course of 1000 hours cyclic exposure. The SEM micrographs show the formation of continuous, compact and adherent surface scale along with the presence of embedded ash particles (Figs. 7.11d, 7.23d, 7.35d, 7.47d and 7.58d). No crack or void is visible on the surface oxide scale. The cross-sectional BSE images also show that the partially oxidised coating has maintained good contact with the substrates in all the Stellite-6 coating-substrate systems without indication of any adherence loss (Figs. 7.20d, 7.44d, and 7.55d). The scale has retained lamellar structure of the as-sprayed coatings and there is no indication of any crack across the cross-section of the scale. The penetration of oxygen is mainly restricted to the scale-substrate interface as indicated by cross-sectional EDAX (Figs. 7.24a and 7.59b) and confirmed by EPMA analysis (Figs. 7.28 and 7.62). The better performance of the Stellite-6 coating found in the present investigation is in good agreement with the results of superior corrosion resistance of Stellite-6B alloy in mixed gas atmosphere reported by Natesan (1980) and plasma sprayed Stellite-6 coating in the coal fired boiler environment reported by Sidhu and Prakash (2006J).

In general, all the Stellite-6 coated superalloys show conformance to parabolic rate law of oxidation during cyclic exposure to boiler environment. The minor deviations from the parabolic rate law is attributed to the formation and rapid growth of inhomogeneous oxides, and their dissolution due to the fluxing action of the molten salt as suggested by Choi et al. (2002). Hence, it can be inferred that the coating shows a tendency to act like a diffusion barrier to the corroding species in the environment of the coal fired boiler. The comparative corrosion rate for the different Stellite-6 coating-substrate systems under study in the given environment can be arranged in the following sequence (Fig. 7.73):

Superni 718 > Superni 601 > Superfer 800H > Superni 75 > Superni 600

The Stellite-6 coated Superni 600 imparted maximum resistance to the degrading species, which is attributed to the formation of dense oxides of chromium and silicon at the boundaries of unoxidised Co-rich splats. The chromium rich thin layer present just above the scale-substrate interface also contributes to its better corrosion resistance (Fig. 7.28). The relatively lower corrosion resistance of the Stellite-6 coated Superni 75 is due

to the outward diffusion of titanium from the substrate forming a continuous thick layer at the topmost part of the scale (Fig. 7.16). It is important to mention here that, as titanium has the highest affinity towards oxygen, it diffuses out very fast through the coating to form less protective oxide of titanium. The diffusion of titanium is considered unfavourable to the corrosion resistance (Li and Gleeson, 2004). The coated Superni 718 and Superni 601 showed almost similar corrosion rate. The presence of discontinuous thin chromium layer at the topmost part of the scale is responsible for the relatively higher corrosion rate of the coated Superni 601 (Fig. 7.40).

The XRD analysis reveals the presence of oxides mainly of cobalt and chromium along with the spinels of cobalt-chromium and nickel-chromium. As can be seen from the EPMA micrographs of the scale (Figs. 7.28 and 7.62), Co-rich splats are surrounded with chromium and the solid-state reaction has occurred to form CoCr_2O_4 spinel. The formation of cobalt-chromium spinel (CoCr_2O_4) blocks the diffusion activities through the cobalt oxide (CoO) by suppressing the further formation of CoO as reported by Luthra (1985). In some cases XRD analysis detected Al_2O_3 , SiO_2 and Fe_2O_3 phases also. The presence of these phases is mostly attributed to the ash deposits. In some cases these elements also have diffused from the substrate (Figs. 7.34, 7.46 and 7.57). Formation of these phases has been supported by the EDAX analysis and also confirmed by EPMA.

The cross-sectional EDAX (Figs. 7.24a and 7.59b) and EPMA (Figs. 7.28 and 7.62) results show that the substrates are safe from the attack of corroding species. The presence of very little amount of oxygen near the scale-substrate interface might be due to penetration of oxygen along the splat boundaries during initial period of the study. These results further reveal that the presence of oxides mainly of chromium and silicon along the boundaries of Co-rich splats has blocked further penetration of oxygen. The probable mode of hot corrosion for Stellite-6 coated superalloy exposed to the coal fired boiler environments at 900 °C for 1000 hours is proposed as shown in Fig. 7.74.

7.3.2.4 Ni-20Cr Coating

The Ni-20Cr coating using wire as a feedstock alloy has provided excellent resistance to corrosion both in the laboratory test as well as in the actual working environment of the coal fired boiler. The weight change and corrosion rate data on different Ni-20Cr coating-substrates systems (Figs. 7.6, 7.18, 7.30, 7.42 and 7.53, and 7.75 respectively), and nearly parabolic behaviour of the weight gain plots indicate the

protective behaviour of this coating. The BSE images of coated alloy obtained after 1000 hours of exposure (Figs. 7.8e, 7.20e, 7.32e, 7.44e and 7.55e) show the formation of uniform and continuous oxide scales without indications of any adherence loss between the partially oxidised coating and the substrates. The surface morphologies also show the formation of compact and protective oxide scale without any indication of spallation tendency or cracks (Figs. 7.11, 7.23, 7.35, 7.47 and 7.58).

The XRD analysis shows the presence of NiO, Cr₂O₃, Al₂O₃, Fe₂O₃, SiO₂ and NiCr₂O₄ as the main phases invariably formed in the surface scale of all the Ni-20Cr coated specimens. The presence of Fe₂O₃, Al₂O₃ and SiO₂ phases are due to mainly ash deposition and partly due to minor diffusion of these elements from the substrates and their subsequent oxidation. The EDAX and EPMA analysis confirm the formation of these phases. The author has reported the presence of these phases in his earlier publication (Sidhu et al., 2006H and 2006L).

The formation of oxides of chromium and nickel, and their spinel upon exposure to the coal-fired boiler environment at 900°C, as revealed by XRD analysis and confirmed by EDAX/EPMA analysis, has contributed to the excellent performance of Ni-20Cr coated superalloys. The splat boundaries of Ni-20Cr coating are found to be rich in chromium oxide due to selective oxidation of chromium as revealed by cross-section EDAX analysis (Figs. 7.24b and 7.48) and confirmed by EPMA (Figs. 7.17, 7.41, and 7.52). These oxides formed at splat boundaries have acted as barrier to the inward diffusion of corrosive species along it. Nicoll and Wahl (1983), Stroosnijder et al. (1994) and Toma et al. (1999) suggested that the Cr₂O₃ inhibits oxidation of the substrate alloys by blocking the diffusion of reacting species. Presence of the spinel NiCr₂O₄ in the surface oxide scales also helps in developing oxidation resistance as these spinel phases usually have much smaller diffusion coefficients for the cations and anions than those in their parent oxides (Chatterjee et al., 2001). The mechanism of Cr₂O₃ formation in Ni-20Cr is described as follows: though NiO and Cr₂O₃ are stable oxides at 1 atm pressure of oxygen, various factors, particularly thermodynamics and kinetics influence the overall scale development. Chromium has higher affinity for oxygen than nickel and forms more stable oxide. NiO is less stoichiometric oxide than Cr₂O₃ (Sundararajan et al., 2003A). This infers that the oxidation of Ni-Cr coating is solely based on the formation of Cr₂O₃. The threshold concentration required to form Cr₂O₃ is around 15%. In the present coating the concentration of chromium is 20%, which is not lowered by diffusion. In the earlier studies, the Ni-20Cr coating using powder as feedstock alloy

showed the high amount of Fe diffusion from the substrate to the coating and Ni from the coating to the substrate (Sundararajan et al., 2003A; Sundararajan et al., 2004A). However in the present case of Ni-20Cr coating using wire as feedstock alloy, the diffusion of Fe and Ni is found to be negligible (Figs. 7.17, 7.41, 7.52). This can be attributed to the presence of uniformly distributed flat splats and very low porosity of the coating as reported by the author (Sidhu et al., 2006G). This is the desired structure when the coatings have to perform in corrosive environment at higher temperature since corrosive species mostly propagate along the splat boundaries and through the pores and voids. Due to dense and flat splat structure of the coatings, the distance from the coating surface to coating/substrate interface along splat boundaries is very long.

The relative performance of the Ni-20Cr coated superalloys based on the combined effects of average scale thickness, scale thickness lost and depth of internal corrosion attack (Fig. 7.75), although not very significantly apart, can be arranged in the following order:

Superni75 > Superni 718 > Superni 600 > Superni 601 > Superfer 800H

The Ni-20Cr coating performed better on the nickel-based superalloys than on the iron-based superalloy. The superior hot corrosion resistance of the coated Superni 75 in the given environment is attributed to the formation of a continuous thin streak of chromium oxide in the top scale and dense network of chromium oxide just above the scale-substrate interface which might have acted as a barrier to the penetration of corrosive species (Fig. 7.17). The corrosion resistance of coated Superni 718 can be ascribed to the formation of Cr₂O₃-rich dense network around the Ni-rich splats as can be seen from Fig. 7.52. The relatively lower hot corrosion resistance of coated Superfer 800H can be attributed to the diffusion of iron, titanium and silicon from the substrate to the coating (Fig. 7.63). Based on the cross-section EDAX analysis along with the support of the results of XRD, EPMA and surface EDAX analyses, the probable mode of hot corrosion of the Ni-Cr coating exposed to the coal fired boiler environments at 900 °C for 1000 hours is proposed as shown in Fig. 7.76.

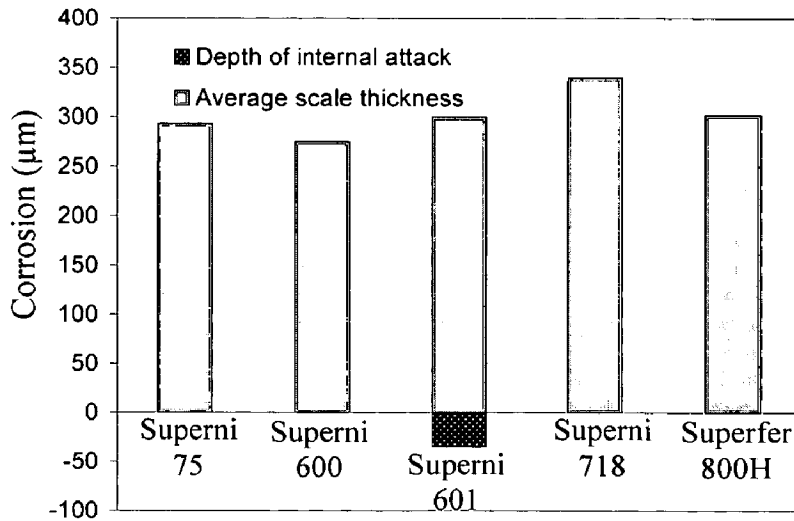


Fig. 7.73 Bar charts indicating the extent of corrosion for the Stellite-6 coated superalloys after 1000 hrs exposure to the coal fired boiler at 900 °C.

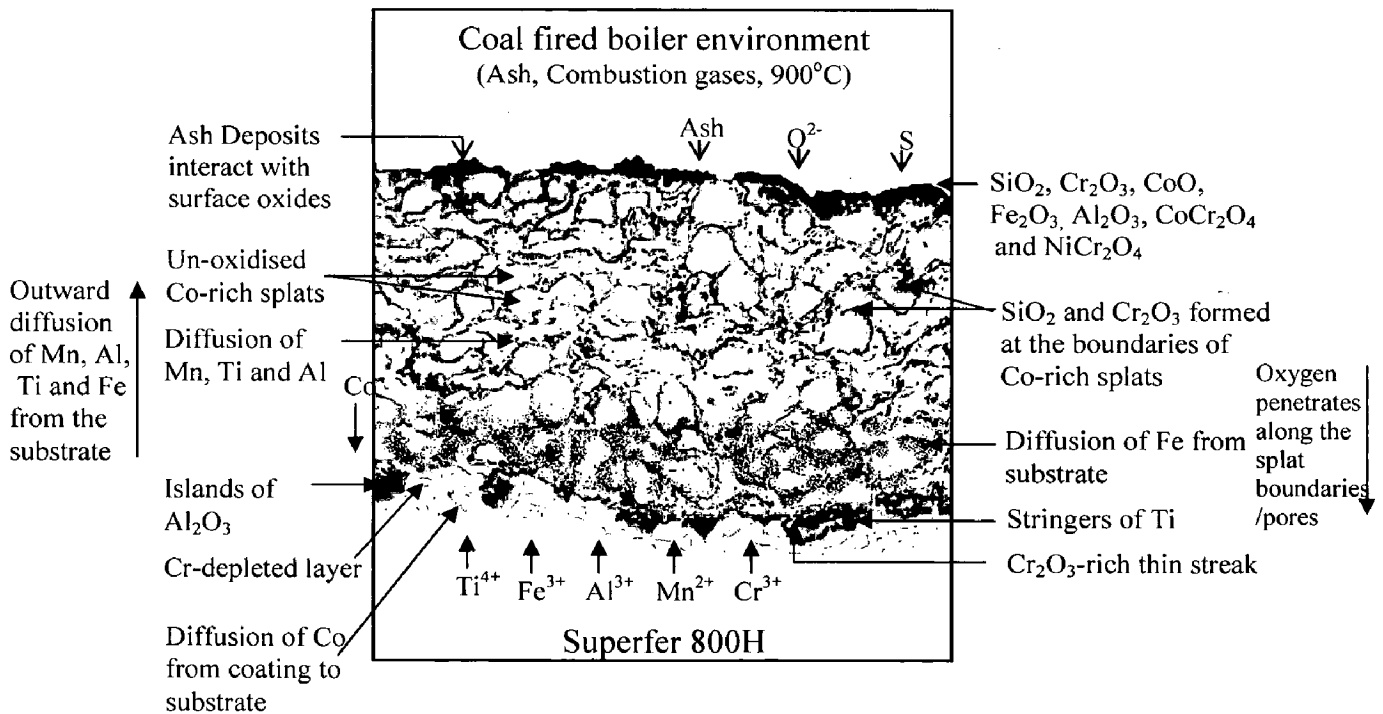


Fig. 7.74 Schematic diagram showing probable hot corrosion mode for the Stellite-6 coated superalloy exposed to 1000 hours in the actual environment of the coal fired boiler at 900 °C.

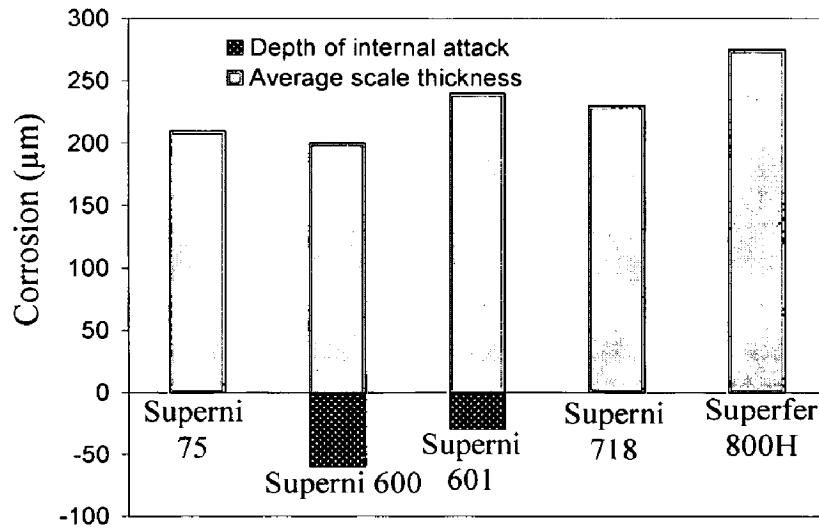


Fig. 7.75 Bar charts indicating the extent of corrosion for the Ni-20Cr coated superalloys after 1000 hrs exposure to the coal fired boiler at 900 °C.

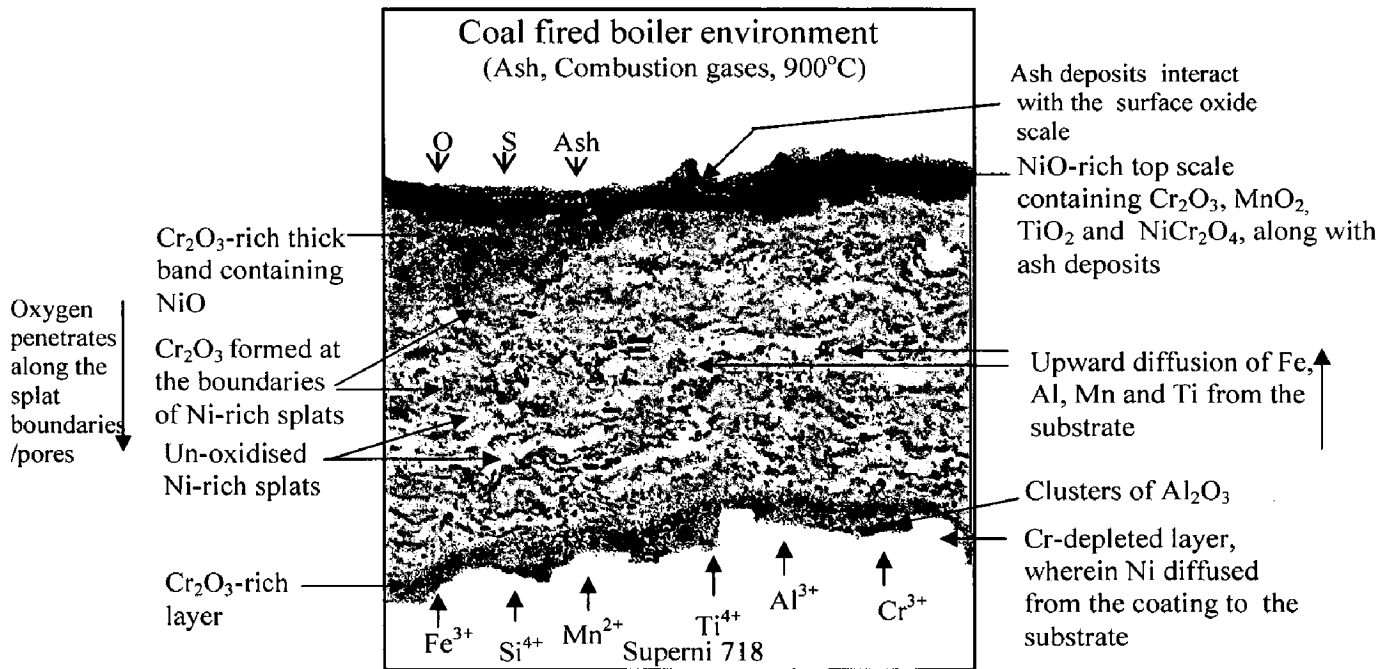


Fig. 7.76 Schematic diagram showing probable hot corrosion mode for the Ni-20Cr coated superalloy exposed to 1000 hours in the actual environment of the coal fired boiler at 900 °C.

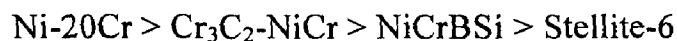
COMPARATIVE DISCUSSION

This chapter describes the comparative performance of the uncoated and HVOF coated superalloys in both the molten salt (Na_2SO_4 -60% V_2O_5) environment as well as in the actual working environment of the coal fired boiler at 900 °C under cyclic conditions.

8.1 MOLTEN SALT ENVIRONMENT

The overall weight gain by the uncoated and coated superalloys, after 50 cycles in the molten salt environment, is presented in Fig. 8.1. It is evident from the bar charts that the coatings, used in the present investigation, have successfully reduced the overall weight gain in all the cases. The EPMA elemental maps obtained after total 50 cycles of exposure to the molten salt environment indicate that all the coatings protect the base superalloys against the penetration of oxygen and other corrosive species, and the BSE images show that the partially oxidised coatings are in good contact with the substrate (Figs. 6.15b, 6.18b, 6.27, 6.29 and 6.40). On the other hand, the oxide scale formed on the bare superalloys is fragile and irregular, and penetrates deeply into the substrates, thereby reducing the thickness of sound metal. The fluxing action of the molten salt on the surface of the bare superalloys is also clearly evident (Figs. 6.22, 6.26, 6.34, 6.38, 6.46, 6.50 and 6.62). All the coatings follow the parabolic rate law of oxidation, whereas the bare alloys show significant deviation from the parabolic rate law. Therefore, it is concluded that the coated superalloys have performed better than the bare superalloys in the given molten salt environment of Na_2SO_4 -60% V_2O_5 salt mixture at 900 °C under cyclic conditions. The coatings get oxidised only at the splat boundaries which act as diffusion barriers against the penetration of corroding species.

Figure 8.1 leads to the conclusion that the Ni-20Cr coating provides the highest hot corrosion resistance, whereas the Stellite-6 coating indicates the least resistance to the molten salt environment at 900 °C. Based on the results of present study, the overall protective behaviour of the coatings deposited on all the substrate superalloys except Superni 718, can be arranged in the following sequence:



The superior performance of Ni-20Cr coatings is mainly attributed to the formation of NiO, Cr₂O₃ and NiCr₂O₄ in the surface scale, and Cr₂O₃ preferentially at the boundaries of Ni-rich splats due to selective oxidation of the chromium. During initial cycles of hot corrosion, oxygen permeates inward along the interconnected splat boundaries and pores, and causes oxidation of the active elements of the coating, mainly chromium at the splat boundaries/pores. The chromium oxide, so formed, plugs/seals the pores and splat boundaries and blocks/slows down the further penetration of oxygen, thereby making the oxidation rate to reach the steady state. In some cases, small amount of corrosive species such as sulphur is found to be present into the substrate alloys near the scale-substrate interface, which might have penetrated along the splat boundaries/pores in the earlier stage of hot corrosion (Fig. 6.42). But with the formation of oxides at the splat boundaries/pores, further penetration of corrosive species is stopped.

In terms of weight gain, the relatively lower hot corrosion resistance of the Cr₃C₂-NiCr coating as compared to the Ni-20Cr coating can be attributed to the presence of higher amounts of chromium in Cr₃C₂-NiCr coating which leads to the formation of a thick network of chromium oxide around the Ni-rich splats (Figs. 6.15b and 6.27). This dense network of chromium oxide might be responsible for spallation of the coating, in some cases, during cyclic study due to difference in the coefficient of thermal expansion of oxides, coating and substrate elements (Fig. 6.3e). However, in case of Ni-20Cr coating, the oxides of chromium are mostly formed as thin stringers or streaks at the boundaries of nickel-rich splats (Fig. 6.18). Hence the Cr₃C₂-NiCr coating shows higher weight gain than the Ni-20Cr coating. Yamamoto and Hashimoto (1995) also reported that the Ni-20Cr coatings showed good resistance to corrosion, while the Ni-50Cr coating collapsed because of a large amount of oxide scales. Recently, Sidhu et al. (2006K) also reported that HVOF Ni-20Cr coating deposited on boiler steel showed better hot corrosion resistance to the molten salt environment of Na₂SO₄-V₂O₅ salt mixture at 900 °C as compared to Cr₃C₂-NiCr coating.

Comparatively lowest corrosion resistance of the NiCrBSi coating can be ascribed, to some extent, to lower content of Cr (15%) in its basic composition. However, the better hot corrosion resistance of this coating as compared to the Stellite-6 coating might be due to the presence of silicon and boron. Wang et al. (2004) reported that the addition of Si and B in the nickel based coating can promote the selective oxidation of the protective

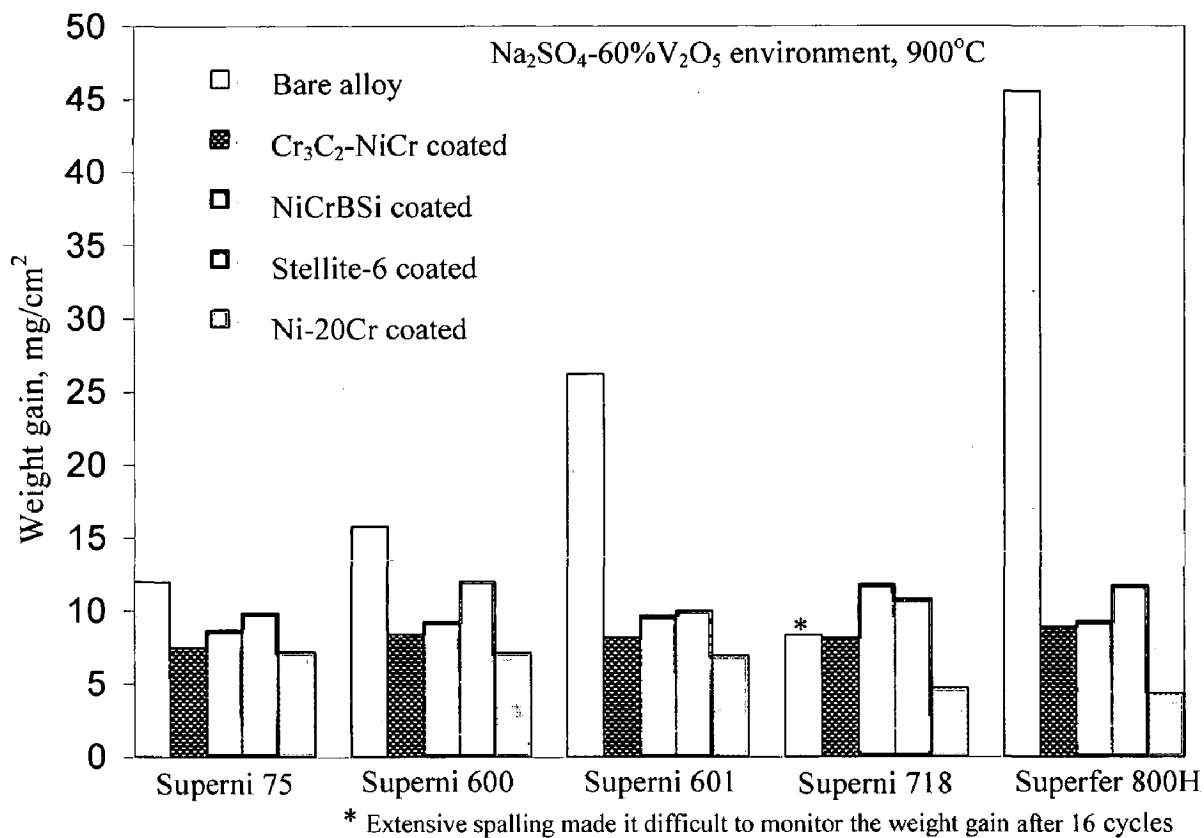


Fig. 8.1 Bar charts showing cumulative weight gain (mg/cm^2) for the coated and uncoated superalloys subjected to cyclic oxidation in $\text{Na}_2\text{SO}_4\text{-60\%V}_2\text{O}_5$ environment at 900 °C for 50 cycles.

scale-forming elements, resulting in the formation of a continuous scale in the initial corrosion stage and improve the adherence of the outer scale to the coating in the subsequent hot corrosion process. The surface scale of the NiCrBSi coated superalloys, enriched in silicon and oxygen, acts as a barrier against the migration of corrosive species inward to the substrate and cation transport outward from the substrate, and thereby reduces the corrosion rate (Fig. 6.40). The relatively least hot corrosion resistance of the Stellite-6 coating might be due to the presence of relatively more porosity and large size globule type splats as compared to other coatings. Due to large size globular splats, the distance along the splat boundaries from the surface to coating-substrate interface is less. Therefore the penetration of degrading species might be easier in Stellite-6 coating. Further the presence of Fe (2.7%) in Stellite-6 coating composition forms less protective oxides of iron. Some spallation of this coating was observed during experimentations. Singh (2005E) also observed least hot corrosion resistance of plasma sprayed Stellite-6 coating in the environment of Na_2SO_4 -60% V_2O_5 salt mixture at 900°C.

In case of Superni 718, the Stellite-6 coating has shown lower weight gain than NiCrBSi coating (Fig. 8.1). The diffusion of various elements of Superni 718 such as Mo and Ti has detrimental effects on the hot corrosion resistance of the NiCrBSi coating (Fig. 6.52). In this coating-substrate combination, the molybdenum diffuses to the surface scale and oxidises in the presence of Na_2SO_4 to form liquid Na_2MoO_4 , which has a high solubility for protective oxides resulting into fluxing of the oxide scale (Peters et al., 1976, Pettit and Meier, 1985). The titanium also diffuses considerably into the coating due to its higher affinity towards oxygen and is considered unfavourable to the corrosion resistance (Li and Gleeson, 2004).

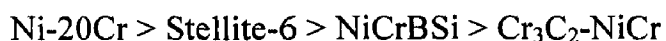
The HVOF sprayed Ni-20Cr and Stellite-6 coatings show better hot corrosion resistance as compared to Plasma sprayed Ni-20Cr and Stellite-6 coatings deposited on same superalloys under the same molten salt environment (Na_2SO_4 -60% V_2O_5) and at the same temperature (900 °C) reported by Singh (2005E). The details have already been discussed under sections 6.3.2.3 and 6.3.2.4.

8.2 INDUSTRIAL ENVIRONMENT

As observed in the molten salt environment, all the coatings, in general, have shown good hot corrosion resistance to the industrial environment consisting of actual working

condition of the coal fired boiler and all the coated superalloys performed better than the bare superalloys. The elemental maps of the coated superalloys indicate that the base alloys are safe from the oxygen and other corrosive species, and the BSE images show that the partially oxidised coatings are in good contact with the substrate (Figs. 7.14, 7.17, 7.26, 7.28, 7.39, 7.41, 7.50, 7.52 and 7.62). In some cases of coated superalloys, only some minor internal attack has been observed during the initials hours of the study (Figs. 7.55, 7.32 and 7.20). On the other hand, the $(\text{weight gain/area})^2$ plots for the bare superalloys show significant deviations from the parabolic rate law, indicating that the surface scale of the bare superalloys might have spalled during experimentations (Figs. 7.7, 7.19, 7.31, 7.43 and 7.54). The BSE images of the bare superalloys also indicate fluxing action of the molten salt and spallation tendency of the scale. Moreover, the oxides formed on the bare superalloy are porous due to reprecipitation by fluxing action (Figs. 7.8, 7.32, 7.44 and 7.55) and are less protective as momentous growth of internal corrosion attack has been seen (Figs 7.13, 7.37, 7.60). Further, the Fig. 8.2 indicates that the bare superalloys show significant thickness loss due to spallation of the scale during experimentations, whereas the coated superalloys do not show any scale thickness loss.

Based on the cumulative effects of the average scale thickness, scale thickness lost and depth of internal corrosion attack which give estimate of the material depth affected by the hot corrosion (Fig. 8.2), the hot corrosion resistance of the coatings on different substrate superalloys under study, except Superni 718, can be arranged in the following sequence:



Similar to the molten salt environment, the Ni-20Cr coating showed best hot corrosion resistance amongst all the coatings in the actual working conditions of the coal fired boiler also. As already explained, the formation of mainly chromium oxide at the boundaries of Ni-rich splats of the Ni-20Cr coating blocks the inward permeation of oxygen and other corrosive species to the substrate (Figs. 7.17, 7.41 and 7.52).

In contrast to the molten salt environment, the NiCrBSi coating has shown relatively lower hot corrosion resistance than the Stellite-6 coating in the actual working conditions of the coal fired boiler. The continuous silicon oxide layer which is formed at the topmost part of the scale of NiCrBSi coating in the molten salt ($\text{Na}_2\text{SO}_4\text{-60\%V}_2\text{O}_5$) environment

(Fig. 6.16, 6.28 and 6.40) could not form in the actual working condition of the coal fired boiler. The silicon oxide layer formed on the surface of NiCrBSi coating in the boiler environment is discontinuous and non-adherent as is evident from the elemental mappings shown in Figures 7.27, 7.39, and 7.51.

The hot corrosion resistance of the Stellite-6 coating may be ascribed to the formation of oxides of chromium and silicon at the boundaries of Co-rich splats, which block the penetration of oxygen and other corrosive species into the substrate (Figs. 7.28 and 7.62). Further the formation of cobalt-chromium spinel (CoCr_2O_4) also has a beneficial effect. Luthra (1985) has reported that CoCr_2O_4 spinel blocks the diffusion activities through the cobalt oxide (CoO) by suppressing the further formation of CoO. Natesan (1980) has also reported the superior corrosion resistance of the Stellite-6 alloy in a mixed gas environment. The high chromium content of the Cr_3C_2 -NiCr coating results in the formation of a thick network of chromium oxide (Figs. 7.14, 7.26 and 7.50) around the Ni-rich splats is considered to be responsible for the spallation and disintegration of the coating in case of (Cr_3C_2 -NiCr)-Superfer 800H combination due to difference in the coefficient of thermal expansion of the oxide scale, the coating and the substrate (Fig. 7.2e). The extent of corrosion of the different coating-substrate systems in the actual working environment of the coal fired boiler is further evaluated by comparing the weight gain after 1000 hours of exposure at 900 °C (Fig. 8.3).

The uncoated Ni-based superalloys have performed better than the uncoated Fe-based superalloy in both the environment under study except Ni-based Superni 718. Further amongst the Ni-based superalloys, the bare Superni 75 has shown the best hot corrosion resistance to both the environments followed by Superni 600. The Superni 718 suffered accelerated hot corrosion in the molten salt environment in the form of intense spalling and sputtering of the scale to such an extent that cumulative weight gain could be determined only up to 16 cycles of the study. The accelerated corrosion of the Superni 718 has been attributed to the diffusion of molybdenum to the surface scale through the porous nickel layer which is formed on bare Superni 718 during exposure to the molten salt environment (Fig. 6.50). The nickel oxide layer has been reported to be relatively loose structured by Wu et al. (2001) and is not able to provide effective protection. This presence of molybdenum in the surface scale causes accelerated corrosion as has already been explained in Chapter 6. However Superni 718 performed well in the actual working

conditions of the coal fired boiler. This may be attributed to the presence of scale rich in oxides of chromium, aluminium and silicon, in the boiler environment, which has restricted the diffusion of molybdenum to reach the surface (Fig. 7.49).

As is evident from the Figures 8.2 and 8.3, the base superalloys affect the hot corrosion resistance of the coatings significantly in the boiler environment, whereas their effect are relatively lower in the laboratory conditions. The variation in hot corrosion behaviour of any particular coating on various superalloys may be attributed to the diffusion of basic elements of the substrate superalloys at higher temperatures. Shifler (2004) discovered that high-temperature coatings on various superalloy substrates behaved differently during 1000 hours of exposure in a Type I hot corrosion environment at 899°C. He reported that difference in chemical compositions between a coating and a substrate alloy can lead to inter-diffusion between these materials which can modify the oxidation and corrosion resistance of the coating.

All the coatings selected for the present study have performed well in both the environments, provided necessary protection to the base alloys, maintained their integrity with the substrates, shown good resistance to the degrading species and indicated minor or negligible spallation of the oxide scale. Though during initial hours of exposure, the coatings have got partially oxidized due to the presence of pores, the coatings have shown good resistance to hot corrosion in both the environments after the formation of oxides in pores or at the boundaries of Ni- or Co-rich splats. Based on the findings of the present study, these coatings are recommended for applications to the super-heater and re-heater tubes of the boilers for protecting them against the given high temperature corrosive environments. Further, Ni-20Cr coating using wire as feedstock materials has given best performance on all the substrates under study in both the environments and is, therefore, recommended as the best coating for the given conditions. The (Ni-20Cr)-Superfer 800H and (Ni-20Cr)-Superni 75 coating-substrate combinations have been found to have the highest hot corrosion resistance to the molten salt and to the coal fired boiler environments, respectively.

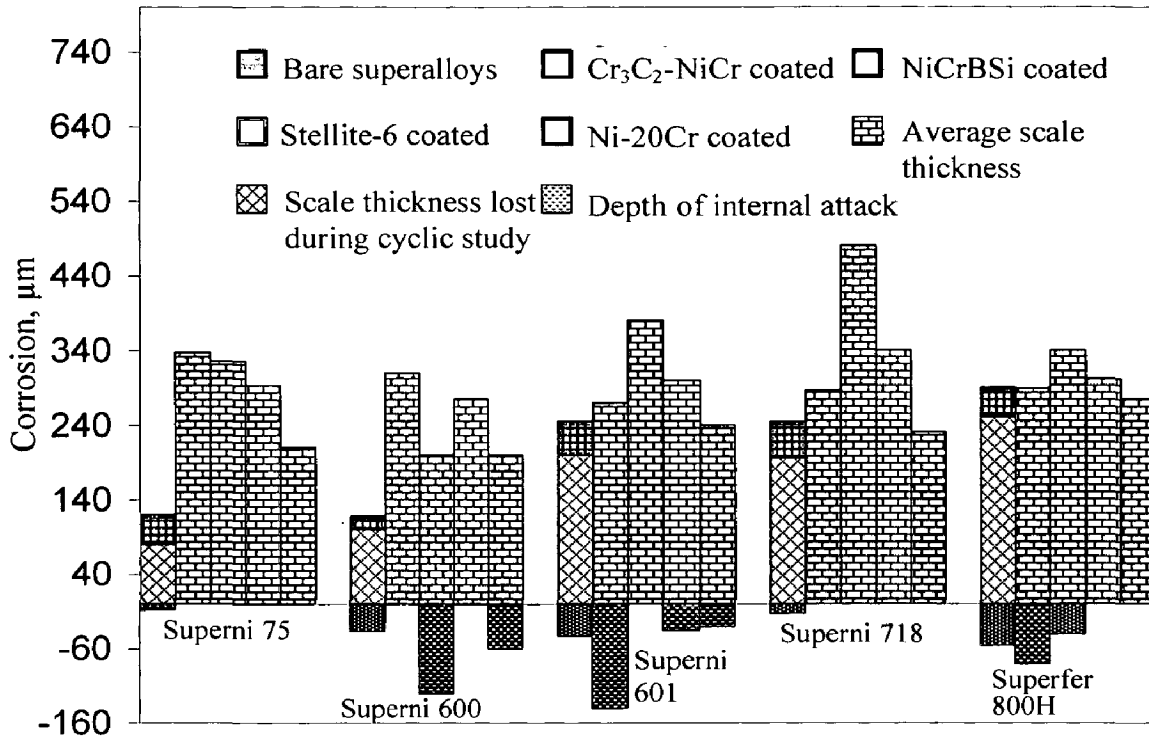


Fig. 8.2 Bar charts showing the extent of corrosion for the coated and uncoated superalloys after exposure to platen super-heater zone of the coal fired boiler at 900 °C for 1000 hours.

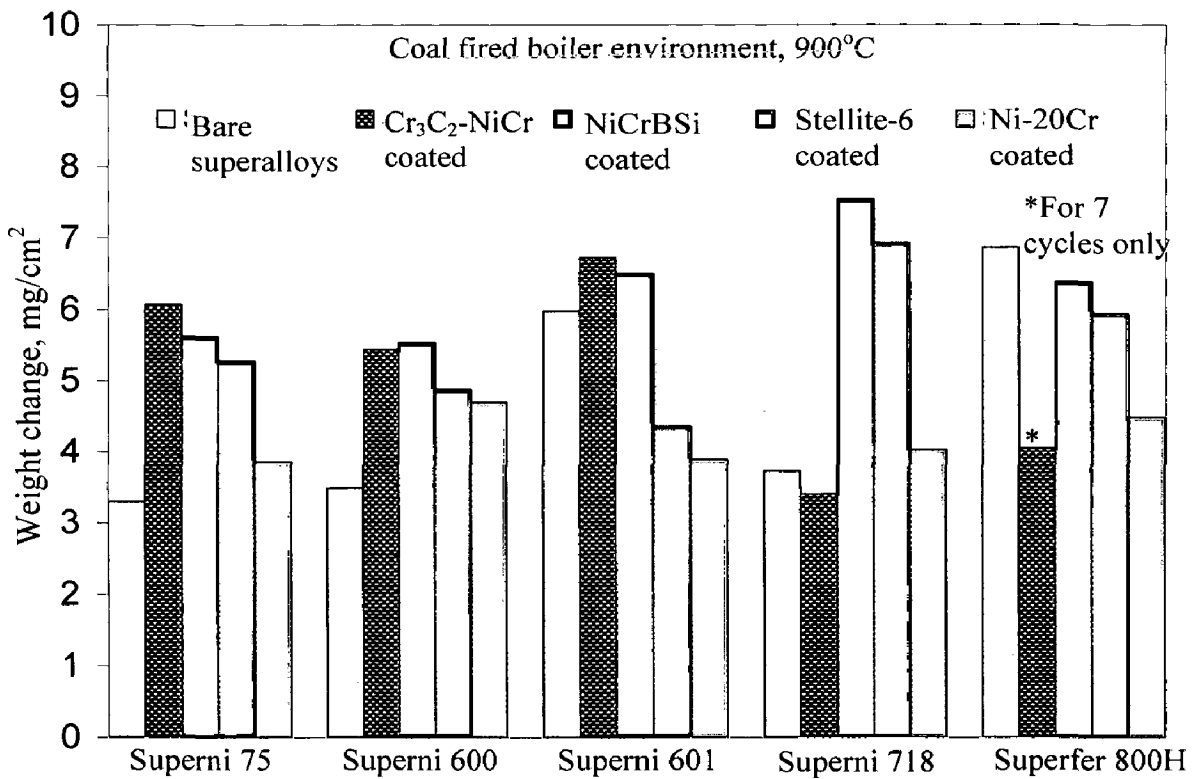


Fig. 8.3 Bar charts showing net weight change (mg/cm²) for the coated and uncoated superalloys after exposure to platen super-heater zone of the coal fired boiler at 900 °C for 1000 hours.

CONCLUSIONS AND RECOMMENDATIONS FOR FUTURE WORK

The hot corrosion behaviour of the bare and Cr₃C₂-NiCr, NiCrBSi, Stellite-6 and Ni-20Cr coated Ni- and Fe-based superalloys has been studied at 900 °C under cyclic conditions in two environments: the molten salt (Na₂SO₄-60%V₂O₅) environment in the laboratory tube furnace and the actual working environment of the coal fired boiler of Guru Nanak Dev Thermal Power Plant, Bathinda, Punjab. The commercially available feedstock alloys were deposited on five types of superalloys namely Superni 75, Superni 600, Superni 601, Superni 718 and Superfer 800H using the HVOF process. The salient conclusions resulting from the present investigation are summarised as follows:

9.1 AS-SPRAYED HVOF COATINGS

- (1) NiCr wire with a composition of 80%Ni and 20% Cr has been successfully deposited by HVOF spraying process to obtain about 200-250 µm thick coating on the Ni- and Fe-based superalloy substrates. It has been established that the HVOF sprayed Ni-20Cr wire coating is a technically viable and effective alternative to the HVOF sprayed Ni-20Cr powder coating obtained by Ak et al., 2003. The wire coating resulted in a dense and uniform lamellar structure consisting of flatter splats with average porosity less than 1% and hardness values in the range of 600-630 Hv.
- (2) Cr₃C₂-NiCr, NiCrBSi and Stellite-6 powders with particle size about -45 µm have been successfully deposited by HVOF process on the given superalloys using liquid petroleum gas (LPG) as a fuel. The coatings have average porosity less than 2% and surface roughness in the range of 4-6 µm.
- (3) The thickness of all the coatings was limited to 250-300 µm in the present study to ensure integrity of the coatings. The thicker coatings were found to disintegrate by themselves.
- (4) All the coatings exhibited dense structure with layered morphology consisting of flat splats. XRD analysis of the as-sprayed Cr₃C₂-NiCr, NiCrBSi, and Ni-20Cr coatings revealed the formation of nickel-based fcc structure as the principal phase, whereas Co-based fcc has been identified as the principal phase in the case of Stellite-6 coating.

- (5) All the coatings have higher hardness values than the substrates. The $\text{Cr}_3\text{C}_2\text{-NiCr}$ coating showed maximum hardness in the range of 870-950 Hv, followed by Stellite-6 and NiCrBSi coatings, whereas the Ni-20Cr wire coating exhibited the lowest hardness in the range of 600-630 Hv.
- (6) The slight increase in hardness of the substrates, near the coating-substrate interface, has been observed in all the coating-substrate combinations. This trend may be attributed partly due to sand blasting of the specimens prior to HVOF coatings and partly due to high impact of the sprayed droplets. There is a noticeable variation in the hardness across the coating thickness in all the coatings, which may be the contribution of porosity, oxide inclusions and partially-melted particles.
- (7) The inter-diffusion of various elements occurred across the coating-substrate interfaces. The diffusion of silicon and aluminium from the substrate to coatings is relatively more, whereas as iron, manganese and titanium reveal marginal diffusion. Further, a marginal diffusion of nickel from the coating to substrate has been found in the case of $\text{Cr}_3\text{C}_2\text{-NiCr}$ coating on Superfer 800H substrate.

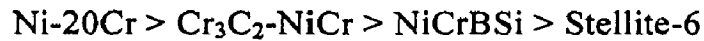
9.2 HOT CORROSION IN MOLTEN SALT ENVIRONMENT

- (8) Based on the overall weight gains after 50 cycles in the molten salt environment, the hot corrosion resistance of the superalloys studied in the present investigation, except Superni 718, has been found in the following order:

Superni 75 > Superni 600 > Superni 601 > Superfer 800H

- i. The superior hot corrosion resistance of the Ni-based superalloys may be attributed to the development of a scale consisting of oxides of nickel and chromium, and to the formation of refractory nickel vanadates, whereas the oxides of iron and iron vanadates are dominantly formed during the hot corrosion of Fe-based superalloy.
- ii. Amongst the nickel-based superalloys, Superni 75 has shown a maximum hot corrosion resistance. The formation of a compact, continuous, and adherent scale about 100 μm thick rich in nickel and chromium might have contributed to better hot corrosion resistance of Superni 75. Superni 718 suffered accelerated hot corrosion in the given molten salt environment in the form of intense spalling and sputtering of the scale may be due to the presence of molybdenum (3.05%) in the alloy.

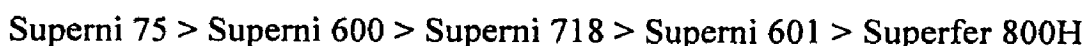
(9) All the coatings under study have imparted resistance to hot corrosion in the given molten salt environment. Based on the thermogravimetric data, the overall protective behaviour of the coatings on different superalloys used in the present study, except on Superni 718, has been found in the following sequence:



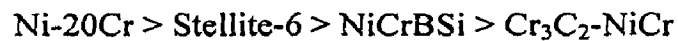
- i. The superior performance of the Ni-20Cr coating is mainly attributed to the formation of oxides of nickel and chromium and their spinel at the topmost part of the scale, and the selective oxidation of chromium to form stringers or globules at the splat boundaries or in pores.
 - ii. The relatively higher oxidation of the $\text{Cr}_3\text{C}_2\text{-NiCr}$ coating as compared to the Ni-20Cr coating has been attributed to the presence of higher amount of chromium which leads to the formation of a thick network of Cr_2O_3 around the Ni-rich splats.
 - iii. Comparatively lower corrosion resistance of the NiCrBSi coating as compared to the Ni-20Cr and $\text{Cr}_3\text{C}_2\text{-NiCr}$ coatings in molten salt environment might be ascribed to some extent to lower content of Cr (15%) in its basic composition. However, the better hot corrosion resistance of NiCrBSi coating as compared to the Stellite-6 coating might be due to the presence of silicon and boron, which promote the selective oxidation of the protective scale-forming elements, and also improve the adherence of the outer scale to the coating as revealed by Wang et al. (2004).
- (10) All the coated superalloys have shown higher rate of hot corrosion during initial cycles of exposure and thereafter the corrosion rate decreases and finally stabilises. Initially, the oxygen permeates inward along the splat boundaries and pores, and causes rapid oxidation. Subsequently, these oxides plug/seal all possible diffusion paths in the coatings, thereby block or slow down the penetration of aggressive species. The corrosion is then confined mainly to the surface of the coatings, thus resulting in the corrosion rate to reach a steady state.

9.3 HOT CORROSION IN THE INDUSTRIAL ENVIRONMENT OF COAL FIRED BOILER

(11) Based on the material depth effected by corrosion after 1000 hours of exposure, the hot corrosion resistance of the superalloys has been found in the following order:



- i. Similar to the molten salt environment, the uncoated Ni-based superalloys have performed better than the uncoated Fe-based superalloy in the coal fired boiler environment also. Similarly, the bare Superni 75 has shown the best hot corrosion resistance to the boiler environment, followed by Superni 600.
 - ii. In contrast to the molten salt environment, Superni 718 performed well in the coal fired boiler environment, may be, due to the formation of a protective scale which restricts the diffusion of molybdenum to reach the surface.
 - iii. The degradation of superalloys in the coal fired boiler environment might be due to the formation of low melting-point alkali-iron trisulphates, which are in molten state at the operating conditions of the boiler and cause dissolution of the protective oxides due to fluxing actions (Srivastava et al., 1997; Weulersse-Mouturat et al., 2004).
- (12) All the coatings used in the present investigation have provided resistance to hot corrosion in the coal fired boiler environment and have shown the following trend of hot corrosion resistance on different superalloys under study, except on Superni 718:



- i. Analogous to the molten salt environment, the Ni-20Cr coating has also shown better hot corrosion resistance amongst all the coatings in the actual working conditions of the coal fired boiler.
- ii. In contrary to the molten salt environment, the NiCrBSi coated superalloys have shown relatively lesser hot corrosion resistance than the Stellite-6 coated superalloys in the boiler environment. In the boiler environment, the NiCrBSi coating partially oxidises up-to the coating-substrate interface, whereas in the molten salt environment, mainly the upper portion of the NiCrBSi coating gets oxidized and the rest portion of the coating remains similar to what has been noted in the as-sprayed coating with negligible amount of oxygen at some spots. In both the environments, the $\text{Cr}_3\text{C}_2\text{-NiCr}$, Stellite-6 and Ni-20Cr coatings got oxidised up to the coating-substrate interface mainly along the splat boundaries.
- iii. The better hot corrosion resistance of the Stellite-6 coated superalloys in the boiler environment may be ascribed to the formation of thick oxides of chromium and silicon, and spinels of cobalt-chromium and nickel-chromium at the boundaries of Co-rich splats due to longer exposure time.

- (13) The hot corrosion resistance of all the coatings under study, in both the environments, can be attributed mainly to the formation of oxides at the surface of the coatings, and at the splat boundaries.

The scale developed on the surface of all the coated superalloys, after exposure to both the environments, consists of protective oxides mainly of chromium, silicon and nickel; and their spinels containing nickel-chromium and/or cobalt-chromium type mixed oxides. These oxides especially Cr_2O_3 and SiO_2 offer a better protection against hot corrosion due to their slow growth rate, strongly bounded compositions and ability to act as effective barriers against ionic migration (Stott, 1989B). The presence of spinel phases may further enhances the hot corrosion resistance due to much lower diffusion coefficients of the cations and anions in the spinel phases than that in their parent oxide phases (Chatterjee et al., 2001).

- (14) It has been established that with the progress of corrosion, the splat boundaries of the coatings are more active in imparting overall hot corrosion resistance as compared to rest of the coating regions. In both the environments, the oxide scale has preferentially formed at the splat boundaries due to oxidation of active elements of the coatings. The Ni- and Co-rich splats of the coatings are mostly in an un-oxidised state.
- (15) Further, the very low porosity and the flat splat structure of the HVOF sprayed coatings might have also contributed to enhanced hot corrosion resistance, as this is the desired structure, when the coatings have to perform in corrosive environment at higher temperature. The distance from the coating surface to coating-substrate interface along the splat boundaries increase significantly in case of a flat splat structure.
- (16) The base superalloys affect the hot corrosion behaviour of the coatings in both the environments, due to outward diffusion of some substrate elements into the coating at higher temperature. However, in some coating-substrate combinations, their effect is noted to be relatively more in the boiler environment as compared to that in the molten salt environment. The performance of the coatings on different substrates follows the following sequence:

(i) Molten salt environment

Cr_3C_2 -NiCr coating: Superni 75>Superni 718>Superni 601>Superni 600>Superfer 800H
NiCrBSi coating : Superni 75>Superni 600>Superfer 800H>Superni 601>Superni 718
Stellite-6 coating : Superni 75>Superni 601>Superni 718>Superni 600>Superfer 800H
Ni-20Cr coating : Superfer 800H>Superni 718>Superni 601>Superni 600>Superni 75

(ii) Coal fired boiler environment

Cr₃C₂-NiCr coating: Superni 718> Superni 600 ≈ Superni 75> Superni 601

NiCrBSi coating : Superni 75 ≈ Superni 600>Superfer 800H> Superni 601>Superni 718

Stellite-6 coating : Superni 600>Superni 75>Superfer 800H>Superni 601>Superni 718

Ni-20Cr coating : Superni75>Superni 718>Superni 600>Superni 601>Superfer 800H

- (17) Titanium has shown significant diffusion into the coating in case of Cr₃C₂-NiCr and Stellite-6 coated Superni 75, and Ni-20Cr coated Superfer 800H after 1000 hour exposure to the boiler environment, as titanium has higher affinity towards oxygen, and it forms a thin layer at the topmost part of the scale.
- (18) The diffusion of some of the other basic elements of the superalloy substrates such as Fe, Al, Mn, Mo, and Si into the scales has been observed in many cases, while the diffusion of Co and Ni from the coatings to substrate is also noticed. In some cases of the coated superalloys, sulphur penetrates into the substrates, while vanadium remains mainly in the top scale.
- (19) The scales formed on all the coated superalloys, in general, show no tendency towards spalling/cracking and are found to be intact, except Cr₃C₂-NiCr coated Superfer 800H. Only minor superficial spalling of the scales has been observed on some coated alloys, which was confined to outer layer of the coatings mostly at the edges and corners of the specimens.
- (20) The Cr₃C₂-NiCr coating on Fe-based superalloy Superfer 800H showed little lower resistance to hot corrosion in both the environments and substantial spalling of the scale has been observed. The spallation of the scale is due to difference in the coefficient of thermal expansion of the oxides, the coating and the substrate.
- (21) The Ni-20Cr coating using wire as feedstock materials has given the best performance on all the substrates under study in both the environments and is, therefore, recommended as the best coating under the given conditions. The (Ni-20Cr)-Superfer 800H and (Ni-20Cr)-Superni 75 combinations have the highest hot corrosion resistance to the molten salt and coal fired boiler environments, respectively.
- (22) Based on the findings of the present study, all the coatings under study are recommended for applications to super-heater and re-heater tubes of the boilers for protecting them from corrosive environments for high temperature applications.

In addition to boilers, any of these coatings can be applied on all those surfaces which are facing the fire side corrosion such as in fluidized beds, industrial waste incinerators, internal combustion engines, gas turbines or steam turbines, to provide the protection against degradation in these environments.

These coatings have a good thermal conductivity (Hidalgo et al., 1999), therefore, they may enhance the service life of the components without affecting the thermal efficiency of the energy generation systems. These coatings are thin and adherent, so they do not cause any appreciable increase in the weight of the coated parts. All the coatings have been tested in the real service environment of the running coal fired boiler at temperature about 900 °C and they performed satisfactory. Therefore, it is proposed that these coatings may be tried on the superheater and reheater tubes of the actual boilers. The coatings under study are generally used for wear resistance, but they are also found to be successful in imparting resistance to hot corrosion. Therefore, these coatings can be applied to other areas of the boiler where erosion-corrosion problems are predominant.

All the coatings used in the present investigation are successfully deposited by HVOF process using LPG as a fuel, which is readily available and is cheap as compared to other fuels used in this process. Further, the deposition of the coating using wire as a feedstock material is convenient for application of the coatings to industrial installation at site. Above all, the HVOF coatings under study have a good resistance to hot corrosion in the given environments due to low porosity and flat splat structure of the coatings, and the HVOF process is convenient, continuous and economical for on-site coating applications to industrial installations.

9.4 RECOMMENDATIONS FOR FUTURE WORK

The results documented in the present research are significant. However recommendations for further works are as follows:

1. In the actual working conditions of the boiler, the thickness of the partially oxidised coatings has been used in the present investigation for evaluating the metal loss due to corrosion. However, a mathematical model could be developed using the laboratory as well as industrial environment data, to predict the corrosive behaviour and life period of the coating. This will also help in designing the coating for high temperature corrosive environment applications.

2. The effects of different HVOF parameters such as spraying distance, fuel/oxygen ratio, powder feed rate etc., of the feedstock alloys used in the present investigation as well as for other feedstock alloys, could be studied for evaluating their influence on the hot corrosion behaviour of the coatings, so as to optimize these HVOF process parameters especially with respect to aggressive environment applications.
3. Hot corrosion behaviours of some feedstock alloys deposited by different thermal spray processes viz-a-viz HVOF process, detonation gun, and plasma spray process, may be evaluated using the cost-effectiveness analysis for these coating processes.
4. The adhesive strength of the as-sprayed coatings as well as the strength after exposure to hot corrosion environment could be evaluated to predict the performance of these coatings for different erosive-corrosive environments.
5. Future work can be extended to other spray materials especially by alloying the coating powders with rare earth elements. High temperature erosion behaviour of the coatings may also be investigated.
6. Hot stage microscopy may be used to understand the development of the scale as well as the mechanism of transport of species during the hot corrosion runs.
7. Some efforts should be made to eliminate the porosity of these coatings so as to further enhance their corrosion resistance. In this regard post coating treatments should be explored.
8. The behaviour of these coatings should further be studied in real service environment for longer duration by applying them on the superheater and reheater tubes of the actual boiler.

Table A.1: Summary of oxidation of Fe-, Ni- & Co- base alloys in Na₂SO₄ and V₂O₅ environments.

Material	Environment	Brief Details
Na₂SO₄ Induced Hot Corrosion		
B-1900	Na ₂ SO ₄	Na ₂ SO ₄ interacted with the alloy to form sodium and sulphur compounds, rapid removal of sulphur from the Na ₂ SO ₄ by unretarded diffusion of sulphur and precipitation of Cr-rich sulphide phases promoted the formation of Na ₂ O. The catastrophic oxidation observed during sulphidation was due to interactions between Na ₂ O and the substrate (Bornstein and DeCrescente, 1970).
Ni-base superalloys and seven binary Ni-base alloys	Pure O ₂ , 825-1000°C	Based upon the results, it was concluded that the reduction of the oxide ion content of Na ₂ SO ₄ was a necessity, but not sufficient condition for sulphidation inhibition. The addition of Mo or V to nickel imparted sulphidation resistance in it because their oxides reacted with and decreased the oxide ion content of Na ₂ SO ₄ . The disagreement in the literature regarding the effect of Molybdenum on hot corrosion was suggested to be largely due to differences in testing techniques and differences in whether the investigators have been more concerned with the initiation or with propagation modes of hot corrosion (Bornstein et al, 1973).
Ni-base industrial superalloys	Static deposits of Na ₂ SO ₄ or NaCl or both in still air, 850-1000°C	The susceptibility to hot corrosion was found to be correlated to the type of scale produced during simple oxidation. Alloys forming an Al ₂ O ₃ scale were found to be susceptible to Na ₂ SO ₄ deposits, independent of their Cr content. The quantity of the Na ₂ SO ₄ deposits dictated the nature of attack and, under certain conditions, the refractory element alloy additions appeared to play an essential role. Alloys containing Cr ₂ O ₃ or TiO ₂ in the simple oxidation scale proved to be sensitive to NaCl attack (Bourhis and John, 1975).
Ni-15Cr-Mo (Peters et al), Fe-, Ni- and Co-base alloys	900°C (Peters et al), 600°C and above (Pettit and Meier), 975°C in oxygen (Fryburg et al)	The effect of Mo on the hot corrosion of superalloys has also been reported by Peters et al (1976), Pettit and Meier (1985) and Fryburg et al (1984). The alloy containing Mo suffered catastrophic degradation. It has been reported that the MoO ₂ reacted with Na ₂ SO ₄ to produce an acid (SO ₂ -rich) salt, leading to acidic fluxing. The MoO ₂ incorporated into the Na ₂ SO ₄ via the formation of compounds such as Na ₂ MoO ₄ , Na ₂ MoO ₄ .MoO ₃ and Na ₂ MoO ₄ .2MoO ₃ . All these phases were liquid and left a high solubility for Al ₂ O ₃ and Cr ₂ O ₃ . Peters et al (1976) added that there is threshold amount of molybdenum below which catastrophic attack is not encountered, e.g. for Ni-15% Cr threshold has been reported to be between 3-4%.

Superalloys HA-188, S-57, IN-617 and TD-NiCrAl	Mach 0.3 burner rig at various temperatures, sea salt concentrations and salt compositions.	Accelerated corrosion of the specimens has been reported in the temperature zones above the calculated dew points of Na ₂ SO ₄ . It was believed that the corrosion occurred by small amount of salt deposit on those temperature zones during heat-up following each cooling cycle or by small amounts of salt migrating from deposits at cooler zones via a wetting action. Large deposits of salt appear to inhibit corrosion that is why less corrosion was noticed at 900°C when flame was doped with 10 ppm sea salt than when it was doped with 5 ppm sea salt (Santoro, 1979).
Ni-30Cr and Co-30Cr	600-900°C	The rapid rate of attack was explained on the basis of sulphation of the transient surface oxides (Ni or Co oxides) and the dissolution of these transition metal sulphates into Na ₂ SO ₄ to yield a liquid phase (Luthra and Shores, 1980).
Pure Iron & Fe-5Cr Alloy, and Fe-13Cr Alloy	1 atmosphere of oxygen, 900°C	Pure iron did not undergo accelerated oxidation, which has been attributed to the thickening of the scale too rapidly for sulphur to penetrate the oxide and interact directly with the metal. Authors further reported an immediate acceleration in oxidation rate of Fe-5Cr alloy in the presence of Na ₂ SO ₄ deposits this was attributed to sulphide formation mechanism which initially restricted spinel formation (Trafford & Whittle, 1980A). In their study conducted on Fe-13% Cr alloy, Na ₂ SO ₄ coating markedly enhanced the oxidation rate and resulted in the formation of thick, compact and stratified scales. They postulated that formation of sulphides in the alloy substrate and mechanical failure of scale was responsible for the enhanced oxidation (Trafford & Whittle, 1980 B).
Nimonic 105	At 900°C	Hot corrosion did not seem to be very detrimental towards the superalloy. It was concluded that SO ₃ pressures below 5x10 ⁻³ atm did not affect the electrokinetic behaviour, but pressures greater than 5x10 ⁻³ atmospheres produced higher corrosion rates which was attributed to the acid fluxing by the sulphate melt. Addition of NaCl to the molten Na ₂ SO ₄ resulted in increased dissolution of Nimonic 105 (Sequeira and Hocking, 1981).
Co-Cr, Co-Al and Co-Cr-Al Alloys.	In O ₂ -SO ₂ -SO ₃ , 600 to 750°C	Co-Cr and Co-Cr-Al alloys reacted non-uniformly, usually in the form of pits and Co-Al alloys suffered broad frontal attack. Under all conditions, a thin sulphur-rich band containing sulphides was observed at the alloy/scale interface and cobalt dissolved near the interface and formed Co ₃ O ₄ /or CoSO ₄ (S) (Luthra, 1982).
Ni-base Superalloys, B-1900 and NASA-TRW IVA	In pure O ₂ , 900°C	After an induction period of little corrosion, local basic fluxing attack of the Cr ₂ O ₃ /Al ₂ O ₃ scale spreaded to cover the surface and generated catastrophic linear kinetics. During catastrophic attack of B-1900, the sulphate ions reacted to release SO ₂ and formed sulphides in the alloy and salt was converted to Na ₂ MoO ₄ (Fryburg et al, 1982).

Nimonic 105, 75, 80A and 90	With and without Cr ₂ (SO ₄) ₃ , NiSO ₄ or CoSO ₄ additions, 650-1000°C	Upto 800°C, the lower oxidation rates for Na ₂ SO ₄ coated alloys were attributed to a scale morphology consisting of inner scales of Cr ₂ O ₃ acting as a protective oxide film and external scales of NiO. This morphology was observed to be maintained at high temperatures (Malik and Ahmad, 1983).
Co-Cr, Co-Al and Co-Cr-Al Alloys	In O ₂ -0.15% (SO ₂ +SO ₃), 750°C	Accelerated oxidation tests at 750°C showed that the corrosion resistance of binary Co-Cr and Co-Al alloys increased with the Cr and Al content of alloys. This protection was offered by the rapid growth of CoCr ₂ O ₄ /Cr ₂ O ₃ and CoAl ₂ O ₄ /Al ₂ O ₃ oxides in comparison to CoO and Co ₃ O ₄ . At high enough Cr (≥40%) and Al (≥15%) concentrations, the growth rates were so fast that liquid did not even form, consequently the corrosion rates were very low. Tests on Co-Cr-Al alloys indicated that simultaneous presence of Cr and Al was deleterious to the resistance against low temperature hot corrosion (Luthra, 1985).
Ni- base superalloys	1 atm O ₂ , 650-1000°C (Goebel et al), O ₂ , 750-950°C (Misra)	The alloys underwent catastrophic corrosion. The accelerated oxidation occurred as a result of the formation of a liquid flux based on Na ₂ SO ₄ which dissolved the normally protective oxide scales. Catastrophic or self-sustaining rapid oxidation can occur in alloys which contain Mo, W or V because solution of oxides of these elements with Na ₂ SO ₄ decrease the oxide ion activity of the molten salts, producing melts which are acidic fluxes for oxide scales (Goebel et al, 1973 and Misra, 1986). The evaporation rate of MoO ₃ from Na ₂ Mo-MoO ₃ melts has been reported to decrease considerably by Misra (1986) when dissolved in Na ₂ MoO ₄ .
Ni-16Cr-2Nb, IN 738, Ni-16Cr and Superalloy 537	900 and 1000°C	Na ₂ SO ₄ coated coupons of Ni-16Cr-2Nb and Ni-16Cr developed dense, protective oxide scales and exhibited good hot corrosion resistance. Alloys 537 and IN 738 experienced a shift from basic fluxing to acidic fluxing and as the temperature was increased, the rate of attack increased significantly (Zho et al, 1987).
Ni and Ni-base Alloy EI 867 with the Aluminide and Cr-Al Diffusion Coatings	Pure Na ₂ SO ₄	Low alloyed aluminide and Cr-Al coatings showed very poor resistance to oxidation. After 24 hrs, these had been almost completely removed. Modification of highly alloyed aluminide coatings with Cr resulted in uniform and relatively slow degradation of the coating. Cr enriched zone is supposed to act as a barrier to the oxidation of refractory metals such as Mo, W and V thus preventing the onset of catastrophic corrosion (Godlewski and Godlewski, 1987).
Pure Nickel and Udimet 700	In a high velocity burner rig, 900°C	Corrosion of Ni in the burner rig produced a relatively compact NiO scale along with some internal grain boundary corrosion. Corrosion of Udimet 700 was observed to occur in two stages. During the first stage, the corrosion proceeded by the reaction of Cr ₂ O ₃ scale with the Na ₂ SO ₄ and evaporation of the Na ₂ CrO ₄ reaction product from the surface of the corroding sample. Cr depletion in the alloy occurred and sulphide particles were formed in the Cr depletion zone.

		Extensive sulphidation occurred during the second stage of corrosion and a thick scale was formed (Misra, 1987).
Fe-, Ni- and Co-base alloys	Atmospheres containing O ₂ , N ₂ and SO ₂ , 729-1076°C	The corrosion rate was lowest when the chromium content of the alloy was highest. Further Mo and Cu were found to increase the corrosion rate. The main corrosion products formed in air were NiO and Cr ₂ O ₃ . In hot corrosion tests NiS and Cr ₃ S ₈ were found (Pehkonen et al, 1987).
Pure Iron	Simulated combustion gas containing SO ₃ , 600-800°C	The accelerated reaction observed in the presence of Na ₂ SO ₄ deposits was attributed to the formation of a liquid salt solution between Na ₂ SO ₄ and the sulphates of the corroded metal with the production of duplex scales consisting of a mixture of metal oxides and sulphides (Gesmundo & Viani, 1988).
Alloys B1900 and IN 100 (Al ₂ O ₃ -formers), Inconel 600, 690, Incoloy 800, IN 738, Nimonic 80A, 100, and 105 (Cr ₂ O ₃ -formers)	In the presence of Na ₂ SO ₄ (s) and NaCl (s) separately, and in combination, air, 850 and 1000°C	The Cr ₂ O ₃ formers got attacked more aggressively by NaCl (s) than Na ₂ SO ₄ (s). Al ₂ O ₃ -formers and to some extent NiO-formers were more resistant to NaCl attack than Cr ₂ O ₃ formers. While Na ₂ SO ₄ induced corrosion preceded by fluxing and sulphidation reactions, the NaCl induced corrosion was observed to follow a reaction path of fluxing, chloridation and oxidation. The Na ₂ SO ₄ -NaCl induced corrosion involved combination of reactions occurring in the presence Na ₂ SO ₄ and NaCl separately (Malik et al, 1988).
Inconel 600 and Incoloy 825	Ar +1% O ₂ , 940°C	Inconel 600 was able to form a protective layer of chromia in Ar +1% O ₂ with or without a thin layer of Na ₂ SO ₄ at a temperature of 940°C, whereas Incoloy 825 was not able to form chromia in the same environment. This was attributed to the formation of nickel and chromium molybdates due to 3.22% Mo present in the alloy. When O ₂ content was only 300ppm, sodium sulphate layer strongly enhanced the corrosion of Inconel 600 and Incoloy 825 (Santorelli et al, 1989).
Review (Shih)	Low-temperature corrosion	Some superalloys containing molybdenum are subjected to sub-melting point hot corrosion when covered with a sulphate, which is associated with the formation of a molybdenum-containing melt resulting from the reaction of MoO ₃ with the sulphate (Shih, 1989).
Single-crystal Ni-base superalloys and DS Mar M 200	704 and 900°C	All the alloys were severely degraded at 900 and 704°C. There was no significant difference between the hot corrosion of these alloys when tested in air or in oxygen with SO ₃ , provided a liquid deposit was present in both cases. It was concluded that all the superalloys under study require a coating if they were to be exposed to any of the hot-corrosion conditions at temperatures of 704°C or higher (Levy et al, 1989).

Pure Nickel	Under $\text{SO}_3 + \text{SO}_2 + \text{O}_2$ gas mixture & SO_2 and O_2 atmospheres, 900°C	The corrosion loss in mixed atmosphere containing SO_3 was reported to be larger than those observed in pure SO_2 and O_2 atmospheres. The corrosion loss was found to correspond to the thickness of the oxide layers. High corrosion losses were attributed to the fact that SO_3 strongly acted as an oxidizing agent for the corrosion process (Hara et al 1991).
Pure Ni and Al and Fe-Cr, Ni-Cr and Fe-Al alloys	In oxygen and air, 750°C	Shi (1995) studied the possibility of $\text{Na}_2\text{SO}_4\text{-Na}_2\text{O}$ eutectic melt formation on the metals deposited with Na_2SO_4 . In case of Ni, Co, Al, Cr and their alloys he could not detect formation of $\text{Na}_2\text{SO}_4\text{-Na}_2\text{O}$. In case of iron base alloy with high Cr or Al content, where Cr_2O_3 or Al_2O_3 were formed, again $\text{Na}_2\text{SO}_4\text{-Na}_2\text{O}$ eutectic was not observed. However, at lower Cr or Al content this eutectic melt was suggested to be the possible cause for accelerated rate of corrosion.
Metal oxides such as Co_3O_4 , NiO, Al_2O_3 , Cr_2O_3 , Fe_2O_3 and SiO_2	$627\text{-}927^\circ\text{C}$ (Malik and Mobin) and $827\text{-}927^\circ\text{C}$ (Mobin et al) in O_2	The interaction of the metal oxides with Na_2SO_4 has been studied. As suggested, the high temperature reaction products usually contain 3-phase structure namely, $\text{Na}_2\text{O-MO-M}_2\text{O}_3$ and metal sulphide and or metal sulphate. The formation of $\text{Na}_2\text{O-M}_2\text{O}$ was further reported to be dependent upon the solid state solubility of metal oxide in the molten salt at high temperature and under limited solubility conditions $\text{Na}_2\text{O-M}_2\text{O}$ was invariably formed, but as soon as conditions got relaxed the oxide M_2O_3 precipitated and was observed to form a separate phase (Malik and Mobin, 1987 and Mobin et al, 1996).
Pure Iron	Na_2SO_4 , $\text{Na}_2\text{SO}_4\text{+NaCl}$, $\text{Na}_2\text{SO}_4\text{+V}_2\text{O}_5$, combustion gas, 600°C	Iron suffered low temperature hot corrosion in the presence of salt deposits at 600°C . The additions of NaCl and V_2O_5 to Na_2SO_4 changed the corrosion kinetics significantly and modified the scale structure (Li et al, 1996).
Binary Iron Aluminide (Fe_3Al)	In pure oxygen, 1100 K, 1225 K and 1330K	The faster kinetics observed in the initial stages of oxidation was related to the formation of $\theta\text{-Al}_2\text{O}_3$ and slower kinetics in the later stages of oxidation to the formation of $\alpha\text{-Al}_2\text{O}_3$. The overall rate of hot corrosion was higher than that of oxidation at all temperatures. The presence of $\alpha\text{-Fe}_2\text{O}_3$ in addition to alumina was indicated by XRD. Cross-sectional microscopy revealed that the metal-scale interfaces were pitted in hot corrosion conditions and the pits contained aluminium sulphide. Sulphides were also detected along grain boundaries in the intermetallic near the scale-metal interface (Das et al, 2002).
Inconel 740	$850 - 1000^\circ\text{C}$	The kinetics curves of the alloy at 950°C without Na_2SO_4 deposit and at 850°C with Na_2SO_4 deposit obeyed the parabolic law, whereas the uniform parabolic growth behaviour of oxide was not followed at 1000°C without Na_2SO_4 deposit and at 950°C with Na_2SO_4 deposit due to oxide spallation at 1000°C and the evaporation of Na_2CrO_4 melt at 950°C , respectively. The oxide scales were found to be consisting of Cr_2O_3 , (Ni, Co) Cr_2O_4 , TiO_2 and Al_2O_3 and internal oxide scales at all temperatures. The internal sulphidation was suggested to take place due to the existence of Na_2SO_4 deposit. The complex layered structure of the oxide scales was reported to be in favour of the resistance to oxidation. The accelerated oxidation of the alloy in the presence of Na_2SO_4 deposit was attributed to the dissolution of Cr_2O_3 induced by basic fluxing in molten Na_2SO_4 (Zhao et al, 2004).

310 Stainless Steel	Various ratios of Na ₂ SO ₄ /NaCl deposit, in air at 750°C	The weight gain kinetics in simple oxidation was found to follow a steady state parabolic rate law after 3 hours, while the kinetics with the salt deposits displayed a multi-stage growth rates. The most severe corrosion took place with 75% NaCl mixtures. Uniform internal attack was the morphology of NaCl-induced hot corrosion, while the extent of intergranular attack was more pronounced as the content of Na ₂ SO ₄ in the mixture was increased (Tsaour et al, 2005).
V₂O₅ Induced Hot Corrosion		
Gas-turbine alloys	750°C and above	Vanadium pentaoxide coatings had a deleterious effect throughout the useful temperature range of all the alloys up to 1120 hrs in 70-hr cycles. The effect was reported to be more pronounced for iron base alloys at temperatures above 750°C (Harris et al, 1955).
Review	-----	Oxidation of pure Cr in V ₂ O ₅ occurs with a very rapid diffusion rate and so only the initial stages of the oxidation curve were supposed to be more important. Later slowing down of the oxidation rate could be attributed mainly to the effect of scale thickening. Loose and spongy appearance of the scale was observed at the beginning of the process; V ₂ O ₅ was present in excess and did dissolve the products of oxidation. At the same point the liquid was saturated with the oxide which subsequently could get precipitated. The presence of various phases in a thin layer of scale would impose such severe strain on the film that cracking and exfoliation could be expected. This would permit liquid phase to reach the metal surface again and the conditions to form a spongy scale were seen to prevail. This mechanism would apply only to iron base alloys, which are susceptible to the catastrophic corrosion (Sachs, 1958).
Technical note (Fairman) Review (Pantony & Vasu)	----	Fairman (1962) reported that the accelerated oxidation due to V ₂ O ₅ is most likely to be the consequence of the catalytic action of vanadium pentoxide. It results in splitting the oxygen molecule at the metal surface, so cause rapid corrosion. Pantony & Vasu (1968A) concluded from the theoretical survey of fireside corrosion of boilers and gas-turbines that in residual fuel ash, V ₂ O ₅ can be the most serious cause of "catastrophic" corrosion.
Pure metals such as iron, cobalt, nickel, molybdenum, titanium, tungsten and 99.5% vanadium rods, and single crystals of chromium	Immersion in the melt, in O ₂	A diffusion controlled corrosion process given by equation below hold good for the initial stages of vanadic corrosion of all metals under study except nickel and chromium. $\Delta w = Kt$ where Δw is the weight change per cm ² at time t, and k is the velocity constant. Whereas nickel obeyed a logarithmic rate law. The velocity constant was found to be inversely proportional to the depth of melt. On the basis of comparison of activation energies of the various rate processes, a single mechanism underlying the corrosion processes of iron, cobalt, vanadium,

		<p>titanium, tungsten and molybdenum was suggested, which involves an inward diffusion of oxygen (or other active species) and a sequential outward diffusion of the corrosion products. In case of nickel and chromium, the existence of a coherent corrosion layer separating the slag from nickel and chromium was revealed, which was named as protective barrier for these metals and was found to be absent for other metals under study (Pantony & Vasu, 1968B).</p>
High temperature alloys	-----	<p>Vanadate-induced corrosion of high temperature alloys has been studied by thermogravimetry in laboratory furnaces (using a limited amount of vanadate deposit), in burner rigs (where small amounts of vanadates are continually being deposited on the surface), or by immersion of specimens in crucibles with molten salt. The reaction products formed during exposure in laboratory furnaces and in burner rigs were qualitatively the same, but the kinetics and reaction rates were differing considerably. The mechanisms were found to be complex (Beltran and Shores, 1972).</p>
Iron, nickel and several alloys containing iron, nickel, and chromium	Crucible and rotating disk testing	<p>The stainless steels and particularly 440 stainless steel (25 wt% Cr) showed the best corrosion resistance to liquid V_2O_5. The rate of corrosion of Armco iron by liquid V_2O_5 has been reported to be controlled initially by the diffusion of oxygen across the metal oxide-liquid vanadate interface. As the available oxygen ions got depleted from the melt, the rate controlling mechanism was observed to be changed to the sorption of oxygen at the liquid vanadate gas phase interface. Whereas in case of nickel, Inconel 600 and the iron alloys, the rates of corrosion were found to be affected by the formation and dissolution of the protective metal oxide layers. They concluded that the presence of Fe and Na in the vanadate melts did not alter the rate controlling process of oxygen diffusion and oxygen sorption, but it increased the non stoichiometry and hence increased the oxygen diffusion. The rate of corrosion was reported to be affected by temperature, oxygen partial pressure and rotational speed, volume of liquid vanadate, composition of the metal and composition of the liquid vanadates. According to them, Inconel showed better corrosion resistance than stainless steels (Kerby and Wilson, 1973).</p>
50Cr-50Ni alloy	In pure V_2O_5 and sodium vanadates, 750-950°C in a rotating disk apparatus	<p>In pure V_2O_5 at 810°C, a Cr_2O_3 scale has been observed on the alloy which subsequently got dissolved slowly into the liquid melt and was thus proposed as a barrier layer by them. In case of NV_6 this barrier layer was not observed. The increased basic character of the melt and its consequently greater fluxing ability toward acidic oxides was thought to be a more important part process than the increased ionic conductivity of NV_6 over V_2O_5 at this temperature. At 950°C the corrosion in terms of both dissolution rate and corrosion rate was reportedly greater in V_2O_5 than in NV_6 (Dooley and Wilson, 1975).</p>

Superalloys	700°C	<p>The relationship of the high temperature corrosion of superalloys with contaminants has been reported by Hancock (1987). It was proposed that to compare contaminant conditions the contaminant flux rate (CFR) rather than the contaminant level in the fuel or environment should be considered. He further suggested that at temperatures above 700°C where vanadates cause fluxing of the protective oxide scales, corrosion could be determined by the CFR and temperature rather than by material selection.</p>
Nickel base superalloy	In air, 700°C	<p>Vanadium, present as vanadium pentoxide, attacked the alloy severely at the temperature of investigation. Study of ternary oxide system and spot tests showed that two low melting eutectics, namely, NiO-V₂O₅-Cr₂O₃ melting at 550°C and V₂O₅-Cr₂O₃-Fe₂O₃ melting at 480°C, were formed. The formation of these liquid eutectics and the presence of corrosive V₂O₅ caused severe damage to the superalloy (Iyer et al, 1987).</p>
Nickel base superalloys Nimonic 80A, Hastelloy C-276 and Superni 600	In air, 923, 973 and 1023 K	<p>The hot corrosion kinetics obeyed a parabolic law with two regions at 973 and 1023 K, the corrosion rate falling with the formation of a solid Ni₃V₂O₈ layer. The acid-base fluxing mechanism and a second mechanism by which nickel vanadate was precipitated from a nickel vanadium compound located in the short circuit diffusion path has been assumed to be occurring in the growing oxide. The corrosion rate for these alloys got decreased with the formation of a compact solid vanadate layer (Swaminathan et al, 1993).</p>

Table A.2: Thermal expansion coefficients of substrate steels, coatings and oxides.

Alloy or oxide	Thermal expansion coefficient (10^{-6} per $^{\circ}\text{C}$)	Reference
Nimonic 75	11	http://www.matweb.com/
Inconel 600	13.3	
Inconel 601	13.75	
Inconel 718	13	
Incoloy Alloy 800H	14.4	
Co-base superalloys	17	http://www.lucasmilhaupt.com/
Ni-20Cr	17.3	Metal Handbook (1961)
S-816 (Co-Cr-Ni based alloy)	15.98	
Al_2O_3	8.5	Niranatlumpong et al (2000)
Cr_2O_3	8.5	
FeCr_2O_4	8.5	
Fe_2O_3	12	Huminik (1963)
NiO	14.5	Duran et al (2003)

REFERENCES

1. **Aalamialeagha, M.E., Harris, S.J. and Emamighomi, M.,** (2003), "Influence of the HVOF Spraying Process on the Microstructure and Corrosion Behaviour of Ni-20%Cr Coatings," *J. Mater. Sci.*, Vol. 38, pp. 4587-4596.
2. **Ak, N.F., Tekmen, C., Ozdemir, I., Soykan, H.S. and Celik, E.,** (2003), "NiCr Coatings on Stainless Steel by HVOF Technique," *Surf. Coat. Technol.*, Vol. 173-174, pp.1070-1073.
3. **Almeraya, C.F., Martinez, V.A., Gaona, C., Romero, M.A. and Malo, J.M.,** (1998A), "Hot Corrosion of the Steel SA213-T22 and SA213-TP347H in 80% V₂O₅-20% Na₂SO₄ Mixture," *Revista de Metalurgia*, Vol. 34, No. 1, pp. 11-17.
4. **Almeraya, C.F., Martinez, V.A. and Gonzalez, R.J.G.,** (1998B), "Electrochemical Studies of Hot Corrosion of Type 347H Stainless Steel," *Brit. Corros. J.*, Vol. 33, No. 4, pp. 288-291.
5. **Anfeng, Z., Yuyue, W., Jiandong, X. and Chanqiu, Li.,** (2003), "Erosion-Corrosion Characteristic and Electrochemical Behavior of High Velocity Oxy-Fuel Sprayed Coatings and Two Types of Steels," *Journal of Xi'an Jiaotong University*, Vol. 37, No. 11, pp 1150-1153, 1158.
6. **Antony, K.C.** (1983), "Wear -Resistant Cobalt-Base Alloys," *Journal of Metals*, Vol. 35, No. 2, pp. 52-60.
7. **Aoh, J.N. and Chen, J.C.,** (2001), "On the Wear Characteristics of Cobalt-based Hardfacing Layer after Thermal Fatigue and Oxidation," *Wear*, Vol. 250, pp. 611-620.
8. **ASM Handbook,** (1995), "Metallography and Microstructures," Vol. 9, Sixth Printing, ASM Publication, Metals Park Ohio.
9. **Atkinson, A.,** (1988) "Wagner Theory and Short Circuit Diffusion," *Mater. Sci. Technol.*, Vol. 4, No.12, pp. 1046-1051.
10. **Bai, C-H., Luo, Y.-J. and Koo, C.-H.,** (2004), "Improvement of High Temperature Oxidation and Corrosion Resistance of Superalloy IN-738LC by Pack Cementation," *Surf. Coat. Technol.*, Vol. 183, pp. 74-88.
11. **Barbezat, G., Nicoll A. R. and Sickinger, A.,** (1993), "Abrasion, Erosion and Scuffing Resistance of Carbide and Oxide Ceramic Thermal Sprayed Coatings for Different Applications," *Wear*, Vol. 162-164, pp. 529-537.

12. **Barbooti, M.M., Al-Madfai, S.H. and Nassouri, H.J., (1988), "Thermochemical Studies on Hot Ash Corrosion of Stainless Steel 304 and Inhibition by Magnesium Sulphate,"** *Thermochim. Acta*, Vol. 126, pp. 43-49.
13. **Batchelor, A.W., Lam, L.N. and Chandrasekaran, M., (2003), "Ch. 6: Discrete Coatings,"** in 'Materials Degradation and its Control by Surface Engineering,' 2nd Edition, Imperial College Press.
14. **Baxter, D.J. and Natesan, K, (1989), "Breakdown of Chromium Oxide Scales in Sulfur-Containing Environments at Elevated Temperatures,"** *Oxid. Met.*, Vol. 31, No. 3-4, pp. 305-323.
15. **Beltran, A.M. and Shores D.A., (1972), "Hot Corrosion,"** In: Sims CT, Hagel WC, editors. *The superalloys*. New York: Wiley, pp. 317-39.
16. **Belzunce, F.J., Higuera, V. and Poveda, S., (2001), "High Temperature Oxidation of HFPD Thermal-Sprayed MCrAlY Coatings,"** *Mater. Sci. & Engg. A*, Vol. 297, No. 1-2, pp. 162-67.
17. **Bhushan, B. and Gupta, B.K., (1991), "Handbook of Tribology: Material Coating and Surface Treatments,"** McGraw-Hill, New York.
18. **Blum, R., (1997), "Advanced (700°C) PF Power Plant,"** EC Contact No SF/1001/97/DK
19. **Bluni, S.T. and Mardar, A.R., (1996), "Effects of Thermal Spray Coating Composition and Microstructure on Coating Response and Substrate Protection at High Temperatures,"** *Corros.*, Vol. 52, No. 3, pp. 213-218.
20. **Bornstein, N.S. and DeCrescente, M.A., (1969), "Relationship Between Compounds of Sodium and Sulfur and Sulfidation,"** *Met. Soc. AIME-Trans.*, Vol. 245, No. 9, pp. 1947-1952.
21. **Bornstein, N. S. and DeCrescente, M.A., (1971), "The Role of Sodium in the Accelerated Oxidation Phenomenon Termed Sulphidation,"** *Metall. Trans.*, No.2, pp. 2875-2883.
22. **Bornstein, N.S., DeCrescente, M.A. and Roth, H.A., (1973), "The Relationship Between Relative Oxide Ion Content of Na₂SO₄, the Presence of Liquid Metal Oxides and Sulfidation Attack,"** *Metall. Trans.*, Vol. 4, pp. 1799-1810.
23. **Bornstein, N.S., Decrescente, M.A. and Roth, H.A., (1975), "Effect of Vanadium and Sodium Compounds on the Accelerated Oxidation of Nickel Base Alloys,"** *Proc. Conf. on Gas Turbine Mater. in the Marine Environment*, MMIC-75-27, Columbus, Ohio, USA, pp. 115-160.
24. **Brandl, W., Marginean, G., Maghet, D. and Utu, D., (2004), "Effects of Specimen Treatment and Surface Preparation on the Isothermal Oxidation Behaviour of the HVOF-Sprayed MCrAlY Coatings,"** *Surf. & Coat. Technol.*, Vol. 188-189, pp. 20-26.

25. **Buchanan, Relva C. and Park, T., (1998), "Materials Crystal Chemistry," Pub. Marcel Dekker, Inc., New York, ISBN 0-8247-9798-1.**
26. **Byrnes, L. and Kramer, M., (1994), "Method and Apparatus for the Application of Thermal Spray Coatings onto Aluminium Engine Cylinder Bores," Proc. of the 7th National Thermal Spray Conference, Boston, (1994), pp. 39-48.**
27. **Calero, J., (1997), "Characterisation of Cr₃C₂-NiCr Coatings Obtained by HVOF Spray System and Process Interpretation Using Mathematical Simulation of the Process," Ph.D. Thesis, Barcelona, Spain.**
28. **Calvarin, G., Molins, R. and Huntz, A.M., (2000), "Oxidation Mechanism of Ni-20Cr Foils and its Relation to the Oxide-Scale Microstructure," Oxid. Met., Vol. 53, No. 1-2, pp. 25-48.**
29. **Castello, P., Guttman, V., Farr, N. and Smith, G., (2000), "Laboratory-Simulated Fuel-Ash Corrosion of Superheater Tubes in Coal-Fired Ultra-Supercritical-Boilers," Mater. Corros., 51, No. 11, pp.786-790.**
30. **Cha, S.C., Gudenau, H.W. and Bayer, G.T., (2002), "Comparison of Corrosion Behavior of Thermal Sprayed and Diffusion-Coated Materials," Mater. Corros., Vol. 53, pp. 195-205.**
31. **Cha, S.C. and Wolpert, P., (2003), "High-Temperature Erosion and Corrosion Measurement of Thermally Sprayed Materials," Adv. Eng. Mater., Vol. 5, No.4, pp. 213-217.**
32. **Chandler, P.E. and Quigley, M.B.C., (1986), "The Application of Plasma-Sprayed Coatings for the Protection of Boiler Tubing," in: Proc. of the 11th International Thermal Spraying Conference, Montreal, Canada, 8–12 September 1986, pp. 29–35.**
33. **Chatterjee, U.K., Bose, S.K. and Roy, S.K., (2001), 'Environmental Degradation of Metals,' Pub. Marcel Dekker, 270 Madison Avenue, New York.**
34. **Choi, H., Yoon, B., Kim, H. and Lee, C., (2002), "Isothermal Oxidation of Air Plasma Spray NiCrAlY Bond Coatings," Surf. Coat. Technol., Vol. 150, No. 2-3, pp. 297-308.**
35. **Chuanxian, C., Bingtang, H. and Huiling, L., (1984), "Plasma Sprayed Wear-Resistance Ceramic and Cermet Coating Materials," Thin Solid Films, Vol. 118, No. 4, pp. 485-493.**
36. **Collazo, A., Novo, X.R. and Perez, C., (1999), "Corrosion Behaviour of Cermet Coatings in Artificial Seawater," Electrochim. Acta, Vol. 44, No. 24, pp. 4289-4296.**
37. **Colot, D., Petelot, D., Hoch, P. and Beranger, G., (1997), Mechanism of Hot Corrosion in Coal Fired Boilers Gas T 91 and Em12 Steels," Mater. Sci. Forum, Vol. 251-54, pp. 641-48.**

38. **Conner, J.A. and Connor W.B., (1994), "Ranking Protective Coatings: Laboratory Vs. Field Experience," JOM, December, pp. 35-38.**
39. **Crawmer, D.C., Krebsback, J.D. and Riggs, W.L., (1992), "Coating Development of HVOF Process Using Design of Experiments," Proc. of the 13th International Thermal Spraying Conference, Florida, pp. 127-136.**
40. **Crook, P. (1993), "Cobalt and Cobalt Alloys," Properties and Selection: Non-Ferrous Alloys and Special-Purpose Materials, In: (10 ed.), Metals Handbook 2, ASM International (1993), p. 446.**
41. **Cuevas-Arteaga, C., Porcayo-Calderon, J., Izquierdo, G., Martinez-Villafane, A. and Gonzalez-Rodriguez, J.G., (2001), "Study of Hot Corrosion of Alloy 800 using Linear Polarization Resistance and Weight Loss Measurement," Mater. Sci. Technol., Vol.17, No. 7, pp. 880-885.**
42. **Cuevas-Arteaga, C., Uruchurtu-Chavarina, J., Porcayo-Calderonb, J., Izquierdo-Montalvob, G. and Gonzaleza, J., (2004), "Study of Molten Salt Corrosion of HK-40m Alloy Applying Linear Polarization Resistance and Conventional Weight Loss Techniques," Corros. Sci., Vol. 46, No.11, pp. 2663-2679.**
43. **Cutler, A.J.B., (1971), "The Effect of Oxygen and SO₃ on Corrosion of Steels in Molten Sulphates," J. Appl. Electrochem, Vol. 1, pp. 19-26.**
44. **Cutler, A.J., (1978), "Fire-Side Corrosion in Power Station Boilers," Central Electricity Generating Board (CEGB) Research Report, London.**
45. **Das, S., Saraswathi, Y.L. and Mondal, D.P., (2005), 'Erosive-Corrosive Wear of Aluminium Alloy Composites: Influence of Slurry Composition and Speed,' Wear, Corrected Proof available on-line.**
46. **De Villiers Lovelock, H.L, Richter, P.W., Benson, J.M. and Young, P.M., (1998), "Parameter Study of HP/HVOF Deposited WC-Co Coatings," J. Therm. Spray Technol., Vol. 7, No. 1, pp. 97-107.**
47. **Deb, D, Iyer, S.R. and Radhakrishnan, V.M., (1996), "A Comparative Study of Oxidation and Hot Corrosion of a Cast Nickel Base Superalloy in Different Corrosive Environments," Mater. Lett., Vol. 29, pp. 19-23.**
48. **DeMasi-Marcin, J.T. and Gupta, D.K., (1994), "Protective Coatings in the Gas Turbine Engine," Surf. Coat. Technol., Vol. 68-69, pp. 1-9.**
49. **Dent, A.H., Horlock, A.J., McCartney, D.G. and Harris, S.J., (2001), "Microstructural Characterisation of a Ni-Cr-B-C Based Alloy Coating Produced by High Velocity Oxy-Fuel Thermal Spraying," Surf. Coat. Technol., Vol. 139, pp. 244-250.**
50. **Dooley, R.B. and Wilson, J.R., (1975), "The Corrosion of 50Cr-50Ni Alloy in Liquid Vanadate Systems in the Temperature Range 750-950⁰C," Trans. ASME, July, pp. 422-428.**

51. **Driver, D., Hall, D.W. and Meetham, G.W., (1981), "The Gas Turbine Engine,"** In: G.W. Meetham, Editor, *The Development of Gas Turbine Materials*, Applied Science Publishers, London, pp. 1-30.
52. **Dube, R.K., (2000), "Spray Atomization and Deposition,"** *J. Mater. Process Tech.*, Vol. 99, No. 1-3, pp. 278-279.
53. **Duh, J.G. and Wang, C.J., (1990), "Formation and Growth Morphology of Oxidation-Induced Ferrite Layer in Fe-Mn-Al-Cr-C Alloys,"** *J. Mater. Sci.*, Vol. 25, No. 4, pp. 2063-2070.
54. **Dwyer, A.L., Jones, S.A., Wykle, R.J., McCaw, B. and Hays, R., (1995), "HVOF Repair of Steering Rams for the USS Saipan,"** *Proc., of the 8th International Thermal Spray Conference*, Houston, pp. 615-620.
55. **Edris, H., McCartney, D.G. and Sturgeon, A.J., (1997), "Microstructural Characterization of High Velocity Oxy-Fuel Sprayed Coatings of Inconel 625,"** *J. Mater. Sci.*, Vol. 32, pp. 863-872.
56. **Eliasz, N., Shemesh, G. and Latanision, R.M., (2002), "Hot Corrosion in Gas Turbine Components,"** *Eng. Fail. Anal.*, Vol. 9, pp. 31-43.
57. **Evans, N.D., Maziasz, P.J., Swindeman, R.W. and Smith, G.D., (2004), "Microstructure and Phase Stability in INCONEL alloy 740 During Creep,"** *Scripta Materialia*, Vol. 51, No. 6, pp. 503-507.
58. **Fairman, L., (1962), "Technical Note: Mechanism of Accelerated Oxidation by Vanadium-Containing Fuel Ash,"** *Corros. Sci.*, Vol. 2, pp. 293-296.
59. **Fantassi, S., Vardelle, M., Fauchais, P. and Moreau, C., (1992), "Investigation of the Splat Formation Versus Different Particulate Temperatures and Velocities Prior to Impact,"** *Proc. of 13th International Thermal Spray Conference*, Florida, USA, pp.755-760.
60. **Fauchais, P., (2004), "Topical Review: Understanding Plasma Spraying,"** *J. Phys. D: Appl. Phys.*, Vol. 37, pp. R86-R108.
61. **Fedrizzi, L., Rossi, S., Cristel, R. and Bonora, P.L., (2004), "Corrosion and Wear Behaviour of HVOF Cermet Coatings Used to Replace Hard Chromium,"** *Electrochim. Acta*, Vol. 49, pp. 2803-2814.
62. **Fryburg, G.C., Kohl, F.J. and Stearns C.A., (1984), "Chemical Reactions Involved in the Initiation of Hot Corrosion of IN-738,"** *J. Electrochem. Soc.*, Vol. 131, No. 12, pp. 2985-96.
63. **Fukuda, Y. and Kumon., M., (1995), "Thermal Spraying, Current Status and Future Trends,"** In: *Proceedings of the 14th International Thermal Spray Conference*, High Temperature Society of Japan, 22-26 May, 1995, Kobe, Japan ASM International, pp. 107-111.

64. **Fukutome, H., Shimizu, H., Yasmashita, N. and Shimizu, Y., (1995), "The Application of Cermet Coating on Piston Ring by HVOF,"** Proceedings of the 14th International Thermal Spray Conference, Kobe, Japan, (1995), pp. 21-26.
65. **Gawne, D.T., Griffiths, B.J. and Dong, G., (1995), "Splat Morphology and Adhesion of Thermally Sprayed Coatings,"** Proceedings of International Thermal Spray Conference (ITSC.95), Kobe, pp. 779-784.
66. **Gil, L. and Staia, M.H., (1999), "Microstructure and Properties of HVOF Thermal Sprayed NiWCrBSi Coatings,"** Surf. Coat. Technol., Vol. 120-121, pp. 423-429.
67. **Gil, L. and Staia, M.H., (2002), "Influence of HVOF Parameters on the Corrosion Resistance of NiWCrBSi Coatings,"** Thin Solid Films, Vol. 420-421, pp. 446-454.
68. **Gitanjaly, Prakash, S. and Singh, S., (2002), "Effects of MgO and CaO on Hot Corrosion of Fe Base Superalloy Superfer 800H in Na₂SO₄-60%V₂O₅ Environment,"** Brit. Corros. J., Vol. 37, No. 1, pp. 56-62.
69. **Gitanjaly, (2003), 'Role of Inhibitors on Hot Corrosion of Superalloys in Na₂SO₄-V₂O₅ Environment,'** Ph.D. Thesis, Met. Mat. Engg. Deptt., Indian Institute of Technology Roorkee, Roorkee, India.
70. **Goebel, J.A. and Pettit, F.S., (1970A), "Na₂SO₄ - Induced Accelerated Oxidation (Hot Corrosion) of Nickel,"** Metall. Trans., Vol. 1, pp. 1943-1954.
71. **Goebel, J.A. and Pettit, F.S., (1970B), "The Influence of Sulphides on the Oxidation Behaviour of Nickel-base Alloys,"** Metall. Trans., Vol.1, pp.3421-3429.
72. **Goebel, J.A., Pettit, F.S. and Goward, G.W., (1973), "Mechanisms for the Hot Corrosion of Nickel-Base Alloys,"** Metall. Trans., Vol. 4, pp. 261-275.
73. **Goward, G.W., (1986), "Overview: Protective Coatings-Purpose, Role, and Design,"** Mater. Sci. Technol., Vol. 2, pp.194-200.
74. **Groshart, E.C., (1995), "Military Aircraft and Aerospace,"** in ASTM, "Corrosion Tests and Standards Manual: Application and Interpretation," American Society for Testing and Materials Society, (1995), pp. 579-581.
75. **Gu, P., Arsenault, B., Beaudoin, J.J., Legoux, J.G., Harvey, B. and Fournier, J., (1998), "Polarization Resistance of Stainless Steel-Coated Rebars,"** Cem. Conc. Res., Vol. 28, No. 3, pp.321-327.
76. **Gudenau, H.W., Bayer, G.T. and Cha, S.C., (2002), "Comparison of Corrosion Behavior of Thermal Sprayed and Diffusion-Coated Materials,"** Mater. Corros., Vol. 53, No. 3, pp. 195-205.
77. **Guilemany, J.M., Cabot, P.L., Fernandez, J., De Paco, J.M. and Sanchez, J., (1997A), Proc. 5th European Conf. on Advanced Materials and Applications (Euromat 97), Maastricht, The Netherlands, April 1997, Fems, ISBN: 90-803513-1-8, Vol.1., pp. 771-774.**

78. **Guilemany, J.M., Fernandez, J. and Delgado, J., (1997B)** "Electrochemical Measurements and Characterisation of a Thermal Sprayed HVOF Cr₃C₂-NiCr Coating in a Corrosive Environment," Proc. of the United Thermal Spray Conference, Düsseldorf, pp. 474-478.
79. **Guilemany, J.M., Fernandez, J., de Paco, J.M. and Sanchez, J., (1998)** "Corrosion Resistance of HVOF WC-Co and TiC/Ni-Ti Coatings Sprayed on Commercial Steel," J. Surf. Engg., Vol. 14, No. 2, pp.133-35.
80. **Guilemany, J.M., Fernandez, J., Delgado, J., Benedetti, A.V. and Climent, F., (2002),** "Effects of Thickness Coating on the Electrochemical Behaviour of Thermal Spray Cr₃C₂-NiCr Coatings," Surf. Coat. Technol., Vol. 153, No. 2-3, pp. 107-113.
81. **Guilemany, J.M., Espallargas, N., Suegama, P.H., Benedetti, A.V. and Fernandez, J., (2005),**"High-velocity Oxyfuel Cr₃C₂-NiCr Replacing Hard Chromium Coatings," J. Therm. Spray Technol., Vol. 14, No. 3, pp.335-341.
82. **Gupta, N., (2003),** "Technical Talk on Cathodic Protection," IIM Metal News, Vol. 16, No.1, pp. 38.
83. **Gurrappa, I., (1999),** "Hot Corrosion Behavior of CM 247 LC Alloy in Na₂SO₄ and NaCl Environments," Oxid. Met., Vol. 51, No. 5, pp. 353-382.
84. **Gurrappa, I., (2001),** "Identification of Hot Corrosion Resistant MCrAlY Based Bond Coatings for Gas Turbine Engine Applications," Surf. Coat. Technol., Vol. 139, No. 2-3, pp. 272-283.
85. **Gurappa, I., (2003),** "Influence of Alloying Elements on Hot Corrosion of Superalloys and Coatings: Necessity of Smart Coatings for Gas Turbine Engines," Mater. Sci. Technol., Vol. 19, pp.178-183.
86. **Halling, J., (1985),** "Introduction: Recent Developments in Surface Coating and Modification Processes," Pub. MEP, London.
87. **Haman, J.D., Lucas, L.C. and Crawmer, D.E., (1995),** "High-Velocity Oxy-fuel Thermal Spray Coatings for Biomedical Applications," J. Therm. Spray. Technol. Vol. 4, No. 2, pp. 179-184.
88. **Hancock, P. and Hurst R.C., (1974),** "The Mechanical Properties and Breakdown of Surface Oxide Films at Elevated Temperatures," in 'Advances in Corrosion Science and Technology,' Vol.4, Eds. Fontana, M.G. and Staehle, R.W., Pub. Plenum Press, New York.
89. **Hancock, P., (1987),** "Vanadic and Chloride Attack of Superalloys," Mater. Sci. Technol., Vol. 3, pp. 536-544.
90. **Harada, Y. and Kawamura, T., (1980),** "Control of Gas Side Corrosion in Oil Fired Boiler," Mitsubishi Heavy Industries Technical Review, Vol. 17, pp. 139.

91. **Harada, Y., Naito, S., Tsuchiya, T. and Nakajima, Y., (1981), "Problems of Low Grade Oil Firing Boilers and Their Solutions," Mitsubishi Heavy Industries- Technical Review, Vol. 18, No. 2, pp. 85-95.**
92. **Harvey, D., Lunder, O. and Henriksen, R., (2000), "The Development of Corrosion Resistant Coatings by HVOF Spraying," Proc. 1st Int. Thermal Spray Conf., Montreal, Canada, May 8-11, 2000, ASM International, pp. 991-997.**
93. **Hawthorne, H.M., Arsenault, B., Immarigeon, J.P., Legoux, J.G. and Parameswaran, V.R., (1999), "Comparison of Slurry and Dry Erosion Behaviour of Some HVOF Thermal Sprayed Coatings," Wear, Vol. 225-229, pp. 825-834.**
94. **Heath, G. R., Heimgartner, P., Irons, G., Miller, R. and Gustafsson, S., (1997), "An Assessment of Thermal Spray Coating Technologies for High Temperature Corrosion Protection," Mater. Sci. Forum, Vol. 251-54, pp. 809-816.**
95. **Helali, M.M. and Hashmi, M.S.J., (1992), "A Comparative Study of Plasma Spraying and High Velocity Oxy-Fuel (HVOF) Thermal Spraying," Proc. of the 10th Conference of the Irish Manufacturing Committee (IMC 10), Galway, Ireland, pp. 377-387.**
96. **Herman, H., Sampath, S. and Mccune, R., (2000), "Thermal Spray: Current Status and Future Trends," MRS Bull, Vol. 25, No. 7, pp.17-25.**
97. **Hidalgo, V.H., Varela, F.J.B. and Rico, E.F., (1997), "Erosion Wear and Mechanical Properties of Plasma-Sprayed Nickel- and Iron-Based Coatings Subjected to Service Conditions in boilers," Tribol. Int., Vol. 30, No. 9, pp. 641-649.**
98. **Hidalgo, V.H., Varela, F.J.B., Martinez, S.P. and Espana, S.G., (1999), "Characterization and High Temperature Behaviour of Cr₃C₂-NiCr Plasma Sprayed Coatings," Proc. of the United Thermal Spray Conf., Germany, pp. 683-686.**
99. **Hidalgo, V.H., Varela, J.B., Calle, J.M. and Menendez, A.C., (2000) "Characterisation of NiCr Flame and Plasma Sprayed Coatings for Use in High Temperature Regions of Boilers," Surface Engg., Vol. 16, No. 2, pp.137-142.**
100. **Hidalgo, V.H., Varela, J.B., Menendez, A.C. and Martinez, S.P., (2001), "High Temperature Erosion Wear of Flame and Plasma Sprayed NiCr Coatings Under Simulated Coal-Fired Boiler Atmospheres, Wear, Vol. 247, pp. 214-222.**
101. **Hocking, M.G., (1993), "Coatings Resistant to Erosive/Corrosive and Severe Environments," Surf. Coat. Technol., Vol. 62, No. 1-3, pp. 460-466.**
102. **Hou, P.Y. and Stringer, J., (1988), "The Influence of Ion-Implanted Yttrium on the Selective Oxidation of Chromium in Co-25wt.% Cr," Oxid. Met., Vol. 29, No. 1-2, pp. 45-73.**

103. **Hwang, Y.S. and Rapp, R.A., (1989), "Thermochemistry and Solubilities of Oxides in Sodium Sulfate-Vanadate Solutions," Corros., Vol. 45, No. 11, pp. 933-937.**
104. **Illavsky, J., Pisacka, J., Chraska, P., Margandant, N., Siegmann, S., Wagner, W., Fiala, P. and Barbezat, G., (2000), "Microstructure-Wear and Corrosion Relationships for Thermally Sprayed Metallic Deposits," Proc. 1st Inter. Thermal Spray Conf., Montreal, Quebec, Canada, May 8-11, pp. 449-454.**
105. **Irons, G. and Zanchuk, V., (1993), "Comparison of MCrAlY Coatings Sprayed by HVOF and Low Pressure Processes," C.C. Berndt (ed.), proc. NTSC, Anaheim, California, 191-197.**
106. **Irving, B., Knight, R. and Smith, R.W., (1993) "The HVOF Process: The Hottest Process in Thermal Spray Technology," Welding J., Vol. 72, pp.25-30.**
107. **Ishikawa, K., Seki, M. and Tobe, S., (1993), "Application of Thermal Spray Coatings to Prevent Corrosion of Construction in Japan," Proc. of the 5th National Thermal Spraying Conference, Anaheim, CA, USA, (1993), pp. 679-684.**
108. **Iyer, S.R., Iyer, K.J.L. and Radhakrishan, V.M., (1987A), "High Temperature Corrosion of a Ni-Base Superalloy by Vanadium," Proc. of 10th ICMC, Madras, India, Vol. IV, pp. 3665-3670.**
109. **Iyer, S.R., Iyer, K.J.L. and Radhakrishan, V.M., (1987B), "Hot Corrosion cracking of Nimonic 80A," High Temp. Technol., Vol. 5, No.3, pp. 145-150.**
110. **Jacobs, L., Hyland, M.M. and De Bonte, M., (1998), "Comparative Study of WC-Cermet Coatings Sprayed Via the HVOF and HVOF Process," J. Therm. Spray Technol., Vol. 7, No. 2, pp. 213-218.**
111. **Jaffee, R.I. and Stringer, J., (1979), "High-Temperature Oxidation and Corrosion of Superalloys in the Gas Turbine (A Review)," In: F. Bradley, Editor, Source book on materials for elevated-temperature applications, ASM, Metals Park (1979), pp. 19-33.**
112. **Jarosinski, W.J., Gruninger, M.F. and Londry, C.H., (1993), "Characterisation of Tungsten Carbide Cobalt Powder and HVOF Coatings," Proc. of the 5th National Thermal Spray Conference, California, pp. 153-158.**
113. **Kanouff, M.P., Neiser, R.A. Jr. and Roemer, T. J., (1998), "Surface Roughness of Thermal Spray Coatings Made with Off-Normal Spray Angles," J. Therm. Spray Technol., Vol. 7 (2), pp.219-228.**
114. **Kapoor, M.L., (1991), "Theory of Electrochemical Processes," Proc. Corrosion and Cathodic Protection, Metallurgical and Materials engineering Department, University of Roorkee, May 20-24, 1991, pp. 18-25.**
115. **Kawahara, Y., (1997), "Development and Application of High Temperature Corrosion-Resistant Materials and Coatings for Advanced Waste-to-Energy Plants," Mater. High Temp., Vol.14, No. 3, pp. 261-268.**

116. **Kawakita, J., Kuroda, S., Fukushima, T. and Kodama, T., (2003),** "Development of Dense Corrosion Resistant Coatings by an Improved HVOF Spraying Process," *Surf. Coat. Technol.*, Vol. 4, pp. 281-289.
117. **Kawase, R. and Nakano, A., (1996),** "Production of Heat and Corrosion-Resistant Plastic Coatings," *Proc. of the 9th National Thermal Spray Conference, Cincinnati, Ohio*, pp. 257-262.
118. **Kerby, R.C. and Wilson J.R., (1972),** "Electrical Conduction Properties of Liquid Vanadates.II. The Sodium Vanadates," *Canadian Journal of Chemistry*, Vol. 58, pp. 2871-2876.
119. **Kerby, R.C. and Wilson J.R., (1973),** "Corrosion of Metals by Liquid Vanadium Pentoxide and the Sodium Vanadates," *Trans. ASME*, January, pp. 36-44.
120. **Khanna, A.S. and Jha, S.K., (1998),** "Degradation of Materials Under Hot Corrosion Conditions," *T. Indian I. Metals*, Vol. 51, No. 5, pp. 279-290.
121. **Kinos, T., Siitonen, P., Kettunen, P. and Laurila, V.J., (1994),** "Thermal Spray Industrial Applications," *Proc. of the National Thermal Spray Conference*, Vol. 7, pp. 537-40.
122. **Knight, R., Smith, R.W., Xiao, Z. and Hoffman, T.T., (1994),** "Particle Velocity Measurements in HVOF and APS Systems," *Proc. 7th National Thermal Spray Conf. [NTSC '94], ASM Int., Boston, MA*. pp. 331-336.
123. **Knotek, O., Lugscheider, E. and Reimann, H., (1975),** "Structure of Ni-rich Ni-Cr-B-Si Coating Alloys," *J. Vac. Sci. Technol.*, Vol. 12, No. 4, pp. 770-772.
124. **Knotek, O., (2001),** "Chapter 3: Thermal Spraying and Detonation Spray Gun Processes," in 'Handbook of Hard Coatings: Deposition Technologies, Properties and Applications,' Ed. Bunshah, R. F., Noyes Pub. Park Ridge, New Jersey, U. S. A./William Andrew Publishing, LLC, Norwich, New York, U.S.A., pp. 77-107.
125. **Koch, G.H., Brongers, M.P.H., Thompson, N.G., Virmani, Y.P. and Payer, J. H., (2002),** "Historic Congressional Study: Corrosion Costs and Preventive Strategies in the United States," *Supplement to Mater. Perfor.*, July, pp. 1-11.
126. **Kofstad, P., (1988),** "Chapter 14" in 'High Temperature Corrosion,' Elsevier Applied Science, London & New York, pp. 495-496.
127. **Kofstad, P., (1990),** "High Temperature Corrosion of Metals," *Microscopy of Oxidation, Proc. Conf., London*, pp. 1-9.
128. **Kolta, G.A., Hewaidy, L.F. and Felix, N.S., (1972),** "Reactions Between Sodium Sulphate and Vanadium Pentoxide," *Thermochim. Acta*, Vol. 4, pp. 151-164.
129. **Kong, G., Zhang, D., Brown, P.D., McCartney, D.G. and Harris, S.J., (2003),** "Microstructural Characterisation of HVOF Thermally Sprayed Stellite 6," *Mater. Sci. Technol.*, Vol. 19, pp.1003-1011.

130. **Kowalsky, K.W., Marantz, D.R., Smith, M.F. and Oberkamp, W.L., (1991),** In: T.F. Bernecki (ed.), *Thermal Spray Research and Applications*, ASM International, Ohio. pp. 587-592.
131. **Kreye, H., (1997),** "Proceedings of 4th Conference HVOF Spraying, German Thermal Spray Society, HÖllriegelskreuth, pp. 13-21.
132. **Krishna, B.V. and Sidhu R.K., (2002),** "Pitting Corrosion of Steel Tubes in an Air Preheater" *Practical Failure Analysis*, ASM International, Vol. 2, No. 5, pp. 61-66.
133. **Lambert, P., Champagne, B. and Arseneault, B., (1991),** "Oxidation and Hot Corrosion in Na₂SO₄-10%V₂O₅ of Ni-17Cr-6Al-0.5Y and Ni-16Cr-5.7Al-0.47Y-5Si, MCrAlY Alloys at 700^oC," *Can. Metall. Quart.*, Vol. 30, No. 2, pp. 125-130.
134. **Lebailly, S. and Hamar, S., (1987),** "Thibault S. Equilibres Liquide-Solide Dans Le Systemr Ni-B-Si Dans la Region Riche en Nickle," *Acta Metall* Vol. 35, No. (3), pp. 701-710, in French.
135. **Lee, C.H. and Min, K.O., (2000),** "Effects of Heat Treatment on the Microstructure and Properties of HVOF-Sprayed Ni-Cr-W-Mo-B Alloy Coatings," *Surf. Coat. Technol.*, Vol.132, No. 1, pp. 49-57.
136. **Lee, W.H. and Lin, R.Y., (2003)** "Hot Corrosion Mechanism of Intermetallic Compound Ni3Al," *Mater. Chem. Phys.*, Vol. 77, No. 1, pp. 86-96.
137. **Levy, A.V., (1993),** "The Erosion-Corrosion of Tubing Steels in Combustion Boiler Environments," *Corros. Sci.*, Vol.35, No. 5-8, pp. 1035-43.
138. **Li, C.-J., Wang, Y.-Y. and Ohmori, A., (2000),** "Effect of Melting State of Spray Particles on the Adhesion Strength of HVOF Nickel-Based Alloy Coatings," *Thermal Spray Surface Engineering via Applied Research: Proc. Int. Therm. Spray Conf., Montreal, QUE, United States, ASM International, May 8-11, pp. 791-796.*
139. **Li, M. H., Sun, X. F., Li, J. G., Zhang, Z. Y., Jin, T., Guan, H.R. and Hu, Z. Q., (2003),** "Oxidation Behaviour of a Single-Crystal Ni-Base Superalloy in Air-I: At 800 and 900^oC," *Oxid. Met.*, Vol. 59, No. 5-6, pp.591-605.
140. **Li, B. and Gleeson, B., (2004),** "Effects of Minor Elements on the Cyclic-Oxidation Behavior of Commercial Fe-Base 800-Series Alloys," *Oxid. Met.*, Vol. 62, No. 1-2, pp. 45-69.
141. **Lianyong, X., Hongyang, J. and Lixing, Huo, (2005),** "High-temperature Corrosion of Protective Coatings for Boiler Tubes in Thermal Power Plants," *Trans. of Tianjin University*, Vol. 11, No. 3, pp.183-189.
142. **Liao, H., Normand, B. and Coddet, C., (2000),** "Influence of Coating Microstructure on the Abrasive Wear Resistance of WC/Co Cermet Coatings," *Surf. Coat. Technol.*, Vol. 124, pp. 235-242.

143. **Link, R. J., Birks, N., Pettit, F. S. and Dethorey, F., (1998), "The Response of Alloys to Erosion-Corrosion at High Temperatures,"** *Oxid. Met.*, Vol. 49, No. 3-4, pp. 213-36.
144. **Liu, Z., Gao, W., Dahm, K. L. and Wang, F., (1998), "Oxidation Behaviour of Sputter-Deposited Ni-Cr-Al Micro-Crystalline Coatings,"** *Acta Mater.*, Vol. 46, No. 5, pp. 1691-1700.
145. **Liu, P.S., Liang, K.M. and Gu, S.R., (2001), "High-temperature Oxidation Behavior of Aluminide Coatings on a New Cobalt-base Superalloy in air,"** *Corros. Sci.*, Vol. 43, pp. 1217-1226.
146. **Longa-Nava and Takemoto, M., (1992), "High-Temperature Corrosion of Laser-Glazed Alloys in Na₂SO₄-V₂O₅,"** *Corros.*, Vol. 48, No. 7, pp. 599-607.
147. **Longa-Nava, Y., Zhang, Y.S., Takemoto, M. and Rapp, R.A., (1996), "Hot Corrosion of Nickel-Chromium and Nickel-Chromium-Aluminum Thermal-Spray Coatings by Sodium Sulfate-Sodium Metavanadate Salt,"** *Corros.*, Vol. 52, No. 9, pp. 680-689.
148. **Lovelock, H.L. de V., Kinds, J. and Young, P.M., (1998), "Characterisation of WC-12Co Thermal Spray Powders and HPHVOF Wear Resistant Coatings,"** *Powder Metall.*, Vol. 41, No. 4, pp. 292-299.
149. **Lugscheider, E., Herbst, C. and Zhao, L., (1998), "Parameter Studies on High-Velocity Oxy-Fuel Spraying of MCrAlY Coatings,"** *Surf. Coat. Technol.*, Vol.108-109, pp. 16-23.
150. **Luthra, K.L. and Spacil, H.S., (1982), "Impurity Deposits in Gas Turbines from Fuels Containing Sodium and Vanadium,"** *J. Electrochem. Soc.*, Vol.129, No. 3, pp. 649-656.
151. **Luthra, K.L., (1983), "Mechanisms of Low Temperature Hot Corrosion,"** in 'High Temperature Corrosion,' Houston, NACE, Ed. Rapp, R.A., pp. 507-518.
152. **Luthra, K.L., (1985), "Kinetics of the Low Temperature Hot Corrosion of Co-Cr-Al Alloys,"** *J. Electrochem. Soc.*, Vol. 132, No. 6, pp. 1293-1298.
153. **Marasco, A.L. and Young, D.J., (1991), "The Oxidation of Iron-Chromium-Manganese Alloys at 900°C,"** *Oxid. Met.*, Vol.36, No. 1-2, pp.157-174.
154. **Marceau, J.A. and Adjorlolo, A.A., (1995), "Commercial Aircraft,"** in ASTM, "Corrosion Tests and Standards: Application and Interpretation." American Society for Testing and Materials Society, (1995), pp. 574-578.
155. **Matsubara, Y. and Tomiguchi, A., (1992), ".Surface Texture and Adhesive Strength of High Velocity Oxy-Fuel Sprayed Coatings for Rolls of Steel Mills,"** *Proc. of 13th Int. Therm. Spray Conf., Florida, USA, (1992), pp. 637-645.*
156. **Matthews, A., Leyland, A., Dorn, B., Stevenson, P.R., Bin-Sudin, M., Rebholz, C., Voevodin, A. and Schneider, J., (1995), Plasma-based Surface Engineering Processes for Wear and Corrosion Protection, J. Vac. Sci. Technol. A, (Vacuum, Surfaces, and Films), Vol. 13, No.3, pp. 1202-1207.**

157. **Matthews, A., Artley, R.J. and Holiday, P., (1998), "Future's Bright for Surface Engineering," Mater.World, Vol. 6, pp. 346-347.**
158. **Metals Handbook, (1972), "Atlas of Microstructures of Industrial Alloys," Vol. 7, ASM Publication, Metals Park OH, USA.**
159. **Metals Handbook, (1975), "Failure analysis and Prevention," Vol.10, ASM Publication, Metals Park OH, USA.**
160. **Metals Handbook, (1990), "Properties and Selection: Iron, Steels, and High-Performance Alloys, 10th Edition," Vol.1, ASM Publication, Metals Park Ohio. pp. 981.**
161. **Mevrel, R., (1989), State of the Art on High-Temperature Corrosion-Resistant Coatings," Mater. Sci. Engg. A, Vol. 120, pp.13-24.**
162. **Meyer, P.J., (1995), In: A. Ohmori (ed), Proc. ITSC, Kobe, Japan, pp 217-222.**
163. **Miguel, J.M., Guilemany, J.M. and Vizcaino, S., (2003), "Tribological Study of NiCrBSi Coating Obtained by Different Processes," Tribol. Int., Vol. 36, No. 3, pp. 181-187.**
164. **Misra, A.K., (1986), "Mechanism of Na₂SO₄-Induced Corrosion of Molybdenum Containing Nickel-Base Superalloys at High Temperatures," J. Electrochem. Soc., Vol. 133, No. 5, pp. 1029-1037.**
165. **Modi, S.C. and Calla, Eklavya, (2001), "Structure and Properties of HVOF Sprayed NiCrBSi Coatings," Thermal Spray 2001: New Surfaces for New Millennium, ASM International, Materials Park, Ohio, USA, pp. 281-284.**
166. **Moreau, C., Cielo, P., Lamontagne, M., Dallaire, S., Krapez, J.C. and Vardelle, M., (1991), "Temperature Evolution of Plasma-Sprayed Niobium Particles Impacting on a Substrate," Surf. Coat. Technol., Vol. 46, pp. 173-181.**
167. **Moreau, C., Cielo, P. and Lamontagne, M., (1992), "Flattening and Solidification of Thermal Sprayed Particles," Proc. of 13th Int. Therm. Spray Conf., Florida, USA, pp. 761-766.**
168. **Moskowitz, L.N., (1992), "Application of HVOF Thermal Spraying to Solve Corrosion Problems in the Petroleum Industry," Proc. of 13th Int. Therm. Spray Conf., Florida, USA, (1992), pp. 611-618.**
169. **Moujahid, S.E., (1987), "High Temperature Corrosion of Cast Iron Chains by Coal Ash," Proc. of 10th ICMC, Madras, India, Vol. 1, pp. 857-60.**
170. **Murthy, J.K.N. and Venkataraman, B., (2004), "Abrasive Wear Behaviour of WC-CoCr and Cr₃C₂-20(NiCr) Deposited by HVOF and Detonation Spray Processes," Surf. Coat. Technol., Vol. 200, No.8, pp. 2642-2652.**
171. **Nakagawa, P.M., Kawakami, F. and Kudoh, T., (1994) "Trends in Automotive Applications of Thermal Spray Technology in Japan." Proc. of the 7th National Therm. Spray Conf., Boston, pp. 1-6.**

172. Natesan, K., (1976), "Corrosion-Erosion Behavior of Materials in a Coal-Gasification Environment," *Corros.*, Vol. 32, No. 9, pp. 364-370.
173. Natesan, K., (1980), *Proc. Symp. Corrosion-Erosion Behavior of Materials, Fall Meeting of TMS-AIME, October 1987*, K. Nagtesan, Ed., AIME, New York, p. 1.
174. Natesan, K., (1985), "High-Temperature Corrosion in Coal Gasification Systems," *Corros.*, Vol. 41, No. 11, pp. 646-655.
175. Natesan, K., (1993), "Applications of Coatings in Coal-Fired Energy Systems," *Surf. Coat. Technol.*, Vol. 56, pp. 185-197.
176. National Materials Advisory Board, (1996), "Coatings for High-Temperature Structural Materials: Trends and Opportunities," National Academy Press Washington D.C., <http://www.nap.edu/openbook/0309053811/html>, pp 1-85.
177. Nelson, H.W., Krause, H.H., Ungar, E.W., Putnam, A.A., Slunder, C.J., Miller, P.D., Hummel, J.D. and Landry, B.A., (1959), "Corrosion and Deposition in Coal- and Oil-Fired Boilers and Gas Turbines," A Report of ASME Research Committee on Corrosion and Deposits from Combustion Gases, published by Pergamon Press, New York and ASME, New York, pp. 1-77.
178. Nguyentat, T., Dommer, K.T. and Bowen, K.T., (1992), "Metallurgical Evaluation of Plasma Sprayed Structural Materials for Rocket Engines," *Proc. of 13th Int. Therm. Spray Conf., Florida, USA*, pp. 321-326.
179. Nicholls, J.R. and Stephenson, D.J., (1991), "High Temperature Coatings for Gas Turbines," *Surf. Engg.*, Vol. 22, pp. 156-163.
180. Nicholls, J.R. and Stephenson, D.J., (1995), "Ch. 22: High-Temperature Coatings for Gas Turbines," in 'Intermetallic Compounds, Principles and Practice, Vol. 2-Practice,' Eds. Westbrook, J.H. and Fleischer, F.L., Pub. John Wiley & Sons Ltd., England.
181. Nicholls, J.R., (2000), "Designing Oxidation-Resistant Coatings," *JOM*, January, pp. 28-35.
182. Nicoll, A.R. and Wahl, G., (1983), "The Effect of Alloying Additions on MCrAlY Systems-An Experimental Study," *Thin Solid Films*, Vol. 95, pp.21-34.
183. Nicoll, A. R., (1984), "Chapter 13: The Production and Performance Evaluation of High Temperature Coatings," in 'Coatings and Surface Treatment for Corrosion and Wear Resistance,' Eds. Strafford, K. N., Datta, P. K. and Googan, C. G., (1984), Institution of Corros. Sci. and Techol., Birmingham, Pub. Ellis Horwood Ltd., Chichester.
184. Nicoll, A.R., (1994), "Production Plasma Spraying in the Automotive Industry: A European Viewpoint," *Proc. of the 7th National Therm. Spray Conf., Boston*, pp. 7-17.

185. **Niranaatlumpong, P., Ponton, C.B. and Evans, H.E., (2000), "The Failure of Protective Oxides on Plasma-Sprayed NiCrAlY Overlay Coatings,"** *Oxid. Met.*, Vol. 53, No. 3-4, pp. 241-58.
186. **Otero, E., Merino, M.C., Pardo, A., Biezma, M.V. and Buitrago, G., (1987), "Study on Corrosion Products of IN657 Alloy in Molten Salts,"** *Proc. of 10th ICMC, Madras, India, Vol. IV,* pp. 3583-3591.
187. **Otero, E., Pardo, A., Hernaez, J. and Perez, F.J., (1990), "The Hot Corrosion of IN-657 Superalloy in Na₂SO₄-V₂O₅ Melt Eutectic,"** *Corros. Sci.*, Vol. 30, pp. 677-683.
188. **Otsubo, F., Era, H. and Kishitake, K., (2000), "Structure and Phases in Nickel-Base Self-Fluxing Alloy Coating Containing High Chromium and Boron." J. Therm. Spray Technol., Vol. 91** pp. 107-113.
189. **Otsuka, N and Rapp, R.A., (1990), "Hot Corrosion of Preoxidized Ni by a Thin Fused Na₂SO₄ Film at 900^oC" J. Electrochem. Soc., Vol. 137,** pp. 46-52.
190. **Otsuka, N, (2002), "Effects of Fuel Impurities on the Fireside Corrosion of Boiler Tubes in Advanced Power Generating Systems-A Thermodynamic Calculation of Deposit Chemistry,"** *Corros. Sci.*, Vol. 44, No. 2, pp. 265-283.
191. **Pantony, D.A. and Vasu, K.I., (1968A), "Studies in the Corrosion of Metals under Melts-I. Theoretical Survey of Fire-Side Corrosion of Boilers and Gas-Turbines in the Presence of Vanadium Pentoxide,"** *J. Inorg. Nucl. Chem.*, Vol. 30, pp. 423-32.
192. **Pantony, D.A. and Vasu, K.I., (1968B), "Studies in the Corrosion of Metals under Melts-III,"** *J. Inorg. Nucl. Chem.*, Vol. 10, pp. 755-79.
193. **Parker, D.W. and Kutner, G. L., (1991), "HVOF-Spray Technology-Poised for Growth,"** *J. Adv. Mater. Process.*, Vol. 139, No.4, pp. 68-72, 74.
194. **Paul, L.D. and Seeley, R.R., (1991), "Oil Ash Corrosion- A Review of Utility Boiler Experience,"** *Corros.*, Vol. 47, No. 2, pp. 152-159.
195. **Pawlowski, L., (1995), "The Science and Engineering of Thermal Spray Coatings,"** Wiley, New York, 1995.
196. **Perkin Elmer, (1989A), "Diamond Jet System and Gun Manual,"** Metco, 1989.
197. **Perkin Elmer, (1989 B), "METCO Thermal Spraying: General Overview,"**
198. **Peters, K.R., Whittle, D.P. and Stringer, J., (1976), "Oxidation and Hot Corrosion of Nickel-Based Alloys Containing Molybdenum,"** *Corros. Sci.*, Vol. 16, pp. 791-804.
199. **Pettit, F.S. and Meier, G.H., (1985), "Oxidation and Hot corrosion of Superalloys,"** *Superalloys 85*, Eds. Gell, M., Kartovich, C.S., Bricknel, R.H., Kent W.B. and Radovich, J. F., Met. Soc. of AIME, Warrendale, Pennsylvania, pp. 651-687.

200. **Pettit, F.S. and Giggins, C.S.**, (1987), "Hot Corrosion, Ch. 12," in 'Superalloys II,' Eds. Sims, C. T., Stoloff, N. S. and Hagel, W. C., Pub. Wiley Pub., N. Y.
201. **Planche, M.P., Liao, H., Normand, B. and Coddet, C.**, (2005), "Relationships Between NiCrBSi Particle Characteristics and Corresponding Coating Properties Using Different Thermal Spraying Processes," *Surf. Coat. Technol.*, Vol. 200, No. 7, pp. 2465-2473.
202. **Pomeroy, M.J.**, (2005), "Coatings for Gas Turbine Materials and Long Term Stability Issues," *Mater. Design*, Vol. 26, pp. 223-231.
203. **Porcayo-Calderon, J., Gonzalez-Rodriguez, J.G. and Martinez, L.**, (1998), "Protection of Carbon Steel against Hot Corrosion using Thermal Spray Si- and Cr-Base Coatings," *J. Mater. Eng. Perform.*, Vol. 7, pp. 79-87.
204. **Prakash, S., Singh, S., Sidhu, B. S. and Madeshia, A.**, (2001), "Tube Failures in Coal Fired Boilers," *Proc. National Seminar on Advances in Material and Processing*, Nov., 9-10, IITR, Roorkee, India, pp. 245-253.
205. **Prakash, S., Puri, D. and Singh, H.**, (2005), "Hot Corrosion Behaviour of Plasma Sprayed Coatings on a Ni-Based Superalloy in Na₂SO₄ -60%V₂O₅ environment," *ISIJ Int.*, Vol.45, No.6, pp. 886-895.
206. **Priyantha, N., Jayaweera, P., Sanjurjo, A., Lau, K., Lu, F. and Krist, K.**, (2003), "Corrosion-Resistant Metallic Coatings for Applications in Highly Aggressive Environments," *Surf. Coat. Technol.*, Vol. 163-64, pp. 31-36.
207. **Provot, X., Burlet, H., Vardayoulias, M., Jeandin, M. and Richard, C.**, (1993), "Comparative Studies of Microstructures, Residual Stress Distributions and Wear Properties for HVOF and APS WC-Co Coatings of Ti₆Al₄V," *Proc. of NTSC, Anaheim, USA*, pp. 159-166.
208. **Rapp, R.A., Devan, J.H., Douglass, D.L., Nordine, P.C., Pettit, F.S. and Whittle, D.P.**, (1981A), "High Temperature Corrosion in Energy Systems," *Mater. Sci. Engg.*, Vol. 50, pp. 1-17.
209. **Rapp, R.A. and Goto, K.S.**, (1981B), "The Hot Corrosion of Metals by Molten Salts," In: J. Braunstein and J.R. Selman, Editors, *Proceedings of the Second International Symposium on Molten Salts*, Vol. 81, No.10, The Electrochemical Society, Pennington, pp. 159-177.
210. **Rapp, R.A.**, (1986), "Chemistry and Electrochemistry of the Hot Corrosion of Metals," *Corros.*, Vol. 42, No. 10, pp. 568-577.
211. **Rapp, R.A.**, (1990), "Hot Corrosion of Materials," *Pure and Appl. Chem.*, Vol. 62, No. 1, pp. 113-122.
212. **Rapp, R.A.**, (2002), "Hot Corrosion of Materials: A Fluxing Mechanism," *Corros. Sci.*, Vol. 44, No. 2, pp. 209-221.
213. **Russo, L. and Dorfmann, M.**, (1995), "Thermal Spraying: Current Status and Future Trends," *High Temperature Society of Japan*, p. 681.

214. **Sadique, S.E., Mollah, A.H., Islam, M.S., Ali, M.M., Megat, M.H.H. and Basri, S., (2000), "High-Temperature Oxidation Behavior of Iron-Chromium-Aluminum Alloys,"** *Oxid. Met.*, Vol. 54, Nos. 5-6, pp. 385-400.
215. **Salmenoja, K., Mäkelä, K., Hupa, M. and Backman, R. (1996) "Superheater Corrosion in Environments Containing Potassium and Chlorine, J Inst Energy,"** Vol. 69, pp. 155–162.
216. **Sampath, S. and McCune, R., (2000), "Thermal-Spray Processing of Materials,"** *MRS Bulletin*, Vol.25, No. 7. pp. 12-16.
217. **Santorelli, R., Sivieri, E. and Reggiani, R.C., (1989), "High-Temperature Corrosion of Several Commercial Fe–Cr–Ni Alloys Under a Molten Sodium Sulphate Deposit in Oxidizing Gaseous Environments,"** *Mater. Sci. Eng. A* Vol. 120, pp. 283–291.
218. **Saunders, S.R.J. and Nicholls, J.R., (1984), "Hot Salt Corrosion Test Procedures and Coating Evaluation,"** *Thin Solid Films*, Vol. 119, pp. 247-269.
219. **Saunders, S. R. J., Gohil, D. D., Banks, J. P., Sheriff, M. U., Tortorelli, P. F., Van, J. H. D. and Wright, I. G., (1997), "Behaviour of FeCr Alloy and Iron Aluminides Alloys in Coal Gasification Atmospheres Containing HCl,"** *Mater. Sci. Forum*, Vol. 251-254, pp. 583-590.
220. **Schmidt, R. D. and Ferriss, D. P., (1975), "New Materials Resistant to Wear and Corrosion to 1000⁰C,"** *Wear*, Vol. 32, pp. 279-289.
221. **Seal, S., Roy, S.K., Bose, S.K. and Kuiry, S.C., (2000), "Ceria-Based High-Temperature Coatings for Oxidation Prevention,"** *JOM-e*, 52 (1) (2000)
222. **Seiersten, M. and Kofstad, P., (1987), "The Effect of SO₃ on Vanadate-Induced Hot Corrosion,"** *High Temp. Technol.*, Vol. 5, No. 3, pp. 115-122.
223. **Seong, B.G., Hwang, S.Y. and Kim, K.Y., (2000), "High-Temperature Corrosion of Recuperators Used in Steel Mills,"** *Surf. Coat. Technol.*, Vol. 126, No. 2-3, pp. 256-265.
224. **Seybolt, A.U., (1968), "Hot Corrosion Mechanism,"** *Trans. TMS-AIME*, Vol. 242, pp. 1955-1961.
225. **Sharma, R.N., (1996), "Hot Corrosion Behaviour of Iron- and Nickel-Base Superalloys in Salt Environments at Elevated Temperatures,"** Ph. D. Thesis, Met. Mat. Engg. Deptt., University of Roorkee, Roorkee, India.
226. **Shifler, David A, (2004), "Substrate-Coating Interactions and Their Effects on Hot Corrosion Resistance,"** *Proc. Electrochemical Society*, v PV 2004-16, High Temperature Corrosion and Materials Chemistry V-International Symposium, Electrochemical Society Inc., Pennington, NJ 08534-2896, United States, Oct 3-8, 2004, pp. 294-305.
227. **Shih, S., Zhang, Y. and Li, X., (1989), "Sub-Melting Point Hot Corrosion of Alloys and Coatings,"** *Mater. Sci. Eng. A-Struct.*, Vol. 120, pp. 277-282.

228. **Sidhu, B.S. and Prakash, S., (2003), "Evaluation of the Corrosion Behaviour of Plasma-Sprayed Ni₃Al Coatings on Steel in Oxidation and Molten Salt Environments at 900⁰C," Surf. Coat. Technol., Vol. 166, pp. 89-100.**
229. **Sidhu, B.S., Puri, D. and Prakash, S., (2004), "Characterisations of Plasma Sprayed and Laser Remelted NiCrAlY Bond Coats and Ni₃Al Coatings on Boiler Tube Steels," Mater. Sci. Eng. A-Struct., Vol. 368, No. 1-2, pp. 149-158.**
230. **Sidhu, B.S., Puri, D. and Prakash, S., (2005A), "Mechanical and Metallurgical Properties of Plasma Sprayed and Laser Remelted Ni-20Cr and Stellite-6 Coatings," J. Mater. Process. Technol., Vol. 159, No. 3, pp. 347-355.**
231. **Sidhu, T.S., Prakash, S. and Agrawal, R.D., (2005B), "State of the Art of HVOF Coating Investigations-A Review," Marine Technol. Soc. J., Vol. 39, No.2, pp. 55-66.**
232. **Sidhu, T.S., Agrawal, R.D. and Prakash, S., (2005C), Studies on the Properties of High Velocity Oxy Fuel Thermal Spray Coatings for Higher Temperature Applications," Physicochemical Mechanics of Materials, Vol. 41 No.6, pp. 80-95.**
233. **Sidhu, T.S, Agrawal, R.D. and Prakash, S., (2005D) "Hot Corrosion of Some Superalloys and Role of High-Velocity Oxy-Fuel Spray Coatings—A Review," Surf. Coat. Technol., Vol. 198, pp. 441-446.**
234. **Sidhu, T.S., Prakash, S. and Agrawal, R.D., (2005E) "Studies of the Metallurgical and Mechanical Properties of High Velocity Oxy-Fuel Sprayed Stellite-6 Coatings on Ni and Fe- Based Superalloys," Surf. Coat. Technol., In Press, Available online.**
235. **Sidhu, T.S., Prakash, S. and Agrawal, R.D., (2006A), "Hot Corrosion Behaviour of HVOF Sprayed NiCrBSi Coatings on Ni- and Fe- Base Superalloys in Na₂SO₄-60%V₂O₅ Environment at 900⁰C," Acta Materialia, Vol. 54, No. 3, pp. 773-784.**
236. **Sidhu, T.S., Agrawal, R.D. and Prakash, S., (2006B), "Performance of High Velocity Oxy-Fuel Sprayed Coatings on a Fe-Based Superalloy in Na₂SO₄-60%V₂O₅ Environment at 900⁰C. Part I: Characterisation of the coatings," J. Mater. Engg. Perform., Vol. 15, No. 1, pp. 122-129.**
237. **Sidhu, T.S., Agrawal, R.D. and Prakash, S., (2006C), "Performance of High Velocity Oxy-Fuel Sprayed Coatings on a Fe-Based Superalloy in Na₂SO₄-60%V₂O₅ Environment at 900⁰C. Part II: Hot Corrosion Behaviour of the Coatings," J. Mater. Engg. Perform., Vol. 15, No. 1, pp. 130-138.**
238. **Sidhu, T.S., Prakash, S. and Agrawal, R.D., (2006D), "Characterisations of HVOF Sprayed NiCrBSi Coatings on Ni- and Fe- Based Superalloys and Evaluation of Cyclic Oxidation Behaviour of Some Ni-Based Superalloys in Molten Salt Environment," Thin Solid Films, In Press, Available on-line.**

239. **Sidhu, T.S., Prakash, S. and Agrawal, R.D., (2006E), "Hot Corrosion Resistance of HVOF Sprayed Coatings on a Ni-Based Superalloy in Molten Salt Environment" J. Therm. Spray Technol., Accepted for publication.**
240. **Sidhu, T.S., Prakash, S. and Agrawal, R.D., (2006F), "Hot Corrosion Studies of HVOF sprayed Cr₃C₂-NiCr and Ni-20Cr Coatings on Nickel Based Superalloy at 900°C," Surf. Coat. Technol., In press, Available on-line**
241. **Sidhu, T.S., Prakash, S. and Agrawal, R.D., (2006G), "Characterisation of NiCr Wire Coatings on Ni- and Fe- Based Superalloys by the HVOF Process, Surf. Coat. Technol., Vol. 200, No. 18-19, pp. 5542-5549.**
242. **Sidhu, T.S., Prakash, S. and Agrawal, R.D., (2006H), Hot Corrosion Performance of a NiCr Coated Ni-based Alloy, Scripta Materialia, Accepted for publication**
243. **Sidhu., B.S. and Prakash, S., (2006I), "Studies on the Behaviour of Stellite-6 as Plasma Sprayed and Laser Remelted Coatings in Molten Salt Environment at 900 °C Under Cyclic Conditions," J. Mater. Process. Technol., Vol.172, No. 1, pp. 52-63.**
244. **Sidhu., B.S. and Prakash, S., (2006J), "Erosion-Corrosion of Plasma As-Sprayed and Laser Remelted Stellite-6 Coatings in a Coal Fired Boiler," Wear, In Press, Available online.**
245. **Sidhu, H.S., Sidhu, B.S. and Prakash, S., (2006K), "The Role of HVOF Coatings in Improving Hot Corrosion Resistance of ASTM-SA210 GrA1 Steel in the Presence of Na₂SO₄-V₂O₅ Salt Deposits, Surf. Coat. Technol., Vol. 200, No. 18-19, pp. 5386-5394.**
246. **Sidhu, T.S., Prakash, S. and Agrawal, R.D., (2006L), "Hot Corrosion Studies of HVOF NiCrBSi and Stellite-6 Coatings on a Ni-Based Superalloy in an Actual Industrial Environment of a Coal Fired Boiler," Surf. Coat. Technol., In Press, Available On-Line.**
247. **Sidky, P.S. and Hocking, M.G., (1987), "The Hot Corrosion of Ni-Based Ternary Alloys and Superalloys for Application in Gas Turbines Employing Residual Fuels," Corros. Sci., Vol. 27, No. 5, pp. 499-530.**
248. **Sidky, P.S. and Hocking, M.G., (1999), "Review of Inorganic Coatings and Coating Processes For Reducing Wear and Corrosion," Brit. Corros. J., Vol. 34, No. 3, pp. 171-183.**
249. **Simons, E.L., Browning, G.V. and Liebhatzky, H.A., Corrosion 11 (1955) 505.**
250. **Sims, C.T., Stoloff, N.S., Hagel, W.C., (1987) "The superalloys," John Wiley and Sons, Inc, New York.**
251. **Singh, P. and Birks, N., (1979), "Attack of Co-Cr Alloys by Ar-SO₂ Atmospheres," Oxid. Met., Vol. 13, pp. 457-474.**

252. **Singh, B.**, (2003A), "Studies on the Role of Coatings in Improving Resistance to Hot Corrosion and Degradation," Ph.D. Thesis, Met. & Mat. Eng. Dept., Indian Institute of Technology Roorkee, Roorkee.
253. **Singh, I.B.**, (2003B), "Corrosion and Sulphate Ion Reduction Studies on Ni and Pt Surfaces in With and Without V₂O₅ in (Li,Na,K)₂SO₄ Melt," Corros. Sci., Vol. 45, No. 10, pp. 2285-2292.
254. **Singh, H., Puri, D. and Prakash, S.**, (2005C), "Some Studies on Hot Corrosion Performance of Plasma Sprayed Coatings on a Fe-Based Superalloy," Surf. Coat. Technol., Vol. 192, No. 1, pp. 27-38.
255. **Singh, H., Puri, D. and Prakash, S.**, (2005D), "Corrosion Behaviour of Plasma Sprayed Coatings on a Ni-base Superalloy in Na₂SO₄-60%V₂O₅ Environment at 900°C," Metall. Mater. Trans. A, Vol. 36, No 4, pp. 1007-1015.
256. **Singh, H.**, (2005E), "Hot corrosion Studies of Plasma Sprayed Coatings over Some Ni- and Fe- Based Superalloys," Ph.D. Thesis, Met. & Mat. Eng. Dept., Indian Institute of Technology Roorkee, Roorkee.
257. **Smeggil, J.G. and Bornstein, N.S.**, (1983), "Study of Interdiffusion Effects on Oxidation/Corrosion Resistant Coatings for Advanced Single Crystal Superalloys," Proc. Sympos. High-Temperature Protective Coatings, March 7-8, Atlanta, GA, USA, Ed. Singhal, S.C., Pub. Metall. Soc of AIME, Warrendale, PA, USA, pp. 61-74.
258. **Smith, R.W. and Knight, R.**, (1995), "Thermal spraying I: Powder Consolidation - From Coating to Forming," J. Mater., Vol. 47, No. 8, pp.32-39
259. **Smith, G.D., Patel, S.J., Farr, N.C. and Hoffmann, M.**, (1999), "The Corrosion Resistance of Nickel Containing Alloys in Coal-Fired Boiler Environments [A]," Corrosion 99 [C], NACE International, Houston, 1999, pp.12.
260. **Sobolev, V.V., Guilemany, J.M. and Nutting, J.**, (2004), "HVOF Spraying," B0655, Maney, IOM3, pp.5.
261. **Srivastava, S.C., Godiwalla, K.M. and Banerjee, M.K.**, (1997), "Fuel Ash Corrosion of Boiler and Superheater Tubes," J. Mater. Sci., Vol.32, No.4, 835-849.
262. **Stein, K.J., Schorr, B.S. and Marder, A. R.**, (1999), "Erosion of Thermal Spray MCr-Cr₃C₂ Cermet Coatings," Wear, Vol. 224, pp. 153-159.
263. **Stokes, J. and Looney, L.**, (2001), "HVOF System Definition to Maximise the Thickness of Formed Components," Surf. Coat. Technol., Vol. 48, No. 1, pp. 18-24.
264. **Stokes, J.**, (2005), "The Theory and Application of the HVOF Thermal Spray Process," Dublin : Dublin City University.
265. **Stott, F.H., Chong, F.M.F. and Stirling, C.A.**, (1984), International Congress on Metallic Corrosion, 9th Edition, pp. 1.

317. **Wu, X., Weng, D., Chen, Z. and Xu, L., (2001),** "Effects of Plasma-Sprayed NiCrAl/ZrO₂ Intermediate on the Combustion Ability of Coatings," *Surf. Coat. Technol.*, Vol. 140, pp. 231-37.
318. **Xiao, C.B., Han, Y.F., Song, J.X. and Li, J.P., (2006),** "Effect of NiCoCrAlYHF Overlay Coating on Performance of Ni₃Al-Based Alloy IC6A," *Surf. Coat. Technol.*, Vol. 200, No. 9, pp. 3095-3101.
319. **Xuefeng, L., (2004),** "Corrosion Behaviours of Two Nickel-Based Coatings in H₂S-Containing Environments," *Surf. Coat. Technol.*, Vol. 183, pp. 212-215.
320. **Yamada, K., Tomono, Y., Morimoto, J., Sasaki, Y. and Ohmori, A., (2002),** "Hot Corrosion Behavior of Boiler Tube Materials in Refuse Incineration Environment," *Vacuum*, Vol. 65, No. 3-4, pp. 533-40.
321. **Yamamoto, A. and Hashimoto, Y., (1995),** "Estimation of High-Temperature Oxidation and Corrosion Resistance on Ni-Cr Alloy Coating with Plasma Transferred Arc Welding," *R&D: Kobe Steel Eng. Reports*, Vol. 45, No. 1, pp. 29-32.
322. **Yoshida, M., (1993),** "Effect of Hot Corrosion on the Mechanical Performances of Superalloys and Coating Systems," *Corros. Sci.*, Vol. 35, No. 5-8, pp. 1115-24.
323. **Zhang, Y.S. and Rapp, R.A., (1987),** "Solubilities of CeO₂, HfO₂ and Y₂O₃ in Fused Na₂SO₄-30 mol% NaVO₃ and CeO₂ in Pure Na₂SO₄ at 900°C," *Corrosion*, Vol. 43, No. 6, pp. 348-352.
324. **Zhang, J.S., Hu, Z.Q., Murata, Y., Morinaga, M. and Yukawa, N., (1993),** "Design and Development of Hot Corrosion-Resistant Nickel-Base Single-Crystal Superalloys by the D-Electrons Alloy Design Theory; II: Effects of Refractory Metals Ti, Ta, and Nb on Microstructures and Properties," *Metall. Trans. A*, Vol. 24A, No. 11, pp. 2451-2464.
325. **Zhang, Y.S. and Rapp, R.A., (1994),** "Solubilities of CeO₂ in Molten Na₂SO₄-10 mol% NaVO₃ Salt Solution 900°C," *Proceedings of the Ninth International Symposium on Molten Salts, Electrochem. Soc.*, May 1994.
326. **Zhang, D., Harris, S.J. and McCartney, D.G., (2003),** "Microstructure Formation and Corrosion Behaviour in HVOF-Sprayed Inconel 625 Coatings," *Mater. Sci. Engg. A*, Vol. 344, pp. 45-56.
327. **Zhao, L., Lugscheider, E., Fischer, A. and Reimann, A., (2001),** "Thermal Spraying of High Nitrogen Duplex Austenitic-Ferritic Steel," *Surf. Coat. Technol.*, Vol. 141, pp.208-215.
328. **Zhao, L. and Lugscheider, E., (2002),** "High Velocity Oxy-Fuel Spraying of a NiCoCrAlY and an Intermetallic NiAl-TaCr Alloy," *Surf. Coat. Technol.*, Vol. 149, pp. 230-35.

329. **Zhao, W.-M., Wang, Y., Han, T., Wu, K.-Y. and Xue, J., (2004A),** "Electrochemical Evaluation of Corrosion Resistance of NiCrBSi Coatings Deposited by HVOF," *Surf. Coat. Technol.*, Vol. 183, pp. 118-125.
330. **Zhao, L., Zwich, J. and Lugscheider, E., (2004B),** "HVOF Spraying of Al₂O₃-Dispersion-Strengthened NiCr Powders," *Surf. Coat. Technol.*, Vol. 182, pp. 72-77.
331. **Zhao, S., Xie, X., Smith, G.D. and Patel, S.J., (2005A),** "The Corrosion of Inconel Alloy 740 in Simulated Environments for Pulverized Coal-Fired Boiler," *Mater. Chem. Phys.*, Vol. 90, No. 2-3, pp. 275-281.
332. **Zhao, W.-M., Wang, Y., Dong, L.-X., Wu, K.-Y. and Xue, J., (2005B),** Corrosion Mechanism of NiCrBSi Coatings Deposited by HVOF," *Surf Coat Technol.*, Vol. 190, pp.293-298.
333. **Zimmermann, S. and Kreye, H., (1996),** "Chromium Carbide Coatings Produced With Various HVOF Spray Systems," *Proc. of the 9th National Therm. Spray Conf., ASM International, Materials Park, Ohio.,USA*, pp. 147-152.

266. **Stott, F.H., Wei, F.I. and Enahoro, C.A., (1989A), "Influence of Manganese on the High-Temperature Oxidation of Iron-Chromium alloys,"** *Werkstoffe und Korrosion*, Vol. 40, No. 4, pp. 198-205.
267. **Stott, F.H., (1989B), "Influence of Alloy Additions on Oxidation,"** *Mater. Sci. Technol.*, Vol. 5, pp. 734-740.
268. **Stott, F. H., Wet, D.J.De. and Taylor, R., (1994), "The Degradation Resistance of Thermal Barrier Coatings to Molten Deposits at very High Temperatures,"** *Trans. Mater. Res. Soc. Jpn.*, Vol. 14A, pp. 135-40.
269. **Strawbridge, A., Evans, H. E. and Ponton, C.B., (1997), "Spallation of Oxide Scales from NiCrAlY Overlay Coatings,"** *Mater. Sci. Forum*, Vol. 251-254, pp. 365-374.
270. **Streiff, R., (1987), "The Effect of Laser Surface Treatment of High-Temperature Oxidation and Corrosion Resistance of Materials and Coatings,"** *Proc. of 10th ICMC, Madras, India*, Vol. II, pp. 1315-1324.
271. **Stringer, J., (1987), "High Temperature Corrosion of Superalloys,"** *Mater. Sci. Technol.*, Vol. 3, No. 7, pp. 482-493.
272. **Stroosnijder, M. F., Mevrel, R. and Bennet, M. J., (1994), "The Interaction of Surface Engineering and High Temperature Corrosion Protection,"** *Mater. High Temp.*, Vol. 12, No. 1, pp. 53-66.
273. **Sturgeon, A.J., et al., (1994), "High Velocity Oxy-Fuel Spraying,"** *T I Met Finish*. Vol. 72, pp. 139-140.
274. **Sturgeon, A.J. and Buxton, D.C., (2000), "The Electrochemical Corrosion Behaviour of HVOF Sprayed Coatings,"** in: *Proc. 1st Int. Thermal Spray Conf.*, Montreal, Canada, May 8–11, 2000, ASM International, pp. 1011-1015.
275. **Suegama, P.H., Fugivara, C.S., Benedetti, A.V., Fernandez, J., Delgado, J. and Guilemany, J.M., (2002), "Electrochemical Behaviour of Thermally Sprayed Cr₃C₂-NiCr Coatings in 0.5 M H₂SO₄ Media" *J. Appl. Chem.*, Vol.32, pp. 1287-1295.**
276. **Suegama, P.H., Fugivara, C.S., Benedetti, A.V., Guilemany, J.M., Fernandez, J. and Delgado, J., (2004), "The Influence of Gun Transverse Speed on Electrochemical Behaviour of Thermally Sprayed Cr₃C₂-NiCr Coatings in 0.5 M H₂SO₄ Solution,"** *Electrochimica Acta*, Vol. 49, pp. 627-634.
277. **Suito, H. and Gaskell, D. R., (1971), "The Thermodynamics of Melts in the System VO₂-V₂O₅,"** *Metall. Trans.*, Vol. 2, pp. 3299-3303.
278. **Sundararajan, T., Kuroda, S., Itagaki, T. and Abe F., (2003A), "Steam Oxidation Resistance of Ni-Cr Thermal Spray Coatings on 9Cr-1Mo Steel. Part 1: 80Ni-20Cr,"** *ISIJ Int.*, Vol. 43, No.1, pp. 95-103.

279. **Sundararajan, T., Kuroda, S., Itagaki, T. and Abe F., (2003B),** "Steam Oxidation Resistance of Ni-Cr Thermal Spray Coatings on 9Cr-1Mo Steel. Part 2: 50Ni-50Cr," *ISIJ Int.*, Vol. 43, No.1, pp. 104-111.
280. **Sundararajan, T., Kuroda, S., Nishida, K., Itagaki, T. and Abe, F., (2004A),** "Behaviour of Mn and Si in the Spray Powders during Steam Oxidation of Ni-Cr Thermal Spray Coatings," *ISIJ Int.*, Vol. 44, No.1, pp. 139-144.
281. **Sundararajan, T., Kuroda, S. and Abe, F., (2004B),** "Steam Oxidation Studies on 50Ni-50Cr HVOF Coatings on 9Cr-1Mo Steel: Change in Structure and Morphology across the Coating/Substrate Interface," *Mater. Trans.*, Vol. 45, No. 4, pp.1299-1305.
282. **Sundararajan, T., Kuroda, S. and Abe, F., (2005),** "Steam Oxidation of 80Ni-20Cr High Velocity Oxy-fuel Coatings on 9Cr-1 Mo Steel: Diffusion-Induced Phase Transformations in the Substrate Adjacent to the Coating," *Metallurgical and Materials Transactions A: Physical Metallurgy and Materials Science*, Vol. 36, No. 8, pp. 2165-2174.
283. **Swaminathan, J. and Raghavan, S., (1992),** "Effect of Vanadic Corrosion on Creep-Rupture Properties of Superni-600 at 650-750⁰C," *Mater. High Temp.*, Vol. 10, No. 4, pp. 242-250.
284. **Swaminathan, J., Raghavan, S. and Iyer, S. R., (1993),** "Studies on the Hot Corrosion of Some Nickel-Base Superalloys by Vanadium Pentoxide," *T. Indian I. Metals*, Vol. 46, No. 3, pp. 175-181.
285. **Swaminathan, J. and Raghavan, S., (1994),** "Vanadic Hot Corrosion-Creep Interaction of Superni-C 276 in the Temperature Range 650-750⁰C," *High Temp. Mater. Processes*, Vol. 13, No. 4, pp. 277-297.
286. **Tan, K.S., Wharton, J.A. and Wood, R.J.K., (2005),** "Solid Particle Erosion-Corrosion Behaviour of a Novel HVOF Nickel Aluminium Bronze Coating for Marine Applications—Correlation Between Mass Loss and Electrochemical Measurements." *Wear*, Vol. 258, No. 1-4, pp. 629-640.
287. **Tani, K., Adachi, M., Nakahira, A. and Takatani, Y., (2000),** "Aqueous Corrosion Behavior of Thermally Sprayed Coatings for Steel Substrate," *Proc. 1st Int. Thermal Spray Conf., Montréal, Québec, Canada, May 8–11, 2000*, ASM International, pp. 1025-31.
288. **Taylor, M.P. and Evans, H. E., (2001),** "The Influence of Bond Coat Surface Roughness and Structure on the Oxidation of a Thermal Barrier Coating System," *Mater. Sci. Forum*, Vol. 369-372, pp. 711-717.
289. **Thilkan, H.R., Lahiri, A.K. and Banerjee, T., (1967),** "Studies on the Resistance of Alloy Steels against Oil Ash Corrosion-Part I," *NML Technical Journal*, May, pp. 20-25.

290. **Tiwari, S. N. and Prakash, S., (1996),** "Hot Corrosion Behaviour of an Iron-Base Superalloy in Salt Environment at Elevated Temperatures," Proc. of Sympos. Metals and Materials Research, Indian Institute of Technology Madras, Madras, 4-5th July, pp. 107-117.
291. **Tiwari, S. N. and Prakash, S., (1997),** "Studies on the Hot Corrosion Behaviour of Some Superalloys in Na₂SO₄-V₂O₅," Proc. of SOLCEC, Kalpakkam, India, 22-24th Jan., Paper C33.
292. **Tiwari, S. N., (1997),** "Investigations on Hot Corrosion of Some Fe-, Ni- and Co-Base Superalloy in Na₂SO₄-V₂O₅ Environment under Cyclic Conditions," Ph. D. Thesis, Met. Mat. Engg. Deptt., University of Roorkee, Roorkee, India.
293. **Tiwari, S. N. and Prakash, S., (1998),** "Literature Review-Magnesium Oxide as Inhibitor of Hot Oil Ash Corrosion," Mater. Sci. Technol., Vol. 14, pp. 467-172.
294. **Toma, D., Brandl, W. and Koester, U., (1999),** "Studies on the Transient Stage of Oxidation of VPS and HVOF Sprayed MCrAlY Coatings," Surf. Coat. Technol., Vol. 120-121, pp. 8-15.
295. **Tran, H.N., Barham, D. and Hupa, M., (1988),** "Fireside Corrosion in Kraft Recovery Boilers-An Overview," Mater. Perform., Vol. 27, pp. 40-45.
296. **Tucker, Jr., R.C., (1994),** "Ch. 11: Advanced Thermal Spray Deposition Techniques," in 'Handbook of Deposition Technologies for Films & Coatings,' Eds. R.F. Bunshah, Noyes Pub. Park Ridge, New Jersey, U. S. A./William Andrew Publishing, LLC, Norwich, New York, U.S.A, pp. 591.
297. **Tuominen, J., Vuoristo, P., Mantyla, T., Ahmaniemi, S., Vihinen, J. and Andersson, P.H., (2002),** "Corrosion Behavior of HVOF-Sprayed and Nd-YAG Laser-Remelted High-Chromium, Nickel-Chromium Coatings," J. Therm. Spray Technol., Vol. 11, No. 2, pp. 233-243.
298. **Tzvetkoff, T. and Gencheva, P., (2003),** "Mechanism of Formation of Corrosion Layers on Nickel and Nickel-based Alloys in Melts Containing Oxyanions- A Review," Mater. Chem. Phys., Vol. 82, No. 3, pp. 897-904.
299. **Ul-Hamid, A., (2003),** "Diverse Scaling Behaviour of the Ni-20Cr Alloy," Mater. Chem. Phys., Vol. 80, No.135-142.
300. **Uusitalo, M.A., Vuoristo, P.M.J. and Mäntylä, T.A., (2003),** "High Temperature Corrosion of Coatings and Boiler Steels in Oxidizing Chlorine-Containing Atmosphere," Mater. Sci. Engg. A, Vol. 346, No. 1-2, pp. 168-177.
301. **Uusitalo, M.A., Vuoristo, P.M.J. and Mantyla, T.A., (2004),** "High Temperature Corrosion of Coatings and Boiler Steels below Chlorine-containing Salt Deposits," Corros. Sci., Vol. 46, No. 6, pp. 1311-1331.
302. **Valdes, C.J., Dooley, R.B. and Wilson, J.R., (1973),** "The Corrosion of A.I.S.I 446 Stainless Steel in Molten Vanadates in the Temperature Range 700-900°C," Report Defence Research Board Canada, Grant No. 7535-14.

303. **Varacalle, D.J.Jr., Couch, K.W. and Budinger, V.S., (1996), "Studies of the Flame Spraying of Polymers," Proc. of the 9th National Thermal Spray Conference, Cincinnati, Ohio, pp. 251-255.**
304. **Verdon, C., Karimi, A. and Martin, J.-L., (1998), "A Study of High Velocity Oxy-Fuel Thermally Sprayed Tungsten Carbide Based Coatings. Part 1: Microstructures," Mat. Sci. Engg. A, Vol. 246, pp. 11-24.**
305. **Vuoristo, P., Niemi, K., Makela, A. and Mantyla, T., (1994), "Abrasion and Erosion Wear Resistance of Cr₃C₂-NiCr Coatings Prepared by Plasma, Detonation and High-Velocity Oxyfuel Spraying," Proc. 7th National Thermal Spray Conf., Boston, June, 20-24, pp. 121-126.**
306. **Wang, B.Q. and Luer, K., (1994), "The Erosion-Oxidation Behavior of HVOF Cr₃C₂-NiCr Cermet Coating," Wear, Vol. 174, No. 1-2, pp. 177-185.**
307. **Wang, F., Lou, H., Bai, L. and Wu, W., (1989), "Hot Corrosion of Yttrium-Modified Aluminide Coatings," Mater. Sci. Engg. A-Struct., Vol. 121, pp. 387-389.**
308. **Wang, B. and Lee, S.W., (2000), "Erosion-Corrosion Behaviour of HVOF NiAl-Al₂O₃ Intermetallic-Ceramic Coating," Wear, Vol. 239, pp. 83-90.**
309. **Wang, J., Zhang, L., Sun, B. and Zhou, Y., (2000), "Study of the Cr₃C₂-NiCr Detonation Spray Coating," Surf. Coat. Technol., Vol. 130, pp. 69-73.**
310. **Wang, B.Q. and Shui, Z.R., (2002), "The Hot Erosion Behavior of HVOF Chromium Carbide-Metal Cermet Coatings Sprayed with Different Powders," Wear, Vol. 253, pp.550-557.**
311. **Wang, C.-J. and Pan J.-Y., (2003) ,"Corrosion of Carbon Steel with NaCl Coating in an Atmosphere Produced by Burning Emulsified Diesel Oil," Mater. Chem. Phys., Vol. 18, no. 3, pp. 965-973.**
312. **Wang, Q.M., Wu, Y.N., Ke, P.L., Cao, H.T., Gong, J., Sun, C. and Wen, L.S., (2004) "Hot Corrosion Behavior of AIP NiCoCrAlY(SiB) Coatings on Nickel Base Superalloys," Surf. Coat. Technol., Vol. 186, No. 3, pp. 389-397.**
313. **Weulersse-Mouturat, K., Moulin, G., Billard, P. and Pierotti, G., (2004), "High Temperature Corrosion of Superheater Tubes in Waste Incinerators and Coal-Fired Plants," Mater. Sci. Forum, Vol. 461-464, pp. 973-980.**
314. **Wong-Moreno, A. and Marchan Salgado, R.I., (1995), "Molten Salt Corrosion of Heat Resisting Alloys," In: Corrosion-95, NACE, Houston, TX (1995), pp. 465-1-465-16.**
315. **Wood, G.C. and Hodgkiess, T., (1966), "Mechanism of Oxidation of Dilute Nickel-Chromium Alloys," Nature, Vol. 211, pp. 1358-1361.**
316. **Wright, I.G., (1987), "High-Temperature Corrosion". In: Metals Handbook, Vol. 13. 9th Ed., Metals Park: ASM, 1987. p. 97-103.**